Spaceborne Antennas for Planetary Exploration

William A. Imbriale, Editor

Jet Propulsion Laboratory
California Institute of Technology

DEEP SPACE COMMUNICATIONS AND NAVIGATION SERIES

DEEP SPACE COMMUNICATIONS AND NAVIGATION SERIES

Issued by the Deep Space Communications and Navigation Systems
Center of Excellence
Jet Propulsion Laboratory
California Institute of Technology

Joseph H. Yuen, Editor-in-Chief

Published Titles in this Series

Radiometric Tracking Techniques for Deep-Space Navigation
Catherine L. Thornton and James S. Border

Formulation for Observed and Computed Values of Deep Space Network Data Types for Navigation
Theodore D. Moyer

Bandwidth-Efficient Digital Modulation with Application to Deep-Space Communications
Marvin K. Simon

Large Antennas of the Deep Space Network
William A. Imbriale

Antenna Arraying Techniques in the Deep Space Network
David H. Rogstad, Alexander Mileant, and Timothy T. Pham

Radio Occultations Using Earth Satellites: A Wave Theory Treatment
William G. Melbourne

Deep Space Optical Communications
Hamid Hemmati, Editor

Spaceborne Antennas for Planetary Exploration
William A. Imbriale, Editor

Spaceborne Antennas for Planetary Exploration

William A. Imbriale, Editor

Jet Propulsion Laboratory
California Institute of Technology

DEEP SPACE COMMUNICATIONS AND NAVIGATION SERIES

Spaceborne Antennas for Planetary Exploration

January 2006

The research described in this publication was carried out at the
Jet Propulsion Laboratory, California Institute of Technology, under
a contract with the National Aeronautics and Space Administration.

Reference herein to any specific commercial product, process, or service
by trade name, trademark, manufacturer, or otherwise, does not constitute
or imply its endorsement by the United States Government or the
Jet Propulsion Laboratory, California Institute of Technology.

Table of Contents

Foreword

The Deep Space Communications and Navigation Systems Center of Excellence (DESCANSO) was established in 1998 by the National Aeronautics and Space Administration (NASA) at the California Institute of Technology's Jet Propulsion Laboratory (JPL). DESCANSO is chartered to harness and promote excellence and innovation to meet the communications and navigation needs of future deep-space exploration.

DESCANSO's vision is to achieve continuous communications and precise navigation—any time, anywhere. In support of that vision, DESCANSO aims to seek out and advocate new concepts, systems, and technologies; foster key technical talents; and sponsor seminars, workshops, and symposia to facilitate interaction and idea exchange.

The Deep Space Communications and Navigation Series, authored by scientists and engineers with many years of experience in their respective fields, lays a foundation for innovation by communicating state-of-the-art knowledge in key technologies. The series also captures fundamental principles and practices developed during decades of deep-space exploration at JPL. In addition, it celebrates successes and imparts lessons learned. Finally, the series will serve to guide a new generation of scientists and engineers.

Joseph H. Yuen
DESCANSO Leader

Preface

Spaceborne Antennas for Planetary Exploration traces the development of the Jet Propulsion Laboratory (JPL) spacecraft antennas from the very first Explorer satellite in 1958 to the present. It primarily deals with the radio frequency (RF) design and performance of the antennas although it includes material on environmental and mechanical considerations. It describes all the new designs and technological innovations introduced throughout their evolution. There is also a thorough treatment of all the analytical and measurement techniques used in the design and performance assessment. This monograph can serve as an introduction to newcomers in the field as well as a reference for the advanced practitioner. The technical terms in the text assume that the reader is familiar with basic engineering and mathematical concepts as well as material typically found in a senior level course in electromagnetics.

This book is complementary to *Large Antennas of the Deep Space Network*[1] published in 2002, which describes all the ground antennas used in support of the spacecraft. Taken together, these books completely describes all JPL antenna technology and is in keeping with the JPL Deep Space Communications and Navigation Series to capture the many technological innovations that helped make significant improvements in deep-space telecommunications over the decades.

As with most Spacecraft antennas, many people contributed to the success of the project, and it would be impossible to include everyone's name on the Chapter. Indeed, this is not the proper place. Proper credit is given by completely and thoroughly citing all the references and sources from which the material is derived. The only person's name on the chapter is the one who actually wrote the contribution and followed it through the editing process, not

[1] William A. Imbriale, John Wiley and Sons, Inc.

that they necessarily did the work described. It also allows someone who was not even involved in the actual design to write or coauthor a chapter. For completeness, this is sometimes required in this type of endeavor. That is because the people who actually did the work may not be available or even be alive, as in the case with some of the very early spacecraft.

William A. Imbriale,
Editor
January 2006

Acknowledgments

I would like to express my appreciation to Joseph H. Yuen for his continued support that made possible the writing of this manuscript. I am also deeply indebted to Cynthia D. Copeland for her typing, Roger Carlson and Pat Ehlers for their editing of the manuscript, and Judi Dedmon for typesetting the monograph in its final form. I would like to thank the authors who contributed chapters or portions of chapters. Each contributing author is identified in the Chapter headings. I would also like to thank Paul W. Cramer, Jr. for supplying much of the material used in Chapters 2 and 3 as well as his review of the chapters, Raul Perez for the Cloudsat data, and Daniel J. Hoppe, Vahraz Jamnejad, and David J. Rochblatt for their careful reading and helpful suggestions on several of the chapters.

William A. Imbriale
January 2006

Contributors

Richard E. Cofield received a BS in applied physics from the California Institute of Technology (Pasadena, California) in 1974, and an MS in electrical engineering from the University of Southern California (Los Angeles, California) (UCLA) in 1982. In 1978 Mr. Cofield joined the Jet Propulsion Laboratory (Pasadena, California) (JPL) to design, analyze, and calibrate antenna and optical systems for spaceborne radar and radiometer instruments observing the Earth. His interests include reflector antennas and quasi-optical feed systems.

Gregory L. Davis holds a PhD in mechanical engineering from Rice University (Houston, Texas). Dr. Davis holds both a BS and an MS in physics from the University of Akron (Akron, Ohio). Dr. Davis has worked for the past 16 years as a member of the technical staff in mechanical engineering at JPL, and is currently the lead technologist for the Mechanical Systems Division. Prior to that, Dr. Davis was the supervisor of the Advanced Deployable Structures Group, which has interests in developing novel, lightweight structures for space applications. Previously, Dr. Davis served as the mechanical systems engineer for cruise, entry, descent, and landing on the Mars Exploration Rover (MER) Project.

Mark S. Gatti received his BS in electrical engineering from New Mexico State University (Las Cruces, New Mexico) in 1980 and his MS in electrical engineering from California State University, Northridge (Northridge, California) in 1986. Mr. Gatti joined JPL in 1981 working in spacecraft radio frequency (RF) systems and in antenna design, analysis, and test. Mr. Gatti has held management positions within the Deep Space Network (DSN) and was the deputy section manager of the Communications Ground System Section. Most

recently, Mr. Gatti has been serving as the system manager during the pre-project activities of the proposed DSN Array project.

Richard E. Hodges received his BS in electrical engineering from the University of Texas at Austin, his MS in electrical engineering from California State University, Northridge, and his PhD in electrical engineering from the University of California, Los Angeles. Dr. Hodges' previous work experience includes Hughes Aircraft Company Radar Systems Group, Rantec/MDM (Chatsworth, California), and Raytheon Antenna/Nonmetallics Technology Center (Los Angeles, California). Dr. Hodges has been at JPL from 1988 through 1993 and from 2001 to the present. Dr. Hodges is the group supervisor for the Spacecraft Antennas Group.

Daniel J. Hoppe received a BS and an MS in electrical engineering from the University of Wisconsin Madison in 1982 and 1983, respectively. Dr. Hoppe received a PhD in electrical engineering from the University of California, Los Angeles (UCLA) in 1994. In 1984 Dr. Hoppe joined JPL, where he is currently a principal engineer. At JPL Dr. Hoppe has developed software for the solution of a number of electromagnetic scattering problems, has designed microwave components for the large antennas of the DSN, and has designed antennas for spacecraft applications. Most recently Dr. Hoppe has focused on diffraction modeling of large space-based telescopes.

John Huang received electrical engineering degrees of BS from Michigan Technology University (Houghton, Michigan) in 1970, MS from the University of California at Berkeley in 1971, and PhD from the Ohio State University (Columbus, Ohio) in 1978. Dr. Huang worked six years at the Naval Weapons Center, China Lake, California. Dr. Huang has been with JPL since 1980, where his research activities involve microstrip antennas, mobile vehicle antennas, antenna miniaturization techniques, spacecraft antennas, phased arrays, reflectarrays, and inflatable antennas.

William A. Imbriale received a BS in engineering physics from Rutgers, the State University of New Jersey (New Brunswick, New Jersey) in 1964; an MS in electrical engineering from UCLA in 1966; and a PhD in electrical engineering from the University of Illinois at Urbana-Champaign in 1969. Dr. Imbriale joined JPL in 1980 and is a senior research scientist in the Communications Ground System Section. Dr. Imbriale has led advanced technology developments for large ground-station antennas, lightweight spacecraft antennas, and millimeter-wave spacecraft instruments and is currently principle investigator on a NASA technology contract. Dr. Imbriale also served as the assistant manager for microwaves in the Ground Antennas

and Facilities Engineering Section and section manager of the Radio Frequency and Microwave Subsystem Section.

Rolando L. Jordan received his BS and MS in electrical engineering from the Massachusetts Institute of Technology (Cambridge, Massachusetts) (MIT) in 1959 and 1962, respectively. Mr. Jordan has been with JPL since 1963 and is a principal engineer in the Radar Science and Engineering Section. Mr. Jordan has been system engineer for a number of spaceborne radar systems including the Apollo 17 Lunar Sounder, the Seasat-A synthetic aperture radar system, the Spaceborne Imaging Radar-C, and the Mars Advanced Radar for Subsurface and Ionospheric Sounding for the Mars Express spacecraft.

Yunjin Kim received his MS and PhD in electrical engineering from the University of Pennsylvania (Philadelphia, Pennsylvania) in 1985 and 1987, respectively. Dr. Kim received his BS in electrical engineering from the California State University, Sacramento, in 1983. Dr. Kim has participated in spaceborne radar development at JPL since 1989. Currently, Dr. Kim is the Hydros project manager.

Roberto Mizzoni received his PhD in physics from the University of Rome, Italy, in 1984. Before joining Alenia Spazio (Rome, Italy) in 1987, Dr. Mizzoni worked on two-dimensional radars and three-dimensional phased arrays at Selenia S.p.A. (Rome, Italy) and on broadband direction finding/ electromagnetic compatible antennas at Elettronica S.p.A. (Rome Italy). Dr. Mizzoni has extensive experience in the design and development of space antennas for telecommunication, Earth observation, navigation and science. Dr. Mizzoni is co-holder of three patents and is head of the antenna electrical design unit at Alcatel Alenia Space (Rome, Italy).

Rebekah L. Tanimoto received her BS in aerospace Engineering from UCLA in 2004. Ms. Tanimoto is currently working on her MS in aerospace engineering at UCLA. Ms. Tanimoto has been with JPL since 2004, working in the area of advanced deployable structures.

Joseph Vacchione received electrical engineering degrees of a BS from Northeastern University (Boston, Massachusetts) in 1985, an MS from the University of Illinois at Urbana-Champaign, and a PhD from the same institution in 1990. Dr. Vacchione joined JPL in 1990 where he has worked on design and development of antennas for space-flight applications. Dr. Vacchione has extensive experience in antennas used for both deep-space telecommunications purposes and for antennas used as part of remote sensing science instruments. Dr. Vacchione is currently the antenna lead for an Earth-orbiting science instrument.

Chapter 1
Introduction

William A. Imbriale, John Huang, and Mark S. Gatti

Spaceborne Antennas for Planetary Exploration traces the development of the antennas used on JPL Spacecraft from their inception on the very first United States Explorer Mission in 1958 to the present. To completely cover all types of spacecraft antennas would be a daunting task indeed, and is not the intent of this monograph. Rather, the focus is only on antennas that have flown on Jet Propulsion Laboratory (JPL) spacecraft or were used for JPL scientific instruments that have flown on other spacecraft. The monograph primarily deals with the RF design and performance of the antennas and associated front-end equipment, but it also includes a chapter on mechanical development. It describes all the new designs and technological innovations introduced by JPL. There is also a thorough treatment of all the analytical and measurement techniques used in the design and performance assessment. This monograph can serve as an introduction to newcomers in the field or a reference for the advanced practitioner. The technical terms in the text assume that the reader is familiar with basic engineering and mathematical concepts including material typically found in a senior-level course in electromagnetics.

This book is complementary to [1], which describes the JPL ground network antennas. However, whereas the ground antennas are primarily for telecommunication, the antennas on spacecraft can serve the dual purpose of a science instrument and/or a means of communicating the science and telemetry data to Earth. JPL's support of the National Aeronautics and Space Administration (NASA) space program has several distinct eras. The very first mission was an Earth orbiter, quickly followed by unmanned exploration of the Moon in preparation for NASA manned flight to the Moon. Missions to the

Moon included the Ranger series that captured pictures of the surface as it flew into the Moon, and the Surveyor spacecraft that successfully landed on the surface of the Moon. The first interplanetary spacecraft were flybys, initially targeting the inner planets of Venus, Mercury, and Mars. The flyby era concluded with the "Grand Tour" Voyager Mission that flew by Jupiter, Saturn, Uranus and Neptune.[1] The next phase of space exploration was planetary orbiters that collected data at Venus, Mars, Jupiter, and Saturn. Probably, the most challenging and exciting missions to date have been the Mars landers, and several of these missions are currently ongoing. In the planning stage are sample-return missions. In addition to planetary exploration missions, there have been a number of missions that have explored planet Earth, including synthetic aperture radar (SAR) missions that have mapped the entire planet.

This monograph is organized around the various eras and has contributions from many of the engineers involved in the development of the missions. The contributors are all identified in the title of the section. Chapter 1 gives a brief introduction and presents the methods of analysis, with supporting mathematical details of the various antenna types described throughout the remainder of the monograph. It also describes some design and measurement techniques. John Huang contributed the sections on microstrip antennas, and Mark Gatti provided the section on near-field measurements. Chapter 1, combined with the first chapter of [1], gives a very thorough reference on spacecraft and ground antenna analysis techniques, and it could be used in a graduate course on electromagnetics.

Chapter 2, "The Early Years," describes some of the antennas used on the very first Earth-orbiting and Moon missions, such as the Explorer, Pioneer, Ranger, and Surveyor spacecraft.

Chapter 3, "The Planetary Flybys," describes the antennas used on the first missions that flew by the planets. It includes the Mariner series of spacecraft that flew by Mars, Venus, and Mercury, as well as the Grand Tour Voyager Mission.

Chapter 4, "The Mars Missions," by Joe Vacchoine, is a comprehensive chapter that covers all the Mars missions including the early orbiters and landers, as well as the more recent orbiters, landers, and rovers. It includes a complete description of the antennas on the Mars Exploration Rover (MER) landers.

Chapter 5, "The Orbiters," with contributions from Roberto Mizzoni and Mark Gatti, describes the antennas on the past and current orbiter missions (not including the Mars Missions) such as the Magellan (Venus Radar Mapper), and the Jupiter and Saturn orbiters. It describes the failed deployable mesh antenna

[1] In 1965 Gary Flandro proposed that, due to a once-per 175-year alignment of planets on one side of the Sun in the 1970s, a multi-planet "Grand Tour" opportunity existed to allow a single spacecraft to explore the four outer planets of the Solar System.

on the Galileo Spacecraft as well as the complicated four-frequency combined radar and communications antenna on the Cassini spacecraft.

Chapter 6, "Spaceborne SAR Antennas for Earth Science," by Yunjin Kim and Rolando Jordan, describes the Earth science SAR missions.

Chapter 7, "Instrument Packages," by Richard Cofield, describes antennas used on various instrument packages for science spacecraft. It includes antennas used on scatterometers and radiometers. Richard Hodges contributed the section on the Wide Swath Ocean Altimeter. There is some overlap in subject material with Chapter 6 as a SAR antenna is also a science instrument, but each chapter has a slightly different perspective and describes different instruments.

Chapter 8, "Mechanical Development of Antenna Systems," by Greg Davis and Rebekah Tanimoto, discusses the various mechanical aspects of spacecraft antenna design. It also discusses the test program necessary to qualify a spacecraft antenna.

Chapter 9, "Miscellaneous Other Antennas," describes a few unique antennas that did not readily fit into the other chapters. Included is the Solar Probe antenna and the Deep Impact antenna by Dan Hoppe.

Finally in Chapter 10, John Huang discusses future spacecraft antenna research and development.

1.1 Technology Drivers

William A. Imbriale

Antennas on board JPL spacecraft are used for telecommunications, as science instruments, or for both purposes. Technology required for science instruments is dictated by the specific science objectives and tends to be mission specific. Technology drivers for deep-space telecommunications are more universal and apply to all missions. The following discusses the main requirements for deep-space telecommunications antennas.

The communication links to deep space are asymmetric, with considerably more data on the downlink (space to Earth) than on the uplink (Earth to space) because the downlink contains the science, and telemetry data and the uplink is primarily used for commanding the spacecraft. The key element of the telecommunications-link performance is the ground-received power signal-to-noise ratio (SNR), which is given by

$$S/N \approx \frac{P_T G_T G_R}{4\pi R^2 N} = \frac{4\pi P_T A_T A_R}{\lambda^2 R^2 k B T_s} \tag{1.1-1}$$

where

P_T = spacecraft transmit power
G_T = transmit gain
G_R = receive gain

R = distance to the spacecraft
N = total noise
A_T = the effective area of the transmit (spacecraft) antenna
A_R = the effective area of the receive ground antenna
T_s = receive system-noise temperature
λ = wavelength
k = Boltzman's constant
B = bandwidth

Thus, data rate is proportional to the spacecraft effective isotropic radiated power (EIRP), or the product of antenna gain and radiated power. High-power spacecraft transmitters and large-aperture antennas are a priority for increasing direct-to-Earth telecommunications performance. Hence, a design that makes the maximum use of the transmit antenna area (high efficiency) is desired. However, not only should the antenna have high gain, but it must be pointed in the right direction. In theory, the main beam pointing could be accomplished electronically or mechanically. But to date, JPL has not used electronic beam pointing, but has relied on mechanically pointing the beam either by gimbaling the antenna or, in the case of a fixed body-mounted antenna, by pointing the entire spacecraft. The necessity to point a high-gain antenna in the proper direction gives rise to the need for antennas that will work when it is not possible to accurately point the antenna. Thus, there is also the need for omni type antennas (antennas that have almost complete spatial coverage) for times when pointing may be completely unknown (emergency situations) or for medium gain (broader beamwidth) when precise pointing may not be available.

There are also a number of environmental factors that must be considered in spacecraft antenna design. The antenna must operate in the vacuum of space and over wide temperature ranges. Sometimes, as in the case of the Solar Probe antenna (Chapter 9), the extreme temperatures dictate the materials that can be used in the design. The antenna must also survive the launch without damage. This includes the launch loads, vibration, shock, and acoustic conditions. Weight and power consumption are at a premium; hence the requirement for light-weight materials. Size is also a major consideration, as the antenna must fit inside the launch-vehicle shroud. For antennas that are too large to fit in the shroud, it is necessary to fold and stow the antenna for launch and deploy it for use.

There are many cases where a direct-to-Earth link, as described above, is not feasible. These applications include small in-situ landers, microprobes, and aerobots as currently in use or planned for Mars missions. These surface or atmospheric probe missions are characterized by their small size (<100 kg) and highly constrained energy budgets (<200 W-hr/sol). Typically, they cannot afford the mass and energy required for any meaningful data return directly over a deep-space link. Rather, these missions require, and are enabled by,

energy-efficient relay communications commonly referred to as proximity links [2,3]. Choice of frequency band is largely dictated by whether directional or omni links are envisioned. For omni-to-omni links, lower frequencies perform better, and the 400-MHz UHF links currently being utilized represent a compromise between communications performance and radio frequency (RF) component size.

1.1.1 Frequency Bands Allocated to Deep-Space Communications

The International Telecommunication Union (ITU) has allocated frequency ranges for use in deep-space and near-Earth research. These ranges are listed in Table 1-1.

1.1.2 Frequency Bands Recommended for Proximity Links

In addition to the formally allocated space-to-Earth links, the Consultative Committee for Space Data Systems (CCSDS) provides a recommendation for space data system standards in the area of proximity space links [4]. Proximity space links are defined to be short-range, bi-directional, fixed, or mobile radio links, generally used to communicate among probes, landers, rovers, orbiting constellations, and orbiting relays. These links are characterized by short time delays, moderate (not weak) signals, and short, independent sessions. The ultrahigh frequency (UHF) frequency allocation consists of 60 MHz between 390 to 450 MHz. The forward frequency band (portion where the caller transmits and the responder receives) is defined from 435 to 450 MHz. The return band (portion where the responder transmits and the caller receives) is defined as from 390 to 405 MHz. There is a 30-MHz deadband between them.

Table 1-1. Allocated frequency bands (GHz).

	Deep-Space Bands for Spacecraft Farther Than 2 Million km from Earth		Near-Earth Bands for Spacecraft Closer Than 2 Million km from Earth	
Band	Uplink[a]	Downlink[b]	Uplink[a]	Downlink[b]
S	2.110–2.120	2.290–2.300	2.025–2.110	2.200–2.290
X	7.145–7.190	8.400–8.450	7.190–7.235	8.450–8.500
Ka	34.200–34.700	31.800–32.300	Not applicable	Not applicable

[a] Earth to space.

[b] Space to Earth.

1.2 Analysis Techniques for Designing Reflector Antennas

William A. Imbriale

Reflector antennas have existed since the days of Hertz. They represent one of the best solutions for high gain and lightweight, easily stowable antenna systems. The use of physical optics (PO) analysis provides the required performance estimate accuracy. Almost all of the spacecraft reflector antennas were either designed or analyzed using PO, and the measured performance is within a few percent of the calculated values.

In addition to PO, there are many other techniques required to completely design and characterize the antenna system. Accurate programs to design and analyze the feed horn, and transform far-field patterns to near field for use in the PO analysis are required. Synthesis programs are used to determine the reflector shape for maximum gain. The sections on PO analysis, Feed Horn analysis, Spherical-Wave Analysis and Dual-Reflector Shaping are covered in [1], but these concepts are so fundamental they are also included in this reference for completeness. Tools to design and analyze frequency-selective surfaces are also needed for use in multi-frequency systems. And, programs to characterize the effect of a mesh surface for a lightweight deployable antenna are also required. The basic mathematical details of each of these techniques are given in this section with examples of their use sprinkled throughout the book.

1.2.1 Radiation-Pattern Analysis

Physical optics (PO) is by far the most important analytical tool, and it is used to calculate the scattered field from a metallic reflecting surface—in this case, a reflector antenna. Electrical currents, which excite the scattered field, are induced on the conducting surface by an incident wave assumed to be of a known amplitude, phase, and polarization everywhere in space (from a feed or other reflecting surface, for example). The PO approximations to the induced surface currents are valid when the reflector is smooth and the transverse dimensions are large in terms of wavelengths. The closed reflecting surface is divided into a region S_1, which is illuminated by direct rays from the source ("illuminated region") and a region S_2, which is geometrically shadowed ("shadowed region") from direct rays from the source (Fig. 1-1). The PO approximations for the induced surface current distribution are

$$\begin{aligned} J_s &= 2\left(\hat{n} \times H_{inc}\right) \quad \text{on } S_1 \\ J_s &= 0 \qquad\qquad\qquad\quad \text{on } S_2 \end{aligned} \tag{1.2-1}$$

where $\hat{n}$ is the surface normal and H_{inc} the incident field. The expressions are then inserted into the radiation integral [5] to compute the scattered field.

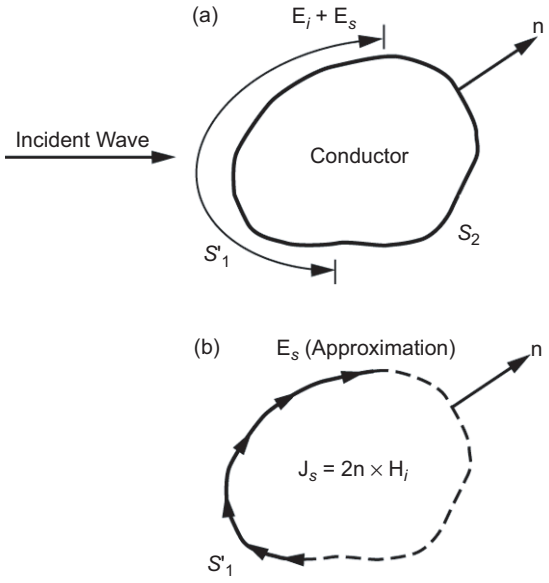

Fig. 1-1. The physical optics approximation: (a) original problem and (b) approximation.

Rusch and Potter [6] provide a good introduction to the early techniques used for analyzing the reflector antennas of the Deep Space Network (DSN). More recently, due primarily to the orders-of-magnitude improvements in computer speed and memory, a very simple but extremely robust algorithm has emerged as the computer program of choice for computing the PO radiation integral. The algorithm is documented in [7 and 8], but because of its extreme importance and to provide a fairly complete reference, it is repeated here.

One of the simplest possible reflector-antenna computer programs is based on a discrete approximation of the radiation integral. This calculation replaces the actual reflector surface with a triangular facet representation so that the reflector resembles a geodesic dome. The PO current is assumed to be constant in magnitude and phase over each facet, so the radiation integral is reduced to a simple summation. This program was originally developed in 1970 and has proven to be surprisingly robust and useful for the analysis of reflectors, particularly when the near field is desired and the surface derivatives are not known. The initial limitation to small reflectors was primarily due to the speed and memory limitations of the then-existing computers.

Two improvements significantly enhanced the usefulness of the computer program: The first was the orders-of-magnitude increase, over time, in computer speed and memory, and the second was the development of a more sophisticated approximation of the PO surface current, which permitted the use of larger facets. The latter improvement is due to the use of a linear-phase

approximation of the surface current. Within each triangular region, the resulting integral is the two-dimensional Fourier transform of the projected triangle. This triangular-shape function integral can be computed in closed form. The complete PO integral is then a summation of these transforms.

1.2.1.1 Mathematical Details. The PO radiation integral over the reflector surface, Σ , can be expressed as [8]

$$\mathbf{H}(\mathbf{r}) = -\frac{1}{4\pi}\int_{\Sigma}\left(jk+\frac{1}{R}\right)\hat{\mathbf{R}}\times\mathbf{J}_s(\mathbf{r}')\frac{e^{-jkR}}{R}ds' \qquad (1.2\text{-}2)$$

in which $\mathbf{r}$ designates the field point, $\mathbf{r}'$ the source point, $R = |\mathbf{r} - \mathbf{r}'|$ is the distance between them, and $\hat{\mathbf{R}} = (\mathbf{r} - \mathbf{r}')/R$ is a unit vector.

For the purpose of analysis, the true surface, Σ, is replaced by a contiguous set of triangular facets. These facets, denoted Δ_i, are chosen to be roughly equal in size with their vertices on the surface, Σ. Figure 1-2 shows a typical facet and its projection onto the *x*-*y* plane. Let (x_i, y_i, z_i) represent the *centroid* of each triangle where the subscript $i = 1, \cdots, N$ is associated with a triangle. Then, the field obtained by replacing the true surface, Σ, by the triangular facet approximation is

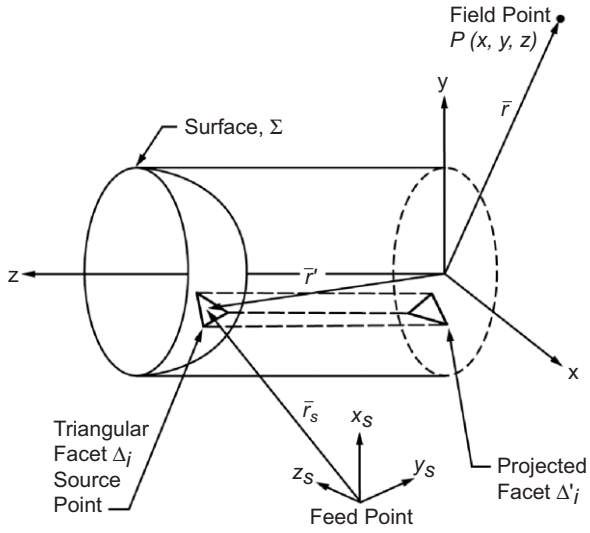

Fig. 1-2. Reflector-analysis coordinate systems and a typical triangular facet.

$$\mathbf{H}(\mathbf{r}) = -\frac{1}{4\partial}\sum_{i=1}^{N}\int_{\Delta_i}\left(jk+\frac{1}{R}\right)\hat{\mathbf{R}}\times\mathbf{J}(\mathbf{r}')\frac{e^{-jkR}}{R}ds' \tag{1.2-3}$$

In Eq. (1.2-3), **J** is now the equivalent surface current evaluated on the triangular facets. Since the triangles are small, it is expected that $\hat{\mathbf{R}}$ and R do not vary appreciably over the area of a given facet. Thus, let $\hat{\mathbf{R}}_i$ and R_i be the value obtained at the centroid (x_i, y_i, z_i) of each facet and approximate Eq. (1.2-3) by

$$\mathbf{H}(\mathbf{r}) = \frac{1}{4\pi}\sum_{i=1}^{N}\left[jk+\frac{1}{R_i}\right]\hat{\mathbf{R}}_i\times\mathbf{T}_i(\mathbf{r}) \tag{1.2-4}$$

$$\mathbf{T}_i(\mathbf{r}) = \int_{\Delta_i}\mathbf{J}_i(\mathbf{r}')\frac{e^{-jkR}}{R_i}ds' \tag{1.2-5}$$

Assume that the necessary transformations have been performed so that the incident field, $\mathbf{H}_{S,}$ is given in terms of the reflector coordinate system. Then

$$\mathbf{J}_i(\mathbf{r}') = 2\hat{\mathbf{n}}_i\times\mathbf{H}_s(\mathbf{r}') \tag{1.2-6}$$

Next, assume that the incident field can be represented by a function of the form

$$\mathbf{H}_S = \mathbf{h}_s(\mathbf{r}_i)\frac{e^{-jkr_s}}{4\pi r_{si}} \tag{1.2-7}$$

where r_S is the distance to the source point and r_{si} is the distance from the triangle centroid to the source point. Then, Eq. (1.2-5) can be written

$$\mathbf{T}_i(\mathbf{r}) = \frac{\hat{n}_i\times\mathbf{h}_s(\mathbf{r}_i)}{2\pi R_i r_{si}}\int_{\Delta_i}e^{-jk(R+r_s)}ds' \tag{1.2-8}$$

Making use of the Jacobian and approximating

$$R(x,y)+r_s(x,y) = \frac{1}{k}\left(a_i-u_i x-v_i y\right) \tag{1.2-9}$$

in which a_i, u_i, and v_i are constants, the expression can be rewritten as

$$\mathbf{T}_i(\mathbf{r}) = \frac{\hat{\mathbf{n}}_i \times \mathbf{h}_s(\mathbf{r}_i)}{2\pi R_i r_{si}} J_{\Delta_i} e^{-ja_i} \int_{\Delta_i'} e^{j(u_i x' + v_i y')} dx'dy' \qquad (1.2\text{-}10)$$

where the surface normal is

$$\mathbf{N}_i = -\hat{\mathbf{x}} f_{xi} - \hat{\mathbf{y}} f_{yi} + \hat{\mathbf{z}} \qquad (1.2\text{-}11)$$

and the Jacobian is

$$J_{\Delta_i} = |\mathbf{N}_i| = \left[f_{xi}^2 + f_{yi}^2 + 1 \right]^{1/2} \qquad (1.2\text{-}12)$$

It may now be observed that this integral is the two-dimensional (2-D) Fourier transform of the i^{th} projected triangle Δ_i', expressed as

$$S(u,v) = \int_{\Delta_i'} e^{j(ux' + vy')} dx'dy' \qquad (1.2\text{-}13)$$

and can be computed in closed form as described in [9]. The full radiation integral is the sum of all the transforms of the individual triangles.

1.2.1.2 Application to Dual-Reflector Antennas. The PO integration methodology is incorporated in a sequential fashion for the analysis of a dual-reflector antenna system. Initially, the feed illuminates the subreflector, and the currents on the subreflector surface are determined. Subsequently, the near fields scattered from the subreflector are used to illuminate the main reflector, and its induced currents are determined. The main reflector scattered fields are then determined by integrating these currents.

Many coordinate systems are required to allow flexibility in locating and orienting the feed, subreflector, main reflector, and output-pattern generation. The relation among the various coordinate systems is depicted in Fig. 1-3 where (x_F, y_F, z_F) is the feed coordinate system, (x_S, y_S, z_S) is the subreflector coordinate system, and (x_M, y_M, z_M) is the main reflector coordinate system.

1.2.1.3 Useful Coordinate Transformations. In the discussion of the preceding sections (1.2.1.1 and 1.2.1.2), the analysis is performed using two distinct coordinate systems: reflector and feed coordinates. In addition, it is sometimes convenient to display the computed patterns in yet another coordinate system. Consequently, one must know the transformation equations that permit coordinates and vectors described in one coordinate system to be expressed in terms of some other coordinate system. The transformation may require both translation and rotation. The required transformations are described below. They are the Cartesian-to-spherical transformation and coordinate rotations using Eulerian angles.

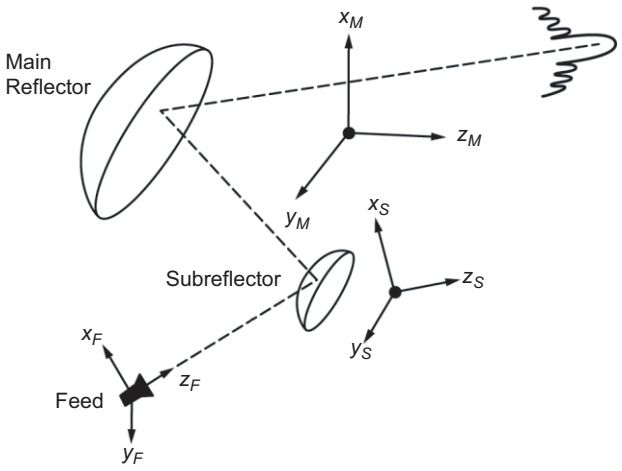

Fig. 1-3. Dual-reflector coordinate systems.

The Cartesian-to-spherical transformation is conveniently summarized in matrix form. With the Cartesian components of a vector, **H**, denoted (H_x, H_y, H_z) and the spherical components (H_r, H_θ, H_ϕ), one finds that the transformation is

$$\begin{bmatrix} H_r \\ H_\theta \\ H_\phi \end{bmatrix} = \begin{bmatrix} \sin\theta\cos\phi & \sin\theta\sin\phi & \cos\theta \\ \cos\theta\cos\phi & \cos\theta\sin\phi & -\sin\theta \\ -\sin\phi & \cos\phi & 0 \end{bmatrix} \begin{bmatrix} H_x \\ H_y \\ H_z \end{bmatrix} \tag{1.2-14}$$

The inverse transformation is just the transpose of the above matrix.

Rotations are handled by the use of the Eulerian angles (α, β, γ). These angles describe three successive rotations that bring one Cartesian system into alignment with another. Let the two systems be denoted (x_1, y_1, z_1) and (x_2, y_2, z_2). As illustrated in Fig. 1-4, the angles are defined as follows:

- α describes a positive rotation about the z_1 axis, which brings the x_1 axis into the x' axis aligned with the *line of nodes* (the line of intersection between the (x_1, y_1) and (x_2, y_2) planes)
- β describes a positive rotation about the line of nodes (the x' axis) that brings the z_1 axis to z_2
- γ describes a positive rotation about the z_2 axis, which brings the x' axis to the x_2 axis.

The phrase "positive rotation" means the direction of increasing angular measure as defined by the right-hand rule with respect to the axis about which

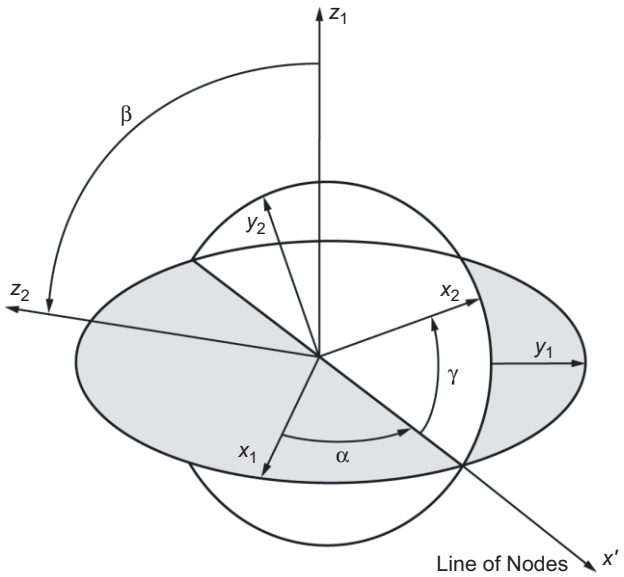

Fig. 1-4. Euler-angle definitions.

the rotation occurs. Each of the rotations just described is performed using the standard rotation of coordinate formulas of plane analytic geometry.

When these expressions are written in matrix form and applied successively as described above, one obtains the following matrix equation that represents a general three-dimensional (3-D) rotation of coordinates.

$$\begin{bmatrix} x_2 \\ y_2 \\ z_2 \end{bmatrix} = \begin{bmatrix} A_{11} & A_{12} & A_{13} \\ A_{21} & A_{22} & A_{23} \\ A_{31} & A_{32} & A_{33} \end{bmatrix} \begin{bmatrix} x_1 \\ y_1 \\ z_1 \end{bmatrix} \tag{1.2-15}$$

where the individual matrix elements are

$$\begin{aligned}
A_{11} &= \cos\gamma\cos\alpha - \sin\gamma\cos\beta\sin\alpha \\
A_{12} &= \cos\gamma\sin\alpha + \sin\gamma\cos\beta\cos\alpha \\
A_{13} &= \sin\gamma\sin\beta \\
A_{21} &= -\sin\gamma\cos\alpha - \cos\gamma\cos\beta\sin\alpha \\
A_{22} &= -\sin\gamma\cos\alpha + \cos\gamma\cos\beta\cos\alpha \\
A_{23} &= \cos\gamma\sin\beta \\
A_{31} &= \sin\beta\cos\gamma \\
A_{32} &= -\sin\beta\cos\alpha \\
A_{33} &= \cos\beta
\end{aligned}$$

The inverse transformation is just the transpose of the matrix given above.

Although the formulas are presented in terms of coordinate transformations, the transformation matrix is equally valid for the Cartesian components of a vector. Thus, the components of a vector, **H**, transform as

$$\begin{bmatrix} H_{x,2} \\ H_{y,2} \\ H_{z,2} \end{bmatrix} = \begin{bmatrix} A_{11} & A_{12} & A_{13} \\ A_{21} & A_{22} & A_{23} \\ A_{31} & A_{32} & A_{33} \end{bmatrix} \begin{bmatrix} H_{x,1} \\ H_{y,1} \\ H_{z,1} \end{bmatrix} \tag{1.2-16}$$

Further information can be found in [10].

1.2.1.4 A Numerical Example of Radiation-Pattern Analysis. In the 1980s, a FORTRAN program was written to perform the linear phase calculations indicated above. The program was extensively verified by comparing the measured data, for example, [11], and many other computer codes.

A simple but interesting example is that of an ellipse, shown in Fig. 1-5. The projected aperture of the ellipse is about 3 m. In the x_p axis, the illuminated function is a $\cos^{42}\theta$ pattern function (22.3-dB gain), and the frequency is 31.4 GHz. The ellipse is about 350λ along the major axis. Figure 1-6 compares the constant-phase approximation for three different grid densities: approximately 4000, 10,000, and 23,000 triangles. This illustrates a general trend of the method; that is, depending on the size of the triangles, there is an angular limit over which the solution is valid. Figure 1-7 compares the linear-phase approximation with the constant-phase approximation for the 4000-triangle case and demonstrates that the angular range is larger with the linear-phase approximation.

1.2.2 Feed-Horn Analysis

An equally critical aspect of the analysis of reflector systems is the ability to accurately compute the radiation pattern of the feed. More details on the design of the feeds will be given later, but the analysis technique for computing the radiation patterns of the feed is summarized below.

Two types of feed horns possessing equal E- and H-plane patterns are commonly used. The first is the dual-mode feed horn [12], and the second is the corrugated feed horn [13]. In the dual-mode horn, a dominant mode circular waveguide is connected to another guide of slightly larger diameter, where modes up to transverse magnetic (TM_{11}) may propagate; the higher order modes being generated by the step transition. The step size is chosen to generate the precise amount of TM_{11} mode from the transverse electric (TE_{11}) mode so that when the two modes travel through the flared horn section that follows, the E- and H-plane patterns are equalized. The bandwidth of this feed

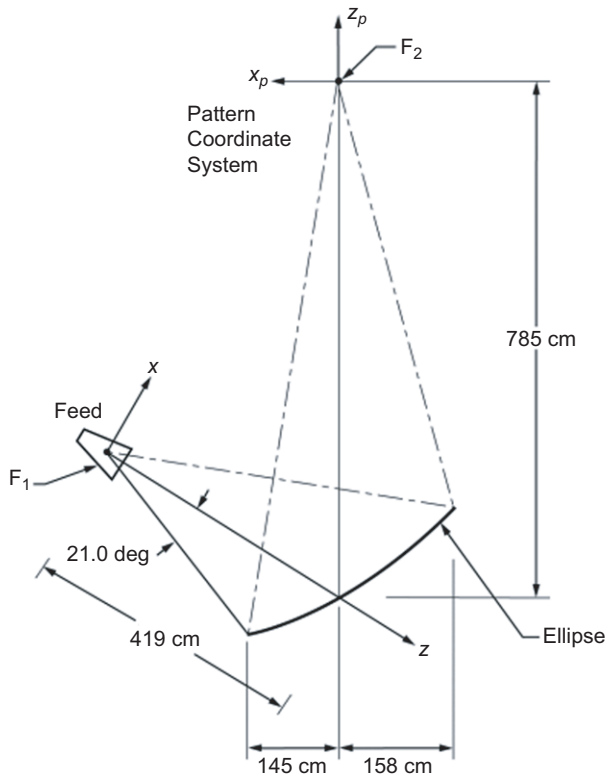

Fig. 1-5. Ellipse geometry.

horn is limited since the two modes must arrive at the horn aperture in phase, and the two modes have phase velocities that vary differently with frequency.

In the corrugated feed horn, the single-mode smooth-wall waveguide is connected to a corrugated waveguide that supports only the hybrid (HE_{11}) mode. Some matching between the waveguides is provided by gradually changing from $\lambda/2$ slot depth to $\lambda/4$ slot depth in a short transition region. Throughout the transition region, only the HE_{11} corrugated waveguide mode may propagate, and the E- and H-plane radiation patterns of this mode become nearly equal when the balanced condition is reached (slot depth = $\sim\lambda/4$). The bandwidth of this horn is larger than that of the dual-mode horn because the transverse electric field patterns and, hence, the radiation pattern of the HE_{11} mode are relatively insensitive to small changes in slot depth around the balanced condition (slot depth = $\sim\lambda/4$). After the HE_{11} mode is established in the single-mode corrugated waveguide, the guide is gradually flared, without changing the slot depth, to the required aperture size.

The corrugated section is analyzed using a computer code developed by Hoppe [14–16]. The analysis follows the method of James [17], expanding the

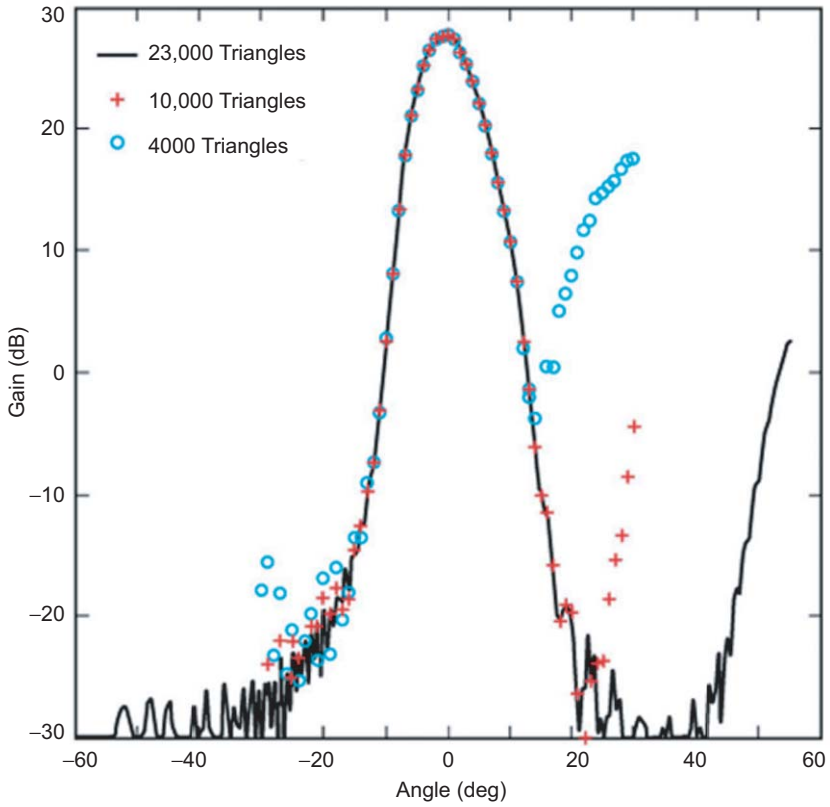

Fig. 1-6. Ellipse example: constant-phase approximation for offset plane.

fields inside each fin and slot in terms of circular waveguide modes, and matching the fields at each slot–fin boundary. All of the possible propagating modes (as well as a sufficient number of evanescent modes) are matched at each boundary, with results for successive edges and waveguide lengths cascading as the analysis moves through the device. In this way, the interactions between the fields of nonadjacent as well as adjacent slots are taken into account. The result of the calculation is a matrix equation relating the reflected and aperture modes to the input modes.

If $\mathbf{a}_1$ is a vector containing the power-normalized amplitudes of the input modes, then we may calculate the reflected modes, $\mathbf{b}_1$, and the aperture modes, $\mathbf{b}_2$, using

$$\mathbf{b}_2 = \left[S_{21}\right] \mathbf{a}_1 \tag{1.2-17}$$

$$\mathbf{b}_1 = \left[S_{11}\right] \mathbf{a}_1 \tag{1.2-18}$$

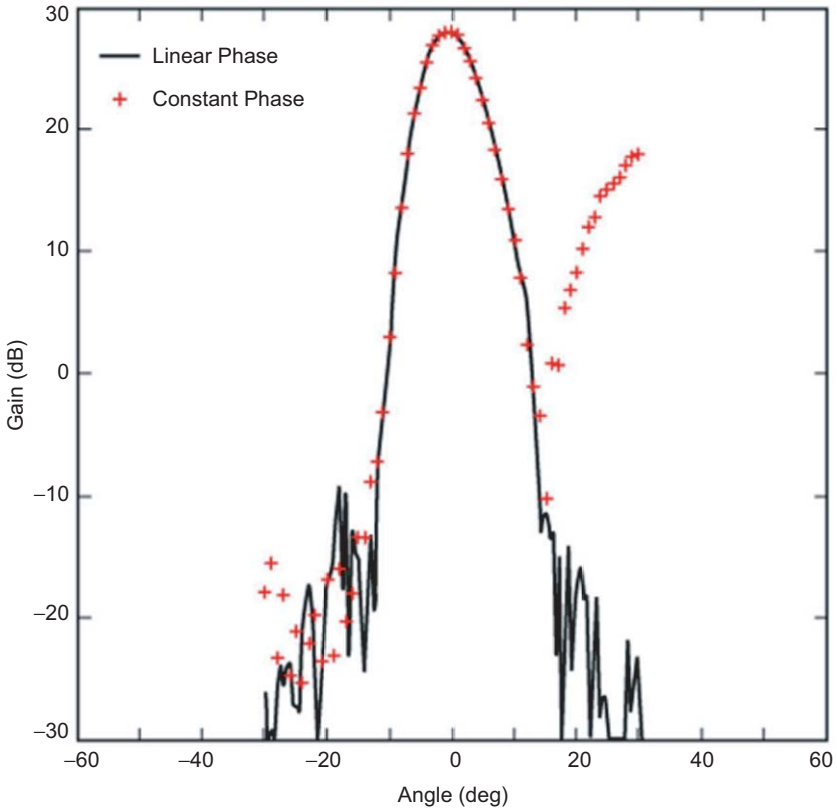

Fig. 1-7. Ellipse example: constant versus linear phase for offset plane.

Here, $[S_{21}]$ and $[S_{22}]$ are the scattering matrices resulting from the computer run. See the appendix of [17]. They depend only on frequency and device dimensions, not input modes. We may therefore specify any input vector $\mathbf{a}_1$ and calculate the reflected and aperture fields. Using the normalized amplitudes calculated above, and the normalized vector functions giving the field distributions for each mode, we find the aperture field $\mathbf{E}_B$. The far field is then calculated by the method described by Silver and Ludwig [18,19].

$$\mathbf{E}_c = \frac{-1}{4\pi} \iint_S \left(-j\mu\omega \left(\hat{n} \times \mathbf{H}_B\right) \phi + \left(\hat{n} \times \mathbf{E}_B\right) \times \nabla\phi\right) ds \qquad (1.2\text{-}19)$$

where

$\mathbf{E}_B$ = aperture electric field
$\mathbf{H}_B$ = aperture magnetic field
$\hat{n}$ = unit vector normal to aperture surface
ds = incremented area on aperture surface

ω = $2\pi f$ angular frequency
f = frequency
μ = free-space permeability
∇ = gradient operator
ϕ = e^{-jkr}/r
k = $2\pi / \lambda o$ wave number
r = far-field point distance from origin (spherical radius)

When $\mathbf{E}_B$ and $\mathbf{H}_B$ are represented in terms of circular waveguide modes, the resulting integrals have already been evaluated by Silver [18]. Therefore, given an input vector and the scattering matrix, we determine the aperture modes and composite far-field patterns. A spherical-wave analysis is then used to compute the feed-horn near-fields pattern for use in the PO software. Throughout the analysis, care must be taken to ensure proper normalization of the field amplitudes in terms of power. The smooth wall conical feed horn is modeled with the same software by approximating the horn taper with small steps and zero-depth corrugated slots.

The mode-matching technique for analyzing corrugated horns yields excellent agreement with the measured patterns—so much so, in fact, that if the computed and measured patterns do not match, it is most likely due to measurement and/or manufacturing errors. There is a recent example of a fairly complicated X-/X-/Ka-band horn described in [1] and [20] that shows excellent agreement between measured and calculated feed patterns. There are also several very good examples given in later chapters with probably the most complicated horn being the Cassini antenna three-frequency horn described in Chapter 5.

1.2.3 Spherical-Wave Analysis

Spherical-wave-expansion coefficients are frequently used in the analysis of reflector systems. Their basic purpose is to transform far-field patterns to the near-field so that PO may be used for reflectors in the near field of their illumination source.

The theory of spherical waves is described in [21] and will only be briefly outlined here. Any electromagnetic field in a source-free region may be represented by a spherical-wave expansion. In general, the expansion must include both incoming and outgoing waves. If the field satisfies the radiation condition, only outgoing waves will be present, and the expansion will be valid outside the smallest sphere enclosing all sources (the sphere center must be at the coordinate origin used for the expansion). The radial dependence of the spherical waves is then given by the spherical Hankel function $h_n^2(kR)$. Another common case is an expansion valid inside the largest sphere enclosing no sources. In this case, the incoming and outgoing waves are present in equal

amounts, producing a radial dependence given by the spherical Bessel function $j_n(kR)$.

Although the spherical-wave expansion can be applied to either of these two most common cases, the version used most typically for antenna analysis assumes outgoing waves.

In either case, the input data that are used to specify the field is the tangential E-field on the surface of a sphere. For the first case, the data-sphere radius must be greater than or equal to the radius of the sphere enclosing the sources. For far-field data, the data-sphere radius is considered to be infinite. For the second case, the data-sphere radius must be less than or equal to the largest sphere enclosing no sources, and must be greater than zero.

The maximum value of the Hankel function index that is needed to closely approximate the field is roughly equal to ka (ka + 10 is typical, but in some cases a lower limit will work), where a is the radius of the sphere enclosing all (or no) sources for the first (and second) case, respectively.

Input data is specified on a grid of points defined by the intersection of constant contours of θ and ϕ. The amplitude and phase of E_θ and E_ϕ are given at each point. The minimum number of θ values is roughly 1.2 times the maximum value of n.

The azimuthal dependence of spherical waves is given by $\sin(m\phi)$ and $\cos(m\phi)$. In general, m runs from 0 to the maximum value of n. As is often the case, symmetry can be used to reduce the number of azimuthal terms. A conical feed radiates only $m = 1$ modes, and reflection from a body of revolution will maintain this behavior. There can be even and odd ϕ dependence, but quite often only one will be present. For the even ϕ dependence, E_θ can be expanded in only $\sin(m\phi)$ terms and E_ϕ in only $\cos(m\phi)$ terms. For the odd case, this is reversed. The minimum number of ϕ values for the data sphere is, in general, $2M + 1$, where M is the maximum value of m.

The output of the computer program is the set of spherical-wave-expansion coefficients. These coefficients may then be used to compute the field anywhere within the region of validity. Therefore, the essential utility the program is to take data consisting of the tangential E-field on a sphere (whose radius may be infinite), and provide the means of computing the field—all three components of E and H—at any other point in the region of validity.

The computer program used is patterned after that in [22].

1.2.4 Dual-Reflector Shaping

The simplest form of a dual reflector system, the Cassegrain, has a parabolic main reflector and a hyperbolic subreflector. The efficiency of these reflectors is primarily determined by (a) the ability of the feed system to illuminate only the reflectors while minimizing the energy that radiates

elsewhere and (b) the ability of the feed plus the subreflector to uniformly illuminate the parabola. Item (a), above, is termed "spillover efficiency" and (b) "illumination efficiency." The illumination efficiency is 100 percent when the energy density on the entire main reflector aperture is a constant.

Feed-horn patterns always taper gradually from their central maxima to nulls. If all this energy is intercepted by the reflector (for maximum spillover efficiency), the illumination is far from uniform, and the illumination efficiency is very poor. Consequently, any attempt to obtain nearly uniform illumination will result in a great loss of energy in spillover. Therefore, a compromise must be made. A common choice for both a prime focus system and the Cassegrain system is a 10-dB taper of the illumination pattern at the parabolic edge. This selection results in a combination of spillover and illumination efficiency of from about 75 to 80 percent.

It is possible, however, to change the shape of the two reflectors to alter the illumination function and improve efficiency. This methodology is termed dual-reflector shaping and was first introduced by Galindo [23], who demonstrated that one could design a dual-reflector antenna system to provide an arbitrary phase and amplitude distribution in the aperture of the main reflector. Thus, if one chose a uniform amplitude and constant phase, 100 percent illumination efficiency could be achieved. With the feed pattern given, the subreflector size would be chosen to give minimal spillover.

1.2.4.1 Theoretical Solution for the Symmetric Case. The complete solution can be found in [23 and 24], and only the uniform aperture case is summarized below.

The geometry of the symmetric dual-reflector system is shown in Fig. 1-8. Due to circular symmetry, the synthesis reduces to the determination of the intersection curve (of the surface) with the plane through the axis of symmetry, that is, the x,y plane.

The synthesis method uses the analytical expressions of geometrical optics (GO) principles together with the reflector geometry to develop a pair of first-order, nonlinear ordinary differential equations of the form

$$\frac{dy}{dx} = f(x,y) \tag{1.2-20}$$

which leads to cross sections of each reflector when subject to boundary conditions such as

$$y\left(x = x_{\max}\right) = 0 \tag{1.2-21}$$

which are then solved by a high-speed digital computer.

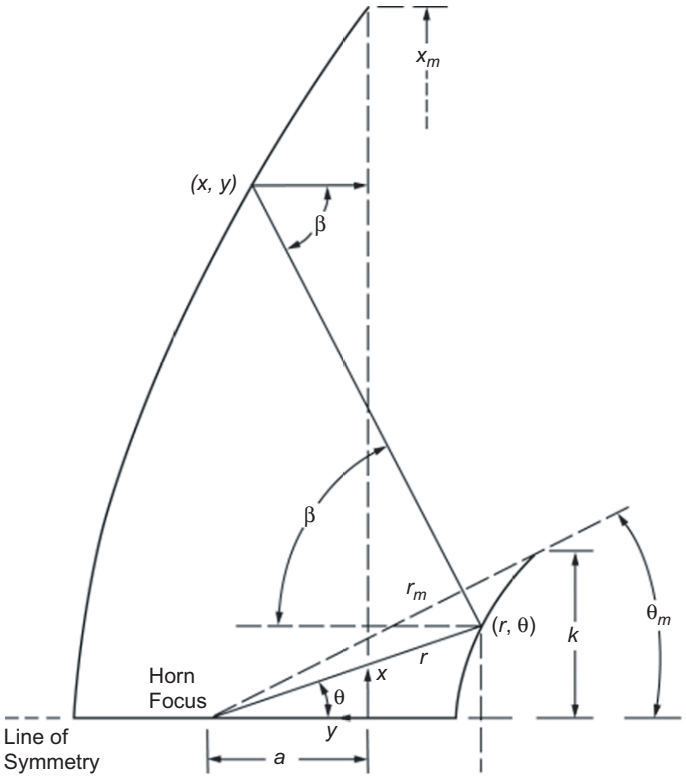

Fig. 1-8. Coordinate system for shaping.

The optical principles that are used to develop the required equations are that (a) the angle of incidence is equal to the angle of reflection (Snell's Law), (b) energy flow is conserved along the ray trajectories, and (c) surfaces of constant phase form normal surfaces to ray trajectories.

The incident field is assumed to have a spherical-phase function, that is, a phase center, and a power-radiation pattern $F(\theta)$. For uniform phase in the aperture, the path length, $r + r' + r''$, must remain constant for all θ. Also, the amplitude function in the aperture $I(x)$ must also be equal to a prescribed distribution (constant for maximum peak gain).

The equation for equal path lengths resulting in the phase front is obtained from trigonometry:

$$r + y + \frac{x - r \sin\theta}{\sin\beta} = C \text{ (constant)} \qquad (1.2\text{-}22)$$

where (x,y) and (r,θ) are the coordinates of points on the main reflector and subreflector, respectively.

The application of Snell's law to the two surfaces defines a relationship between the angles shown and the first derivates (slopes) of the surfaces. These are

$$\frac{1}{r}\frac{dr}{d\theta} = \tan\frac{\theta+\beta}{2} \tag{1.2-23}$$

$$\frac{-dy}{dx} = \tan\frac{\beta}{2} \tag{1.2-24}$$

Since the dual-reflector system is symmetrical about the *y*-axis, the total power within the increment $d\theta$ of the pattern $F(\theta)$ will be $F(\theta)2\pi\sin\theta d\theta$. Similarly, the total power within the increment *dx* of the main antenna aperture is $I(x)2\pi dx$, where *I*(*x*) is the illumination function of the antenna aperture. Making *I*(*x*) constant and equating the total power from $\theta = 0$ to angle θ to that within *x*, and normalizing by the total power, one obtains

$$x^2 = x_{\max}^2 \frac{\int_0^{\theta} F(\theta)\sin\theta d\theta}{\int_0^{\theta\max} F(\theta)\sin\theta d\theta} \tag{1.2-25}$$

These four equations now have five dependent variables (*x*, *y*, *r*, θ, and β) and can be solved to provide equations for the surfaces. This procedure yields an optimum-gain antenna. The antennas used on the Voyager, Galileo, and Cassini spacecraft described in Chapter 5 were all dual-shaped systems.

1.2.4.2 Offset-Shaped Reflector Antennas. The formulation shown in Section 1.2.4.1 (above) is for circularly symmetric reflector geometries. The exact solution has also been developed for offset geometries [25,26]. The offset geometry will have higher efficiency than the symmetric geometry because the central blockage due to the subreflector can be eliminated. In the early 1980s, an antenna with an offset geometry was designed and built that had an efficiency of 84.5 percent—the highest ever recorded [27].

1.2.5 Dichroic Reflector Analysis

The ability to transmit and receive simultaneously at multiple frequency bands is an important requirement for deep-space communications. It is usually accomplished by using either a dual-band feed horn or separate feed horns and a frequency selective surface (FSS), typically referred to as a dichroic reflector. Dichroic reflectors are important components for both ground and spacecraft antennas. The most frequently used type of surface for ground antennas is a flat metal plate that passes the higher frequency and reflects the lower frequency.

The analysis for those types of surfaces is given in reference [1]. However, for spacecraft antennas, the typical use is for a dichroic subreflector that reflects the higher frequencies and passes the lower frequencies. Examples are the Voyager, Galileo, and Cassini (Chapter 5) high-gain antennas. As these dichroic surfaces play an important role in the telecommunications antennas, this section presents a typical technique for analyzing them.

1.2.5.1 Theoretical Formulation. Dichroic surfaces are analyzed using a combination of Floquet modes and the method of moments. The theory is well documented in references [28–30] and will only be summarized here. In particular, the following is derived from reference [28]. Consider the printed dipole array shown in Fig. 1-9. The surface is assumed infinite in the *xy* plane. Expanding the fields in the three regions in Floquet modes and applying the appropriate boundary conditions allows the development of an integral equation for the unknown current distribution $J(x,y)$ on the dipoles. If $J(x,y)$ is approximated as follows:

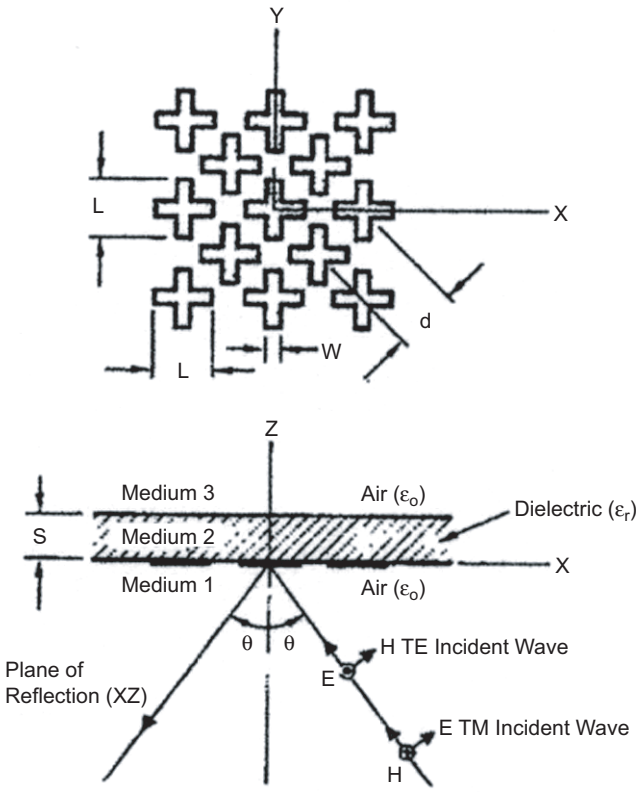

Fig. 1-9. Geometry of the dichroic surface.

$$J(x,y) = \sum_{n=1}^{N} c_n h_n(x,y), \tag{1.2-26}$$

where the functions $h_n(x,y)$ are complete and orthonormal over a crossed dipole and N is finite for computability, then the integral equation is easily solved using the method of moments. The resulting system of equations is:

$$\begin{aligned} &\sum_{m=1}^{2}\left(1 + R_{m00}^{\ slab}\right) b_m \hat{\kappa}_{m00} \cdot g_i{}^*(\mathbf{k}_{00}) \\ &= \sum_{n=1}^{N} c_n \frac{1}{d^2} \sum_{m=1}^{2} \sum_{p} \sum_{q} \\ &\quad \cdot \frac{\hat{\kappa}_{mpq} \cdot g_i{}^*\left(\mathbf{k}_{pq}\right) \hat{\kappa}_{mpq} \cdot g_n\left(\mathbf{k}_{pq}\right)}{\eta_{mpq}^{\ eq}}, \\ &\quad i = 1,2,\cdots,N \end{aligned} \tag{1.2-27}$$

where a time-dependence $\exp(j\omega t)$ is assumed, $m = 1$ corresponds to the TM mode, $m = 2$ corresponds to the TE mode, and

$$g_l\left(\mathbf{k}_{pq}\right) = \int_{\text{dipole}} h_l(x,y) \exp\left(j\mathbf{k}_{pq} \cdot \rho\right) dx\, dy, \tag{1.2-28}$$

d = array spacing,
ρ = $x\hat{x} + y\hat{y}$,
$\mathbf{k}_{pq}$ = $\left(k_0 \sin\theta\cos\phi + \sqrt{2}\pi p/d\right)\hat{x} + \left(k_0 \sin\theta\sin\phi + \frac{\sqrt{2}\pi}{d} + \frac{2\sqrt{2}\pi q}{d}\right)\hat{y}$,
k_0 = $2\pi/\lambda_0$,
λ_0 = free-space wavelength,
(θ,ϕ) = direction of incidence,
b_m = incident field magnitude of mth mode,
$\hat{\kappa}_{1pq}$ = $\mathbf{k}_{pq} \big/ \left|\mathbf{k}_{pq}\right|$,
$\hat{\kappa}_{2pq}$ = $\hat{z} \times \hat{\kappa}_{1pq}$,
$\eta_{mpq}^{\ eq}$ = $\eta_{mpq}^{\ \text{air}} + \eta_{mpq}^{\ \text{diel}}\left(\frac{1 - R_{mpq}}{1 + R_{mpq}}\right)$,
η_{1pq} = $\frac{k\eta}{\gamma_{pq}}$,

$$\eta_{2pq} = \frac{\gamma_{pq}\eta}{k},$$

η = $\sqrt{\varepsilon/\mu}, \varepsilon, \mu$ are the permittivity and permeability of medium,

k = propagation constant of the medium,

$$\gamma_{pq} = \left(k^2 - \left|\mathbf{k}_{pq}\right|^2\right)^{1/2}, \quad k^2 > \left|\mathbf{k}_{pq}\right|^2,$$

$$= -j\left(\left|\mathbf{k}_{pq}\right|^2 - k^2\right)^{1/2}, \quad k^2 < \left|\mathbf{k}_{pq}\right|^2,$$

$$R_{mpq} = \frac{\eta_{mpq}^{\text{diel}} - \eta_{mpq}^{\text{air}}}{\eta_{mpq}^{\text{diel}} + \eta_{mpq}^{\text{air}}} \exp\left(-j2\gamma_{pq}s\right),$$

$$R_{mpq}^{\text{slab}} = \frac{2\eta_{mpq}^{\text{air}} - \eta_{mpq}^{eq}}{\eta_{mpq}^{eq}}.$$

Once we select a suitable set of functions $\mathbf{h}_n$, the unknown coefficients c_n can be easily obtained by solving Eq. (1.2-27). The reflected and transmitted far fields contain only the propagating Floquet modes for which γ_{pq} is real. In a suitable design, by using a small array spacing, the higher order Floquet modes $(|p|>0, |q|>0)$, which correspond to the grating lobes, are made evanescent. Thus the reflection and transmission coefficients are computed from the following expressions:

$$\mathbf{R}(\theta) = \sum_{m=1}^{2}\left\{R_{m00}^{\text{slab}} b_m - \frac{1}{d^2\eta_{m00}^{eq}}\sum_{n=1}^{N} c_n g_n(\mathbf{k}_{00})\cdot\hat{\kappa}_{m00}\right\}\hat{\kappa}_{m00} \tag{1.2-29}$$

$$\mathbf{T}(\theta) = \sum_{m=1}^{2}\left\{t_{m00}\left(1+R_{m00}^{\text{slab}}\right)b_m - \frac{t_{m00}}{d^2\eta_{m00}^{eq}}\sum_{n=1}^{N} c_n g_n(\mathbf{k}_{00})\cdot\hat{\kappa}_{m00}\right\}\hat{\kappa}_{m00}$$

where

$$t_{mpq} = \frac{\exp\left\{j\left(\gamma_{pq}^{\text{air}} - \gamma_{pq}^{\text{diel}}\right)s\right\} + R_{mpg}\exp\left\{j\left(\gamma_{pq}^{\text{air}} + \gamma_{pq}^{\text{diel}}\right)s\right\}}{1+R_{mpq}},$$

$b_1 = 1, \quad b_2 = 0$ for TM incidence,

and

$$b_1 = 0, \qquad b_2 = 1 \quad \text{for TE incidence}.$$

1.2.5.2 Examples on a Flat Dielectric Sheet. Most of the applications for telecommunications require circular polarization; therefore, an array of crossed dipoles is a popular choice for the element. The array becomes reflective near the dipole resonance and is almost transparent at lower frequencies. In practice, these surfaces are often constructed by printing metal dipoles on supporting dielectric layers. The exact reflection and transmissions characteristics, therefore, depend on the length, width, and spacing of dipoles; the dielectric constants; and the thickness of the layers. The reflection coefficient is also a function of incident angle. When the application is a dichroic subreflector, there is a range of incident angles on the surface. There are two ways to handle the varying incident angles, by redesigning the element to be reflective at the given incident angle, or, more simply, selecting dimensions for the element that work over the entire range of incident angles. Since the exact resonance frequency is fairly sensitive to the parameters and some of the parameters are not accurately known (dielectric constant of the materials, for example), a flat-sheet test sample is sometimes manufactured and tested to verify the design. A comparison of the calculated and measured reflection coefficient is given below.

A computer program was written for calculating the reflection coefficients for a dipole element using a Fourier expansion in Eq. (1.2-26). Upon comparison with the experimental results, it was found that a three-term expansion of the current on each dipole was sufficient. Thus, for the crossed dipole at the origin we have

$$\mathbf{h}_1 = \hat{y}\sqrt{\frac{2}{WL}}\cos(\pi y/L), \qquad \mathbf{h}_2 = \hat{y}\sqrt{\frac{2}{WL}}\sin(2\pi y/L),$$
$$\mathbf{h}_3 = \hat{y}\sqrt{\frac{2}{WL}}\cos(3\pi y/L), \quad \mathbf{h}_4 = \hat{x}\sqrt{\frac{2}{WL}}\cos(\pi x/L),$$
$$\mathbf{h}_5 = \hat{x}\sqrt{\frac{2}{WL}}\sin(2\pi x/L), \quad \mathbf{h}_6 = \hat{x}\sqrt{\frac{2}{WL}}\cos(3\pi x/L),$$

The computed reflection coefficient for $L = 0.97$ cm, $d = 0.92$ cm, and $W = 1.016$ mm is shown in Fig. 1-10. Fig. 1-10(a) assumes an absence of the dielectric ($\varepsilon_r = 1$, $s = 0$), and Fig. 1-10(b) is with a sheet of dielectric constant $\varepsilon_r = 4.25$ and thickness $s = 0.127$ mm. Figure 1-10(c) shows the measured reflection coefficient of an experimental surface with the same parameters as used in the computation of the curves of Fig. 1-10(b). This experimental surface is shown in Fig. 1-11, and the method of measurement is described in [28]. As

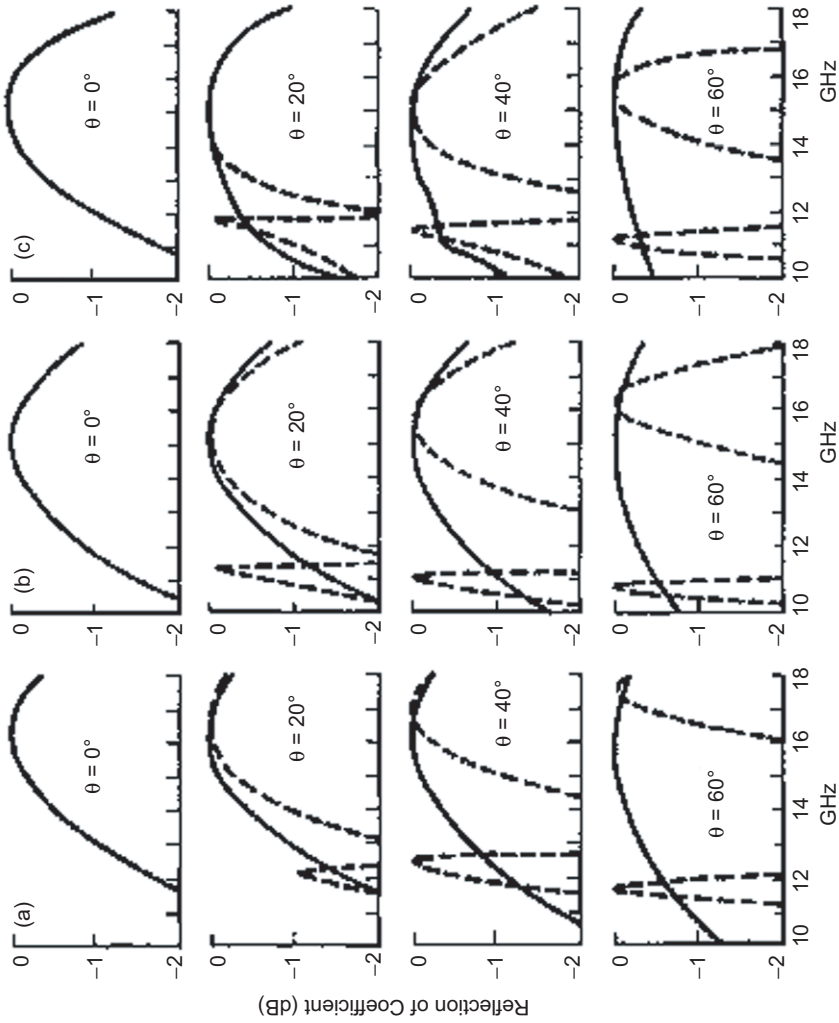

Fig. 1-10. Computed and measured reflection coefficient, —TE, ---TM: (a) theory $\varepsilon_r = 1$, s = 0 mm; (b) theory $\varepsilon_r = 4.25$, s = 0.127 mm; and (c) experiment $\varepsilon_r = 4.25$, s = 0.127 mm.

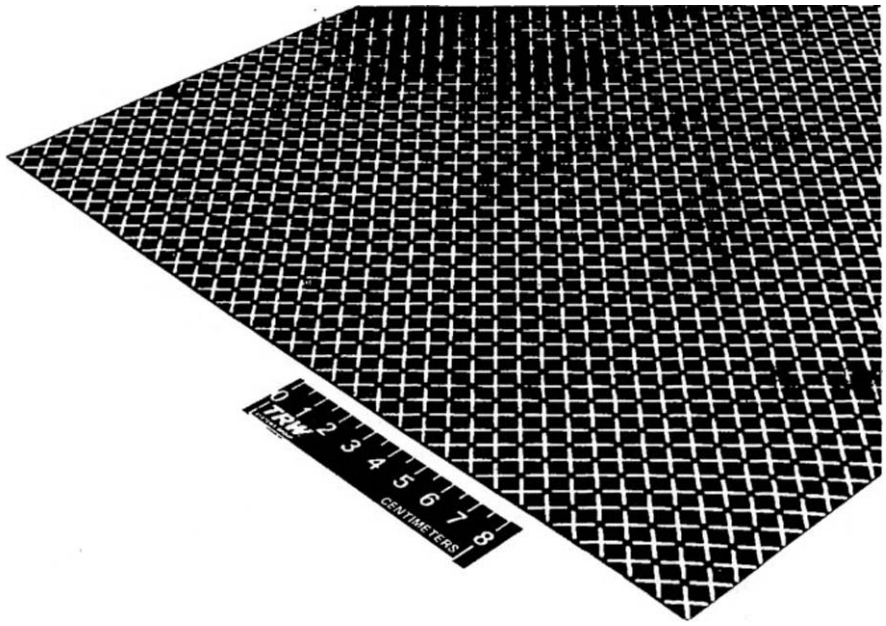

Fig. 1-11. Experimental dichroic surface of copper dipoles printed on 5-mil Kapton sheet (s = 0.127 mm).

can be seen in Fig. 1-10, the theoretical results are in close agreement with the experiment. A major influence of the dielectric sheet appears to be in lowering the resonance frequency at which the surface becomes a perfect reflector.

1.2.6 Mesh Analysis

The use of a mesh for the surface of a reflector antenna is a very attractive solution for large deployable antennas such as those on the Tracking and Data Relay Satellite System (TDRSS) and the Galileo spacecraft. These mesh surfaces are typically constructed from gold-plated molybdenum wires, which are woven in a periodic pattern. A commonly used pattern is the tricot knit. The fineness of the wires (typically 1.2 mil [31 μm] in diameter) and the complexity of the weave made the problem of an exact numerical diffraction analysis quite formidable. Nonetheless, Imbriale, Galindo and Rahmat-Samii [31] solved the problem using a Floquet-mode expansion to establish an integral equation for the mesh wire currents that was solved using the method of moments technique with piecewise triangular basis functions. It was observed that it was necessary to give special attention to the junction treatment among different branches of the mesh configuration. For analytic convenience, the mesh was modeled as flat strips on a plane surface. This does not limit the validity of the results since the wire diameters are so small that there are only longitudinal currents. An

equivalent radius of one-fourth the strip width is used to equate round wire and flat strips.

1.2.6.1 Theoretical Formulation. Since the tricot weave is essentially periodic, Floquet's theorem can be applied in the analysis of a plane wave incident upon the mesh. Currents induced along the strip are modeled as a series of overlapping triangular basis functions (splines)—the coefficients of each triangle to be determined by inversion of the matrix obtained when tangential **E** is set to zero on the flat strips.

The multiwire junction points are carefully modeled so that the currents are naturally continues through the junctions and no additional conditions are necessary. Conditions of good electrical contact, no contact, or partial contact at the junctions are included in the model. Finite conductivity can be included as well.

The formulation follows very closely the development described in the previous section on dichroic surfaces. In fact, using Floquet's theorem and the method of moments results in the identical set of equations to be solved, i.e., Eq. (1.2-27). The differences stem from the different basis functions used in the formulation and the fact that medium 2 is air instead of a dielectric. However, if the dielectric constant is included in the formulation, the resulting computer code can also be used to analyze dichroic surfaces. In addition, it allows experimental verification of the computer code by comparing with various flat-strip meshes printed on a dielectric sheet.

As indicated above, the reflection and transmission coefficients are computed using Eq. (1.2-29). The major difference in the formulation is the representation of the currents to be used in Eq. (1.2-26).

The actual curved strip is represented as a series of straight segments. The currents are modeled as piecewise triangular along the strip and constant in the transverse direction. The geometry is shown in Fig. 1-12. In particular the currents on the *n*th segment are

$$h_n(x',y') = \hat{\mathbf{x}}' \frac{(x'+l)}{wl}, \quad -l \le x' \le 0, \quad -\frac{w}{2} \le y' \le \frac{w}{2}$$

$$\mathbf{h}_n(x',y') = \hat{\mathbf{x}}' \frac{(l-x')}{wl}, \quad 0 \le x' \le l, \quad -\frac{w}{2} \le y' \le \frac{w}{2} \tag{1.2-30}$$

where

$$x = x_n + x'\cos\Psi - y'\sin\Psi, \quad y = y_n + x'\sin\Psi + y'\cos\Psi.$$

By substituting Eq. (1.2-30) into Eq. (1.2-28) and integrating, we obtain

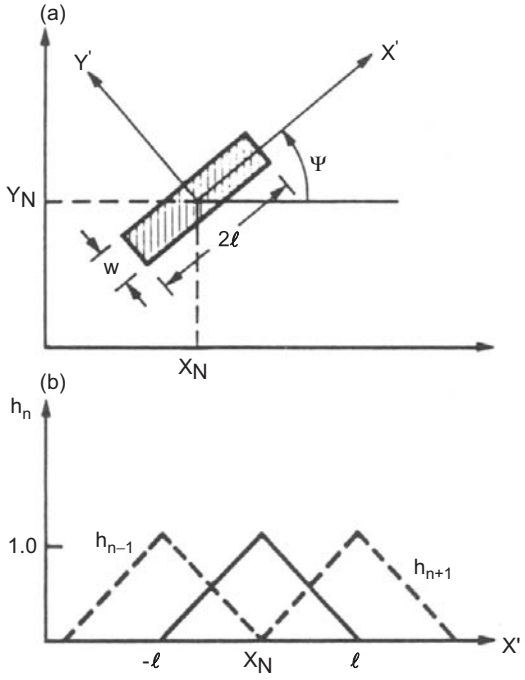

Fig. 1-12. Basic function geometry: (a) geometry of nth segment and (b) triangular basis function.

$$\mathbf{g}_{npg} = \mathbf{g}^{-}_{npq} + \mathbf{g}^{+}_{npq}$$

where

$$g^{-}_{npq} = \hat{\mathbf{x}}' e^{jC}\left[\left(\frac{1}{Z^2} - \frac{jl}{Z}\right)e^{jlz} - \frac{1}{Z^2}\right]\frac{\sin\dfrac{Vw}{2}}{\dfrac{Vw}{2}} \times \frac{e^{-jlk}}{l}$$

$$g^{+}_{npq} = \hat{\mathbf{x}}' e^{jC}\left[\left(\frac{1}{Z^2} - \frac{jl}{Z}\right)e^{-jlz} - \frac{1}{Z^2}\right]\frac{\sin\dfrac{Vw}{2}}{\dfrac{Vw}{2}} \cdot \frac{e^{jlk}}{l} \qquad (1.2\text{-}31)$$

with

$$Z = k_x \cos\Psi + k_y \sin\Psi,$$

$$V = -k_x \sin\Psi + k_y \cos\Psi, \text{ and } C = k_x x_n + k_y y_n.$$

The complete solution for reflectivity is thus obtained by first using Eq. (1.2-31) and Eq. (1.2-28) and solving for the unknown coefficients c_n using Eq. (1.2-27), and then using the c_n in Eq. (1.2-29) to compute reflectivity.

At the bends in the wire and at wire junctions, special treatment is required to insure that the analytical model provides for the vector continuity of current from one segment to the next segment.

If the vector continuity is not provided, then the current along the strip "senses" a termination of the conductor, and the coefficient of the end point basis function goes to zero.

Setting tangential **E** equal to zero is the *only constraint* required if current continuity is insured in the *vector* sense by the addition of a "wedge" current as illustrated in Fig. 1-13.

The *wedge* current in Fig. 1-13a is represented by

$$\mathbf{h}_n = \frac{-\hat{\mathbf{x}}\sin\Psi + \hat{\mathbf{y}}\cos\Psi}{w}. \tag{1.2-32}$$

This is a circular current of constant amplitude as depicted in Fig. 1-13(a). We need to evaluate g_{npq} for this segment. The result is

$$g_{npq} = e^{jC}\int_{\Psi_{n-1}}^{\Psi_n}\left[\frac{-\hat{\mathbf{x}}\sin\Psi + \hat{\mathbf{y}}\cos\Psi}{w}\right]\cdot\left[\frac{e^{jZw} - jZwe^{jZw} - 1}{Z^2}\right]d\Psi \tag{1.2-33}$$

where the integration is carried out numerically with C and Z is as described above.

At the junction of more than one strip, a superposition of all possible wedge currents is required. For example, if two strips cross and make contact, then this junction is treated as a four "port" with six interconnecting wedges necessary to permit current flow from any given strip to any other strip. In general, for N' strips at a common junction point,

$$\left[(N'-1)+(N'-2)+\cdots\right] = \left[\frac{N'(N'-1)}{2}\right]$$

wedge currents are required.

Figure 1-13(b) illustrates a crude schematic of three wire strips meeting at a junction. Hence $N' = 3$ and three connecting "wedge" currents are required. Since wire 3 connects *straight* into wire 2, one wedge current, $\mathbf{I}_{32}$, degenerates into a *straight connecting section*. Current $\mathbf{I}_{c2}$ and $\mathbf{I}_{c3}$ are circular currents.

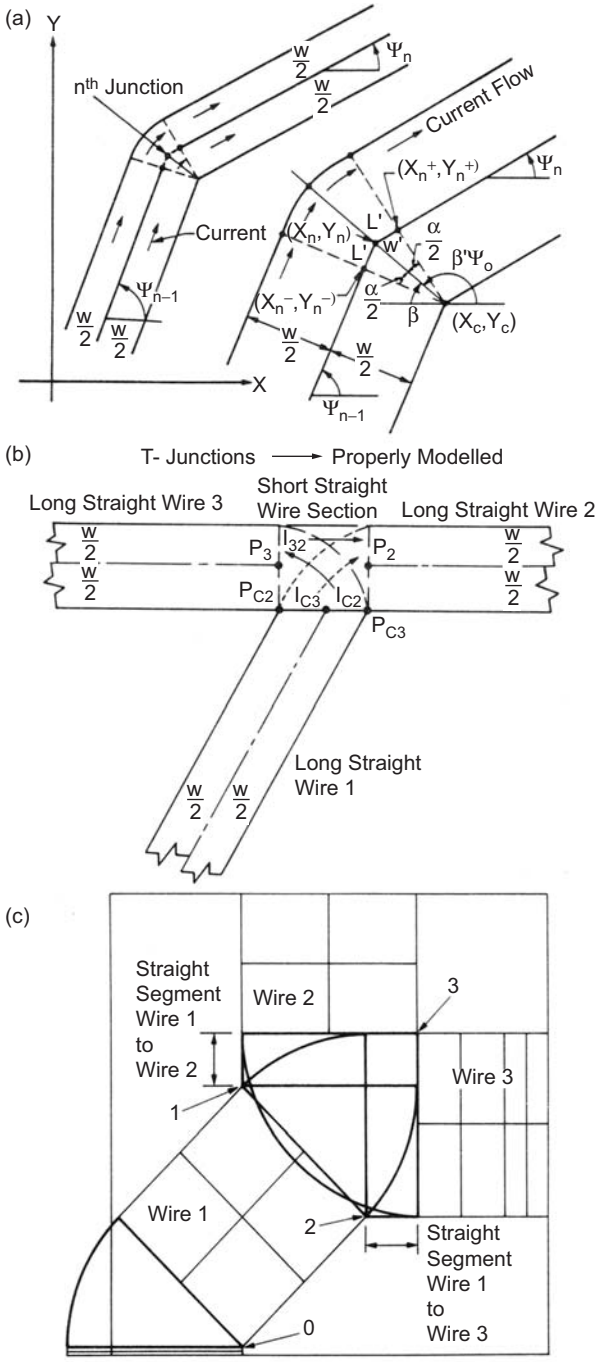

Fig. 1-13. Wire junction geometry: (a) wire bend geometry, (b) three strips meeting at a junction, and (c) General three wire junction with connecting straight sections.

In order to use simple cylindrical currents in the wedge segment, as described earlier, it is necessary to introduce some additional "straight connecting segments" into the geometry. This is illustrated in the three-wire junction of Fig. 1-13(c). The lower left of the figure contains a simple two-wire junction (i.e., a bend) wherein the current wedge is easily introduced and centered at point 0 in the figure.

For the three-wire junction, two straight segments must be introduced in order to use circular wedge currents. For an N' wire junction, we need $(N'-1)$ straight wire connecting segments at the junction. Figure 1-13(c) indicates the required two straight segments. The cylindrical wedge currents are centered at points 1, 2, and 3 (P_1, P_2, P_3) in the figure. The $\mathbf{g}_{npq}$ for these segments are readily evaluated. It is not necessary to introduce an additional unknown for each connecting straight segment.

A number of examples, including experimental results to validate the theory, are given in reference [31].

1.2.6.2 Galileo Mesh Calculations. The mesh that was used on both the Galileo high-gain antenna and the TDRSS single access antennas was a complex tricot knit, with 10 openings per inch (4 openings per centimeter) and a 1.2-mil (31-μm) diameter wire. Since the analysis uses a flat strip model and the actual mesh is composed of round wire, it was necessary to demonstrate equivalence between wires and strips. It was shown in [31] that the equivalent radius is one-fourth of the strip width. Using the equivalent radius and the complex mesh geometry (shown in Fig. 1-14), a computation for the Galileo type mesh is shown in Fig. 1-15, along with the measured reflectivity at 8 and 15 GHz. In Fig. 1-15 it was assumed that all the junctions make perfect contact, as is the case if there is no corrosion or oxides on the wires. It has been experimentally observed, that under certain unfavorable conditions, a loss of mesh reflectivity of several dB can occur. This has been attributed to lack of electrical contact at the junctions and occurs in part because the tricot knit has wires predominantly in one direction. This phenomenon is further discussed in [31].

1.3 Wire Antennas

William A. Imbriale

Since the dipole antenna is a very simple and lightweight antenna, many of the early spacecraft made use of such antennas (Explorer I for example). For some of the same reasons small rovers and instruments also make use of simple wire-type antennas. For completeness on the analysis tools, this section provides a short summary on the analysis of wire antennas. There are many papers and textbooks that describe the use of the method of moments for the

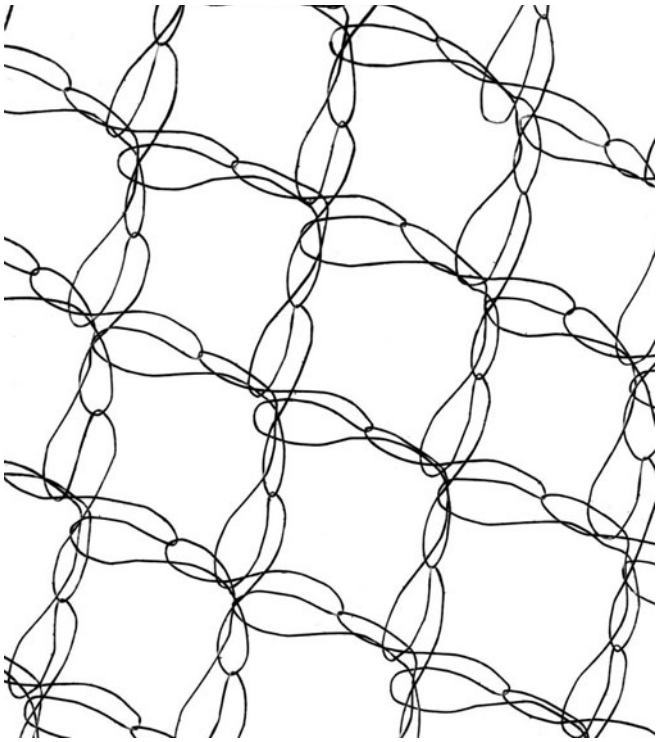

Fig. 1-14. Complex tricot knit geometry.

solution of wire antennas, with [32] probably the classic reference. The following formulation follows the development given in [33] and [34].

1.3.1 Theoretical Formulation

In the moments solution the method of subsectional basis functions is applied with both the expansion and testing functions being sinusoidal distributions. This allows not only a simplification of near-field terms but also the far-field expression of the radiated field from each subsegment, regardless of length. Sinusoidal basis functions are extremely useful for the analysis of large arrays of dipoles since the use of one subsegment per dipole is equivalent to the induced electromotive force (EMF) method of calculating mutual impedances and therefore give a physically meaningful result. For an array of N dipoles, this allows the use of the minimum matrix size of N × N to achieve a good "first order" approximation to the solution.

1.3.1.1 Basic Theory. Figure 1-16 shows a straight section of wire of circular cross section and defines the coordinate system. The wire with radius a extends from $z = 0$ to $z = L$ along the z-axis. It is assumed that the radius is small

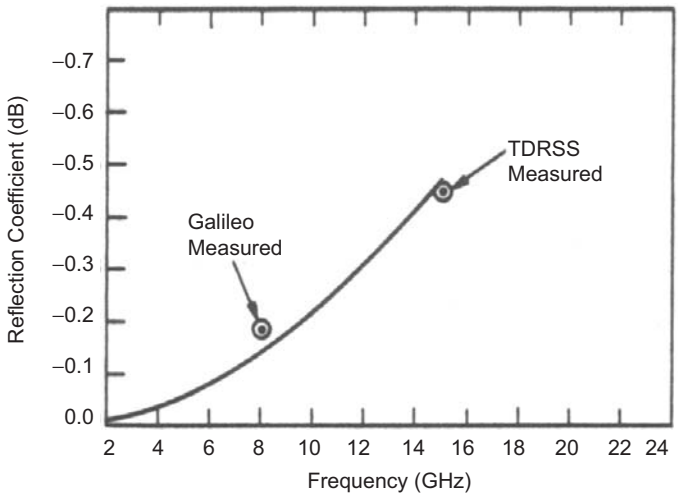

Fig. 1-15. Computed and measured Galileo mesh reflectivity.

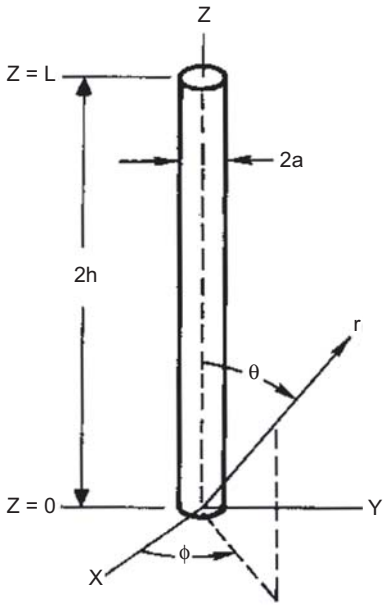

Fig. 1-16. Straight wire and coordinate system.

compared to a wavelength, but the ratio of a to L need not be small. The only significant component of current on the wire is the axial component, which can be expressed in terms of the net current $I(z)$ at any point z along the wire. The current distribution is modeled as an infinitely thin sheet forming a tube of

radius a, with the density of current independent of the circumferential position on the tube. An integral equation for the problem is given by

$$L\{I(z)\} = j(4\pi\omega\varepsilon)^{-1}\left(d^2/dz^2 + k^2\right)\oint_c \int_0^L \left[\exp(-jkR)/R\right]\cdot I(z')dz'dc = E_z^i(z) \tag{1.3-1}$$

where $E_z^i(z)$ is the z component of the impressed electrical field at the wire surface, $I(z')$ is surface current density, $\oint_c dc$ represents the integration around the circumference, R is the distance from the source point to the field point, and L is a shorthand notation for the integral operator.

The integral equation is solved using the method of moments with sinusoidal subsectional currents and Galerkin's method [34].

Let the wire be broken up into N segments (each of length $2H$, and let $I(z)$ be expanded in a series of sinusoidal functions

$$I(z) \approx \sum_{n=1}^{N-1} I_n S(z - nH), \tag{1.3-2}$$

where I_n are constants and

$$S(z) = \begin{cases} \sin k\left(H - |z|\right), & |z| < H \\ 0, & |z| < H \end{cases}.$$

Substitute Eq. (1.3-2) into Eq. (1.3-1), multiply each side by $S(z - mH)$, $m = 1, 2, \cdots, N-1$ and integrate from z to L on z. This results in the matrix equation

$$[Z][I] = [V] \tag{1.3-3}$$

where the elements of $[I]$ are I_n, those of $[Z]$ are

$$Z_{mn} = \int_0^L S(z - mH) L\{S(z - nH)\} dz \tag{1.3-4}$$

and those of $[V]$ are

$$V_m = \int_0^L S(z - mH) E_z^i(z) dz\,. \tag{1.3-5}$$

Inverting the $[Z]$ matrix to solve for $[I]$ and substituting in Eq. (1.3-2) gives the solution for the unknown current.

In solving thin wire antennas, the integration around the current tube is normally removed by replacing the integral with the value of the integrand at one point. This then reduces the equation to a single integral and obviates the singularity of the integrand, which occurs when the source and field points coincide during the calculation of the self and first adjacent mutual terms. The singularity is, of course, integrable; and by suitably expanding the integrand, special series for these terms can be obtained and the integral performed in closed form. However, many authors have used an "average" value equal to the radius *a*. This approximation is described as assuming the current to be totally located on the center axis and the distance *a* is used to represent an average distance from the current filament to the true current surface. A thorough discussion of this singularity and its effect on numerical convergence is given in [33]. However, if the radius is sufficiently small and the number of subsegments limited to the condition when a/H is small, then this approximation is sufficient. The Z_{mn} term for an infinitely thin current filament is given as

$$Z_{mn} = 30\int_{H_{m-1}}^{H_{m+1}} [-j\exp(-jkR_1)/R_1 - j\exp(-jkR_2)/R_2 + 2j\cos kH_n \cdot \exp(-jkR_0)/R_0] \cdot \sin\left[k\left(H_m - |z|\right)\right] dz, \tag{1.3-6}$$

where R_1 and R_2 are the distances from the end points, and R_0 the distance from the center of subsegment H_n to the field point on H_m when integrating over subsegment H_m. For the self-term and the first adjacent subsegment where the source and field terms coincide, the impedance term is computed by separating the source and field *E* by the radius *a*.

1.3.1.2 Far-Field Evaluation. The radiation pattern of a wire antenna is obtained by superposition of the fields of the many small subsegments with sinusoidal current distributions. Utilizing the general expression for the electric field of a subsegment of any half-length *H* oriented along the *z*-axis the far-zone field is given by

$$E(\theta,\phi) = j\eta(4\pi r)^{-1}\exp(-jkr)\sum_{n=1}^{N} I_n[\cos(kH\cos\theta) - \cos kH] \cdot \exp(jk\eta H)/\sin\theta\,\hat{u}_\theta, \tag{1.3-7}$$

where η is the intrinsic impedance of free space and $\hat{u}_\theta$ is a unit vector.

The power gain pattern of the radiation field is

$$g(\theta,\phi) = 4\pi r^2 \eta^{-1} \left| E(\theta,\phi) \right|^2 / P_{in}, \tag{1.3-8}$$

where P_{in} is the power input to the antenna

$$P_{in} = \mathrm{Re}[\tilde{V}][I^*], \tag{1.3-9}$$

where $[\tilde{V}]$ denotes the transpose of $[V]$, and * denotes conjugation.

1.3.2 Arbitrarily Shaped Wires and Wire Junctions

The procedure for solving arbitrarily shaped wires is similar to that used for straight wire as the wire is divided into subsections, over each of which a sinusoidal current distribution is assumed, and a generalized impedance matrix [*Z*] obtained to describe interactions between subsections. The junction of two or more straight segments can be thought of as the intersection of two or more half subsegments superimposed on one another. Thus, Kirchoff's current law is not invoked at the junction; it is a consequence of Maxwell's equations.

To complete the description of arbitrarily shaped wires we need to obtain the mutual impedances between two full subsegments, between a full subsegment and a half subsegment, and between two half subsegments. The details for computing these impedance terms are given in [34].

1.4 Microstrip Antenna: Analysis, Design, and Application

John Huang

1.4.1 Introduction

Since the invention of the microstrip antenna a half-century ago [35,36], the demand for its application [37–43] has been increasing rapidly, especially within the past two decades. Because of microstrip antennas' many unique and attractive properties, there seems to be little doubt that they will continue finding many applications in the future. These properties include low profile, light weight, compact and conformable to mounting structure, easy to fabricate, and integratable with solid-state devices. Although, the microstrip antenna is well known for its shortcoming of narrow bandwidth, recent technology advances have improved its bandwidth from a few percent to tens of percent. To understand a microstrip antenna's performance and to simplify its design process, several numerical analysis techniques have been developed and converted to computer-aided-design (CAD) tools. Some of these analysis techniques also allow the designer to know the physical insight of the antenna's electrical operating mechanism. It is the purpose of this section to discuss some of the microstrip antenna's technical features, its advantages and disadvantages,

as well as its material considerations for space application. Analysis techniques, design processes, and CAD tools are briefly presented. Several spacecraft applications of the microstrip antenna are also highlighted.

1.4.2 Technical Background

This subsection presents the technical background of the microstrip antenna, which is separated into three areas: features of the microstrip antenna, advantage and disadvantage tradeoffs, and material considerations.

1.4.2.1 Features of the Microstrip Antenna. A microstrip antenna [44,45], as shown in Fig. 1-17, consists of a radiating metallic patch or an array of patches situated on one side of a thin, nonconducting, substrate panel with a metallic ground plane situated on the other side of the panel. The metallic patch is normally made of thin copper foil or is copper-foil-plated with a corrosion resistive metal, such as gold, tin, or nickel. Each patch can be designed with a variety of shapes, with the most popular shapes being rectangular of circular. The substrate panel generally has a thickness in the range of 0.01 to 0.05 free-space-wavelength (λ_0). It is used primarily to provide proper spacing and mechanical support between the patch and its ground plane. It is also often used with high dielectric-constant material to load the patch and reduce its size. The substrate material should be low in insertion loss with a loss tangent of less than 0.005, in particular for large array application. Generally, substrate materials [45] can be separated into three categories in accordance with their dielectric constant:

1) Having a relative dielectric constant (ε_r) in the range of 1.0 to 2.0. This type of material can be air, polystyrene foam, or dielectric honeycomb.
2) Having ε_r in the range of 2.0 to 4.0 with material consisting mostly of fiber-glass reinforced Teflon.
3) With an ε_r between 4 and 10. The material can consist of ceramic, quartz, or alumina.

Although there are materials with ε_r much higher than 10, one should be careful in using these materials. As is discussed later, they can significantly reduce the antenna's radiation efficiency.

A single microstrip patch can be excited either by a coaxial probe or by a microstrip transmission line as shown in Fig. 1-17. For an array of microstrip patches, the patches can be combined either with microstrip lines located on the same side of the patches or with microstrip-lines/striplines designed on separate layers placed behind the ground plane. For the separate-layer configuration, each patch and its feed line are electrically connected either by a small-diameter metal post or by an aperture-coupling slot [46]. Regardless of the different layer configurations, tens or hundreds of patch elements in an array can be fabricated

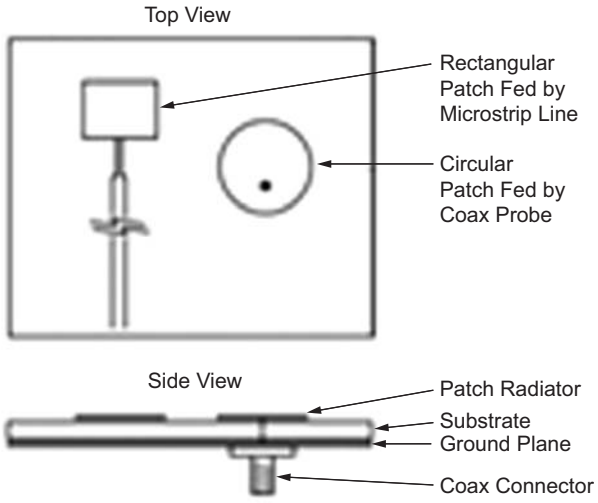

Fig. 1-17. Rectangular and circular microstrip patch antenna configurations.

by a single low-cost chemical etching process, and each single patch element does not need to be fabricated individually (as many other types of radiating elements do), which will lead to an overall lower antenna manufacturing cost.

1.4.2.2 Advantage and Disadvantage Trade-offs. There are advantages as well as disadvantages associated with the microstrip antenna. By understanding them well, one can readily design a microstrip antenna with optimum efficiency, minimum risk, and lower cost for a particular application.

The advantages of microstrip antennas when compared to conventional antennas (helix, horn, reflector, etc.) are:

- The extreme low profile of the microstrip antenna makes it lightweight, and it occupies very little volume of the structure or vehicle on which it is mounted. It can be conformally mounted onto a curved surface so it is aesthetically appealing and aerodynamically sound. Large aperture microstrip arrays on flat panels can be made mechanically foldable for space applications [47,48].
- The patch element or an array of patch elements, when produced in large quantities, can be fabricated with a simple etching process, which can lead to greatly reduced fabrication cost. The patch element can also be integrated or made monolithic with other microwave active/passive components.
- Multiple-frequency operation is possible by using either stacked patches [49] or a patch with a loaded pin [50] or a stub [51].

- There are other miscellaneous advantages, such as the low antenna-radar cross section (RCS) when conformally mounted on aircraft or missiles, and the microstrip antenna technology can be combined with the reflectarray technology [52] to achieve very large aperture requirement.

The disadvantages of the microstrip antennas are:

- The microstrip antenna generally has a narrow bandwidth of less than 5 percent. However, with technology advancement, up to 50 percent bandwidths have been achieved. Some of the techniques used are multiple stacked patches, thicker substrates with aperture slot coupling [53,54], external matching circuits [55], a sequential rotation element arrangement [56,57], parasitic coupling [58], U-slot feed [59], and L-shaped probe feed [60]. It is generally true that wider bandwidth is achieved with the sacrifice of increased antenna physical volume.
- The microstrip antenna can handle relatively lower RF power due to the small separation between the radiating patch and its ground plane (equivalent to small separation between two electrodes). Generally, a few tens of watts of average power or less is considered safe. However, depending on the substrate thickness, metal edge sharpness, and the frequency of operation, a few kilowatts of power for microstrip lines at X-band have been reported [61]. It should be noted that for space application, the power-handling capability is generally less than that for ground application due to a mechanism called multipacting breakdown [62].
- The microstrip array generally has a larger ohmic insertion loss than other types of antennas of equivalent aperture size. This ohmic loss mostly occurs in the dielectric substrate and the metal conductor of the microstrip line power-dividing circuit. It should be noted that a single patch element generally incurs very little loss because it is only a one-half wavelength long. The loss in the power-dividing circuit of a microstrip array can be minimized by using several approaches, such as the series feed power-divider lines [45, 63], waveguide and microstrip combined power dividers, and honeycomb or foam low-loss substrates. For very large arrays, transmit/receive (T/R) amplifier modules can be used on elements or subarrays to mitigate the effect of large insertion loss.

1.4.2.3 Material Consideration. The purpose of the substrate material of a microstrip antenna is primarily to provide mechanical support for the radiating patch elements and to maintain the required precision spacing between the patch and its ground plane. With higher dielectric constant of the substrate material, the patch size can also be reduced due to a loading effect to be discussed later. Certainly, with reduced antenna volume, higher dielectric

constant also reduces bandwidth. There is a variety of types of substrate materials. As discussed in Section 1.4.2.1, the relative dielectric constant of these materials can be anywhere from 1 to 10. Materials with dielectric constants higher than 10 should be used with care. They can significantly reduce the radiation efficiency by having overly small antenna volumes. The most popular type of material is Teflon-based with a relative dielectric constant between 2 and 3. This Teflon-based material, also named PTFE (polytetrafluoroethylene), has a structure form very similar to the fiberglass material used for digital circuit boards, but it has a much lower loss tangent or insertion loss. The selection of the appropriate material for a microstrip antenna should be based on the desired patch size, bandwidth, insertion loss, thermal stability, cost, etc. For commercial application, cost is one of the most important criteria in determining the substrate type. For example, a single patch or an array of a few elements may be fabricated on a low-cost fiberglass material at the L-band frequency, while a 20-element array at 30 GHz may have to use higher-cost, but lower loss, Teflon-based material. For a large number of array elements at lower microwave frequencies (below 15 GHz), a dielectric honeycomb or foam panel may be used as substrate to minimize insertion loss, antenna mass, and material cost with increased bandwidth performance. A detailed discussion of substrate material can be found in reference [45].

1.4.2.3.1 Space Application. When a microstrip antenna is used in space, its substrate material must survive three major effects related to the space environment: radiation exposure, material outgassing, and temperature change. These effects are separately discussed below.

Radiation exposure. Exposure to cosmic high-energy radiation is an important factor in space applications. Cosmic radiations, such as beta, gamma, and X-rays, are similar to nuclear radiation in many respects. They can damage materials after the prolonged exposure typical of a long space mission. The most popular substrate material, as discussed earlier, for the microstrip antenna is the Teflon-based PTFE. This material is generally combined with glass microfibers or ceramic filler to strengthen its mechanical properties. In either case, the component that is most susceptible to space radiation exposure damage is the PTFE. This is because of the low cohesive forces between PTFE molecular chains [64,65]. The primary effect of radiation on PTFE is the reduction of molecular weight by breaking the large polymer molecule into smaller parts. Oxygen is essential to some of the possible radiation induced reactions. Thus, the damage due to radiation is minimized in an oxygen-free environment such as space. The effect of molecular weight reduction is primarily on mechanical properties. There will be an increase in brittleness and reduction in tensile strength, modulus, and elongation. The electrical properties, such as dielectric constant and loss tangent, are also affected by electrical charge distributions in the resin which decays with time; and thus, the radiation

dose rate is important. The degree to which PTFE is affected is essentially a function of the amount of energy absorbed and is generally regardless of the types of radiation. For examples, beta, gamma, X-ray, etc. all have about the same effect. The radiation dose unit is the "rad" with one rad being equal to 100 ergs/gram. Table 1-2 is a summary of radiation doses in rads related to damage levels to PTFE.

Frequently, the dose rate of 10 rads/hour is quoted for the Van Allen Radiation Belt. At this rate, PTFE could operate for 5 to 50 years before a threshold level of damage would occur.

Material outgassing. Outgassing is another phenomenon that needs to be concerned when flying material in space. Outgassing causes a material to lose its mass in the form of gases or volatile condensable matter when subject to a vacuum, especially when it is heated as the antenna is exposed to sunlight in space. Losing mass will certainly affect the material's mechanical and electrical properties. Several substrate materials manufactured by Rogers Corporation have passed the outgassing test and are approved for space usage. Rogers' composites of PTFE with either glass microfibers, ceramic filler, or Thermoset Microwave Material (TMM) temperature stable hydrocarbon have all shown outstanding resistance to outgassing (see Table 1-3), according to data

Table 1-2. Radiation amount in rads for damage to PTFE material.

	In Air	In Vacuum
Threshold level	$2–7 \times 10^4$	$2–7 \times 10^5$ or more
50% tensile strength remains	10^6	10^7 or more
Retains 100% elongation	$2–5 \times 10^5$	$2–5 \times 10^6$

Table 1-3. Outgassing test results of Rogers substrate material.

Material Type	Rogers Duroid 5870	Rogers Duroid 5880	Rogers Duroid 6002	Rogers Duroid 6010	TMM 3	TMM 10
Material Composition	PTFE with Glass Microfiber	PTFE with Glass Microfiber	PTFE with Ceramic Filler	PTFE with Ceramic Filler	Thermoset Polymer Composite	Thermoset Polymer Composite
Dielectric constant	2.3	2.2	2.9	10.0	3.0	10.0
% TML	0.05	0.03	0.02	0.03	0.04	0.06
% CVCM	0.0	0.0	0.01	0.0	0.0	0.0
% WVR	0.04	0.02	0.01	0.02	0.03	0.04

compiled by NASA test procedure SP-R-0022A [66,67]. The test procedure consists of vacuum heating of 100- to 300-mg specimens in an enclosure. The total mass loss (TML), collected volatile condensable materials (CVCM), and water vapor recovered (WVR) are expressed as a percentage of the original specimen mass. In general, materials with a TML greater than 1 percent or a CVCM greater than 0.1 percent should be avoided in space application.

Temperature change. The effect of temperature in space on electrical and physical properties of the substrate material must be taken into consideration when designing a microstrip antenna. Since the space is a vacuum without conduction medium, the temperature of an object could be extremely cold, e.g., –100 deg C, when it is not exposed to the sunlight or it could become very hot, e.g., +100 deg C, when it is directly illuminated by the Sun over a period of time. The effects of these extreme temperatures could cause change to the microstrip substrate material include dielectric constant (ε) and substrate thickness, which will together cause an impedance change of the microstrip patch or transmission line. Table 1-4 gives examples of the expected response of microstrip transmission line to temperature change [45,68] for both non-woven-glass PTFE and ceramic-loaded PTFE.

In addition to the above two substrate materials, Rogers corporation developed a substrate material that is very insensitive to temperature changes and is named the Thermoset Microwave Material (TMM). It is a highly filled inorganic resin composite with tightly controlled dielectric constant value. Over a temperature range of ±100 deg C, the TMM only changed its dielectric constant value by less than 0.5 percent. At the high temperature of 300 deg C, the TMM exhibited a thermal expansion amount of 1/3 of that of the PTFE material. This TMM is highly recommended for space applications where there is a concern regarding wide ranges of temperature variation.

Table 1-4. Example of microstrip substrate property change vs. temperature change in vacuum.

Temperature (deg C)	Percent Change from 20 deg C Value; Frequency = 18 GHz, 50-ohm Line					
	Non-Woven-Glass PTFE			Ceramic-Loaded PTFE		
	Thickness	ε	Impedance	Thickness	ε	Impedance
–100	–1.31	1.36	–1.60	–0.26	5.06	–2.2
–60	–0.89	1.02	–1.20	–0.19	3.38	–1.4
+70	1.31	–0.53	1.20	0.15	–2.27	1.0
+110	2.37	–0.87	2.20	0.19	–3.42	1.6
+150	3.42	–1.50	3.40	0.26	–4.47	2.0

1.4.3 Analysis, Design, and CAD Tools

1.4.3.1 Analysis Techniques. The main reason for developing an analytic model for the microstrip antenna is to provide a means of designing the antenna without costly and tedious experimental iteration. Also, it may help the designer to know the physical mechanisms of how the microstrip antenna operates. With an analysis technique, the engineer should be able to predict the antenna performance qualities, such as the input impedance, resonant frequency, bandwidth, radiation patterns, and efficiency. There are many different analysis techniques that have been developed for analyzing the microstrip antennas. However, the most popular ones can be separated into four groups: transmission-line circuit model, multimode cavity model, moment method, and finite difference time domain (FDTD) approach. They are briefly discussed below:

1.4.3.1.1 Transmission-Line Circuit Model. A microstrip patch, operating at its fundamental mode, is essentially a ½λ-long microstrip transmission line and can be represented by an equivalent circuit network [69,70]. For a rectangular or square patch, its radiation is basically generated from its two edges with two equivalent slots along the resonating dimension, as shown in Fig. 1-18. Thus, the microstrip radiator can be characterized by two slots separated by a transmission line, where each slot is represented by a parallel circuit of conductance (G) and susceptance (B). The complete patch antenna can be represented by the equivalent network shown in Fig. 1-19 [69]. This transmission line model is simple, intuitively appealing, and computationally fast, but it suffers from limited accuracy. For examples, this model lacks the radiation from the non-radiating edges of the patch, and it has no mutual coupling between the two radiating slots. Although, this model has led to a much improved version [70], it lacks the flexibility and generalization of analyzing other shapes of patches.

1.4.3.1.2 Multimode Cavity Model. Any microstrip radiator can be thought as an open cavity bounded by the patch and its ground plane. The open edges can also be represented by radiating magnetic walls. Such a cavity will support multiple discrete modes in a manner similar to that of a completely enclosed metallic cavity. As an example, for a rectangular patch with relatively dielectric constant of ε_r, substrate thickness of h, and patch dimensions of $w \times l$ as that shown in Fig. 1-18, its total electric field in the cavity can be expressed as the sum of the fields associated with each sinusoidal mode [71]:

$$E_z(x,y) = \sum_m \sum_n C_{mn} \bullet \cos\left(\frac{m\pi}{w}\right)x \bullet \cos\left(\frac{n\pi}{l}\right)y \qquad (1.4\text{-}1)$$

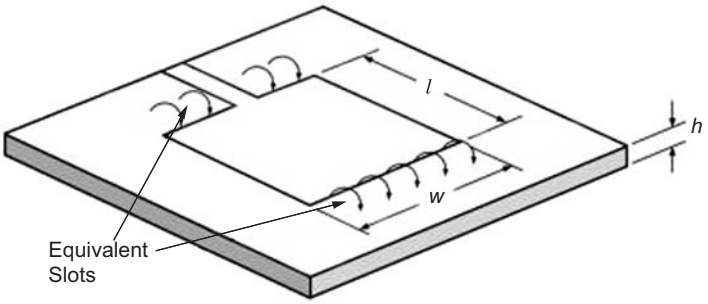

Fig. 1-18. Microstrip patch with two equivalent radiating slots.

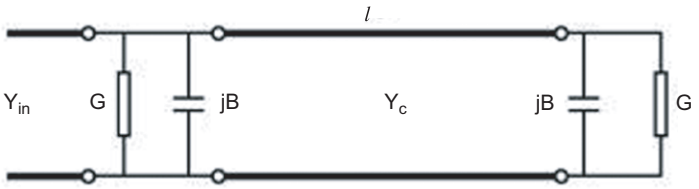

Fig. 1-19. Equivalent network of microstrip patch element.

where C_{mn} is a constant that depends on the feed location, *w* and *l* dimensions, and the dielectric constant. Due to the very thin substrate, the fields are assumed to be *z*-directed only with no variation in the *z*-direction. The most important dominant mode is the TM_{10} mode, which can be obtained if the dimension *l* is approximately $\lambda_g/2$ (λ_g is the effective wavelength in the dielectric). By knowing the fields at the edges of the patch, the equivalent edge magnetic currents can be determined and integrated to find the far-field radiation patterns. By knowing the total radiated power and the input power, one can also determine the input impedance. The cavity model technique allows one to know the mode structure underneath the patch; and therefore, its physical mechanisms are more easily understood, such as its resonating and cross-polarization behaviors. However, because it assumes the field has no *z*-variation, its solution is not very accurate; in particular, when the substrate becomes thick (for wider bandwidth consideration). Also the calculation of mutual coupling between patches in an array environment is very tedious and not accurate.

1.4.3.1.3 Moment Method. The radiated fields of a microstrip antenna can be determined by integrating all the electrical currents on its metallic surfaces via the integral equation approach whose solution is obtained by the so-called moment method. This integral equation approach [72–75] is analyzed by first

solving the vector potential $\vec{A}(x,y,z)$ which satisfies the wave equation with J_s being the patch surface current:

$$\nabla^2\vec{A}^I + k^2\vec{A}^I = -juJ_S(x,y) \quad \text{in the dielectric (region I)} \tag{1.4-2}$$

and

$$\nabla^2\vec{A}^{II} + k_0^2\vec{A}^{II} = 0 \quad \text{in the free space (region II)} \tag{1.4-3}$$

then the vector potential may be given as

$$\vec{A}^{I,II}(x,y,z) = \iint_{patch} \vec{J}_S(x',y') \bullet \overline{\overline{G}}^{I,II}\left(\frac{x,y,z}{x',y',z'}\right) dx',dy' \tag{1.4-4}$$

where $\overline{\overline{G}}^{I,II}$ is the dyadic Green's function for regions I and II. Region I contains the substrate, while region II being the free-space area above the substrate. The electric field $\vec{E}$ everywhere is given by

$$\vec{E}(x,y,z) = -j\omega\vec{A} + \frac{j\omega}{k^2}\vec{\nabla}(\vec{\nabla}\bullet\vec{A}) \tag{1.4-5}$$

By weighting the Green's function of Eq. (1.4-4) with the unknown electrical current density and integrating over the patch, the radiated electric or magnetic field can be calculated anywhere outside the dielectric. An integral equation for the unknown current is obtained by forcing the total tangential electric field on the patch surface to zero. Using the proper basis and testing functions for the unknown current, the integral equation is then discretized and reduced to a matrix equation:

$$[E] = [Z_{mn}][J] \tag{1.4-6}$$

where the impedance matrix element has the form:

$$\begin{aligned} Z_{mn} = \int_x\int_y\int_{x'}\int_{y'}\int_{k_x}\int_{k_y} & J^m(x,y)\cdot G(k_x,k_y)\cdot J^n(x',y') \\ & \cdot e^{-jk_x(x-x')}\cdot e^{-jk_y(y-y')} dk_y dk_x dy' dx' dy dx \end{aligned} \tag{1.4-7}$$

where $G(k_x,k_y)$ is the Fourier transform of the Green's function given in Eq. (1.4-4), J^m is the *m*th expansion mode, and J^n is the *n*th weighting or testing mode. Equation (1.4-7) has been solved by two different approaches. One uses the space domain approach [74,75], where the spectral variables k_x

and k_y are transformed to spatial polar coordinates α and β. The other approach uses the spectral domain approach [72,73] where the spatial integrations in Eq. (1.4-7) are done in closed form, which results in an integral in spectral domain only. Nevertheless, both approaches are derived to solve, via the method of moment and matrix inversion, for the patch surface current, which is then used to determine the properties of the microstrip antenna, such as the input impedance and radiation patterns. The moment method, a two-dimensional integration technique, is considered very accurate and includes the effects of mutual coupling between two surface current elements as well as the surface wave effect in the dielectric. It is computationally more time consuming than the transmission-line model and the cavity model. However, it is more computationally efficient than the three-dimensional technique to be discussed in the following subsection.

1.4.3.1.4 Finite-Difference Time-Domain (FDTD) Method. The previous moment method is basically a two-dimensional solver. It solves for the 2-D surface current on the microstrip patch. The FDTD method, on the other hand, is a three-dimensional solver. It solves for the electromagnetic fields in a 3-D volumetric space. Thus, it can solve more complex problems with 3-D interfaces and connections, such as the multi-layer microstrip antenna with complicated multi-layer connections. However, it suffers from laborious computation time, and it is not suitable (with current computer capability) for solving large microstrip array problems. The FDTD method [76–78] uses Yee's algorithm [79] to discretize Maxwell's equation in three-dimensional space and in time. The volume-space of interest is discretized into many cubes, and the E and H fields are then solved through Maxwell equations with given boundary conditions from cube to adjacent cubes. This is illustrated briefly in the following Maxwell's curl equations:

$$\mu \cdot \frac{\partial H}{\partial t} = -\nabla \times E \tag{1.4-8}$$

$$\varepsilon \cdot \frac{\partial E}{\partial t} = \nabla \times H \tag{1.4-9}$$

With time and space discretized, the E- and H-fields are interlaced within the spatial 3-D grid. For example, Eq. (1.4-9) can be discretized for the x-directed E field:

$$E_x^{n+1}(i,j,k) = E_x^n(i,j,k) + \frac{\Delta t}{\varepsilon}\left[\frac{H_z^{n+1/2}(i,j+1,k) - H_z^{n-1/2}(i,j,k)}{\Delta y}\right] - \frac{\Delta t}{\varepsilon}\left[\frac{H_y^{n+1/2}(i,j,k+1) - H_y^{n-1/2}(i,j,k)}{\Delta z}\right] \tag{1.4-10}$$

where Δx, Δy, and Δz are the space steps in the x-, y-, and z-directions, and Δt is the time step. The same discretization can be carried out for Eq. (1.4-8).

Now, Maxwell's equations have been replaced by a set of computer-recognizable finite-difference equations, which can be solved sequentially from cube to cube once the known boundary conditions are applied. Certainly, this cube-to-cube solver cannot continue indefinitely outside the volume of interest and must be terminated. However, the fields will bounce back from any terminating boundary (which does not happen in reality) and disturb the correct solution. The solution is to use the electromagnetic absorbing boundaries to be set up outside the areas of interest and to absorb all outgoing fields. One significant advantage of the FDTD method is that, by discretizing time, one is able to see on a computer screen how the field is actually traveling and radiating in time sequence in a complicated antenna/circuit configuration.

1.4.3.2 Design Methodology. The previous section presented different techniques to analyze the microstrip antenna. To ease the design process, these different analysis techniques have been developed into several user-friendly computer-aided-design (CAD) tools by several institutions. However, an analysis technique or a CAD tool, by itself, cannot generate an antenna design. It can only analyze a design and provide calculated performance results for a design. The basic antenna design has to originate from human experience, knowledge, and innovation, even though an optimal and accurate design often cannot be achieved without an analysis tool. Figure 1-20 depicts a typical microstrip antenna development process. The block labeled "Computer Analysis Software" represents the central processing unit into which a human must enter the proper design data to initiate the design process. The block labeled "Antenna Design Techniques" represents the knowledge for generating a set of preliminary input design data, which is the main subject of this section. It includes techniques to design array configurations, patch elements, and power division transmission lines, which are separately discussed in the following subsections.

1.4.3.2.1 Array Configuration Design. Before performing a detailed design, it is critically important to lay out the most suitable array configuration for a particular application. Array configuration variables include series feed or parallel feed, single layer versus multiple layers, substrate thickness, dielectric

constant, array size, patch-element shape, element spacing, etc. The selection of the proper configuration depends upon many factors, such as the required antenna gain, bandwidth, insertion loss, beam angle, grating/sidelobe level, polarization, and power-handling capability. Several important microstrip array configurations that often challenge the skills of antenna designers are presented below.

Series feed. In a series feed configuration [45,80], multiple elements are arranged linearly and fed serially by a single transmission line. Multiples of these linear arrays can then be connected together serially or in parallel to form a two-dimensional planar array. Figure 1-21 illustrates two different configurations of the series feed method. The in-line feed [81,82] has the transmission line serially connected to two ports of each patch and is sometime called the two-port series feed. The out-of-line feed [63] has the line connected to one port of each patch and is thus called one-port series feed. The in-line

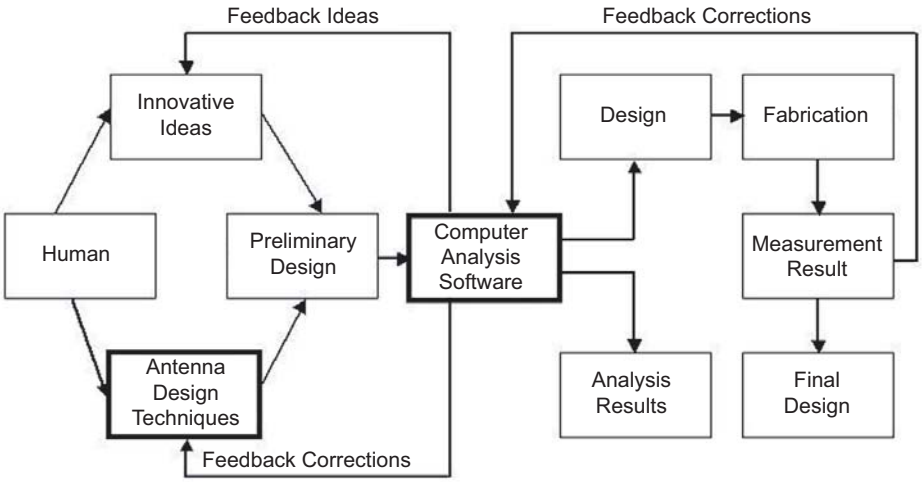

Fig. 1-20. Microstrip antenna development procedures.

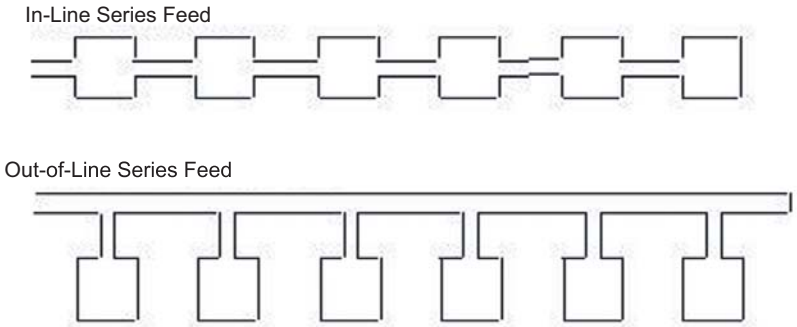

Fig. 1-21. Series-fed microstrip arrays.

feed array occupies the smallest real estate with the lowest insertion loss, but it generally has the least polarization control and the narrowest bandwidth. The in-line feed, as shown in Fig. 1-21, is generally more suitable for generating linear polarization than circular polarization. It has the narrowest bandwidth because the line goes through the patches, and, thus, the phase between adjacent elements is not only a function of line length but also of the patches' input impedances. Since the patches are amplitude weighted with different input impedances, the phases will be different for different elements and will change more drastically as frequency changes due to the narrow-band characteristic of the patches.

The series feed can also be classified into two other configurations: resonant and traveling-wave [45,80]. In a resonant array, the impedances at the junctions of the transmission lines and patch elements are not matched. The elements are spaced multiple integrals of one wavelength apart so that the multiply bounced waves, caused by mismatches, will radiate into space in phase coherence in the broadside direction. Because of this single- or multiple-wavelength element spacing, the beam of the resonant array is always pointed broadside. For the same reason, the bandwidth of a resonant array is very narrow, generally less than 1 percent. With a slight change in frequency, the one-wavelength spacing no longer exists, thereby causing the multiply bounced waves not to radiate coherently but, instead, to travel back to the input port as mismatched energy. Both the in-line and out-of-line feed arrays can be designed to be of the resonant type.

For the traveling-wave array type, the impedances of the transmission lines and the patches are generally all matched, and the element spacing can be one wavelength for broadside radiation, or less than one wavelength for off-broadside radiation. Because the energy travels toward the end of the array without multiple reflections, there is generally a small amount of energy remaining after the last element. This remaining energy can be either absorbed by a matched load or reflected back to be re-radiated in phase for broadside radiation [63]. The array can also be designed such that the last element radiates all of the remaining energy [63]. The traveling-wave array has a wider impedance bandwidth, but its main beam changes in direction as frequency changes. A general rule-of-thumb for the frequency-scanned beam of a traveling-wave array is one degree of beam scan per one percent of frequency change. For an instantaneous wideband signal, such as a pulsed system, a beam broadening effect will occur. Both the in-line and out-of-line series-fed arrays of Fig. 1-21 can be designed as the traveling-wave type. There are also other forms of series-fed microstrip arrays: chain, comb line, rampart line, Franklin, and coupled dipole [45,80]. These arrays operate similarly to the arrays shown in Fig. 1-21, except that they use microstrip radiators with different radiating mechanisms.

Parallel feed. The parallel feed, also called the corporate feed [83], is illustrated in Fig. 1-22. In the parallel feed, the patch elements are fed in parallel by the power-division transmission lines. The transmission line divides the power into two branches, and each branch divides again until it reaches the patch elements. In a broadside-radiating array, all the parallel division lines have the same length. For a series-fed array, the insertion loss is generally less than that of a parallel-fed array because most of the insertion loss occurs in the transmission line at the first few elements, and very little power remains at the end of the array. Most of the power has already been radiated by the time the end elements are reached. Despite its higher insertion loss, the parallel-fed array does have one significant advantage over the series-feed, which is its wideband performance. Since all elements in a parallel-fed array are fed by equal-length transmission lines, when the frequency changes, the relative phases between all elements will remain the same; and thus, no beam squint will occur. The bandwidth of a parallel-fed microstrip array is limited by two factors: the bandwidth of the patch element and the impedance matching circuit of the power-dividing transmission lines, such as the quarter-wave transformer. Whereas a series-fed array can only achieve a bandwidth of 1 percent or less, a parallel-fed array can achieve a bandwidth of 15 percent or more.

Hybrid series/parallel feed. An example of a hybrid series/parallel-fed array is depicted in Fig. 1-22, where a combination of series and parallel feed lines is used. In a hybrid array [63], the smaller series-fed subarray has a broader beamwidth, which will suffer only a small gain degradation due to beam squint with frequency change. Hence, a hybrid array will achieve a wider bandwidth than a purely series-fed array having the same aperture size. Of course, because of its partial parallel feed, the insertion loss of hybrid array is higher than that of a purely series-fed array. This hybrid technique gives the

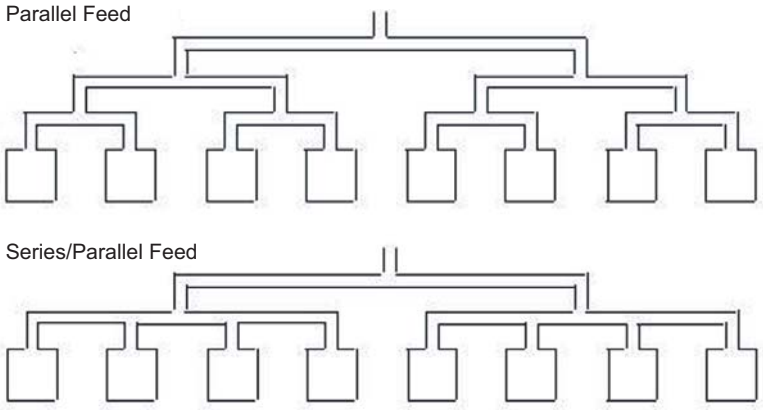

Fig. 1-22. Configurations of parallel feed and hybrid parallel/series feed microstrip arrays.

designer an opportunity to make design trade-offs between bandwidth and insertion loss.

Regardless of whether the array is parallel or series fed, two recently developed arraying techniques can be employed to significantly improve the array's performance. The first is to reduce cross-polarization (cross-pol) radiation in a planar array by oppositely exciting adjacent rows or columns of elements in phase and in orientation [63], as shown in Fig. 1-23(a). Another technique is shown in Fig. 1-23(b) for a circularly polarized array, in which every adjacent four elements placed in a rectangular lattice can be sequentially

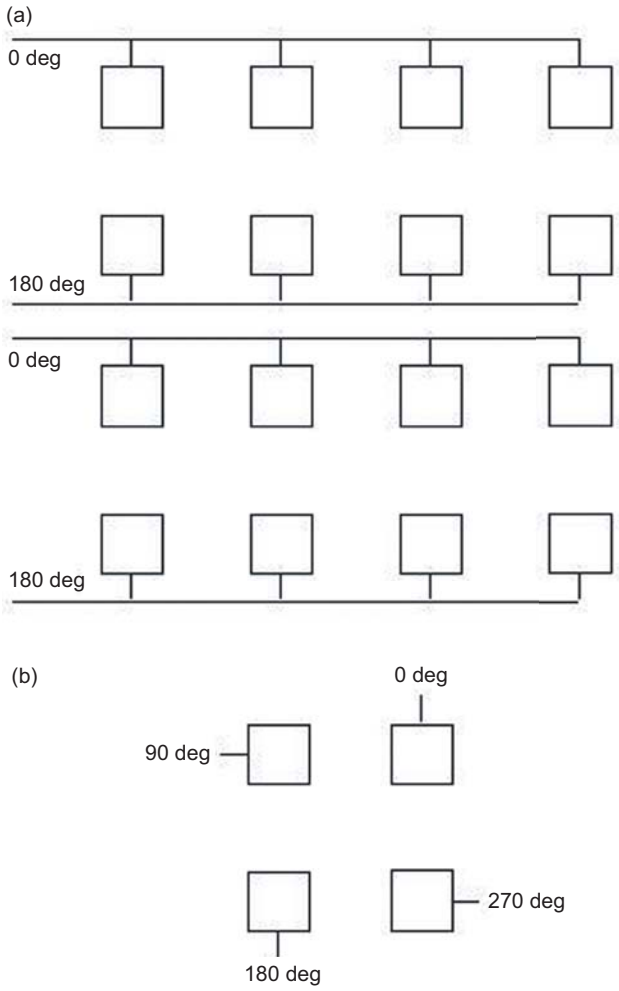

Fig. 1-23. Microstrip array configuration: (a) rows excited by opposite phases and orientations and (b) sequentially arranged four-element subarray.

arranged in both phase and orientation to achieve good circular polarization over a wide bandwidth [56,57].

Single-layer or multilayer design. A microstrip array can be designed in either a single-layer or multilayer configuration. The factors that determine this choice are complexity and cost, sidelobe/cross-pol level, number of discrete components, polarization diversity, bandwidth, and so on. When the given electrical requirements are relaxed, a single-layer design will generally suffice. If all transmission lines and patch elements are etched on the same layer, it will be low in manufacturing cost. However, when extremely low sidelobe or cross-pol radiation (e.g., less than –30 dB) is required, the double-layer design seems to be the better choice. With all transmission lines etched on the second layer behind the radiating patch layer, the ground plane in the middle will shield most of the leakage radiation of the lines from the patch radiation. This leakage radiation becomes more pronounced when discrete components, such as monolithic microwave integrated circuit (MMIC) T/R modules and phase shifters, are placed in the transmission line circuits. Thus, it is more desirable to place all discrete components behind the radiating layer in a multilayer configuration. When dual-linear or dual-circular polarization is required with high polarization isolation, it is often more desirable to design the feed circuits of the two polarizations on two separate layers, as shown in Fig. 1-24. When a radiating patch having a thick substrate is used to achieve wider bandwidth, it is best to design the transmission lines on a separate layer because the lines may become too wide to be practical if designed on the same thick layer as the radiating patches. In other cases, when an extremely wide bandwidth requirement can be met only by using multiple stacked patches [53], the multilayer design becomes the obvious choice. With the advancement of the

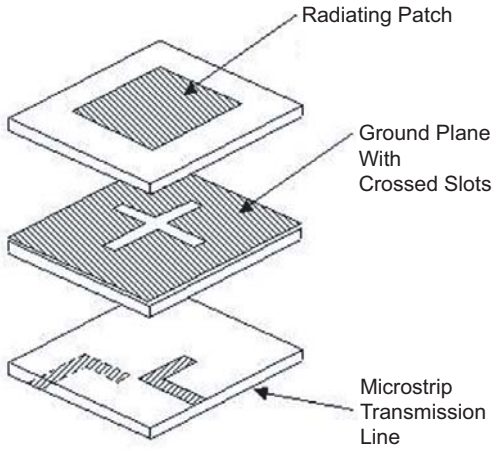

Fig. 1-24. Multilayer dual-polarized microstrip patch element.

aperture-coupling technique that allows the transmission line to feed the patch, the multilayer design becomes much more feasible than those using many feed-through pins.

Other array configuration. When designing a microstrip array, various antenna parameters, such as substrate thickness, dielectric constant, and element spacing, can all play important roles in determining an array's performance. Substrate thickness determines bandwidth, as well as the antenna's power handling capability [61]. The thicker the substrate, the more power it can handle. For ground applications, a thicker microstrip antenna (>0.05 λ_0 thick) can generally handle several hundred to a few thousand watts of peak power. For space applications, due to the effect of multipacting breakdown [62], only tens of watts are attainable. The dielectric constant of the substrate material also affects the bandwidth: the higher the dielectric constant, the narrower the bandwidth. Because of the loading effect, a higher dielectric constant reduces the patch resonant size and, hence, increases the element beamwidth. A wider element beamwidth is desirable for a large-angle-scanning phased array. Another important array design parameter is element spacing. It is often desirable to design a microstrip array with larger element spacing so that more real estate can be made available for transmission lines and discrete components. However, to avoid the formation of high grating lobes, element spacing is limited to less than 1 λ_0 for broadside beam design and less than 0.6 λ_0 for a wide-angle scanned beam. In designing a wide-angle scanned microstrip phased array, substrate thickness, dielectric constant, and element spacing are all important parameters that need to be considered for reducing mutual coupling effects and avoiding scan blindness [84].

1.4.3.2.2 Patch Element Design. Patch elements come in various shapes, such as rectangular, square, circular, annular ring, triangular, pentagonal, and square or circular with perturbed truncations. These different shapes can often be used to meet various challenging requirements. For example, the rectangular patch, used for linearly polarized applications, can achieve slightly wider bandwidth than the square or circular patch. However, the square or circular patch, unlike the rectangular patch, can be excited orthogonally by two feeds to achieve circular polarization. In addition, the circular patch can be designed to excite higher-order modes for generating different-shaped patterns [85,86]. The pentagonal patch, as well as the square or circular patch with a small perturbation, can be used to generate circular polarization with only a single feed [45], which is often a desirable feature when simplicity and low insertion loss are required.

It should be noted that all of these patch shapes can be accurately analyzed and designed by the full-wave moment method discussed in Section 1.4.3.1.3. However, designing a patch using the moment method or any other rigorous technique requires a priori knowledge of the approximate size of the patch so

that appropriate dimensions, rather than random numbers, can be input to the analysis computer code. With a few iterations of the computer code, the designer should be able to determine the precise dimensions of the microstrip antenna. Once the dimensions are known, other parameters (e.g., input impedance, bandwidth, and radiation patterns) can be accurately computed by the full-wave moment method. The above-mentioned a priori knowledge of the approximate patch size can be acquired through experience, or derived by simple closed-form equations if available. Fortunately, the two most popular and often-used patch shapes, rectangular (or square) and circular, do have simple closed-form equations available. These equations, in predicting the resonant frequency, can generally achieve an accuracy of within 2 percent. For the fundamental-mode rectangular patch, the simple equation [44] is given by

$$f = \frac{c}{2(L+h)\sqrt{\varepsilon_e}} \tag{1.4-11}$$

where

$$\varepsilon_e = \frac{\varepsilon_r + 1}{2} + \frac{\varepsilon_r - 1}{2}\left(1 + \frac{12h}{w}\right)^{-1/2} \tag{1.4-12}$$

f is the resonant frequency, c is the speed of light, L is the patch resonant length, h is the substrate height, ε_r is the relative dielectric constant of the substrate, and w is the patch non-resonant width.

For the circular patch with TM_{mn} mode, the simple design equation is given by [44,85]

$$f = \frac{\chi_{mn} c}{2\pi a_e \sqrt{\varepsilon_e}} \tag{1.4-13}$$

where

$$a_e = a\left\{1 + \frac{2h}{\pi a \varepsilon_r}\left[\ln\left(\frac{\pi a}{2h}\right) + 1.7726\right]\right\}^{1/2} \tag{1.4-14}$$

f, c, h, and ε_r are as defined for the rectangular patch design equation, a is the patch's physical radius, χ_{mn} is the mth zero of the derivative of Bessel's function of order n, n represents the angular mode number, and m is the radial mode number.

There is no significant difference in performance between the fundamental-mode rectangular patch and a fundamental-mode circular patch. A circular patch does have the advantage of offering higher-order-mode performance with

different diameters and differently shaped radiation patterns [85,86]. These patterns can be either linearly or circularly polarized, depending on the configuration of the feed excitations.

1.4.3.2.3 Power Division Transmission Line Design. One of the principal shortcomings of a microstrip array with a coplanar feed network is its relatively large insertion loss, especially when the array is electrically large or when it is operating at a higher frequency. Most of the losses occur in the power-division transmission line's dielectric substrate at microwave frequencies. At millimeter-wave frequencies, the loss in the copper lines becomes significant. It is thus crucially important to minimize insertion loss when designing the power division transmission lines. In order to minimize insertion loss, the following principles should be observed: The impedances of the power-division lines should be matched throughout the circuit; low-loss material should be used for the substrate; at higher frequencies, the roughness of the metal surfaces that face the substrate should be minimized; and the array configuration should be designed to minimize line length (as described in Section 1.4.3.2.1). This section discusses the impedance-matching techniques for power division circuits. Every designer has a somewhat different approach to design a microstrip circuit, but they all require the knowledge of the fundamental circuit theory and basic equations presented in the following subsections. In a good design with well matched lines, the microstrip circuit will suffer less from mismatch losses and radiation leakage losses. Although most of the microstrip circuit components shown here are very fundamental and have been presented elsewhere in separate articles, they are collected here for microstrip array designs.

A very important circuit component in most microstrip array design is the quarter-wave transformer (see Fig. 1-25), which transforms one impedance to another. The proper impedances for this transformation are given by the following equation:

$$Z_2 = \sqrt{Z_1 \times Z_3}\,. \tag{1.4-15}$$

In Fig. 1-25, the symbol λ_g is the effective wavelength in the microstrip line, and its equation is given in [87]. This quarter-wave transformer is not only used to transform between two different impedances, but it also should be used where there is a possible impedance mismatch. For example, for the single-patch circuit shown in Fig. 1-26, the quarter-wave section should be used at the coax input feed location and at the input to the patch. At both of these locations, there may be some residual mismatches. For instance, the 250-ohm input impedance of the patch may not be accurately predicted by a CAD due to inaccuracy in the model or inaccurate specification of the dielectric constant by the manufacturer, and the coax feed may not be perfectly matched to the

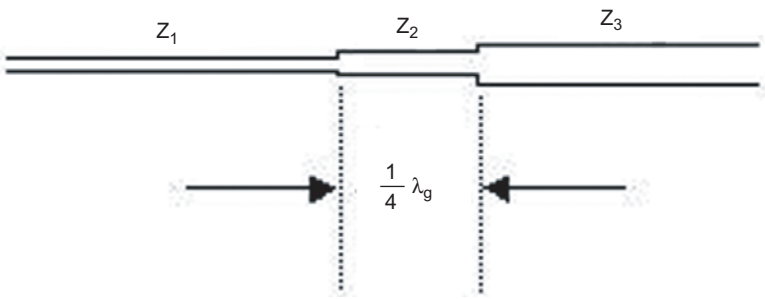

Fig. 1-25. Microstrip quarter-wave impedance transformer.

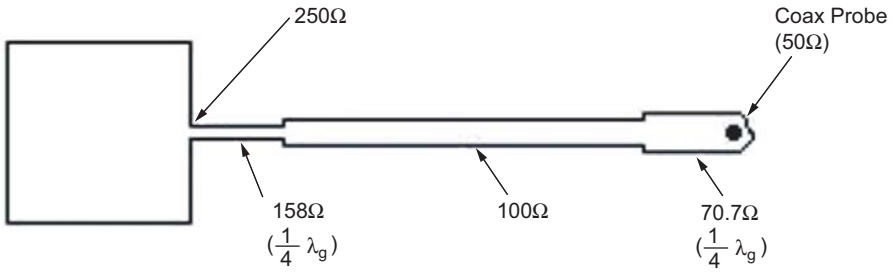

Fig. 1-26. Microstrip line feeding a patch element with impedance-matched quarter-wave sections.

microstrip line due to possible air gap, fabrication tolerance, etc. The quarter-wave transformer can be used to minimize such mismatches. This is because of the quarter-wave line's round-trip phase delay (180 deg), and thus the reflected signal due to mismatch occurring at one location will cancel with that reflected from another location a quarter-wave distance away.

In a microstrip line with a given substrate height and dielectric constant, the width of line governs the characteristic impedance. To determine the microstrip line width with a specified line impedance, simple closed-form equations are given in [87]. These equations are generally accurate enough without resort to a full-wave analysis or a CAD tool, unless there is a significant amount of mutual coupling between lines.

Another important microstrip circuit component used quite often is the two-way power divider illustrated in Fig. 1-27. In this figure, the input power P_1 with microstrip line width W_1 and impedance Z_1 is split into powers P_2 and P_3 with line widths W_2 and W_3 and impedances Z_2 and Z_3, respectively. The fundamental equations for this simple power division are

$$Z_1 = Z_2 \times Z_3 \div \left(Z_2 + Z_3\right), \quad P_2 = \left(Z_1 / Z_2\right) \times P_1, \quad P_3 = (Z_1 / Z_3) \times P_1$$
$$angle \;\; A = \arctan\left(W_3 / W_1\right) \tag{1.4-16}$$

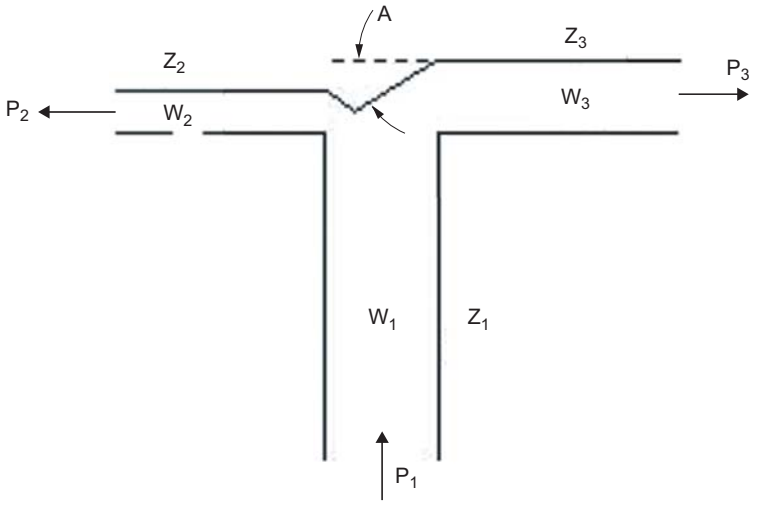

Fig. 1-27. Microstrip two-way power divider.

Since there could be a small amount of impedance mismatch due to fabrication tolerance or other types of inaccuracies, it is more practical, as explained previously, to design the power divider with a quarter-wave transformer as shown in Fig. 1-28.

A three-way power divider, illustrated in Fig. 1-29, can also be designed based on the equations of the two-way power divider. The design equations for this three-way divider are

$$Z_1 = \frac{Z_4 \times Z_S}{Z_4 + Z_S}, \qquad Z_S = \frac{Z_2 \times Z_3}{Z_2 + Z_3}$$
$$P_4 = \frac{Z_1}{Z_4} \times P_1, \qquad P_3 = \frac{Z_1}{Z_3} \times P_1, \qquad P_2 = \frac{Z_1}{Z_2} \times P_1 \tag{1.4-17}$$

With the above equations for the two-way and three-way power dividers, one should be able to derive the equations for any multiple power division with different combinations of power ratios.

The above power dividers are named reactive power dividers because the power divisions are based on the reactive impedances of the lines. In addition to these reactive power dividers, two other types of power dividers are briefly presented here. One is the branch-line hybrid divider shown in Fig. 1-30, and the other is the Wilkinson power divider shown in Fig. 1-31. A reactive power divider does not provide isolation between the divided ports. Any mismatch at the end of a divided port will send portion of the returned power into other

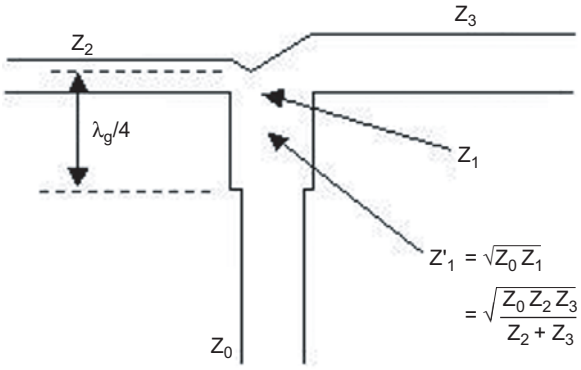

Fig. 1-28. Microstrip two-way power divider with a quarter-wave transformer.

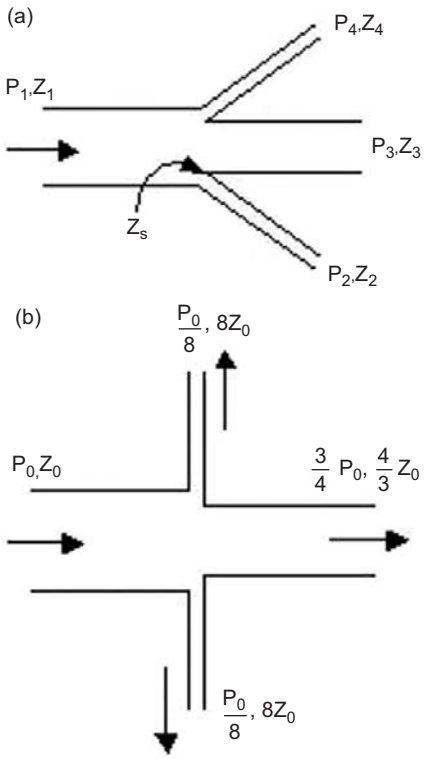

Fig. 1-29. Two methods (a and b) to configure microstrip three-way power dividers.

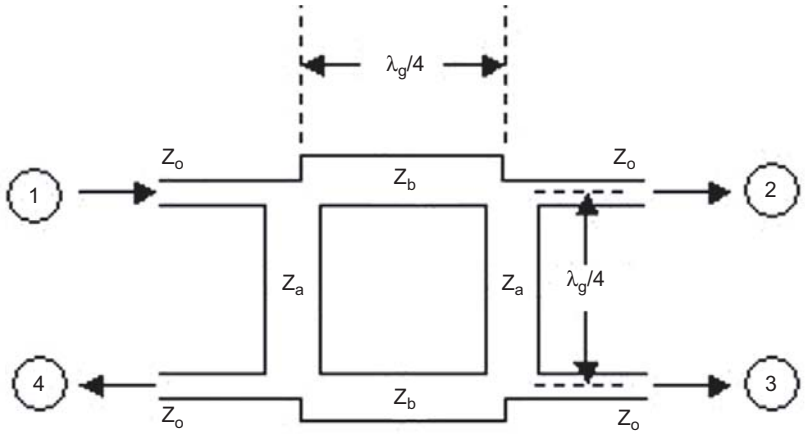

Impedances: $\frac{Z_o}{Z_a} = a$; $\frac{Z_o}{Z_a} = b$

$b^2 - a^2 = 1$ ····· Matched Condition

Power Ratios: $\frac{P_2}{P_1} = (\frac{1}{b})^2$; $\frac{P_3}{P_1} = (\frac{a}{b})^2$

Fig. 1-30. Microstrip hybrid branch-line power divider.

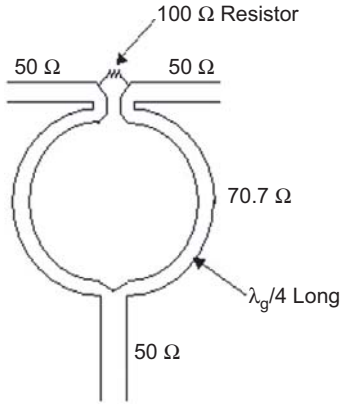

Fig. 1-31. Microstrip Wilkinson power divider.

ports, which can cause high radiated sidelobe and cross-pol levels. Both the branch-line hybrid and the Wilkinson dividers can generally provide more than 20 dB of isolation between divided ports. The branch-line hybrid, in addition to its capability of providing 90-deg phase difference between its two output ports, can also achieve different power divisions. In Fig. 1-30, any mismatch-reflected power from port 2 or 3 will go into the loaded port 4 and not into the input

port 1. For the Wilkinson divider depicted in Fig. 1-31, mismatch-reflected power from the two divided ports will be mostly absorbed by the 100-ohm resistor.

1.4.3.3 CAD Tools. In the previous section, design methodology, a typical microstrip antenna development process is depicted in a block diagram (see Fig. 1-20). Although all CAD tools available today can only provide analysis and not a design, they do assist significantly in achieving the final design. For example, an engineer generates an initial design and then inputs the design dimensions and configuration into a CAD to calculate a set of performance results, such as input return loss and radiation patterns. Generally, the initial results will not meet the given requirements, in particular, for a complicated design. The engineer, using his experience and knowledge, will perform corrections on the design and then input to the CAD again as indicated in Fig. 1-20. This iterative process may take several times until satisfactory results are achieved. Before CAD tools were available, the engineer could only perform hardware verification of the design and might have needed many iterations. This hardware verification step requires significantly longer time with higher cost than computer simulation. For a large array, the cost of iterative hardware verification soars with array size and complexity. Academic researchers have been prolific in generating analytical and numerical solutions for a wide variety of microstrip antennas and arrays, often with a high degree of accuracy and efficiency. But this area of work is generally performed primarily for graduate student theses or publications, and the software are seldom completely written, validated, or documented for other users. Researchers in industry may be more pragmatic when developing comparable solutions for specific antenna geometry, but such software is often considered proprietary.

From the above discussion, there is a clear need for a CAD tool. The first commercial CAD tool for microstrip antennas became available in the early 1990s, and in the past decade, the number of commercial tools has mushroomed with more than ten available in the world. Table 1-5 lists some commercial software packages that can be used for microstrip antenna analysis and design.

Among the CAD tools, the Ensemble and IE3D, that use full-wave moment method, are the most popular. These two PC-based software were on the market much earlier than the other ones for microstrip antenna application. Through up-grades and modifications, they became more efficient, less prone to errors, and with more capabilities. Designs with multilayer, conductive via connections, finite ground plane, etc. can all be accurately analyzed. With a 1-gigabyte (GB) random-access memory (RAM) capability, a current personal computer (PC), by using either Ensemble or IE3D, can handle a microstrip array with approximately 30 elements and some microstrip power-division lines. Some of the other softwares, which use finite difference time domain (FDTD) or finite element (FE) methods, take a three-dimensional approach by

Table 1-5. Some commercially available microstrip antenna CAD tools.

Software Name	Theoretical Model	Company
Ensemble	Moment method	Ansoft
IE3D	Moment method	Zeland
Momentum	Moment method	HP
EM	Moment method	Sonnet
PiCasso	Moment method/Genetic	EMAG
FEKO	Moment method	EMSS
PCAAD	Cavity model	Antenna Design Associates, Inc
Micropatch	Segmentation	Microstrip Designs, Inc.
Microwave Studio (MAFIA)	FDTD	CST
Fidelity	FDTD	Zeland
HFSS	Finite element	Zeland

modeling the entire antenna space, including dielectric, metal components, and some surrounding volume. This approach allows a high degree of versatility for treating arbitrary geometries, including inhomogeneous dielectrics and irregularly shaped structures, but the price paid is computer time. With a current PC, only a few patch elements can be calculated. Regardless of the method used, future advancement in CAD tools is vested in two areas: (1) PCs with high capacity and faster computation; and (2) more efficient mathematical algorithms. With these advancements, large microstrip arrays can be more effectively analyzed and designed.

One important conclusion [88] should be made here for all CAD users that, while CAD software can be an invaluable analysis/design tool, it is not a substitute for design experience or a thorough understanding of the principles of operation of microstrip antennas and arrays. While microstrip antenna design is based on solid science, it also retains a strong component of intuitive understanding and a creative problem-solving approach that can only come from experience. It also can be concluded that, at least for the near future, CAD tools will continue to aid, rather than actually replace, the experienced designers.

1.4.4 Spacecraft Applications

1.4.4.1 Introduction. The demand for microstrip antenna application has been increasing rapidly in the past two decades. Initial applications have been primarily in the defense sector. Because of their extremely thin profiles and lightweight, printed microstrip antennas have found many applications for conformal mounting on military aircraft, missiles, rockets, etc. In the commercial sector, the adoption of microstrip antennas had not been as rapid during the 1980s, primarily due to their relatively higher material cost and the newness of the technology. During the earlier years, the costs of the microstrip antenna's substrate material, design effort, and manufacturing processes were considered non-competitive when compared to monopole, helix, horn, or parabolic reflector antennas. In addition, at the time, the configuration and environment of most terrestrial communication systems did not warrant the use of microstrip antennas. During the past decade, however, the cost to develop and manufacture microstrip antennas has dropped significantly. This is because the maturity of the microstrip antenna technology, the reduction in cost of the substrate material and manufacturing processes, and the simplified design process using newly developed versatile CAD tools. Furthermore, modern communication systems, such as cellular phone and station antennas, benefit greatly from the small size and low profile features of the microstrip antenna. In the space sector, the demand for using microstrip antennas is also increasing, but rather gradually since spacecraft are not produced in large quantities. Because of the increasing demand for smaller spacecraft and high-capability large-aperture antennas, smaller antenna mass to save launch vehicle fuel, and smaller antenna stowage volume to save launch vehicle space, there is an increasing need for more applications of microstrip antennas.

1.4.4.2 JPL/NASA Programs. Starting in the late 1970s, JPL/NASA began using microstrip antennas for space applications. For JPL-related programs, the following spacecraft have used or are using microstrip antennas: Seasat [89], Shuttle Imaging Radar (SIR) – A, B, C series [90,91], Mars Pathfinder, and Mars Exploration Rovers (MER). Among these programs, the antennas for Seasat and the SIR-A, -B, and -C series are all large-panel microstrip arrays (>10-m dimension) operated at L-band and/or C-band frequencies. These antennas are part of the synthetic-aperture radars (SARs) used to perform Earth remote sensing functions. These large arrays, except the SIR-C, are all designed with fixed main beams.

The SIR-C/X-SAR antenna is the most massive piece of hardware (10,500 kg) ever assembled at JPL, and measures 12 m by 4 m. The SIR-C instrument was built by JPL and the Ball Communication Systems Division for NASA and provides the L-band and C-band measurements at different polarizations. The L-band and C-band antennas employ phased-array

technology, which allows the antenna beam pointing to be adjusted electronically. The X-SAR instrument was built by the Dornier and Alenia Spazio companies for the Deutsche Agentur für Raumfahrtgelenheiten (DARA, German Space Agency) and the Agenzia Spaziale Italiana (ASI, Italian space agency), and it operates at a single frequency, X-band. The X-SAR antenna is a slotted waveguide type (12 m × 0.4 m at the top of Fig. 1-32), which uses a mechanical tilt to change the beam pointing direction.

The SIR-C antenna, flew three times (1994, 1995, and 2000) on the Space Shuttle, has electronic beam scanning capability with solid-state transmit/receive (T/R) modules and phase shifters. The antenna, shown in Fig. 1-32, has separate L-band (12-m × 3-m aperture size) and C-band (12 m × 0.75 m at bottom of Fig. 1-32) microstrip array panels developed by Ball Aerospace Corporation under a JPL contract.

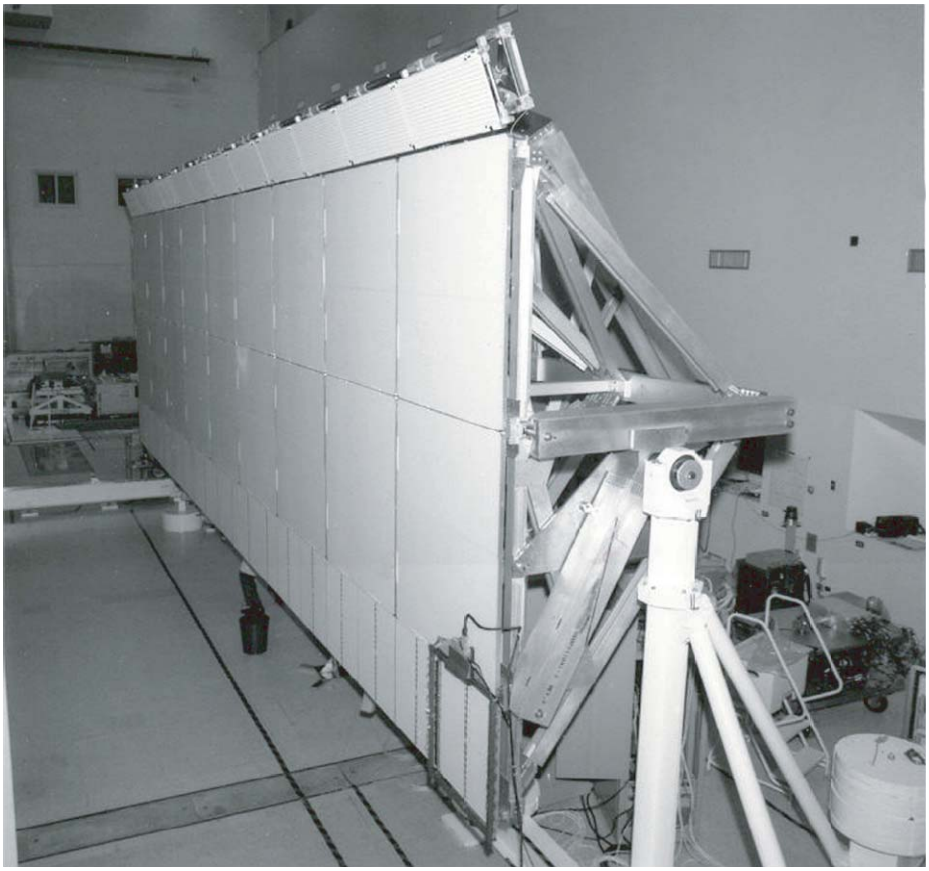

Fig. 1-32. SIR-C antenna in laboratory configuration. (The middle large L-band panels and the bottom small C-band panels are microstrip phased arrays with distributed T/R modules and phase shifters; the top slightly tilted panels are a fixed-beam X-band slotted waveguide array.)

For the Mars Pathfinder program, a relatively small (25-cm diameter) X-band microstrip dipole array, developed by Ball under JPL contract, was used as a telecommunication high-gain antenna on the Mars Pathfinder spacecraft launched in 1996 for Mars exploration. This antenna provided circular polarization with a peak gain of 25 dB. It was constructed with a corporate feed power divider and electromagnetically coupled dipoles, which allowed the antenna to have wide bandwidth and operate at both the transmit frequency of 8.4 GHz and the receive frequency of 7.1 GHz. The divider and the dipoles were printed on multilayer honeycomb substrates with open vented cells for space application. A polarizing cover sheet was used to achieve circular polarization.

Another Mars exploration program launched two MER spacecraft in 2003 to send two rovers to further explore the Mars surface. The two spacecraft successfully landed in late 2003 and in early 2004. On each lander vehicle, there are four petals (protective shielding panels) that opened up after landing to allow the rover to exit. An X-band antenna is mounted on the outside of one of the petals. It sent an indicator signal to Earth to confirm that the lander had landed and was functioning on the Martian surface. This X-band antenna is a single-element square patch with two orthogonal input ports to provide circular polarization. The patch and its microstrip lines are gold plated to avoid moisture corrosion in Earth environment prior to its launch. It is mounted in a circular protective cavity with a protective radome cover. The cavity has a 7-cm diameter, and the complete antenna has a mass of only 20 g. This single-patch antenna provides a peak gain of 7 dB with a –3 dB beamwidth of 85 deg. The microstrip patch antenna was selected for this application because of its unique features of small size and very little mass. Pictures of the Mars Pathfinder and MER microstrip antennas can be found in Chapter 4.

1.4.4.3 Areas of Attention for Space Application. In designing microstrip antennas for space applications, several critical areas need to be considered. In addition to the substrate material's radiation, outgassing, and temperature characteristics (discussed in Section 1.4.2.3.1), there are three other critical areas to be briefly discussed here. One is that the antenna must be able to survive the violent vibration during launch from the Earth. Generally, a vibration shock on the order of 10 gs or more must be tolerated. The soldering points of the coax connectors, via-through-hole connectors, discrete component attachments, and laminating epoxy material between different layers of a multilayer design all need to be made strong enough to survive the vibration.

The second area of attention is the large temperature variations that can occur in space. At an Earth-like distance from the Sun, the temperature can vary between 173 and 373 K (±100 K). At Venus the temperature can exceed 473 K, and at Jupiter it can get as low as 50 K. A spacecraft like Cassini that uses a gravity assist from Venus to get to Jupiter must be designed for both extremes.

The substrate material, as well as its laminating adhesive material, must survive physically and electrically throughout a wide temperature range over the lifetime of the spacecraft. In particular, the microstrip antenna is a narrow-band device. Its resonant frequency may shift out of the required operating bandwidth and lose its performance due to the temperature change.

The third area of attention is the antenna's RF power-handling capability. The power-handling capability of a microstrip antenna is generally an order of magnitude less in space than in Earth's atmosphere. Due to the vacuum in space, a particular breakdown phenomenon known as multipacting [62] generally occurs at pressures lower than 10^{-2} torr (1.3 Pa). At this low gas pressure, the electrons are freer to leave an electrode and move across to the opposite electrode. For a microstrip antenna, the two electrodes are the patch and its ground plane. Thus, in order to handle higher power in space, the microstrip antenna or microstrip transmission line must be designed with the proper thickness. The thicker it is, the more power it can handle. For a patch with conventional thickness ($<0.02\ \lambda_0$), a few tens of watts or less may considered to be safe in space. For more than 50 watts of average power, one should perform theoretical power breakdown analyses [62] and actual high-power-in-vacuum tests.

1.4.5 Summary and Conclusion

In this chapter, the design methodologies and various analysis techniques for microstrip antennas have been presented. In particular, the full-wave moment method is the most popular technique due to its computation accuracy and efficiency. Practical design techniques for the array configuration, radiating patch element, and power-division lines have been thoroughly discussed. Commercial available CAD tools were also presented. Space applications of microstrip antennas were highlighted. It is expected that, because of their small size and low mass, the demand for microstrip antennas in space applications will continue to increase. On the other hand, there is also an unabated demand for improving the performance of microstrip array antennas, such as widening of the bandwidth, reduction of the insertion loss, and improving the computation efficiency to handle large-size arrays. By utilizing the analysis techniques and design methods presented in this chapter, in conjunction with innovative ideas, the performance of microstrip antennas can be further enhanced to broaden their applications in the future.

1.5 Antenna Measurements

Mark S. Gatti

One area where spacecraft and ground antennas differ significantly is in the methods used to verify antenna performance parameters. Because of the requirements for low mass and the need to fit into the launch vehicle,

spaceborne antennas are generally small and quite amenable to direct measurements of their antenna radiation patterns. There are even standards written that define such measurements [92]. Two basic techniques have been developed to measure spacecraft far-field antenna parameters. A direct measurement of the far-field pattern can be done if enough distance can be reached between a source antenna and the antenna under test (AUT). In this mode a transmitter can be connected to either antenna, but traditionally, the source antenna is connected to a transmitter that radiates a signal at the frequency or frequencies of interest, and the AUT is connected to a suitable receiver. If the separation distance between the two antennas is sufficient that spherical phase error is negligible, then accurate main-beam and sidelobe measurements of the AUT are possible. This type of measurement is referred to as a "far-field" antenna measurement. An alternate method of determining the far-field antenna performance makes use of the relationship between the field surrounding the antenna on a closed surface at any distance from the antenna and the field at a great distance. One could, for example, measure the entire field around an antenna and use a Fourier relationship to calculate the field at an infinite distance. Typically, the enclosing surface chosen is in the immediate vicinity of the antenna and measures the near-field power of the antenna. The far-field performance of an antenna is calculated using this indirect measurement and is referred to as a "near-field" measurement. Figure 1-33 illustrates both the direct and indirect categories of antenna measurements. This section discusses both of these measurements and how they have been applied to several spacecraft antennas over the past 40 years.

In deciding which technique to use, an antenna engineer must determine the shortest distance that defines the beginning of the far field. Other factors include the ruggedness of the AUT, its total size, compatibility with the environment (for outdoor measurements), deformation in the effects of gravity, etc. Some spacecraft antennas are susceptible to gravity such that they distort. Others can only be rotated around one axis to measure patterns. An example of an antenna that should be tested indoors is a fragile deployable antenna similar to the Galileo high-gain antenna (HGA) (see Chapter 5). The long "stick" antenna used on the NASA Scatterometer and SeaWinds is easily rotated about its long axis, whereas a special fixture is required to rotate about any other axis. Some antennas, such as the HGAs used on the Mariner, Viking, Voyager, Magellan, and Cassini spacecraft, are not only stiff, but are rugged and lend themselves to periodic cleaning of any dust that may accumulate due to being in the outdoors. More flexibility in choosing the type of measurement is allowed for such antennas. Finally, the symmetric properties of the AUT can also be used in determining which type of measurement to be done. Often, rotating the AUT about an axis of mechanical symmetry provides a smaller

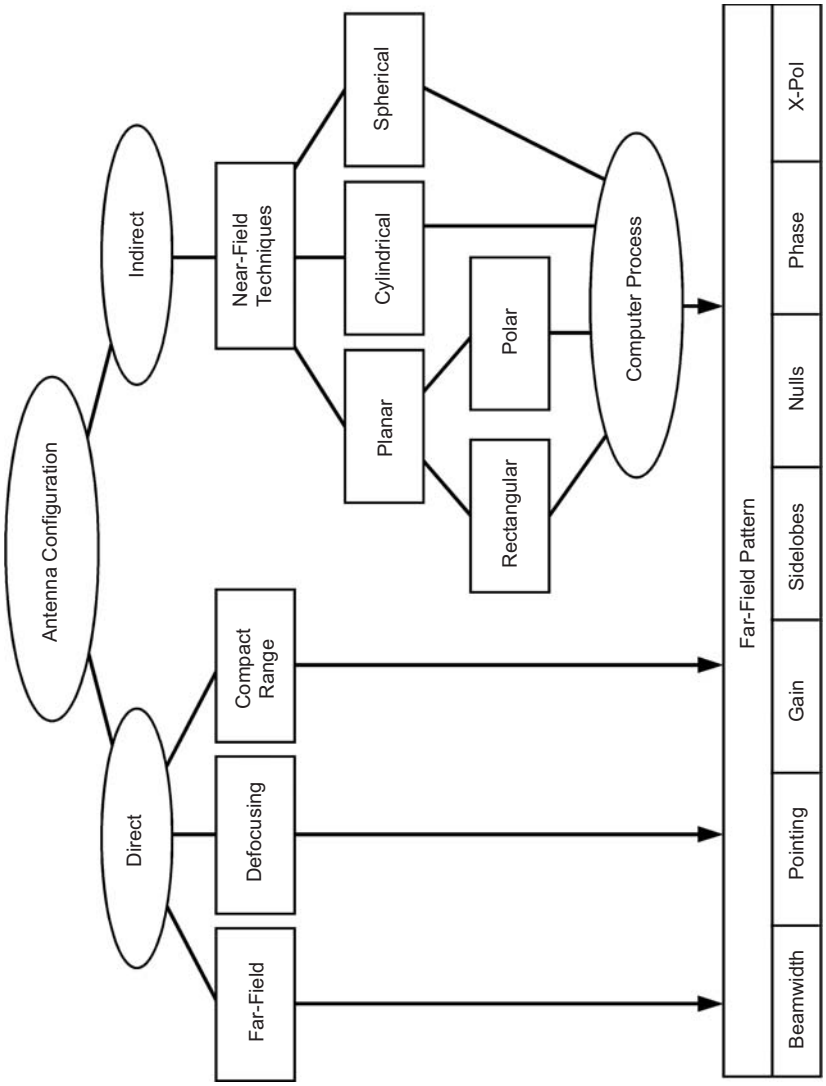

Fig. 1-33. Categorization of measurement techniques for antenna far-field patterns.

total suspended moment and a smaller total size of the required measurement facility.

1.5.1 Far-Field Measurements

The far-field measurement of an antenna's performance is the most straightforward technique as the quantity measured is exactly what is desired. The techniques described in this section are fully developed in great detail in [93] as well as most texts on antenna theory and design. The AUT and another source antenna, either of which can be connected to either a transmitter or receiver, are placed at a distance such that the measurements of the coupled power represent the far-field parameters of the AUT (see Fig. 1-34). This separation distance is somewhat arbitrary; however, it has been shown that the measured parameters very closely match the infinite distance far-field when the phase across the aperture of the antenna is less than 22.5 deg (equivalently 1/16 of a wavelength). This minimum separation is at a distance defined by the *largest* antenna in the measurement (either the AUT or the source antenna), and is given by $2D^2/\lambda$ where λ is the wavelength of the measurement and D is the diameter of the *largest* antenna in the measurement setup. For microwave antennas this can be quite far, ranging from 100–1000 meters. Finally, when making far-field measurements, one has to be aware that the reflection off objects between the source antenna and AUT will effect the measurement. The main error comes from the reflection off the ground between the antennas. Other reflections include the towers that the antennas are mounted on as well as other structures. Careful test-range design and characterization are required before an antenna should be calibrated on any far-field range. Typical difficulties with far-field antenna ranges are the huge real estate required, the uncontrolled environment (especially for fragile spacecraft antennas), the unbalanced gravitational forces, and the ground reflections. Nevertheless, for many spacecraft antennas a far-field range measurement is the most direct method to verify antenna performance.

1.5.1.1 Antenna Pattern Measurements. For this discussion, assume that the source antenna is transmitting a signal at the frequency or frequencies of interest. Furthermore, assume that this source antenna is of the same polarization as the AUT. Alternatively, the source antenna can be of linear polarization regardless of the AUT's polarization. The AUT is connected to an appropriate receiver and detector to measure the power received from the transmitter. To measure the patterns of the AUT, it is often mounted on a fixture such that it can be rotated about (or close to) the phase center. In doing so the measured power is directly proportional to the antenna pattern. Figure 1-34 shows such a configuration. For this measurement, one can either

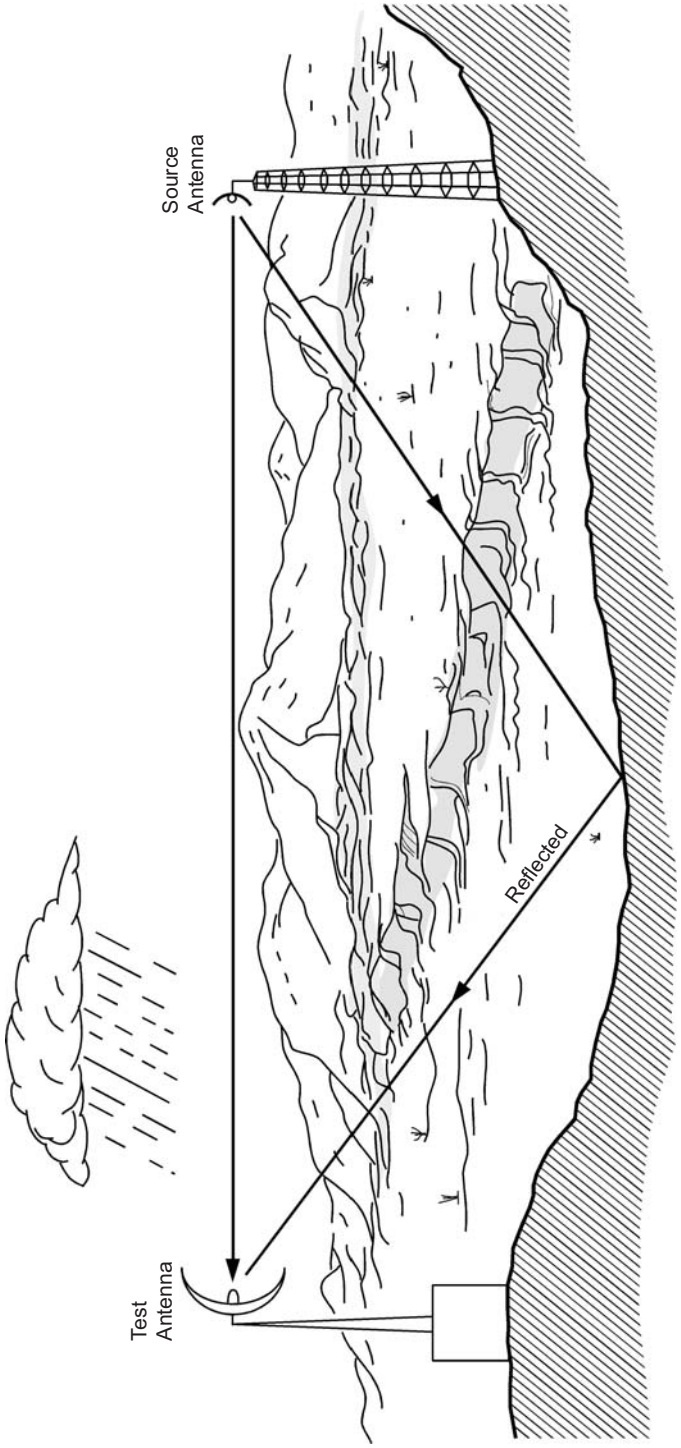

Fig. 1-34. Typical far-field antenna range.

eliminate reflections from the ground by using screens or by taking measurements at slightly different distances (separated by multiples of $\frac{1}{4}\lambda$). Alternatively, one can use geography to advantage. By placing the source antenna and the AUT on the sides of a hill, one will be able to reduce the ground reflections by as much as 60 dB.

Modern antenna ranges include the capability to rotate the AUT in the presence of the transmitted wave, detect the signal, and record the data in digital form. The antenna engineer will then display the data as the power versus direction in an appropriate coordinate system for the AUT. Throughout this book there will be examples of measured radiation patterns describing the performance of various antennas.

Given that the antenna test range has been properly constructed and that any extraneous objects are not within the field of view of either the test antenna or the AUT, the "free-space" far-field patterns can be measured. The term free-space refers to the performance of the AUT when not perturbed by any other object. After the antenna is characterized, the antenna engineer will often have to estimate the effects of the surrounding equipment, including the spacecraft body itself or booms, masts, and other antennas.

Finally, a careful comparison of the measurements of a particular antenna before and after an event can be useful in identifying if the event affected the antenna. Typical events for a spacecraft antenna include thermal tests, vibration tests, acoustic tests, launch pressure profile tests, among others. Careful measurement of antenna patterns is required to properly qualify an antenna for space flight.

1.5.1.2 Gain. Here we assume that the reader is familiar with the concept of antenna gain. There are two basic types of gain measurements. The first is an absolute gain measurement where no prior knowledge of the gain of any antenna in the measurement is required. The second is a gain transfer measurement requiring knowledge of the gain of at least one of the antennas, called a "standard gain antenna." Sometimes this second method is referred to as a gain-comparison method.

If two antennas having gains of G_a and G_b, are separated by a distance R, then the power received at one antenna as transmitted by the other is given by Friis' transmission formula as:

$$P_{rB} = P_{tA} G_A G_B \left(\frac{\lambda}{4\pi R} \right)^2 \tag{1.5-1}$$

It is sometimes useful to express this equation in decibels (dB) by taking the appropriate logarithms. Then, Eq. (1.5-1) can be written as:

$$p_{rb} = p_{ta} + g_a + g_b - SL \tag{1.5-2}$$

where the powers and gains are $p_r = 10\log_{10}(P_r)$, $p_t = 10\log_{10}(P_t)$, $g_a = 10\log_{10}(G_A)$, $g_b = 10\log_{10}(G_B)$, and the SL is the term that relates to the separation distance and is given by $SL = 20\log_{10}(4\pi R/\lambda)$. Note that the SL term is the reciprocal of the factor in Eq. (1.5-1). The literature refers to this as the space loss, or the loss in signal due to the distance between the transmitter and receiver. Therefore, in Eq. (1.5-2) the negative sign for space loss is used to suggest a loss in power.

By measuring the received power between a pair of antennas, one can use these equations to determine the gain of the antenna under test. In Eq. (1.5-1) it is assumed that the two antennas are perfectly matched to the transmission lines connecting their receiver and transmitter and that each is of exactly the same polarization. This equation and the subsequent development of gain measurement can be done with these factors included. The following describes the most commonly used gain measurement techniques used.

1.5.1.2.1 Substitution (Two-Antenna Technique). There are two useful versions of the two-antenna technique. In one case, in which the AUT and the source antennas are the same, the gain is calculated from the direct measurements. In this case, no knowledge of the gain of either antenna is required. Another case is where one knows very accurately the gain of one of the antennas. This is often referred to as the "standard gain antenna" (SGA). Usually, some other method (see the three-antenna technique below) is used to determine the gain of the SGA.

If the two antennas are identical, then G_A and G_B are equal. In this case Eq. (1.5-2) simplifies, and the gain of either antenna is given in decibels by:

$$g_a = g_b = \frac{1}{2}\left(p_r - p_t - SL\right) \tag{1.5-3}$$

This technique is simple in principle; however, it can be difficult in practice to implement. Small differences in the antenna manufacture also reflect in gain-measurement errors. As always, proper care should be given to the range and proper correction for errors.

The two-antenna substitution method is nearly as simple as above, with the exception that the standard gain antenna must be calibrated by some other technique. A calculation (as opposed to measurement) of the gain is also possible if the antenna is simple in nature, for example that of a horn antenna. In this case, the gain of the AUT is measured directly and calculated by rearranging either Eq. (1.5-1) or Eq. (1.5-2) as appropriate. Here Eq. (1.5-2) is used to yield the gain of the AUT.

$$g_b = p_r - \left(p_t + g_a - SL\right) \tag{1.5-4}$$

1.5.1.2.2 Three-Antenna Technique. The measurement of gain using the three-antenna technique is similar to the two-antenna technique. However, in this technique no two antennas need be the same. The measured parameters are such that one can solve for the gain of all three antennas without the knowledge of any one antenna. A generalized three-antenna method has been described that even accounts for the finite separation distance between the antennas [94] allowing for measurements to be done at less than the requisite far-field distance. This method of measuring gain consists of three separate measurements similar to that of the two-antenna method. In particular, measurements are made with each possible pair of antennas. For each measurement, Eq. (1.5-2) can be written. Subsequently, a system of three equations and three unknowns is developed for which any one of many methods can be used to solve for the individual antenna gains. For this technique the measurements can be expressed in the following equations:

$$\begin{aligned} g_a + g_b &= p_{rb} - p_{ta} + SL \\ g_a + g_c &= p_{rc} - p_{ta} + SL \\ g_b + g_c &= p_{rc} - p_{tb} + SL \end{aligned} \tag{1.5-5}$$

This set of equations can be cast in matrix form as:

$$\begin{bmatrix} 1 & 1 & 0 \\ 1 & 0 & 1 \\ 0 & 1 & 1 \end{bmatrix} \begin{bmatrix} g_a \\ g_b \\ g_c \end{bmatrix} = \begin{bmatrix} p_{rb} - p_{ta} + SL \\ p_{rc} - p_{ta} + SL \\ p_{rc} - p_{tb} + SL \end{bmatrix} \tag{1.5-6}$$

1.5.1.2.3 Polarization. The polarization characteristics of an antenna are important to know prior to using it in a communications link. The coupling of an antenna with the free-space wave is at a maximum when each shares the same polarization. Polarization of an elliptical wave includes the sense and the tilt angle. For elliptically polarized antennas, both the sense of polarization and the axial ratio are important. Both sense and polarization can be measured in one of several ways. The simplest way to measure the polarization as a function of direction is to use a linearly polarized antenna that is spinning around the polarization axis. When such a signal is received by the AUT, the measured signal will describe an envelope of polarization. Several examples of this type of measurement are given elsewhere in the book. Other measures of polarization are possible and are described in [93].

1.5.1.2.4 Input Impedance. Modern network analyzers make simple the measurement of impedance. Prior to that, other techniques were used including slotted lines and systems of couplers and power meters.

1.5.2 Near-Field Measurements

The basis of this technique is that the measured fields on a closed surface surrounding the antenna under test can be related to the far-field patterns, gain, and polarization by a Fourier transform-type relationship. See for example Fig. 1-35. If the tangential field is known on a closed surface ***S***, then the field anywhere external to ***S*** is given by

$$\vec{E}(\vec{R}) = \int_S \int \left\{ j\omega\mu_0 \left[\hat{n} \times \vec{H}(\vec{R}') \right] \bullet \overline{\overline{G}}\left(\vec{R}', \vec{R} \right) + \left[\hat{n} \times \vec{E}(\vec{R}') \right] \bullet \nabla' \times \overline{\overline{G}}\left(\vec{R}', \vec{R} \right) \right\} ds' \tag{1.5-7}$$

where

$\vec{E}(\vec{R})$ is the electric field at $\vec{R}$

$\vec{H}(\vec{R})$ is the magnetic field at $\vec{R}$

$\hat{n}$ is the unit normal

$\overline{\overline{G}}\left(\vec{R}', \vec{R} \right)$ is the Green's function

Theoretically, the far field of an antenna can be calculated from measurements over any arbitrary surface surrounding an antenna; however, it is advantageous to select a surface for which the relationship between the near field and the far field can be easily determined. Typically, measurements are

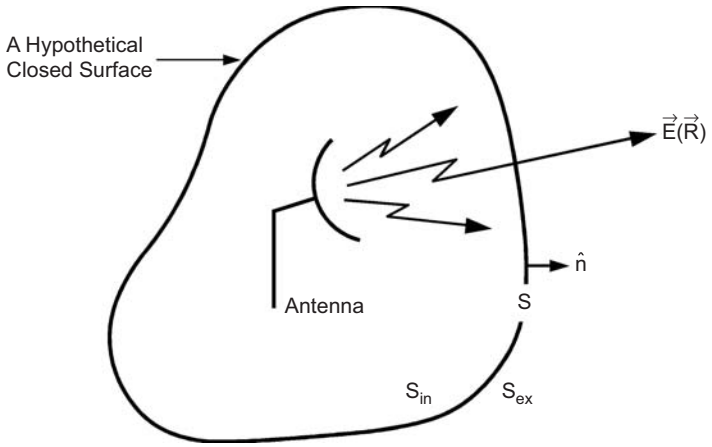

Fig. 1-35. Generalized Huygens theorem.

made over either a planar, a cylindrical, or a spherical surface as illustrated in Fig. 1-36. Early development [95–98] of this indirect technique for planar measurements suggested that very accurate measurements could be made. By the mid 1980s, near-field measurements became popular due to the fact that

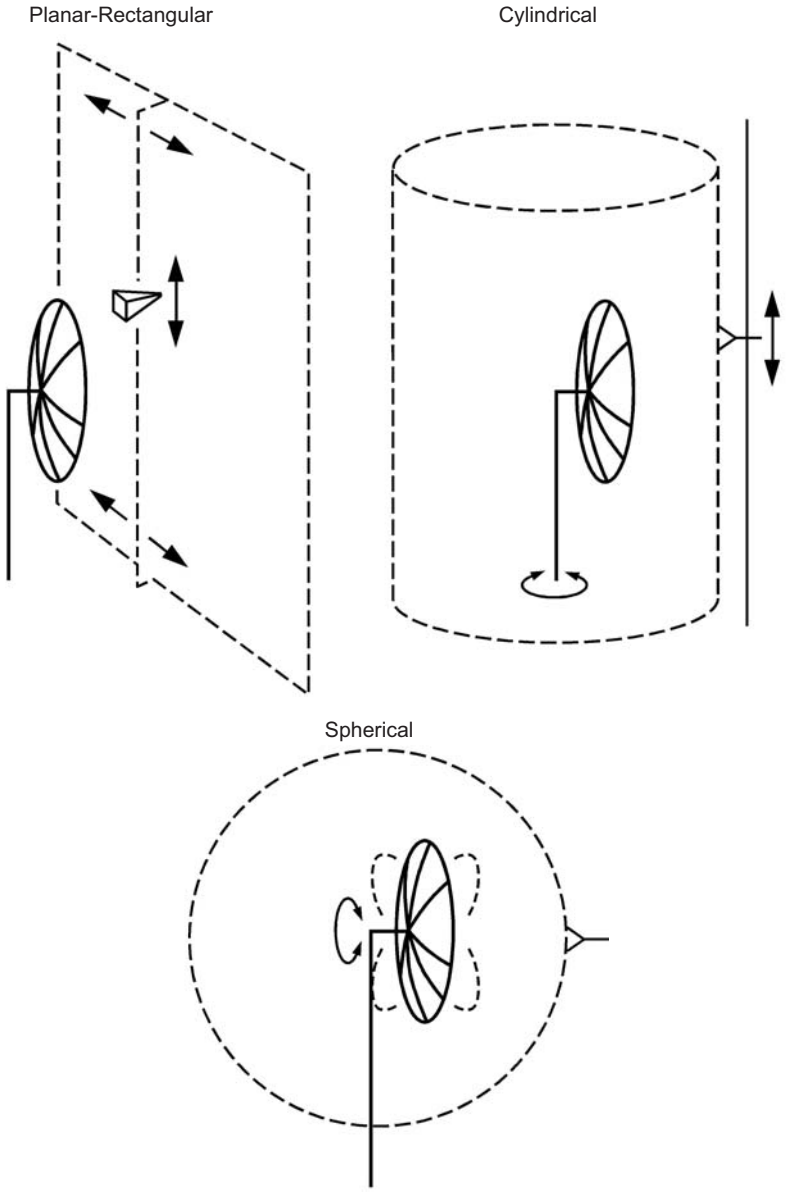

Fig. 1-36. Conventional mechanical setups for near-field measurements.

most ranges were indoors, lending themselves to the measurement of delicate or even classified antennas. Many developments were made during this time [99,100] during which JPL made the first deep-space spacecraft antenna calibrations using a near-field range [101]. Also during this time, the collection of many of these techniques was published in a special issue of the IEEE Transactions on Antennas and Propagation [102]. Note that both a Cartesian and a polar coordinate system of measurement have been developed for the planar measurement system. Even the use of Cartesian formulations using data measured on plane-polar ranges was developed [103]. Also, while planar near-field measurements were the most popular, being the most developed, there was a need for cylindrical near-field measurements as well. As a result JPL developed a cylindrical near-field range to augment its plane-polar facility [104] and measured the NASA Scatterometer and SeaWinds antenna performances [105,106]. Of these three types of surfaces, only the spherical surface can provide a complete near-field measurement. Measurements of the near field of an antenna on a planar or cylindrical surface are, by their very nature, truncated measurements of the entire antenna field. This truncation will cause some error in the calculation of the far field. Much work has been done to quantify the calculated far-field error due to this truncation as well as other effects, including the effects of the probe that is used to sense the fields, and the interaction of the probe with the antenna under test. Even in the early development of near-field measurements, experimenters knew that errors and corrections were necessary [107]. Since then, there has been much development in the analysis of these truncation errors, their causes, and mitigating steps to be taken in making such measurements [108–111]. It has been demonstrated that exceptionally accurate calculations of an antenna's far-field performance can be made using near-field measurements.

1.5.2.1 Calculation of Far-Field Patterns. The near-field measurement scheme normally consists of an AUT connected to a transmitter and a small probe antenna located in the near field of the AUT that samples the resulting electric and magnetic fields, $\overline{E}_a$ and $\overline{H}_a$. Application of the Lorentz reciprocity theorem shows that the output voltage of this probe is proportional to these fields. Also, it can be shown that the relation between the motion of the probe and the antenna is a convolution expression of the probe fields and the antenna fields. Finally, for the case of an open-ended waveguide probe sensitive to the magnetic field, an expression can be written to relate the apparent induced current given by $\overline{q_m}\left(\overline{\rho'}\right) = 2\hat{n} \times \overline{H}_a$ as defined in the scan plan to an integration integral, which is in the form of a Fourier transform as given in Eq. 1.5-7 [99,103]. This radiation integral can be written in any of several coordinate systems depending on the scanning motion of the probe with respect to the AUT. Many spacecraft microwave antennas lend themselves to a planar

measurement system. There are two planar coordinate systems frequently used; the polar and Cartesian systems. The plane-polar geometry is shown in Fig. 1-37. The probe moves along the *x*-axis, and the antenna rotates on the *z*-axis to measure a set of ring data at various radii from the center of the antenna.

In the plane-polar system, the radiation integral can be written by:

$$\vec{T}(\theta,\phi) = \int_{-\infty}^{\infty}\int_{-\infty}^{\infty} \overline{q_m}\left(\overline{\rho'}\right) e^{jk\left(\hat{r}\bullet\overline{\rho'}\right)} \rho\delta\rho\delta\phi \qquad (1.5\text{-}8)$$

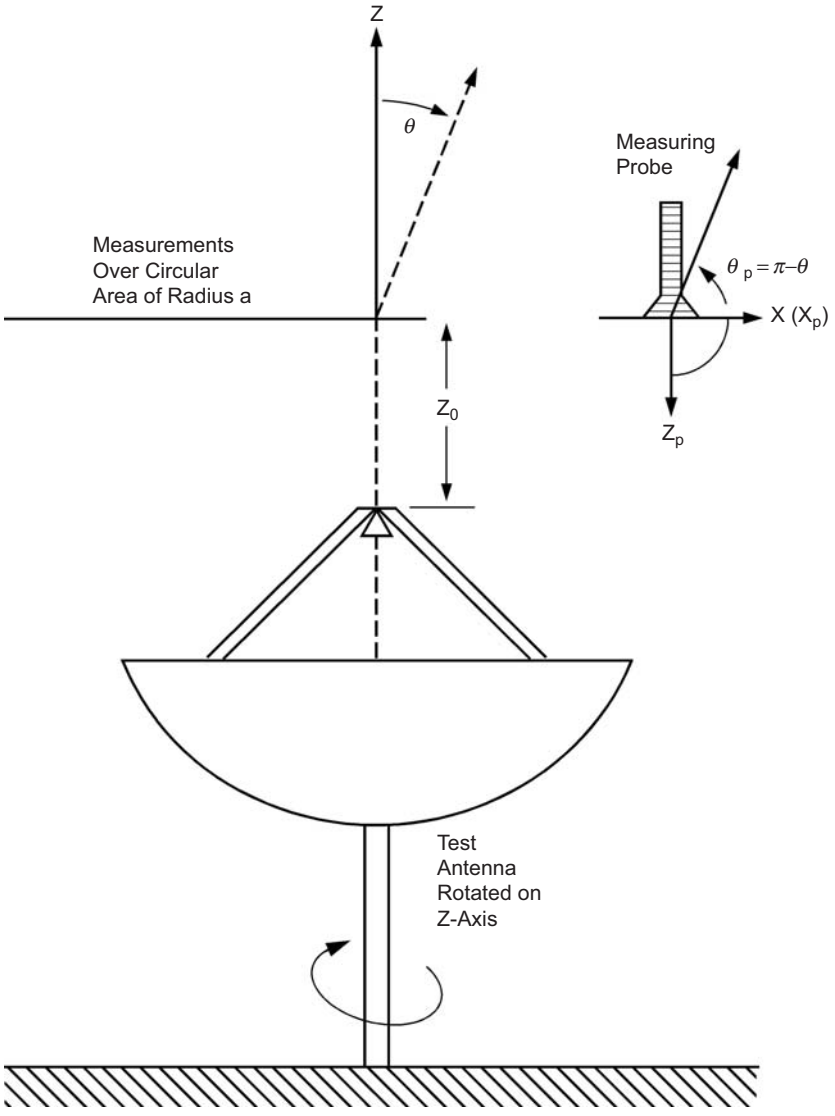

Fig. 1-37. Plane polar geometry.

Given that the measured data are from a plane-polar measurement, the numerical solution to Eq. 1.5-8 can be most readily be solved using the Jacobi-Bessel expansion of the integrand. The resulting expressions yield a set of coefficients for which the integrand is replaced by a summation given by:

$$\vec{T}(\theta,\phi) = 2\pi a^2 \sum_n \sum_m \left[\vec{C}_{nm}\cos n\phi + \vec{D}_{nm}\sin n\phi\right] \times \sqrt{2(n+2m+1)}\,\frac{J_{n+2m+1}(ka\sin\theta)}{ka\sin\theta} \tag{1.5-9}$$

where J is the Bessel function and one chooses n and m such that the resulting summation converges in the angular region of interest. This simple summation is used for all angles θ,ϕ. This suggests that, once the coefficients are calculated, all pattern information can be rapidly calculated for many directions. The calculation of the coefficients is where the time-consuming computations occur. These coefficients are given by

$$\vec{C}_{nm} = \frac{\varepsilon_n}{2\pi}\int_0^1\int_0^{2\pi}\vec{Q}(\vec{a}s')\cos n\phi\, F_m^n(s')s'd\phi'ds' \tag{1.5-10}$$

$$\vec{D}_{nm} = \frac{\varepsilon_n}{2\pi}\int_0^1\int_0^{2\pi}\vec{Q}(\vec{a}s')\sin n\phi\, F_m^n(s')s'd\phi'ds' \tag{1.5-11}$$

where ε is the Neumann factor (1 for $n = 0$, 2 otherwise) and s' is ρ'/a.

1.5.2.2 Measurement of Gain. Measurement of gain using near-field techniques can be done in either of two ways. One technique uses a substitution method very similar to that described in the far-field gain measurement where a second antenna of known gain is also measured by near-field techniques, and a comparison of the peak fields is done. For this technique, no knowledge of the probe antenna characteristics is required. Another substitution technique uses the knowledge of the probe gain and the loss of the transmission line to make a direct measure of the gain. This is done by removing the transmission line between the transmitter and the probe and in the lab using a variable attenuator to duplicate power levels found in the near-field measurement. The gain is determined directly from the settings of the attenuator. These techniques have been described in detail for near-field measurements using any of the typical coordinate systems.

1.5.2.3 The JPL Near-field Ranges

1.5.2.3.1 The Plane-Polar Range. A plane-polar near-field range was developed in the early 1980s and first used for the Galileo project high-gain

antenna test program [99,101]. The plane-polar technique, together with the series expansion algorithm, has a number of important mechanical and computational features.

The mechanical features can be readily inferred from the geometry shown in Fig. 1-37. The advantages of the plane-polar geometry are that both the probe and the antenna are gravitationally balanced and that the probe only moves in one direction. This allows for larger antennas for the same near-field facility than the planar-rectangular geometry. Also, the antennas always point in the same direction, which can be skyward. This is especially important for the measurement of gravitationally sensitive lightweight spacecraft antennas. Thus, this geometry is very suitable for high-gain reflector-type spacecraft antennas.

From the use of the Jacobi-Bessel series expansion from the plane-polar geometry, the following computational features apply:

1) Plane-polar data are used directly without interpolation in a rectangular grid.
2) The Jacobi-Bessel series computations require numerical manipulations proportional to N for N data and N observation points.
3) The numerical value of N that is required is determined only by the informational content of the measured field. No aliasing errors are introduced no matter how sparsely spaced the data points are located, and no zero fill is required.
4) The value of N can be substantially reduced by taking full advantage of any rotational symmetry in the antenna patterns.
5) The choice and number of observation points are not constrained.
6) The integrations involved can be performed piecewise over the aperture plane with no added complexity. Thus, large quantities of data can be readily handled.
7) Once the far field is computed at one observation point, it can be determined at any other observation point with relatively little effort.

For the early use of near-field ranges, it was extremely important to verify that the computation of the far-field patterns from near-field data actually matched the data measured on a far-field range. The first verification of this with the JPL plane-polar range was made using the 1.47-m Viking high-gain antenna (HGA). The Viking antenna was first measured on a far-field range and then measured in the plane-polar near-field range (see Fig. 1-38). The comparison of the direct far-field measurement and the constructed far field from the near-field measurement is shown in Fig. 1-39. As can be seen in the figure, there is good agreement, validating the use of the near-field range. Subsequently, the Galileo HGA performance was verified by near-field measurements in the plane polar near-field facility [101].

Fig. 1-38. Viking spacecraft HGA in the near-field facility.

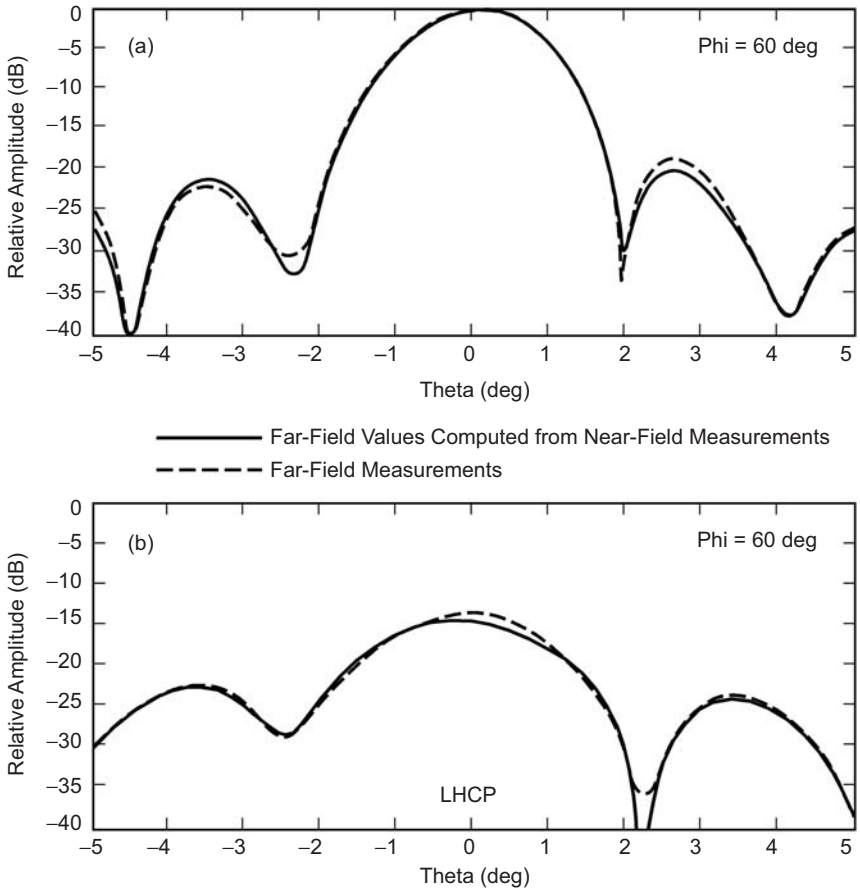

Fig. 1-39. Far-field patterns of the circulary-polarized Viking HGA at X-band: (a) RHCP and (b) LHCP.

1.5.2.3.2 Cylindrical Range. Several of JPL's instrument antennas to be described in Chapter 7 (NSCAT, SeaWinds Radar Antenna, and Wide Swath Ocean Altimeter) have a very long slender footprint and are best measured in the near field using a cylindrical rather than a planar geometry. Consequently, a cylindrical near-field scanning range [104–106,110,111] was assembled at JPL and used in the measurement of these antennas.

1.5.3 Conclusions

Regardless of the method chosen to characterize an antenna, such characterization is paramount in validating the performance of the antenna. Telecommunications systems engineers develop their system with specific performance expectations and associated tolerances. Verification of the performance assures the telecommunications system engineer that adequate

margin will exist over the life of the mission. The accuracy with which the performance is known is sometimes even more important than the actual performance itself. Antennas in instrument systems often fall into this category. The gain defines the total sensitivity; however, the precision is often affected by the total accuracy in performance prediction. This chapter has exposed some of the methods available to the antenna engineer to provide this validation. The amount of literature available to support antenna measurements seems limitless, possibly because of the importance placed on the activity. Research into the available methods for antenna measurements, development of the test facility to support the measurements, validation of the test facility, and a thorough analysis of the potential errors is mandatory prior to the measurement of any antenna. Only then will the final results of a validation and verification program be full acceptable.

References

[1] W. A. Imbriale, *Large Antennas of the Deep Space Network,* John Wiley & Sons, Inc., Hoboken, New Jersey, 2003.

[2] C. D. Edwards, Jr. and F. M. Naderi, "Telecommunications and Navigation Strategies for Mars Exploration," *52nd International Astronautical Congress*, Toulouse, France, 1–5 October 15, 2001, IAF-01-M.4.08, International Astronautical Federation, Paris, France, 2001.

[3] C. D. Edwards, J. T. Adams, D. J. Bell, R. Cesarone, R. DePaula, J. F. Durning, T. A. Ely, R. Y. Leung, C. A. McGraw, and S. N. Rosell, "Strategies for Telecommunications and Navigation in Support of Mars Exploration," *Acta Astronautica*, vol. 48, issue 5-12, pp. 661–668, March–June 2001.

[4] *Recommendation for Space Data Systems Standards, Proximity-1 Space Link Protocol–Physical Layer*, CCSDS 211.1-B-1, Consultative Committee for Space Data Systems, Matera, Italy, April 2003.

[5] R. F. Harrington, *Time Harmonic Electromagnetic Fields*, McGraw-Hill, New York, New York, 1961.

[6] W. V. T. Rusch and P. D. Potter, *Analysis of Reflector Antennas*, Academic Press, New York, New York, 1970.

[7] W. A. Imbriale and R. E. Hodges, "Linear-Phase Approximation in the Triangular Facet Near-Field Physical Optics Computer Program," *Telecommunications and Data Acquisition Progress Report 42-102, April–June 1990*, Jet Propulsion Laboratory, Pasadena, California, pp. 47–56, August 15, 1990.
http://ipnpr.jpl.nasa.gov/progress_report/issues.html

[8] W. A. Imbriale and R. E. Hodges, "The Linear Phase Triangular Facet Approximation in Physical Optics Analysis of Reflector Antennas," *Applied Computational Electromagnetic Society*, vol. 6, no. 2, pp. 74–85, Winter 1991.

[9] S. W. Lee and R. Mittra, "Fourier Transform of a Polygonal Shape Function and Its Application in Electromagnetics," *IEEE Transactions on Antennas and Propagation,* vol. 31, no. 1, pp. 99–103, January 1983.

[10] Y. Rahmat-Samii, "Useful Coordinate Transformations for Antenna Applications," *IEEE Transactions on Antennas and Propagation*, vol. 27, pp. 571–574, July 1979.

[11] J. R. Withington, W. A. Imbriale, and P. Withington, "The JPL Beamwaveguide Test Facility," *Antennas and Propagation Society Symposium*, London, Ontario, Canada, pp. 1194–1197, June 24–28, 1991.

[12] P. D. Potter, "A New Horn Antenna with Suppressed Sidelobes and Equal Beamwidths," *Microwave Journal*, pp. 71–78, June 1963.

[13] S. A. Brunstein, "A New Wideband Feed Horn with Equal E- and H-plane Beamwidths and Suppressed Sidelobes," *Space Programs Summary 37-58*, *Vol. II*, *The Deep Space Network*, Jet Propulsion Laboratory, Pasadena, California, pp. 61–64, July 1969.

[14] D. Hoppe, "Scattering Matrix Program for Circular Waveguide Junctions," *Cosmic Software Catalog*, NASA-CR-179669, NTO-17245, National Aeronautics and Space Administration, Washington, D.C., 1987.

[15] D. Hoppe, "Modal Analysis Applied to Circular, Rectangular, and Coaxial Waveguides," *Telecommunications and Data Acquisition Progress Report 42-95*, *July–September 1988*, Jet Propulsion Laboratory, Pasadena, California, pp. 89–96, November 15, 1988.
http://ipnpr.jpl.nasa.gov/progress_report/issues.html

[16] D. J. Hoppe, W. A. Imbriale, and A. M. Bhanji, "The Effects of Mode Impurity on Ka-Band System Performance," *Telecommunications and Data Acquisition Progress Report 42-80*, *October–December 1984*, Jet Propulsion Laboratory, Pasadena, California, pp. 12–23, February 15, 1985.
http://ipnpr.jpl.nasa.gov/progress_report/issues.html

[17] G. L. James, "Analysis and Design of TE_{11} and HE_{11}, Corrugated Cylindrical Waveguide Mode Converters," *IEEE Transactions on Microwave Theory and Techniques*, vol. MTT-29, pp. 1059–1066, October 1981.

[18] S. Silver, *Microwave Antenna Theory and Design*, Radiation Laboratory Series, vol. 12, McGraw-Hill, New York, New York, pp. 336–338, 1949.

[19] A. C. Ludwig, "Radiation Pattern Synthesis for Circular Aperture Horn Antennas," *IEEE Transactions on Antennas and Propagation*," vol. AP-14, pp. 434–440, July 1966.

[20] P. H. Stanton, D. J. Hoppe, and H. Reilly, "Development of a 7.2-, 8.4-, and 32-Gigahertz (X-/X-/Ka-Band) Three-Frequency Feed for the Deep Space Network," *Telecommunications and Mission Operations Progress Report 42-145, January–March 2001*, Jet Propulsion Laboratory, Pasadena, California, pp. 1–20, May 15, 2001. http://ipnpr.jpl.nasa.gov/progress_report/issues.html

[21] A. C. Ludwig, "Spherical Wave Theory," section in *Handbook of Antenna Design* (A. W. Rudge, K. Milne, A. D. Olver, and P. Knight, editors), Peter Peregrinus, Limited, London, England, 1982.

[22] A. C. Ludwig, *Calculation of Scattered Patterns from Asymmetrical Reflectors*, Ph.D. dissertation, University of Southern California, Los Angeles, 1969. Also Technical Report 32-1430, Jet Propulsion Laboratory, Pasadena, California, February 1970.

[23] V. Galindo, "Design of Dual-Reflector Antennas with Arbitrary Phase and Amplitude Distributions," *IEEE Transactions on Antennas and Propagation*, vol. AP-12, pp. 403–408, July 1964.

[24] W. F. Williams, "High Efficiency Antenna Reflector," *Microwave Journal*, vol. 8, pp. 79–82, July 1966.

[25] V. Galindo-Israel, W. A. Imbriale, and R. Mittra, "On the Theory and Synthesis of Single and Dual Offset Shaped Reflector Antennas," *IEEE Transactions on Antennas and Propagation*, vol. AP-35, no. 8, pp. 887–896, August 1987.

[26] V. Galindo-Israel, W. A. Imbriale, R. Mittra, and K. Shogen, "On the Theory of the Synthesis of Offset Dual-Shaped Reflectors—Case Examples," *IEEE Transactions on Antennas and Propagation*, vol. 39, no. 5, pp. 620–626, May 1991.

[27] A. G. Cha, "The JPL 1.5-meter Clear Aperture Antenna with 84.5 Percent Efficiency," *Telecommunications and Data Acquisition Progress Report 42-73*, *January–March 1983*, Jet Propulsion Laboratory, Pasadena, California, pp. 1–14, May 15, 1983. http://ipnpr.jpl.nasa.gov/progress_report/issues.html.

[28] V. D. Agrawal and W. A. Imbriale, "Design of a Dichroic Cassegrain Subreflector," *IEEE Transactions on Antennas and Propagation*, vol. AP-27, pp. 466–473, July 1979.

[29] J. P. Montgomery, "Scattering by an Infinite Periodic Array on Thin Conductors on a Dielectric Sheet," *IEEE Transactions on Antennas and Propagation*, vol. AP-23, pp. 70–75, January 1975.

[30] V. Galindo, N. Amitay, and C. P. Wu, *Theory and Analysis of Phased Array Antennas*, Wiley-Interscience, New York, New York, 1972.

[31] W. A. Imbriale, V. Galindo, and Y. Rahmat-Samii, "On the Reflectivity of Complex Mesh Surfaces," *IEEE Transactions on Antennas and Propagation*, vol. AP-39, pp. 1352–1365, September 1991.

[32] R. F. Harrington, *Field Computations by Moment Methods*, The Macmillan Company, New York, New York, 1968.

[33] W. A. Imbriale and P. G. Ingerson, "On Numerical Convergence of Moment Solutions of Moderately Thick Wire Antennas using Sinusoidal Basis Functions," *IEEE Transactions on Antennas and Propagation*, vol. AP-21, pp. 363–366, May 1973.

[34] W. A. Imbriale, "Applications of the Method of Moments to Thin-Wire Elements and Arrays," Chapter 2 in *Topics in Applied Physics,* vol. 3, *Numerical and Asympotic Techniques in Electromagnetics*, Editor: R. Mittra, Springer-Verlag, Berlin, Germany, and New York, New York, 1975.

[35] G. A. Deschamp, "Microstrip microwave antennas," *Proceedings of the Antenna Applications Symposium*, Robert Allerton Park, Monticello, Illinois, University of Illinois, [no page numbers in proceedings], September 1953.

[36] H. Gutton and G. Baissinot, "Flat Aerial for Ultra High Frequencies," French patent No. 703113, 1955.

[37] R. E. Munson, "Conformal microstrip antennas and microstrip phased arrays," *IEEE Transactions on Antennas and Propagation*, vol. AP-22, pp. 74–78, January 1974.

[38] K. R. Carver and J. W. Mink, "Microstrip antenna technology," *IEEE Transactions on Antennas and Propagation*, vol. AP-29, pp. 2–24, January 1981.

[39] R. J. Mailloux, J. McIlvenna, and N. Kernweis, "Microstrip array technology," *IEEE Transactions on Antennas and Propagation*, vol. AP-29, pp. 25–38, January 1981.

[40] J. Q. Howell, "Microstrip antenna," *IEEE Transactions on Antennas and Propagation*, vol. AP-23, pp. 90–93, January 1975.

[41] A. G. Derneryd, *Linear microstrip array antennas*, Tech. Rep. 7505, Chalmer University of Technology, Goteborge, Sweden, October 1975.

[42] J. L. Kerr, "Microstrip polarization techniques," *Proceedings of the Antenna Applications Symposium*, Robert Allerton Park, Monticello, Illinois, University of Illinois, [no page numbers in proceedings], September 1953.

[43] J. Huang, "Microstrip antennas for commercial applications," *Microstrip Antennas*, D. M. Pozar and D. H. Schaubert, editors, IEEE Press, Piscataway, New Jersey, pp. 371–379, 1995.

[44] I. J. Bahl and P. Bhartia, *Microstrip Antennas*, Artech House, Dedham, Massachusetts, 1980.

[45] J. R. James and P. S. Hall, *Handbook of Microstrip Antennas*, Peter Peregrinus Limited, London, England, 1989.

[46] D. M. Pozar, "Microstrip antenna aperture-coupled to a microstripline," *Electronics Letters*, vol. 21, pp. 49–50, January 1985.

[47] L. Murphy, "Seasat and SIR-A microstrip antennas," *Proceedings of the Workshop on Printed Circuit Antenna Technology* (Las Cruces, New Mexico), paper 18, October 1979.

[48] J. Huang, M. Lou, B. C. Lopez, and E. Gama, "Foldable Frame-Supported Thin-Membrane Array," *Proceedings of the International Symposium on Antennas and Propagation (ISAP)*, Institute of Electronics, Information and Communications Engineers, Fukuoka, Japan, pp. 213–216, August 2000.

[49] S. A. Long and M. D. Walton, "A Dual-Frequency Stacked Circular Disc Antenna," *IEEE Transactions on Antennas and Propagation*, vol. AP-27, pp. 270–273, March 1979.

[50] S. S. Zhong and Y. T. Lo, "Single-Element Rectangular Microstrip Antenna for Dual-Frequency Operation," *Electronics Letters*, vol. 19, pp. 298–300, 1983.

[51] J. L. Kerr, "Terminated Microstrip Antenna," *Proceedings of the Antenna Applications Symposium*, Robert Allerton Park, Monticello, Illinois, University of Illinois [no page numbers in proceedings], September 1978.

[52] J. Huang, "Microstrip reflectarray," *IEEE AP-S/URSI Symposium* (London, Ontario, Canada, June 1991), pp. 612–615, 1991.

[53] F. Crog and D. M. Pozar, "Millimeter Wave Design of Wideband Aperture Coupled Stacked Microstrip Antennas," *IEEE Transactions on Antennas and Propagation*, vol. 39, pp. 1770–1776, December 1991.

[54] R. Q. Lee, K. F. Lee, and J. Bobinchak, "Characteristics of a Two-Layer Electromagnetically Coupled Rectangular Patch Antenna," *IEEE Transactions on Antennas and Propagation*, vol. AP-38, pp. 1298–1302, August 1990.

[55] H. F. Pues and A. R. Van De Capelle, "An Impedance-Matching Technique for Increasing the Bandwidth of Microstrip Antennas," *IEEE Transactions on Antennas and Propagation*, vol. AP-37, pp. 1345–1354, November 1989.

[56] T. Teshirogi, M. Tanaka, and W. Chujo, "Wideband Circularly Polarized Array with Sequential Rotation," *Proceedings of the International Symposium on Antennas and Propagation (ISAP)*, Institute of Electronics, Information and Communications Engineers, Fukuoka, Japan, pp. 117–120, August 1985.

[57] J. Huang, "A Technique for an Array to Generate Circular Polarization with Linearly Polarized Elements," *IEEE Transactions on Antennas and Propagation*, vol. AP-34, pp. 1113–1123, 1986.

[58] D. H. Schaubert and F. G. Farrar, "Some Conformal Printed Circuit Antenna Designs," *Proceedings of the Workshop on Printed Circuit Antenna Technology* (State University Las Cruces, New Mexico), pp. 5/1–5/21, October 1979.

[59] K. F. Lee, K. M. Luk, K. F. Tong, and T. Huyuh, "Experimental Study of the Rectangular Patch with a U-Shaped Slot," *1996 International IEEE Antennas and Propagation Symposium Digest* (Baltimore, Maryland), vol. 1, pp. 10–13, 1996.

[60] C. L. Mak, K. M. Luk, K. F. Lee, and Y. L. Chow, "Experimental Study of a Microstrip Antenna with an L-Shaped Probe," *IEEE Transactions on Antennas and Propagation*, vol. 48, pp. 777–783, May 2000.

[61] H. Howe, Jr., "Stripline Is Alive and Well," *Microwave Journal*, vol. 14, p. 25, July 1971.

[62] R. Woo, *Final Report on RF Voltage Breakdown in Coax Transmission Lines*, JPL Technology Report 32-1500, Jet Propulsion Laboratory, Pasadena, California, October 1970.

[63] J. Huang, "A Parallel-Series-Fed Microstrip Array with High Efficiency and Low Cross-Polarization," *Microwave and Optical Technology Letters*, vol. 5, pp. 230–233, May 1992.

[64] *Radiation Resistance of Teflon in a Simulated Space Environment*, TM-6871, Components and Material Laboratory, Hughes Aircraft Company, August 1961.

[65] "Radiation Tolerance of Teflon Resins," *The Journal of Teflon*, vol. 10, no. 1, Dupont Company, January–February 1969.

[66] W. A. Campbell, Jr. and R. S. Marriott, *Outgassing Data for Selecting Spacecraft Materials*, NASA Reference Publication 1124, National Aeronautics and Space Administration, Washington, District of Columbia, August 1987.

[67] "Standard Test Method for Total Mass Loss and Collected Volatile Condensable Materials from Outgassing in a Vacuum Environment," *Annual Book of Standards*, ANSI/ASTM E595-77, American Society for Testing and Materials, West Conshohocken, Pennsylvania, pp. 1–8, 1980.

[68] R. K. Kirby, "Thermal Expansion of PTFE Teflon from -190 to 300°C," *Journal of Research of the National Bureau of Standards*, vol. 57, pp. 91–94, 1965.

[69] A. G. Derneryd, "A Theoretical Investigation of the Rectangular Microstrip Antenna," *IEEE Transactions on Antennas and Propagation*, vol. AP-26, pp. 532–535, July 1978.

[70] H. Pues and A. Van de Capelle, "Accurate Transmission-Line Model for the Rectangular Microstrip Antenna," *Proceedings of the IEE*, vol. 131, part H, pp. 334–340, December 1984.

[71] W. F. Richards, Y. T. Lo, and D. Harrison, "An Improved Theory for Microstrip Antennas and Applications," *Transactions on Antennas and Propagation*, vol. AP-29, pp. 38–46, January 1981.

[72] M. D. Deshpande and M. C. Bailey, "Input Impedance of Microstrip Antennas," *IEEE Transactions on Antennas and Propagation*, vol. AP-31, pp. 740–747, September 1983.

[73] D. M. Pozar, "Input Impedance and Mutual Coupling of Rectangular Microstrip Antennas," *IEEE Transactions on Antennas and Propagation*, vol. AP-30, pp. 1191–1196, November 1982.

[74] I. E. Rana and N. G. Alexopoulos, "Current Distribution and Input Impedance of Printed Dipoles," *IEEE Transactions on Antennas and Propagation*, vol. AP-29, pp. 99–105, January 1981.

[75] J. R. Mosig and F. E. Gardiol, "General Integral Equation Formulation for Microstrip Antennas and Scatterers," *Proceedings of the IEE*, vol. 132, Part H, pp. 424–432, 1985.

[76] A. Reineix and B. Jecko, "Analysis of Microstrip Patch Antennas Using Finite Difference Time Domain Method," *IEEE Transactions on Antennas and Propagation*, vol. 37, pp. 1361–1368, November 1989.

[77] X. Zhang and K. K. Mei, "Time-Domain Finite-Difference Approach to the Calculation of the Frequency-Dependent Characteristics of Microstrip Discontinuities," *IEEE Transactions Microwave Theory and Techniques*, vol. 36, pp. 1775–1787, 1988.

[78] C. Wu, K. L. Wu, Z. Q. Bi, and J. Litva, "Accurate Characterization of Planar Printed Antennas Using Finite-Difference Time-Domain Method," *IEEE Transactions on Antennas and Propagation*, vol. 40, pp. 526–534, May 1992.

[79] K. S. Yee, "Numerical Solution of Initial Boundary Value Problems Involving Maxwell's Equations in Isotropic Media," *IEEE Transactions on Antennas and Propagation*, vol. AP-14, pp. 302–307, 1966.

[80] J. R. James, P. S. Hall, and C. Wood, *Microstrip Antenna: Theory and Design*, Peter Peregrinus, Limited, London, England, 1981.

[81] A. G. Derneyd, "Linearly Polarized Microstrip Antennas," *IEEE Transactions on Antennas and Propagation*, vol. AP-24, pp. 846–851, November 1976.

[82] T. Metzler, "Microstrip Series Array," *IEEE Transactions on Antennas and Propagation*, vol. AP-29, pp. 174–178, January 1981.

[83] T.-S. Horng and N. G. Alexopoulos, "Corporate Feed Design for Microstrip Arrays," *IEEE Transactions on Antennas and Propagation*, vol. 41, pp. 1615–1624, December 1993.

[84] D. M. Pozar, "Scanning Characteristics of Infinite Arrays of Printed Antenna Subarrays," *IEEE Transactions on Antennas and Propagation*, vol. 40, pp. 666–674, June 1992.

[85] J. Huang, "Circularly Polarized Conical Patterns from Circular Microstrip Antennas," *IEEE Transactions on Antennas and Propagation*, vol. AP-32, pp. 991–994, September 1984.

[86] G. Kumar and L. Shafai, "Generation of Conical Patterns from Circular Patch Antennas and Their Performance," *Canadian Electrical Engineering Journal*, vol. 10, pp. 108–112, 1985.

[87] I. J. Bahl and D. K. Trivedi, "A Designer's Guide to Microstrip Line," *Microwaves*, pp. 174–181, May 1977.

[88] D. M. Pozar and J. R. James, "A Review of CAD for Microstrip Antennas and Arrays," in *Microstrip Antennas*, IEEE Press, New York, D. M. Pozar and D. H. Schaubert, editors, pp. 51–56, 1995.

[89] A. G. Brejcha, L. H. Keeler, and G. G. Sanford, "The Seasat-A Synthetic Aperture Radar Antenna," presented at *Synthetic Aperture Radar Technology Conference*, Las Cruces, New Mexico, March 1978.

[90] H. Schaeper and H. A. Nitschke, "Spaceborne SAR Antenna Technology and the Shuttle Imaging Radar – B (SIR-B) Antenna Development," *IEEE International Radar Conference* (Arlington, Virginia), May 1985.

[91] R. L. Jordan, B. L. Huneycutt, and M. Werner, "The SIR-C/X-SAR Synthetic Aperture Radar System," *IEEE Transactions on Geoscience and Remote Sensing*, vol. 33, pp. 829–839, July 1995.

[92] Antenna Standards Committee, *IEEE Standard Test Procedures for Antennas*, IEEE, distributed in cooperation with Wiley, 1979.

[93] J. S. Hollis, T. J. Lyon, L. Clayton, Jr., *Microwave Antenna Measurements*, Scientific-Atlanta, Inc., Atlanta, Georgia, 1969.

[94] A. C. Newell, R. C. Baird, and P. F. Wacker, "Accurate Measurement of Antenna Gain and Polarization at Reduced Distances by an Extrapolation Technique, *IEEE Transactions on Antennas and Propagation*, vol. 21, pp. 418–431, July 1973.

[95] R. C. Johnson, H. A. Ecker, and J. S. Hollis, "Determination of Far Field Antenna Pattern from Near Field Measurements," *Proceedings of the IEEE*, vol. 61, pp. 1668–1694, December 1973.

[96] D. T Parris, W. M. Leach, Jr., and E. B. Joy, "Basic Theory of Probe-Compensated Near-Field Measurements," *IEEE Transactions on Antennas and Propagation*, vol. 26, pp. 373–379, May 1978.

[97] G. V. Borgiotti, "Integral Equation Formulation for Probe Corrected Far-Field Reconstruction from Measurements on a Cylinder," *IEEE Transactions on Antennas and Propagation*, vol. 26, pp. 572–578, July 1978.

[98] D. M. Kerns, *Plane-Wave Scattering-Matrix Theory of Antennas and Antenna-Antenna Interactions*, NBS Monograph 162, United States National Bureau of Standards, June 1981.

[99] Y. Rahmat-Samii, V. Galindo-Israel, and R. Mittra, "A Plane-Polar Approach for Far-Field Construction from Near-Field Measurements, *IEEE Transactions on Antennas and Propagation*, vol. AP-28, pp. 216–230, March 1980.

[100] A.D. Yaghjian, "An Overview of Near-field Antenna Measurements," *IEEE Transactions on Antennas and Propagation*, vol. 34, no. 1, pp. 30–45, January 1986.

[101] Y. Rahmat-Samii and Mark S. Gatti, "Far-Field Patterns of Spaceborne Antennas from Plane-Polar Near-Field Measurements," *IEEE Transactions on Antennas and Propagation*, vol. AP-33, no. 6, pp. 638–648, June 1985.

[102] Special Issue on Near-Field Scanning Techniques, *IEEE Transactions on Antennas and Propagation*, vol. AP-36, no. 6, June 1998.

[103] M. S. Gatti and Y. Rahmat-Samii, "FFT Applications to Plane-Polar Near-Field Antenna Measurements," *IEEE Transactions on Antennas and Propagation*, vol. AP-36, no. 6, pp. 146–149, June 1988

[104] *Efficient and Fast Reconstruction of the Far-Field Radiation pattern from Knowledge of the Near-Field on a Cylindrical Surface*, JPL Document D-9124 (internal document), Jet Propulsion Laboratory, Pasadena, California, November 8, 1991.

[105] Z. Hussein and Y. Rahmat-Samii, "Application of Cylindrical Near-Field Measurement Technique to the Calibration of Spaceborne Radar Antennas: NASA Scatterometer and SeaWinds," *IEEE Transactions on Geoscience and Remote Sensing*, vol. 37, no. 1, January 1999.

[106] Z. A. Hussein and Y. Rahmat-Samii, "On the Accurate Calibration of the SeaWinds Radar Antenna: A Cylindrical near-Field Measurement Approach," *International Geoscience and Remote Sensing Symposium (IGARSS) Digest* (Lincoln, Nebraska, May 27–31) vol. 1, *Technical Papers*, A96-42751 11-43, Institute of Electrical and Electronics Engineers, Inc., Piscataway, New Jersey, pp. 515–519, 1996.

[107] D.M. Kearns, "Correction of Near-Field Antenna Measurements Made with an Arbitrary But Known Measuring Antenna," *Electronics Letters*, vol. 6, pp. 347–347, May 1978.

[108] *Upper Bound Errors in far-field antenna parameters determined from planar near-field measurements*, *Part 1: Analysis*, Technical Note 667, National Bureau of Standards, Boulder, Colorado, 1975.

[109] A. C. Newell, "Error Analysis Technique for Planar Near-Field Measurements, *IEEE Transactions on Antennas and Propagation*, vol. AP-36, pp. 754–768, June 1988

[110] Z. Hussein and Y. Rahmat-Samii, "Cylindrical Near-Field Measurement Error Models for NASA Scatterometer Fan-Beam Array Antenna, *1992 IEEE AP-S International Antennas and Propagation Symposium Digest* (Chicago, Illinois, July 1992), pp. 1558–1561, 1992.

[111] Z. A. Hussein and Y. Rahmat-Samii, "Probe Compensation Characterization in Cylindrical Near-Field Scanning," *IEEE AP-S International Symposium Digest* (Ann Arbor, Michigan), vol. 3, pp. 1808–1811, July 1993.

Chapter 2
The Early Years

William A. Imbriale

It would be difficult to portray an accurate portrait of the Jet Propulsion Laboratory (JPL) spaceborne antennas without giving a brief introduction of how JPL got into the spacecraft business in the first place [1]. JPL started in 1936 as the Guggenheim Aeronautical Laboratory, California Institute of Technology (GALCIT) rocket project, a collection of six amateurs working for the eminent Hungarian-born professor, Theodore von Karman. During World War II they made fundamental breakthroughs in the theoretical and applied aspects of both solid- and liquid-propellant rocketry. The project developed into a full-fledged, permanent installation operated by the California Institute of Technology for the Army Ordnance Corps and was renamed the Jet Propulsion Laboratory in 1944. The laboratory's major responsibility was basic research in missile technology and the development of the country's first tactical nuclear missiles, Corporal and Sergeant.

It was this rocketry background that eventually lured JPL into space exploration. JPL teamed with the German V-2 group at White Sands, New Mexico in 1949 to launch the Bumper-WAC, the "first recorded man-made object to reach extraterrestrial space." JPL engineers speculated that it was possible to cluster some Loki rockets (a solid-propellant antiaircraft missile based on the Germans World War II Taifun) on a Corporal missile and land an empty beer can on the moon. (What? No antenna!)

Scientists won approval for a satellite as a United States' contribution to the 1957–58 International Geophysical Year. JPL became involved in Project Orbiter, a joint effort between the Army Ballistic Missile Agency (ABMA) and the Office of Naval Research (ONR). Orbiter's first stage would be an updated

Redstone missile, and the upper stages would be a scaled down version of the Sergeant rocket motors. Based upon proven technology, it almost certainly would have made possible a launch by August 1957. However, based primarily on the desire by then President Eisenhower for the space program to be nonmilitary, Project Orbiter was cancelled, and the go-ahead was given to the Naval Research Laboratory's Vanguard, a smaller rocket that was still under development.

However, JPL and ABMA found an institutional outlet for their Orbiter studies in the reentry test vehicle (RTV) that was claimed to test the nose cone for the Army's Jupiter intermediate-range ballistic missile. The nose-cone test missile would be launched above the atmosphere then point straight down and aim at the Earth. To counteract the intense heat encountered reentering the atmosphere at high velocity, ABMA planned to use a blunt ablation-type nose cone, in which the various layers burned away during reentry. The RTV was extraordinarily similar to Orbiter, only needing a forth stage rocket and payload to create a satellite. JPL's Orbiter electronics were readily adaptable to the RTV program. The laboratory's telemetry could send data back to the ground on the heating effects of the missile during flight, and its tracking mechanism made it possible to recover the nose cone at the end of the flight. The main JPL electronic contribution was Microlock, a phased lock loop tracking system that could lock to a very low-level signal. There were three launches of the system, with the third firing, on August 8, 1957 succeeding brilliantly. All major systems worked satisfactorily, and the nose cone was recovered at a range of 1,160 miles (1,870 km). After validating the design, the RTV project was terminated, and the several sets of flight hardware left over were put in controlled storage, from which it could be made flight ready in less than four months.

With the launch of Sputnik on October 4, 1957 President Eisenhower cautiously accepted the suggestion to use the army as a backup to Vanguard. Then, on December 6, 1957 under the hot glare of international television, Vanguard exploded and burned up on the launch pad. The go-ahead was then given to JPL and the ABMA to launch the first U.S. satellite. This culminated in the launch of Explorer I at 10:48 p.m. on January 31, 1958 using the Jupiter-C, which had already been flight-tested as part of the RTV program.

2.1 Explorer I

Explorer-I (see Fig. 2-1 and [2]) was placed in an orbit with a perigee of 224 miles (360 km) and an apogee of 1575 miles (2535 km) having a period of 114.9 minutes. Its total weight was 30.66 pounds (13.91 kg), of which 18.35 pounds (8.32 kg) were instrumentation. The instrument section at the front end of the satellite and the empty scaled-down Sergeant fourth-stage rocket casing

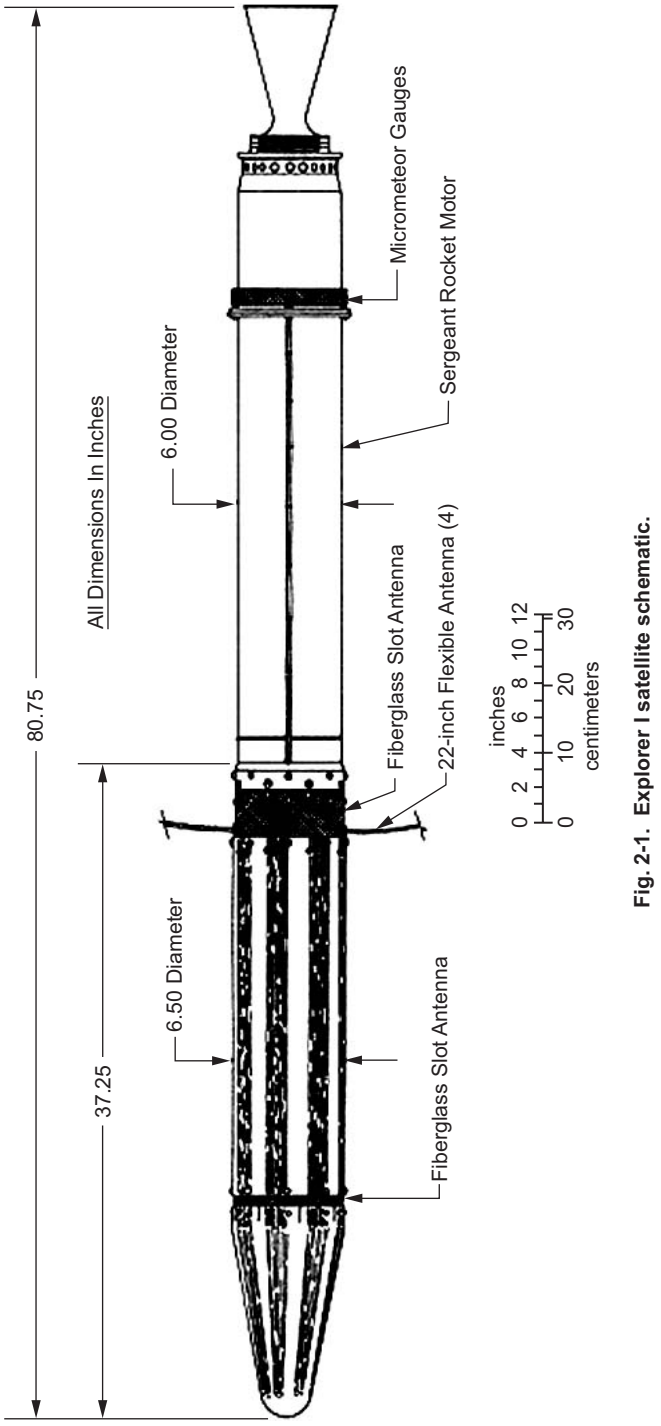

Fig. 2-1. Explorer I satellite schematic.

orbited as a single unit, spinning around its long axis at 750 revolutions per minute.

Instrumentation consisted of a cosmic-ray sensor, an internal temperature sensor, three external temperature sensors, a nose-cone temperature sensor, a micrometeorite impact microphone, and a ring of micrometeorite erosion gauges. The cosmic-ray sensor detects the penetration of high-energy atomic particles through the stainless-steel wall of the Geiger-Mueller tube.

A 60-mW transmitter operating on 108.03 MHz and a 10-mW transmitter operating on 108.00 MHz transmitted data from these instruments to the ground. Transmitting antennas consisted of two fiberglass slot antennas in the body of the satellite itself and four flexible whips forming a turnstile antenna. The rotation of the satellite about its long axis kept the flexible whips extended. The flexible whips caused instability in the attitude of the satellite and were deleted for subsequent flights.

The external skin of the instrument section was painted in alternate strips of white and dark green to provide passive temperature control of the satellite. The proportions of the light and dark strips were determined by studies of shadow-sun-light intervals based on firing time, trajectory, orbit, and inclination.

Nickel-cadmium chemical batteries, which made up approximately 40 percent of the payload weight, provided electrical power. These provided power that operated the high power transmitter for 31 days and the low-power transmitter for 105 days.

Because of the limited space available and the requirements for low weight, the Explorer-I instrumentation was designed and built with simplicity and high reliability in mind. It was completely successful.

Once in orbit, the cosmic ray equipment of Explorer-I registered at least a thousand times what had been expected; counts exceeded 35,000 per second at the highest altitudes, over South America, and saturated the Geiger-Muller counter. Dr. James Van Allen theorized that the equipment might have been saturated by very strong radiation caused by the existence of a belt of charged particles trapped in space by the Earth's magnetic field. The existence of these Van Allen Belts, discovered by Explorer-I, was confirmed by Explorer-III, which was launched by a Jupiter-C on March 26, 1958. There were five Explorer launches in all, of which three were successful.

The discovery of the Van Allen Belts by the Explorer satellites was considered to be one of the outstanding discoveries of the International Geophysical Year.

2.2 Pioneers 3 and 4

With the President's approval, on March 27, 1958, Secretary of Defense Neil McElroy announced that the Advanced Research Projects Agency (ARPA) space program would advance space flight technology and "determine our

capability of exploring space in the vicinity of the moon, to obtain useful data concerning the moon, and to provide a close look at the moon" [3]. Conducted as part of the United States' contribution to the International Geophysical Year, the lunar project would consist of three Air Force launches using modified Thor ballistic missiles with liquid-propellant Vanguard upper stages, followed by two Army launches using modified Jupiter-C missiles and JPL solid-propellant upper stages. JPL was to design the Army's lunar probe and arrange for the necessary instrumentation and tracking. ARPA directed the Air Force to launch its lunar probes "as soon as possible consistent with the requirement that a minimal amount of useful data concerning the moon be obtained."

The ARPA lunar program approved in March 1958, generally known as the "Pioneer program," offered five flight opportunities, three for the Air Force and two for the Army. The three Air Force probes were called Pioneer 0, 1, and 2. Only Pioneer 1 was partially successful. The Pioneer 3–4 payload (Fig. 2-2) antenna is basically an unsymmetrically fed dipole built in the shape of a cone [4]. The antenna cone is 12 in. (30.5 cm) high and 9 3/8 in. (23.8 cm) in diameter with a 2 ¾-inch (7.0-cm) aluminum probe at its apex. The cone was fabricated of a cloth epoxy laminate 0.016 in. (0.04 cm) thick. Weight of the cone was 4.6 lb (2.1 kg). Metallization of the cone was accomplished by depositing a 0.0006-in. (0.0015-cm) coating of silver and then plating with gold on the outside of the cone. Electrically, the antenna had a characteristic impedance of 50 ohms and a gain of 3 ±0.5 decibels (dB). Vibration tests on the

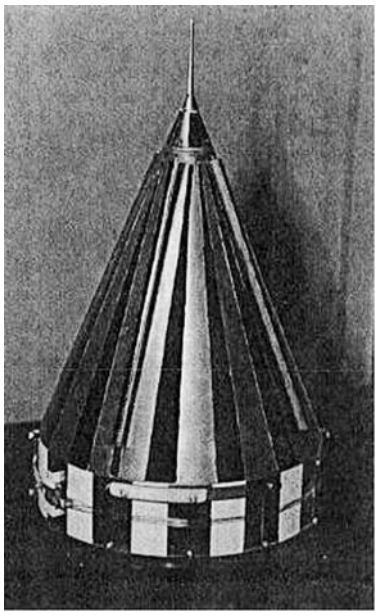

Fig. 2-2. Pioneer 4 antenna.

fiberglass cone at 20 g root mean square (rms) revealed several mechanical resonances. In order to provide the necessary mechanical rigidity, four longitudinal half-round external stiffeners and one internal bulkhead were added. Pioneer 3 was launched December 6, 1958 and transmitted 180 mW at 960.5 MHz. Because of a slight error in the satellite's velocity and angle after burnout of the Juno II rocket, it did not reach the Moon; instead it achieved a peak altitude of 102,320 km (63,580 miles). The satellite did, however, discover a second radiation belt around Earth during its flight. Pioneer 3 reentered Earth's atmosphere over equatorial Africa a day after launch. Pioneer 4 was launched March 3, 1959, and successfully passed within 60,000 km (37,300 miles) of the Moon the following day. The satellite was tracked for 82 hours to a distance of 655,000 km (407,000 miles) from Earth, a record at that time. Pioneer 4 is now orbiting the Sun, the first U.S. spacecraft placed in solar orbit and the first to escape the Earth's gravitational field. Pioneer 3 was the original object tracked by the first Deep Space Network (DSN) antenna, which was appropriately named the Pioneer antenna [5].

2.3 Project Ranger

Pioneer 4 was the last of the ARPA-initiated lunar probes. By mid-1958 responsibility for a coherent program of civilian space research had been vested in the new National Aeronautics and Space Administration, familiarly known as NASA. JPL was mandated by NASA to conduct unmanned "deep space" exploration—research at lunar distances and beyond. By the end of 1959, NASA specifically directed JPL to undertake a series of unmanned lunar missions. Actually, many JPL engineers and scientists tended to favor investigating the planets and space medium ahead of the Moon. However in 1959 and 1960, NASA did not have a reliable launch vehicle capable of planetary missions. The decision was to adopt the Atlas-Agena B as NASA's interim launch vehicle until the larger Atlas-Centaur rocket, capable of an interplanetary launch, became available in 1962. It was deemed mandatory that NASA acquire early experience with the next generation of American spacecraft for deep-space missions—vehicles attitude stabilized on three axes and guided by means of midcourse and terminal (lunar or planetary approach) maneuvers—before trying to develop still larger spacecraft. The Ranger project was to launch probes directly toward the Moon. The craft were designed to relay pictures and other data as they approached the Moon and finally crash-landed into its surface. Although the first attempts failed, the later Rangers were a complete success [6].

JPL had been working on a Martian spacecraft, but the Juno IV program was cancelled in October 1958. However, the fundamental design elements of a planetary spacecraft were formulated. To communicate adequately from planetary distances, the spacecraft would require a high-gain antenna (HGA, a

reflector antenna or "dish") mounted and hinged so as to point continuously at the Earth. On the ground, sensitive receivers, powerful transmitters, and very-high-gain ground antennas would complete the circuit. All the while, the spacecraft antenna would have to be kept pointing in the right direction through an appropriate method of stabilizing the attitude of the spacecraft itself. Spinning the vehicle along its roll axis had stabilized both the Explorers and Pioneers. For flights to the planets, it was deemed necessary to have complete control of the spacecraft in all three axes, roll, yaw, and pitch. This would ensure precise pointing of the experiments and the antenna, and it would maximize solar power collection and thermal control. With full attitude control, igniting a rocket engine on board in a "midcourse maneuver" could also refine the flight trajectory of a planetary spacecraft. A small rocket would be able to compensate for minor guidance errors introduced by the launch vehicle, thus permitting the spacecraft to approach more closely or even hit a celestial target. In addition to the features of an HGA and full attitude stabilization, the spacecraft would be designed so that its longitudinal axis would point continuously toward the Sun (except during midcourse or terminal maneuvers), since it was uncertain whether the Earth could be "seen" by onboard sensors at planetary distances. This decision simplified the problem of maintaining thermal equilibrium on the spacecraft and permitted the use of solar cells on fixed panels as a primary source of electrical power.

When NASA decided to emphasize the lunar objective in July 1959, JPL did not abandon the Martian spacecraft. They preferred to stick with it even though on a 66-hour flight to the Moon batteries could suffice in place of solar panels, and an HGA was unnecessary for communicating to a distance of 400,000 km (a quarter million miles). Adapted to lunar missions, the HGA, instead of being used for long-range, narrowband communication would now be used for relatively wideband transmission such as television at lunar distances. The bus and passenger concept, three-axis attitude stabilization, and solar power, its designers reasoned, could be used to develop the technology required for the planetary flights postponed to 1962.

Ranger was originally designed in three distinct phases, called "blocks." Each block had different mission objectives and progressively more advanced system design. The JPL mission designers planned multiple launches in each block, to maximize the engineering experience and scientific value of the mission and to assure at least one successful flight [7].

Block 1, consisting of two spacecraft launched into Earth orbit in 1961, was intended to test the Atlas/Agena launch vehicle and spacecraft equipment without attempting to reach the Moon.

Block 2 of the Ranger project launched three spacecraft to the Moon in 1962, carrying a television camera, a radiation detector, and a seismometer in a separate capsule slowed by a rocket motor and packaged to survive its low-speed impact on the Moon's surface. The three missions together demonstrated

good performance of the Atlas/Agena B launch vehicle and the adequacy of the spacecraft design, but unfortunately not all on the same attempt.

Ranger's Block 3 embodied four launches in 1964–65. These spacecraft boasted a television instrument designed to observe the lunar surface during the approach; as the spacecraft neared the Moon, they would reveal detail smaller than the best Earth telescopes could show, and finally details down to dishpan size.

The first of the Block 3 series, Ranger 6, had a flawless flight, except that the television system was disabled by an in-flight accident and could take no pictures. The next three Rangers, with a redesigned television, were completely successful. Ranger 7 photographed its way down to target in a lunar plain, soon named Mare Cognitum, south of the crater Copernicus. It sent more than 4,300 pictures from six cameras to waiting scientists and engineers.

The problem of providing antennas for the Ranger spacecraft involved two general requirements [8]. The first requirement was to provide a high-efficiency communication link for telemetry, to be utilized for the later portions of the Ranger flight. This function demanded a high-gain, vehicle-mounted antenna that could be directed toward the Earth. However, there are times when an HGA is incapable of being-oriented toward the Earth: (1) before the spacecraft is stabilized in space; (2) during the period when the spacecraft is undergoing its midcourse maneuver; and (3) any time when the spacecraft is in a failure mode such that the HGA cannot be pointed toward Earth.

A second type of antenna is required to accommodate such situations, incorporating "quasi" omnidirectional pattern characteristics. With such a radiation pattern, communications can be provided almost independently of the spacecraft orientation. However, this increased pattern coverage is obtained at the penalty of reduced antenna performance. This antenna can be used for telemetry purposes during the early portion of the spacecraft flight, when the spacecraft is undergoing attitude stabilization and during the period of midcourse maneuvers. When this antenna is used for long-distance communication, it provides low information bandwidth.

Therefore, there are basically two antennas systems required. An omnidirectional system providing telemetry coverage during the early portions of the flight, and an HGA system, giving required science communication-system performance during the long-distance phases of the flight.

A third requirement is the capability of receiving commands sent to the spacecraft. Since one of the purposes of the ground command system is to override various spacecraft-generated commands or maneuvers when the spacecraft malfunctions, it is necessary to get commands through to the spacecraft no matter what the spacecraft orientation happens to be. This means that an omnidirectional antenna is required for command purposes. Since there is already an omni antenna aboard for telemetry, it is logical to use it to satisfy the omnidirectional command requirement. A diplexer is needed to allow both

the transmitter and receiver of the spacecraft transponder to operate on the same omni antenna.

The antenna system must have a rotary joint to point the HGA back at the Earth through two degrees of rotational freedom. One degree of freedom is obtained by rolling the spacecraft on its axis. The second degree of freedom results from moving the antenna relative to the spacecraft. This means the transmission line, which connects between the antenna and the spacecraft communication pan, must have bending capability. The best way to meet this requirement is to use a rotary joint.

2.3.1 High-Gain Antenna System

The original constraints imposed on the HGA system were that its maximum size would be 4 ft (1.2 m) in diameter, and the weight of the reflector and feed structure should be less than 10 lb (4.5 kg). The HGA was a 4-ft (1.2-m) paraboloidal reflector, with a focal length-to-diameter ratio of 0.35 (Fig. 2-3). The reflective surface of the dish consisted of ¼-in. (0.63-cm) square

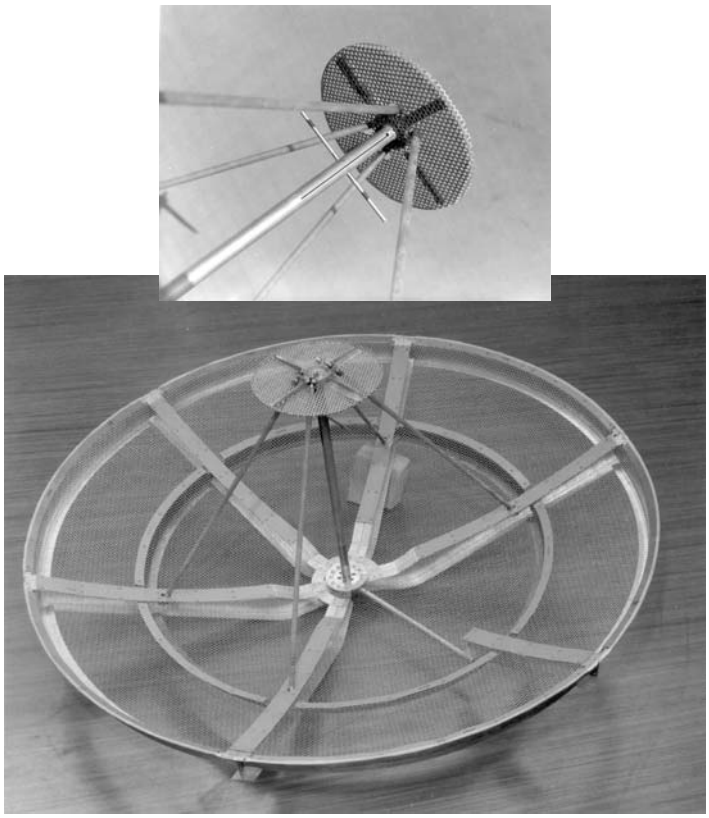

Fig. 2-3. Rangers 1 through 5 high-gain antenna.

mesh. This mesh was supported by a structural system consisting of six radial arms and three concentric hoops. The feed for this antenna consisted of a dipole mounted 1/4 wavelength in front of a 9-in. (23-cm) diameter ground plane. For the first five Ranger spacecraft, a linear polarized radiator was chosen for simplicity; it matched the polarization of the omni antenna. For this particular configuration, the antenna was slightly defocused. Displacing the feed from the nominal focus has certain advantages. With the feed at the focus of the reflector, very sharp nulls were produced at either side of the maximum lobe whenever there was no phase variation in the illumination of the antenna aperture. By slightly moving the antenna and causing a variation in the phase of illumination, these nulls fill in, and therefore provide additional reliable angular coverage when the antenna is not closely directed toward the Earth. This advantage, however, can be utilized only during the early portions of the spacecraft flight when there is a sufficient signal margin. The performance parameters for the antenna were as follows, all measurements being made at 960 MHz: The voltage standing wave ratio was 1.1 to 1. The half-power beamwidth in the E plane was 17½ deg and in the H plane it was 15½ deg. The 1-dB beamwidth in the E plane was 10.5 deg and in the H plane was 9.5 deg. The highest side lobe level in the E plane was down by 22.5 dB, whereas in the H plane it was down by 16 dB. The gain of the antenna was 19.5 dB. The Ranger E-plane and H-plane antenna patterns are shown in Fig. 2-4.

The matching section of the antenna system consisted of a quarter-wave coaxial transformer located approximately 1 in. (2.54 cm) below the balun slot (toward the base of the reflector). The balun slot itself was resonant at 0.454 wavelength or 5.587 in. (14.19 cm). The final length of the dipole element was 6.25 in. (15.9 cm) over-all, and it was spaced 3.13 in. (8.0 cm) from the 9-in. (23-cm) diameter ground plane.

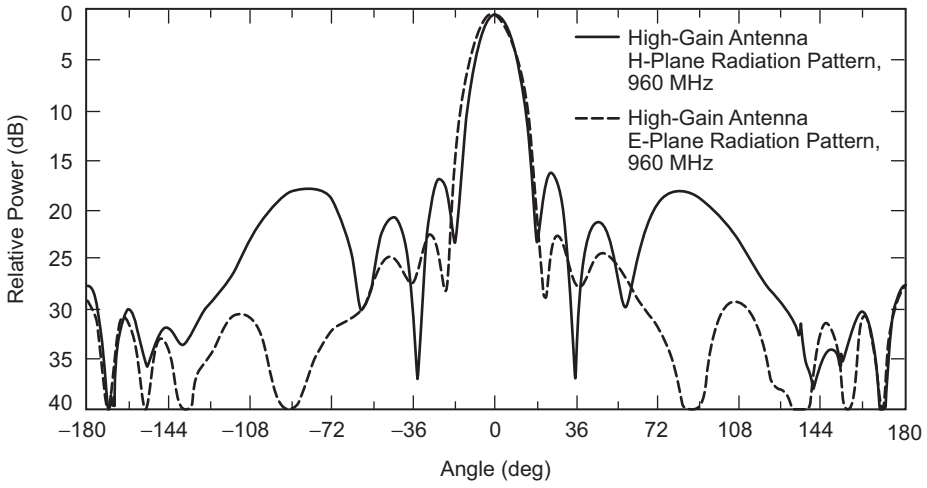

Fig. 2-4. Rangers 1 through 5 high-gain antenna patterns.

Since this feed was driven from an unbalanced coaxial transmission line, and the feed was a balanced type of antenna, some type of balun was required. The balun type selected consisted of a one-half wavelength axial slot cut into either side of the outer conductor of the coaxial transmission line, thus splitting the outer conductor into two halves. Half of the way along the slot, one side of the outer conductor was shorted to the center conductor of the coaxial transmission line; the dipole feed was driven at this point. The 9-in. (23-cm) ground plane was mounted onto the outer end of the balun slot. The other end of the balun slot became the coaxial transmission line, which ran from the feed area down to the base of the reflector. The feed structure position was stabilized by a fiberglass quadripod.

For Rangers 6 and 7 it was decided to use a circular polarized HGA. In order to circularly polarize the antenna, the ½-wave dipole on the feed of the antenna used for Rangers 1 through 5 was replaced by a turnstile (two crossed dipoles). The dipoles were of unequal length to get the 90-deg shift required for circular polarization. Since the turnstile changed the impedance of the HGA, the ¼-wave matching transformer required redesign. This involved changing the diameter and location of a ¼-wavelength enlarged section of the center conductor of the coaxial transmission line. Some mirror modifications were made to the reflector structure to enhance the reliability of the reflector surface and the focus was adjusted. With the HGA right-hand circularly polarized, its performance was essentially the same as the antenna used for Rangers 1 through 5.

2.3.1.1 High-Gain Antenna Development for Rangers 8 and 9. The performance required of the HGA for Rangers 8 and 9 was the same as that for Rangers 6 and 7 at 960 MHz. However, Rangers 8 and 9 carried an S-band communication and tracking experiment, and it was required that an HGA be used with the S-band experiment. Because it was not feasible to put a second HGA on the spacecraft, the decision was made to broadband the existing antenna to cover the S-band frequencies, as well as the 960-MHz frequency. A design was borrowed from the Mariner program (Fig. 2-5). The reflector was the same as that used for Rangers 6 and 7. The major difference was in the feed design and the feed support structure. To meet the bandwidth requirement for the feed, a conical spiral periodic antenna structure was used. Since this type of antenna has to be fed at the small end of the cone, by a balanced line with an impedance of over 100 ohms, a broadband balun transformer was required to connect the antenna to the 50-ohm unbalanced coaxial line. The design used consisted of a coaxial line, which had been peeled open so the end was transformed into a twin line. Since the impedance on the twin line end was higher than that of a closed coaxial line, and also was a function of the width of the twin line, this type of balun could be used to give the required impedance transformation.

Fig. 2-5. Rangers 8 and 9 high-gain antenna.

During the development of this broadband feed, it became apparent that conducting material in close proximity to the feed was highly undesirable. Therefore, the final configuration incorporated a dielectric feed-support structure. Gain measurements versus focal distance (Fig. 2-6) of the original Mariner (a high-gain broadband antenna) indicated that the minimum distance for good operation at all three frequencies required (960, 2113, and 2295 MHz) was about 22 in. (56 cm). This focal distance was also the maximum allowable feed protrusion into the Rangers 1 through 7 sterilization diaphragm without requiring a change to that structure.

2.3.1.2 Rotary Joint. Two different types of rotary joints were required for the *Ranger* program. The rotary joint for Rangers 1 through 7 was required to operate at 960 MHz only; and, therefore, it was a single-frequency design. The rotary joint used for Rangers 8 and 9 had to pass 960 MHz and S-band, since the HGA would be operating both at 960 MHz and at S-band. Since there were no commercially available rotary joints adequate for a space environment, JPL developed a suitable rotary joint. The basic configuration chosen was a rotary joint with radio frequency (RF) chokes since this technique eliminates any metal-to-metal relative motion joints at low impedance levels, which could cause seizing of the rotary joint or could cause noise because of corrosion or dirt in the joint. The conventional joint, where the relative motion was taken through fingerstock, was eliminated at the start since it was believed that the fingers could conceivably weld to the mating portion of the joint. The choke for the center conductor of the rotary joint consisted of an open-circuit ¼-wavelength choke. It reflected the high impedance at the open end of the choke into very low impedance at the point where the ¼-wavelength choke entered the transmission line. The choke in the outer conductor was a shorted

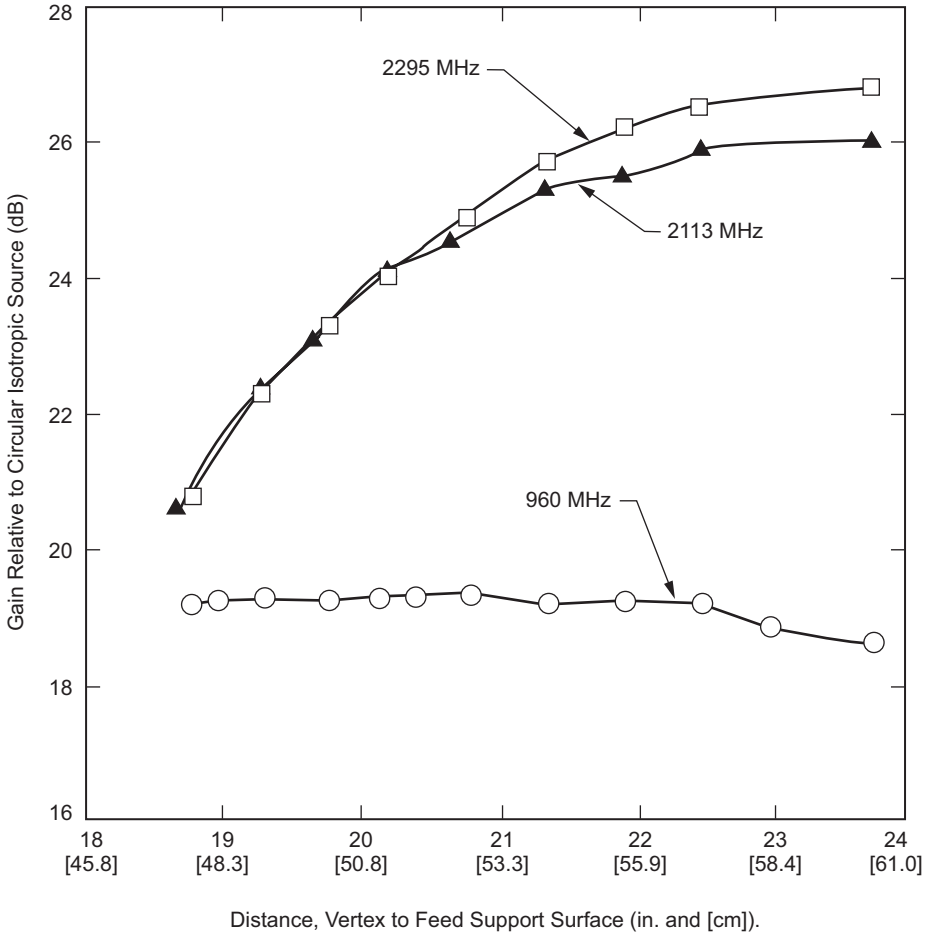

Fig. 2-6. Rangers 8 and 9 high-gain antenna gain versus feed position, fiberglass struts.

½-wavelength choke; the short was reflected through ½ wavelength into a short at the point where the choke entered the transmission line at the outer conductor. The only metal-to-metal contact in the rotary joint occurred in the center of this ½-wavelength choke. However, this was not critical since at this point the choke was at a very high impedance level, and noisy or erratic performance would be greatly attenuated by transformation through ¼ wavelength down to the point where the choke intercepted the outer conductor.

It was desired to optimize the performance of the rotary joint at the spacecraft transmitting frequency. However, sufficient broadbanding was included so the rotary joint could be used at the receiving frequency in case a two-way system ultimately was needed. Considerable effort was expended designing the bearing system of the rotary joint. Due to the low expected

angular rates of the antenna, the rotary joint was designed with dry bearings. This eliminated the problem of lubricants and the probability that the lubricants would evaporate in a vacuum environment. The selection of the bearings for the rotary joint was complicated for several reasons:

1) Due to the size of the rotary joint, conventional ball bearings would not fit.
2) Lubrication of conventional bearings would be difficult because of the basic requirement that the rotary joint could not be pressurized.
3) The bearings within the coaxial section of the rotary joint itself could not be allowed to degrade the electrical performance of the joint.

In the final design, one main bearing was used at the rotating end of the joint and was located in the center of the ½-wavelength outer choke (Fig. 2-7). This arrangement consisted of a sleeve bearing with silicon copper running on

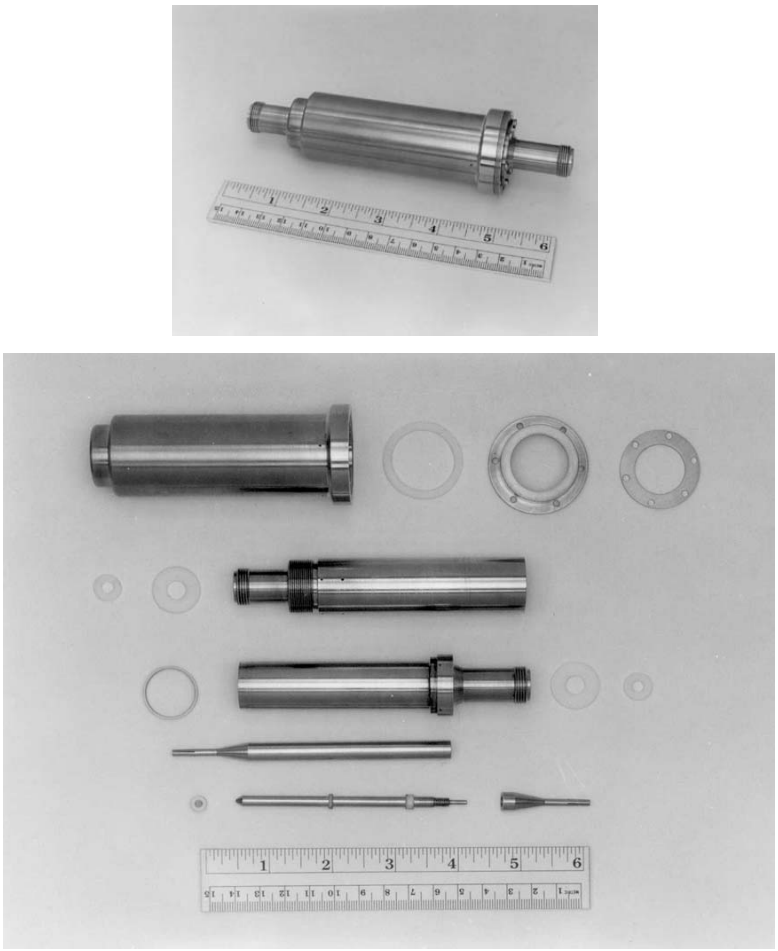

Fig. 2-7. Prototype rotary joint, disassembled.

303 stainless steel, with a molybdenum disulfide dry lubricant. A tungsten carbide needle bearing, running dry in an aluminum oxide ceramic jewel, carried the axial loads of the rotary joint in a compressive direction. This bearing was located within the ¼-wavelength open-circuit choke, which was within the center conductor of the rotary joint. A 303 stainless-steel collar on the sleeve bearing kept the rotary joint from separating in the axial direction. To maintain the concentric tubes of the joint in line, aluminum oxide spacers were used. Aluminum oxide was ideal in this application because it has low RF losses and is a very hard material. The design approach on the bearings was conservative due to the lack of information on bearing performance at extremely low pressures.

The final version of the rotary joint was 5-1/2 in. (14 cm) long and 1-3/8 in. (3.5 cm) in diameter and weighed 0.99 lb (0.45 kg) (Fig. 2-8). The chokes in the rotary joint were determined to be quite broad, providing a voltage standing wave ratio (VSWR) of less than 1.1 over a frequency range of 770 to 1000 MHz. The insertion loss turned out to be 0.05 dB at 960 MHz, and the wow was within 0.01 dB (the measuring accuracy of the insertion loss measurement).

2.3.1.3 Rotary Joint for Rangers 8 and 9. Since on Rangers 8 and 9 an S-band experiment was to be flown that would use the HGA, the rotary joint had to be redesigned to handle not only the 960 MHz, but also 2295 MHz (which was the S-band transmitter frequency) and 2113 MHz (which was the S-band transponder receiver frequency). See [8] for further details on the rotary joint redesign.

Fig. 2-8. Flight RF coaxial rotary joint.

2.3.2 Omni Antennas

The basic requirement of an omni antenna is to provide coverage over as large an angular region of space as possible. This provides for communication if the spacecraft is not properly oriented, or it allows the spacecraft to assume different attitudes in flight. The Ranger spacecraft required omni communications within 40 deg to 140 deg of the spacecraft roll axis and for any angle about the roll axis.

Constraints were imposed on the spacecraft to help meet this communication requirement. One such constraint was that no spacecraft hardware could lie within the specified communication angle. A second was that the bulk of the spacecraft below the antenna should appear symmetrical. A number of antenna configurations were considered and evaluated (Fig. 2-9), and these configurations included a sleeve dipole, a ¼ wavelength stubbed cone, and a disc-cone antenna.

To meet the requirement that the spacecraft should not interfere with the antenna field of view, the only location acceptable for the antenna was above the spacecraft, on its roll axis. It was in this location that the above configurations were tested. To maintain the requirement that the spacecraft appear symmetrical and to control the points where reflections could originate, a diffraction structure or ground plane was used to isolate the antenna from the spacecraft.

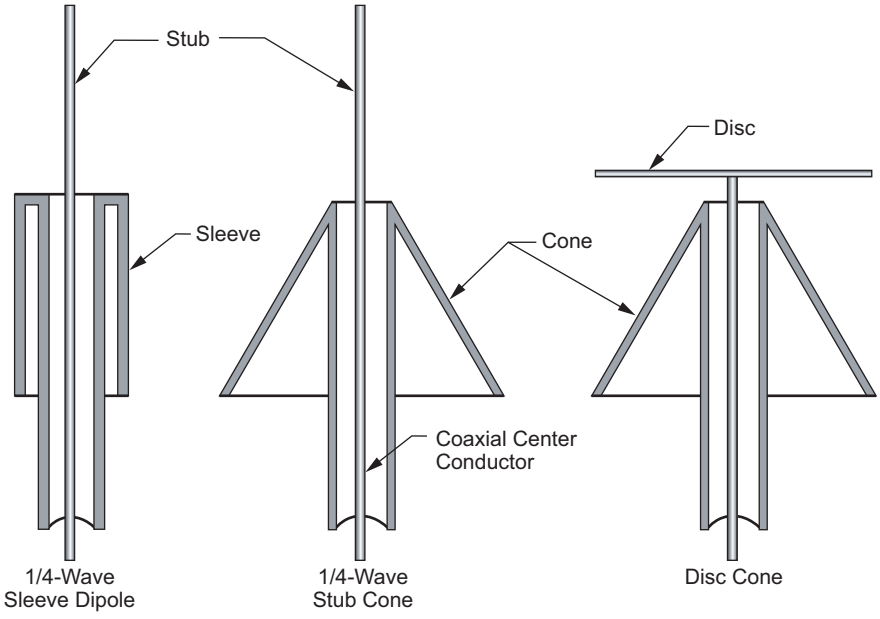

Fig. 2-9. Omnidirectional antenna types.

The disc-cone antenna was selected because it was sufficiently broadband to handle both the 890 and 960 MHz, and it had a lower silhouette, thus allowing it to be mounted higher while still providing a shorter all-around spacecraft system. This antenna was found to be versatile, since there are many parameters (the length and the angle of the cone and the diameter of the disc) that can be used to vary the pattern shape. The pattern shape of a disc-cone antenna with a ¼-wavelength diameter disc and a ¼-wavelength cone is similar to that of a dipole. Tests made with the Ranger disc-cone antenna indicated that the radiation could be directed toward the aft end of the antenna when either the cone angle was made smaller (i.e., going from an 80-deg to a 60-deg cone), or if the length of the cone was increased. Increasing the diameter of the disc to more than ¼ wavelength shifted the pattern toward the forward end of the antenna. It was found that a combination of increasing the length of the cone and increasing the diameter of the disc provided the required pattern coverage. The final configuration used a disc approximately ¾ wavelength in diameter and a cone approximately ½ wavelength long with an angle of 80 deg. The pattern of a full-scale disc-cone without the spacecraft is shown in Fig. 2-10.

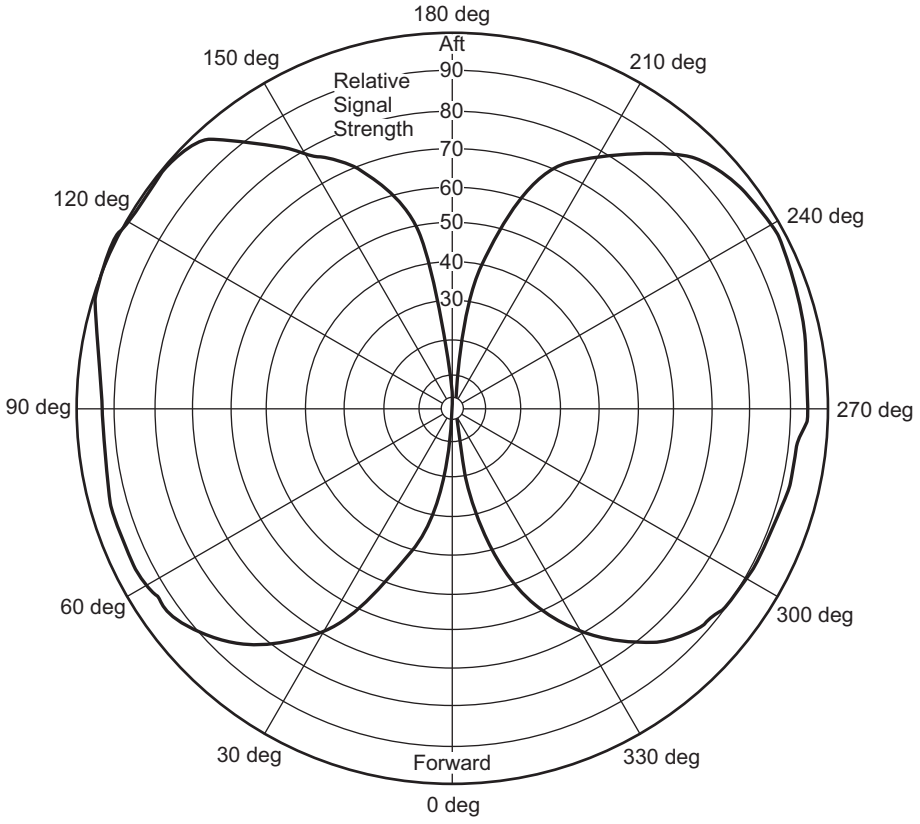

Fig. 2-10. Full-scale disc-cone antenna pattern.

Next, measurements were made to determine the effect of a diffraction disc on the disc-cone antenna pattern. It was found that the diffraction disc had an appreciable effect on the resultant pattern of the disc-cone antenna. Depending upon the position of this disc, a pattern could be produced which was predominately forward-directed or aft-directed. It was found that a 16-in. (41-cm) diameter diffraction disc placed 16 in. (41 cm) from the forward end (i.e., the disc) of the antenna gave the best results (Fig. 2-11). By comparing with the previous pattern (Fig. 2-10), it can be seen that the disc caused approximately a 1-dB dip at the equatorial plane of the pattern, and somewhat reduced the energy radiated toward the aft end of the antenna. In order to determine whether the effect of the diffraction disc could be minimized, absorbers were mounted on the side of the diffraction disc facing the antenna. It was found that the absorber only had a small effect on the diffraction disc. Since the absorber would add considerable weight to the antenna and would provide mechanical problems, the small increase in antenna performance was not sufficient to warrant its use. The prototype antenna is shown in Fig. 2-12.

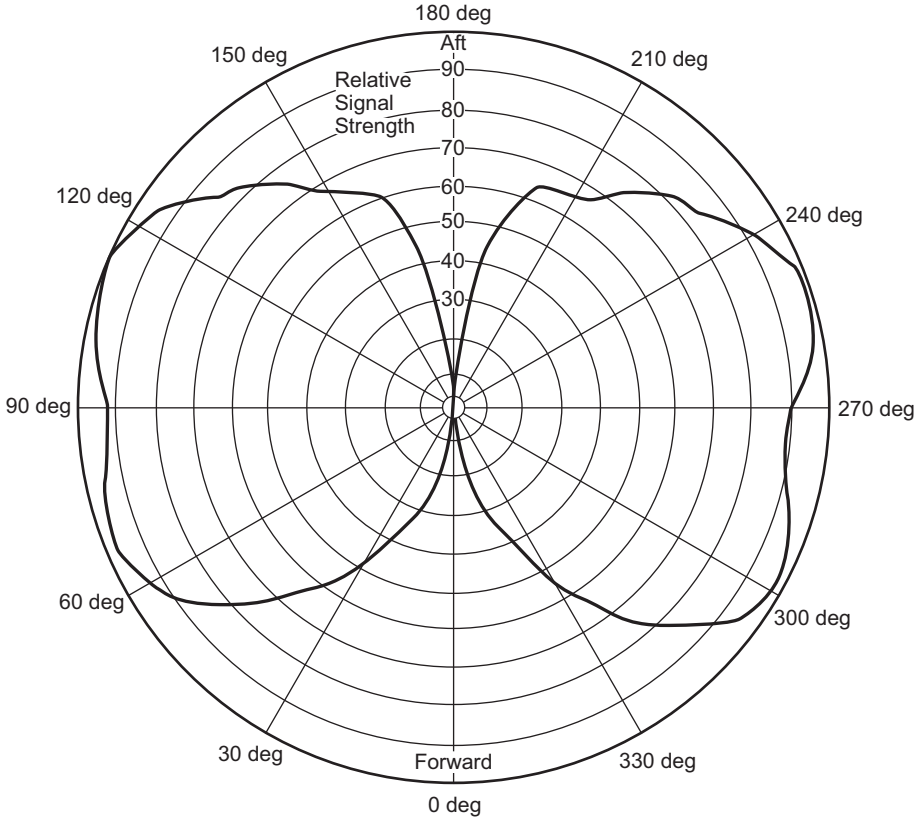

Fig. 2-11. Full-scale disc-cone antenna pattern with diffraction disc.

Fig. 2-12. Disc-cone antenna with diffraction disc.

Figure 2-13 shows the final flight configuration of the omni antenna. A fiberglass cylinder was used to support both the disc at the top of the antenna and the rim of the cone. The fiberglass cylinder mated with the ground plane. Because the outer rim of the ground plane supported the antenna, buttresses were used to carry the loads up from the edge of the ground plane to the fiberglass cylinder. A coaxial transmission line that traveled up the center of the fiberglass cylinder fed the disc-cone antenna. Within this transmission line was a ¼-wavelength matching transformer located where the phase of both the 890- and the 960-MHz impedance was the same. The original design of the antenna had a lip at the top of the antenna where the disc and the fiberglass cylinder were laced together. It was feared that this lip might hang up on the shroud, as it was ejected. To eliminate this possibility, a modification was made to the antenna by adding a small fairing. The fairing began approximately 2 in. (5 cm) below the top of the antenna and ran up to the edge of the disc. This

Fig. 2-13. Rangers 1 and 2 omnidirectional antenna.

modification did not appreciably affect the electrical characteristics of the antenna.

The VSWR of the antenna at both 890 MHz and 960 MHz was below 1.2. The gain was approximately 1.6 dB above isotropic at 960 MHz, and 1.7 dB at 890 MHz. Its weight was approximately 3.3 lb (1.5 kg).

The Pioneer 3 and 4 antenna was adapted for the omni antenna design for Rangers 3, 4, and 5 since the spacecraft was designed to carry a lunar landing capsule. However, since none of these rangers had a successful mission, its design is not included here.

Diplexer. A diplexer (Fig. 2-14) was required on the Ranger series so that the command receiver and the telemetry system could operate over the same omni antenna. A diplexer serves two basic functions. It isolates the power of the transmitter from the receiver, since the high power level could disturb the operation of the receiver. Second, the diplexer matches the transmitter to the antenna so that no power is lost into the receiver, which would cut down the efficiency of the transmitter communications link. The Ranger diplexers were designed and built by Rantec Corporation. The diplexer had four coaxial

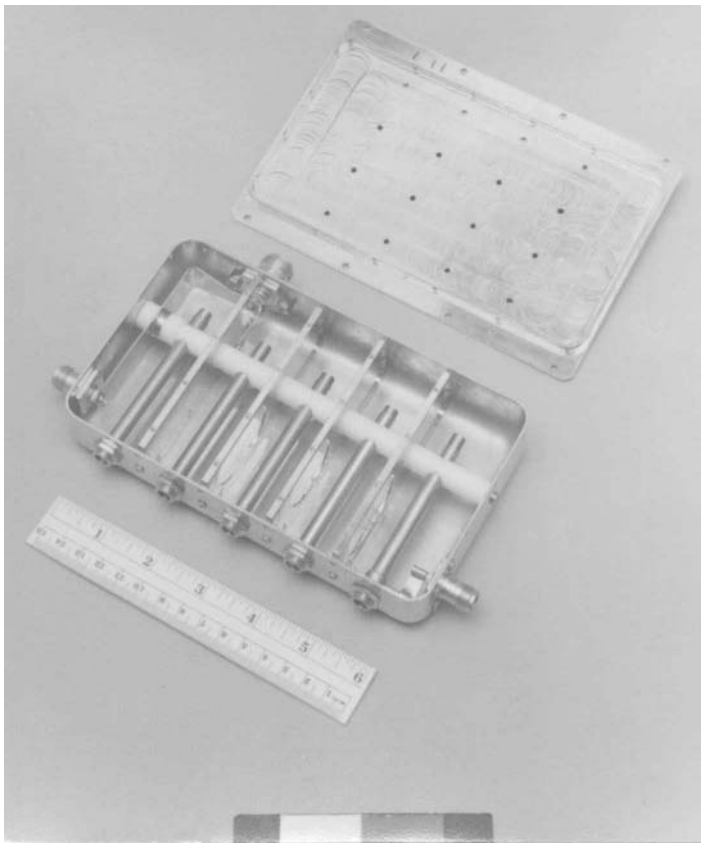

Fig. 2-14. Ranger diplexer.

cavities in the receive arm and one in the transmitter arm. Further details on the design and performance of the diplexer can be found in [8].

2.4 Surveyor

Following up on the Rangers, the Surveyor series (Fig. 2-15) was the first United States' effort to make a soft landing on the Moon. The Surveyor missions tested a new high-energy Atlas/Centaur rocket, a new spacecraft design, two-way communications to control spacecraft activities from the ground, and a new and elegant landing method (with three steerable rocket engines controlled by onboard radar). The Surveyor project began its development in 1961 with the selection of Hughes Aircraft Company as spacecraft system contractor to JPL, which managed the project.

Delayed repeatedly by the extended development of the launch vehicle's Centaur booster and the difficulties of its own development, Surveyor underwent many evolutions of management, engineering, and science before

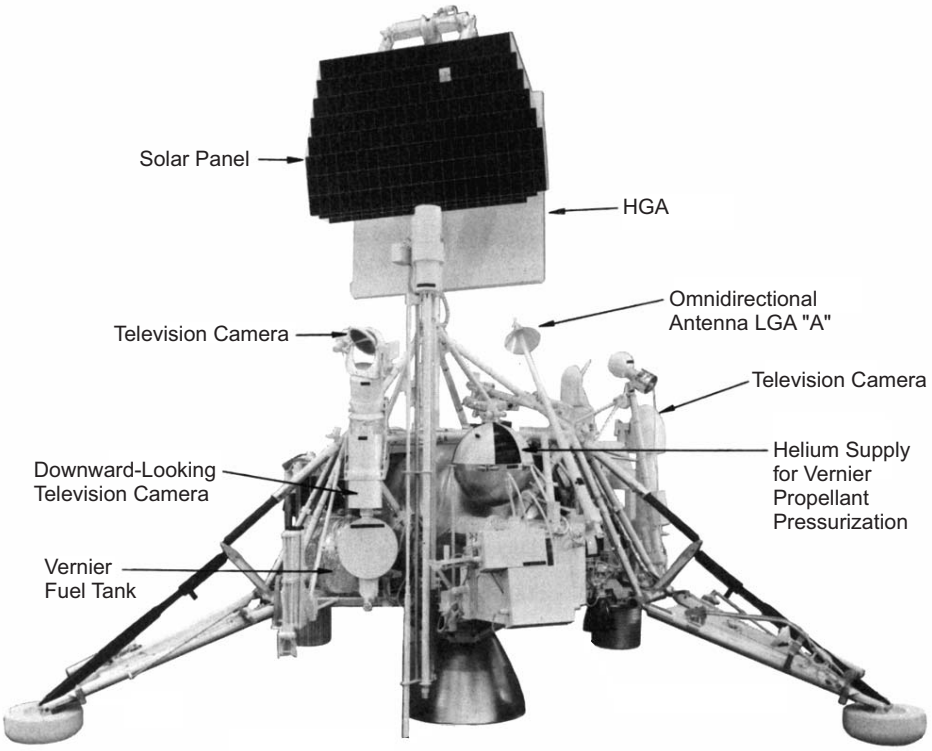

Fig. 2-15. Surveyor Spacecraft.

successfully landing with a remote-controlled TV camera at *Flamsteed* in *Oceanus Procellarum* in June 1966.

2.4.1 Surveyor Radio Switching and Antenna System

The Surveyor radio switching and antenna system contained [9,10]:

1) Two omni antennas (A and B).
2) Planar array directional antenna.
3) Two diplexers (A and B).
4) Two RF power monitors.
5) Antenna transfer switch.
6) Omni antenna selector switch.

The purpose of this system was to connect the output of the operating transmitter to the appropriate antenna and to radiate and receive RF energy.

The two low-gain, omnidirectional turnstile antennas, which were circularly polarized, were used for simultaneous reception of command information and transmission of TV and engineering data. They were positioned on the

spacecraft so that their composite antenna pattern ensured reception of command information for all spacecraft attitudes. The omni antennas had patterns that may be visualized as cardioids of revolution with the null centered back along the antenna support in the direction of the spacecraft. Thus, together both antennas provided the required full 4π steradian coverage at near 0-db gain.

Each omni antenna was permanently connected to a receiver through a diplexer. Located at the ends of fiberglass booms, the antennas were extended away from the main body of the spacecraft during flight and lunar operations.

The high-gain planar-array antenna was a slotted waveguide array, had a gain of 27 dB, and had a beamwidth of approximately 6 deg. It was used for transmitting only, so it operated at 2295 MHz. In normal mission operations, the planar array antenna was used only on the lunar surface, and to take full advantage of the directional gain properties of the antenna, the unit was positioned by command from the controlling ground station.

Each diplexer was permanently connected to one of the omni antennas, and it provided for simultaneous reception and transmission via that single antenna. Each unit was a double-tuned cavity device that had one arm tuned to pass 2.113 GHz and the other to pass 2.295 GHz. A minimum of 60 dB of isolation was provided between the two arms.

The transmitter RF output from the diplexer was applied to the stripline power monitor. A small portion of the transmitter RF, during both high- and low-power transmission, was rectified and filtered by the power monitor and fed to the spacecraft signal processing system for transmission to ground control as an indication of transmitter output power.

Both the antenna transfer switch and the omni antenna selector switch were relay-operated coaxial switches commanded from ground control. The antenna transfer switch was a double-pole, double-throw unit connected to provide, as desired, the output of either of the transmitters to the input of the omni antenna selector switch or the planar array antenna. The omni antenna selector switch was a single-pole, double-throw device that directed the power to either of the two omni antennas.

2.4.2 The High-Gain Planar Antenna Array

The Surveyor spacecraft was designed to soft-land a package of scientific instruments on the lunar surface. One of its requirements was that it be capable of transmitting television pictures of the surrounding terrain back to Earth. The relatively high data rate required for this television signal necessitated the use of an HGA on the spacecraft. It was additionally required that this antenna be circularly polarized to preclude the necessity of polarization tracking. Restricted stowage space and stringent weight limitations demanded the highest possible efficiency from the antenna in a lightweight configuration. A planar-

array antenna designed to satisfy these requirements was 38.5 in. (98 cm) square and weighed only 8.5 lb (3.86 kg). The overall aperture efficiency of 70 percent gave a gain of 27.0 dB. The measured ellipticity of the polarization was 1.0 dB. The Surveyor antenna based on this design is shown in Fig. 2-16. The material which follows was abstracted from reference [11].

2.4.2.1 Design Concept. Circularly polarized arrays can be constructed by using crossed slots on the broad wall of a waveguide at the point of circular polarization of the magnetic fields within the guide [12]. However, efficient aperture illumination is difficult to obtain using these slots alone since they must be spaced a full guide wavelength apart in order to keep the radiated fields in phase. This results in a free-space distance between elements of approximately $1.4\lambda_0$ for typical air-filled waveguides, thereby causing generation of secondary maxima (also known as second-order beams or grating lobes). It has been shown that adequate suppression of these lobes is required in order to obtain high aperture efficiencies. This can be accomplished by using interelement spacing between 0.5 and $0.9\lambda_0$, depending on the array length [13].

One approach considered for obtaining the proper spacing with the crossed slots was to reduce λ_g. It was rejected because none of the usual techniques of reducing λ_g satisfied both weight and gain requirements. A satisfactory solution was found in the form of additional slots in a new arrangement that together with a slow wave structure produced adequate interelement spacing.

The additional slots are of the complex type. The manner in which they solve the interelement spacing can be understood by considering a pair of them as one element. The two slots of each such pair are oriented 90 deg with respect to each other and are longitudinally separated by $\lambda_g/2$, as shown in Fig. 2-17. Each slot radiates the same power. A crossed slot and a complex slot pair located on opposite sides of the centerline radiate the same sense of circular polarization, but are 180 deg out of phase when the complex pair is centered on the same transverse plane as the crossed slot. By shifting the complex slot pair $\lambda_g/2$, in-phase radiation is obtained. Hence, this new slot element allows a commonly used technique of linearly polarized array design (i.e., staggering slot offsets to obtain in-phase radiation from $\lambda_g/2$ spacing) to be used for circularly polarized arrays.

The slow wave structure required for the slot spacing consisted of a series of transverse ridges located in the non-radiating broad wall of each linear array.

2.4.2.2 Array Configuration. The planar array slot configuration required two types of linear arrays, designated 1 and 2 in Fig. 2-18. The two arrays were designed as traveling-wave types with a beam tilt of 6 deg incorporated into the

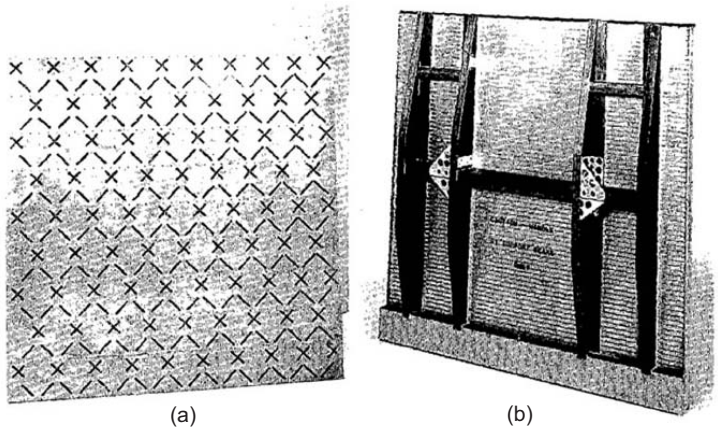

Fig. 2-16. Productized circularly polarized planar array antenna for surveyor: (a) front and (b) back.

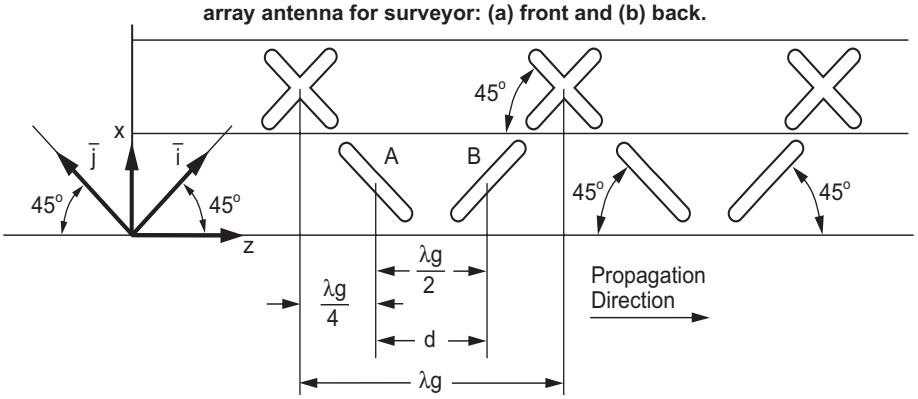

Fig. 2-17. Crossed slot-complex slot pair arrangement.

design for proper input impedance match. The design of each of these arrays was based on the assumption that a single complex slot coupled half as much power as a crossed slot. In both types of arrays, 5 percent of the input power was dissipated in the load termination. In the final design arrays 1 and 2 had 10 and 9 crossed slots, respectively, and 9 complex slot pairs each. No attempt was made to keep the complex slots in pairs since the effect of an additional slot in an array of this length is negligible.

The out-of-phase feeding of adjacent linear arrays was suggestive of a multimode waveguide. However, the slot arrangement resulted in a non-mirror image symmetry about the virtual walls and multimode operation was therefore not possible without heavy mode suppression. Mode suppression was used, and took the form of partial walls between the top of the corrugations and the top plate.

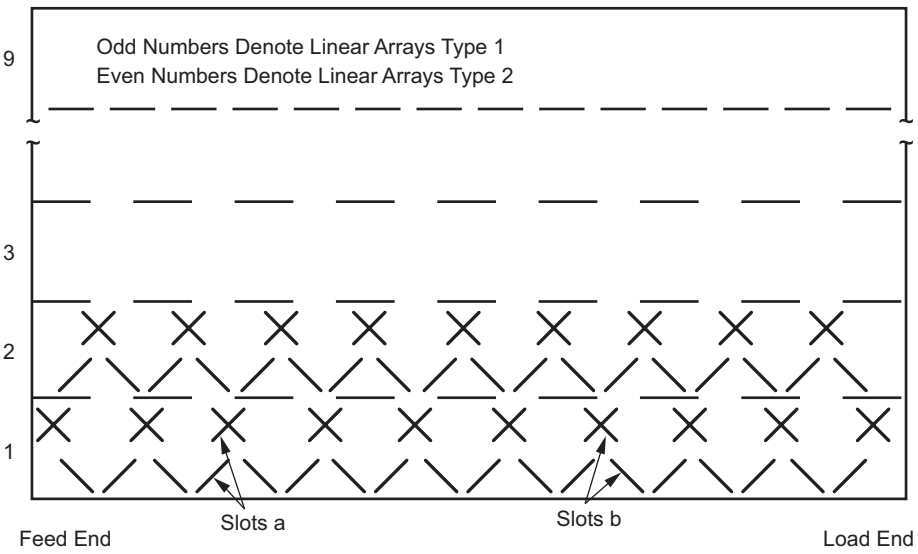

Fig. 2-18. Slot arrangement of circularized polarized planar array for maximum aperture efficiency.

The feedline was a standing-wave array with shunt-type slots coupling from the feedline into the bottom of the first corrugation gap of each linear array. The feedline was in turn centerfed by means of a magnetic loop coax-to-waveguide transition.

2.4.2.3 Performance. The coordinate system for the planar array patterns is shown in Fig. 2-19. The plane of the cut is given by the angle ϕ. The *z*-axis goes through the main lobe peak (thus, it is not perpendicular to the planar array surface), and the *y*-axis is parallel to the feedline. The polar axis, for all cuts except $\phi = 0$ deg, is the *z*-axis. For $\phi = 0$ deg, the polar axis is the dash line z', which is in the $\phi = 0$ deg plane and broadside to the array; accordingly, the pattern angle is θ'. The reason for showing angle θ' in the $\phi = 0$ deg plane is to bring out the existing beamtilt.

Measured patterns of the developmental model antenna showing both linear polarization components for the principal planes ($\phi = 0$ and $\phi = 90$) are shown in Fig. 2-20. The measured axial ratio of the full array is 1.5 dB. The two components are within 0.2 deg of being coincident, and the measured beamwidths are in good agreement with the 6.8-deg beamwidths computed for this aperture size. The large 1st sidelobes in the E_θ component, $\phi = 0$ deg plane, are due to the radiation from the end of the guides. In this particular array the guides are open ended.

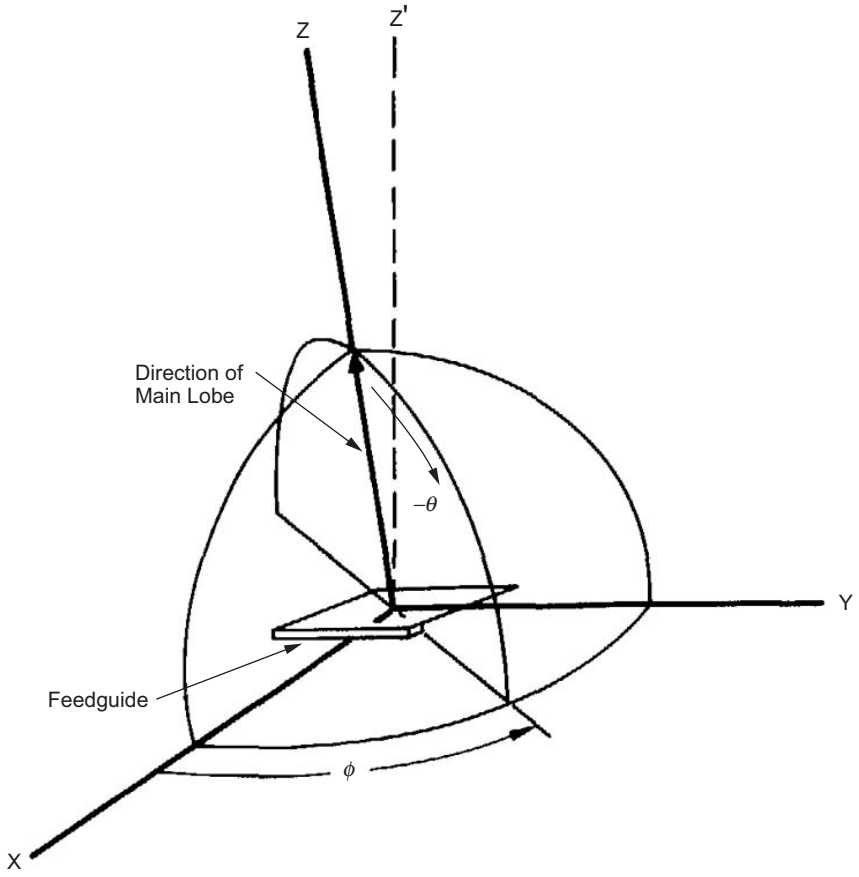

Fig. 2-19. Coordinate system for planar array patterns.

The antenna gain with a waveguide input was 27.2 dB, corresponding to an overall efficiency of 73 percent. However, with the coax input the best gain achieved was 27.0 dB.

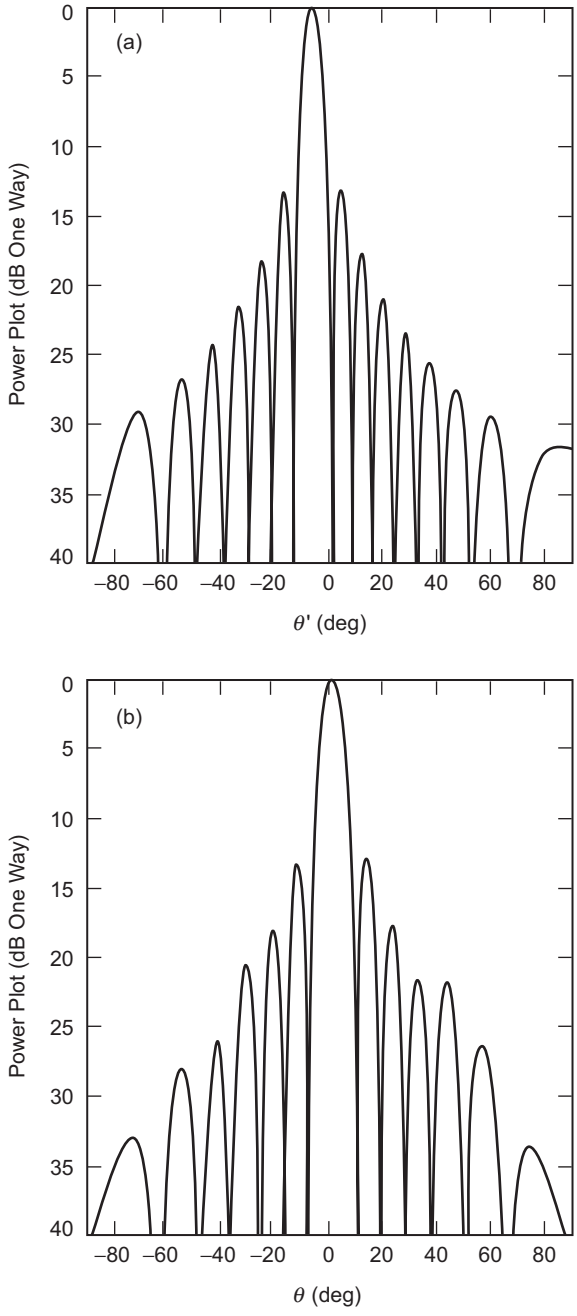

Fig. 2-20. Measured antenna patterns: (a) ϕ = 0 deg plane and (b) ϕ = 90 deg plane.

References

[1] C. R. Koppes, *JPL and the American Space Program*, Chapter 6, Yale University Press, New Haven, Connecticut, and London, England, 1982.

[2] "Explorer-I and Jupiter-C," Headquarters, Public Affairs Office web site, National Aeronautics and Space Administration, site accessed July 6, 2005. http://www.hq.nasa.gov/office/pao/History/sputnik/expinfo.html

[3] *Secretary McElroy Announces New Space Program*, DOD News Release No. 288-50, Department of Defense, Washington, District of Columbia, March 27, 1958.

[4] *Space Programs Summary No. 1*, Jet Propulsion Laboratory, Pasadena, California, February 1, 1959.

[5] W. A. Imbriale, *Large Antennas of the Deep Space Network,* Chapter 2, John Wiley & Sons, Inc., Hoboken, New Jersey, 2003,

[6] R. C. Hall, *Lunar Impact: A History of Project Ranger,* NASA SP 4210, National Aeronautics and Space Administration, Washington, District of Columbia, 1977.

[7] "Rangers and Surveyors to the Moon," *NASA Facts*, Jet Propulsion Laboratory, Pasadena, California, May 1996, also available at JPL web site accessed July 25, 2005. www.jpl.nasa.gov/news/fact_sheets/rangsurv.pdf

[8] *The Ranger Project: Annual Report for 1961*, Technical Report No. 32-241, Jet Propulsion Laboratory, Pasadena, California, June 15, 1962.

[9] *Surveyor Project Final Report*, Part 1 *Project Description and Performance*, Technical Report 32-1265, Jet Propulsion Laboratory, Pasadena, California, July 1, 1969.

[10] *Summary of the Surveyor Spacecraft System*, Technical Memorandum No. 33-54, Jet Propulsion Laboratory, Pasadena, California, September 1, 1961.

[11] A. F. Seaton and G. A. Carnegis, "A Novel Circularly Polarized Planar Array for Surveyor," *1963 IEEE International Convention Record*, pp. 2–9, March 1963.

[12] A. J. Simmons, "Circularly Polarized Slot Radiators," *IRE Transactions on Antennas and Propagation*, vol. AP-5, iss. 1, pp. 31–36, January 1957.

[13] H. E. King, "Directivity of a Broadside Array of Isotropic Radiators," *IRE Transactions on Antennas and Propagation*, vol. AP-7, pp. 197–198, April 1959.

Chapter 3
The Planetary Flybys

William A. Imbriale

The next era in Solar System exploration included flybys of the planets with spacecraft carrying scientific instruments designed to study the characteristics of the planets and intervening space. The Mariner series of spacecraft was designed to study the inner Solar System, and the two Voyager spacecraft were targeted for the outer planets.

Between 1962 and late 1973, The National Aeronautics and Space Administration's (NASA's) Jet Propulsion Laboratory (JPL) designed and built 10 spacecraft named Mariner to explore the inner Solar System [1]—visiting the planets Venus, Mars, and Mercury for the first time, and returning to Venus and Mars for additional close observations. The next-to-last mission, Mariner 9, became the first spacecraft to orbit another planet when it reached Mars for about a year of mapping and measurement. The final mission in the series, Mariner 10, flew past Venus before going on to encounter Mercury, after which it returned to Mercury for a total of three flybys.

The Mariners were all relatively small robotic explorers, each launched on an Atlas rocket with either an Agena or Centaur upper-stage booster, and each weighed less than half a ton (without onboard rocket propellant). Each of their missions was completed within a few months to a year or two, though one of them outlived its original mission and continued to send useful scientific data for three years.

The Voyager mission [2] was designed to take advantage of a rare geometric arrangement of the outer planets in the late 1970s and the 1980s. This layout of Jupiter, Saturn, Uranus, and Neptune (which occurs about every 175 years) allows a spacecraft on a particular flight path to swing from one

planet to the next without the need for large onboard propulsion systems. The flyby of each planet bends the spacecraft's flight path and increases its velocity enough to deliver it to the next destination. Using this "gravity assist" technique, the flight time to Neptune, with the rockets available at that time, was reduced from 30 years to 12. This mission has become known as The Grand Tour.

3.1 The Mariner Series

The Mariner series of missions were designed to be the first U.S. spacecraft to other planets, specifically Venus and Mars. This chapter focuses on the Venus and Mercury flybys, and Chapter 4 describes the Mars missions.

3.1.1 Mariners 1 and 2

Mariners 1 and 2 (Fig. 3-1) were nearly identical spacecraft developed to fly by Venus. The rocket carrying Mariner 1 went off-course during launch on July 22, 1962, and was blown up by a range safety officer about 5 minutes into flight. A month later, Mariner 2 was launched successfully on August 27, 1962, sending it on a 3-1/2-month flight to Venus. On the way, it measured for the first time the solar wind, a constant stream of charged particles flowing outward from the Sun. It also measured interplanetary dust, which was found to be scarcer than predicted. In addition, Mariner 2 detected high-energy charged particles coming from the Sun, including several brief solar flares, as well as cosmic rays from outside the Solar System. As it flew by Venus on December 14, 1962, Mariner 2 scanned the planet with infrared and microwave radiometers, revealing that Venus has cool clouds and an extremely hot surface. Because the bright, opaque clouds hide the planet's surface, Mariner 2 was not outfitted with a camera.

3.1.1.1 Mariner Antennas. The radio frequency (RF) subsystem [3,4] employed four antennas for the various in-flight communications requirements. Reception of ground-transmitted signals was through the Command Antenna System; a dipole antenna and a turnstile antenna mounted above and below the outboard end of a solar panel. Both antennas relayed the received 890-MHz energy to the communications transponder through a flexible coaxial cable.

Prior to spacecraft midcourse maneuver, an omnidirectional antenna located at the apex of the spacecraft structure transmitted 960-MHz signals to the ground. A separate L-band cavity amplifier provided power to the antenna. Following midcourse maneuver and after the attitude of the spacecraft had been corrected, the radio frequency (RF) power was radiated by a high-gain directive antenna located at the base of the spacecraft hex structure. A separate cavity amplifier also drove this antenna. The high-gain antenna (HGA) was nested at

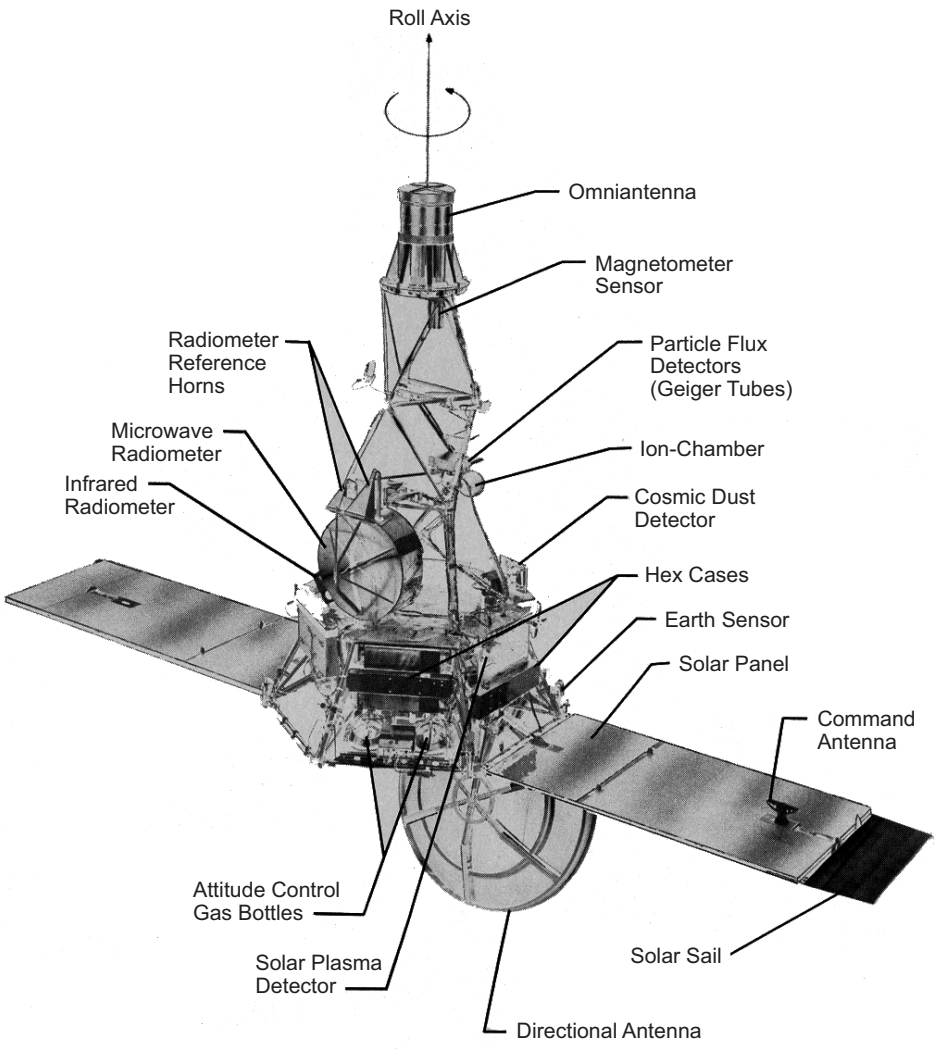

Fig. 3-1. Mariner 2 spacecraft.

the base of the spacecraft structure until midcourse maneuver, when it swung into position and faced the Earth. RF power was fed from the cavity amplifier to the HGA through flexible coaxial cables and a rotary joint. The cavity amplifiers were switched to provide either an omnidirectional pattern or an Earth-directed lobe.

A substantial portion of the antenna system was inherited from the Ranger Spacecraft. The omni antenna, for early flight telemetry, was the Ranger disc-cone antenna. The directional HGA used the Ranger 1 feed modified for circular polarization and a Ranger type parabolic reflector. This feed was then also used on Rangers 6 and 7. Radio-frequency continuity between the HGA

and the communications system during relative motion of the antenna and bus was provided by a Ranger 1-type coaxial rotary joint and associated cabling.

Omni antenna. The omni antenna, having been taken directly from the Ranger configuration, required no design work, but some structural strengthening was necessary. The omnidirectional antenna was located at the apex of the spacecraft structure and was driven by a separate L-band cavity amplifier.

Command antenna subsystem. The command antenna subsystem consisted of a turnstile antenna mounted on the backside of the solar panel and a dipole antenna mounted on the forward side of the solar panel (Fig. 3-2). To split the power between the two antennas, a directional coupler was used, with the dipole being driven 6 dB below that of the turnstile.

High-gain antenna. Requirements for the Mariner HGA design were the following:

1) The existing paraboloidal reflector had to be used with a minimum of modifications.
2) The design had to provide an efficient circularly polarized feed at 960 MHz.
3) The feed structure had to be compatible with the adapter diaphragm of the Ranger-Agena B vehicle.

A feed design was quickly accomplished by modifying the existing Ranger 1 configuration. The modification involved the replacement of the linearly polarized dipole elements with circularly polarized turnstile elements consisting of two dipoles oriented 90 deg from each other and 45 deg from the balun slot on the outer conductor. In the design, circular polarization was achieved by the phase quadrature of the essentially equal currents flowing in the crossed dipoles when one dipole was cut appropriately shorter than that required for resonance and the other appropriately longer than that required for resonance.

Several focal-length positions were examined in order to optimize the gain. At each position, the element lengths were adjusted to produce nearly circular polarization, meeting the criterion that the gain variation versus incident linear polarization angle be less than 0.2 dB. The 1-dB and 3-dB beamwidths of the antenna were 10.3 and 16.5 deg, respectively. Absolute gain relative to right-hand circular polarization (RHCP) of the antenna was measured to be 20.0 ±0.5 dB. Gain variation of the antenna versus incident linear polarization angle (ellipticity) was measured to be 0.33 dB.

3.1.2 Mariner 5

The Mariner 5 spacecraft was originally built as a backup to Mariner 4, a Mars craft launched in 1964. When Mariner 4 completed its mission

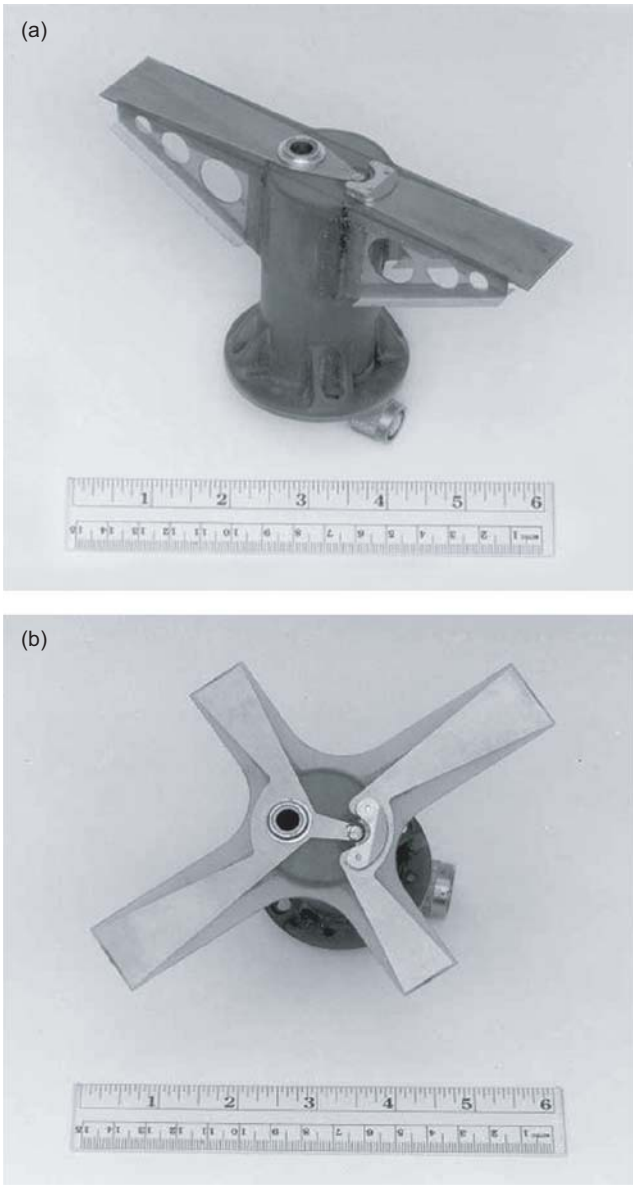

Fig. 3-2. Mariner 2 command antennas: (a) dipole and (b) turnstile.

successfully, the backup was rechristened Mariner 5 and reoutfitted for a flyby of Venus. Launched from Cape Canaveral, Florida, in June 1967, Mariner 5 (Fig. 3-3) flew within about 4,000 km (approximately 2,500 miles) of Venus some four months later. Mariner 5's flight path following its Venus encounter brought it closer to the Sun than any previous probe.

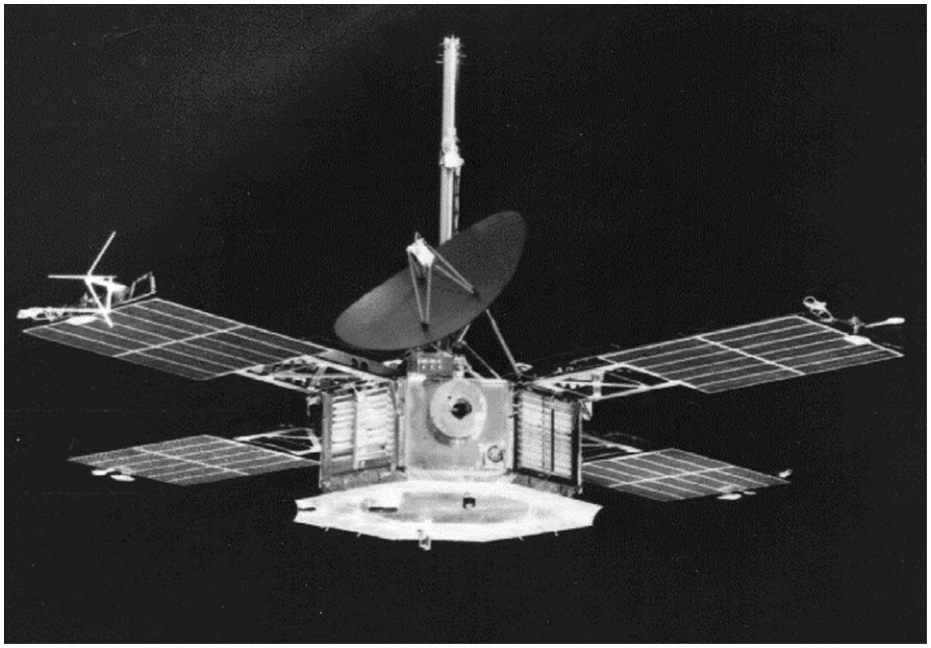

Fig. 3-3. Mariner 5 spacecraft.

The spacecraft antenna subsystem included a low-gain antenna (LGA), an HGA, and their transmission lines [5]. The function of the LGA was to receive commands from Earth and to transmit telemetry to Earth during the first half of the mission and during midcourse maneuver. The primary function of the HGA was to transmit telemetry to Earth during the last half of the transfer orbit and for a period after planetary encounter. The Earth-look angles were somewhat different than those for the Mariner 4 mission. Look angles for Venus continued away from the low-gain peak after encounter, while those at Mars reversed and retraced through the low-gain beam. Thus, the trajectories put the Earth-look angles on the opposite sides of the spacecraft. This placement of these angles would not have been a difficult problem if only telemetry and command requirements had to be met, since the encounter range of Venus was only 80 million km, whereas it was 222 million km for Mars in 1965. Hence, for the Venus encounter, the antenna gain required was about 9 dB less than that for Mariner 4 at Mars. If this antenna gain, then, was the only requirement, a relatively small antenna could have been packaged on the opposite side of the Mariner 4 type-spacecraft to accomplish the encounter antenna coverage. However, the S-band occultation experiment had to be considered as a key element, and for this, a nominal peak gain of 21.5 dB was required, which was approximately the gain required for telemetry return from Mars by Mariner 4.

This fact sized the Mariner 5 HGA to something approximately the same as the Mariner 4 HGA.

Since an antenna of this size would be impossible to position between the spacecraft and the Agena or between the bus and the shroud adapter, the antenna would have had to be stowed above the bus during launch and deployed after planetary injection, or the solar axis of the spacecraft would have had to be reversed. Of these two choices, the reversal of the solar axis appeared to be not only inherently the most reliable but also the easiest to implement.

In this configuration, the Mariner 4 LGA could be used without changes for Mariner 5, since the cone angle variations of Earth with time from launch to loss of LGA signal would now be similar. Clock-angle variations were not of significance in the LGA selection, since its pattern was essentially symmetrical about the roll axis.

Hence, S-band antennas made for Mariner 4 were used for Mariner 5 with only minor changes. The LGA consisted of an RHCP mode launcher in the base of a 2.1-m-long, 0.10-m-diameter circular aluminum waveguide, with a crossed slot radiator and a ground-plane system at the other end (Fig. 3-4). The base of the antenna was mounted in a fixed position on the spacecraft structure with the waveguide extending parallel to the spacecraft Z-axis.

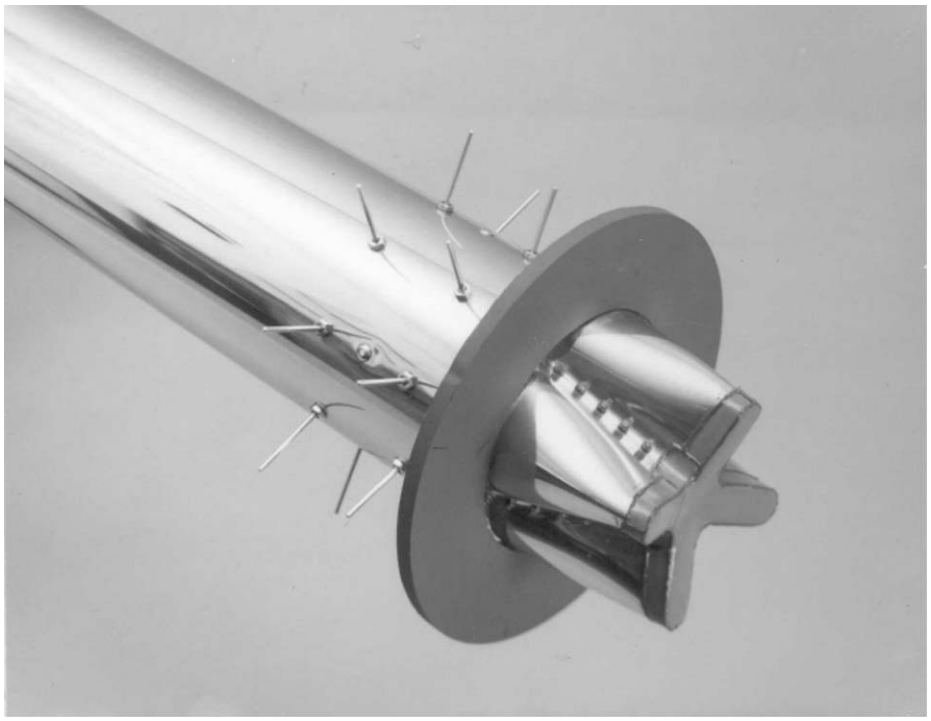

Fig. 3-4. Mariner 5 low-gain antenna.

The HGA consisted of a reflector and feed (Fig. 3-5). The reflector was a sectoral paraboloid, with an elliptic aperture that had a major axis of 1.17 m and a minor axis of 0.53 m. The feed was an array of two turnstile elements driven in phase through a stripline power divider and matching network. The HGA was right-hand circularly polarized. A fiberglass feed support truss joined the feed and reflector, an antenna support truss joined the reflector to the spacecraft, and a section of rigid coax tubing (supported by the feed and antenna support trusses) passed from the feed through the reflector.

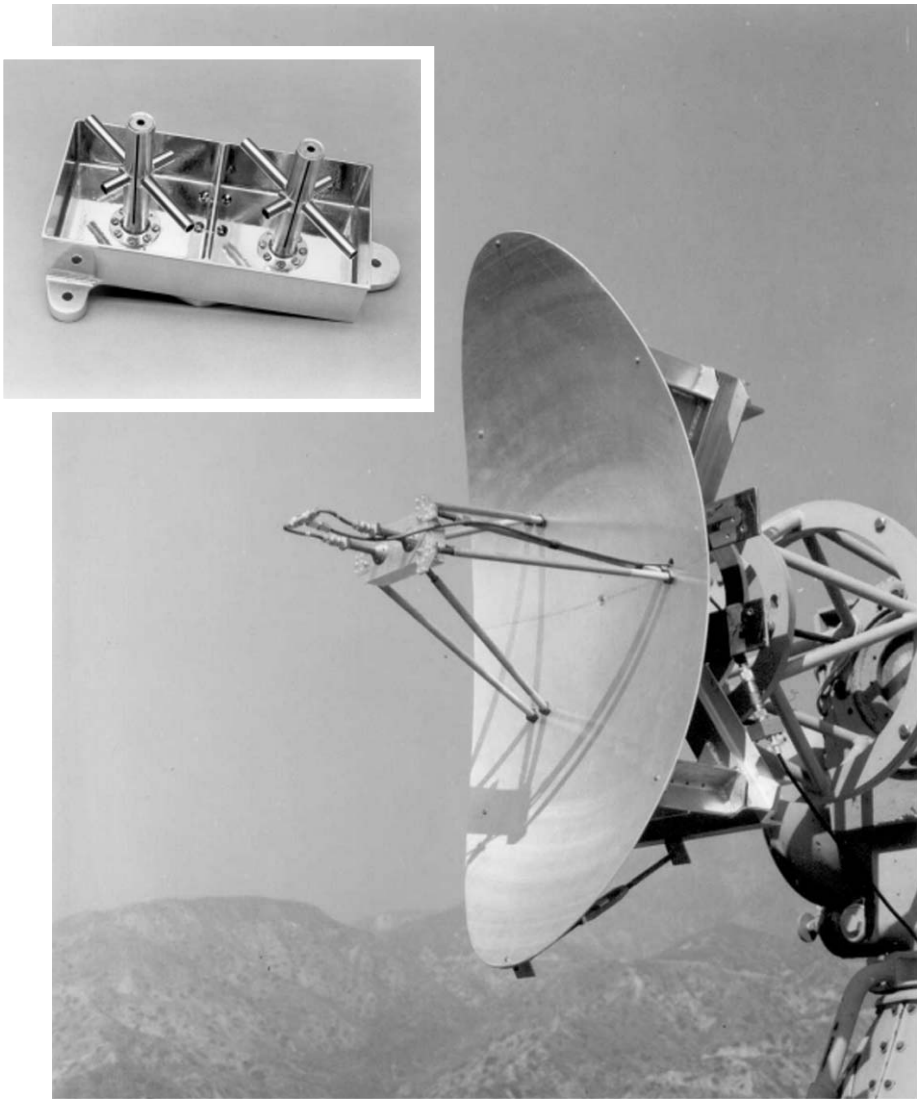

Fig. 3-5. Mariner 5 breadboard high-gain antenna.

Unlike Mariner 4, the Mariner 5 HGA had two separate positions to accommodate the occultation experiment. For a fixed on-board antenna, the occultation experiment required two peaks with approximately 21.5 dB nominal gain, each spaced 53 deg apart in the plane containing the earth track with sufficient cross Earth track to account for out-of-plane bending of the occultation whiskers. Various antenna studies narrowed the logical choice to the Mariner 4 HGA with its 23.2-dB peak gain and 2.06:1 beamwidth aspect ratio, along with a simple one-step position change to be made while the spacecraft was behind the planet. This choice would allow optimum pointing of the antenna back along the Earth track when entering occultation, then, allow it to be placed to a second position behind the planet allowing optimum pointing for the outgoing occultation. The offset angle chosen for the first position of the HGA was a compromise between occultation optimization and telemetry return to Earth after encounter in the event that the antenna pointing angle change did not occur. Hence, the first offset angle was –8.2 deg, while the exit occultation offset was 9.5 deg.

Changes made to accommodate the two positions included the addition of a new mounting interface structure and revision of the coaxial cabling between the antenna and the electronic cases. A tuned mismatch was inserted in the LGA transmission line as a result of an interferometer problem on Mariner 4 caused by insufficient isolation between the high-gain and low-gain antennas. A detailed discussion of this problem may be found in [5].

3.1.3 Mariner 10

With Mariner 10, JPL engineers embarked on an experiment with an ingenious way of traveling through the Solar System using the gravity of one planet to help propel the craft on to the next destination—somewhat like a series of bank shots in a game of billiards [6].

With the scorched inner planet Mercury as its ultimate target, the final Mariner pioneered the use of a "gravity assist" swing by the planet Venus to bend its flight path. Using a near-ultraviolet filter, it produced the first clear pictures of the Venusian chevron clouds and performed other atmospheric studies before moving to the small, airless, cratered globe of Mercury. Here a fortuitous gravity assist enabled the spacecraft to return at six-month intervals for close mapping passes over the planet, covering half the globe (Mercury's slow rotation left the other half always in the dark when Mariner 10 returned).

The S/X-band antenna subsystem requirements provided for transmission and reception of S-band signals between the DSN and the Mariner spacecraft and for transmission of X-band signals from the spacecraft to the DSN [7,8]. The subsystem consisted of one HGA, one LGA, an HGA coupler, plus the necessary RF transmission lines and associated connectors. The HGA requirements were to downlink S-band (2295 + 5 MHz) and X-band (8415 + 20

MHz) using an RHCP signal. The gain requirements were S-band 27.6 ±0.25 dB and X-band 38.2 ±0.4 dB. The LGA requirements were to uplink and downlink S-band (2115 ±5 MHz receive and 2295 ±5 MHz transmit). The polarization was RHCP, and the minimum gains at mercury encounter when the Sun was acquired were receive –4.1 dB and transmit –3.1 dB.

A schematic of the antenna subsystem is shown in Fig. 3-6. The HGA was a steerable parabolic dish 54 in. (137.2 cm) in diameter with a focal length of 21.6 in. (54.88 cm). It used a collocated S-and X-band focal point feed where the S-band feed was an annular cavity, and the X-band feed was an open-ended circular waveguide. The LGA was a boom-mounted biconical antenna with the boom used as an air-dielectric coaxial transmission line. It was fixed mounted after deployment from stowed position, but it had a post-Mercury encounter redeployment capability. The transmission lines used 50-Ω semi-rigid coax, and the deployment and articulating joints used 50-Ω flexible coax.

There was some heritage from the earlier Mariner missions for the HGA dish materials, but the feed was new, and the LGA was a new design patterned after a lunar orbiter LGA design but with simplified feed and thermal expansion joint. The antenna subsystem weight was 7.24 lb (3.3 kg).

Pictures of the HGA feed are shown in Figs. 3-7 and 3-8. Studies were made of the vertex-to-feed distance, and the outer cup depth and the measured data for S-band are shown in Fig. 3-9. The selected design was 22.2 in. (56.4 cm) focal distance and 1.6 in. (4.1 cm) cup. The measured gains were 27.6 dB at S-band and 38.74 dB at X-band.

The Mariner LGA configuration is shown in Fig. 3-10. Typical patterns compared to the specification are shown in Fig. 3-11.

3.2 Voyager Mission to the Outer Planets

The Voyager mission [2] was designed to take advantage of a rare geometric arrangement of the outer planets in the late 1970s and the 1980s. This layout of Jupiter, Saturn, Uranus, and Neptune, which occurs about every 175 years, allows a spacecraft on a particular flight path to swing from one planet to the next without the need for large onboard propulsion systems. The flyby of each planet bends the spacecraft's flight path and increases its velocity enough to deliver it to the next destination. Using this "gravity assist" technique, the flight time to Neptune was reduced from 30 years to 12.

While the four-planet mission was known to be possible, it was deemed to be too expensive to build a spacecraft that could go the distance, carry the instruments needed, and last long enough to accomplish such a long mission. Thus, the Voyagers were funded to conduct intensive flyby studies of Jupiter and Saturn only. More than 10,000 trajectories were studied before choosing the two that would allow close flybys of Jupiter and its large moon Io, and

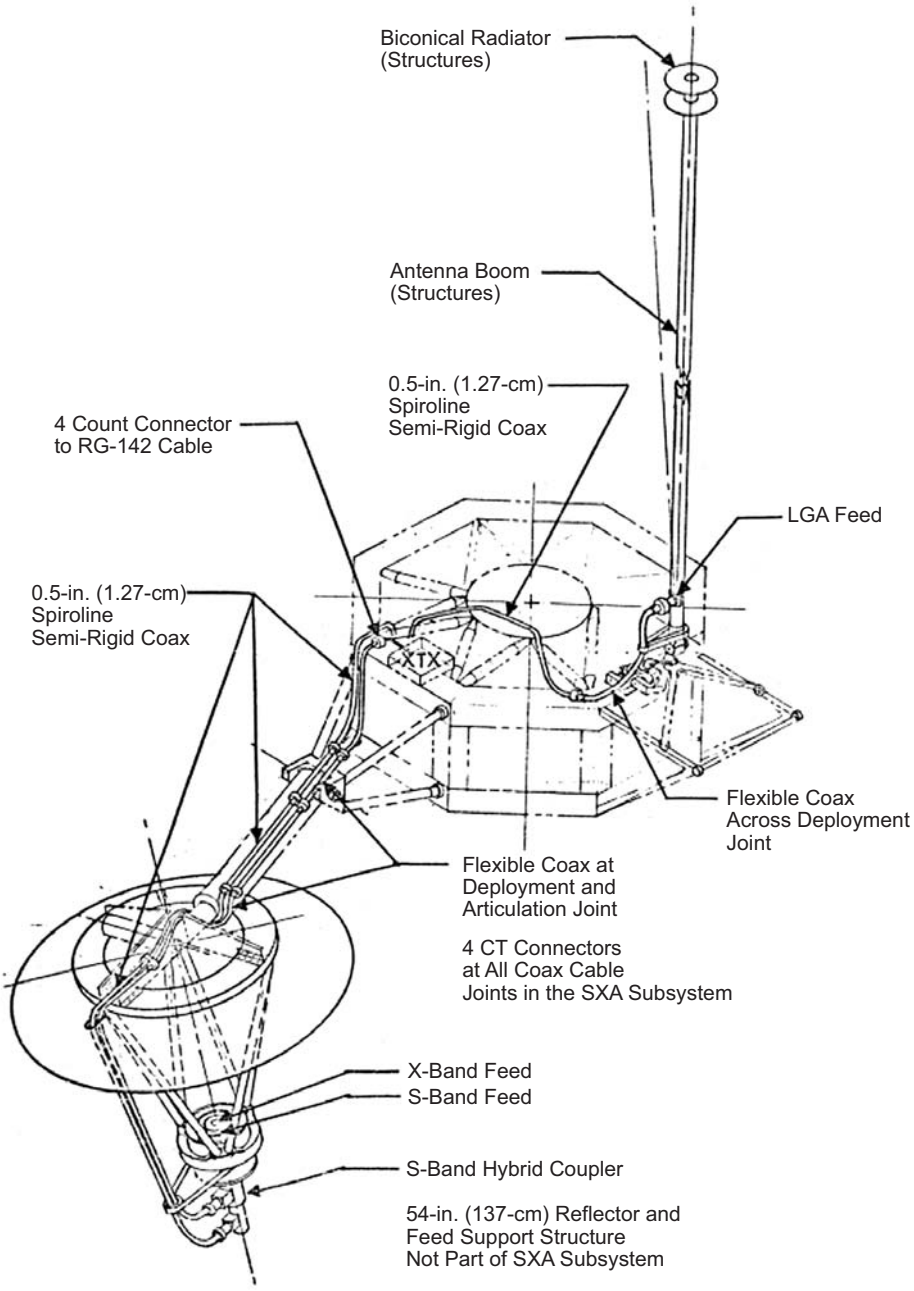

Fig. 3-6. Mariner 10 antenna subsystem (CT = coil terminal).

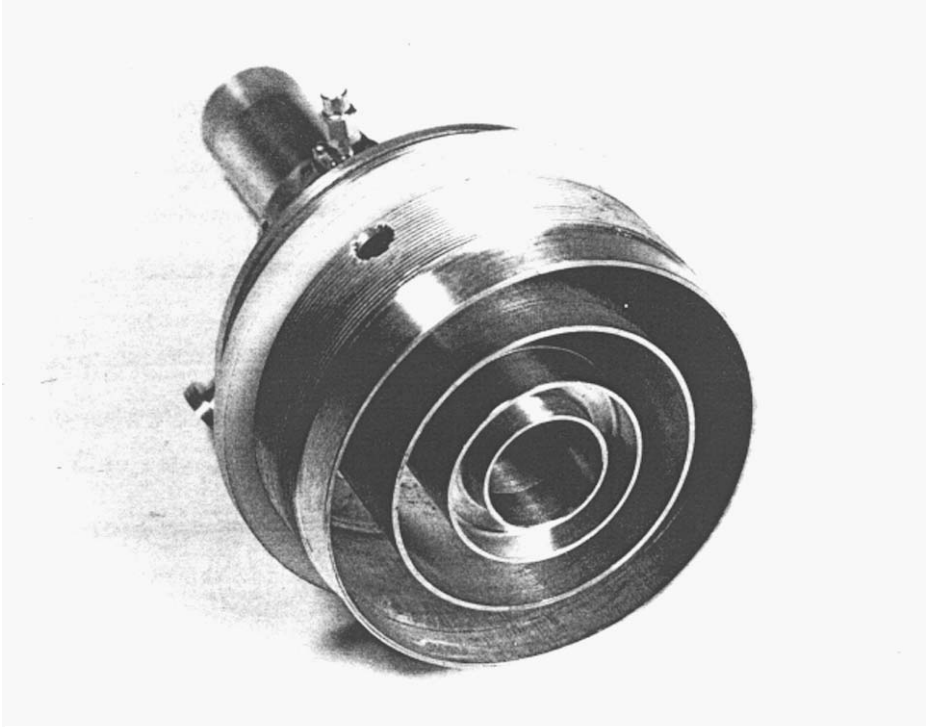

Fig. 3-7. Mariner 10 HGA feed.

Saturn and its large moon Titan. The chosen flight path for Voyager 2 also preserved the option to continue on to Uranus and Neptune.

From the NASA Kennedy Space Center at Cape Canaveral, Florida, Voyager 2 was launched first, on August 20, 1977; Voyager 1 was launched on a faster, shorter trajectory on September 5, 1977. Both spacecraft were delivered to space aboard Titan-Centaur expendable rockets. The prime Voyager mission to Jupiter and Saturn brought Voyager 1 to Jupiter in 1979 and Saturn in 1980, while Voyager 2 flew by Jupiter in 1979 and Saturn in 1981. Voyager 1's trajectory, designed to send the spacecraft closely past the large moon Titan and behind Saturn's rings, bent the spacecraft's path inexorably northward out of the ecliptic plane—the plane in which most of the planets orbit the Sun. Voyager 2 was aimed to fly by Saturn at a point that would automatically send the spacecraft in the direction of Uranus.

After Voyager 2's successful Saturn encounter, it was shown that Voyager 2 would likely be able to fly on to Uranus with all instruments operating. NASA provided additional funding to continue operating the two spacecraft and authorized JPL to conduct a Uranus flyby. Subsequently, NASA also authorized the Neptune leg of the mission, which was renamed the

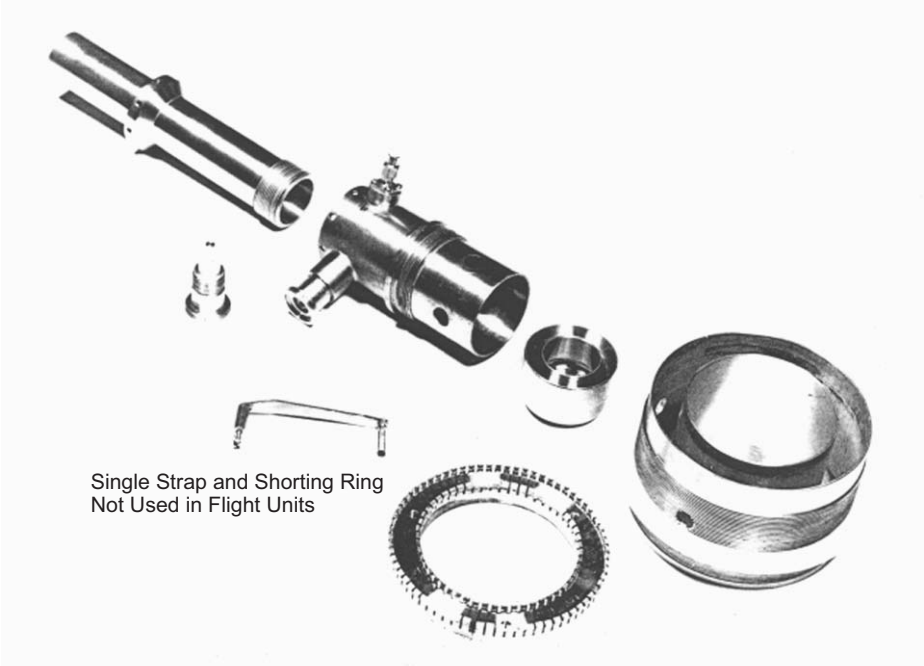

Fig. 3-8. Mariner 10 HGA feed, exploded view.

Voyager Neptune Interstellar Mission. It should be pointed out, however, that although Voyager 2 was targeted to fly by Uranus and Neptune, the telecommunications link was only designed for operation at Jupiter and Saturn. Since it was not possible to change the spacecraft, significant improvements in the ground portion of the link were necessary for a successful mission at Uranus and Neptune. A description of the many improvements to the ground antenna system can be found in [9]. It included, among other things, an addition of another 34-m antenna subnet, increasing the size of the existing 64-m antennas to 70-m, and arraying 34-m and 70-m antennas.

Voyager 2 encountered Uranus on January 24, 1986, returning detailed photos and other data on the planet, its moons, its magnetic field, and its dark rings. Voyager 1, meanwhile, continued pressing outward, conducting studies of interplanetary space. Eventually, its instruments may be the first of any spacecraft to sense the heliopause—the boundary between the end of the Sun's magnetic influence and the beginning of interstellar space.

Following Voyager 2's closest approach to Neptune on August 25, 1989, the spacecraft flew southward, below the ecliptic plane and onto a course taking it, too, to interstellar space. Reflecting the Voyagers' new transplanetary destinations, the project name was changed to the Voyager Interstellar Mission.

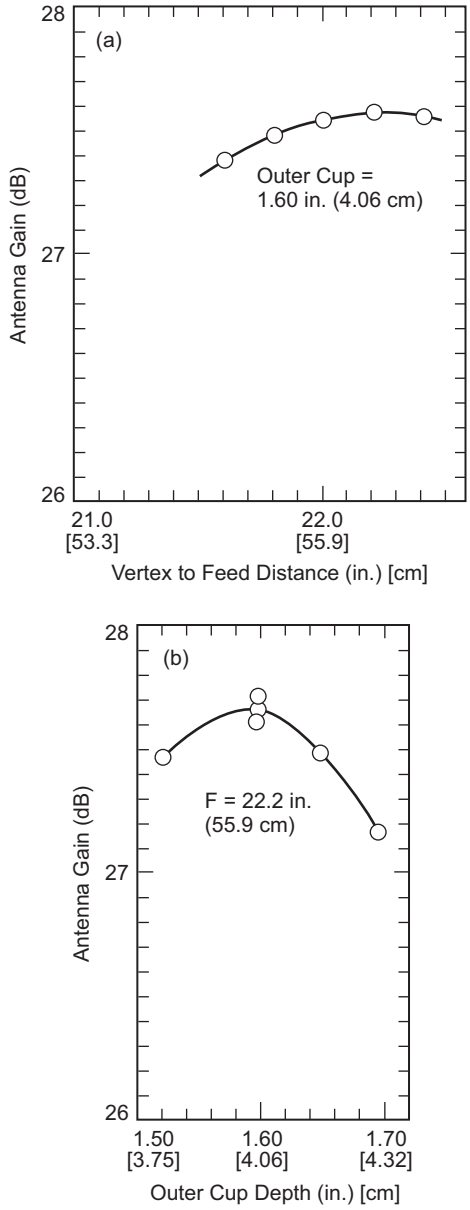

Fig. 3-9. Mariner 10 HGA S-band gain measurements (measurements obtained using linear standard gain horn): (a) vertex to feed distance and (b) outer cup depth.

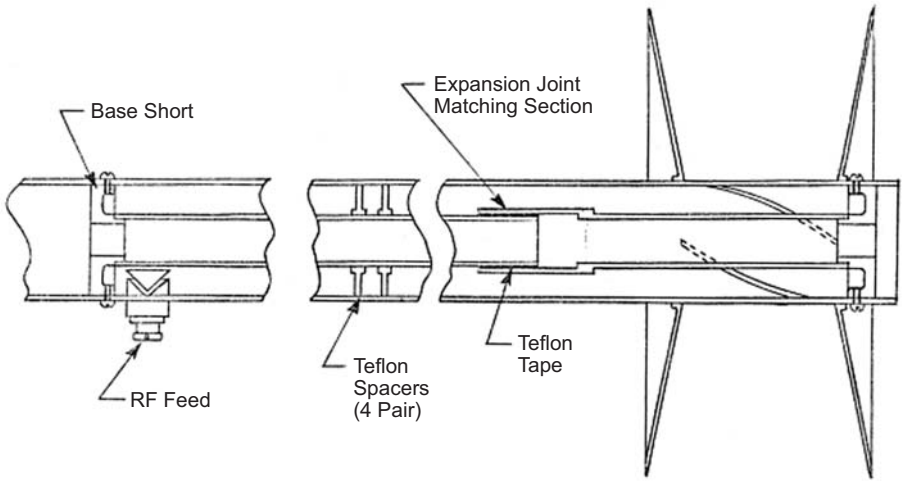

Fig. 3-10. Mariner 10 LGA configuration.

Voyager 1 is now leaving the Solar System, rising above the ecliptic plane at an angle of about 35 degrees at a rate of about 520 million kilometers (about 320 million miles) a year. Voyager 2 is also headed out of the Solar System, diving below the ecliptic plane at an angle of about 48 degrees and a rate of about 470 million kilometers (about 290 million miles) a year.

Both spacecraft will continue to study ultraviolet sources among the stars, and the fields and particles instruments aboard the Voyagers will continue to search for the boundary between the Sun's influence and interstellar space. The Voyagers are expected to return valuable data for two or three more decades. Communications will be maintained until the Voyagers' nuclear power sources can no longer supply enough electrical energy to power critical subsystems.

3.2.1 Voyager S-/X-Band Antenna Subsystem

The Voyager spacecraft (Fig. 3-12) S-/X-band antenna subsystem (SXA) is required to (1) receive S-band signals from the DSN and conduct them to the radio frequency subsystem (RFS), (2) transmit S-band signals from the RFS to the DSN, and (3) transmit X-band signals from either RFS X-band traveling wave tube assembly (TWTA) to the DSN [10,11].

A schematic diagram of the SXA is shown in Fig. 3-13. It consists of an HGA, an LGA, transmission lines (including waveguide and X-band power monitors), and RF power probes located on the HGA main reflector and the LGA cavity.

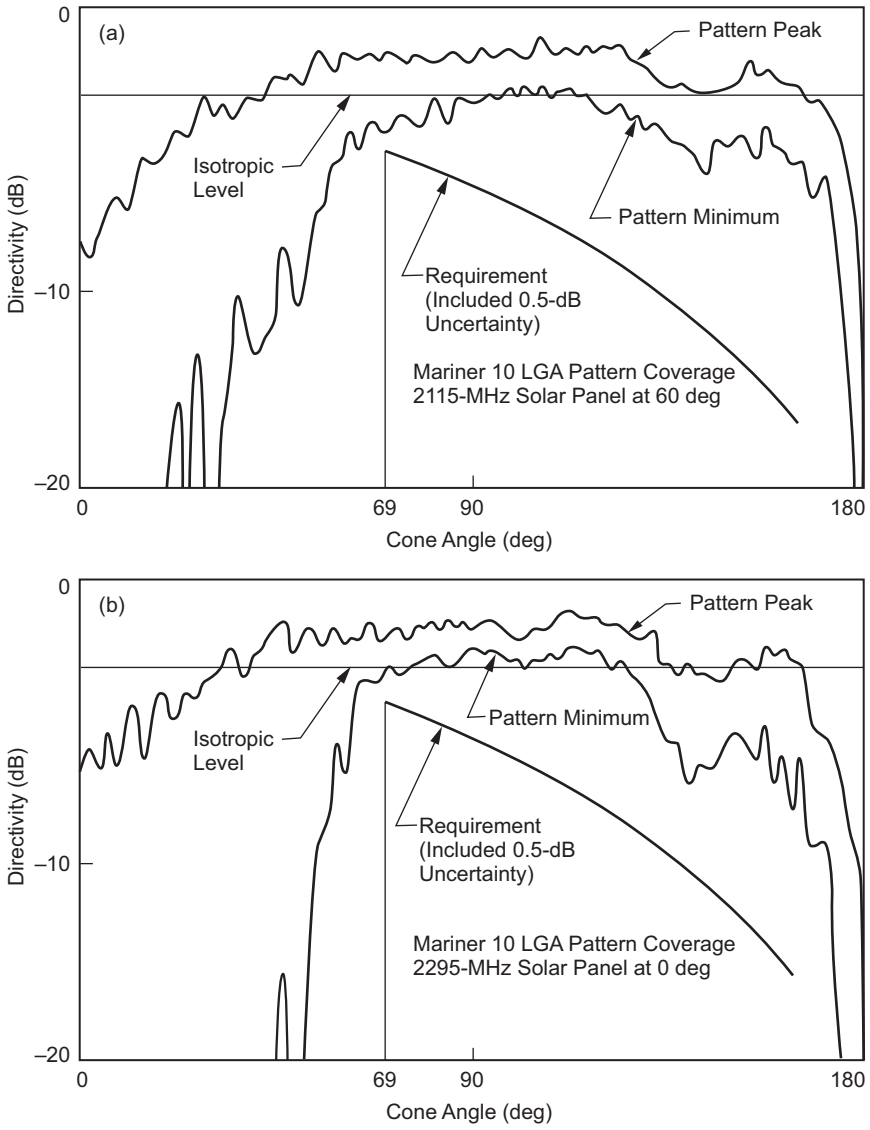

Fig. 3-11. Mariner 10 LGA patterns: (a) 2115 MHz and (b) 2295 MHz.

3.2.2 Requirements

The HGA consists of a paraboloidal reflector with a 3.66-m (12-ft.) diameter circular aperture and suitable S- and X-band feeds. The X-band feed utilizes dual shaped Cassegrain optics, and the S-band feed utilizes a prime focus feed. A frequency selective subreflector (FSS) reflects the X-band signal and passes the S-band signal. The HGA has a focal length to diameter (F/D) ratio of 0.338. The HGA is RHCP and operates over the frequency ranges of

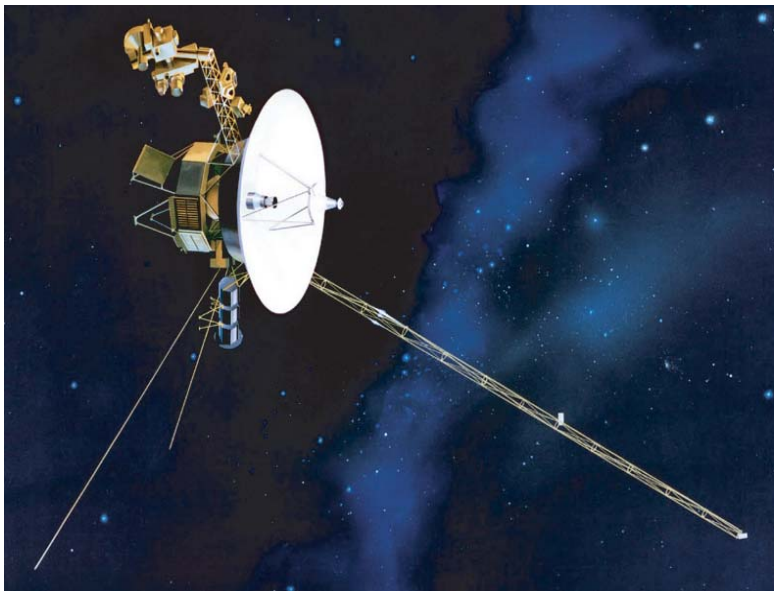

Fig. 3-12. The Voyager spacecraft.

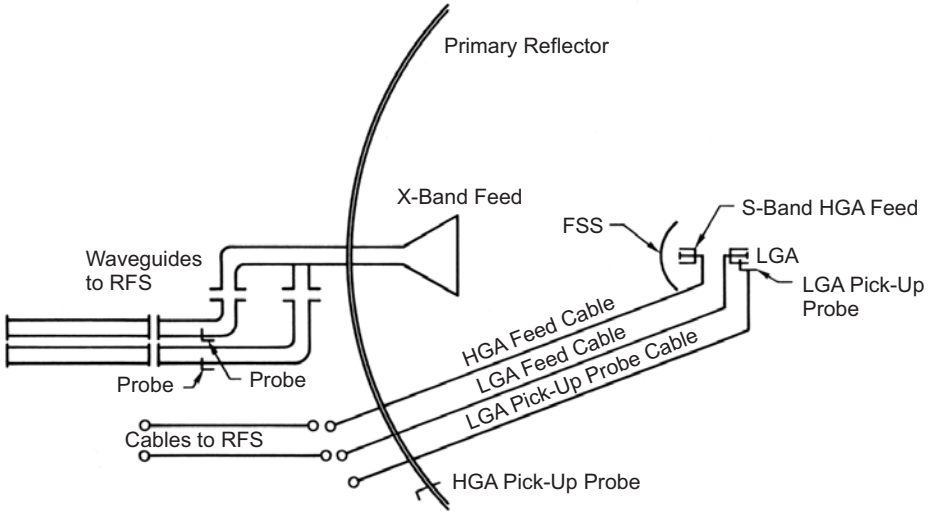

Fig. 3-13. Voyager SXA subsystem.

2115 ±5 and 2295 ±5 MHz. It also operates over the frequency range of 8422 ±20 MHz, with a dual polarized feed that yields a right-hand or left-hand circularly polarized wave from the HGA depending on which of its input ports is excited by the RFS. S-band signals are received by the HGA at 2115 ±5 MHz and routed to the RFS receiver. S-band signals at 2295 ±5 MHz from the RFS

S-band transmitter are radiated via the HGA. X-band signals at 8422 ±20 MHz from the RFS X-band transmitter are radiated via the HGA.

The LGA radiates a circularly polarized, broadbeam pattern directly to Earth. The LGA requirements are summarized in Table 3-1.

3.2.3 Voyager High-Gain Antenna

Since a 3.66-m reflector was the largest solid reflector diameter that could fit into the nose cone fairing without deployment, it was desirable to have the highest aperture efficiency possible. A high-efficiency dual-reflector system generally requires that (1) most of the feed energy be intercepted by the reflectors (i.e., low spillover), and (2) the field in the aperture of the main reflector be distributed as uniformly as possible. Ordinarily, reduction of spillover requires tapering the aperture distribution, and a uniform aperture distribution generally involves substantial spillover. Consequently, optimum performance traditionally involves a compromise that has limited efficiencies of conventional systems to about 55–60 percent. The shaped dual-reflector concept permits the apparent contradiction between the two requirements for high efficiency to be overcome with the following rationale: a feed is selected with a high taper at the edge of the subreflector to minimize forward spillover; the subreflector profile is designed to distribute the highly tapered energy uniformly over the aperture of the main reflector. By designing for constant aperture illumination (see Section 1.2.4), the classical hyperboloid subreflector is transformed into an empirical contour with a smaller radius of curvature than a hyperboloid in the central section to deflect more of the rays to the outer part of the main reflector. Thus, there is little spillover and, at the same time, a nearly uniform aperture distribution. The main reflector must then be slightly

Table 3-1. Voyager low-gain antenna requirements.

Parameter	Requirement
Frequency bands	2115 ±5 MHz (receive) 2295 ±5 MHz (transmit)
Power handling	120 W continuous wave (CW)
Polarization	RHCP
Axial ratio	2115 MHz band: ≤6 dB, For ±90-deg cone angle; ≤2 dB, On boresight
	2295 MHz band: ≤11 dB, For ±90-deg cone angle; ≤2 dB, On boresight
Boresight gain (at input connector) pattern	≥7.5 dBi for 2115-MHz band ≥7.6 dBi for 2295-MHz band
VSWR	≤1.2 : 1 for both bands

reshaped from its original paraboloidal contour to produce a constant-phase distribution

The HGA was dual-shaped for optimum efficiency at X-band (see Fig. 3-14). The dichroic subreflector is transparent to radiation from an S-band prime-focus horn nestled behind it. At S-band, the main reflector differs little from a paraboloid. The focus of the resultant best-fit paraboloid was chosen as the prime focus for the S-band feed.

3.2.3.1 X-band Feed. The X-band feed [12] is required to illuminate the subreflector with circularly symmetric, circularly polarized energy of a prescribed pattern shape with constant pattern phase. A subreflector edge illumination level of 17.5 dB below the boresight pattern level was chosen as the best comprise between the –25 dB optimum gain edge illumination and typical feed phase patterns, which have large rates of change past the –17.5 dB points.

The subreflector shape was calculated based on a computer-predicted pattern for the dual-mode horn baseline feed. Therefore, the computer-predicted

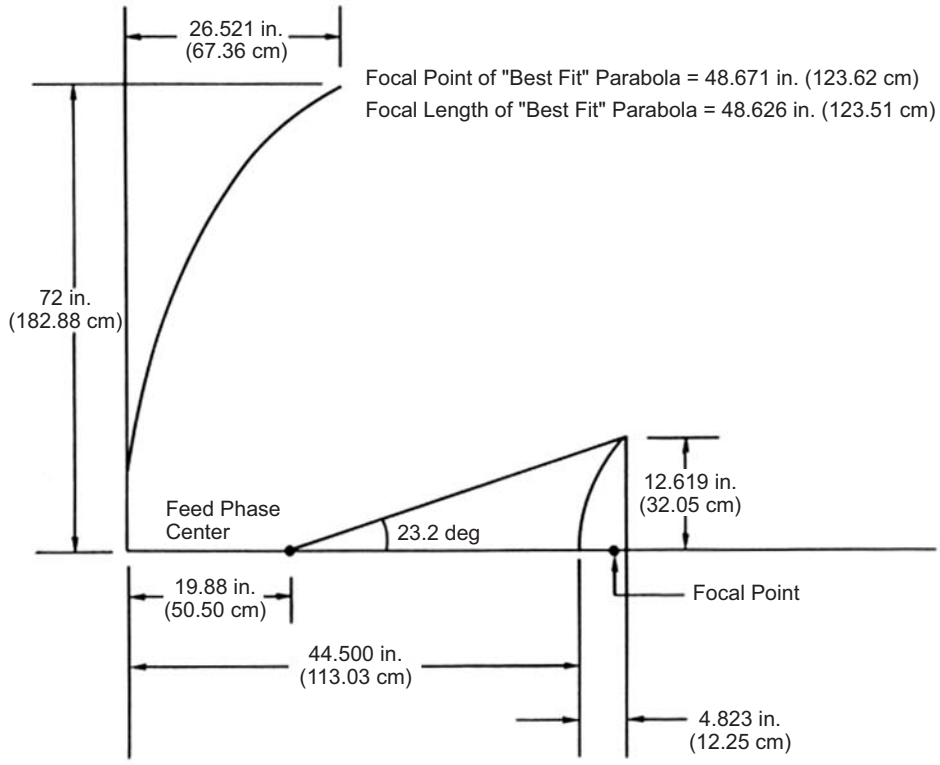

Fig. 3-14. Voyager HGA geometry.

pattern was the design goal for the X-band breadboard feed. The X-band feed requirements are summarized in Table 3-2.

3.2.3.2 Trade-off Studies. Circular polarization consists of two spatially orthog-onal E-field components 90 deg out of time phase. Good circular polarization for a given feed horn pattern can occur only if the pattern is closely matched in orthogonal planes and has nearly identical phase-centers in orthogonal planes. Radiation patterns in the dominant transverse electric (TE_{11}) circular waveguide mode have narrower E-planes than H-planes due to the more nearly uniform E-field aperture distribution in the E-plane. Radiation in the transverse magnetic (TM_{11}) mode, in phase with the TE_{11} mode at the horn aperture, increases E-plane beamwidth and reduces E-plane sidelobe levels without affecting H-plane radiation patterns.

Potter [13] found that TM_{11} power in the proper ratio to the TE_{11} mode could nearly equalize E- and H-plane beamwidths. Ludwig [14] found that radiation from the TE_{12} and TM_{12} modes in combination with the TE_{11} mode and TM_{11} mode could produce beams with fairly flat tops and steep skirts, or shaped beams with nearly equal E-and H-plane beamwidths. The combination of the TE_{11} and TM_{11} mode is the hybrid HE_{11} mode, and the combination of TE_{12} mode and TM_{12} mode is the HE_{12} mode. An antenna radiating in the HE_{11} and HE_{12} modes is a dual hybrid-mode antenna.

Therefore, the X-band feed candidate antennas considered were the dual mode horn, the corrugated horn, and the dual hybrid-mode horn. The operation of each of these type horns is described in the following paragraphs.

3.2.3.2.1 Dual Mode Horn. TM_{11} mode power is generated at the step change in circular waveguide size as a result of the boundary condition requiring tangential E-fields to vanish at a perfectly conducting wall. The ratio of waveguide diameter left of the step to the waveguide diameter to the right of the step, or step ratio, determines the ratio of TM_{11} mode power to TE_{11} mode power to the right of the step.

Table 3-2. Voyager X-band feed specifications.

Parameter	Required Performance
Frequency band	8422 ±20 MHz
Polarization	RHCP and LHCP from two different input ports
Power handling	105 W CW
VSWR	≤1.2 : 1.0
Axial ratio	≤1.0 dB*

* Internal specification. The X-band system axial ratio specification is 1.5 dB on the boresight axis.

The waveguide size at the left of the step was chosen such that the TM_{11} mode is below cutoff. The TM_{11} mode and TE_{11} mode propagate with different phase velocities, and therefore change their relative phase relationship in the horn flare section.

The phasing section also yields a differential phase shift between the two modes. Its length was adjusted during testing so that the two modes are in phase at the aperture. For the Voyager antenna, the phasing section length was determined experimentally because, although the differential phase shift between the two modes in the flare section could be calculated, the computer program did not calculate the initial phase relationship at the step. The dependence on the absolute length of the phasing and flare sections for proper performance limits the dual mode horn bandwidth to between 5 and 10 percent.

3.2.3.2.2 Corrugated Horn. The corrugated horn utilizes TE_{11} and TM_{11} mode radiation to equalize E- and H-plane beamwidths. The bandwidth limitations of the stepped dual mode horn are overcome by using corrugations to generate TM_{11} mode power in a distributed manner along the flare section, thus eliminating the phase difference between the two modes. The corrugations, which are $\lambda/4$ deep, may be viewed as providing equal boundary conditions in the E- and H-planes. There should be enough corrugations per wavelength such that the corrugated wall performs as an anisotropic surface.

3.2.3.2.3 Dual Hybrid-Mode Horn. It is possible to add hybrid modes in a corrugated waveguide analogously to adding individual TE and TM modes in a smooth waveguide. The TM_{11}, TE_{12}, and TM_{12} modes are generated at the step and propagate through the corrugated flare section, unlike in the dual-mode horn that attenuates the HE_{12} mode in its phasing section. The combination of the two hybrid modes can produce radiation patterns with nearly equal and shaped E- and H-plane beams over a narrow band. JPL [15] has tested a dual-hybrid-mode horn from 8.3 GHz to 8.6 GHz and has developed computer analysis programs for the horn.

3.2.3.2.4 Choice of Dual-Mode Horn as X-Band Feed. The Voyager X-band bandwidth is 0.475 percent, which is well within the 5-percent bandwidth capability of the dual-mode horn; therefore, the wideband, corrugated horn design offers no advantage over the dual-mode horn and is more expensive to fabricate. Although the beam-shaping property of the dual-hybrid-mode horn could yield some advantages over the dual-mode horn, the use of dual-shaped optics for the reflector system negates that advantage. Also the increased complexity, fabrication cost, weight, and blockage at S-band of the dual-hybrid-mode horn over the dual-mode horn makes the dual-mode horn the clear choice as the X-band feed.

3.2.3.2.5 Detailed Design of the Voyager X-Band Feed Horn. Figure 3-15 gives the dimensions of the feed, the polarizer, and the orthomode transducer, and the following describes the process used to determine the design. Some of the parameters were determined empirically, as the computer programs used at that time did not provide a complete solution. The program described in Section 1.2.2 could be used today to completely design the horn without the need for measurements.

Aperture diameter. The addition of the TM_{11} mode radiation pattern to the TE_{11} mode pattern broadens the E-plane beam to match the H-plane beam, without affecting the H-plane beam; therefore, the diameter of the dual-mode horn was chosen based on the H-plane pattern of a dominant mode horn. A 4.905-in. (12.46-cm) diameter (~3.5 wavelengths) aperture yields a –17.5-dB pattern taper at the 23.2-deg subreflector edge cone angle. A computer program computed the radiation pattern for a TM_{11}/TE_{11} mode voltage ratio of 10.626, both modes in phase, and a 4.905-in. (12.46-cm) diameter aperture. This computer pattern was then used as the design goal for the feed because the subreflector shape was determined from the computer-predicted feed pattern.

Phasing section design. The phasing section diameter, 2.05 in. (5.21 cm), was chosen to be 20 percent above the TM_{11} mode cutoff diameter at 8422 MHz. The closer the TM_{11} mode is to cutoff, the more effective is a given length of phasing section in providing the required TE_{11} to TM_{11} mode differential phase shift to put the two modes in phase at the aperture. However, if the TM_{11} mode is too close to cutoff, its guide wavelength varies radically with frequency, thus severely limiting the antenna bandwidth. A phasing section diameter 20 percent above the TM_{11} mode cutoff diameter is a

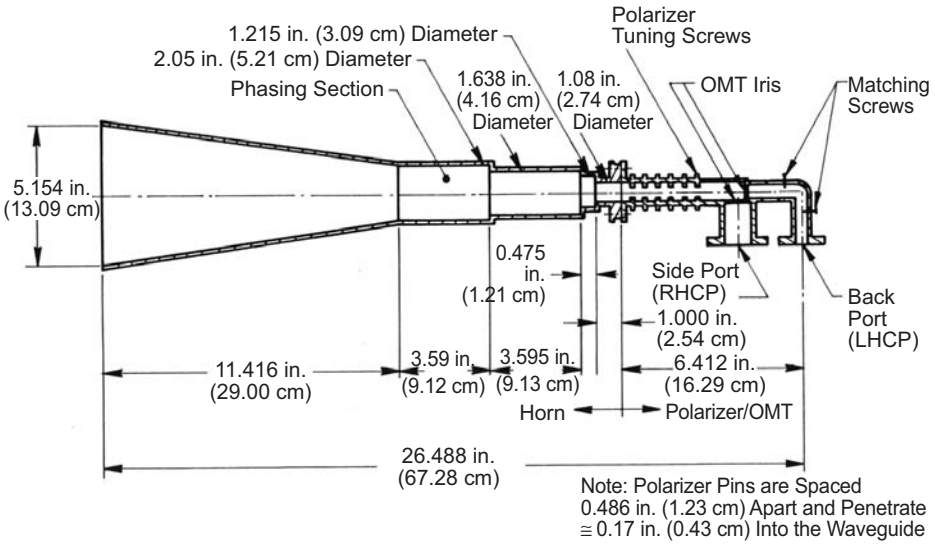

Fig. 3-15. Voyager HGA X-band feed horn cross section and dimensions.

compromise between phasing section effectivity and antenna bandwidth. Also, a small diameter phasing section is effective in attenuating modes of higher order than TM_{11} generated at the step.

Step ratio. The E-plane pattern of the dual-mode horn is only an approximation to the H-plane pattern. One design factor in a dual-mode horn is the pattern level at which the E- and H-plane coincide. The feed breadboard step ratio was chosen such that the –10 dB points coincide. Designing the step so that the E- and H-plane beams coincide at the –10 dB pattern levels causes the beams to be in close agreement for the 23.2-deg portion subtended by the subreflector. Breadboard tests determined that a step ratio of 0.799 optimized the beamwidth match.

Input matching section. A quarter-wave transformer and a linear taper were each considered for matching the input or feed waveguide impedance to the waveguide impedance at the step section input. The linear taper was not used because it was 3 in. (7.62 cm) longer than the quarter-wave transformer and more suited to wideband applications.

3.2.3.3 X-Band Performance Summary. The performance of the antenna system at X-band is summarized in Table 3-3.

3.2.4 Voyager S-Band Feed and Low-Gain Antenna Design

The S-band feed and LGAs [16] are back-to-back in the SXA system (Fig. 3-13). The S-band feed is required to illuminate the main reflector with

Table 3-3. Voyager X-band performance summary at 8422 ±20 MHz.

RF Parameter		Specification	Measured Performance	
			RHCP	LHCP
Gain (dB)		≥48.3	47.96	47.98
Efficiency (η) (percent)		64.9	60.0	60.2
Axial ratio (on-axis) (dB)		≤1.5	0.6	0.6
3-dB beamwidth (deg)		≥0.5	0.58	0.58
10-dB beamwidth (deg)		≥0.9	0.97	0.97
First sidelobe angle from boresight (deg)		≥0.9	0.9	0.9
First sidelobe level (dB)		>15.0	13 to 17	13 to 17
VSWR	8402 MHz	≤1.2 : 1	1.06 : 1	1.17 : 1
	8422 MHz		1.03 : 1	1.05 : 1
	8442 MHz		1.03 : 1	1.06 : 1
Isolation (dB)	8402 MHz	>20	20.5	
	8422 MHz		19.5	
	8442 MHz		18.6	

circularly polarized power in a circularly symmetric pattern with a prescribed edge taper. The feed position is the focal point of the best-fit parabolic approximation of the main reflector. The LGA radiates a circularly polarized, broadbeam pattern directly to Earth. Fig. 3-16 is the LGA pattern specification. Tables 3-4 and 3-5 summarize the LGA and S-band feed design requirements. A calculated prime focus fed parabola efficiency curve versus reflector edge illumination shows that the S-Band HGA efficiency will be nearly identical for feed patterns rolling off from –8 dB through –11 dB with respect to boresight at the 73-deg cone angle subtended by the main reflector. This wide range of feed patterns for high efficiency performance of the HGA S-band system allowed use of an antenna design that meets both the LGA patterns and S-band feed specifications, thereby reducing system cost and complexity. The sense of circular polarization is the only difference between the two antennas. Because the S-band feed and the LGA are of the same design, they shall hereafter be referred to as the S-band feed/LGA.

3.2.4.1 Design Summary. The initially proposed S-band feed and LGA was a self-phased crossed dipole matched by a triple tuner. Concern about the thermal stability and reliability of the triple-stub tuner resulted in a change of the S-Band feed/LGA to a hybrid-fed crossed dipole (HFCD). The HFCD design, Fig. 3-17, provides the four-way equal power split and 0, –90, –180, –270 deg phase progression required for circular polarization from a 180-deg ring hybrid feeding two 90-deg "over and under" couplers. The four outputs of the two 90-deg hybrids are connected to the four printed circuit radiating elements by sections of 0.141-in. (0.36-cm) diameter semi-rigid cables. The cables run the length of the square, beam-shaping cavity. An alternate approach to feeding the four radiating elements would have been to use a single 90-deg hybrid feeding the two orthogonal pairs of radiating elements; the opposite elements dividing current using a quarter-wave balun.

The balun design, however, required close feed-cable spacing and a cross strap between opposite radiating element pairs; both susceptible to voltage breakdown. The radiating cavity dimensions are such that the S-band feed pattern at 73 deg illuminates the main reflector edge at –11 dB. This edge illumination is in the maximum efficiency region for the primary reflector.

The breadboard LGA design is an S-band feed element with two 1/2-in. (1.27-cm) spaced, 6-in. (15.24-cm) diameter conductive disks conforming to the radiating cavity wall and with the upper disk at the level of the radiating element. The upper disk forms a ground plane that narrows the pattern half-power beamwidth from ~94 deg to ~77 deg and increases the gain from ~6.3 dBi to ~8.0 dBi, so that the LGA gain specification can be met. The lower disk, upper disk, and cavity wall roughly form a quarter-wave, short-circuited channel that "chokes off" edge currents and reduces the back lobe from –18 dB

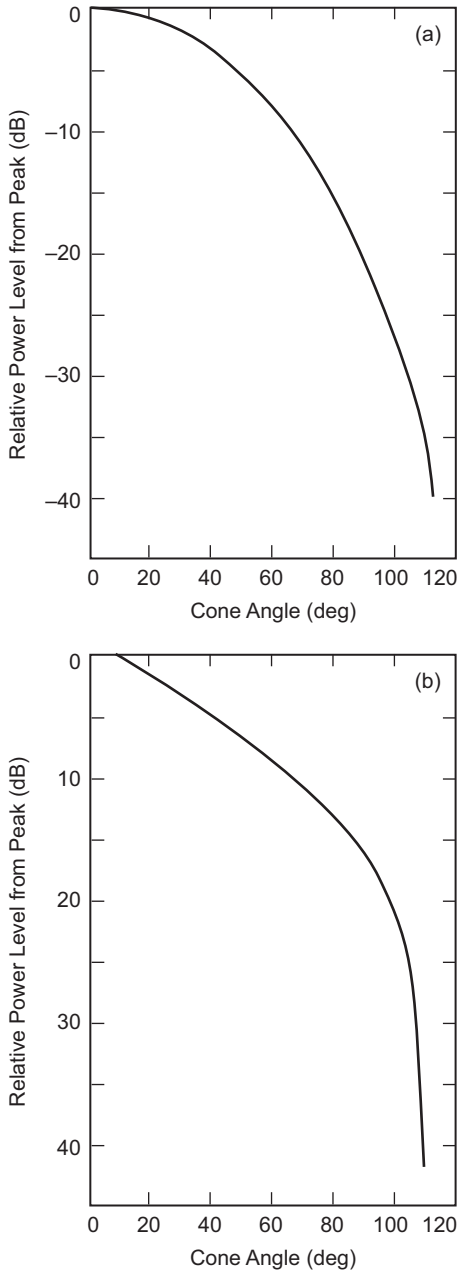

Fig. 3-16. Voyager low-gain antenna pattern performance criteria for: (a) 2115 ±5 MHz and (b) 2295 ±5 MHz.

Table 3-4. Voyager low-gain antenna requirements.

Parameter	Requirement
Frequency bands	2115 ±5 MHz (receive) 2295 ±5 MHz (transmit)
Power handling	120 W CW
Polarization	RHCP
Axial ratio	2115 MHz band: ≤6 dB For ±90-deg cone angle; ≤2 dB On boresight
	2295 MHz band: ≤11 dB For ±90-deg cone angle; ≤2 dB On boresight
Boresight gain (at input connector) pattern	≥7.5 dBi for 2115-MHz band ≥7.6 dBi for 2295-MHz band
VSWR	≤1.2 : 1.0 for both bands

Table 3-5. Voyager S-band feed requirements.

Parameter	Requirement
Frequency bands	2115 ±5 MHz (receive) 2295 ±5 MHz (transmit)
Power handling	120 W CW
Polarization	LHCP
Axial ratio	≤1.5 dB average within ± 73-deg cone angle
Pattern rolloff	−8 dB through −11 dB with respect to boresight at 73-deg cone angle (space taper is 4 dB)

to –23 dB. This back-lobe reduction decreases the effect of the primary reflector collimating the LGA back radiation and generating interference ripple in the LGA pattern.

3.2.4.2 Radiation Performance of the LGA in the Presence of the Primary Reflector. As discussed above, a choke channel was added to the LGA that reduced the back radiation level from –18 dB to –23 dB. This reduced, but did not eliminate the effect of interference from the primary reflector. Interference ripples are due to the primary reflector collimating the back radiation of the LGA and producing an interference pattern. To reduce the effect of primary reflector interference on the LGA pattern, the LGA was moved as far from the primary reflector focal point as system considerations would allow, thus defocusing the back radiation and reducing the level of the interference signal. Spacing ranging from the original initial baseline of 55.5 in. (141 cm) (the primary reflector subtends at a 136.15-deg angle from the LGA) to 64.5 in.

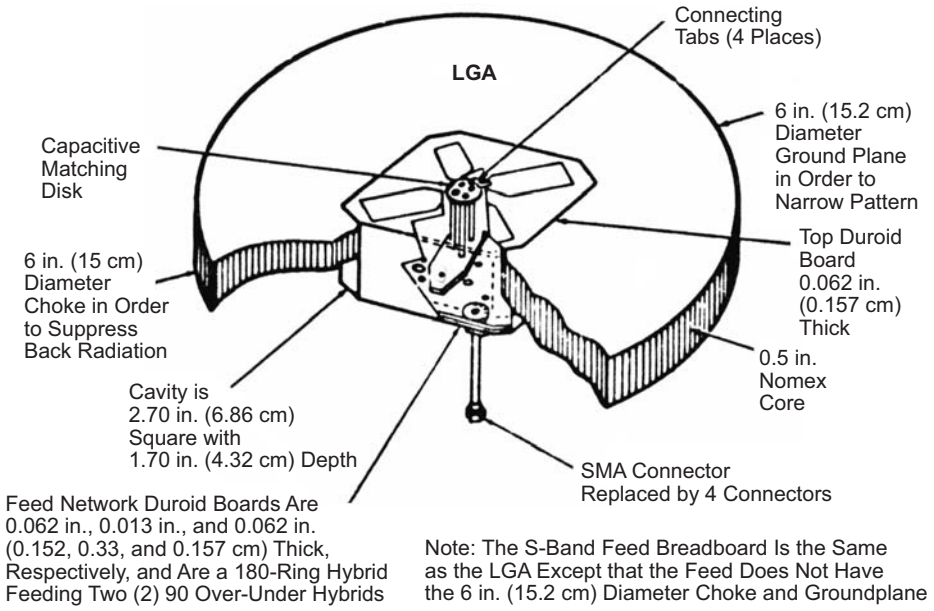

Fig. 3-17. Voyager S-band feed and LGA outline diagram.

(163.8 cm) (the primary reflector subtends a 124.4-deg angle from the LGA) was studied. The nominal spacing chosen as the prototype baseline, based on a compromise between RF performance and system considerations, was 62.9 in. (159.8 cm) (126.4 deg of LGA angle subtended by the primary reflector). Figures 3-18 and 3-19 are LGA patterns at the 62.9-in. (159.8-cm) spacing at 2115 MHz and 2295 MHz, respectively.

3.2.4.3 HGA S-band Performance Summary. Table 3-6 summarizes the S-band HGA final performance with 0.75-in. (1.9-cm) metal struts at one half the radius with the hybrid-fed cross dipole feed. The only significant parameter that the S-band feed system fails to meet is the gain at the transmit frequency (2295 MHz). The gain includes the Spiroline cable loss of 0.4 dB at 2295 MHz and 0.35 dB at 2115 MHz.

3.2.4.4 S-band Strut/Feed Measurements. An extensive investigation was made of the S-band gain for various strut and S-band feed configurations. The HGA with the HFCD feed gave superior performance when compared to the HGA gain with the self-phased feed—particularly with the 3/4-in. (1.9-cm) metal struts. This higher gain was justification for changing the baseline feed from the self-phase dipole to the HFCD. The Kevlar struts configuration gave higher gain than the metal struts for all configurations. However, the Kevlar

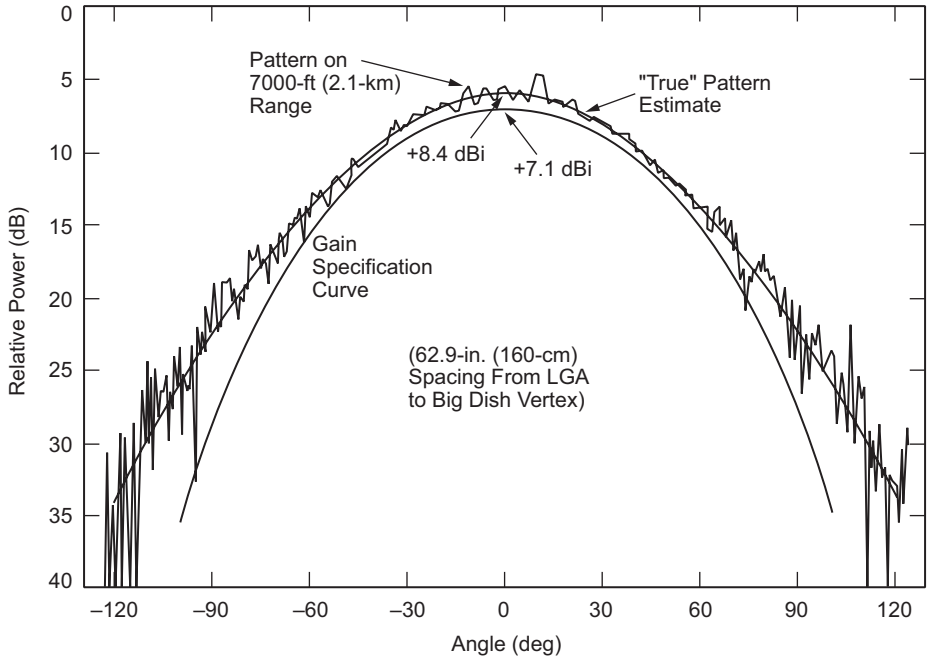

Fig. 3-18. Voyager 2215-MHz LGA pattern in the presence of the main reflector.

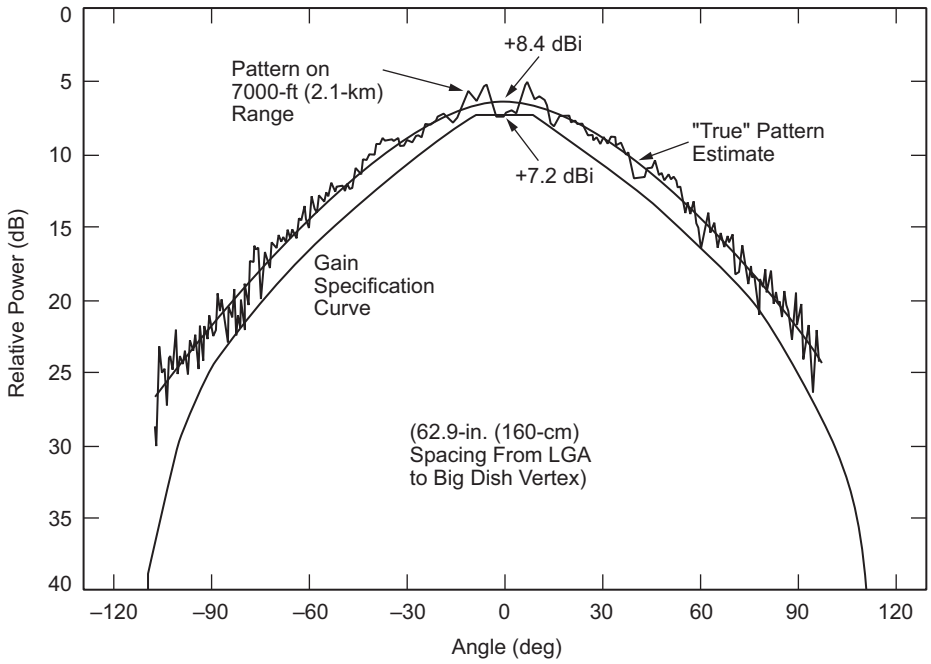

Fig. 3-19. Voyager 2295-MHz LGA pattern in the presence of the main reflector.

Table 3-6. Voyager HGA S-band performance summary with 0.75-in. (1.9-cm) metal struts.

RF Parameter	2115 MHz		2295 MHz	
	Specified	Measured	Specified	Measured
Gain (dB)	≥35.5	35.59	≥36.3	36.14
Efficiency (percent)	≥54.2	55.1	≥55.3	53.1
Axial ratio on-axis (dB)	≤2.0	0.5	≤1.5	0.8
3-dB beamwidth (deg)	2.8 ±0.3	2.8	2.6 ±0.3	2.5
10-dB beamwidth (deg)	5.2 ±0.3	4.8	4.8 ±0.3	4.3
First sidelobe angle from boresight (deg)	≤4.3	4.25	≥4.0	3.8
First sidelobe level (dB)	≤–20.0	–22.2 to –26.0	≤–20.0	–20.7 to –25.5
VSWR (at feed)	1.2 : 1	1.17 : 1	1.2 : 1	1.20 : 1

struts are a marginal mechanical design and consequently 3/4-in. (1.9-cm) graphite struts were selected as the baseline.

3.2.5 Voyager Frequency Selective Surface (FSS) Subreflector

The HGA utilizes prime focus/Cassegrainian geometry with an FSS to separate the frequencies. The FSS is transparent at low frequencies to allow prime focus operation, and it is reflective at the high frequency for Cassegrainian operation [17]. The FSS utilizes two layers of X-band aluminum resonant crossed dipoles printed on Mylar. The subreflector is constructed from a Kevlar/Nomex honeycomb-core sandwich (see Fig. 3-20). The size and geometry of the resonant dipoles are determined from flat panel tests (see Section 1.2.5), and the second layer is used to match the lower frequency. The performance goal was that the loss introduced at both frequency bands be less than 0.2 dB. Measured data confirmed a loss of <0.1 dB at S-band and between 0.1 and 0.2 dB at X-band. Figure 3-21 is a picture of the FSS subreflector.

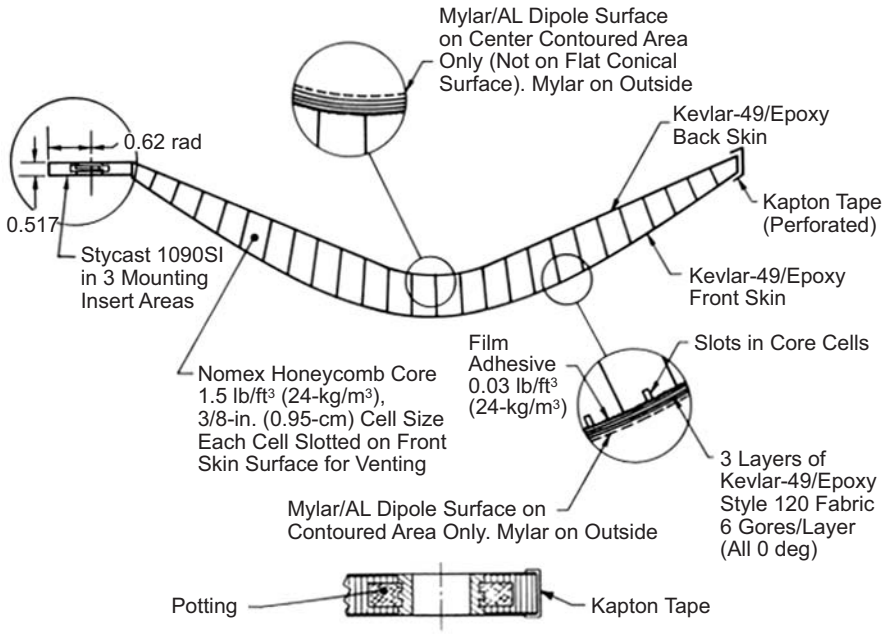

Fig. 3-20. Voyager FSS subreflector materials and construction.

Fig. 3-21. Voyager FSS subreflector.

References

[1] *NASA Facts: Mariner to Mercury, Venus and Mars* (web site), Jet Propulsion Laboratory, Pasadena, California, May 1996, accessed July 7, 2005. http://www.jpl.nasa.gov/news/fact_sheets/mariner.pdf

[2] *NASA Facts: Voyager Mission to the Outer Planets* (web site), Jet Propulsion Laboratory, Pasadena, California, May 1996, accessed July 7, 2005. http://www.jpl.nasa.gov/news/fact_sheets/voyager.pdf

[3] *The Mariner R Project: Progress Report September 1, 1961 – August 31, 1962*, JPL Internal Technical Report No. 32-353, Jet Propulsion Laboratory, Pasadena, California, also NASA-CR-135806, National Aeronautics and Space Administration, Washington, District of Columbia, January 1, 1963.

[4] J. N. Bryden, *Mariner (Venus '62) Flight Telecommunication System*, Technical Report No. 32-377, Jet Propulsion Laboratory, Pasadena, California, January 15, 1963.

[5] *Mariner Venus 67 Final Project Report*: Volume 1. *Launch through Midcourse Maneuver*, Technical Report 32-1203, Jet Propulsion Laboratory, Pasadena, California, June 15, 1968.

[6] *Past Missions - Mariner 10* (web page), Jet Propulsion Laboratory, Pasadena, California, accessed July 7, 2005. http://www.jpl.nasa.gov/missions/past/mariner10.html

[7] *S/X Band Antenna Subsystem FDR Data Package*, W.U. 33-2-1, Contract Mariner Venus/Mercury 1973 JPL Contract 953000, contract to Jet Propulsion Laboratory, Pasadena, California, Boeing Company, Seattle, Washington, November 4, 1971.

[8] MVM'73-4-2017, *Functional Requirement MVM'73 Spacecraft Equipment S/X-Band Antenna Subsystem*, MVM'73-4-2017 JPL Contract 953000, Contract to Jet Propulsion Laboratory, Pasadena, California, Boeing Company, Seattle, Washington, November 14, 1971.

[9] W. A. Imbriale, *Large Antennas of the Deep Space Network*, Chapters 5 and 6, John Wiley & Sons, Inc., Hoboken, New Jersey, 2003.

[10] *Functional Requirement Mariner Jupiter/Saturn 1977 Flight Equipment S/X-Band Antenna Subsystem*, MJS77-4-2017A, in JPL 618-205, *MJS77 Functional Requirements Book* (set of internal documents), Jet Propulsion Laboratory, Pasadena, California, February 3, 1977.

[11] *Mariner Jupiter/Saturn 1977 SXA Subsystem*, Vol. 1, *Critical Design Review*, Aeronutronic Ford Corporation, Palo Alto, California, November 1975.

[12] *Mariner Jupiter/Saturn 1977 S/X-Band Antenna Subsystem, Design Analysis Report*, Volume II *HGA/LGA Feed RF Analysis*, WDL Technical Report 5717, Philco-Ford Corporation, Palo Alto, California, March 18, 1975.

[13] P. D. Potter, *A New Horn with Suppressed Sidelobes and Equal Beamwidth*, Technical Report No. 32-354, Jet Propulsion Laboratory, Pasadena, California, February 25, 1963.

[14] A. C. Ludwig, *Antennas for Space Communication*, JPL SPS 37-33, Vol. IV, Supporting Research and Advanced Development, Jet Propulsion Laboratory, Pasadena, California, also NASA-CR-64605, National Aeronautics and Space Administration, Washington, District of Columbia, pp. 261–266, June 30, 1965.

[15] R. F. Thomas and D. A. Bathker, "A Dual Hybrid Horn Feedhorn for DSN Antenna Performance Enhancement," *The Deep Space Network Progress Report 42–22, May and June 1974*, Jet Propulsion Laboratory, Pasadena, California, pp. 101–108, August 15, 1974. http://ipnr.jpl.nasa.gov/progress_report/

[16] *Mariner Jupiter/Saturn 1977 S/X-Band Antenna Subsystem, Breadboard Development Report Addendum A*, WDL-TR5740, Aeronutronic Ford Corporation, Palo Alto, California, August 22, 1975.

[17] G. H. Schennum, "Frequency Selective Surfaces for Multiple-Frequency Antennas," *Microwave Journal*, pp. 56–59, March 1973.

Chapter 4
The Mars Missions

Joseph Vacchione

4.1 Overview of Missions to Mars

Of all the planets of the inner Solar System, Mars is the most intriguing. While Venus is geologically our twin sister, its high surface temperatures, the result of a greenhouse effect run amuck, make it quite alien and a poor candidate for human exploration and search for evidence of present or past life. Mars, on the other hand, offers different opportunities. While today Mars is very cold and dry on its surface, and its atmosphere is a thin veil of mostly carbon dioxide (CO_2), there is a great deal of evidence that the planet may have had vast quantities of surface water. Since the days when Percival Lowell and Giovianni Schiaparelli peered at the red planet, reporting what they referred to as "Canali" or canals (this was an optical illusion, but it raised the scientific interest in Mars), data have been mounting of what appears to be extensive water erosion. Of course, where there is water, there is increased chance of present or past life. In addition, further evidence indicates that just beneath the surface of Mars may be permafrost containing frozen water. This water could become a resource for future manned exploration.

From the earliest years of space flight, Mars has been a favorite destination; however, it has not proven to be the easiest locale to reach. Table 4-1 provides a historical overview of unmanned missions to Mars [1–4]. As can be seen, only about one-third of the attempts have been successful, however, those that succeeded have provided a wealth of knowledge about our intriguing red neighbor.

Table 4-1. Historical overview of Mars missions.

Country/Mission	Launch Date	Purpose	Results
USSR*/Korabl 4	10/10/60	Mars flyby	Did not reach Earth orbit
USSR/Korabl 5	10/14/60	Mars flyby	Did not reach Earth orbit
USSR/Sputnik 22 or Korabl 11	10/24/62	Mars flyby	Achieved Earth orbit only
USSR/Mars 1	11/1/62	Mars flyby	Radio failed at 65.9 million miles (106 million km)
USSR/Sputnik 24 or Korabl 13	11/4/62	Mars flyby	Achieved Earth orbit only
US/Mariner 3	11/5/64	Mars flyby	Launch vehicle shroud failed to jettison
US/Mariner 4	11/28/64	Mars flyby	First successful Mars mission—arrived 7/14/65, returned 21 photos
USSR/Zond 2	11/30/64	Mars flyby	Passed Mars but radio failed, returned no planetary data
US/Mariner 6	2/24/69	Mars flyby	Arrived 7/31/69, returned 75 photos
US/Mariner 7	3/27/69	Mars flyby	Arrived 8/5/69, returned 126 photos
US/Mariner 8	5/28/71	Mars orbiter	Failed during launch
USSR/Kosmos 419	5/10/71	Mars orbiter/lander	Achieved Earth orbit only
USSR/Mars 2	5/19/71	Mars orbiter/lander	Achieved orbit 11/27/71—unfortunately lander crashed on surface
USSR/Mars 3	5/28/71	Mars orbiter/lander	Achieved orbit 12/3/71, lander soft-landed on Mars—sent 20 seconds of data, including an image of the surface—lander destroyed by a dust storm
US/Mariner 9	5/30/71	Mars orbiter	In orbit from 11/13/71–10/27/72—returned 7,329 photos
USSR/Mars 4	7/21/73	Mars orbiter	Flew past Mars 2/10/74—did not achieve orbit
USSR/Mars 5	7/25/73	Mars orbiter	Achieved orbit 2/12/74—lasted a few days after which contact was lost.
USSR/Mars 6	8/5/73	Mars flyby/lander	Arrived 3/12/74—lander crashed on surface—sent some atmospheric data back during descent
USSR/Mars 7	8/9/73	Mars flyby/lander	Arrived 3/9/74—lander flew past Mars after separation from parent spacecraft
US/Viking 1	8/20/75	Mars orbiter/lander	In orbit 6/19/76–1980; Lander 7/20/76–1982 Orbiter & lander returned thousands of photos
US / Viking 2	9/9/75	Mars orbiter/lander	In orbit 8/7/76–1987; Lander 9/3/76–1980 Orbiter & lander returned thousands of photos
USSR/Phobos 1	7/7/88	Mars/Phobos/lander	Lost en route to Mars

Table 4-1. Historical overview of Mars missions (cont'd.).

Country/Mission	Launch Date	Purpose	Results
USSR/Phobos 2	7/7/88	Mars/Phobos/lander	Lost en route near Phobos
US/Mars Observer	9/25/92	Mars orbiter	Lost just before Mars arrival
US/Mars Global Surveyor	11/7/96	Mars orbiter—data relay	Arrived 9/12/97—surface mapper; still operating
Russia/Mars 96	11/16/96	Mars orbiter/lander	Launch vehicle failed
US/Mars Pathfinder	12/4/96	Mars lander and rover	Landed 7/4/97—last transmission 9/27/97
Japan/Nozomi	7/4/98	Mars orbiter	Extend sun orbit due to propulsion problem—Mars arrival expected 12/03—missed Mars.
US/Mars Climate Orbiter	12/11/98	Mars orbiter—data relay	Lost on arrival at Mars
US/Mars Polar Lander / Deep Space 2	1/3/99	Mars lander/descent probe	Lost on arrival 12/3/99
US/Mars Odyssey	4/7/01	Mars orbiter—data relay	Arrived 10/24/01—Mars mapper and other science
Europe/Mars Express/Beagle II	6/2/03	Mars orbiter/lander	Arrived 12/25/03—orbiter successfully achieved Mars orbit—Beagle II lander lost during landing.
US/Mars Exploration Rover-A (Spirit)	6/10/03	Mars lander and rover	Arrived 01/03/04—successfully landed on the Martian surface—very successful mission
US/Mars Exploration Rover-B (Opportunity)	7/703	Mars lander and rover	Arrived 01/24/04—successfully landed on the Martian surface—very successful mission

* USSR or Union of Soviet Socialist Republics; dissolved in the early 1990s; most of the USSR space program is now in the Russian space program.

In the following sections, the technology and some of the challenges associated with the spacecraft and lander antennas used for the United States program of Mars exploration will be examined.

4.2 NASA Mars Orbiters/Landers

This section presents an overview of the antennas used on the many National Aeronautics and Space Administration (NASA) Mars orbiters and landers (without rover technology). However, it is mainly as an overview of the technology. In a few cases, a further detailed examination of the antenna technology is presented.

4.2.1 Mariners 3 and 4

The twin Mariner 3 and 4 spacecraft (Fig. 4-1) represented the United States entry into in-situ Mars exploration. Mariner 3 was lost shortly after

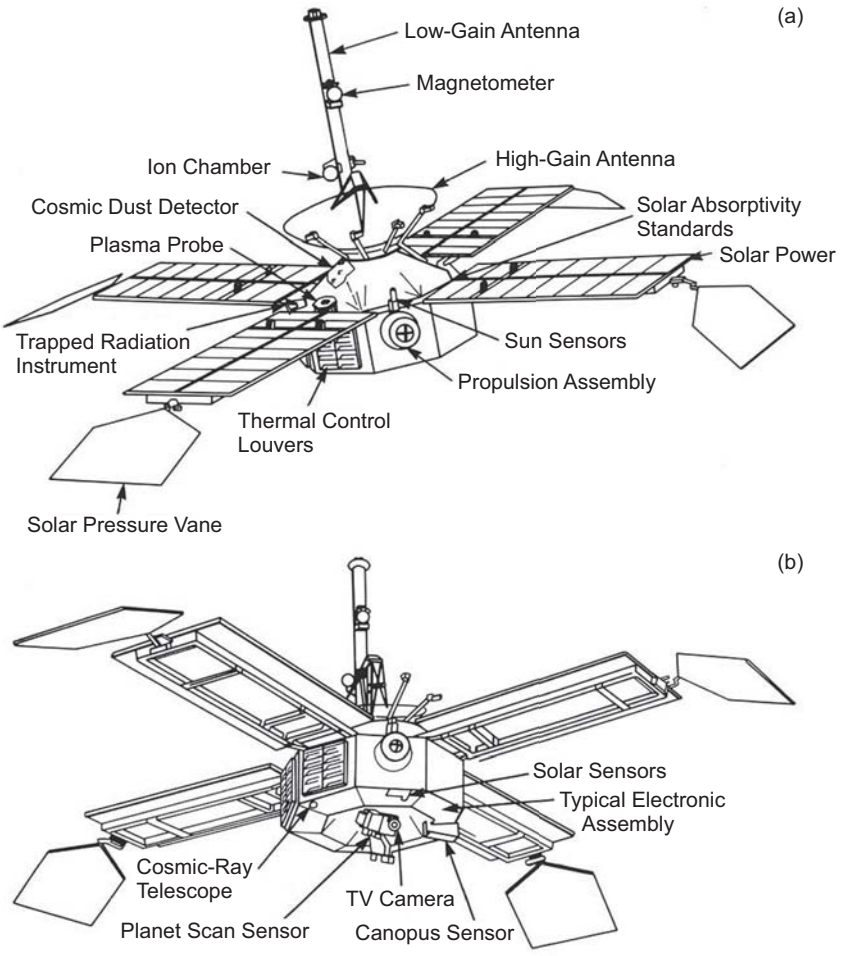

Fig. 4-1. Diagrammatic views of Mariners 3 and 4 (Mariner Mars 1964) spacecraft: (a) upper and (b) lower.

launch due to shroud separation failure; however, Mariner 4 achieved its mission objectives and returned the first comprehensive close-up views of the red planet [5,6].

Mariner 5 was originally intended as a backup to Mariner 4. When Mariner 4 successfully completed its mission, Mariner 5 was re-outfitted for a flyby of Venus. The antenna complement consisted of a high-gain antenna (HGA) and a low-gain antenna (LGA). The HGA was a 46×21-in. (116.8×53.3-cm) elliptical parabolic sector with a peak gain at S-band of 23 decibels (dB) mounted on the spacecraft so that the look angles to Earth

during the last half of the flight would fall within the main lobe of the antenna. The antenna's primary function was to transmit telemetry to Earth during the last half of the transfer orbit and for 20 days after planetary encounter during the video playback period. The S-band LGA was mounted on a 253.3-cm tall mast next to the HGA. Its function was to receive commands from Earth during the entire flight and to transmit flight telemetry to Earth during the first half of the mission when the spacecraft was near Earth and the look angles to Earth varied widely. The telecommunications system used a dual S-band 7-W triode cavity amp/10-Watt (W) traveling wave tube amplifier (TWTA) transmitter and a single receiver, which could send and receive data via the LGA and HGA [7].

Both the HGA and the LGA are further described in Chapter 3 in the Mariner 5 section.

4.2.2 Mariners 6 and 7

The Mariner 6 and 7 missions [8] used a twin set of spacecraft and employed a design very similar to the Mariner 3 and 4 spacecrafts (see Fig. 4-2). Both missions were considered a success. The antenna compliment was similar to the Mariner 3 and 4 system in that it contained both an LGA and an HGA. However, both designs were modified for improved performance [9].

The earlier Mariner LGA was a simple design, but it had some fabrication problems. Its conical feed and waveguide diameter had to be held to very tight tolerances, or polarization losses would be high due to the use of a circular polarization in the waveguide. Its return loss was high due to the manner in which the cruciform aperture was formed by crimping one end of the waveguide tube. The antenna also had high back radiation due to currents on the outer surface of the circular waveguide.

Using linear polarization from waveguide input to the aperture and converting to circular polarization at the aperture relieved tolerance requirements on the feed since linear polarization is less sensitive to dimensional changes than circular polarization. The aperture design was also modified to give the highest gain at the 40-deg cone angle while still above the minimum requirement at the 90-deg cone angle.

The LGA is shown in Fig. 4-3. It consisted of a circular waveguide mast with a series of mode-suppression pins. Toward the end of the waveguide, near the radiating aperture a four-pin polarizer was employed to provide circular polarization. The antenna achieved a gain of ~7.5 dB and a 3-dB beamwidth of 88 deg. This LGA design (or slight variations) was reused on Mariners 8 and 9, as well as the Viking orbiter spacecraft.

The Mariner 4 HGA gain was too low to support the higher data rate requirement, and its gain contours did not fit the trajectory geometry. For the higher gain, a 40-in. (101-cm) diameter circular diameter with a suitable left-hand circularly polarized (LHCP) turnstile feed was used (see Fig. 4-4). The

focal length to diameter F/D radio was chosen to use the existing Mariner 4 reflector forming tool.

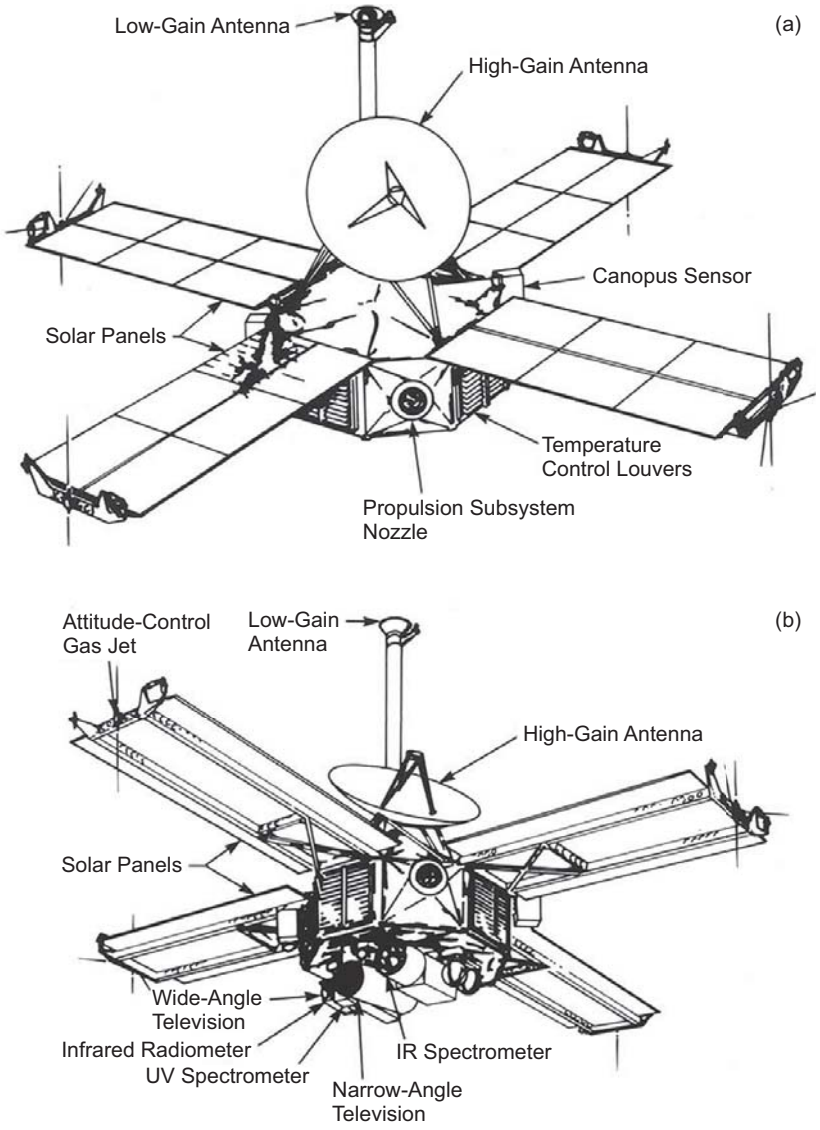

Fig. 4-2. Diagrammatic views of Mariners 6 and 7 (Mariner Mars 1969) spacecraft: (a) upper and (b) lower.

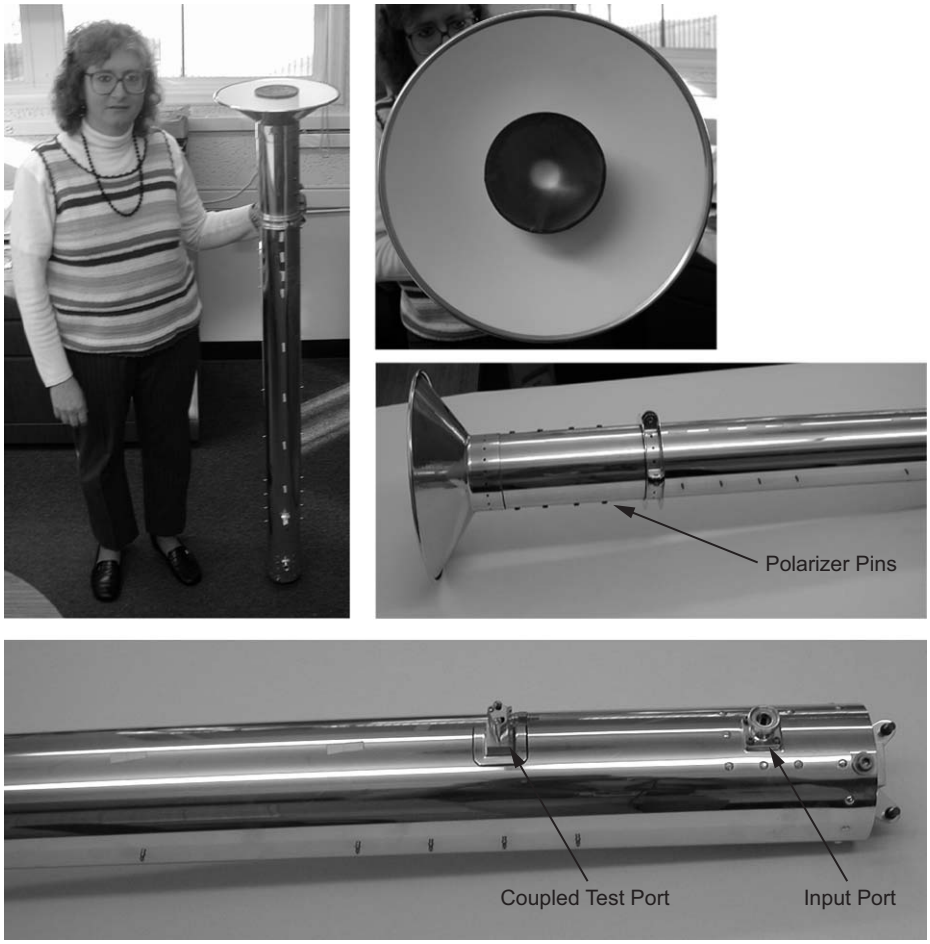

Fig. 4-3. Mariner S-band LGA (this particular unit was used for the Mariner 9 spacecraft).

4.2.3 Mariners 8 and 9

Mariners 8 and 9 were (once again) twin spacecraft [10]. Of the two, only Mariner 9 was successful, Mariner 8 failed on the launch pad. These spacecraft represented a gradual evolution of Mars-bound craft. They used a slightly modified S-band LGA on a 1.44-m long mast. They also employed a medium-gain horn antenna in addition to a Mariner 7-type high-gain parabolic antenna. Telecommunications were facilitated via dual S-band 10 W/20 W transmitters and a single receiver.

Fig. 4-4. Mariner 9 HGA with spacecraft mockup at the Jet Propulsion Laboratory (JPL) Mesa Antenna Range.

4.2.4 Viking

The Viking spacecraft represented the first U.S. attempt to land on Mars [11,12]. It could also be considered the first truly successful mission of its kind, although the Soviet Mars 3 did successfully land and did return a fuzzy video of the surface before succumbing to a violent sand storm.

The twin Viking spacecraft (Viking 1 and Viking 2) each consisted of an orbiter and a landing module, as shown in Figs. 4-5 and 4-6. Upon arrival into Mars orbit, the lander module was deployed to the surface, leaving the orbiter behind as a signal relay from the Martian surface back to Earth as shown in Fig. 4-7 [13].

The orbiter antenna compliment consisted of a fixed S-band HGA, the now familiar S-band LGA on a mast, and an ultra-high frequency (UHF) quadrafiler helix mounted on a ground plane.

The lander antennas [14,15] included a gimbaled S-band HGA direct-to-Earth link, an S-band turnstile LGA direct-to-Earth link, and a UHF turnstile antenna for link with the orbiter. The use of a direct-to-Earth link in conjunction with an orbiter relay link became the standard model for all future surface-operation missions.

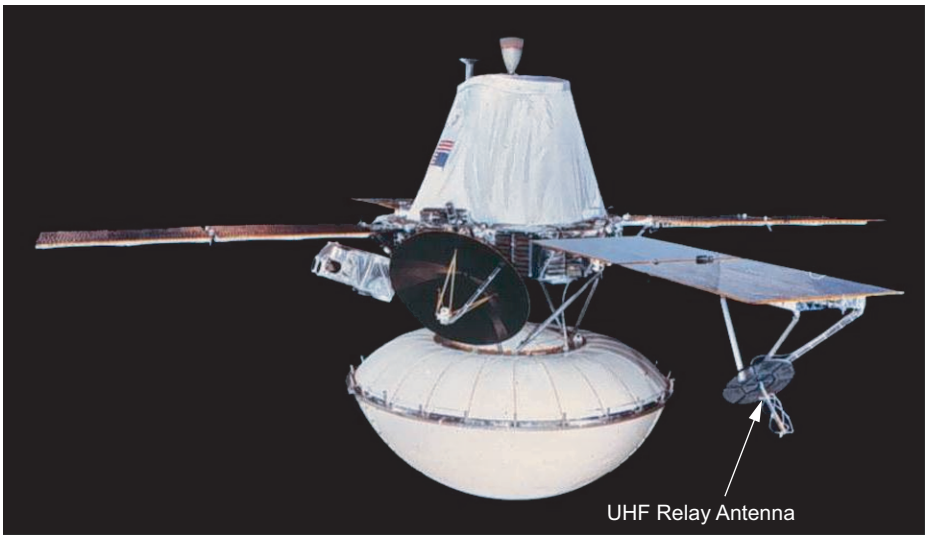

Fig. 4-5. Viking orbiter.

The Viking spacecraft begin a trend toward highly populated/integrated spacecraft. Evidence of this is seen as its traditionally isolated LGA field of view is impinged upon by various spacecraft assemblies. In addition, the highly populated lander incorporated two LGAs in close proximity to the top deck instruments. This trend makes antenna pattern predictions very difficult (particularly at UHF). To retire some of the uncertainty, mathematical models are sometimes employed, but as a safer approach, mock-ups of the vehicles are constructed, and antenna patterns are measured.

Of some interest is the use of UHF as the surface-to-orbiter link frequency. It was highly desirable to cover as much of the planet at a single time as possible in order to maximize the available link time with the lander. During the early years of balloon-borne and other high-altitude experiments on Earth by the French and others, it was determined that UHF provides a broad and very pervasive coverage, bending around objects and generally facilitating a reasonable link. The UHF band thus became the choice for surface links with the first Mars landers, and that tradition continues through the present.

Another point of interest that is of particular importance for landers on the Martian surface is the potential for ionization and multipactor breakdown within and around the antennas and their associated microwave components. On the surface of Mars, the atmospheric pressure is approximately 4–12 T (533 Pa–1600 Pa) versus 760 T (101,325 Pa) at sea level on Earth. These low pressures, also known as critical pressures, are nearly ideal for the occurrence of ionization of the antennas with powers as low as 5 W. This ionization

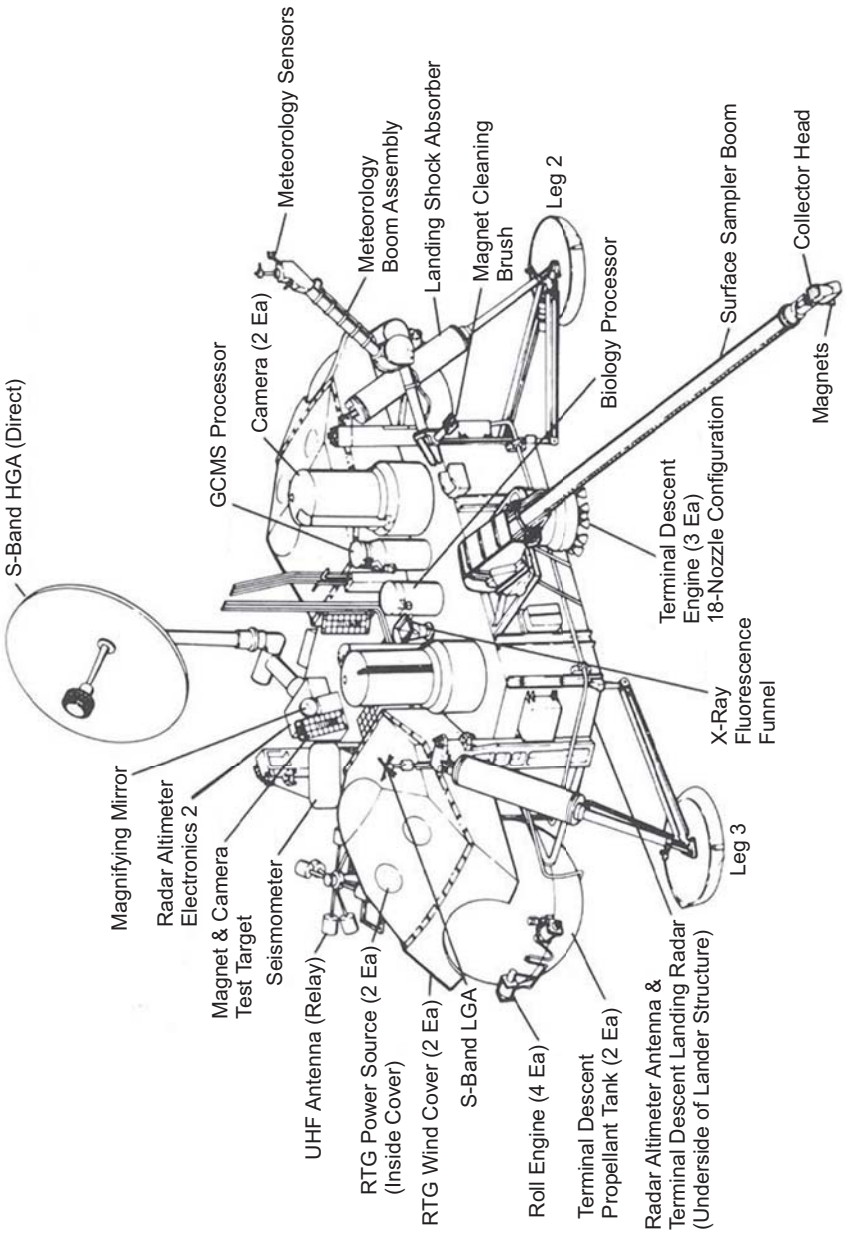

Fig. 4-6. Viking lander detailed diagram (RTG = radioisotope thermoelectric generator; GCMS = gas chromatograph-mass spectrometer).

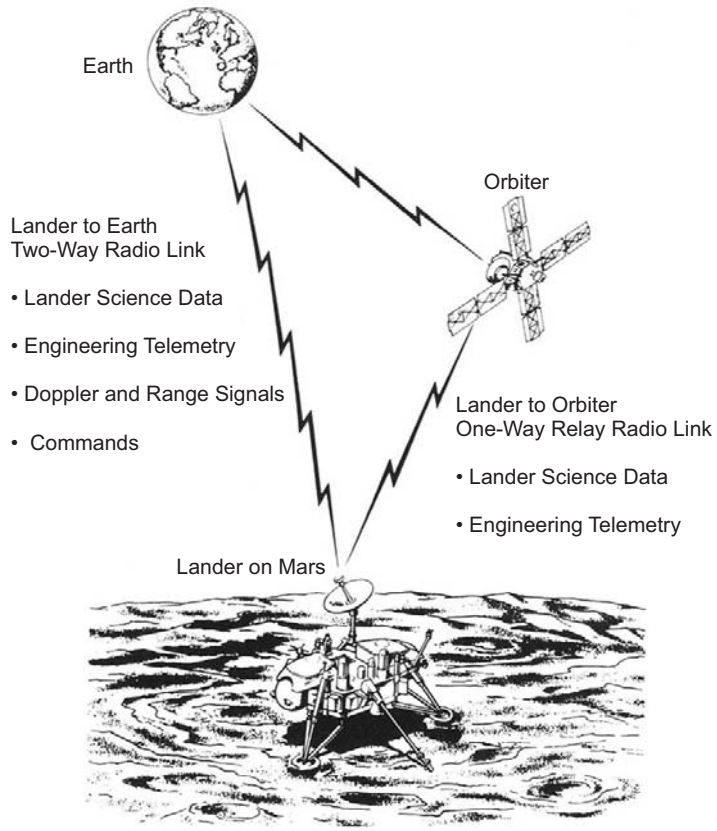

Fig. 4-7. Viking–Earth–Orbiter–Lander communication links.

phenomenon and its impact on the antenna design is discussed in more detail in Section 4.3.2. In order to mitigate the occurrence of the ionization for the Viking UHF antennas, the radiating elements have their ends rounded. This avoidance of sharp points in the presence of electric fields is a well-known approach to avoid coronal ionization in high voltage systems and other applications. At the low Martian pressures, the use of large radii may not be enough. As seen in Fig. 4-8, the radiating elements are also covered with foam-filled end caps. The figure shows one of the end caps removed revealing the high-radius radiating elements. The addition of the foam-filled cap provided further minimization of the corona potential. This is discussed further in Section 4.3.2.

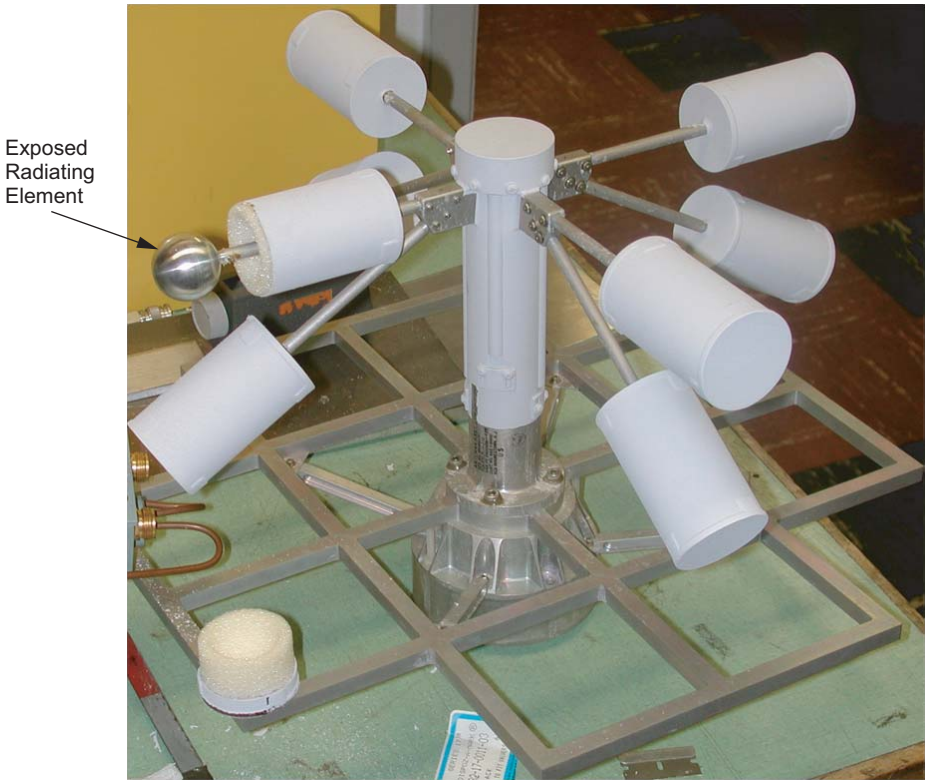

Fig. 4-8. Viking lander UHF "turnstile" antenna.

4.2.5 Mars Observer

After an absence of nearly 20 years from the Martian scene, on September 25, 1992, the U.S. launched the Mars Observer (MO). This began a concerted effort to thoroughly explore the red planet and gather information about, water, potential life, and the building blocks for a possible manned mission. The MO spacecraft, unfortunately, was lost (probably due to a thruster malfunction) just prior to Mars orbit insertion [16]. While this was a great disappointment, it was followed four years later by the very successful Mars Global Surveyor and the Mars Pathfinder lander/rover missions.

The MO orbiter (see Fig. 4-9) used a mechanically articulated X-band 1.5-m HGA on a 5.5-m long boom [17]. It also used a choked circular X-band waveguide LGA. This was the first NASA spacecraft in a long series to follow which employed the choked circular waveguide LGA. One set of variations of this design is detailed in Section 4.3.1. The spacecraft also employed a long UHF helix antenna that was to be used as a communications link to a Russian

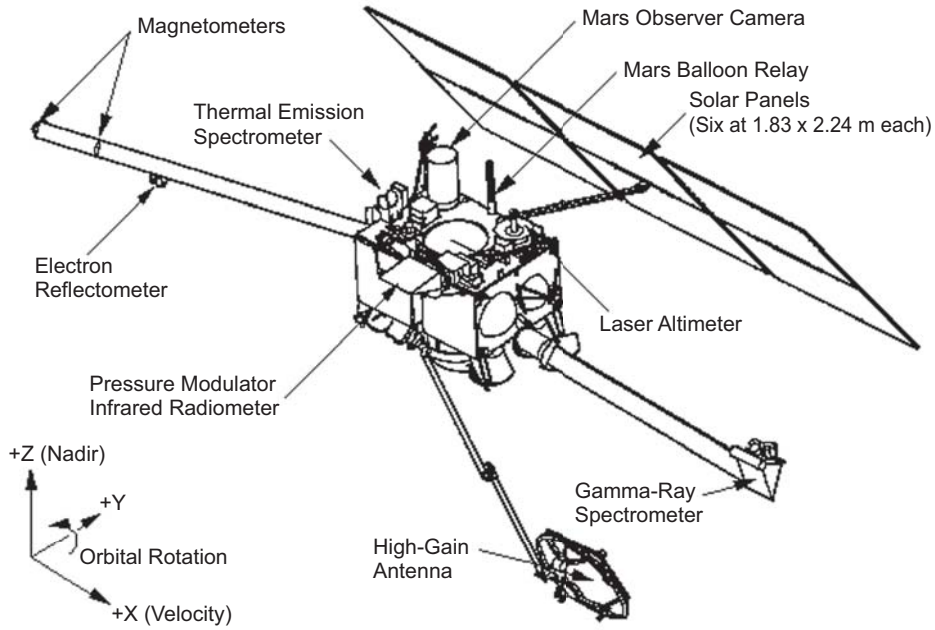

Fig. 4-9. Mars Observer spacecraft diagram.

surface balloon experiment (Mars Balloon Relay) that was to arrive in 1994. The Russian mission never materialized.

As can be seen, this next generation of spacecraft had switched from S-band as the primary link frequency to X-band. This evolution began with the twin Voyager spacecraft and continued on through the end of the 20th Century. The wider bandwidths and other features made this frequency band an obvious choice over the S-band frequencies. In addition to using the X-band frequencies for the primary link to Earth, the MO spacecraft was set to begin a push to an even higher frequency/wider bandwidth links. The MO HGA had a set of Cassegrain optics, which employed a special purpose subreflector (see Fig. 4-10). The backside of the HGA subreflector was itself a prime focal-fed reflector. A Ka-band feed was mounted out at the focal point of this small reflector, facilitating an "experimental" Ka-band link. This experiment was to provide information to radio scientists and telecommunications engineers that would lead to the possible evolution from X-band to Ka-band telecom [18].

4.2.6 Mars Global Surveyor

As a continuation of the mission to Mars, the Mars Global Surveyor (MGS) [19] yielded a wealth of data. It also was to serve as a UHF relay for Mars surface missions that were planned by the Europeans and others. Those surface

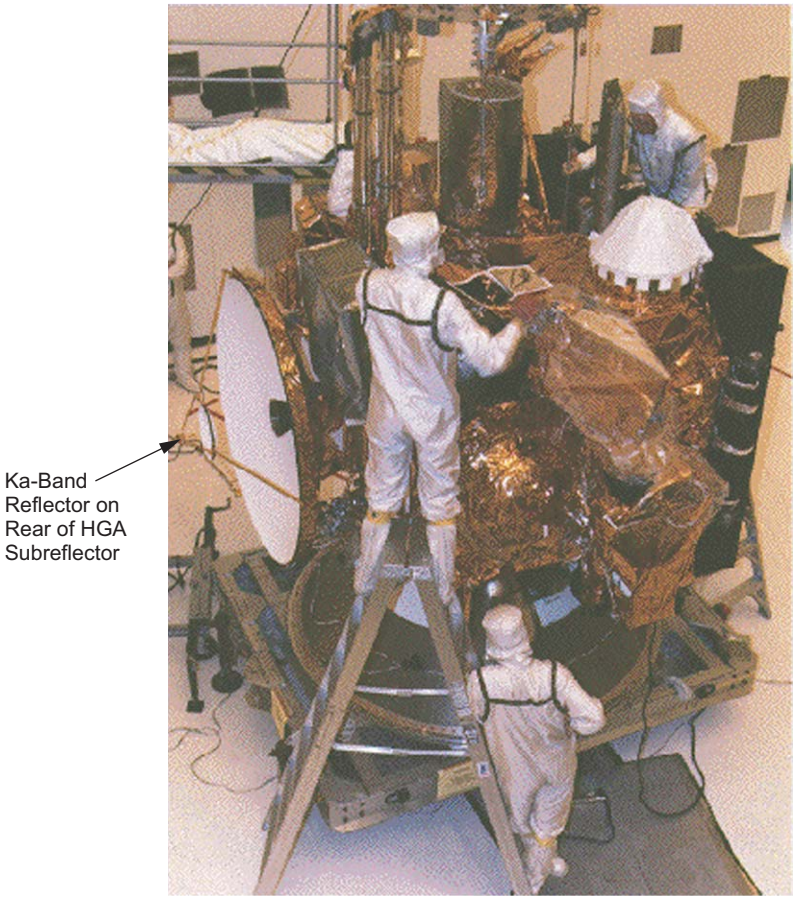

Fig. 4-10. Mars Observer spacecraft during assembly and checkout.

missions never materialized; however, due to the longevity of the spacecraft, this UHF link was used (in concert with Mars Odyssey) to support communications with the twin Mars Exploration Rovers (Section 4.3.2).

The MGS spacecraft design borrowed many features of the MO spacecraft [20]. In fact, this mission was in some ways a replacement of the MO mission. The craft uses the same UHF surface link helix antenna. It also uses the MO HGA design (Fig. 4-11) except that it employs a germanium Kapton radome over its aperture whereas the MO HGA had no radome. The MGS HGA does not utilize the dual-purpose subreflector (the back side of the subreflector could be used as a small prime focal-fed reflector) for a Ka-band link, instead, the telecommunications engineers decided to implement a Ka-band link "experiment" using a dual-band feed at the Cassegrain antenna feed point. This Ka-band link would thus take full advantage of the HGA aperture. The dual-

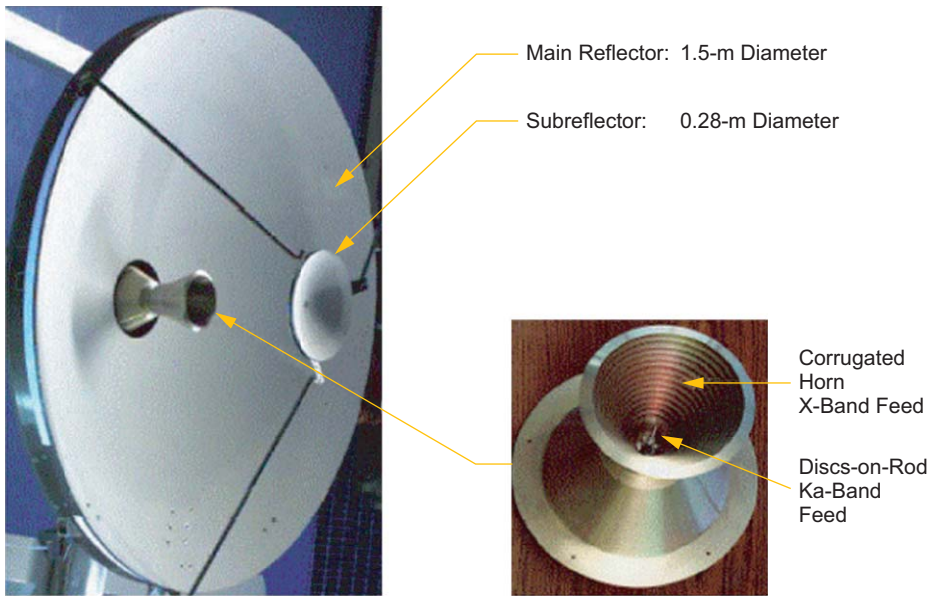

Fig. 4-11. Mars Global Surveyor HGA.

band feed incorporated a coaxial fed X-band corrugated horn and a disc-on-rod Ka-band feed down the center of the X-band horn (a detailed description of a very similar dual-band feed for the Mars Reconnaissance Orbiter mission is shown in Section 4.4).

One other difference between the MGS and the MO spacecraft antenna complement is that MGS employs a set of microstrip patch LGAs (two receive LGAs and two transmit LGAs) in place of the choked circular waveguide design (see Fig. 4-12). Each LGA has a boresight gain of about 6.5 dBi (X-band uplink and downlink) and a half-power beamwidth of about ±40 deg. The LGAs include a pair of circularly polarized microstrip path antennas, tuned to 8.4 GHz (transmit) and tuned to 7.1 GHz (receive). The circular polarization was achieved by using a 3-dB hybrid and feeding the patches at orthogonal feed points [20].

The MGS spacecraft uses a 25-W traveling wave tube amplifier (TWTA), which is mounted in a module on the back of the HGA, in order to minimize RF loss and to reduce power requirements. This approach to minimizing RF path losses became a model for all the future orbiters described in this chapter. The Ka-band experiment utilized a 1-W amplifier for this link.

4.2.7 Mars Climate Orbiter

The Mars Climate Orbiter (MCO) together with the Mars Polar Lander (MPL) had the objective of studying the Martian climate history [21].

Fig. 4-12. LGAs used on the Mars Global Surveyor spacecraft.

Unfortunately, this spacecraft was lost when it crashed into the planet due to an error in unit conversions in the navigation software.

The MCO (see Fig. 4-13) used a 1.3-m HGA with a 15-W solid-state power amplifier (SSPA) mounted at the back of the two-axis gimbaled reflector, a transmit-only medium-gain antenna (MGA), and one receive-only LGA. The orbiter also was to serve as the primary link for the MPL via a helix antenna driven by a 10-W UHF radio.

The MGA was a square flared horn mounted to the prime-focal fed HGA through a hole in its aperture approximately two-thirds of the way out from the center of the reflector.

4.2.8 Mars Polar Lander

The Mars Polar Lander (MPL) was to work in conjunction with the Mars Climate Orbiter in an effort to explore the climate history of Mars [22]. In a spate of bad luck, this lander mission also met with an unfortunate fate. The lander successfully reached Mars and entered the atmosphere for a rocket-controlled soft landing. It is thought that a software error caused the lander's rocket engines to turn off too soon, dropping the craft from a large height.

The MPL utilized a fixed X-band medium-gain antenna to communicate with the Earth during the cruise phase. During the surface operations, the lander was to communicate via a UHF link between the Mars Climate Orbiter and/or the MGS. As a backup to the UHF link, a direct-to-Earth (DTE) link via an articulated X-band MGA could also be used.

In addition to the lander functions, the MPL carried two micro-probes called Deep Space 2 (see Fig. 4-14). These microprobes were to eject from the

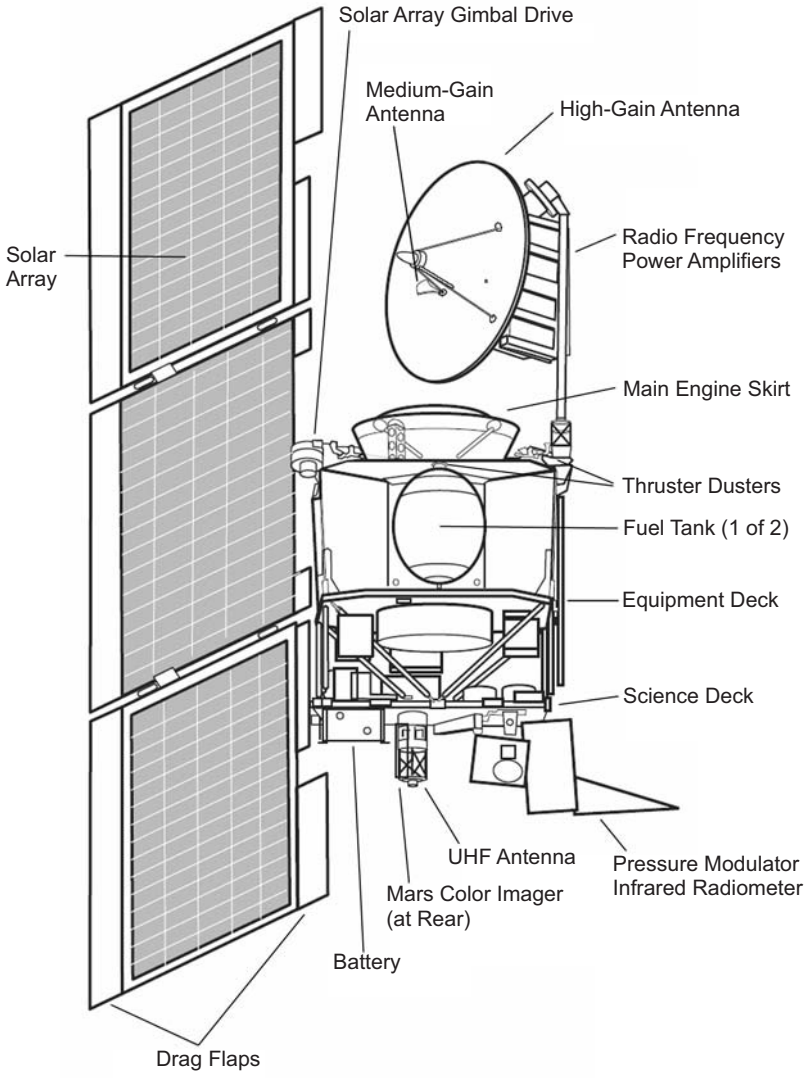

Fig. 4-13. Mars Climate Orbiter spacecraft.

orbiter and be shot into the Mars surface as penetrators. The microprobes each had a small UHF radio with a monopole antenna, and they were to relay their data back through the UHF system on the orbiting MPL spacecraft [23].

4.2.9 Mars Odyssey

The Mars Odyssey spacecraft (launched April 7, 2001) has continued the detailed exploration of Mars with the specific objectives of mapping chemical elements and minerals on the surface of Mars, looking for water in the shallow

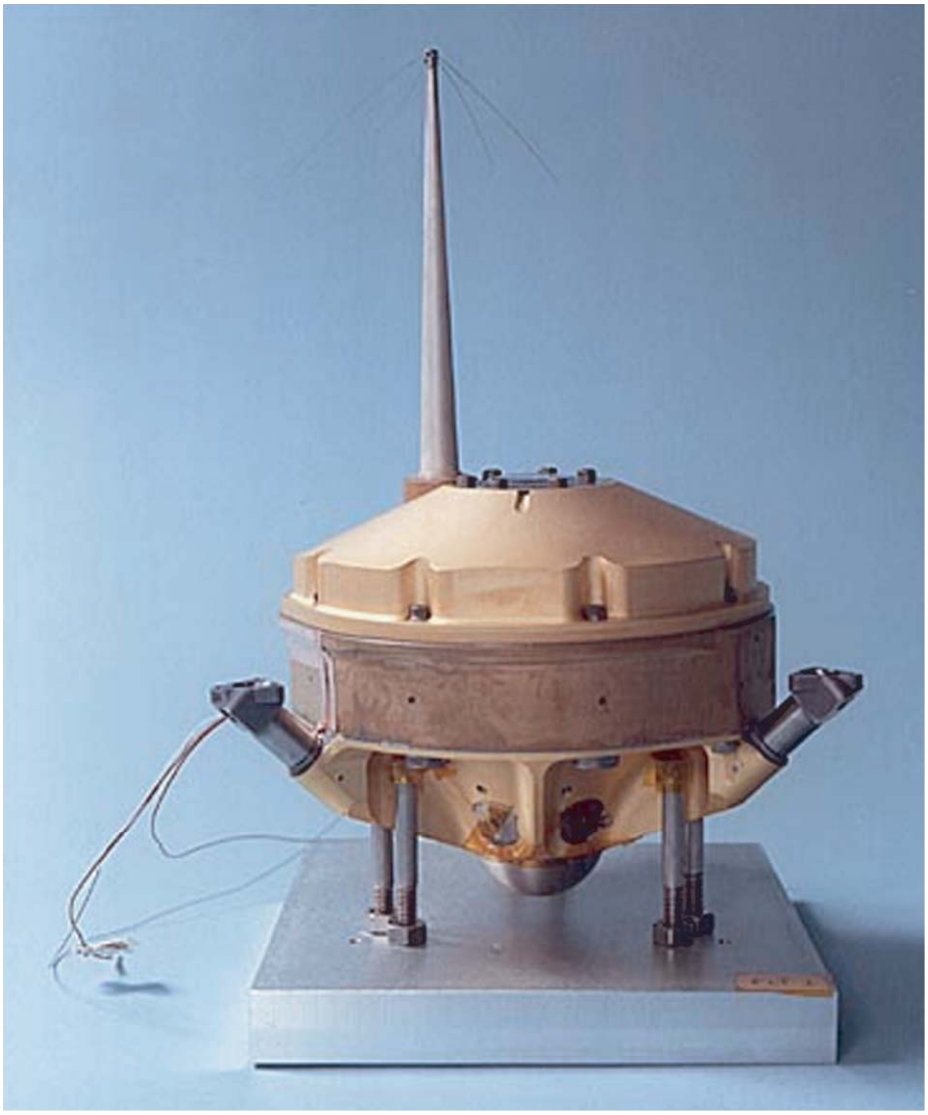

Fig. 4-14. Deep Space 2 microprobe—UHF antenna matched using top-loading "whiskers" [26].

subsurface, and analyzing the radiation environment to determine its potential effects on human health [24]. The spacecraft design followed many of the characteristics that began with and continued on from the Mars Observer spacecraft [25].

The Mars Odyssey telecommunications package is quite similar to the MGS and MCO spacecraft. It consists of a boom-mounted HGA with an MGA

mounted within its reflector aperture (like the Mars Climate Orbiter). It also has a four-arm quadrafiler helix UHF antenna (Fig. 4-15) for communications with any surface vehicles that may arrive during its tenure. The height of the antenna is 26.7 cm, and the diameter is 16.5 cm. Odyssey is one of the primary relay links for the Mars Exploration Rovers.

4.3 Mars Rovers

This section provides a detailed description of antennas used on the Mars rovers, the Mars Pathfinder, and the twin Mars Exploration Rovers (Spirit and Opportunity). It includes antenna design information as well as special considerations and constraints applied to the designs.

4.3.1 Mars Pathfinder

The Mars Pathfinder mission represented the first U.S. attempt to return to the surface of Mars since the 1975 Viking Missions [26]. This mission was considered to be highly successful, and it generated an excitement about the

Fig. 4-15. Mars Odyssey four-arm quadrafiler helix UHF antenna.

space program and Mars the likes of which had not been seen since the first Apollo missions. The Pathfinder mission was a product of a paradigm shift in the U.S. unmanned exploration program in that it sought to develop the spacecraft lander in a more cost-effective manner. Under this new approach, some of the formal approaches to space flight hardware development and production were relaxed. An emphasis was placed on a close-knit team effort that employed old and new ideas to address the very challenging task of landing a small rover, called Sojourner, onto the surface. The resulting approach was a unique and highly integrated spacecraft architecture and a novel method of entry, descent, and landing. The integrated approach had a rather dramatic effect on the antenna assembly. With a goal of maintaining communications with the Earth throughout all phases of cruise, Mars entry, descent, and landing, a novel "antenna stack" design was developed [27]. The following subsections provide a detailed examination of the Mars Pathfinder antennas used throughout the mission.

4.3.1.1 Mars Pathfinder Communications During Cruise, Entry, Descent, and Landing. With the objectives of high reliability, high performance, low mass, and low cost, the spacecraft antenna subsystem enabled the Mars Pathfinder spacecraft to transition through four configuration changes en route to its landing site—using only one switch and no pyrotechnic events while maintaining constant telemetry. Continuous telemetry, an important mission goal, provided all possible engineering data, including failures, for use as proof of spacecraft design.

The four mission phases are shown in Fig. 4-16, along with the associated gains and edge of coverage requirements. As seen in Fig. 4-16(a), the first portion of the mission employed an MGA during the spacecraft's cruise to Mars. The radiating aperture of this antenna consisted of a simple flared aluminum conical horn, which achieved a 13.1 decibels referenced to a circularly polarized, theoretical isotropic radiator (dBic) 10-deg edge of coverage RHCP gain at its downlink frequency of 8.4 GHz and 10.8-dBic 10-deg edge-of-coverage RHCP gain at the uplink frequency of 7.2 GHz. In order to accommodate launch vehicle interface requirements, the antenna was flush mounted to the spacecraft cruise stage. The antenna geometry was adjusted so that the side lobe region of the pattern maintained a relatively flat 30-dB floor (with no nulls) so that spacecraft maneuvers during cruise could be made without loss of signal. This antenna performance was validated using a full-scale mockup of the spacecraft cruise stage. Unfortunately, as the cruise stage design progressed a launch adaptor ring, which raised the edge of the cruise stage ring 1 to 2 in. (2.5–5.0 cm), was added to the spacecraft. This design change was not captured in the cruise stage mockup.

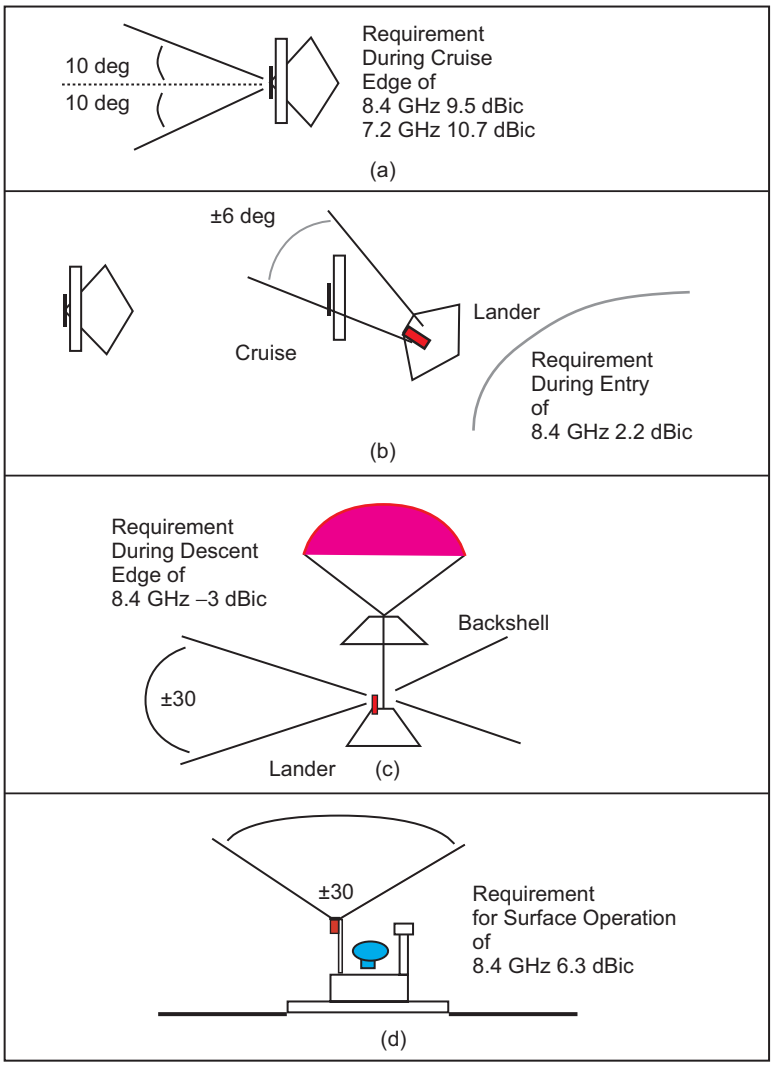

(a) Cruise from Earth to Mars; used MGA located on cruise stage.
(b) Entry; after cruise stage ejection before lander/backshell separation; used LGA located in backshell.
(c) Descent; after backshell separation through landing; used descent antenna located on top of lander petal.
(d) Surface operation; initial downlink of entry, descent, and landing telemetry and emergency communications; used lander LGA.

Fig. 4-16. Mars Pathfinder requirements vs. mission phase [28].

This ring caused an obstruction of the MGA pattern over a small azimutal angle in the pattern. Since the spacecraft was spun at a few revolutions per minute during cruise, there was a periodic drop out of the signal during flight.

While there was an operational work-around for this difficulty, this provides a good example of the risks associated with highly integrated spacecraft whose antennas are placed in close proximity to spacecraft structure.

Upon reaching the planet (July 4, 1997), the cruise stage and MGA were jettisoned; exposing the backshell LGA, and a choked circular waveguide horn antenna, which up to this point functioned as waveguide feeding the MGA (see Fig. 4-17). It had a broad field of view with a ±6-deg edge of coverage and an RHCP gain of 6.3 dBic at 8.4 GHz, and it only functioned to transmit data back to Earth. The unique feature of this waveguide/antenna was that it employed innovative self-aligning slip-fit waveguide interfaces, allowing passive transitions during the stage separations. Cruise stage separation marked the beginning of the entry phase of the mission (Fig. 4-16(b). Although the Martian

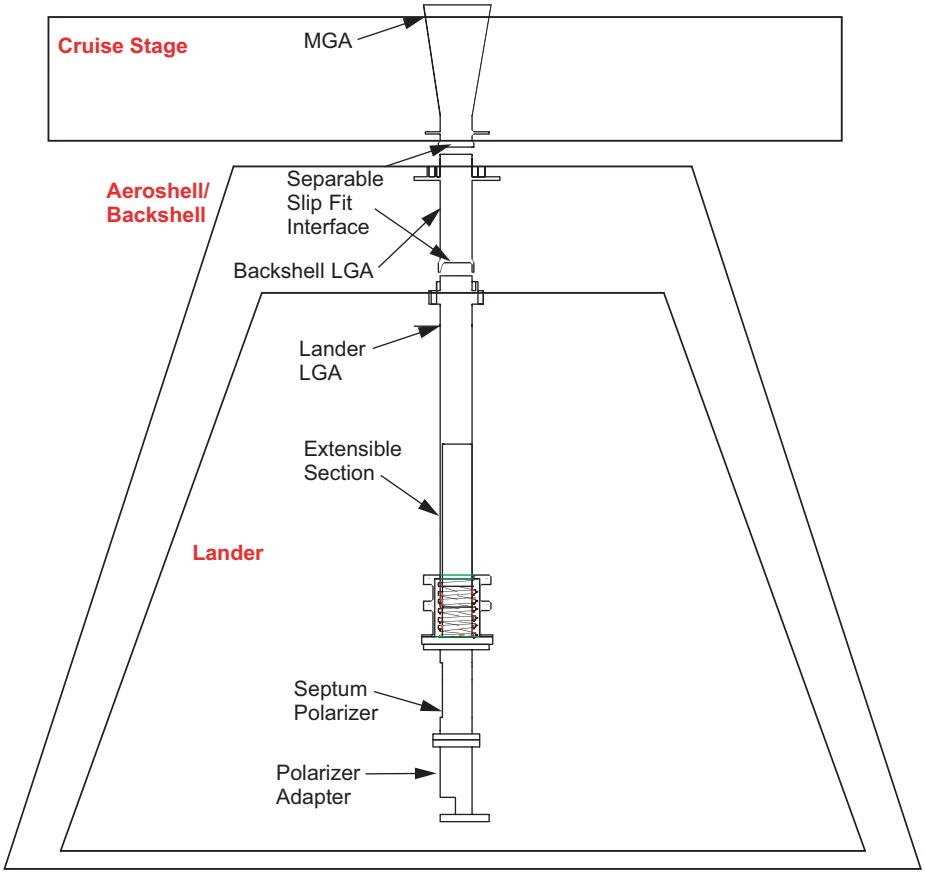

Fig. 4-17. Exploded view of Mars Pathfinder antenna assembly including lander LGA, backshell LGA, and MGA. The MGA was mounted to the cruise stage and was ejected with the cruise stage; the backshell LGA was mounted to the aeroshell/backshell; it separated from the lander LGA when the lander dropped away from the backshell.

atmosphere is very thin, it still causes significant friction and generates very high surface temperatures on the entry vehicle. The spacecraft was protected by an ablating thermal tile heat shield. In order to protect the antenna and the open transmission line, ceramic-coated Lockheed HTP-6 shuttle tile was employed. A radome/plug prevented the superheated gas from flowing through and down the waveguide assembly. Additional tile material was placed over the choke rings. Since an annular interface region between the backshell LGA and the MGA was left exposed, and the superheated gas stream approached temperatures of 2000 deg F (1366 K, above the melting point of aluminum), the backshell LGA material was chosen to be beryllium copper, a high-temperature metal with excellent RF properties. Arcjet tests at NASA's Ames Research Center verified that this combination of beryllium copper and shuttle tile provide adequate thermal isolation.

Following the ballistic entry, the spacecraft deployed a descent parachute that reduced the spacecraft speed and altered the Earth probe angle, as shown in Fig. 4-16(c). Once the parachute was deployed, the bottom of the heat shield was ejected, and the lander was lowered via a tether from the backshell, separating the backshell LGA from the lander LGA. The backshell-LGA-to-Lander-LGA interface employed a slip fit similar to the MGA-to-backshell-LGA interface. Originally, it was hoped that descent communications could be achieved through the Lander LGA, a choked circular waveguide horn, but the required coverage region in conjunction with overwhelming spacecraft blockage made this unfeasible. As the spacecraft descended, it spun on the tether and swung in a pendulum-like motion. This, in addition to the Earth's location at the horizon, gave rise to the requirement for an antenna with a torroidal pattern whose coverage extended ±30 deg. This descent antenna (DEA) (see Fig. 4-18) was accessed by switching via a waveguide transfer switch just prior to parachute deployment. The DEA consisted of a simple X-band disc-cone wire antenna. The antenna was fabricated from a 0.25-in. (0.635-cm) diameter semi-rigid cable with its center conductor exposed approximately ¼ of a wave length. A small conical skirt was used as a "ground plane," and a top-loading disc at the end of the exposed center conductor was used for matching. The antenna used a thimble-shaped Astroquartz radome. The antenna assembly was mounted on a small spring-loaded mast, which popped up after the backshell aeroshell ejected.

During operations it was found that the descent antennas provided marginal link returning data in a sporadic fashion. In particular, during the high-temperature entry, an unexpected blackout occurred. It is speculated that this may have been caused by plasma effects.

At the appropriate altitude, retro-rockets fired to bring the probe to a complete stop many meters above the surface. The tether was released, dropping the lander, which deployed an array of large airbags to cushion the impact of landing. After the lander was grounded, the airbags deflated and

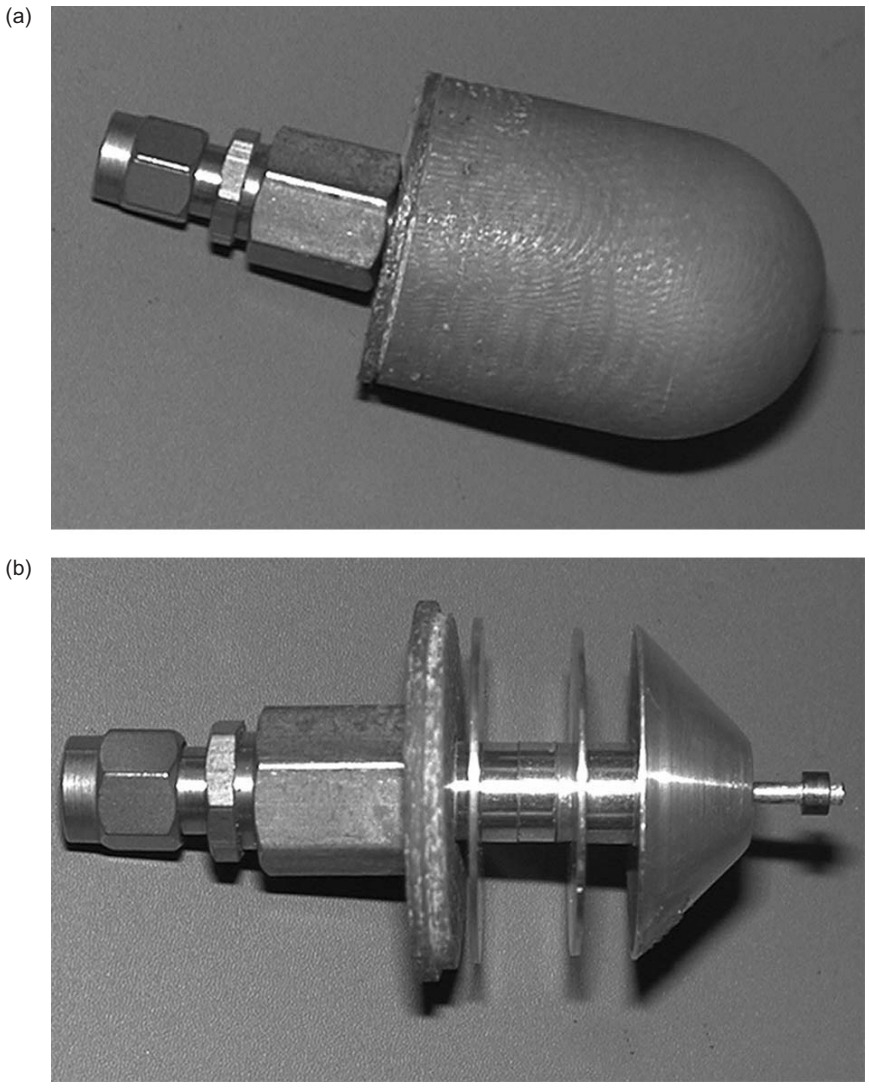

Fig. 4-18. Mars Pathfinder descent antenna (DEA): (a) with radome and (b) with radome removed.

retracted, and the pyramid-shaped lander, composed of a base and three petals, opened (Fig. 4-16(d)). The action of the opening petals served to right the lander, regardless of which side it would have landed.

After the lander came to a roll stop and prior to opening the lander, signals were sent back to Earth via the small descent antenna. It was not certain whether the lander would crush this antenna due to impacts from bouncing on the airbags. Further, there was no guarantee that the lander would come to a

stop in an upright position; the DEA was located atop the lander petals, so there was a 1-in-3 chance it would have been broadcasting into the ground. (Actually the center of gravity of the lander skewed the odds to better than 1-in-3 toward causing it to roll into its upright position.) However, almost on cue, a set of tones was received from the tiny antenna shortly after it was estimated that it should have come to rest on the surface.

4.3.1.2 Communications Link Between Lander and Earth. Once upright, the opened lander revealed the LGA, a two-axis gimbaled HGA, a camera on a deployable mast, a small robotic rover, and a number of other instruments (see Fig. 4-19). The lander LGA was then used to download a replay of the sequence of events that occurred during the entry and descent in the event that the real-time communications had been interrupted. Following this transmission, the antenna subsystem was switched to the actuated HGA array (a printed dipole array). The HGA consisted of an array of printed dipoles, which was used for all major direct-to-Earth communications. The Lander LGA was

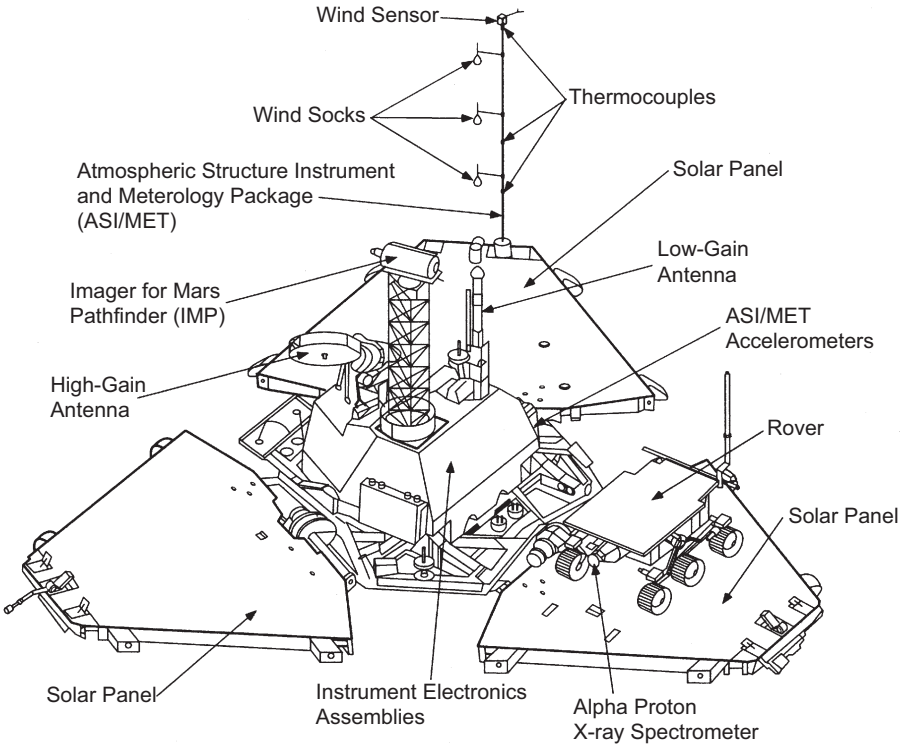

Fig. 4-19. Mars Pathfinder lander in its deployed (opened) configuration.

used periodically throughout the mission to relay commands and telemetry. Its broad-beam LGA pattern (7-dBiC boresight gain with an approximately ±40-deg 3-dB beamwidth) made it useful during periods when the HGA could not be actuated into view of Earth.

The lander LGA functioned as the transmission line feeding the 17-W signal from the warm electronics box (WEB) mounted X-band SSPA to the backshell LGA and MGA. This dual transmission line/antenna feature made it an innovative and challenging design. Large launch and entry displacements between the backshell and the lander (the two items it connects) made use of a single rigid waveguide impossible. Other constraints made flexible waveguide or coaxial cable impractical. However, by constructing two sections of circular waveguide of different diameters, a tube-within-a-tube extensible waveguide was formed. The two sections, connected with a compression spring contained by a cylindrical spring retainer (Fig. 4-17), allowed the waveguide to shorten and lengthen.

Mechanical/electrical discontinuities throughout the antenna subsystem were among the many engineering challenges of this antenna system design. Some sources of these discontinuities included two diameter steps in the waveguide, one at the interface between the polarizer and the first tube of the extensible waveguide section, and the other at the interface between the two tubes of the extensible waveguide section. A linear taper was used to counter the effects of the second of these waveguide steps. Another source of discontinuity was interactions with and between the pair of ceramic radomes used in the lander and backshell LGAs. It was necessary to adjust the thickness of these radomes to prevent filtering effects at the operating frequencies.

The HGA was used for the majority of the data transfer between the lander and the Earth. This antenna was designed and manufactured by Ball Aerospace and Technologies Corporation. It consisted of an array of printed dipoles mounted over a ground plane (separated by a Nomex honeycomb layer) (see Fig. 4-20). It also made use of a set of printed meander-line polarizers to achieve the required circular polarization. The polarizers were layered atop the printed dipoles and were separated by a Nomex honeycomb layer. Due to the resonant nature of the dipole elements, this antenna functioned best over a transmit frequency band (8.4 GHz) with a better than 1.2:1 voltage standing wave ratio (VSWR) but provided acceptable performance at the receive frequency band (7.1 GHz) achieving better than 2.4:1 VSWR. The antenna transmit and receive gains were 24.5 dBic and 20.6 dBic, respectively.

4.3.1.3 Communications Link Between Rover and Lander. The microrover telecommunications system used a two-way UHF radio link between the lander and the rover. The microrover radio had a signal range similar to a walkie-talkie. The telecommunications system was composed of two UHF radios and two UHF whip antennas. The microrover radio was located inside the Rover

(a)

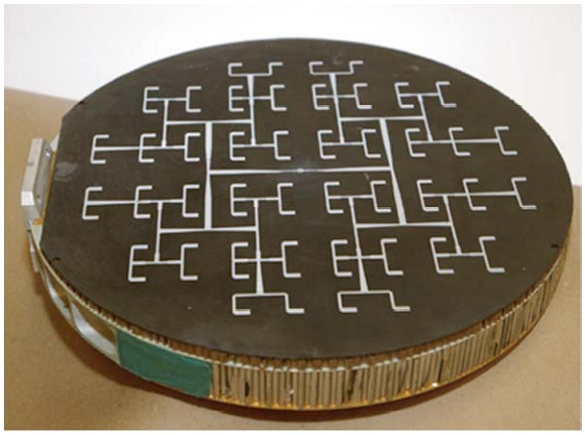

(b)

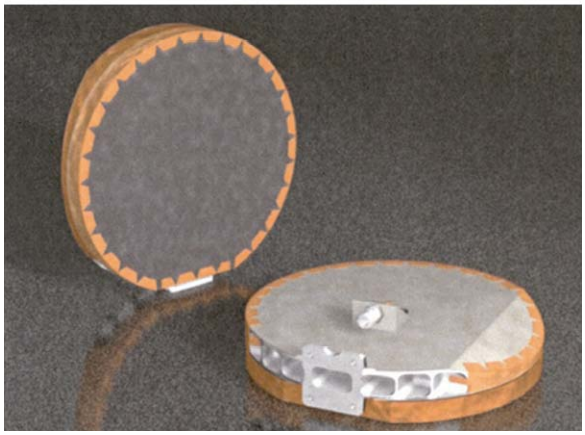

Fig. 4-20. Mars Pathfinder HGA (same design used for MER) designed and fabricated by Ball Aerospace: (a) dipole array exposed prior to installation of the meanderline polarizer layer and (b) final product.

WEB where it was protected from the extreme cold of the Martian environment. The radio was connected to the microrover antenna using a short piece of coaxial cable that passed through the wall of the WEB (see Fig. 4-21). Table 4-2 provides a list of specifications for the lander UHF antenna.

The antenna patterns of Fig. 4-22 were taken on the JPL Mesa Antenna Range using a static lander model. A flight-like lander-mounted rover equipment (LMRE) antenna was mounted to the LGA (mast and placed a height of 83 cm from the ground. A radio modem operating in continuous wave (CW) mode was used to transmit a 459.7-MHz, 100-mW signal from the LMRE antenna to a receiving antenna attached to a spectrum-analyzer receiver.

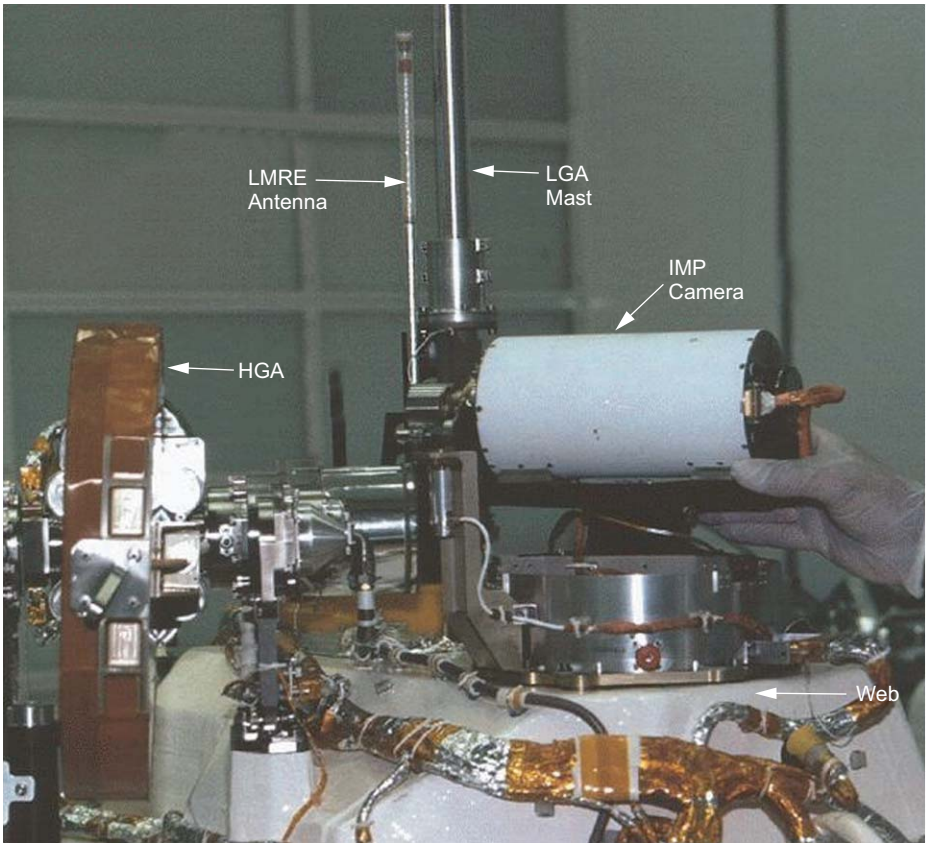

Fig. 4-21. Mars Pathfinder LMRE antenna atop the warm electronics box (WEB) mounted to the lander LGA [31].

The receive antenna was a flight-like rover antenna set to a height of 80 cm and connected to the receiver via a coaxial cable. The antenna pattern taken at a distance of 3 m looks quite irregular. In particular, at 10 deg and 330 deg, there are noticeable null zones. This is due primarily to scattering and out-of-phase reflections of the RF energy from the metallic components (e.g., LGA, HGA, Imager for Mars Pathfinder (IMP) mast, and solar panels) of the lander structure. Farther away, beyond 5 m, the LMRE antenna is away from this near-field scattering, and the shape of the antenna's radiation pattern becomes better defined.

The Pathfinder rover antenna (see Fig. 4-23) specifications are provided in Table 4-3. The rover antenna radiation patterns of Fig. 4-24 were taken on the JPL Mesa Antenna Range using a static model rover. A flight-like rover antenna was mounted to the rover mast and placed a height of 83 cm from the ground. A radio modem operating in CW mode was used to transmit a

Table 4-2. Mars Pathfinder lander LMRE UHF antenna specifications.

Parameter	Value
Overall length	33.6 cm
RF: connector type	Coaxial SMA
RF center frequency	459.7 MHz
RF bandwidth	16 MHz for <2:1 VSWR
RF gain	1.4 dBi-vertical polarization
Free space match	1.25:1 VSWR at center frequency
Materials	Fiberglass tube, aluminum tube, Teflon supports

459.7-MHz, 100-mW signal from the rover to a receiving antenna attached to a spectrum analyzer receiver. The receive antenna was a flight-like LMRE antenna mounted to the receiver at a height of 80 cm. The antenna pattern taken at a distance of 2 m looks quite irregular. This is due to near-field distortion and scattering of the RF energy. Farther away, beyond 3 m, the rover antenna is in the far field, and the true shape of the Rover antenna's radiation pattern becomes more visible.

4.3.2 Mars Exploration Rovers

The Mars Exploration Rover (MER) mission consists of a twin set of rovers (Spirit and Opportunity) [28]. These rovers were intended to be an incremental evolution of the Mars Pathfinder design. The key difference between the two spacecraft/rover designs is that whereas the Mars Pathfinder configuration consisted of a small rover and a stationary lander/base station, which hosts most of the mission instruments and the telecommunications equipment, the MER configuration uses a single large rover which carries all the instruments and telecommunications equipment. The lander is merely a shell used to carry the rover to the ground. One spacecraft design objective for the MER mission was to employ as much heritage from Mars Pathfinder as possible. As a result, the antenna assembly looks very much like the Pathfinder design. The “antenna stack” approach was once again employed; the same HGA design was used. There were some variations, which are discussed in the following subsections.

4.3.2.1 Cruise Stage Antennas. Whereas the Pathfinder program used a single low-medium gain antenna to facilitate the link back to Earth during cruise, the MER mission required a higher gain to provide sufficient link margin, particularly when the two craft approached Mars. This led to a high-medium gain antenna design. In order to satisfy the need for a broad-beam antenna for wide-angle applications (such as emergency situations), an LGA was also

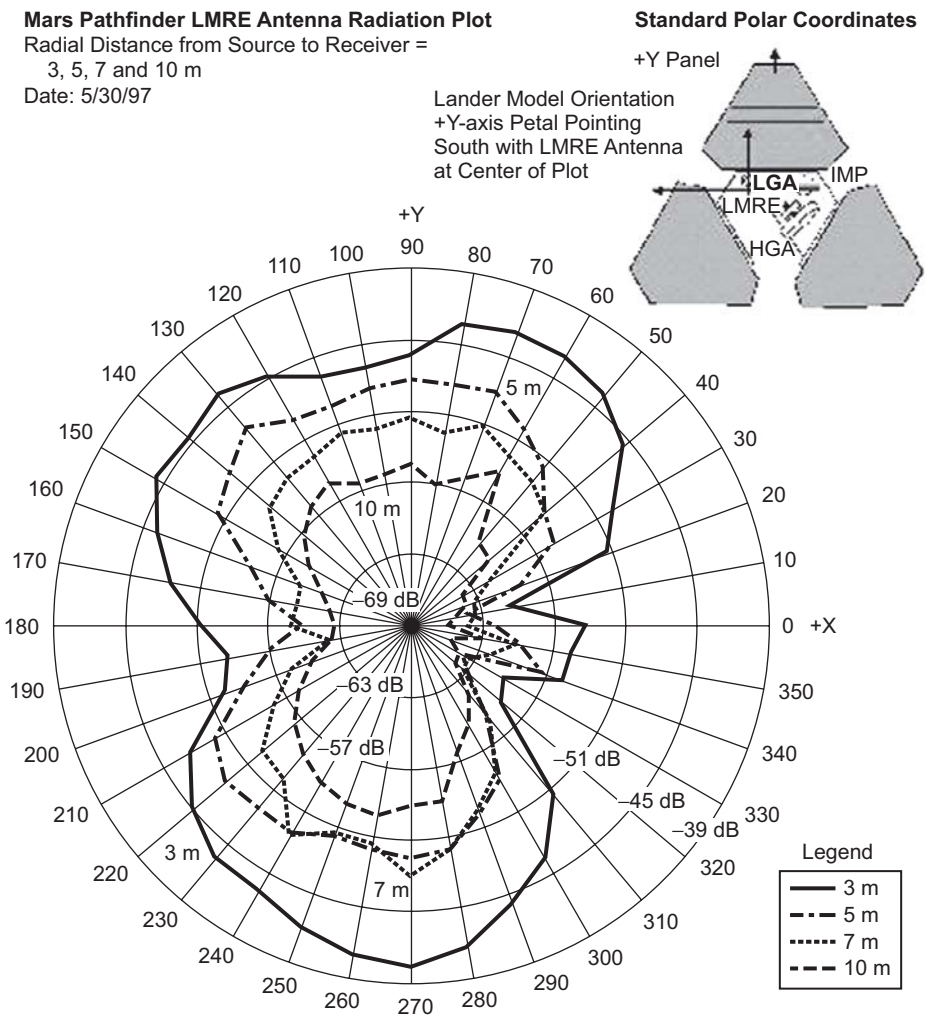

Fig. 4-22. Mars Pathfinder LMRE antenna pattern measurements [32].

added. Figure 4-25 shows the MGA and LGA mounted on the cruise-stage mockup.

The MGA consists of a simple smooth wall conical horn with an aperture that produces approximately 19 dBic at the transmit frequency of 8.439 GHz (18 dBic at the receive frequency of 7.181 GHz). The antenna is in series with a hybrid septum polarizer designed and manufactured by Atlantic Microwave Inc. to achieve the required LHCP. This polarizer design was used on several previous JPL missions (including on the Mars Pathfinder spacecraft) at the bottom of the antenna stack (see Fig. 4-17). This hybrid polarizer also provides access to a RHCP feed port. While this was not used during flight, this port was

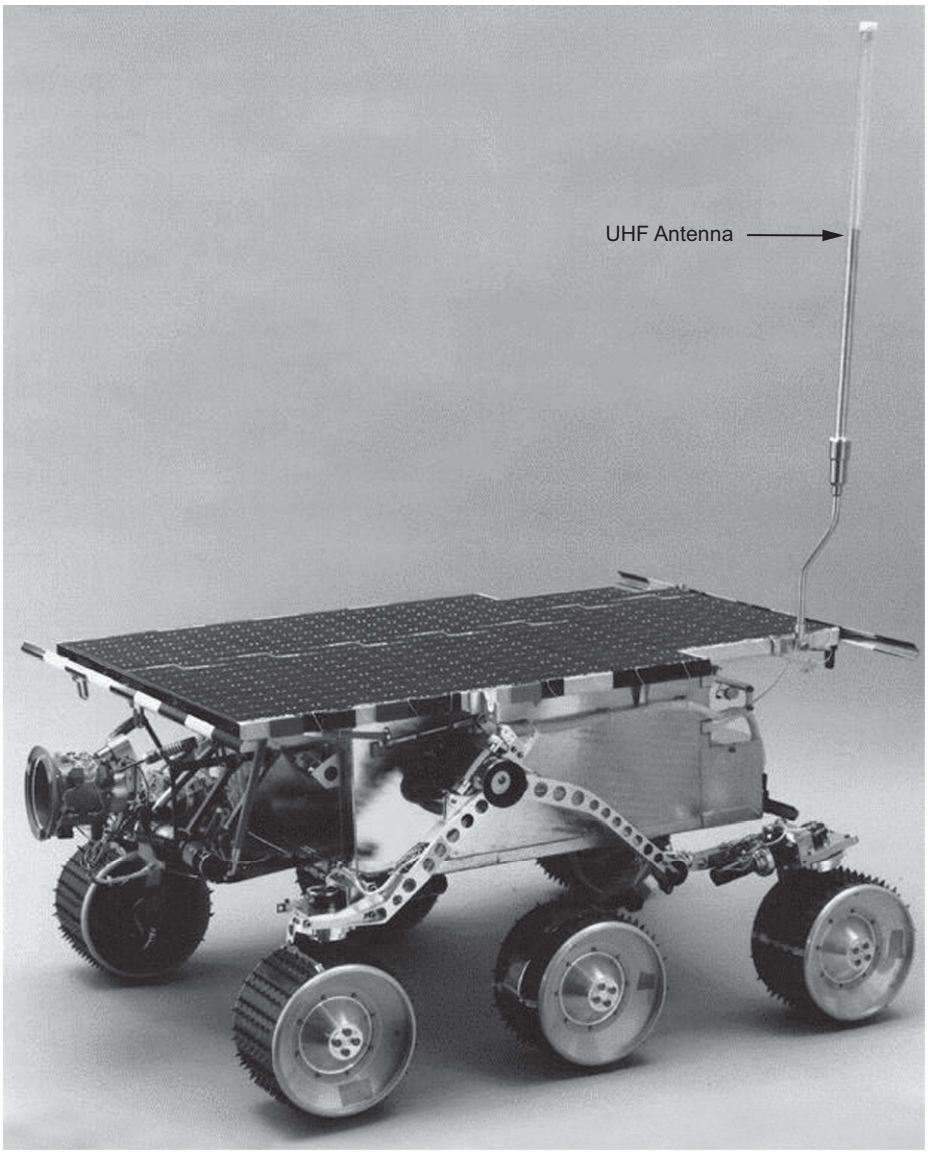

Fig. 4-23. Mars Pathfinder rover (Sojourner) with its UHF antenna deployed.

used as a handy test port. Placing a short over the antenna aperture reflected the incident left hand polarized signal back to the polarizer. The then right-hand polarized reflected signal was routed to the right-hand-circular-polarized test port on the polarizer.

This antenna was mounted near the outer diameter of the cruise stage through a hole in the cruise-stage solar array. The fact that this spacecraft was a

Table 4-3. Pathfinder Rover antenna specifications.

Parameter	Value
Overall length	45.0 cm (includes support tube)
RF: connector type	Coaxial SMA
RF center frequency	459.7 MHz
RF bandwidth	700 KHz for < 2:1 VSWR
RF gain	1.4 dBi-vertical polarization
Free space match	1.09:1 VSWR at center frequency
Materials	Fiberglass tube, aluminum tube, Teflon supports, coaxial cable

spinner meant that the MGA signals had a phase "wow." This phase modulation was factored into the telecommunications link design and was handled through ground processing. Antenna patterns of the MGA while mounted to a cruise-stage mockup are provided in Fig. 4-26. In this instance, care was taken to assure that the cruise-stage mock-up agreed with the final flight cruise-stage design. In-flight measurements show that the link performed as expected.

The cruise-stage LGA employed the choked circular waveguide design concept employed by the LGAs on Pathfinder and used in the antenna stack on this spacecraft. There were some subtle variations in the choke rings and the use of internal matching irises to maximize antenna performance, but the basic design was the same. In series with this antenna was a hybrid septum polarizer of the same design as that used with the MGA to achieve the required RHCP. Notice that the MGA used LHCP while the LGA used RHCP, this was done to provide some polarization isolation between the two antennas. Patterns for the cruise LGA while mounted to the cruise stage mock-up are provided in Fig. 4-27.

Whereas the Mars Pathfinder cruise-stage antenna was directly connected to the antenna stack, the MER assembly used an intermediate connection point, a hybrid septum polarizer, to split the signal into two oppositely polarized signals (See Fig. 4-28). The two polarized signals could then use the same circular waveguide that made up the antenna stack. There was another septum polarizer At the bottom of the stack. This polarizer sent the two signals to their proper locations in accordance with their polarization.

4.3.2.2 Entry, Descent, and Landing Antennas. As with the Pathfinder mission, there was a design requirement to maintain communications with the lander throughout all phases of entry, descent, and landing (EDL). This was especially emphasized after the loss of the Mars Polar Lander in which there

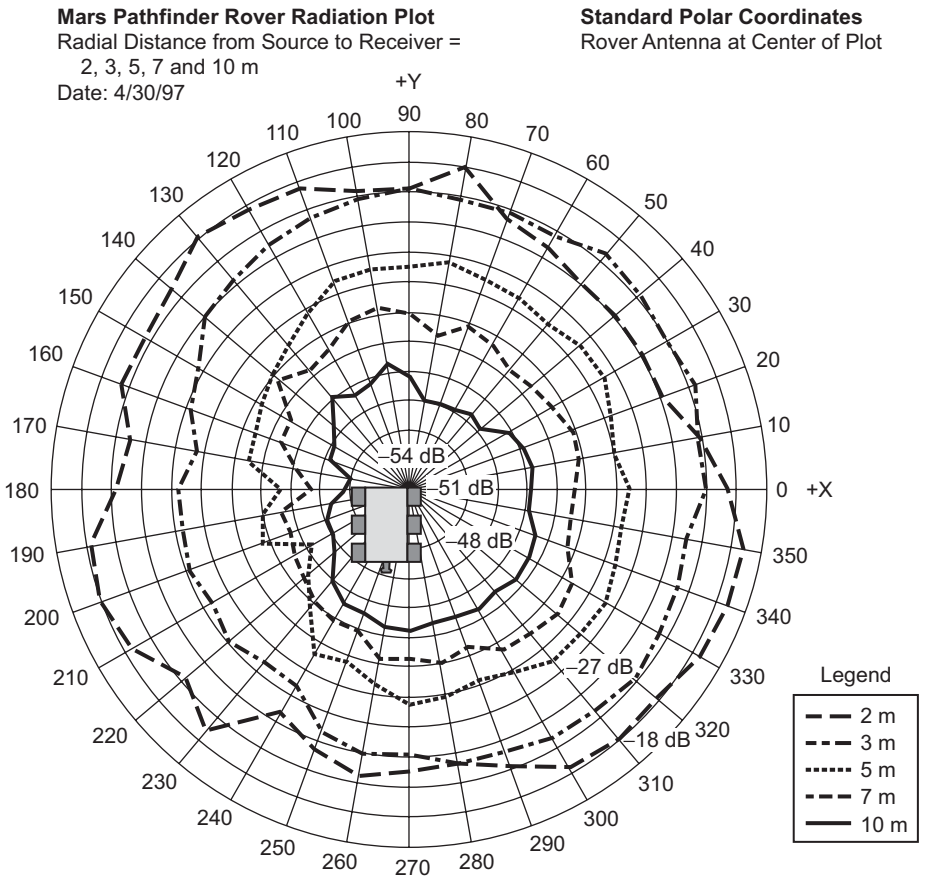

Fig. 4-24. Mars Pathfinder rover UHF antenna measurements [33].

was no link back to Earth during EDL. Receiving telemetry during descent may have provided better clues as to what caused the mission failure.

In order to facilitate the EDL requirements, the antenna stack concept from the Pathfinder mission was reused (see Fig. 4-17). Once again the backshell LGA was used as the link antenna during entry.

For the parachute descent, a slightly different concept was used. The Pathfinder spacecraft used a direct-to-Earth X-band link via the disc-cone antenna. The two MERs used the lander LGA, peering over the top of the lander for the X-band direct-to-Earth link. In addition, a new, UHF monopole antenna was implemented.

The MER lander design allowed the top of the rover LGA to protrude above the lander petals. This provided just enough clearance to facilitate a reasonable (albeit noisy) antenna pattern (see Figs. 4-29 and 4-30). Since the lander swayed back and forth during descent and the Earth was close to the

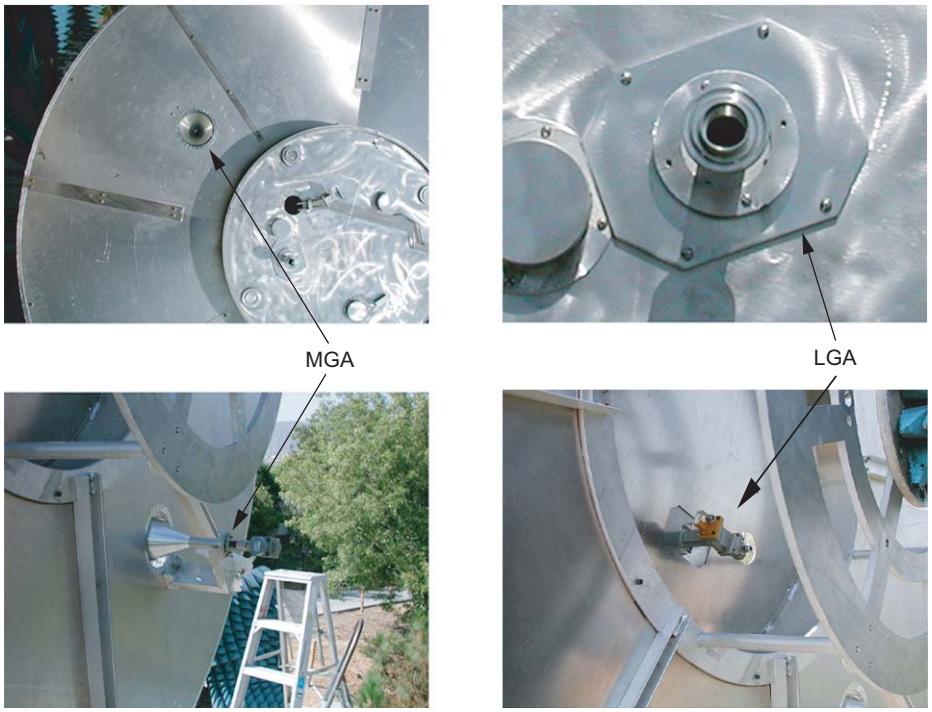

Fig. 4-25. Mars Exploration Rover MGA and LGA mounted on the cruise-stage mock-up.

horizon, this pattern did not provide an ideal angular coverage, but it provided an adequate link back to Earth.

For both MER Spirit and Opportunity, the descent UHF antenna was the primary link for descent. The UHF descent antenna communicated in a one-way (transmit only) mode of operation with MGS. The UHF monopole was mounted to the top of one of the lander petals as was done with the Mars Pathfinder X-band EDL antenna. This spring-loaded monopole popped up into action after lander separation from the aeroshell/backshell. The simple design consisted of a coaxial cable with an extended center conductor radiator. A solid Vespel radome was used to provide support and some measure of tuning. (see Fig. 4-31) The use of the Vespel replaced an earlier design that used a hollow fiberglass radome with a small metallic ball on the end to support the center conductor wire. This earlier design was found to be highly susceptible to ionization/corona at the operational powers of 15 W at 401 MHz. The new Vespel radome provided some relief from this problem, as is discussed in more detail in Section 4.3.2.4. Patterns were taken of this antenna mounted to a full-scale mock-up of the lander. The performance of this monopole was highly influenced by the lander. This less-than-ideal pattern due to the close proximity

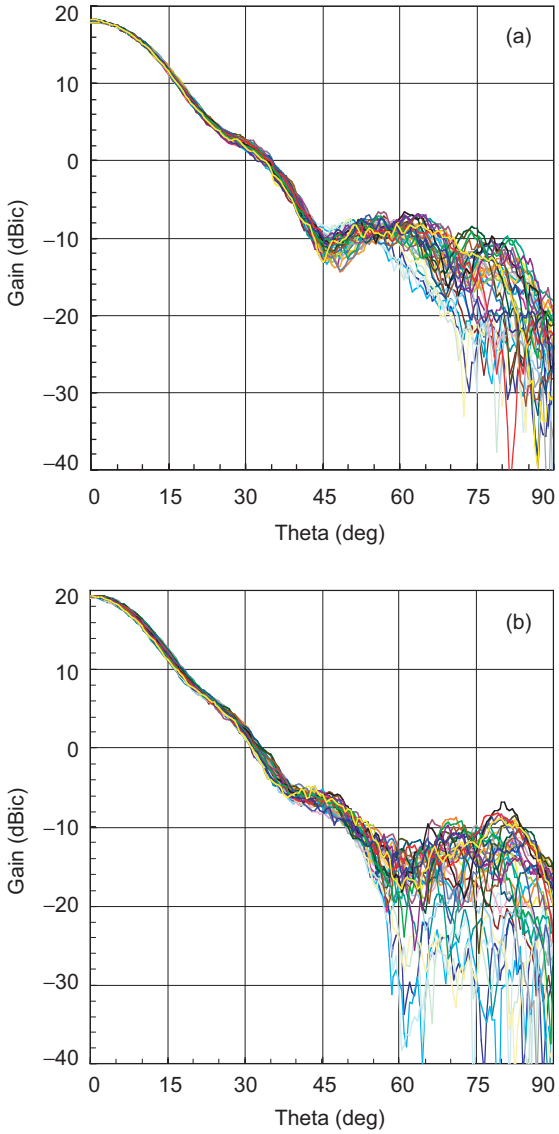

Fig. 4-26. Mars Exploration Rover measured radiation patterns from the MGA mounted on a cruise-stage mock-up: (a) 7.1 GHz, boresight gain = 18.1 dBiC and (b) 8.4 GHz, boresight gain = 19.3 dBiC.

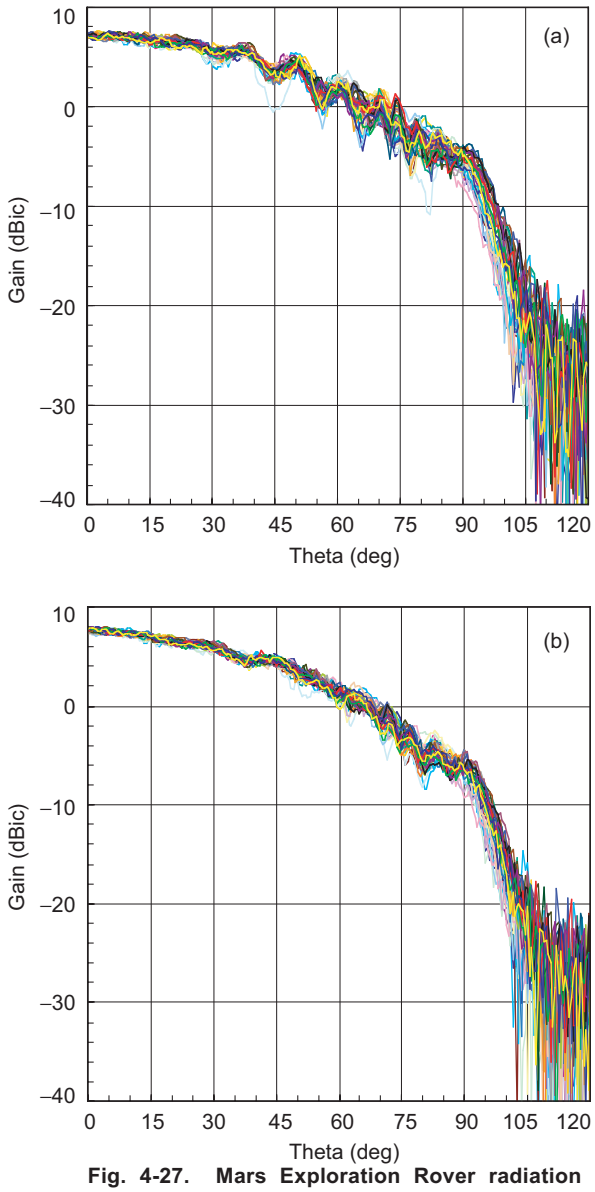

Fig. 4-27. Mars Exploration Rover radiation patterns for the LGA on a cruise-stage mock-up: (a) 7.1 GHz, boresight gain = 7.1 dBiC and (b) 8.4 GHz, boresight gain = 7.8 dBiC.

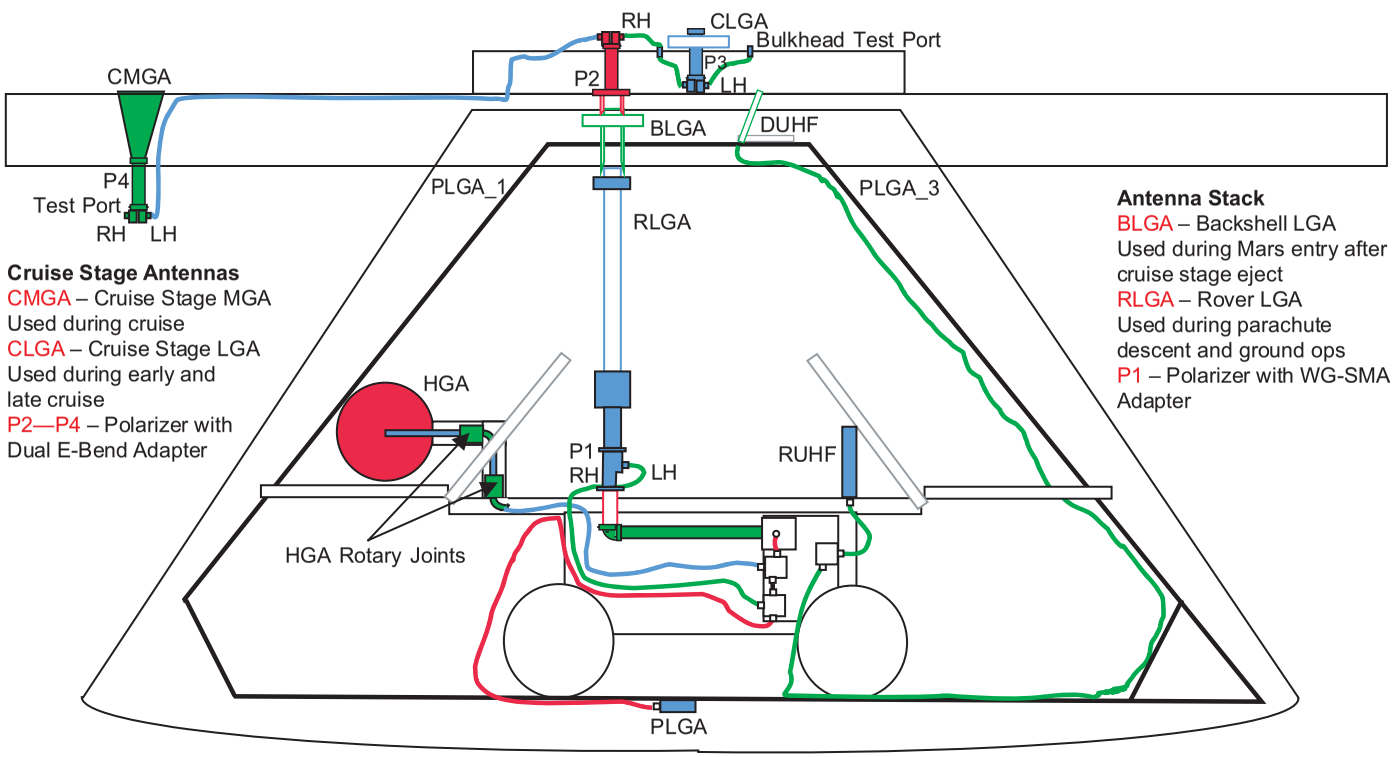

Fig. 4-28. Configuration of Mars Exploration Rover antennas during cruise stage.

Fig. 4-29. Mars Exploration Rover lander LGA mounted inside a full-scale lander mock-up. This antenna is used as a direct-to-Earth link during descent.

to the lander was a compromise that had to be made. The lander geometry was highly constrained and did not leave room to implement other more elaborate concepts. Of course, cost and schedule played in the compromise space as well.

4.3.2.3 Direct-to-Earth Rover Communications Antennas for Landed Operations. The rover deck was populated with two X-band direct-to-Earth antennas. Both of these mirrored the design used for the Mars Pathfinder mission. A rover LGA was used periodically for sending telemetry and receiving commands. The two-axis gimbaled HGA was used to send science data and telemetry as well as receive commands. The HGA design used is identical to that used for the Pathfinder mission. The LGA used the same design principals and varied only in that it incorporated a few matching irises and an RF choke near the interface between the two circular waveguides that form the spring-loaded strut-like configuration used to take up loads incurred during landing. Radiation patterns for the rover LGA while mounted to a full-scale mock-up of the rover are provided in Fig. 4-32.

In addition to the rover-mounted antennas, there was also one other direct-to-Earth link antenna that was mounted to the base petal of the lander. This antenna was to provide one of three possible data links from the time right after

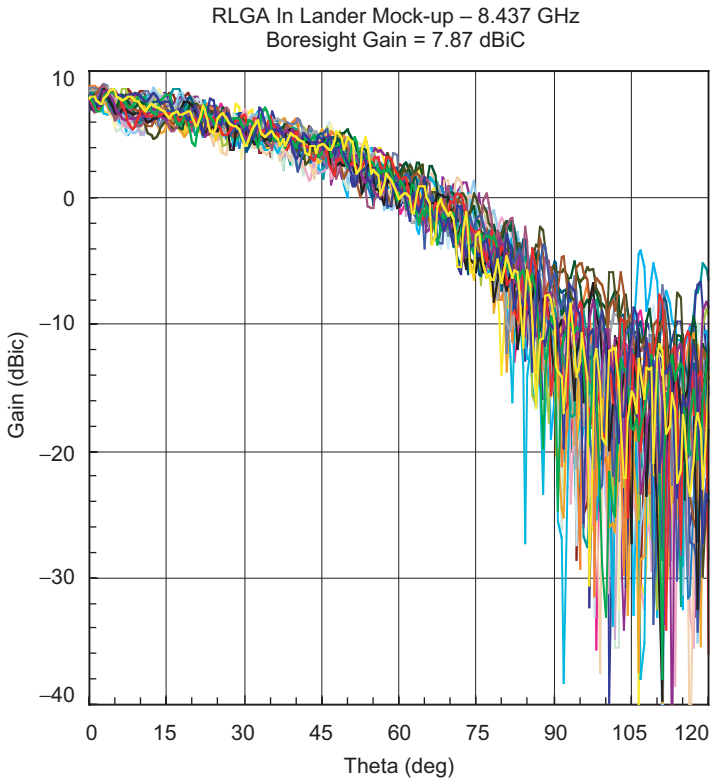

Fig. 4-30. Radiation pattern of Mars Exploration Rover LGA mounted inside a full-scale lander mock-up.

the lander came to a roll-stop after descent through the time just before opening the lander petals. This antenna would be necessary in the event the lander came to rest on one of the side petals. With the rover LGA providing coverage in the region above the base petal, this antenna would provide coverage behind the base petal. In addition, the descent UHF antenna might have provided link, depending on its orientation after landing.

The base petal LGA (PLGA) is a X-band microstrip patch tuned to the transmit frequency of 8.437 GHz (Fig. 4-33). The antenna employs a thin Last-A-Foam radome for protection and as a spacer to prevent contact with the airbag hardware. Like the descent UHF antenna, this antenna was forced into a non-ideal location. Since the lander was surrounded by large inflated air bags at this phase of the mission, there were few places to mount the antenna in order to provide coverage behind the base petal. As a result, the antenna was mounted in the center of the base petal underneath the airbags. All three antennas used for the link at this phase of the mission were subject to some amount of airbag

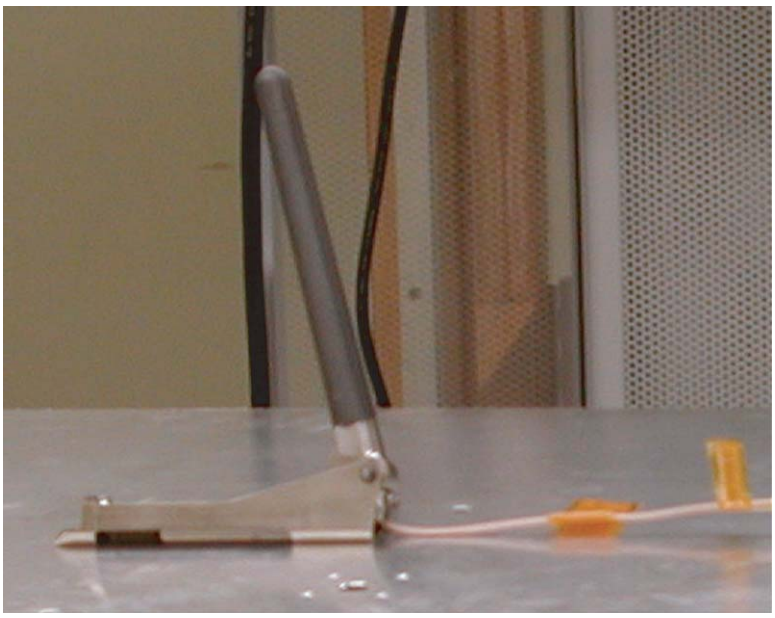

Fig. 4-31. Mars Exploration Rover descent UHF antenna.

blockage. The radiation patterns for the PLGA when mounted on a simulated base petal with a single air bag attached are shown in Fig. 4-34.

4.3.2.4 Rover-to-Orbiting-Asset UHF Relay Link Antenna. In addition to the X-band direct-to-Earth link antennas, the MER rovers use a UHF link for relaying science data back to Earth via one of the orbiting assets, either MGS or Mars Odyssey.

Each rover's deck-mounted UHF antenna consists of a simple one quarter wavelength monopole (see Fig. 4-35). This antenna was not the first choice for this function. Its free space radiation pattern sends it energy out to the sides across the rover deck in a torroidal pattern. This energy interacts with the many vertical structures mounted to the rover deck. In addition, due to configuration constraints, the monopole had to be placed close to the edge of the rover deck, which did not provide an ideal ground plane for the antenna. These effects resulted in patterns that are fairly unrecognizable relative to a classical monopole pattern. As has been mentioned several times in this chapter, any LGA should be installed as far from spacecraft structure as possible, or the user link should have lots of margin (greater than 20 dB). Unfortunately, neither choice was possible in this mission. The highly crowded rover deck could only fit a very small antenna whose volume had to fit within an envelope about the size of the monopole. Alternate designs (such as the turnstile antenna used on Viking) could not be used.

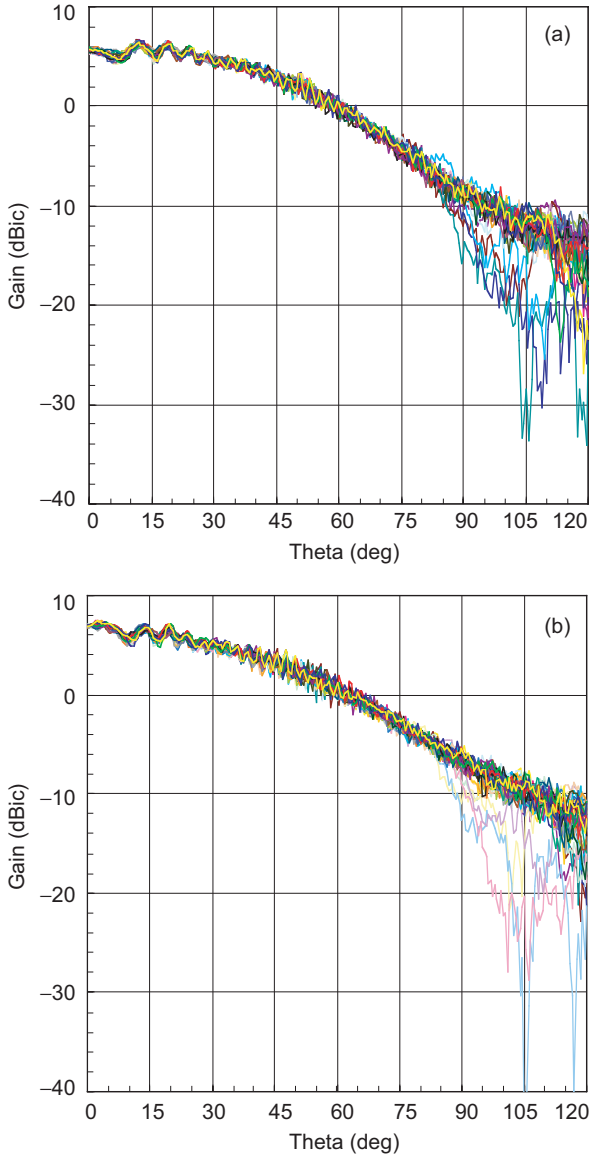

Fig. 4-32. Radiation patterns of the Mars Exploration Rover LGA measured with antenna mounted to a full-scale mock-up of the rover deck and its major instruments: (a) 7.181 GHz, boresight gain = 5.73 dBiC and (b) 8.437 GHz, boresight gain = 6.85 dBiC.

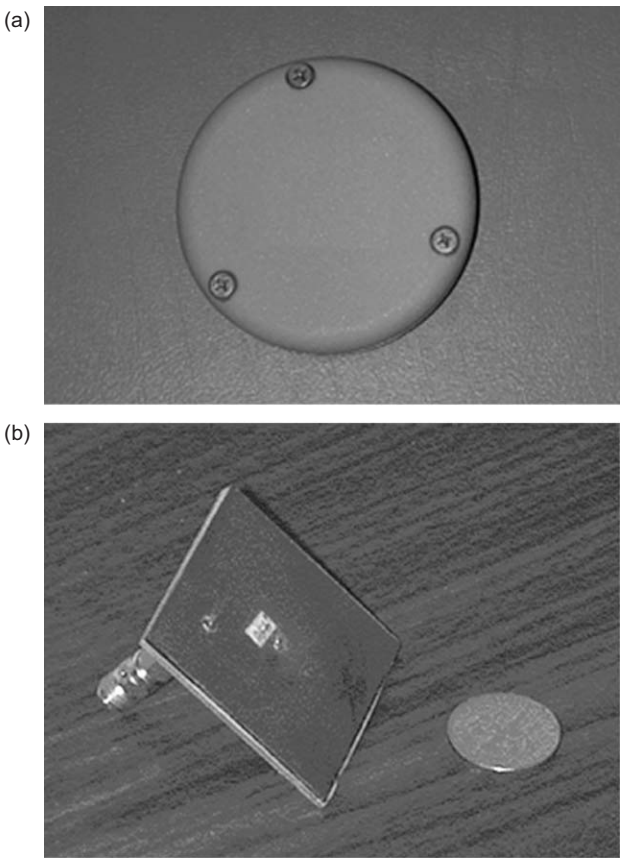

Fig. 4-33. Mars Exploration Rover (a) breadboard petal LGA patch antenna and (b) its flight unit Last-A-Foam radome (note dime for size).

Another design consideration that was particularly relevant to the UHF frequency band is ionization/corona effects on the Martian surface. It turns out that the 4- to 12-T (533- to 1600-Pa) Martian atmospheric pressure is just about ideal for corona to occur. This is true for radiation power even as low as 5 W. For this mission, the 15-W UHF transmit power provided ample opportunity for corona. The corona effect occurs when electric fields are strong enough to strip electrons from surrounding gas atoms; these electrons then recombine, giving rise to the corona glow. In addition to optical radiation, accelerated free electrons can radiate broadband noise, and in the case of antennas, the shroud of ionized gas can cause the antenna to electrically look larger than its radiating elements. This causes the antenna to be mismatched, sometimes severely, as is the case with a resonant antenna like a monopole. This problem can usually be

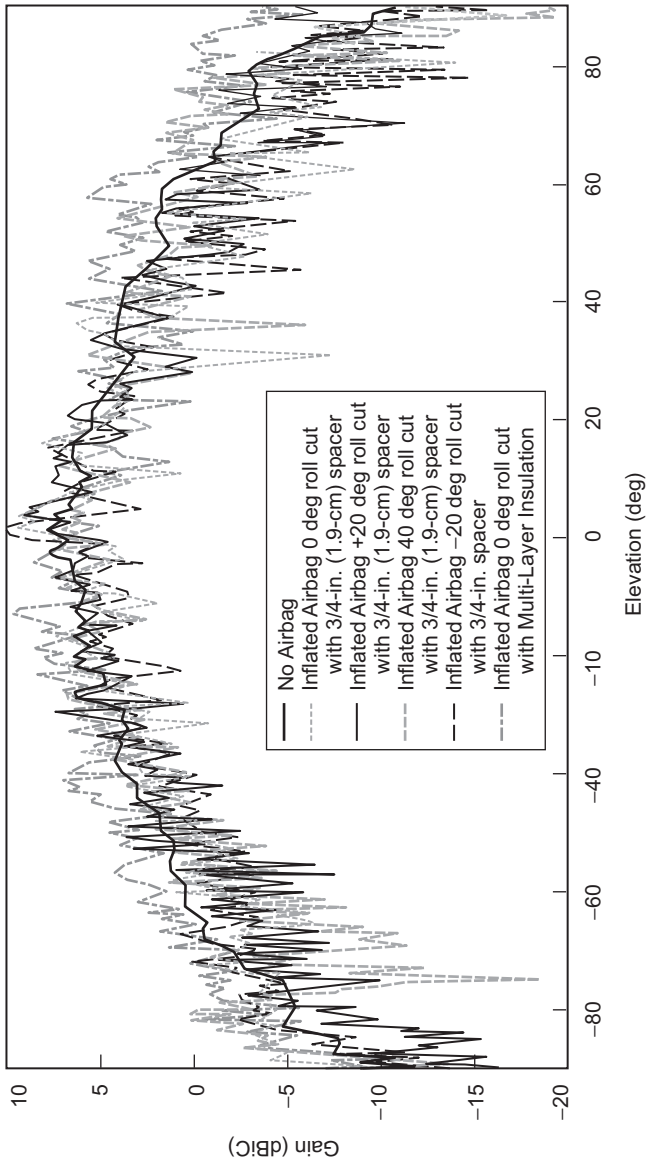

Fig. 4-34. Mars Exploration Rover base petal X-band LGA and its radiation patterns in the presence of the base petal and a single lander airbag. Note: the flight unit low-gain patch antenna uses a Last-A-Foam radome for protection and as a spacer to prevent contact with the airbag.

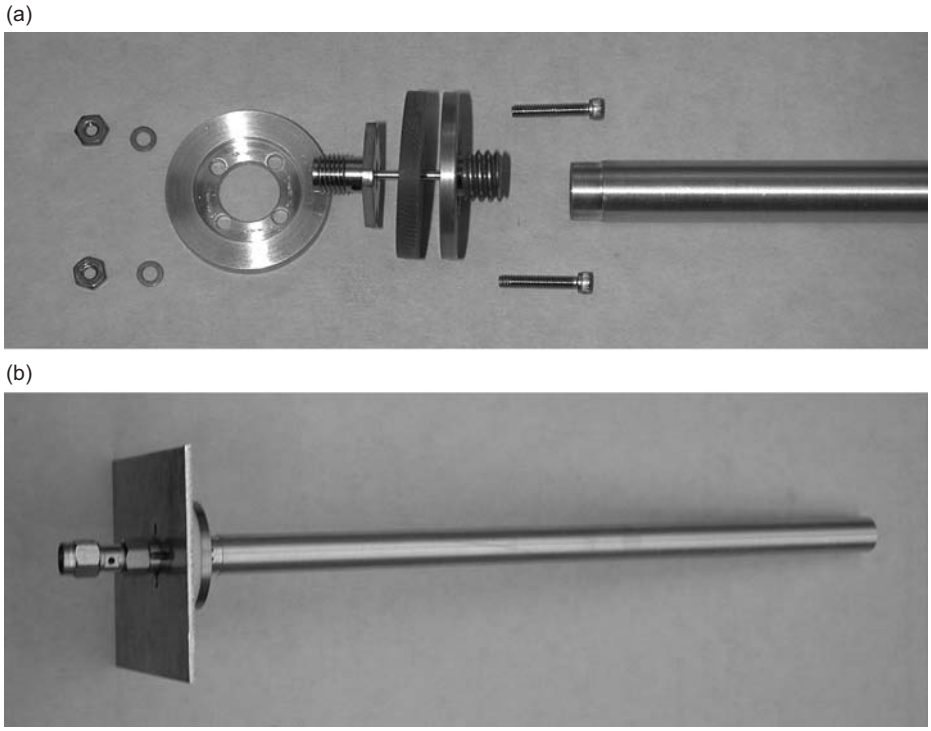

Fig. 4-35. Breadboard version of MER rover UHF antenna: (a) exploded view of breadboard monopole antenna and (b) assembled breadboard monopole antenna.

avoided by using rounded tips on the radiating elements as was done for the Viking antenna (see Fig. 4-13). As is well known, pointed tip (very small radius of curvature) radiating elements have high electric fields in the vicinity of the point, these fields give can facilitate the corona/ionization problem. In the case of a Mars-based antenna, the problem is even more difficult. When the gas pressure is very low, in addition to stripping electrons off of neighboring gas atoms, electrons are emitted from the radiating element metal itself. These electrons have fairly large mean-free paths. In the oscillating fields with long wavelengths, such as at UHF (~0.75-m wavelength), this allows the electron to be accelerated to high velocities before it comes in contact with a gas atom. This is opposed to the higher-pressure case where the electrons emitted from the surface do not get very far before coming in contact with a gas atom or (for higher frequencies with short wavelengths) cannot gather enough momentum. In the low-pressure case when the electron does reach the atom, it has sufficient energy to knock off electrons before it finally recombines. This process can start an avalanche effect. At these lower pressures, rounding the element tips is not sufficient. It has been found that one needs to raise the work-function (the measure of how readily a material will emit electrons) of the element. In the

case of the Viking UHF antenna, this was done by surrounding the element with a foam cap. For the MER program, it was found that wrapping the antenna in black (carbon-loaded) Kapton tape raised the work function enough to prevent corona at our operational power of 15 W.

Figure 4-36 shows the rover UHF antenna operated in a vacuum chamber with a back-fill of simulated Mars gas (mostly CO_2). The pressure of the gas was varied while a fixed excitation power fed the antenna. As this was done, the antenna began to generate corona/ionization. At first the effect was quite local, around the tip of the monopole. As the pressure was lowered, the mean free path increased, increasing the area over which the corona occurred. Finally, when the pressure was so low that there was no longer any gas to ionize, the effect stopped. It should be noted that this type of ionization is rather benign in terms of its ability to damage the RF hardware. In the case where there is extremely high potentials, an ionization event can break down the intervening gas generating a instantaneous arc of electric current which has sufficient heat energy to damage the equipment. This type of ionization is not a problem for the MER rover UHF antenna.

As was mentioned in Section 4.3.2.2, the original descent UHF antenna design was susceptible to the corona effect. This antenna employed an exposed metal ball at the tip of the radiating element. It was found that by encasing the radiating element in Vespel, the work function was raised sufficiently high to eliminate the corona at our operational powers.

4.4 Continued Mars Exploration

As of the writing of this book chapter, there are several new missions planned for the further exploration of Mars. These include the Mars Reconnaissance Orbiter [29], Mars Science Laboratory (MSL), Mars Scout Missions, and a Mars Sample Return mission [30].

The Mars Reconnaissance Obiter (MRO) mission (launched August 12, 2005) will be the highest data-rate mission ever flown by NASA. Its 3-m HGA and 100-W X-band TWTA will facilitate data rates on the order of 6 megabits per second (Mbps). In addition to the X-band link frequency, the MRO antenna also hosts a Ka-band “experimental” link. As with the MGS, the MRO Ka-band signal is fed to the high-gain dish through a dual-band feed. Once again the X-band is fed coaxially through a corrugated horn, and the Ka-band is fed via a central disc-on-rod antenna (See Fig. 4-37). The optics for the MRO HGA use a derivative of the Gregorian type optics. This so called “displaced-axis” optics design is shown in Fig. 4-38. The advantage of this reflector assembly is that rays are reflected from the subreflector in such a manner as to avoid re-reflection back into the feed, thus minimizing the central blockage of the feed. The as-built reflector is shown in Fig. 4-39. The main reflector and the

Inside Vacuum Chamber

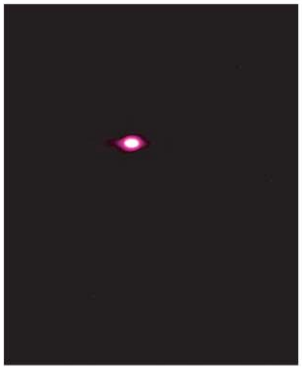

2 T (267 Pa)
60 W Peak (15 W Avg)

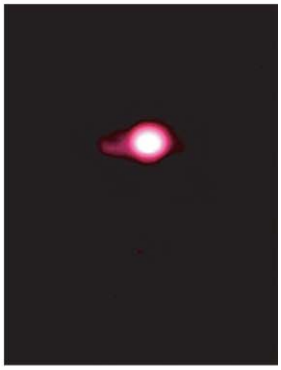

1 T (133 Pa)
60 W Peak (15 W Avg)

0.1 T (13.33 Pa)
60 W Peak (15 W Avg)

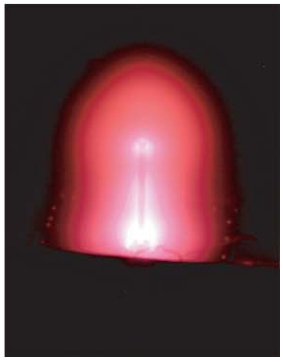

0.05 T (6.67 Pa)
60 W Peak (15 W Avg)

Fig. 4-36. Corona effects due to the MER Rover UHF (RUHF) antenna when operated in pulse mode at 60-W peak power (15-W average power) at various pressures of simulated Mars gas (mostly CO_2).

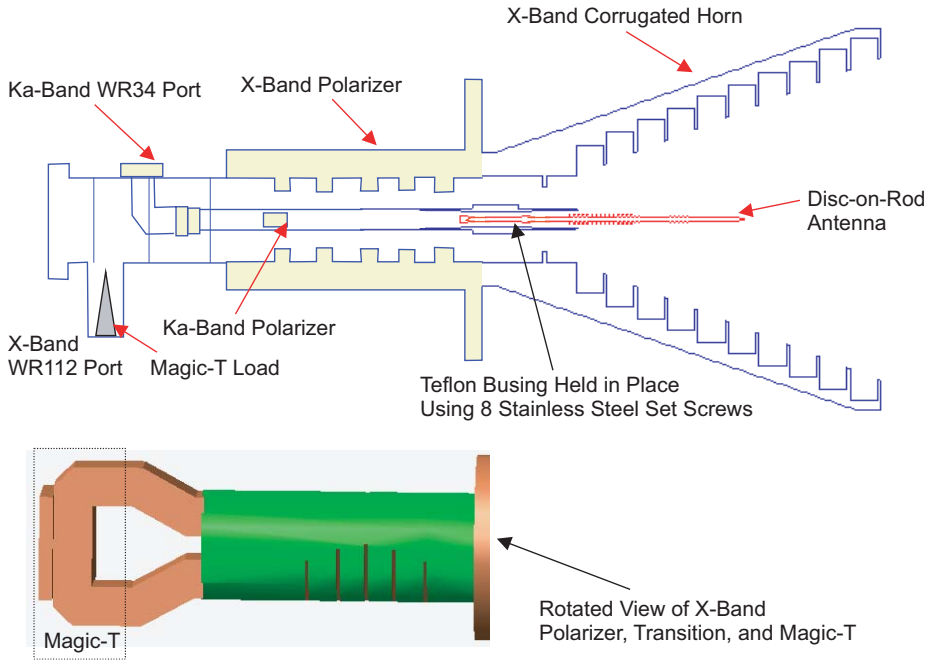

Fig. 4-37. Two views of X-/Ka-band feed assembly (without the long X-band and Ka-band waveguides; this configuration used with MGS and MRO).

subreflectors achieved better than 7 mils (178 µm) root mean square (rms) and 3 mils (76 µm) rms, respectively, manufacturing surface accuracy. The as-measured antenna was found to be 60 percent efficient at X-band and 48 percent efficient at Ka-band. Some of the major loss elements in this system were strut losses, estimated at ~0.5 dB at each frequency; surface reflectivity loss, estimated at ~0.3 dB at both frequencies; and ~1.4 dB of feed losses for the Ka-band frequencies. In addition to the dual-frequency HGA, the MRO spacecraft uses two X-band LGAs mounted as shown in Fig. 4-40. The LGAs were designed to provide as broad of a beam as possible while trying to minimize the interaction with the nearby HGA and spacecraft structure. The LGAs also make use of the septum polarizer produced by Atlantic Microwave, Inc., to achieve the necessary circular polarization. The design, predicted performance, and flight-unit article are shown in Fig. 4-41.

The Mars Science Laboratory mission will utilize the next generation of Mars surface rovers. Planned for the 2009 time frame, this rover will be the size of a small automobile and will host a new generation of scientific instruments to study the surface.

The Mars Scout Missions are a series of lower cost missions selected from proposals from the science community. The first of the scout missions,

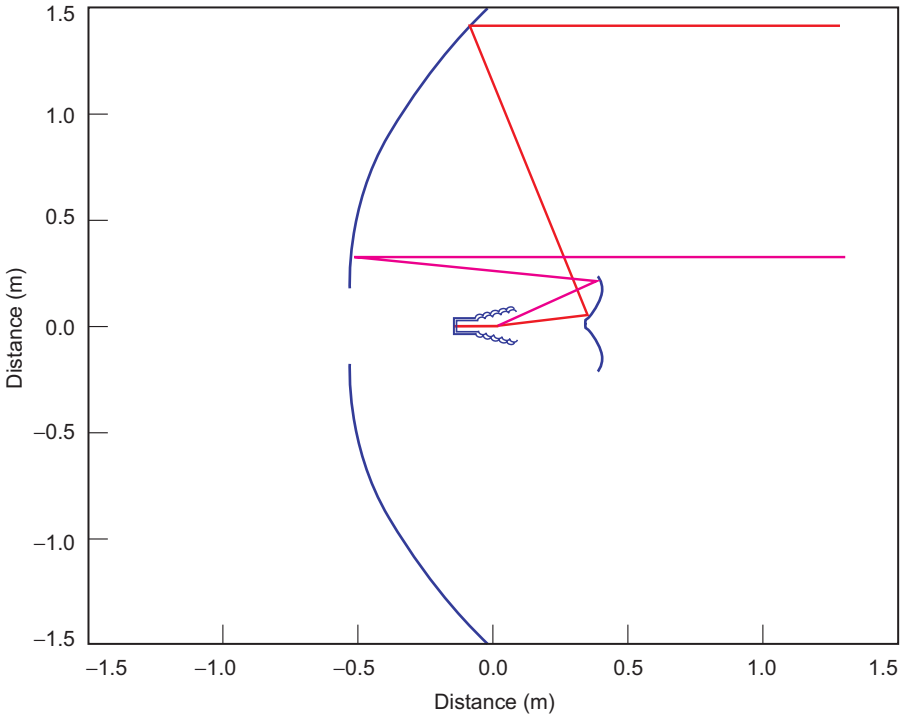

Fig. 4-38. Mars Reconnaissance Orbiter displaced-axis HGA optics.

Phoenix, a refurbished version of the Mars Polar Lander, is anticipated for the year 2007 time frame.

The Mars Sample Return mission is an ambitious endeavor to attempt to return a sample of Mars soil and rock from the surface back to Earth. This mission would involve a lander with a module that can retrieve a sample and launch back into Mars orbit. An orbiter would seek out the sample module and then return back to Earth. This mission is anticipated for some time in the second decade of the 21st Century.

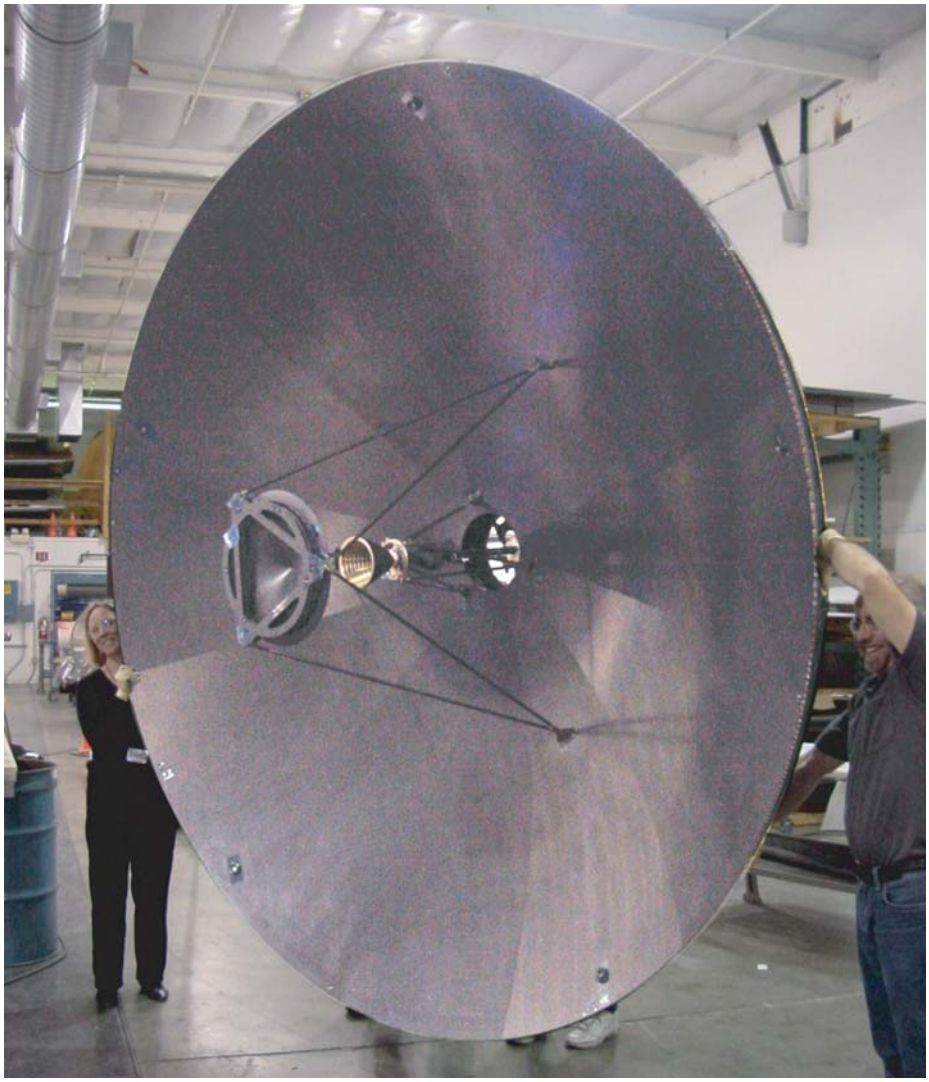

Fig. 4-39. Mars Reconnaissance Orbiter HGA and its X-/Ka-band feed.

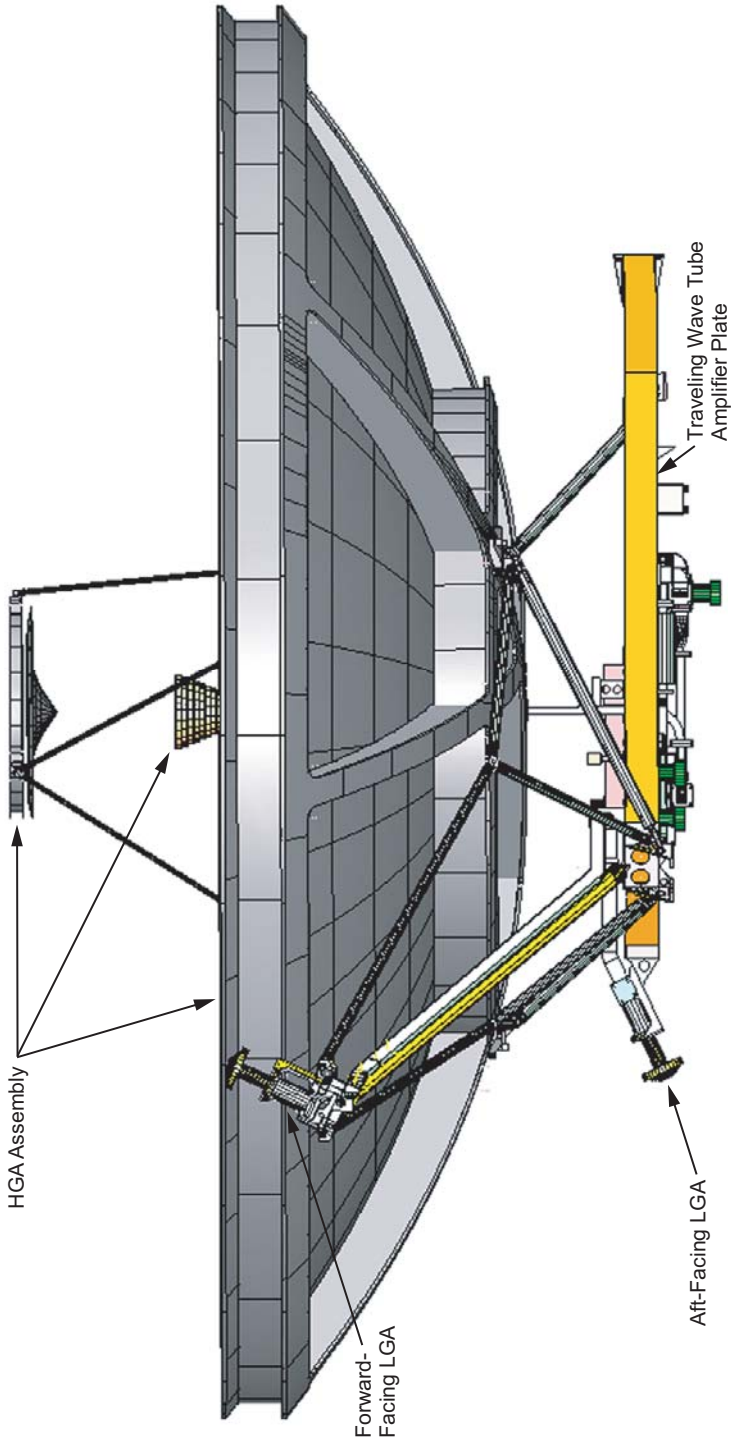

Fig. 4-40. Mars Reconnaissance Orbiter HGA and LGA configuration.

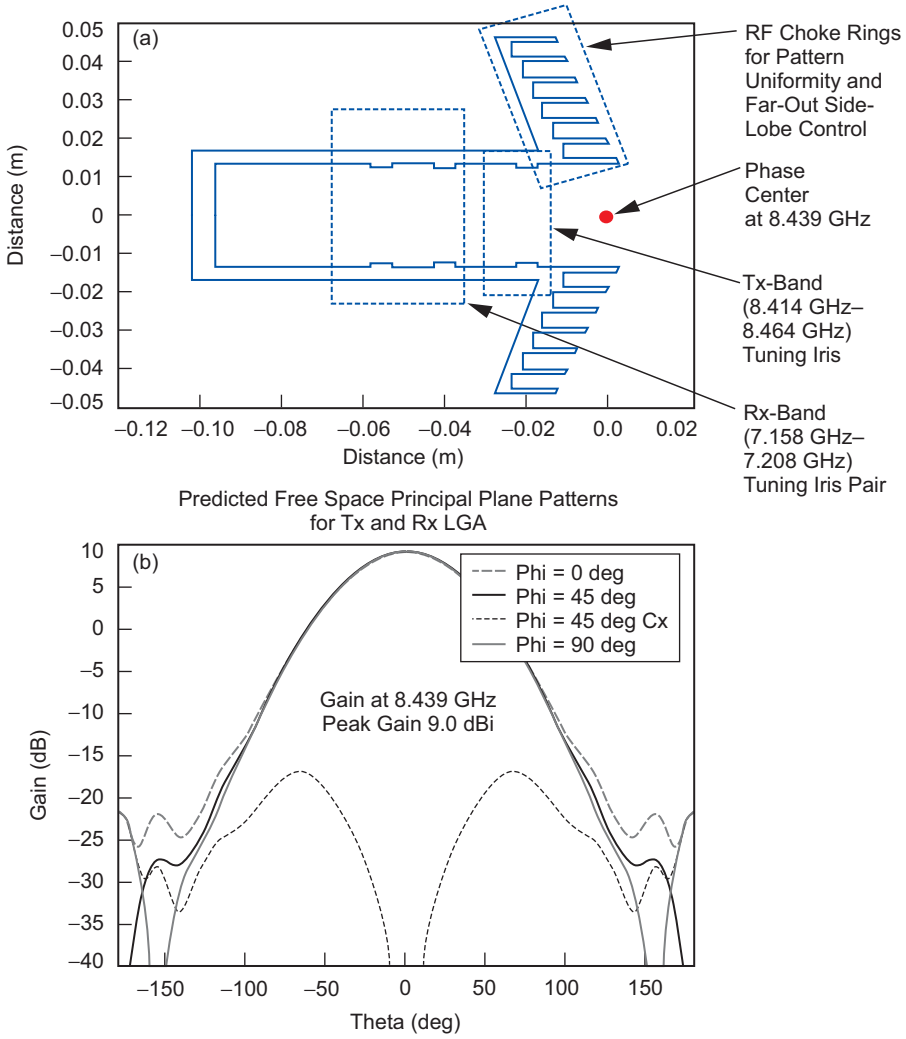

Fig. 4-41. Mars Reconnaissance Orbiter LGA (a) design, (b) predicted performance at transmit frequency, (c) predicted performance at receive frequency, and (d) flight unit.

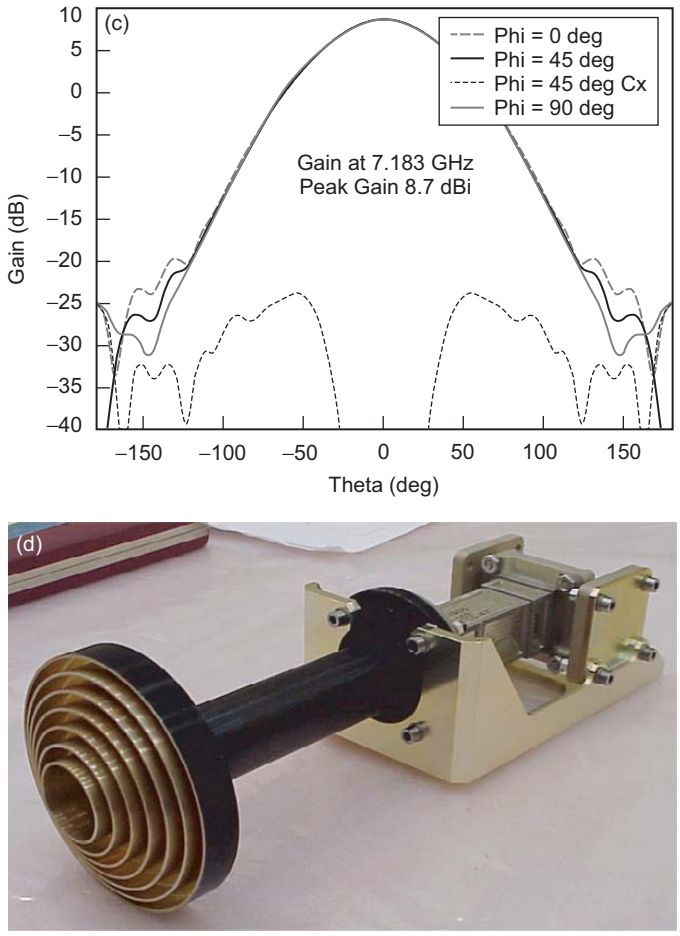

Fig. 4-41. Mars Reconnaissance Orbiter LGA (a) design, (b) predicted performance at transmit frequency, (c) predicted performance at receive frequency, and (d) flight unit (cont'd.).

References

[1] "Historical Log," *NASA's Mars Exploration Program*, website, Jet Propulsion Laboratory, Pasadena, California, accessed July 14, 2005. http://mars.jpl.nasa.gov/missions/log

[2] C. Lethbridge, "International Mars Missions Span Four Decades of Successes, Failures," article posted on *Space.com*, October 20, 1999, accessed July 14, 2005. http://www.space.com/scienceastronomy/solarsystem/marsmissions_991020.html

[3] E. C. Ezell, L. N. Ezell, *On Mars: Exploration of the Red Planet. 1958-1978***,** SP-4212, National Aeronautics and Space Administration, Washington, District of Columbia, 1984, (also on NASA web site, accessed July 14, 2005). http://history.nasa.gov/SP-4212/contents.html

[4] *Mariner Space Probes*, web site, NASA History Office, Washington, District of Columbia, accessed July 14, 2005. http://www.hq.nasa.gov/office/pao/History/mariner.html

[5] *Past Missions–Mariner to Mars*, website, Jet Propulsion Laboratory, Pasadena, California, accessed August 1, 2005. http://www.jpl.nasa.gov/missions/past/mariner3-4.html

[6] E. C. Ezell, L. N. Ezell, "Mariner Mars 1964," *On Mars: Exploration of the Red Planet. 1958-1978***,** SP-4212, National Aeronautics and Space Administration, Washington, District of Columbia, 1984 (also on NASA web site, accessed July 14, 2005). http://history.nasa.gov/SP-4212/p164.html

[7] *Mariner Mars 1964 Project Report: Mission and Spacecraft Development*, Vol. 1. *From Project Inception through Midcourse Maneuver*, Technical Report 32-740, Jet Propulsion Laboratory, Pasadena, California, March 1, 1965.

[8] E. C. Ezell, L. N. Ezell, "Chapter 6, Viking Orbiter and Its Mariner Inheritance," *On Mars: Exploration of the Red Planet. 1958-1978***,** SP-4212, National Aeronautics and Space Administration, Washington, District of Columbia, 1984 (also on NASA web site, accessed July 14, 2005). http://history.nasa.gov/SP-4212/ch6.html

[9] *Mariner Mars 1969*, Technical Report 32-1460, Jet Propulsion Laboratory, Pasadena, California, pp. 266–270, November 1, 1970.

[10] *Mariner Mars 1971 Project Final Report*, Vol. 1 *Project Development Through Launch and Trajectory Correction Maneuver*, JPL Technical Report 32-1550, Jet Propulsion Laboratory, Pasadena, California, April 1, 1973.

[11] *Viking 1 Orbiter*, Goddard Space Flight Center, Greenbelt, Maryland, Internet website, accessed July 14, 2005. http://nssdc.gsfc.nasa.gov/database/MasterCatalog?sc=1975-075A

[12] E. C. Ezell, L. N. Ezell, *On Mars: Exploration of the Red Planet. 1958–1978*, SP-4212, p. 201 (Viking Orbiter/cruise vehicle), National Aeronautics and Space Administration, Washington, District of Columbia, 1984 (also on NASA web site, accessed July 14, 2005). http://history.nasa.gov/SP-4212/p201.html

[13] E. C. Ezell, L. N. Ezell, *On Mars: Exploration of the Red Planet. 1958–1978*, SP-4212, p. 250 (communication links between Earth, orbiter, and lander), National Aeronautics and Space Administration, Washington, District of Columbia, 1984 (also on NASA web site, accessed July 14, 2005). http://history.nasa.gov/SP-4212/p250.html

[14] (Viking Lander (model, image on web site), Goddard Space Flight Center, Greenbelt, Maryland, accessed July 14, 2005. http://nssdc.gsfc.nasa.gov/image/spacecraft/viking_lander_model.jpg

[15] E. C. Ezell, L. N. Ezell, *On Mars: Exploration of the Red Planet. 1958–1978*, SP-4212, National Aeronautics and Space Administration, Washington, District of Columbia, p. 246 (Viking lander details), 1984 (also on NASA web site, accessed July 14, 2005). http://history.nasa.gov/SP-4212/p246.html

[16] *Past Missions – Mars Observer*, web site, Jet Propulsion Laboratory, Pasadena, California, accessed July 14, 2005. http://www.jpl.nasa.gov/missions/past/marsobserver.html

[17] "Mars Observer Spacecraft Diagram," *Exploring Mars*, web site, Los Angeles, California, accessed July 15, 2005. http://www.exploringmars.com/missions/mars-observer/spacecraft.html

[18] (Mars Observer spacecraft during assembly and checkout), image on web site), Goddard Space Flight Center, Greenbelt, Maryland, accessed July 14, 2005. http://heasarc.gsfc.nasa.gov/Images/marsobs/marsobs_2.gif

[19] *NASA Facts: Mars Global Surveyor*, web site, Jet Propulsion Laboratory, Pasadena, California, accessed July 15, 2005. http://www.jpl.nasa.gov/news/fact_sheets/mgs.pdf

[20] J. Taylor, K.-M. Cheung, and C.-J. Wong, *Mars Global Surveyor Telecommunications*, DESCANSO Design and Performance Series, Article 1, May 1, 2001, Jet Propulsion Laboratory, Pasadena, California, May 1, 2001 (also available at web site, accessed July 14, 2005). http://descanso.jpl.nasa.gov/DPSummary/MGS_07Aug01.pdf

[21] *Mars Climate Orbiter Science Goals*, web site, Jet Propulsion Laboratory, Pasadena, California, accessed July 26, 2005. http://mars.jpl.nasa.gov/msp98/orbiter/science.html

[22] *Mars Polar Lander*, web site, Jet Propulsion Laboratory, Pasadena, California, accessed July 14, 2005. http://mars.jpl.nasa.gov/msp98/lander

[23] "Flight 1 probe in Pre-Impact Configuration," page in *Deep Space 2 Microprobe*, web site, Jet Propulsion Laboratory, Pasadena, California, accessed July 14, 2005. http://mars.jpl.nasa.gov/msp98/ds2/pictures/flight/microprobe.html

[24] "2001 Mars Odyssey," page in *NASA's Mars Exploration Program*, web site, Jet Propulsion Laboratory, Pasadena, California, accessed July 14, 2005. http://mars.jpl.nasa.gov/missions/present/odyssey.html

[25] A. Makovsky, A. Barbieri, and R. Tung, *Odyssey Telecommunications*, DESCANSO Design and Performance Series, Article 6, Jet Propulsion Laboratory, Pasadena, California, October 2002. http://descanso.jpl.nasa.gov/DPSummary/odyssey_telecom.pdf

[26] *Mars Pathfinder*, web site, Jet Propulsion Laboratory, Pasadena, California, accessed July 14, 2005. http://mars.jpl.nasa.gov/MPF

[27] J. Vacchione, K. Burke, J. Huang, T. Otoshi, and H. Smith, "A Novel Waveguide Antenna System for the Mars Pathfinder Spacecraft /Lander," *IEEE AP-S International Symposium Digest*, vol. 3, pp. 1704–1707, July 25, 1996.

[28] *Mars Exploration Rover Mission*, web site, Jet Propulsion Laboratory, Pasadena, California, accessed July 14, 2005. http://marsrovers.jpl.nasa.gov/home/index.html

[29] *Mars Reconnaissance Orbiter*, web site, Jet Propulsion Laboratory, Pasadena, California, accessed July 14, 2005. http://marsprogram.jpl.nasa.gov/mro

[30] *NASA's Mars Exploration Program*, web site, Jet Propulsion Laboratory, Pasadena, California, accessed July 14, 2005. http://mars.jpl.nasa.gov/missions/future/2005-plus.html

Chapter 5
The Orbiters

William A. Imbriale, Mark S. Gatti, and Roberto Mizzoni

After planetary flybys, the next great quest in Solar System exploration was to put a spacecraft in orbit about each of the planets. The purpose of this effort was to enable long-term climatic studies and gravity-field and surface mapping. Mariner 9, the very first orbiter, arrived at Mars in November 1971. Magellan arrived at Venus in August 1990, Galileo at Jupiter in December 1995, and Cassini at Saturn in July 2004. This chapter describes these three non-Mars orbital missions. (Mars orbiters are discussed in Chapter 4.)

5.1 Magellan to Venus

William A. Imbriale

In the latter part of 1972, the Jet Propulsion Laboratory (JPL) began the concept studies of a radar-imaging mission to map the Venusian surface [1]. Due to uncertainty about funding in the Advanced Studies Program and the mission's role and rationale, a decision was made to conduct the study in two parts: a science and mission activity first, and a spacecraft system activity later. The project was named Venus Orbiting Imaging Radar (VOIR), and science investigators were selected in 1979.

Hughes Aircraft Company was selected to conduct the design development of the VOIR, scheduled to launch in 1983. However, complex cost estimates due to considerable science input from non-NASA, non-JPL scientists through consultants, informal work, and contractor science steering groups created an expensive complex spacecraft. Consequently, VOIR was deemed too costly and was cancelled in 1982.

However, in October 1983, the Venus mission was reinstated as a National Aeronautics and Space Administration (NASA) budgetary new start and named the Venus Radar Mapper (VRM). The new mission was a reduced undertaking that eliminated all experiments except the gravity-field experiment and the synthetic-aperture radar (SAR), which included imaging, altimetry, and radiometry. Also, to accommodate a reinstatement provision of reduced funding, the spacecraft would be built for about half the originally estimated cost. VRM used mission-proven technologies and spare components from other flight programs, such as Voyager, Galileo, and Ulysses. VRM was officially renamed Magellan in 1986, after the Sixteenth Century Portuguese explorer who first circumnavigated the Earth by sea.

Thus, with a scaled-down experiment package and with other compromises, such as the use of an elliptical orbit rather than the circular one planned for, the Venus mission was on track again, with a launch planned for May 1988. Magellan's simpler design also meant that some components had to perform more complex tasks than they had originally been designed for. For example, instead of using separate antennas for mapping and telemetry, the primary antenna would perform both of these functions.

The loss of the Space Shuttle Challenger in 1986 and the 32-month suspension of Shuttle missions delayed and reshuffled many planned space activities, including Magellan. One factor that influenced Magellan's launch date was the cancellation of the Centaur G-Prime booster as cargo on the Space Shuttle. (The Centaur had the most powerful upper stage ever designed. Its explosive liquid-oxygen and liquid-hydrogen propellants, however, were deemed too dangerous to carry along with humans into space). A second factor was the scheduled launch of the Galileo mission to Jupiter, set for October 1989—the date initially set for Magellan. A third factor was the alignment of the planets, which added a two-year delay to Magellan's launch date.

Therefore, the U.S. Air Force's less-powerful Inertial Upper Stage (IUS) replaced Centaur as the booster for Magellan; this required some modification of the spacecraft design and mission plans. The result for Magellan was that its earliest launch would be May 1989 with the use of a Type-IV trajectory. This meant that the spacecraft would spend 15 months traveling one-and-a-half times around the Sun before arriving at Venus. The original May 1988 launch date would have allowed Magellan to reach Venus in 4 months by traveling less than 180 degrees around the Sun on a Type-I trajectory.

The $551-million Magellan was the first planetary spacecraft to be launched by a Space Shuttle; the Atlantis carried it aloft from Kennedy Space Center in Florida on May 4, 1989. Atlantis took Magellan into low-Earth orbit, where it was released from the Shuttle's cargo bay. The solid-fuel IUS then fired, sending Magellan on a 15-month cruise before it arrived at Venus on August 10, 1990. A solid-fuel motor on Magellan then fired, placing the spacecraft in orbit around Venus. Magellan's initial orbit was highly elliptical,

taking it as close as 294 km (182 mi) from Venus and as far away as 8,543 km (5, 296 mi). The orbit was polar, meaning that the spacecraft moved from south to north or vice versa during each looping pass, flying over Venus' north and south poles. Magellan completed one orbit every 3 hours and 15 minutes.

During the part of its orbit closest to Venus, Magellan's radar mapper imaged a swath of the planet's surface approximately 17 to 28 km (10 to 17 mi) wide. At the end of each orbit, the spacecraft radioed back to Earth a map of a long, ribbon-like strip of the planet's surface captured on that orbit. Venus itself rotates once every 243 Earth days. As the planet rotated under the spacecraft, Magellan collected strip after strip of radar image data, eventually covering the entire globe at the end of the 243-day orbital cycle.

By the end of its first such 8-month orbital cycle between September 1990 and May 1991, Magellan had sent to Earth detailed images of 84 percent of the Venusian surface. The spacecraft then conducted radar mapping on two more 8-month cycles, from May 1991 to September 1992. This allowed it to capture detailed maps of 98 percent of the planet's surface. The follow-on cycles also allowed scientists to look for any changes in the surface from one year to the next. In addition, because the "look angle" of the radar was slightly different from one cycle to the next, scientists could construct three-dimensional views of the Venusian surface.

During Magellan's fourth 8-month orbital cycle at Venus from September 1992 to May 1993, the spacecraft collected data on the planet's gravity field. During this cycle, Magellan did not use its radar mapper but instead transmitted a constant radio signal to Earth. If it passed over an area of Venus with higher than normal gravity, the spacecraft would slightly speed up in its orbit. This would cause the frequency of Magellan's radio signal to change very slightly due to the Doppler effect—much like the pitch of a siren changes as an ambulance passes. Thanks to the ability of radio receivers in the NASA/JPL Deep Space Network (DSN) to measure frequencies extremely accurately, scientists were able to accumulate a detailed gravity map of Venus.

At the end of Magellan's fourth orbital cycle in May 1993, flight controllers lowered the spacecraft's orbit using a then-untried technique called aerobraking. This maneuver sent Magellan dipping into Venus's atmosphere once every orbit; the atmospheric drag on the spacecraft slowed down Magellan and lowered its orbit. After the aerobraking was completed between May 25 and August 3, 1993, Magellan's orbit then took it as close as 180 km (112 mi) from Venus and as far away as 541 km (336 mi). Magellan also circled Venus more quickly, completing an orbit once every 94 minutes. This new, more circularized orbit allowed Magellan to collect better gravity data in the higher northern and southern latitudes near the Venusian poles.

After the end of that fifth orbital cycle in April 1994, Magellan began a sixth and final orbital cycle, collecting more gravity data and conducting radar

and radio science experiments. By the end of the mission, Magellan captured high-resolution gravity data for about 95 percent of the planet's surface.

In September 1994, Magellan's orbit was lowered once more in another test called a "windmill experiment." In this test, the spacecraft's solar panels were turned to a configuration resembling the blades of a windmill, and Magellan's orbit was lowered into the thin outer reaches of Venus's dense atmosphere. Flight controllers then measured the amount of torque control required to maintain Magellan's orientation and keep it from spinning. This experiment gave scientists data on the behavior of molecules in the Venusian upper atmosphere, and lent engineers new information useful in designing spacecraft.

On October 11, 1994, Magellan's orbit was lowered a final time, causing the spacecraft to become caught in the atmosphere and plunge to the surface; contact was lost the following day. Although much of Magellan was believed to have vaporized, some sections probably hit the planet's surface intact.

5.1.1 The Magellan Spacecraft

Built partially with spare parts from other missions, the Magellan spacecraft was 4.6 m (15.4 ft) long, topped with a 3.7-m (12-ft) high-gain antenna (HGA) (see Fig. 5-1). Mated to its retrorocket and fully tanked with propellants, the spacecraft weighed a total of 3,460 kg (7,612 lb) at launch.

The HGA, used for both communication and radar imaging, was a spare from the Voyager mission to the outer planets, as were Magellan's 10-sided main structure and a set of thrusters. The command data computer system, attitude control computer, and power distribution units were spares from the Galileo mission to Jupiter. Martin Marietta Corporation was the primary subcontractor for the Magellan spacecraft, while Hughes Aircraft Company was

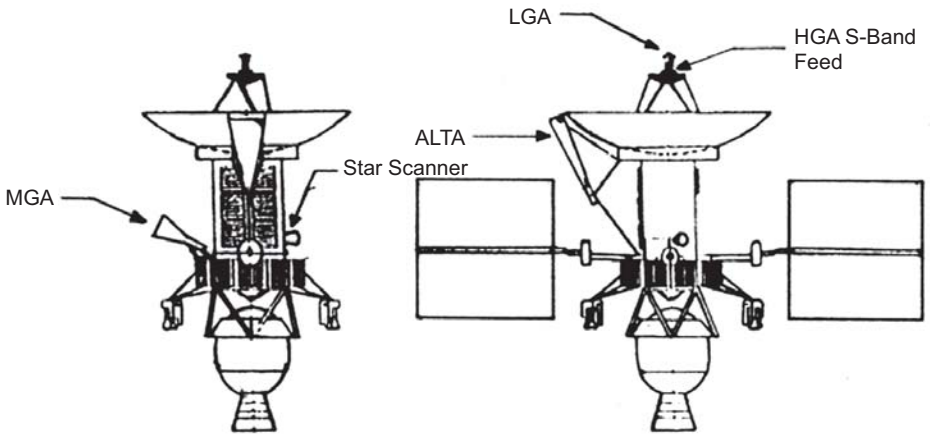

Fig. 5-1. Magellan spacecraft (ALTA = altimeter antenna, HGA = high-gain antenna, MGA = medium-gain antenna).

the primary subcontractor for the radar system. The altimeter antenna was designed and built by Hughes Aircraft Company and is described in detail in the following section.

Magellan was powered by two square solar panels, each measuring 2.5 m (8.2 ft) on a side; together they supplied 1,200 W of power. Over the course of the mission, the solar panels gradually degraded, as expected. By the end of the mission in the fall of 1994, it was necessary to manage power usage carefully to keep the spacecraft operating.

Because a dense, opaque atmosphere shrouds Venus, conventional optical cameras could not be used to image its surface. Instead, Magellan's imaging radar used bursts of microwave energy somewhat like a camera flash to illuminate the planet's surface.

Magellan's HGA sent out millions of pulses each second toward the planet; the antenna then collected the echoes returned to the spacecraft when the radar pulses bounced off the Venus surface. Because the radar pulses were not sent directly downward but rather at a slight angle to the side of the spacecraft, it was sometimes called "side-looking radar." In addition, special processing techniques were used on the radar data to result in higher resolution as if the radar had a larger antenna, or "aperture." The technique is known as synthetic aperture radar, or SAR [2].

NASA first used SAR on JPL's Seasat oceanographic satellite in 1978; it was later developed more extensively for the Spaceborne Imaging Radar (SIR) missions on the Space Shuttle in 1981, 1984, and 1994.

Besides imaging, Magellan's radar system was also used to collect altimetry data showing the elevations of various surface features. In this mode, pulses were sent directly downward (from the altimeter antenna), and Magellan measured the time required for a radar pulse to reach Venus and return in order to determine the distance between the spacecraft and the planet.

5.1.2 The High-Gain Antenna Subsystem

Magellan's HGA/low-gain antenna (LGA) was a spare from the Voyager spacecraft; it is described in detail in Chapter 3. However, the mounts for the S-band feed and the LGA were redesigned for radar and communications use. There was also some cabling redesign because of the higher power requirements for the radar [3].

In addition to transmitting 2298 megahertz (MHz) and receiving 2115 MHz, the S-band feed also needed to transmit and receive the 2385-MHz radar frequency. The polarization was linear. The S-band feed was essentially a 3.6-in. (9.1-cm) inner-diameter open-ended waveguide surrounded by an 8.8-in. diameter (22.4-cm) cup 4.05 in. (10.3 cm) deep, as shown in Fig. 5-2.

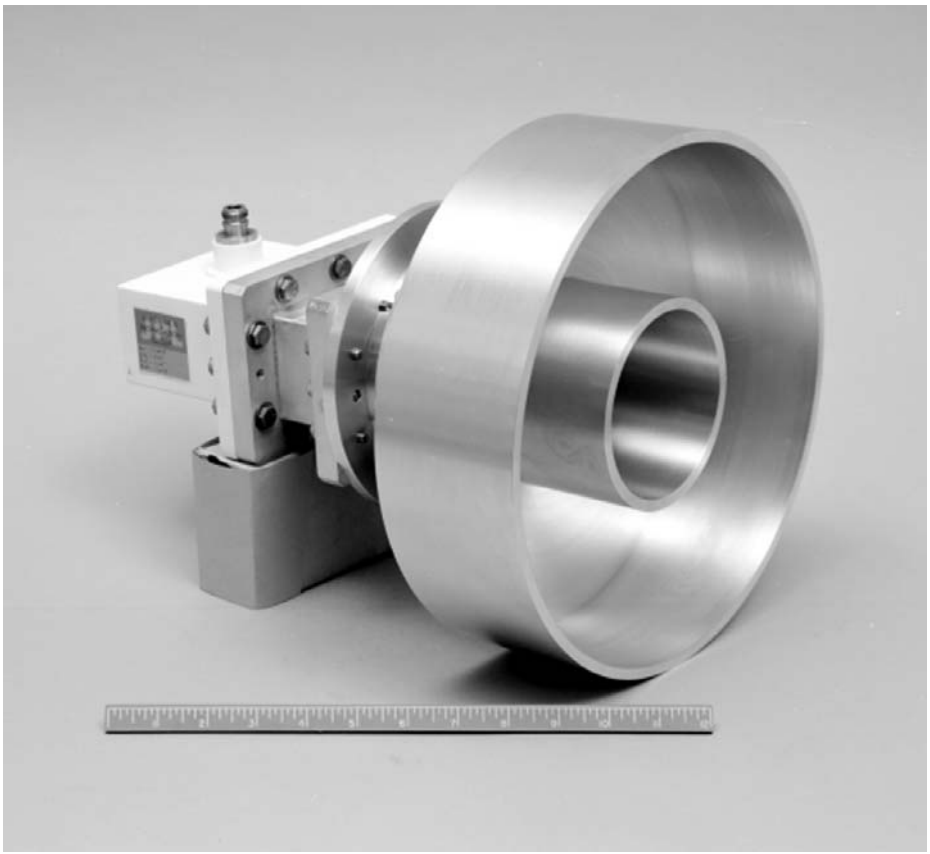

Fig. 5-2. Magellan S-band feed.

5.1.3 The Medium-Gain Antenna

The medium-gain antenna (MGA) [4] was required to transmit 2298 ±5 MHz, with a peak gain of 19.0 decibels referenced to an isotropic radiator (dBi) and receive 2116 ±5 MHz, with a peak gain of 18.5 dBi. The polarization was right-hand circular polarization (RHCP) with an axial ratio of less than 2 dB over the 3-dB beamwidth. The antenna was mounted on the spacecraft bus in the x–y plane and pointed nominally at 70 deg body cone angle and 270 deg body clock angle. It was decided to use the Mariner 9 spare MGA, which was a conical horn antenna. However, the Mariner 9 horn diameter was 14 in. (36 cm) while an approximately 18.5-in. (47-cm) diameter was required to meet the gain specification. Therefore, the Mariner 9 MGA was modified with a cone extension (see Fig. 5-3), and thereby met all the performance requirements.

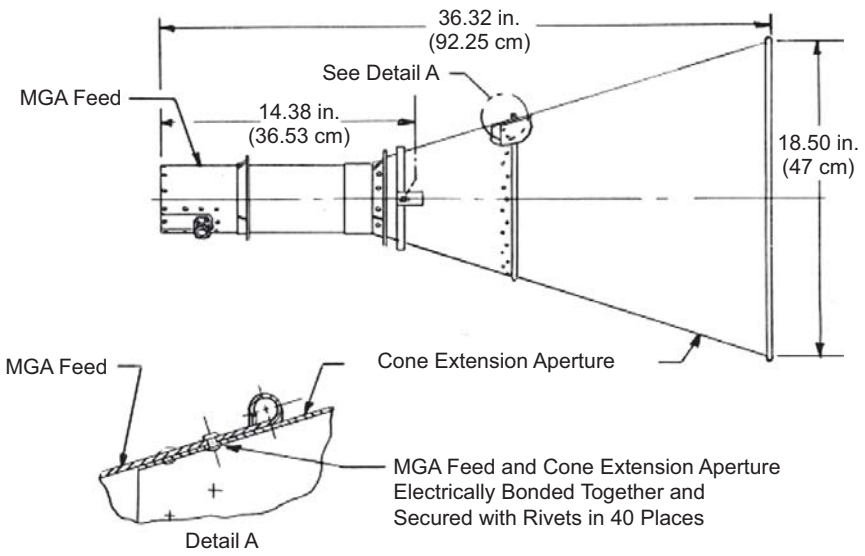

Fig. 5-3. Magellan medium-gain antenna.

5.1.4 The Magellan Altimeter Antenna

The altimeter antenna (ALTA) subsystem radiated the high-power-altimeter burst generated by the sensor subsystem transmitter. It also received the altimeter-burst echo and transmitted it to the sensor subsystem receiver [5].

The ALTA provided a peak gain of at least 18.5 dB and a 3-dB beamwidth of not less than 30 by 10 deg. The antenna was mounted alongside the HGA, as shown in Fig. 5-1. Its boresight was offset 25 deg relative to that of the HGA. The broad beamwidth of the ALTA radiation pattern was in the plane of the boresight axis of the HGA. During the sensor data collection portion of the mission, the ALTA was pointed to the approximate subsatellite point, while the HGA was looking toward the side of the planet to provide the synthetic aperture data processing capability.

The ALTA consisted of two basic elements: the horn and the waveguide transition. The horn provided the rectangular aperture that shaped the wavefront of the microwave signal and determined the directivity and beamwidths of the radiation pattern. The waveguide transition element transformed the microwave signal transmitted by a coaxial cable into a waveguide propagating waveform. It excited the waveguide in the appropriate mode to radiate a polarized signal in a plane parallel to the large dimension of the rectangular aperture. This plane contained the smallest beamwidth pattern.

The requirements for the ALTA, including expected performance, are summarized in Table 5-1. In all cases, the specified requirements were exceeded.

Table 5-1. Magellan altimeter antenna requirements summary.

Parameter	Required	Expected
Frequency	2385 MHz ±5 MHz	2385 MHz
Peak gain	18.5 dBi, absolute	19.6 dB (est losses)
Beamwidth, E-plane	10 deg min (3 dB)	11.0 deg (theoretical)
Beamwidth, H-plane	30 deg min (3 dB)	31.1 deg (theoretical)
Polarization	Linear—parallel to aperture large dimension	Linear
Cross polarization	–20 dB over 3 dB beamwidth	–24 dB (est)
Gain at 25 deg off boresight in H-plane	13 dBi max	11.5 dB (theoretical)
Input connection	TNC (female on antenna)	TNC
VSWR	1.2:1 max	1.2:1
Electrical-to-mechanical boresight error	±0.25 deg max	±0.10 deg (est)
Gain calibration error	≤0.3 dB relative, ≤0.5 dB absolute	≤0.3 dB relative, ≤0.5 dB absolute
Size	Less than 80 × 165 × 34 cm envelope	60.9 × 26.7 × 130.9 cm
Aperture cover	Not removed for flight	0.005-in. (0.01-cm) kapton with germanium coat
Power handling	320 W peak, 3.2 W average	≥4 dB above required

5.1.4.1 Electrical Design. Consideration of sidelobe levels in the E-plane of a standard horn design, particularly in an environment of potential excitation of an adjacent antenna, led to the selection of a trifurcated horn (Fig. 5-4). A trifurcated horn is one that divides the E-plane dimension of the aperture into three sections. This is done via conducting plates that convert the horn from a single large aperture to a central aperture and two adjacent radiating sections. These other sections are of the same H-plane dimensions as the central unit. The amplitude and phase of these outer radiating horn sections can be used to improve pattern shapes in the E-plane. Typically, a small percentage of the power is coupled from the input waveguide and throat geometry of the horn to the outer sections. Since in this case the "a" dimension of the horn is the same for all three-aperture illumination horn divisions, the phases for the three sections are nearly identical. A small phase difference of 6 deg was predicted in the ALTA design.

The gaps created near the throat of the horn controlled the percentage power split. The computed patterns assumed gaps that were adjusted to provide

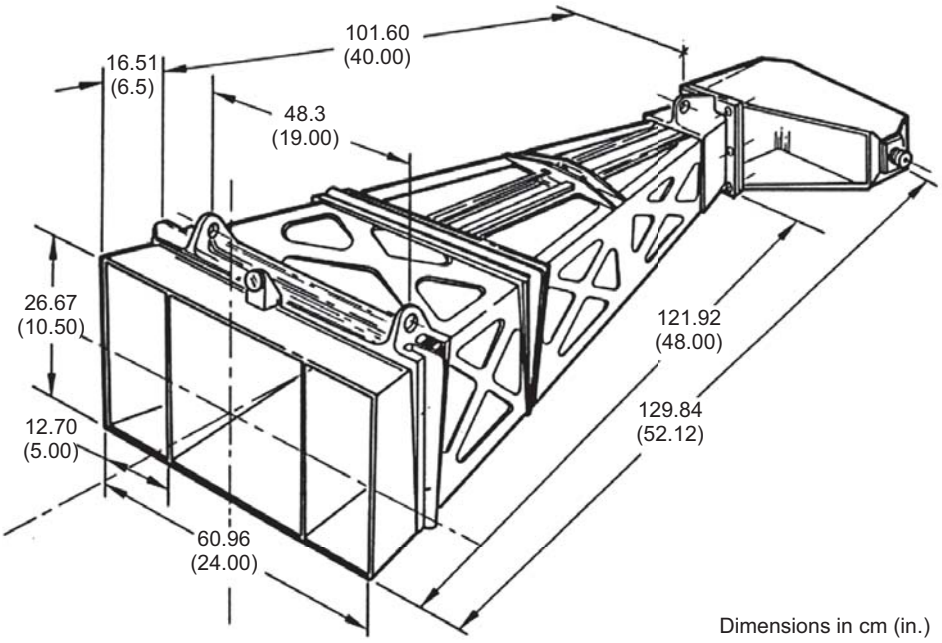

Fig. 5-4. Magellan altimeter antenna (ALTA).

both outer sections of the horn at 16 percent power, leaving 68 percent power for the center. In addition to power and phase, the relative percent of the physical aperture assigned to the outer sections could be varied to optimize antenna pattern shape and gain.

An additional advantage of the trifurcated horn, as compared to standard horns of large size and area, is structural integrity. The septa dividing the horn into three sections provides inherent means of making the horn very strong and less susceptible to motion or distortion of the large areas of the horns.

Since very low sidelobes (i.e., larger than 20 dB below the peak of the beam) are not a specification requirement of this horn, there was considerable freedom in the selection of aperture dimensions, relative power and phase distributions, and horn length.

Figure 5-4 shows the dimensions of the Magellan trifurcated horn mode, which generated the gain and radiation patterns shown in Fig. 5-5 and cited in Table 5-1.

There are two types of coaxial line to waveguide probes: (a) capacitive and (b) inductive. There are advantages and disadvantages to each. The main advantage of the inductive type, which was selected for the ALTA, is the use of a probe that is rigidly attached to the broad wall of the transition waveguide assembly. This makes the unit a very structurally strong device. Also, the

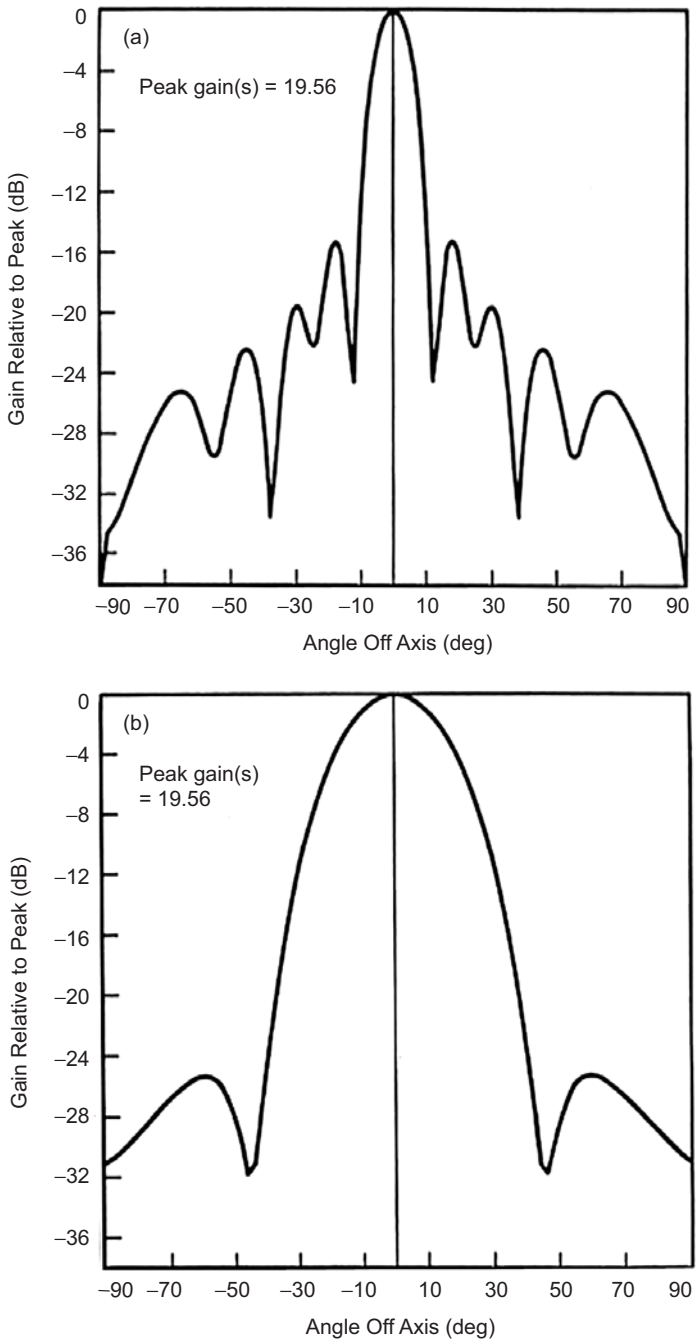

Fig. 5-5. Magellan altimeter antenna radiation patterns in (a) E-plane and (b) H-plane.

inductive probe can use physical geometries that lead to low input voltage standing wave ratio (VSWR) without need for extensive tuning screws and/or encapsulating dielectric. Thus, it is easier to design for handling high power with low probability of multipactor breakdown. To set up the proper node excitation in the waveguide requires the inductive probe to be located in the back (i.e., short circuit) wall of the transition. Since mechanically it is more desirable to place the RF connector on the side of the horn, the transition incorporates a right angle. Careful attention was given to shape the transition so no sharp edges and tuning elements would compromise its power handling.

5.1.4.2 Mechanical Design. The ALTA (shown in Fig. 5-4) consisted of three major components: horn, transition, and connector. The transition and horn were aluminum, fabricated specifically for the mission, while the connector was an off-the-shelf item.

The transition section was made of a thin-walled aluminum housing and flange. Attached to the exterior was the threaded Neill-Concelman (TNC) connector. A dielectric disk was inserted between the conductor joining the connector and the inductive probe to avoid multipacting. The probe was machined aluminum, mounted inside the transition housing.

The horn consisted of four pieces of aluminum, plate cut and machined for the walls of the horn. Machining was required for weight savings. The thinner sections were 0.030 in. (0.8 mm) thick while the stiffeners were 0.055 in. (1.4 mm) thick. There were three mounting flanges, each containing a self-aligning bearing. This bearing design was rated for 8150-lb (3705-kg) radial and 700-lb (276-kg) axial static unit loads. The two septa, which divided the horn aperture into three rectangular sections, were 0.030-in. thick (0.8-mm) aluminum plates extending 36 in. (91.4 cm) into the horn. The flange of the horn contained one of the mounting flanges and a sleeve that slipped onto the horn. All components of the horn were joined by electron beam welding or dip brazing.

The ALTA weight was specified to be less than or equal to 7 kg (15.4 lb). The machined aluminum antenna weight was 4.54 kg (10 lb).

5.2 The Galileo Antenna System

Mark S. Gatti

Planning for the Galileo mission started almost immediately after the launch of the Voyager spacecraft. Galileo's mission was to place a spacecraft in orbit around Jupiter after the successful Voyager flybys, equipped with the most advanced telecommunications system yet flown on a deep-space mission. The telecommunications system would operate at X-band with 134.4 kilobits per second (kbps) and would require the use of an HGA that was the largest flown of any deep-space mission [6]. As with Voyager, Galileo would operate

at both S- and X-band. Unlike Voyager, however, X-band would be the prime operating frequency for this mission. The telecommunications system would require an LGA for near-Earth and emergency communications. The Space Shuttle would provide the launch, while the direct-to-Jupiter interplanetary trajectory would use the Centaur upper stage. Finally, the Galileo Probe mission, carrying a payload of science instruments, was to relay its signals through the orbiter via an L-band communications system.

In the late 1970s, the typical telemetry antennas used in deep-space missions were solid reflectors ranging in size from 1 m to 3.66 ms [7]. However, due to the growing need for increased data rates, higher antenna gain was required. As a result, during the planning for the mission telecommunications system, much activity was undertaken to determine the most cost effective, reliable, deployable antenna system that could support the Galileo mission [8–10]. After some effort, the "radial-rib" antenna developed by Harris Corporation for the Tracking and Data Relay Satellite System (TDRSS) spacecraft antenna [11] was selected for development to meet Galileo mission requirements.

Between 1981 and 1985, the Galileo antenna system, consisting of the high-gain system and a coaxially mounted low-gain antenna were designed, developed, fabricated, tested, and delivered to the Galileo Project. It was at the end of this period that the Shuttle Challenger was lost during launch with all aboard. Subsequent investigation and return-to-service of the Shuttle fleet required several years, during which it was determined the Centaur upper stage did not meet safety requirements for transport aboard the Shuttle. Instead, the U.S. Air Force Inertial Upper Stage (IUS) was selected for the injection into the interplanetary trajectory between the Earth and Jupiter. As a result of the inability for the IUS to support a direct-to-Jupiter trajectory, the spacecraft would now require the assistance of the planetary gravity of both Venus and the Earth. This trajectory is depicted in Fig. 5-6. The most obvious result of this trajectory is that it required the spacecraft to fly closer to the Sun than it would on a direct trajectory to Jupiter. Many of the systems on the spacecraft had to be redesigned and/or retrofitted in order to survive in the new solar environment. The most significant redesign for the antenna system was the addition of a sunshield mounted on the tip of the central tower structure, behind which the stowed HGA would remain until it was safe to deploy. Since the HGA was designed to be no closer than 0.98 astronomical units (AU) from the Sun, it would be several years after launch before deployment. Furthermore, other Galileo systems required shade from the Sun, provided by a large sunshield below the HGA. For all of the sunshields to perform properly, the spacecraft HGA/LGA axis had to be continuously Sun-pointed. As a result, there were many times in the mission where Earth would be in the aft-facing direction of the spacecraft. In order to maintain communications during these (long)

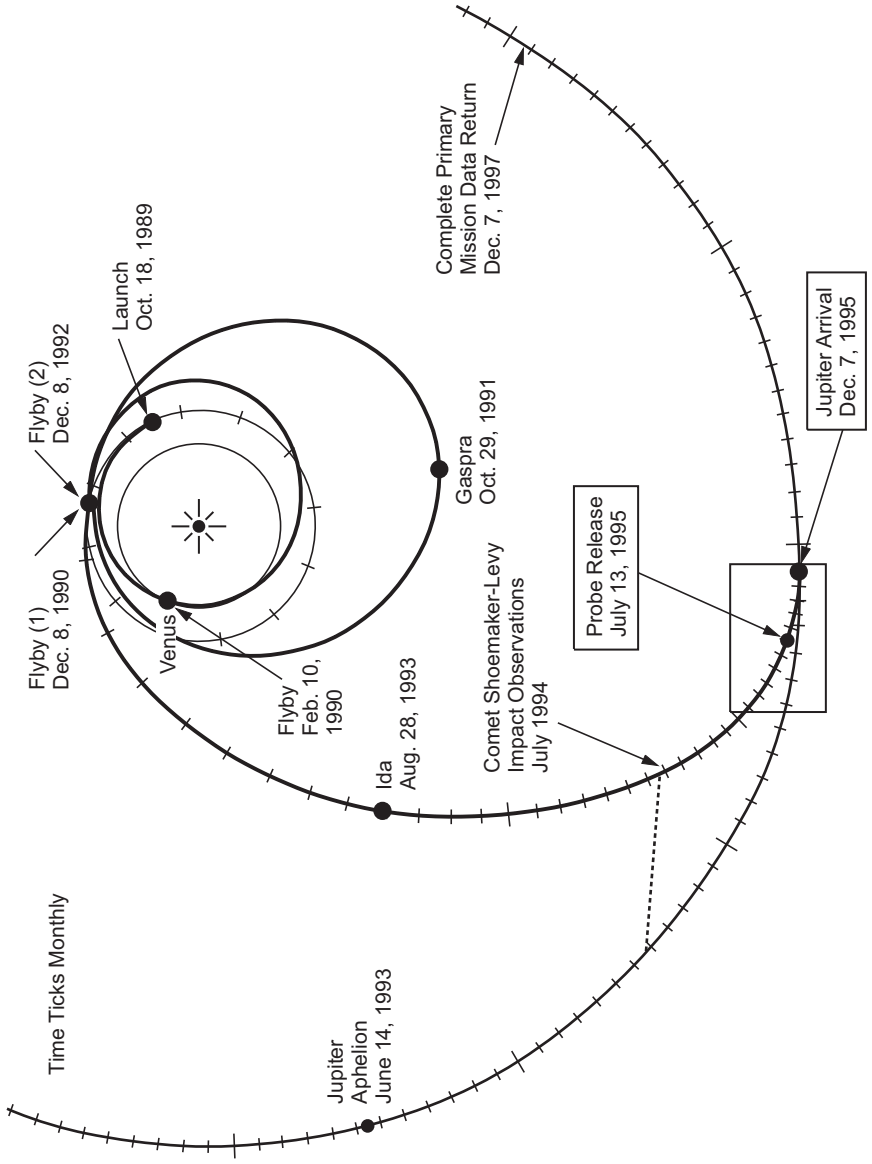

Fig. 5-6. Galileo flight trajectory.

periods, a second aft-facing LGA was added to the telecommunications system. Figure 5-7 shows the spacecraft as configured for the new trajectory that took it to Venus once and Earth twice before finally traveling to Jupiter.

This chapter describes the telecommunications antennas for the Galileo-to-Earth link. The spacecraft had an L-band antenna for relay communications to the probe. The L-band relay antenna was a 1.1-m parabolic reflector with a 21.0-dBi peak gain and a 25-deg half-power beamwidth [6]. The description of the HGA and the two LGAs are provided. Design detail, where available, is also provided. All RF measurements on the HGA that were performed in the JPL Plane-Polar Near-Field Antenna Range are also provided. The HGA was a complex mechanism. A description of its mechanics is also provided. Finally, measurement data for both low gain antennas (LGA1 and LGA2) are also provided.

On April 11, 1991 the deployment of the HGA failed. This chapter will not describe the anomaly or the subsequent investigation. Information regarding these events, as well as recovery attempts, can be found in [12–14]. The mission continued without the use of the HGA. The Galileo mission team developed techniques that utilized the LGAs [15].

5.2.1 Mission Description

The Galileo spacecraft was launched on the Space Shuttle Atlantis (STS-34) on October 18, 1989. Its mission was to conduct long-term observations of the Jovian system (Jupiter and its major moons) and included

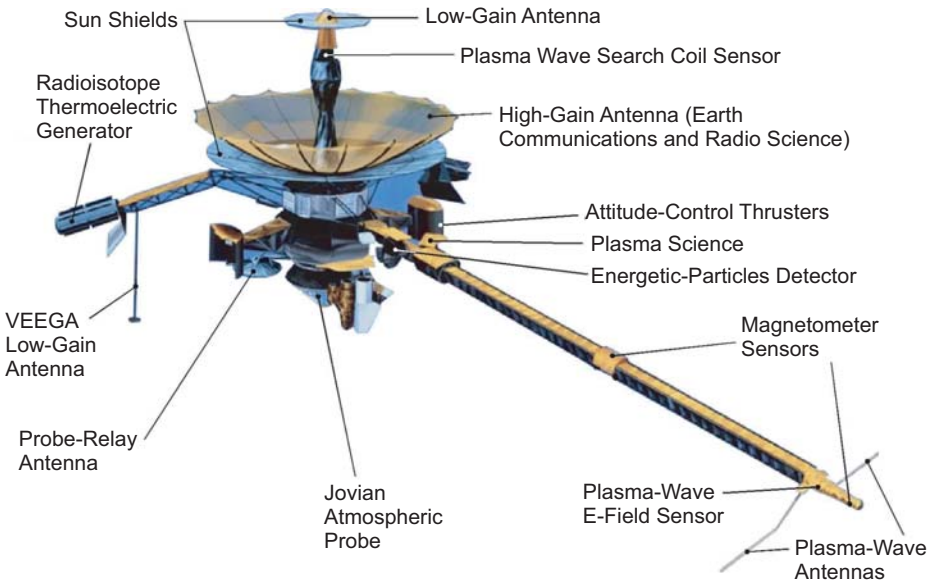

Fig. 5-7. Galileo spacecraft.

the first-ever direct measurements of the atmosphere using a descent probe. The primary mission was a 23-month, 11-orbit tour of the Jovian system, including 10 close encounters of Jupiter's natural satellites, or moons. The mission was extended three times, taking advantage of the spacecraft's durability, with 24 more orbits. The extensions made it possible to encounter all four of Jupiter's major moons: Io, Europa, Ganymede, and Callisto, as well as the small moon Amalthea.

The unique interplanetary trajectory used by the spacecraft in reaching its target is shown in Fig. 5-6. This trajectory used the gravity of both Venus and the Earth to "slingshot" the spacecraft at ever-greater velocity until finally it could begin its cruise to Jupiter. The trajectory was named Venus, Earth, Earth gravity assist (VEEGA), due to its encounters with these planets and the use of the planets' gravity. Of particular note is the duration of the cruise phase of the mission: just over six years from launch to Jupiter orbit insertion in December 1995.

Galileo observed several interesting things during its cruise: the Earth, the Moon, and mid-level clouds at Venus, all of which it mapped. Also, Galileo became the first spacecraft to encounter an asteroid when it passed within 1600 km of Gaspra on October 29, 1991, and an even larger asteroid, Ida, on August 28, 1993. Startlingly, Ida was found to have its own moon, about 1.5 km in diameter, named Dactyl, making it the first asteroid known to have a natural satellite. Finally, in March 1993, as the comet Shoemaker–Levy 9 impacted Jupiter, the Galileo spacecraft was the only observation platform with a direct view of the impact area on Jupiter's far side.

The mission carried a descent probe along with the orbiter during its interplanetary cruise. This probe weighed 339 kg and carried seven science experiments. Probe mission duration was planned for 40–75 minutes. Prior to Jupiter orbit insertion, the probe was released on a ballistic trajectory towards the planet. As the probe entered the atmosphere, and after its rapid deceleration, it deployed a parachute; then it relayed its scientific data through the L-band system on the orbiter and subsequently via the LGA1 communications system to Earth.

Figure 5-7 shows the spacecraft after deployment of the HGA. Also shown are the forward-facing and aft-facing LGAs. The HGA tip-mounted sunshield and the spacecraft bus sunshield, shown just below the HGA, provided protection from the Sun. The gross attitude stability for Galileo was provided by a spinning section of the spacecraft. However, in order to provide a stable platform for the various science instruments and cameras, a despun section was also provided. The HGA was mounted on the spin side of the spacecraft. The orbiter weighed 2223 kg and carried 12 experiments. Two radioisotope thermoelectric generators (RTG) provided spacecraft power. The telecommunications system included a 20-W S-band transmitter with a

maximum 1.2 kbps data rate and a 20-W X-band transmitter with a maximum 134-kbps data rate.

On September 21, 2003, the mission ended after the spacecraft was commanded to plunge into Jupiter's atmosphere, where it burned up after its 14-year mission. The spacecraft, mission, and scientific observations are summarized in *NASA Facts* [16].

5.2.2 Requirements

The communications requirements for the Galileo spacecraft were based on the large amount of data return expected during the mission's launch, interplanetary cruise, and orbital phases. A single antenna would not meet all of the system requirements. Therefore, the spacecraft telecommunications system consisted of three antennas: one HGA and two LGAs. Furthermore, simultaneous operation at both S-band (2115 MHz and 2295 MHz) and X-band (8415 MHz) were required. The entirety of the telecommunications antenna system, including both the HGA and the LGAs, was referred to as the S/X-band Antenna (SXA) System. This section describes all of major requirements for the Galileo SXA. The two classes of requirements described here are the functional and the design.

5.2.2.1 S-/X-Band Antenna Subsystem (SXA) Functional Requirements. The functional requirements were developed in cooperation with the spacecraft system engineer and documented in the project requirements book [17]. The basic antenna functions required were to:

- Deploy the HGA reflector after launch vehicle/spacecraft separation.
- Receive S-band signals from the DSN and conduct them to the RF subsystem (RFS) on the spacecraft).
- Transmit S-band signals from the RFS to the Tracking and Data Relay Satellite (TDRS) and to the DSN.
- Transmit X-band signals from the RFS X-band traveling-wave tube amplifier (TWTA) to the DSN.
- Receive X-band signals from the DSN and conduct them to the X/S downconverter subsystem (XSDC) on the spacecraft.

In order to meet these functions for all phases of the mission, the following equipment was required:

- HGA
- Forward-facing LGA (LGA1)
- Aft-facing LGA (LGA2)
- Transmission lines, including waveguides and associated connectors
- RF power probes located on the HGA main reflector, LGA1, and LGA2 (used for ground test)

- HGA deployment mechanism, including the rib-restraint release device with redundant non-explosive initiators, HGA deploy indicator microswitches, and motors
- HGA tip sunshield

5.2.2.1.1 RF Performance Requirements. Table 5-2 summarizes the polarization, VSWR, and gain requirements for each antenna in both transmit and receive mode. Figure 5-8 illustrates the main antenna components that provide the required functions.

5.2.2.1.2 Mass and Power. The total mass requirement of the HGA/LGA1, including the plasma wave search-coils (PWS), was 36.12 kg. Of this total, the HGA mass, including both the RF and structural components, was 32.46 kg, LGA1 and associated coaxial cable mass was 1.23 kg, and that of the PWS and its support structure was 2.43 kg. The mass of LGA2 and its transmission lines was 2.16 kg. Of that total, the LGA2 was 0.33 kg, and the transmission lines were 1.83 kg.

Prior to the Galileo mission, no other deep-space communications antenna had required input power to become operable. However, with the advent of the decision to use a deployable antenna equipped with dual redundant motors, power would be required to deploy the structure. For this antenna, the nominal voltage was 30 V (+6/–5), current was less than 0.5 amp (A) (with a maximum surge current of 1 A/s), and a nominal power was 3 W (with a 15-W maximum).

5.2.2.2 Design Requirements. The design requirements for the antenna system as derived from the functional requirements follow [18]. Derived requirements included both physical and performance parameters. Physical parameters

Table 5-2. Galileo SXA polarization, VSWR, and gain requirements summary.

Antenna	Mode	Frequency (MHz)	Polarization	VSWR	Gain (dBi)	Gain Tolerance (dBi)
HGA	Receive	2115	Linear	1.54 : 1	35.7	+0.6/-0.8
HGA	Transmit	2295	Linear	1.38 : 1	38.1	+0.6/–0.8
HGA	Receive	7167	RHCP	1.60 : 1	46.0	+0.5/–0.9
HGA	Transmit	8418	RHCP	1.20 : 1	50.1	+0.5/–0.9
HGA	Transmit	8418	LHCP	1.20 : 1	50.1	+0.5/–0.9
LGA1	Receive	2115	RHCP	1.43 : 1	6.8	+2.0/–2.4
LGA1	Transmit	2295	RHCP	1.43 : 1	7.1	+2.0/–2.4
LGA2	Receive	2115	RHCP	1.43 : 1	4.0	±1.5
LGA2	Transmit	2295	RHCP	1.43 : 1	4.5	±1.5

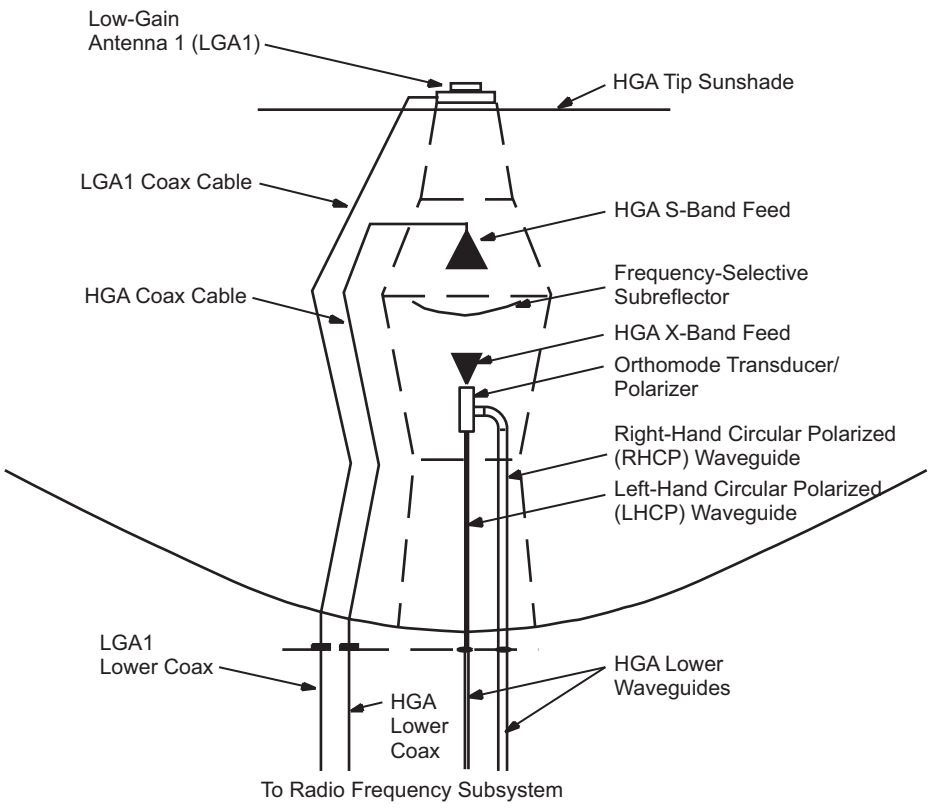

Fig. 5-8. Functional layout of the Galileo antenna system.

included the mass, optical configuration, sunshields, micrometeoroid shields, venting properties, specific connector types, and even specific dimensions such as those for reflector diameters and shapes. Performance parameters included deployment motor power, pointing requirements, power handling requirements, and the apportionment of the system gain into various components, such as the HGA and its transmission lines.

The subsystem mass summary allocations to the components that constitute the SXA are shown in Table 5-3. The antenna system engineer defined these allocations as targets to meet the total functional requirement. A summary of the S- and X-band HGA RF performance requirements is given in Table 5-4. These performance requirements are set higher so that there is margin in meeting the overall functional requirements. The system LGA1 and LGA2 RF performance requirements are given in Table 5-5. Finally, Figs. 5-9 and 5-10 illustrate the minimum required LGA gain patterns for communications to Earth for the uplink and downlink frequencies. Note that these figures represent the required gain, independent of the LGA used. As discussed in Section 5.2.7,

this requirement was met by the use of two antennas, one pointed forward (the LGA1) and the other pointed aft (the LGA2).

The antenna designs that were proposed to meet these requirements are described in the next section. The final selection of the antennas was based on meeting these requirements for all conditions.

5.2.3 High-Gain Antenna Trade-off Studies

The antenna engineering team considered many options [7,8] to meet the mission requirements for the high-data-rate phases of the mission. These

Table 5-3. Galileo SXA mass summary.

Component Description	Mass (kg)
RF Components	
HGA X-band feed	0.94
HGA S-band feed	0.36
HGA frequency selective surface	0.61
HGA S-band cable assembly	0.58
HGA X-band RHCP waveguide assembly	0.50
HGA X-band LHCP waveguide assembly	0.50
LGA1	0.40
LGA1 cable assembly	0.83
LGA2	0.33
LGA2 cable assembly	1.83
RF Component Total	**6.88**
Structural Components	
Hub assembly	6.44
Rib assembly	6.63
Surface assembly	1.80
Support structure	9.37
Thermal control	2.78
Non-RF wiring	0.39
Sunshield	0.59
Micrometeoroid shield	0.97
PWS/LGA1 support structure	1.97
PWS preamp adapter plate	0.17
PWS conduit	0.26
Optical alignment assembly	0.03
Structure Total	**31.40**
High/Low Gain Antenna Assembly Total	**38.28**

Table 5-4. Galileo high-gain RF performance requirements.

Frequency (MHz)	2295 ±5	2115 ±5	8418 ±23
Polarization	Linear	Linear	RHCP, LHCP
Gain (dBi)	37.6	36.4	50.1
3-dB beamwidth (deg)	>1.8	>2.0	>0.45
10-dB beamwidth (deg)	>3.1	>3.4	>0.75
First sidelobe location (deg from peak)	>3.0	>3.2	>0.70
First sidelobe level (dB)	>15	>15	>14
Axial ratio (on axis to –3 dB level, dB)	n/a	n/a	1.5
Axial ratio (–3 dB level to –10 dB level, dB)	n/a	n/a	3.0
Cross-polarized component (dB)	>20	>20	n/a
VSWR	1.38:1	1.54:1	1.2:1
Power handling (W, CW)	120	n/a	100
Isolation (between polarizations, dB)	n/a	n/a	18
RF axis alignment (to mechanical boresight, deg)	0.03	0.03	0.03
System mode of operation	Transmit	Receive	Transmit

considerations included a review of what had been previously flown on JPL/NASA missions, what was currently available from industry, and what could be developed to meet the requirements. The three options at the forefront of consideration, one classical and two deployable, for the HGA are described below.

5.2.3.1 Solid Fixed-Size Reflectors: The Voyager Design/Spare. The use of spare antennas from the Voyager Project was initially considered for the mission. Since Galileo planned on a Space Shuttle launch, a maximum volume was defined that could (barely) be met by Voyager's 3.6-m antenna. Nevertheless, because there were spare Voyager Project HGAs in storage, this option seemed a reasonable way to economically meet requirements. However, in the early stages of project planning, the desired data rate was increased such that it became apparent that an antenna of somewhat larger diameter would be required, eliminating the Voyager option as a solution. (Voyager's spare antenna remained in storage until used by the Magellan mission to Venus years later.)

5.2.3.2 Deployable Antennas: Lockheed Wrap-Rib and the TDRSS Antennas. Since a 3.6-m antenna was the largest antenna that could be fit into the Shuttle cargo bay, it became apparent that some technology for a deployable

Table 5-5. Galileo LGA system RF performance requirements.

	LGA1		LGA2	
Frequency (MHz)	2295 ±5	2115 ±5	2295 ±5	2115 ±5
Polarization	RHCP	RHCP	RHCP	RHCP
Gain (dBi)	7.1	7.1	4.5†	4.0†
3-dB beamwidth (deg)	>45	>36	>40, <60	>35, <50
10-db beamwidth (deg)	>65	>70	n/a	n/a
Axial ratio (boresight, dB)	2.0	2.0	<8	<10
Axial ratio (45 deg off boresight, dB)	n/a	n/a	<4	<6
Axial ratio (90 deg off boresight, dB)	11	6	<17	<20
VSWR	1.43:1	1.43:1	1.4:1	1.4:1
Power handling (W, CW)	120	n/a	120	n/a
RF axis alignment (to mechanical boresight, deg)	1.0	1.0	1.0	1.0
System mode of operation	Transmit	Receive	Transmit	Receive

† Measured at the peak of the gain curve, not coincident with mechanical boresight

antenna would be required. During the early phases of the project, two candidate technologies being developed by industry were investigated. First was a design proposed by Lockheed Space Systems that consisted of a set of flexible ribs that supported a mesh surface and that were wrapped about and constrained to a central hub. The stored energy of the ribs provided for the deployment of the reflector system. Deployment of this antenna would occur in a matter of seconds once the constraint system was released. The second design under consideration was that being developed by Harris Corporation for the orbital element of TDRSS. It consisted of a set of stiff graphite ribs supporting a mesh surface. The deployment of this system required several minutes and is best described as opening much like an umbrella. After careful consideration, the TDRSS configuration was selected and detail design of RF components started.

5.2.4 Post-Challenger Modifications

After the Shuttle Challenger accident, the passage to Jupiter was modified. The new trajectory would require the spacecraft to fly closer to the Sun than originally planned. Whereas the original design margin allowed solar flux at 0.98 AU, the new route was to fly close to Venus. As a result, several hardware modifications and operational changes were required. Operationally, it was determined that the HGA would remain stowed and shielded from the Sun

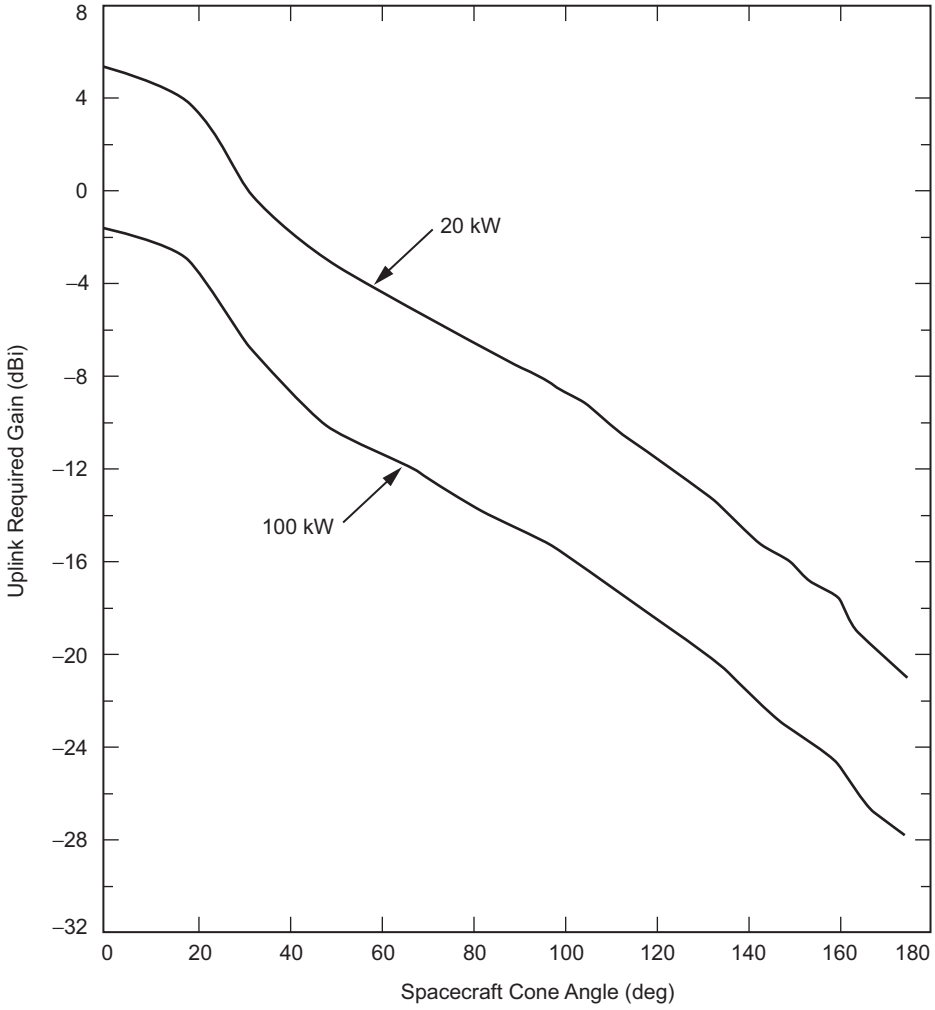

Fig. 5-9. Galileo LGA minimum required gain vs. cone angle, 2115 MHz.

behind a new sunshield placed at the tip of the antenna. In this configuration, the spacecraft could remain Sun-pointed, thus protecting the HGA behind the sunshield. However, the single LGA (LGA1) that was planned to support the mission, and which was already mounted to the HGA, could not support Earth coverage because of the need to have it continuously Sun-pointed. In other words, there would be times in the early phases of the mission that Earth would be in the back lobes of LGA1. The total gain requirement (as illustrated in Figs. 5-9 and 5-10 could not be met by the LGA1 alone. It was determined that a second LGA would be required. Furthermore, this LGA2, pointing in the aft-direction, would require a gain pattern that was peaked at some angle off its

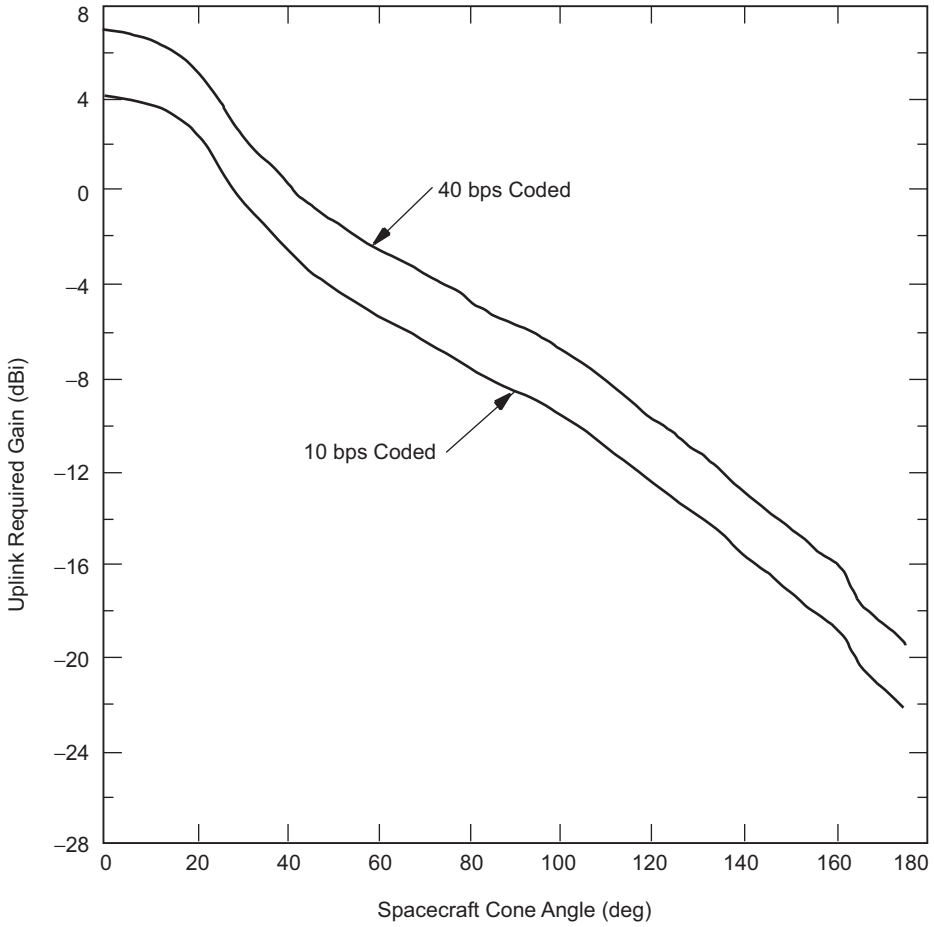

Fig. 5-10. Galileo LGA minimum required gain vs. cone angle, 2295 MHz.

mechanical boresight in order to meet the total system gain requirement. A design effort was undertaken to meet the new requirements.

5.2.4.1 Tip Sunshield. A basic requirement for the tip sunshield was to be transparent to the radio signals sent to and from the HGA. This suggested a nonconductive dielectric material. However, electrostatic discharge (ESD) requirements for spacecraft hardware included a path for charged particles to reach the electrical bus ground. These seemingly conflicting requirements were met because the discharge path was allowed to be through a fairly large resistance, including a dielectric material acceptable to the antenna designers. The sunshield for this function consisted of a carbon-coated Kapton. The material was stretched between a set of radial spokes. made of invar, a

conductive nickel-iron alloy. The shade mounting was designed to fit to the tower structure, using the LGA1 mounting holes, after which LGA1 was mounted to the sunshield. The vibration environment that the tip of the HGA would be exposed to during the Shuttle launch was to exceed 50 g. As a result, it was essential that the total mass be limited. The entire structure and shade material had a total mass of 0.6 kg. The sunshield that provided shelter for the HGA is shown in Fig. 5-11. The picture shows the sag in the sunshield due to gravity. In flight, this sunshield assumes a flat shape. RF measurements of the sunshield showed negligible gain loss [19]. Furthermore, the effect to the LGA1 patterns was also negligible.

5.2.4.2 Aft-Facing Low-Gain Antenna. The new, aft-facing (LGA2) antenna was used during the early mission stages. LGA requirements, shown in Section 5.2.2, included all cone angles for both the uplink and downlink frequencies. Even though the required gain in the region from 90 to 180 deg was low, it was not insignificant. However, it was important that all areas of this curve be met. The design selected is described in Section 5.2.7. Section 5.2.7.3 illustrates the total gain versus the requirements.

Fig. 5-11. Galileo tip sunshield being tested on the lateral vibration fixture.

5.2.5 High-Gain Antenna Design Selected

Armed with the knowledge gained from the industry surveys, the project decided that a selection of the HGA system could be made based on engineering criteria. As mentioned earlier, the Harris Corporation radial-rib design was chosen to meet the Galileo antenna system requirements.

5.2.5.1 High-Level Overview. One of the basic considerations in selecting not only the HGA, but also the feeds and other microwave components, was hardware heritage, or having been flown on previous missions. The initial design for the Galileo SXA was based on that of TDRSS antennas, which had recently been developed for TRW, Inc. However, due to the difference in frequencies from the TDRSS mission, the feeds had to be changed. Furthermore, the optics had to be designed to allow for simultaneous S/X band operation. The successful Voyager mission had just flown, and during its development, an X-band feed and polarizer had been designed. By leveraging the Voyager antenna design, both the cost and the RF performance risk of the Galileo antenna was reduced.

Figs. 5-12, 5-13, and 5-14 illustrate the salient features of the Galileo HGA and LGA1, discussed below, in top-down order. (Missing from these figures is the sunshield added to the structure as a result of the redesign for the VEEGA trajectory). The RF components are all located in the tower structure. LGA1 is atop the plasma wave search-coil support structure. The S-band feed is at the prime focal point of the main reflector, looking downward through the frequency selective subreflector (FSS). The X-band feed is connected to a dual polarization orthomode transducer (OMT). When the antenna is deployed, the graphite ribs support a surface of gold-plated wire mesh that is connected to a set of stand-offs and ties that hold it in the desired shape. The mesh, which is a 0.0013-in. (0.03-mm) gold-plated molybdenum wire, woven into a tricot fabric is discussed in Chapter 1. This weave is exactly the same as that used for nylon stockings, but with a very loose 10 holes per inch (4 holes/cm) weave. The optics design of the fully deployed system is that of a dual-shaped Cassegrain X-band system and a focal feed S-band system.

The mechanical system included the eighteen ribs, the tip restraint used to circumferentially constrain the stowed ribs during launch, the central release mechanism and upper structure, the radome, the truss supports, the hub assembly, the hub carrier, and the dual-drive motors. Deployment was accomplished by the hub being moved upwards by a motor and ballscrew combination, and the deflection of the ribs that are pinned to the hub at the pivot point. The method was very much like opening an umbrella.

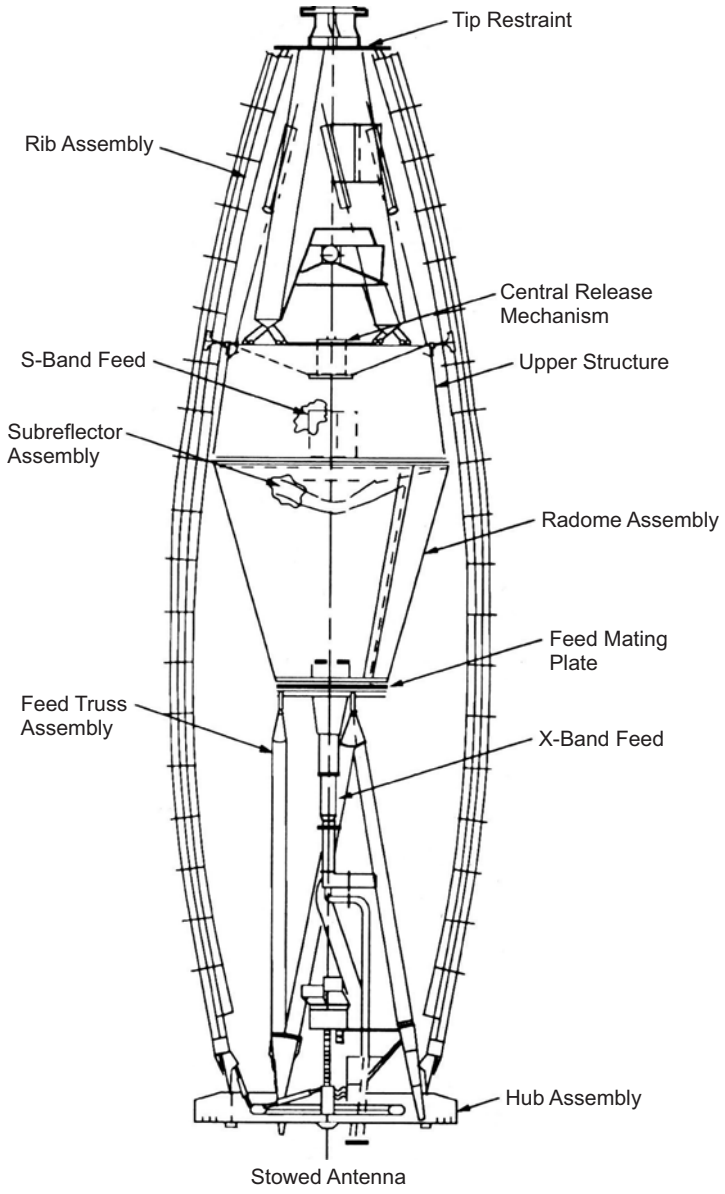

Fig. 5-12. Galileo HGA stowed configuration.

5.2.5.2 Mechanical Mechanisms and Structural Components. Although this chapter focuses on the RF and electrical characteristics and design of the Galileo SXA, a brief overview of the mechanical and structural system is useful. At the time of development, this antenna design was clearly the most mechanically complex device flown for deep-space science missions. The

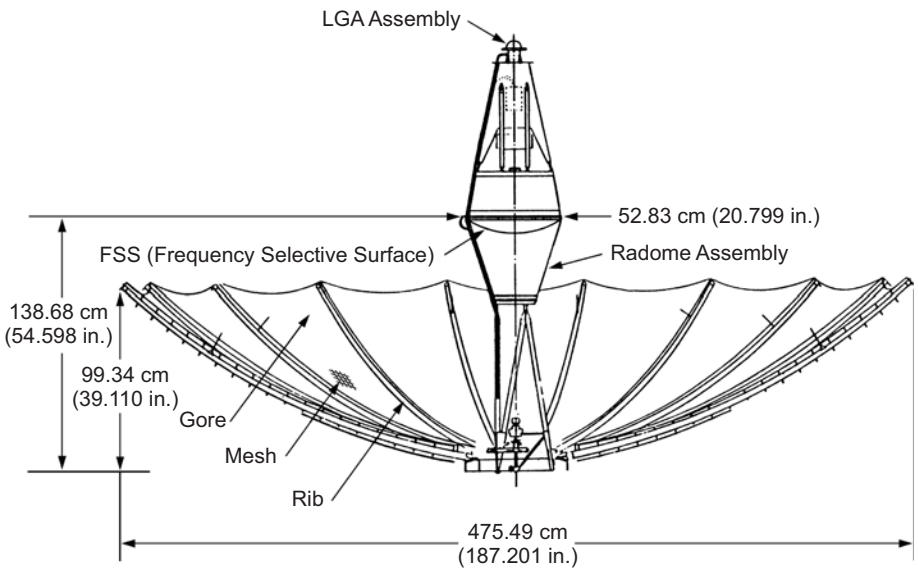

Fig. 5-13. Galileo HGA deployed configuration.

fundamental purpose for the antenna was to act as an RF device to capture RF energy, route it to a focal point and further to the receivers, or vice versa, from the transmitters to the antennas. Nevertheless, because it fit into the Shuttle bay, the Harris design was a mechanical marvel for its time. An excellent description of the mechanical system can be found in the literature on the TDRSS antenna [11].

Construction. The construction of the antenna system differed in several areas from that of the TDRSS antenna. Notwithstanding these differences, the construction of the antenna followed the same process as the many previous TDRSS antennas. The system included 18 carbon fiber ribs curved in approximately the required shape. The gold-wire mesh was supported along the radius of the ribs by a series of stand-offs. Between ribs, a set of circumferential cords at different radial distances was strung below the mesh surface and tied with short wires to the surface of the mesh, forming the required final surface shape.

Non-HGA structure: plasma-wave search-coils. The feed tower was required to support the plasma-wave search-coils (PWS). To accomplish this, a fiberglass A-frame structure was mounted on the subreflector support cone. The other significant changes to the TDRSS design were constrained to the deployment system, and are described below.

Deployment system. By its very nature, a deployable antenna requires a system to bring it to its final state. For the Galileo SXA, the deployment system included the motors required to turn a ballscrew, which in turn moved upward a carrier connected to the ends of 18 ribs. As the carrier moved upwards, the ribs,

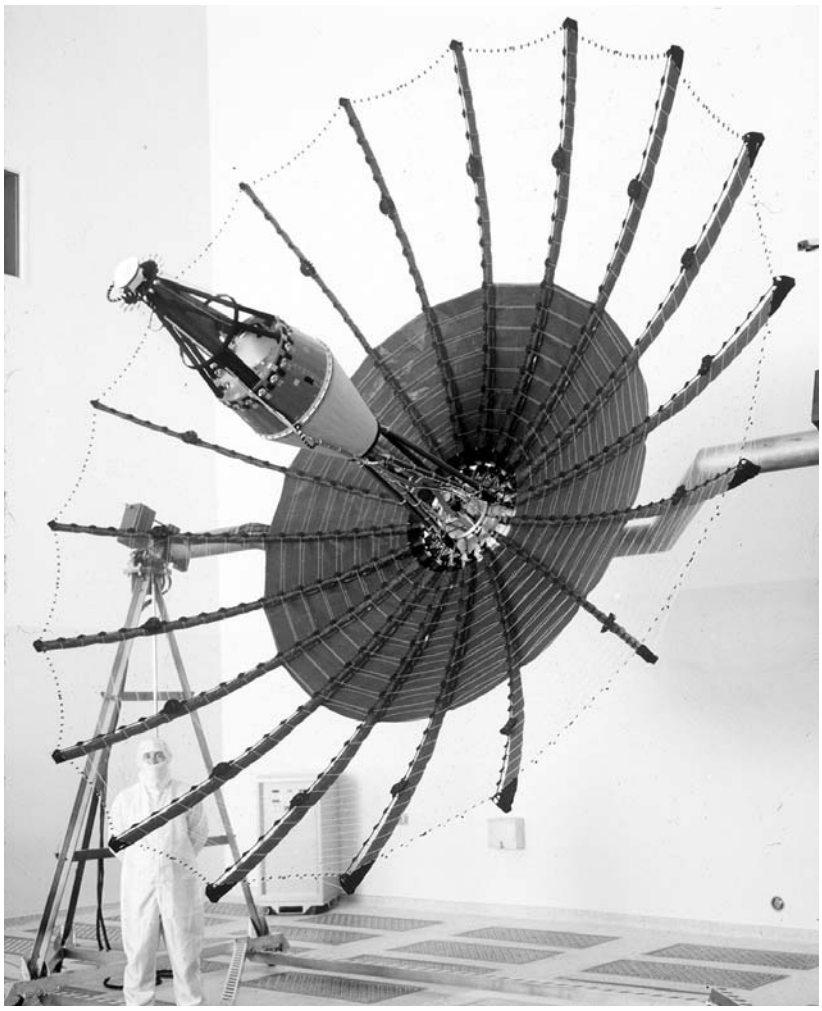

Fig. 5-14. Galileo antenna deployed on its ground handling fixture.

which were pinned several inches above the carrier at a fulcrum point, began to rotate outward, deploying the antenna and forming the surface of the reflector. The deployment system also included a mechanism that held the ribs close and tight to the structure in order to withstand the high vibration loads experienced during the launch phase. Finally, because of the addition of the PWS and LGA1 support structure, an anti-snag system was added at the outermost tip, or maximum diameter, of the antenna. A brief description of each of the major elements of the deployment system follows.

Redundant dual-drive motors. The motors used to deploy the Galileo SXA were different than those of the TDRSS system. They were developed at

JPL, specifically to be used in flight missions where high reliability, high torque, and total redundancy were required. The dual-drive motors used included two motors, each of which was connected to the rotating ballscrew. The torque delivered was to be adequate to tear mesh in the event of a mesh snag.

Central release mechanism. Another part of the deployment system that differed from that of TDRSS was the device that held the 18 ribs tightly to the central tower for the launch phase. This device was called the central release mechanism (CRM); it held 18 wires that were connected to each rib of the antenna. The end of each wire was fitted with a swage ball, which fit into the CRM and was held in place until released. The release occurred when a nonexplosive initiator, or burn wire, was activated. (The ultimate nondeployment of the system was traced to the sticking of several ribs to the central tower structure after the nonexplosive initiator released all 18 ribs. See [13,14] on the deployment anomaly.)

Anti-snag system. During the testing of the SXA, it was found that an occasional snag of mesh would occur at the tip of the stowed antenna after launch-load lateral vibration. Accordingly, part of a panel of mesh was added that followed the back of the rib from the tip, down several inches. This cocoon of mesh prohibited the mesh from becoming entangled with either the LGA1 support structure or the tip of the ribs. After installation, no further snags of this nature occurred in test.

5.2.6 Radio Frequency System—High-Gain Antenna

5.2.6.1 HGA Optics. Shaping a reflector system optimizes for the highest frequency of operation and, in the case of Galileo, was done to maximize the gain. Thus, the aperture distribution was very nearly uniform across the face of the deployed dish, with a very sharp fall-off of power at the edges of the dish. The S-band feed, located at the primary focal point of the dish illuminated the reflector by viewing it through the shaped subreflector. The main reflector was shaped by the use of 18 rows of circumferential cords stretching from rib to rib on the back side of the ribs and connecting to the surface of the mesh using ties that were individually set to hold the mesh in its prescribed shape. The importance of this shaping system cannot be overstated. While the project was investigating methods to eliminate these cords as potential snags for antenna deployment, an analysis was done [20] to determine the gain loss. With all the cords removed, the X-band loss would be approximately 5.4 dB while the S-band loss would be approximately 0.5 dB. Alternatively, removing only the outermost four rows of cords would cause a loss of approximately 1 dB [21]. Ultimately, this loss in gain was deemed unacceptable, and the antenna was not modified.

The optics configuration is summarized in Fig. 5-15. The positions of the feed horns with respect to the vertex of the reflector are provided. The surface of the main reflector is defined by a sixth-order polynomial. The coefficients of this polynomial are given in Table 5-6.

5.2.6.2 S-Band. The S-band feed is shown in Figs. 5-16 and 5-17. This feed was an E-plane sectoral horn, and it received and transmitted only linearly

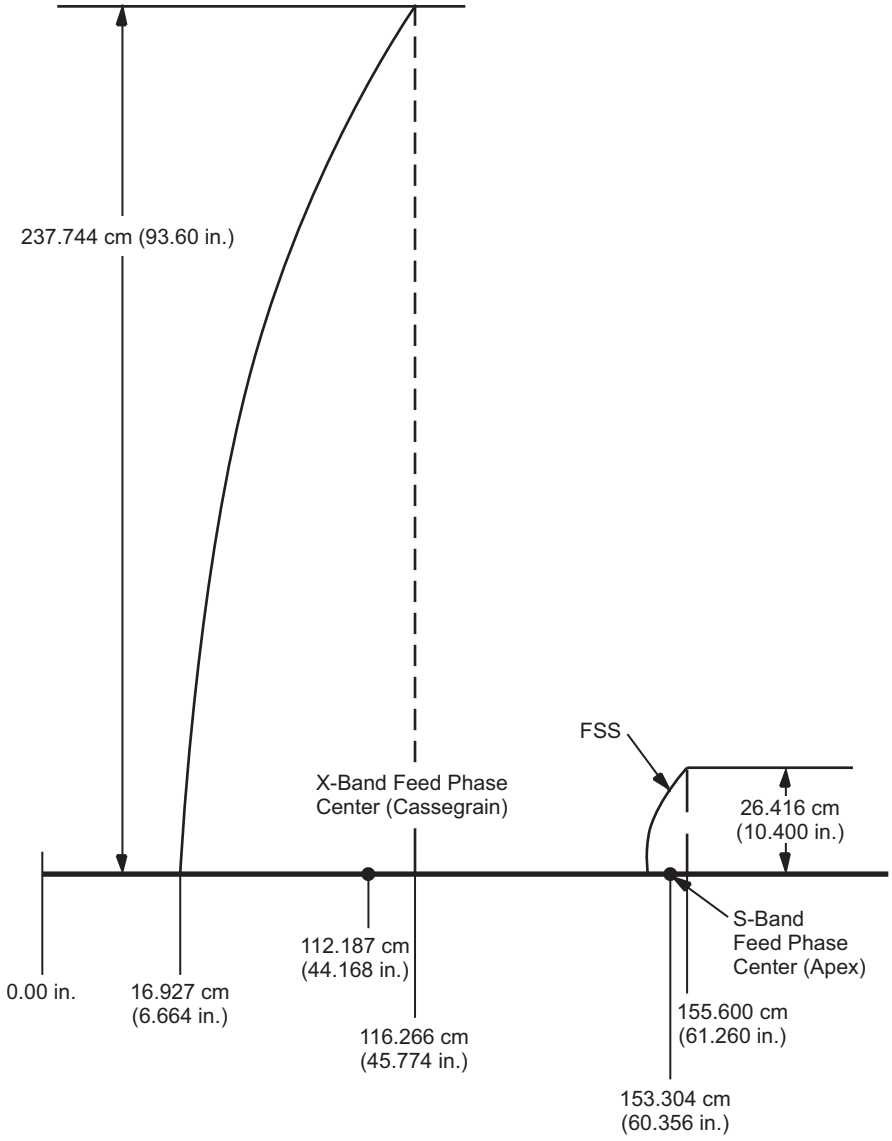

Fig. 5-15. Galileo optics configuration.

Table 5-6. Equation and coefficients defining shape of the Galileo HGA main reflector.

Coefficient	Value
6	$0.134268864 \times 10^{-10}$
5	$-0.410523382 \times 10^{-8}$
4	$0.455319128 \times 10^{-6}$
3	$-0.24178805 \times 10^{-4}$
2	$0.522080064 \times 10^{-2}$
1	$-0.21984271 \times 10^{-2}$
0	5.583933584

$$F(x) = A_6x^6 + A_5x^5 + A_4x^4 + A_3x^3 + A_2x^2 + A_1x + A_0$$

polarized energy. Note that the horn flared out in only one dimension. This feedhorn was designed to have 37.3 dBi gain at 2115 MHz, 38.1 dBi gain at 2295 MHz, and to be symmetric in the two orthogonal planes. During the design and breadboard phase of the project, it was determined that there was a resonance in the tower structure between the X-band feed and the upper support structure. The presence of the FSS radically changed this resonance at 2295 MHz but had little effect at 2115 MHz. Two shorting plates were fabricated, one to electrically tune the depth of the upper structure around the S-band horn, and the other to electrically match out the center blockage reflections. Figure 5-18 illustrates the configuration of the tuning plates. The precise location of these plates was determined empirically by measuring the system gain as a function of the separation of the plates and the location with respect to the feedhorns. The radiation patterns of this feed in the final configuration, including tuning plates, are shown in Fig. 5-19.

Given the feed and its associated radiation patterns, the performance of the system was measured in a near-field facility constructed specifically for this project [22,23]. The project chose this path for antenna characterization based on the recent advances in near-field calibration techniques at the U.S. National Institute of Standards and Technology (NIST) and at JPL [24,25]. The measured far-field radiation patterns were measured at both the uplink (2115 MHz) and downlink (2295 MHz) frequencies. Figure 5-20 shows the results of these measurements [26].

5.2.6.3 X-Band. The X-band feed design was inherited directly from Voyager. Known as a Potter horn, it was smooth walled, with a launching section that ultimately resulted in a fairly narrow-banded feed that provided very symmetric patterns in any two orthogonal cuts. See Chapter 3 of this book for a detailed description. Note, however, that because of the difference in the ratio of the

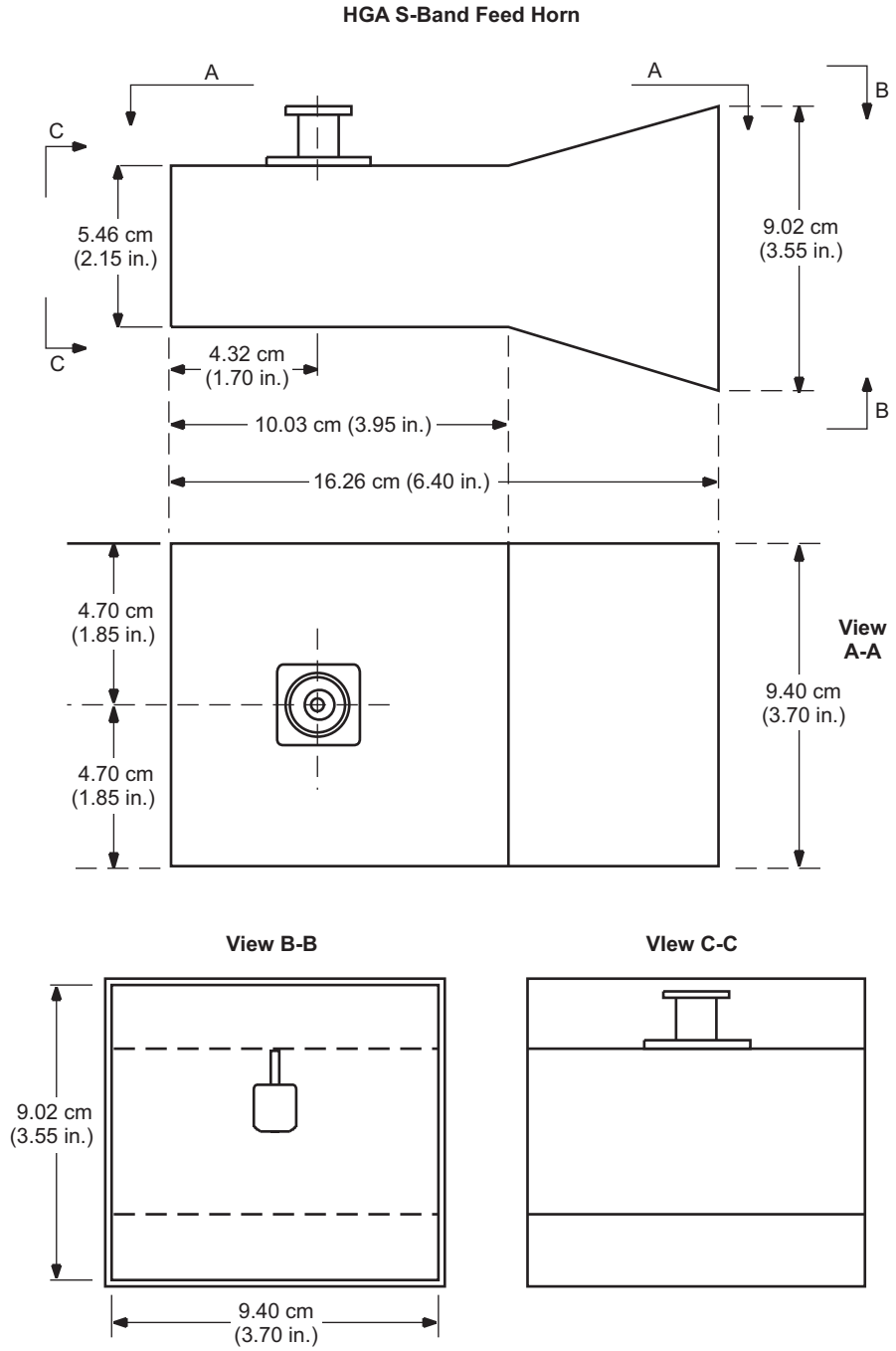

Fig. 5-16. Galileo S-band feed showing three views of the sectoral horn.

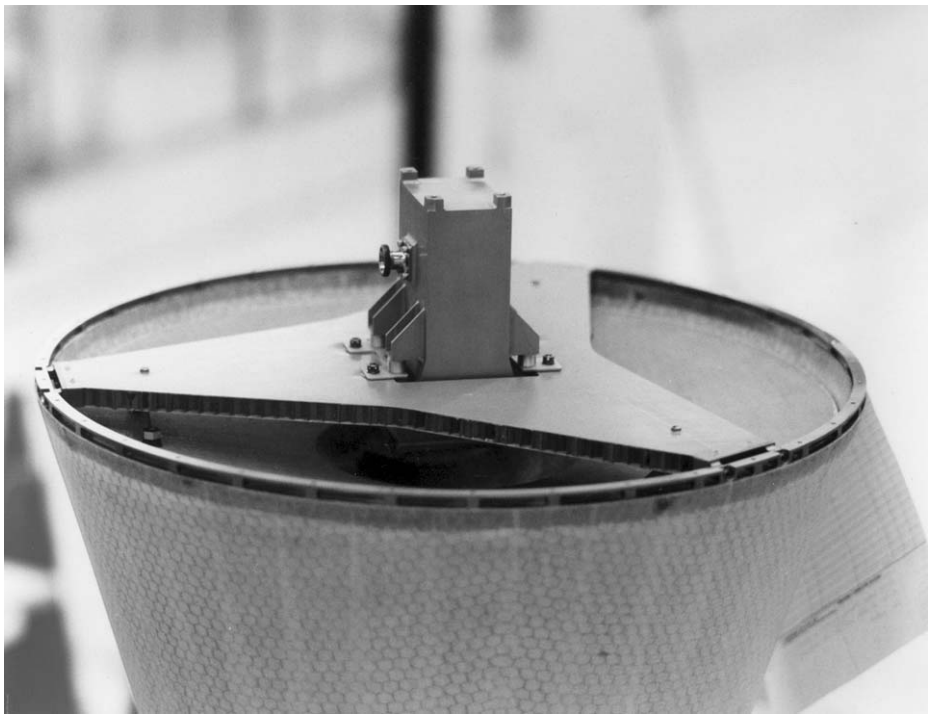

Fig. 5-17. Galileo S-band feed mounted on the top of the radome.

focal length to diameter of the main reflector (f/d), the edge taper had to be different than that of the Voyager feed. This was easily accomplished by using a feed with lower gain. Thus, the Galileo feed, while being *exactly* the same as the Voyager feed from the dual-polarized orthomode transducer and through the phasing section, was shorter by several inches to provide the wider pattern necessary for the different reflector. The radiation patterns of this feed are shown in Fig. 5-21, and the resulting far-field patterns are given in Fig. 5-22.

5.2.6.4 Frequency Selective Subreflector. An FSS was used to enable dual-frequency response to both X- and S-band. It consisted of a series of crossed dipoles that were resonant at the frequencies of interest. In this case, the FSS was invisible to S-band radiation but looked like a solid reflector at X-band. The subreflector was a dual-surfaced fiberglass and NOMEX honeycomb material with copper etched into the surface for the dipoles. During development tests, the X-band gain was measured alternatively with the FSS and with a solid subreflector. The gain loss due to this FSS at X-band was approximately 0.24 dB. This reflector is shown in Fig. 5-23.

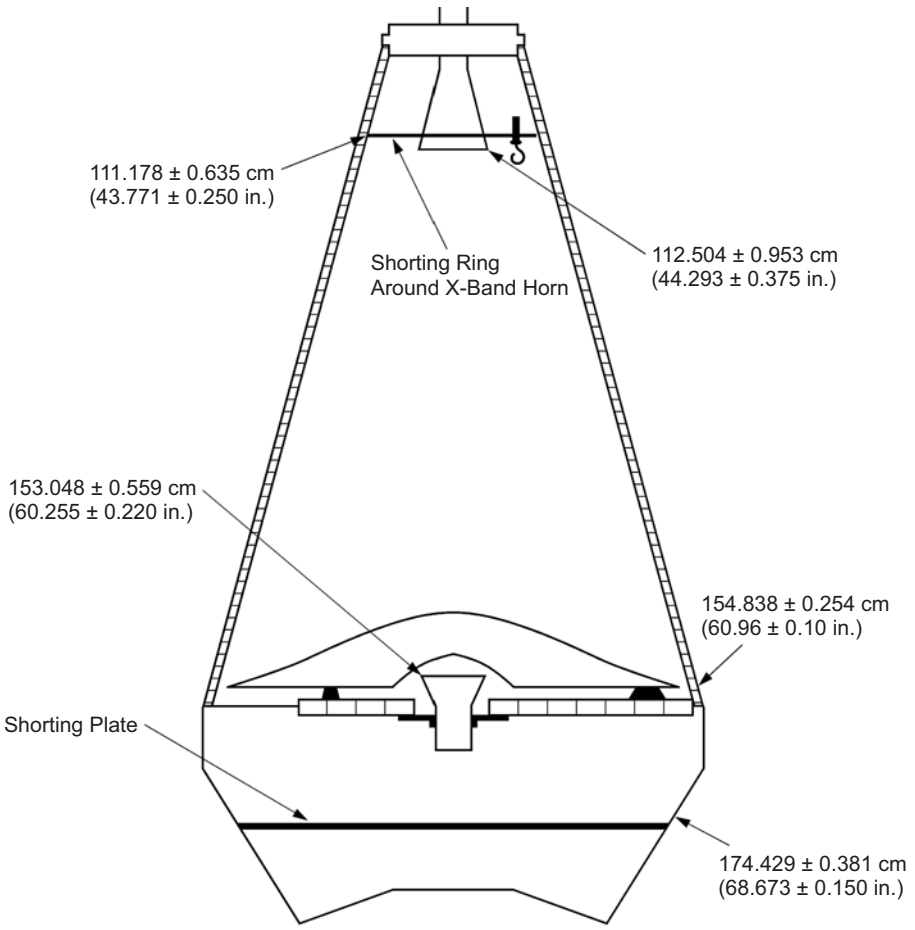

Fig. 5-18. Configuration of the tuning plates in the Galileo upper structure and radome.

5.2.7 Low-Gain Antenna System

The LGA requirements were set such that a communications link could be maintained during all phases of the mission. The original requirements for this mission were for coverage only in the forward direction, which was in the same direction as the main beam of the HGA. When the trajectory was changed later in the mission, the requirements were changed; and, as a result, coverage in both forward and aft directions was included. After much investigation, an LGA system consisting of two antennas was selected. This section describes the design of the two different LGAs and compares their performance to the system requirements.

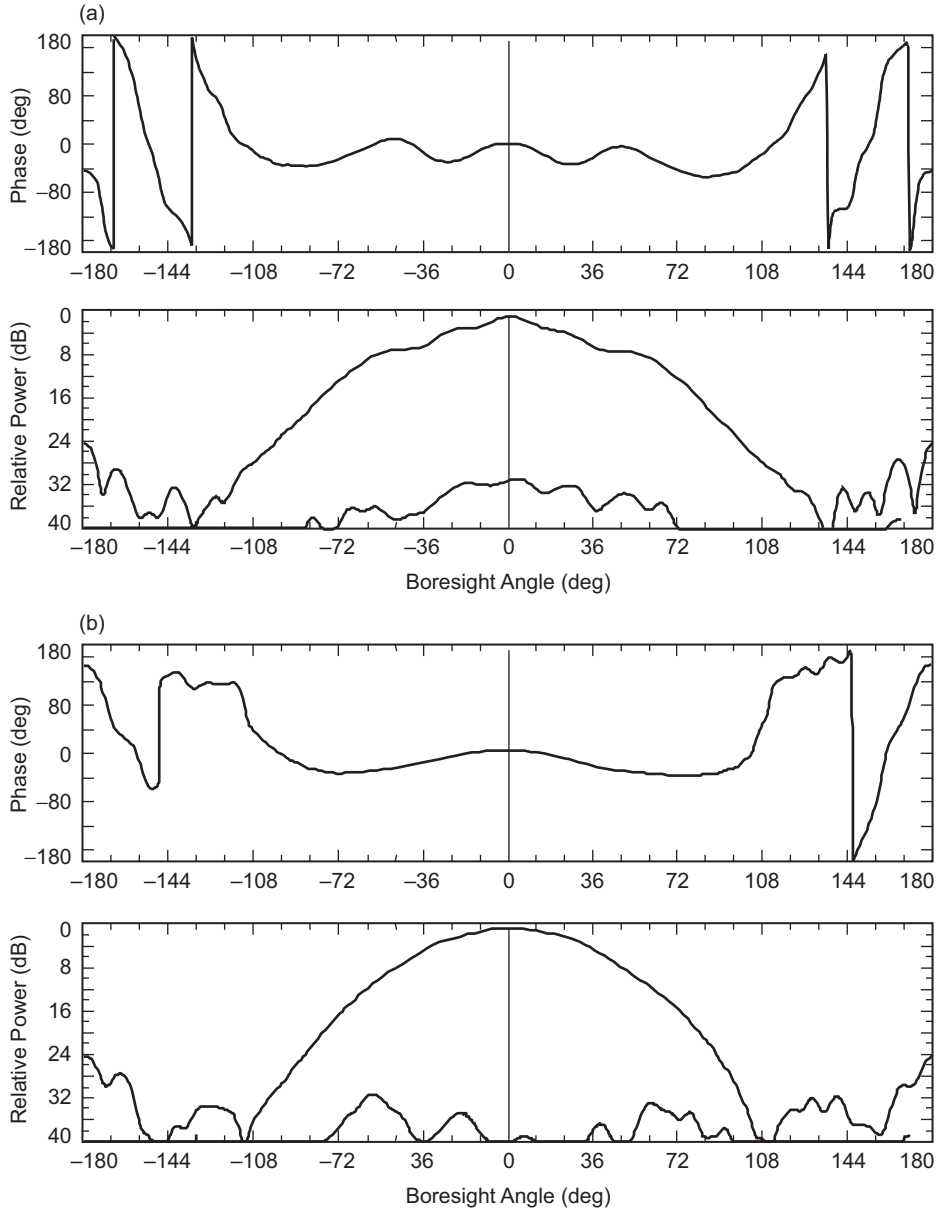

Fig. 5-19. Galileo S-band feed pattern cuts, f = 2295 MHz, for (a) E-plane and (b) H-plane.

5.2.7.1 LGA1 (Forward Facing) RF Design. The LGA1 for the Galileo spacecraft was also inherited directly from the Voyager LGA as shown in Chapter 3. The LGA1 was simply a build-to-print of the Voyager LGA. Its

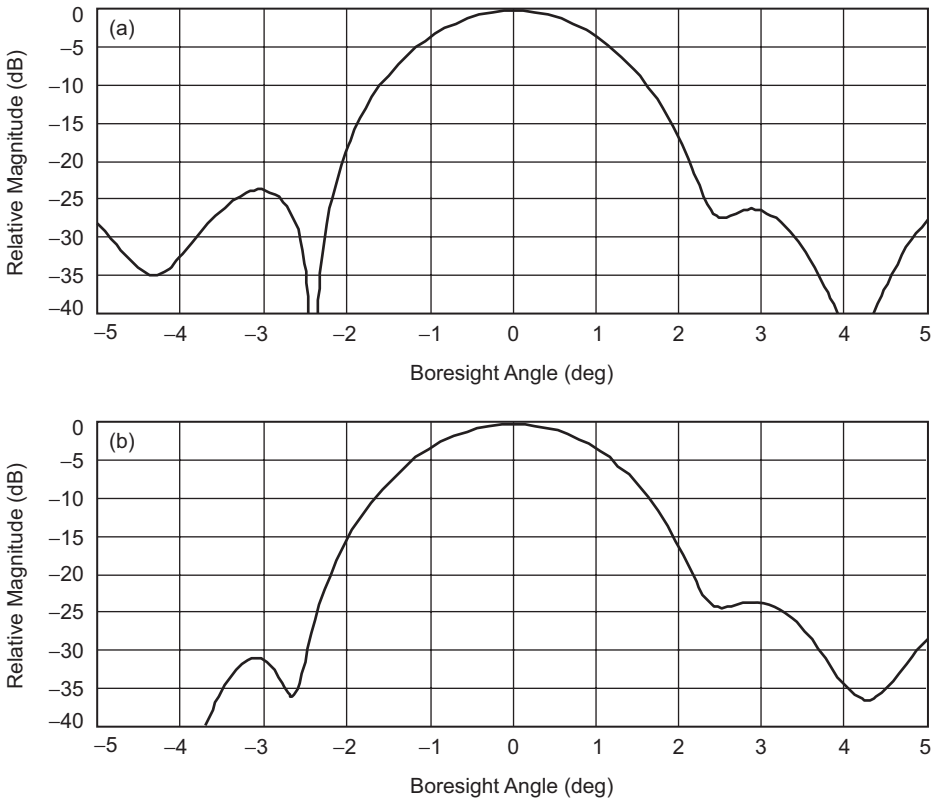

Fig. 5-20. Far-field patterns of the Galileo HGA, f = 2295 MHz, for (a) phi = 0 deg and (b) phi > 90 deg.

mounting position was also similar to that of the Voyager LGA; however, a significant difference was that there was a small ground plane separating the LGA1 aperture from the main reflector behind it. It was expected that there would be considerable currents on the rim of the LGA1 that could, in turn, interact with the main reflector. This may have prevented the LGA1 from meeting requirements. Figure 5-24 show the free-space far-field patterns of the LGA1. These patterns were of just the antenna without the main HGA reflector behind it. In order to put a bound on the problem, a series of far-field measurements of the LGA1 was made where it was placed in front of a 5-m test reflector [27]. Figure 5-25 provides the results of this testing. There is high (spatial) frequency ripple across the pattern, with a predominant peak in the boresight direction. When this pattern is compared to specifications in Section 5.2.3.7, one finds that even with the ripple, the requirements are met.

5.2.7.2 LGA2 (Aft Facing). A review of the LGA system gain requirements (Section 5.2.2) shows that the required gain decreased monotonically as the

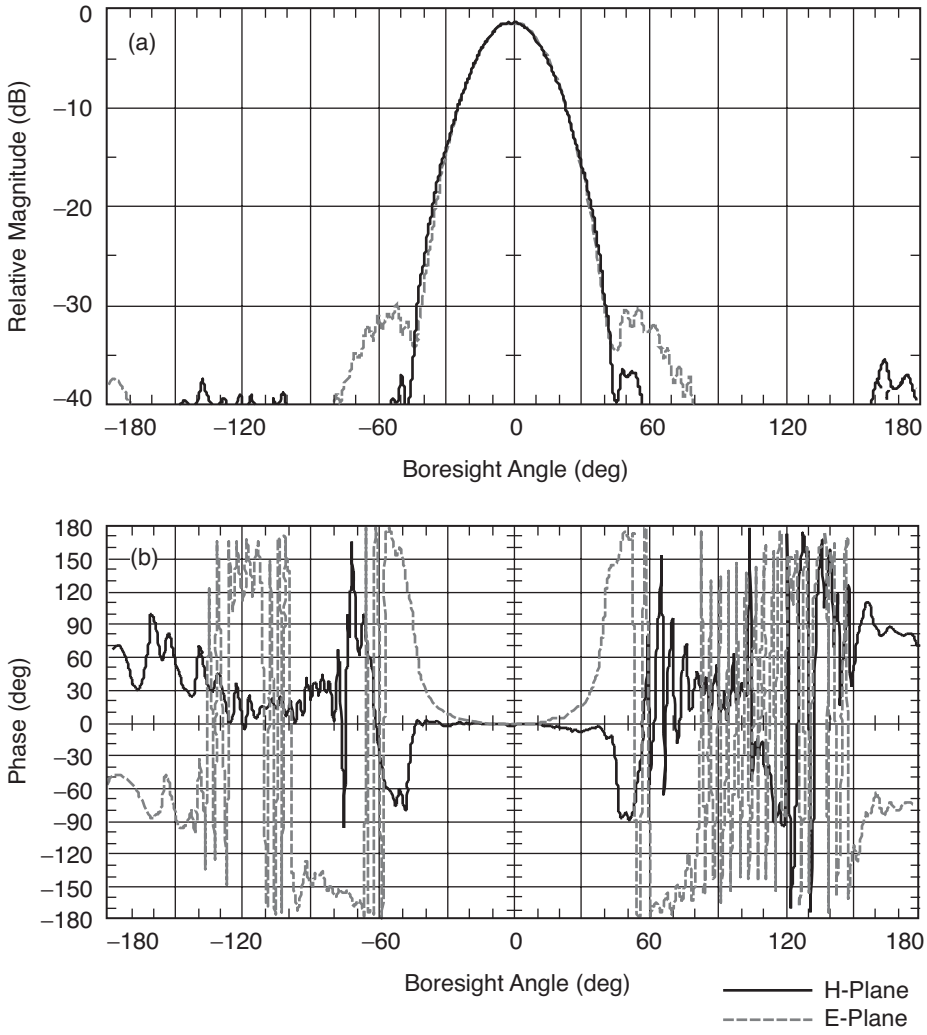

Fig. 5-21. Galileo X-band feed pattern cuts, f = 8415 MHz, with (a) amplitude patterns and (b) phase patterns.

direction angle increased from the forward direction (0-deg spacecraft cone angle) towards the aft direction (180-deg spacecraft cone angle). LGA1 was designed to meet the requirements from 0 deg to 120 deg, while LGA2 was designed to meet the requirements from 120 deg to 180 deg. Note that the requirements were to be met for all azimuth angles at every cone angle. Therefore, since LGA2 was to be mounted so that its mechanical axis was pointed at the spacecraft 180 deg, the design choice was to either provide an antenna with enough boresight gain so that at the antenna's 60-deg angle the requirement was still met; or to provide an antenna with lower gain on its

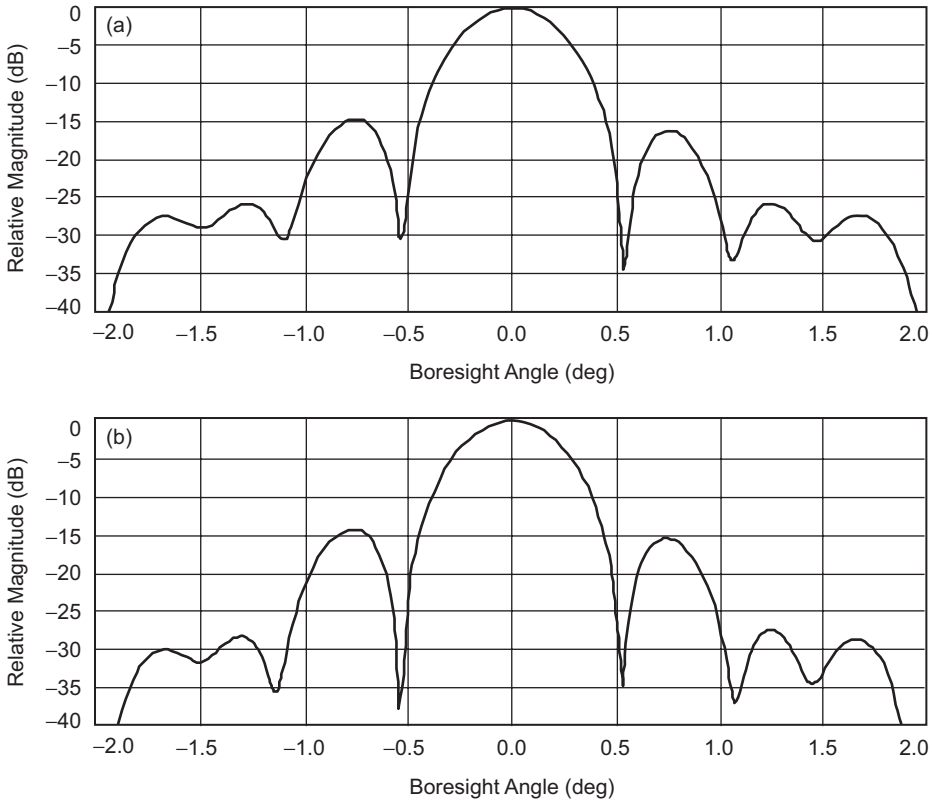

Fig. 5-22. Far-field patterns of Galileo HGA, f = 8415 MHz, with (a) phi = 0 deg and (b) phi = 90 deg.

boresight in order to spread the energy out to a wider angle off of its boresight. The latter design choice was made after it was determined that the gain and beamwidth relationship conspired to make it impossible to meet the requirement with a typical LGA. Specifically, the system gain coverage 60 deg off boresight (at the spacecraft 120-degree cone angle) could not be met since, as the gain of the antenna increased, the beamwidth decreased. This section describes how the system gain requirements for the aft direction were met.

5.2.7.2.1 LGA2 RF Design. As stated above, it was required that the LGA2 be designed such that the gain at some direction away from the mechanical boresight be higher than the gain in the boresight direction. One type of antenna that meets that requirement is a crossed drooping-dipole antenna [28]. This type of antenna consists of crossed dipoles of different lengths, held over a ground plane, drooping with respect to the normal to the ground plane. Finally, the match of the dipoles is obtained by using a split-tube balun [29] between the

(a)

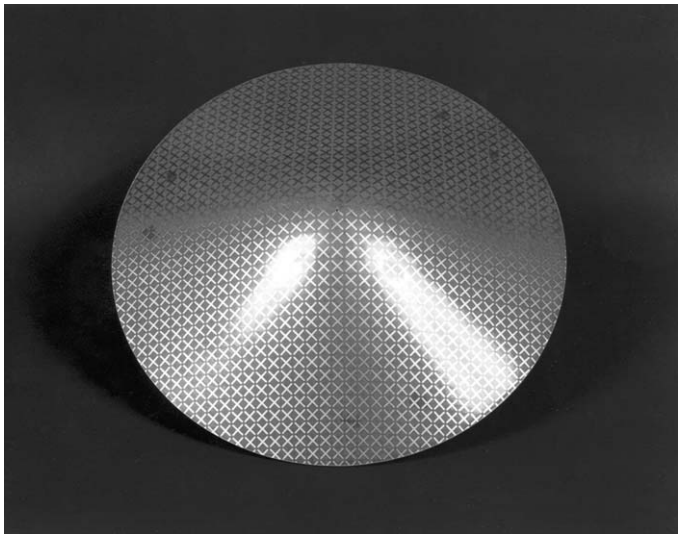

(b)

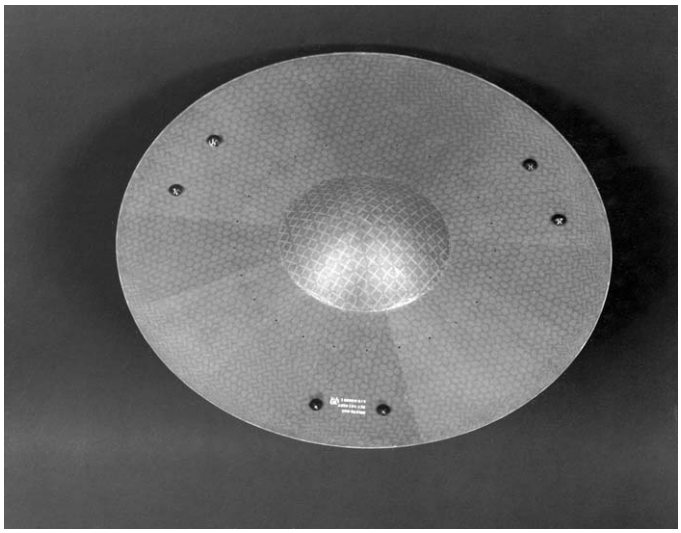

Fig. 5-23. Galileo frequency selective surface (FSS) subreflector: (a) front and (b) back.

inner and outer conductors of the coaxial feeding structure. This antenna type is constructed on the structure of a 0.5-in. (1.26-cm) semi-rigid coaxial cable. This aluminum cable uses a series of Teflon tubes to locate the center conductor. The cap of the LGA2 was soldered to the top of the coaxial cable joining the inner and outer conductors. The balun slots were shorted at the

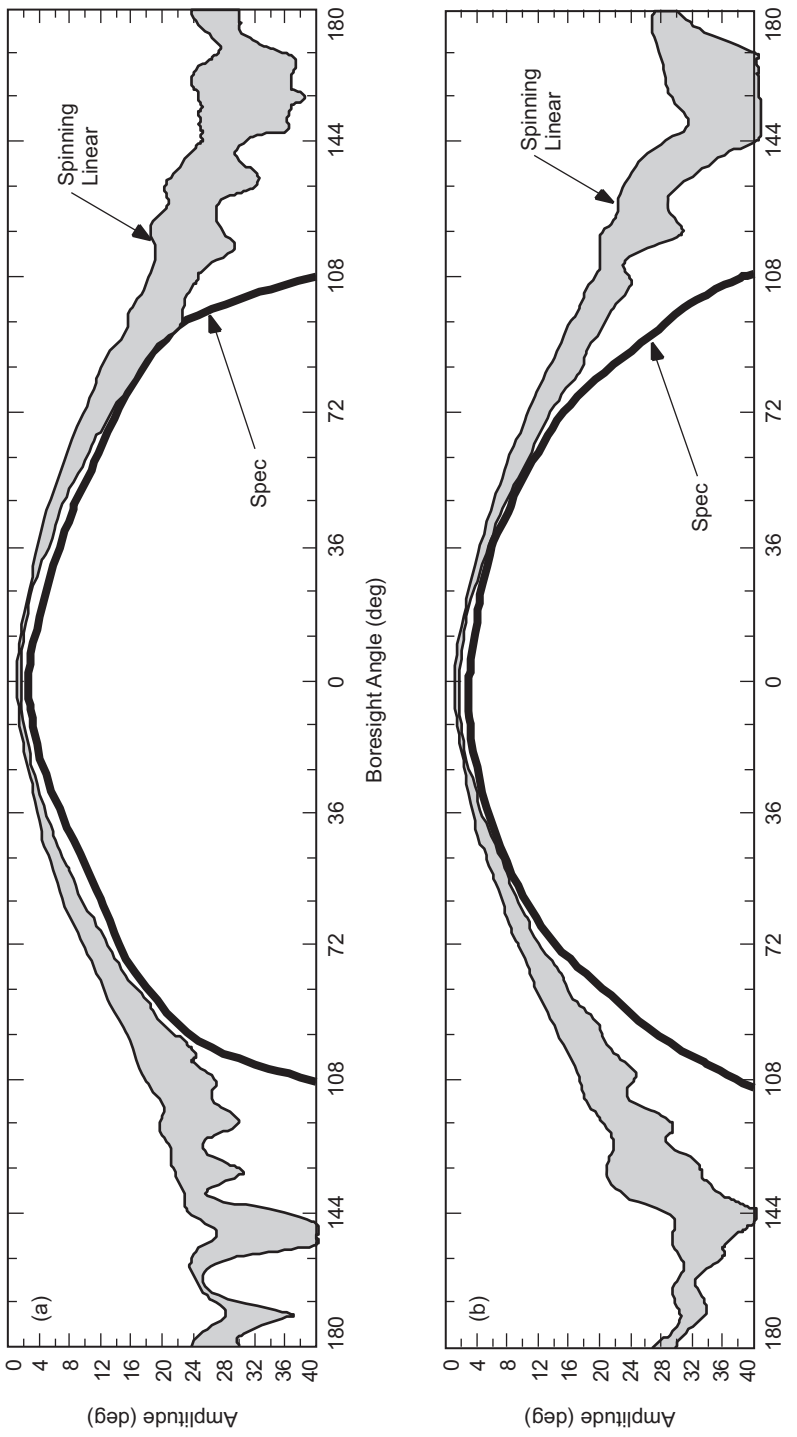

Fig. 5-24. Galileo LGA1 free-space pattern measured with a spinning linear probe compared to the required specification at (a) 2295 MHz and (b) 2115 MHz.

proper length by a ring that was empirically located by measurement of the VSWR and then soldered into place. Other parameters that could have been varied in the design of the antenna are shown in Fig. 5-26, and the parameter values selected after the design and breadboard testing are given in Table 5-7 [30,31]. The resulting far-field patterns are given in Fig. 5-27, and performance values are shown in Table 5-8. Finally, Figs. 5-28(a) and 5-28(b) are photographs of the spacecraft hardware as built.

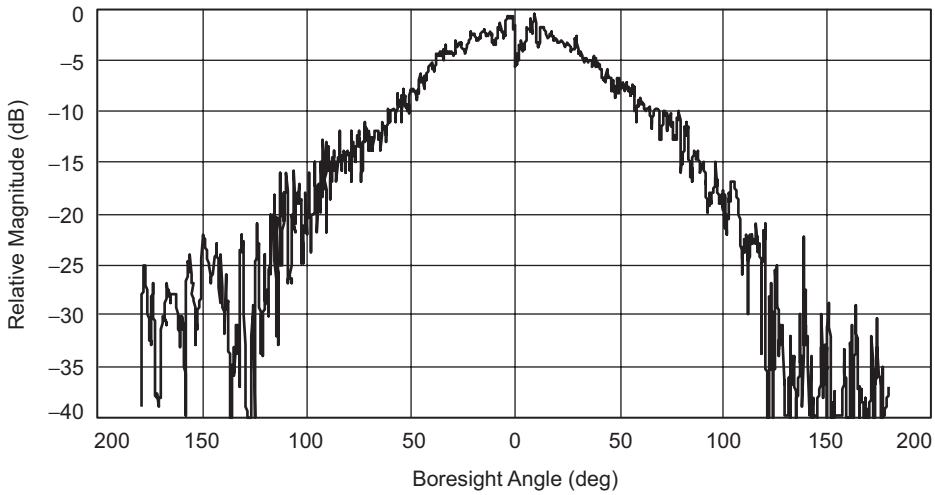

Fig. 5-25. Galileo LGA1 RF pattern in the presence of a 5-m reflector.

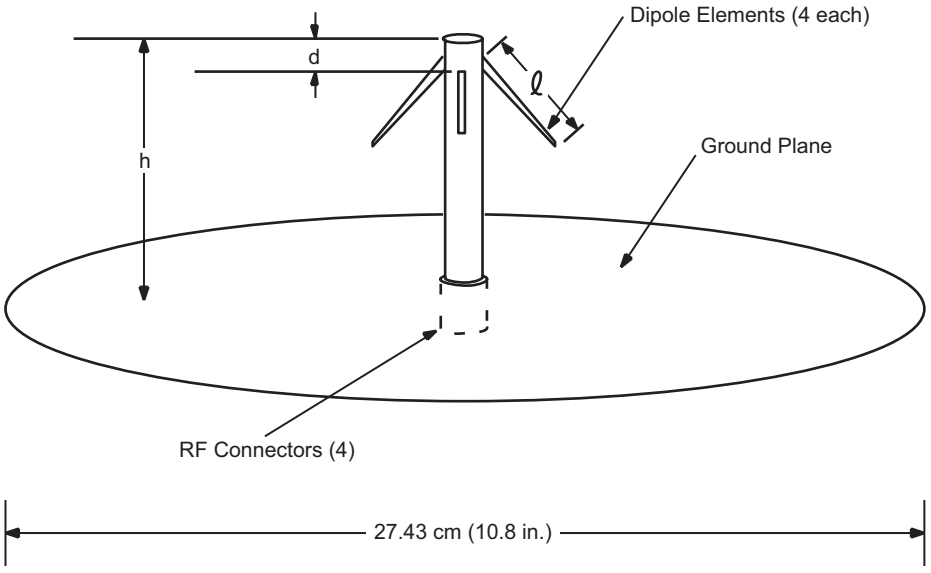

Fig. 5-26. Variable parameters of the Galileo LGA2.

Table 5-7. Values of the design variables for the Galileo LGA2.

Variable	Description	Dimension (in.	cm)
h	Post tip to ground plane	2.9	7.5
d	Post tip to dipole element	0.3	0.8
l_s	Length of short-dipole element	0.8	2.0
l_l	Length of long-dipole element	1.3	3.3

5.2.7.2.2 Articulated Spacecraft Mounting Boom. LGA2 was mounted on a mast that in turn was mounted on one of the RTG booms, as shown in Fig. 5-6. However, during the launch phase, the RTG boom was folded into the body of the spacecraft. Therefore, the LGA2 mast also had to be folded out of the way during launch. This was accomplished by a rotational motorized mechanism that swung from the mast in an arc from its stowed position to one that was pointed directly in the aft direction.

5.2.7.3 Performance of the LGA System Versus Requirements. The performance of the LGA system is illustrated in Fig. 5-29, where the gain patterns of LGA1 and LGA2 are shown relative to each other and to the requirements. It is apparent that the gain requirements were met for all but the very fewest directions centered about the 90-deg spacecraft angle. The spacecraft system engineering team analyzed the results, estimated the expected number of days that Earth would be in that direction, and determined that the results were satisfactory.

5.2.8 Conclusions

The 14-year Galileo mission came to an end at 11:57 a.m. Pacific Daylight Time (PDT) on Sunday, September 21, 2003, when the spacecraft was intentionally commanded to plunge into the atmosphere of Jupiter. (The reason for this action was because the onboard fuel was nearly expended and mission planners did not want to risk an unwanted impact with Jupiter's moon Europa. During its mission, the spacecraft received more than four times the cumulative dose of radiation that it was designed to withstand.) The DSN at Goldstone, California, received the last signal from the spacecraft at 12:23:14 a.m. PDT.

The Galileo spacecraft traveled approximately 4.7 billion kilometers, orbited Jupiter 35 times, and conducted the first long-term observations of the Jovian system. During this time, Galileo made the first observations of ammonia clouds in another planet's atmosphere; observed moon Io's volcanic activity, which may be 100 times greater than that of Earth; provided evidence

supporting a theory that a liquid ocean exists under Europa's icy surface; and showed that Europa, Ganymede, and Callisto each have a thin atmospheric layer [32].

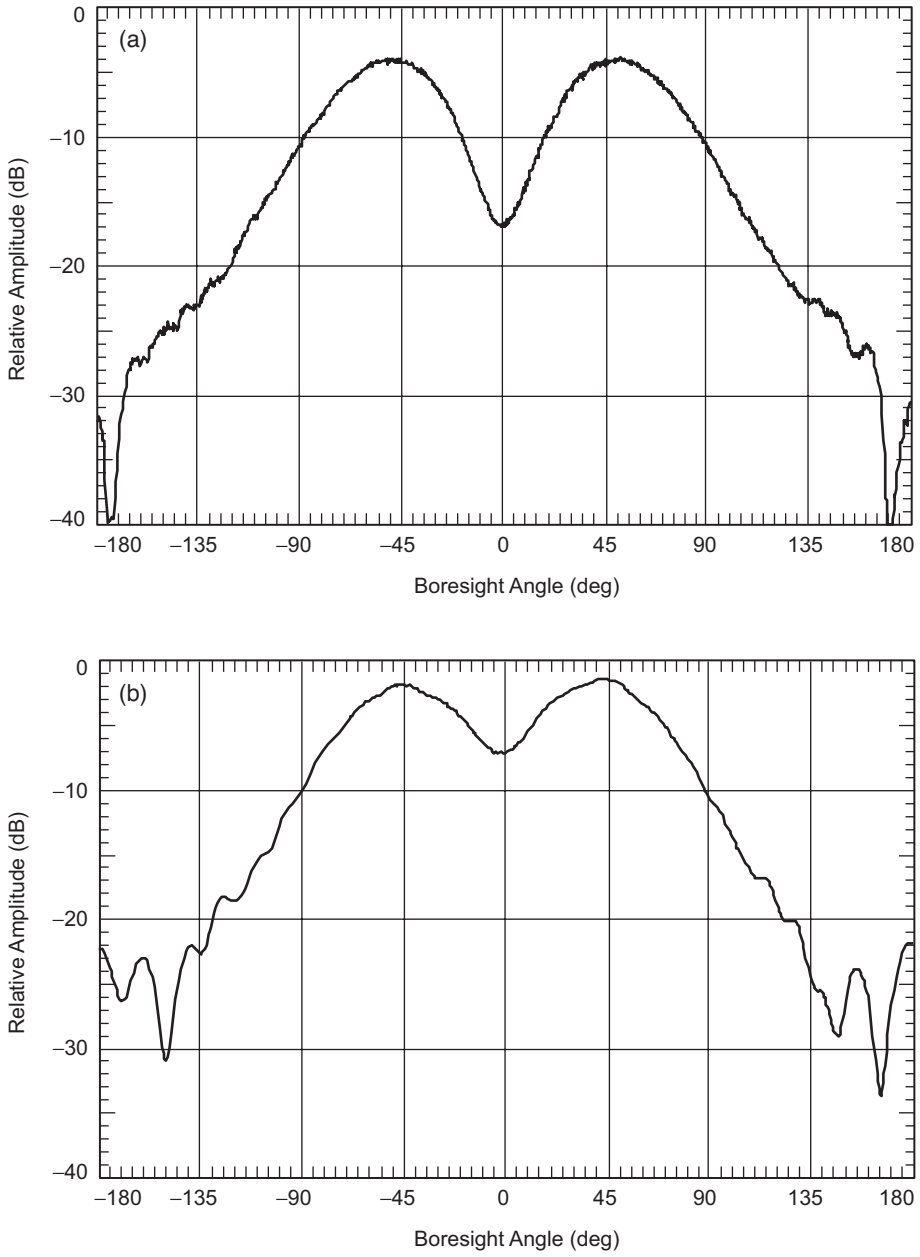

Fig. 5-27. Free-space far-field patterns of Galileo LGA2 at (a) 2295 MHz and (b) 2115 MHz.

Table 5-8. Galileo LGA2 performance measurements.

	Frequency = 2295 MHz		Frequency = 2115 MHz	
Parameter	Requirement	Measurement	Requirement	Measurement
Gain	≥4.5 dBi	5.3 dBi	≥4.0 dBi	5.3 dBi
Axial ratio	≤8 dB	≤11 dB	≤8 dB	≤7 dB
VSWR	≤1.30:1	1.23:1	≤1.30:1	1.22:1

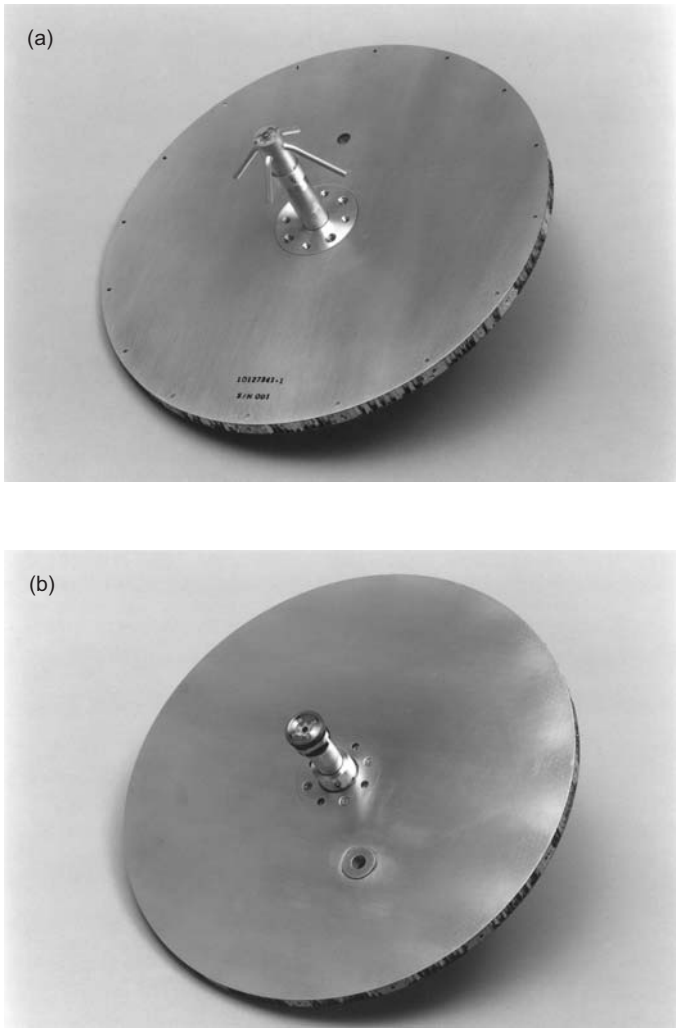

Fig. 5-28. Galileo aft-facing LGA2 for (a) front and (b) back.

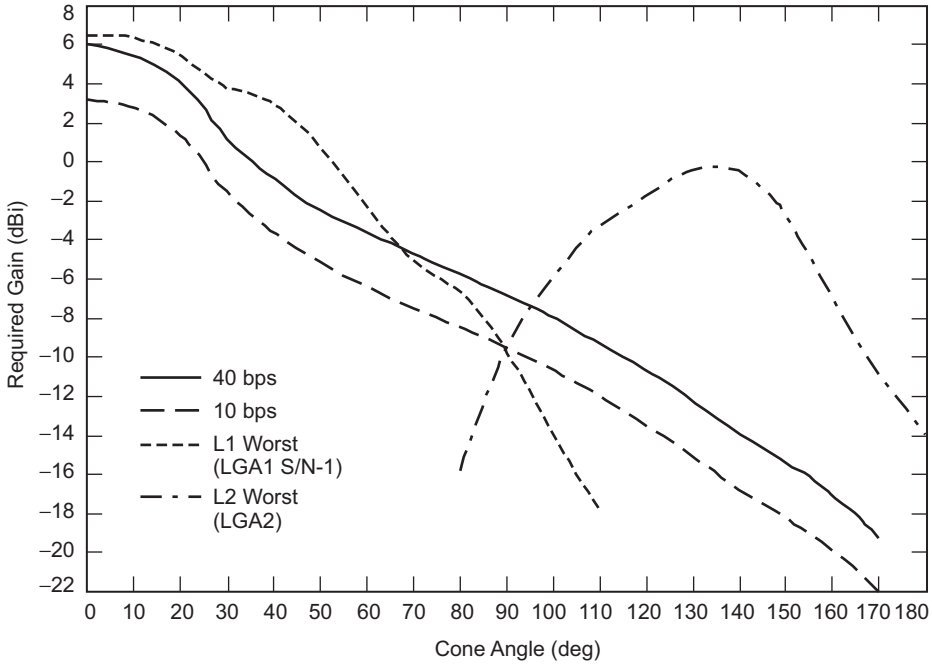

Fig. 5-29. Galileo LGA system performance vs. requirements.

During its entire life cycle, Galileo telecommunications were supported by only the LGA system of antennas. Had the HGA deployed as planned, the amount of discoveries might not have been greater, but the volume and quality of data would have no doubt been awe inspiring, given the more than 40 dB of gain between the HGA and LGA systems. The lessons learned from this project will be used in the development of future large deployable antennas that will be required in order for future missions to achieve the extremely high data rates that will be used to return scientific data.

5.3 The Cassini High-Gain Antenna Subsystem

Roberto Mizzoni, Alenia Spazio S.p.A, Rome, Italy

The Cassini-Huygens deep-space mission is a U.S.–European science program having as primary objective the exploration of Saturn and its largest moon, Titan [33]. The orbiter probe, launched in October 1997, arrived at the Saturnian system in July 1, 2004. Cassini's 4-year scientific mission at Saturn is dual: to complete a multispectral orbital surveillance of Saturn, and to investigate Titan. The U.S. Cassini orbiter, during its 74-orbit tour of the Saturnian system, will measure the planet's magnetosphere, atmosphere, and rings, and will observe some of its icy satellites and Titan during close flybys.

The Cassini's investigation of Titan was augmented by an instrumented European probe, called the Huygens Probe, which dropped through Titan's dense atmosphere on January 14, 2005. The Huygens probe reached the surface of Titan and transmitted data from there for 1 hour and 10 minutes before shutting down.

The Cassini data will be a major contribution to our scientific modeling of planetary atmospheres, important to our understanding of the evolution of Earth's own atmosphere. Cassini's multiple close flybys of Saturn's icy satellites also will provide insight into the nature of the population of small planet-like bodies that may once have been prevalent in the outer Solar System.

The mission, managed by NASA, is fully international in scope. The Huygens probe was provided by the European Space Agency, and elements of three of Cassini's science instruments were provided by the Italian Space Agency, along with the orbiter's HGA [34].

Cassini's orbit is shown in Fig. 5-30, and the spacecraft, at an intermediate integration phase at JPL, is shown in Fig. 5-31. The HGA (top) and the Huygens probe (side) can be seen on the spacecraft. The Cassini mission benefited from the gravity-assisted swing-bys of Venus, Earth, and Jupiter, without which it would be impossible to reach Saturn.

Cassini–Huygens is a three-axis stabilized spacecraft equipped for 27 diverse science investigations. The Cassini orbiter has 12 instruments, and the Huygens probe has six. The instruments often have multiple functions, equipped to thoroughly investigate all the important elements that the Saturn system may uncover. The spacecraft communicates through one HGA and two LGAs. It is only in the event of a power failure or other such emergency situation however, that the spacecraft will communicate through one of its LGAs, known as LGA1. This section describes the most important RF subsystem: the HGA.

5.3.1 High-Gain Antenna Requirements and Constraints

Table 5-9 summarizes the HGA–LGA1 modes and functions. Radio science experiments and radio relay linkage to the Huygens probe were allocated to S-band. Telecommunication is provided at X-band while radar imaging to Titan and altimetry of Titan are implemented at Ku-band. Precision Doppler experiments are done at Ka-band, to search for gravitational waves and measure relativistic bending of solar rays. Dual circular polarization is required at all bands except Ku, which is linear vertical (aligned with spacecraft motion). The HGA subsystem has a total of 11 physical ports, 5 of them diplexed at payload level, providing a total number of 16 input/output ports, while the LGA1 has got two Tx/Rx lines.

The top-level electrical parameters are summarized in Table 5-10, according to the operating frequencies detailed in Table 5-9.

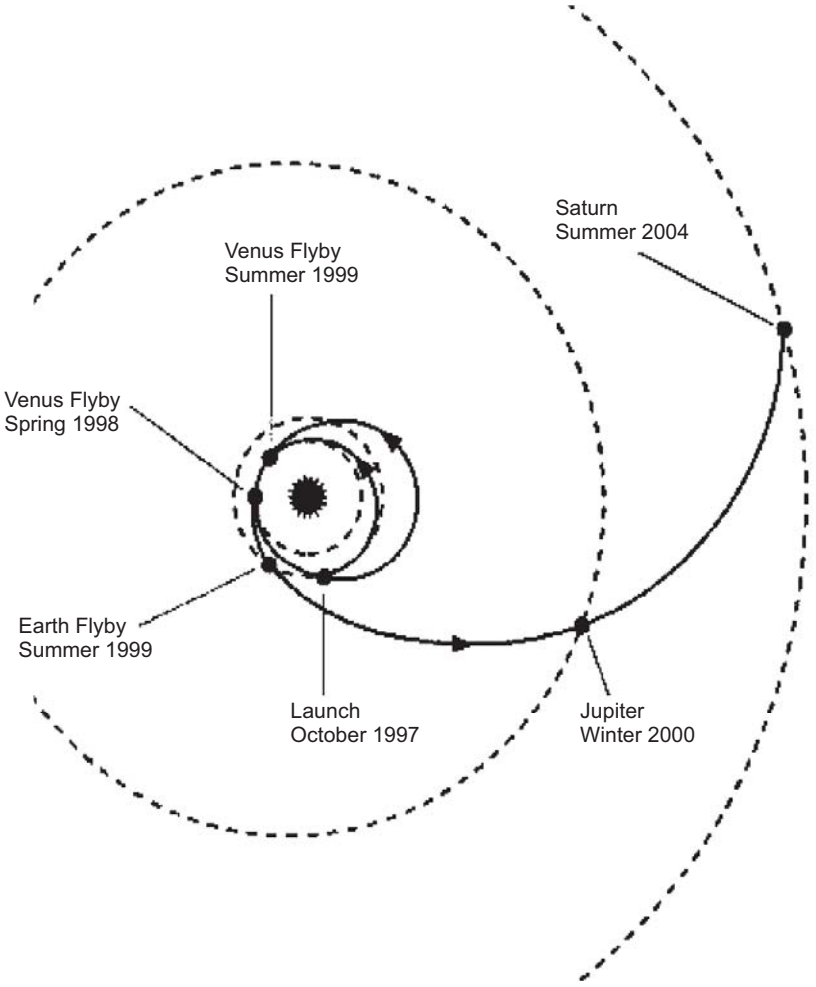

Fig. 5-30. Cassini journey to Saturn.

On-axis pencil beams are required at all bands, according to the beam scenario depicted in Fig. 5-32.

In addition, four fan beams (with five-to-one beamwidth ratio) are required for the radar imaging mode at Ku-band. Those beams form, together with the center pencil beam, a whole coverage line of about 5.8 deg along the range plane. Good cross polarization discrimination (<–20 dB), relatively low peak sidelobes (<–15 dB), a regular 3-dB contour (0.35 deg ±0.05 deg) in the along-track direction, and minimum gain along the range plane line (MGL) are important to SAR operation.

As an appropriate compromise between peak gain and spacecraft attitude control capability, the 3-dB beamwidth at Ka-band was required to be

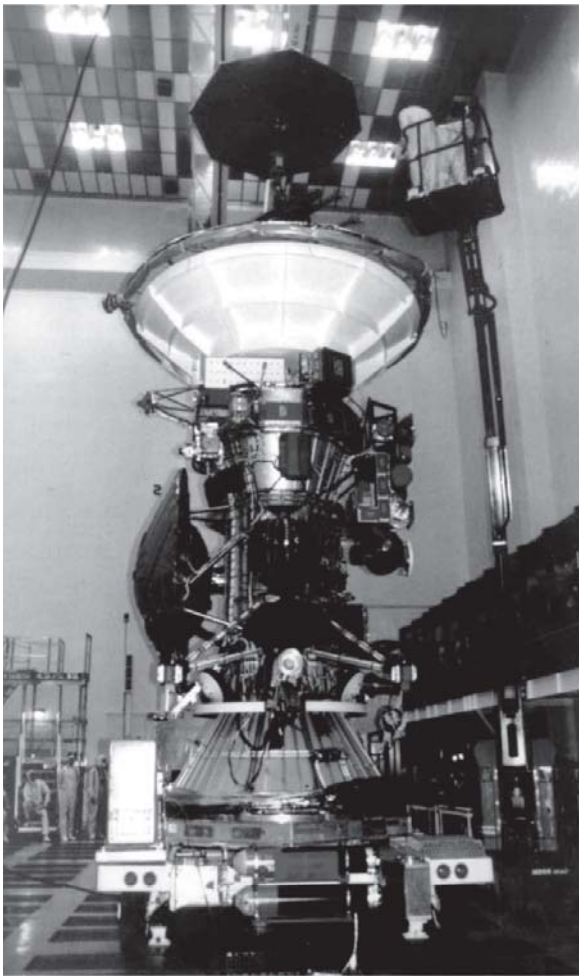

Fig. 5-31. Cassini spacecraft.

approximately 1.6 times larger that what is typical for the given aperture size. This then requires some form of beam-broadening at Ka-band. Maximum gain at the X-band downlink frequency is a priority in antenna configuration since the communication link is at the limit of feasibility.

The electrical design was heavily constrained by the launch vehicle envelope and the severe mechanical and thermal design requirements. This led to a symmetric dual-reflector antenna with a 4-m maximum reflector diameter and a focal length to diameter ratio lower than 0.33. Additionally, six thick struts were placed well inside the main reflector, to survive the dynamic loads at launch. The mechanical constraints and potential solutions are summarized in Table 5-11.

Table 5-9. Cassini HGA/LGA1 functions.

Antenna	Frequency (MHz)	Mode (*)	Function	Polarization
HGA	2040 ±5	R	Probe relay antenna	Circular, left hand
HGA	2098 ±5	R	Probe relay antenna	Circular, right hand
HGA	2298 ±5	T	Radio science	Circular, right hand
HGA	7175 ±25	R	Telecommunications	Dual circular
HGA	8425 ±25	T	Telecommunications	Dual circular
HGA	13776.5 ±100	T,R	Radar-SAR	Linear, vertical
HGA	32028 ±100	T	Radio science	Dual circular
HGA	34316 ±100	R	Radio science	Dual circular
LGA1	7175 ±25	R	Telecommunications	Dual circular
LGA1	8425 ±25	T	Telecommunications	Dual circular

* T–Transmit, R–Receive

Table 5-10. Cassini HGA driving electrical requirements.

S-Band	X-Band	Ku-Band	Ka-Band
On-axis beam	On-axis beam	On-axis and off-axis beams	On-axis beam
Maximize peak gain	Maximize peak gain	Maximize MGL gain	Beamwidth 1.6 times larger than the physical aperture
Beam circularity	Dual CP operation	Minimize SLL	Dual CP operation
Dual CP operation		Minimize ISLR	
		Fan beam requirements	
		Linear polarization	

CP = circular polarization

ISLR = integrated sidelobe ratio

SLL = sidelobe level

5.3.2 Configuration Selection

The selected antenna configuration is shown in Fig. 5-33. The X-, Ku- and Ka-band subsystems are located at the Cassegrain focus of the dual-reflector system while the S-band feed system is located at the prime focus. The

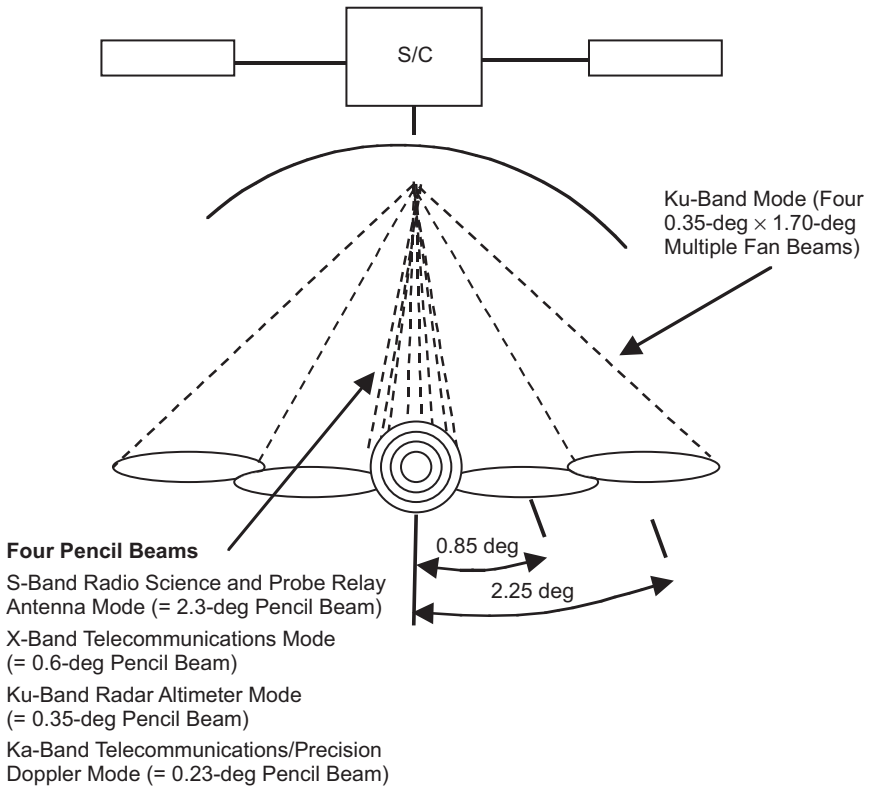

Fig. 5-32. Cassini HGA beam scenario.

Table 5-11. Cassini HGA mechanical/configuration constraints.

Parameter	Impact
Overall envelope	D <4.0 m, F/D <0.33
Spacecraft survivability	at 0.625 AU (Venus flyby), HGA Sun pointed (T_{ant} = + 160 deg C)
Antenna operation at 10 AU	Close to Saturn, T_{ant} = –210 deg C
Spacecraft/launcher envelope, interfaces, and loads	Center-fed antenna with 6-strut tripod inside main dish
Priority to X-band	X Cassegrain
Multiple-band operation	Wideband reflectors profiles, front feeds, Cassegrain feeds, FSS subreflector

T_{ant} = antenna temperature

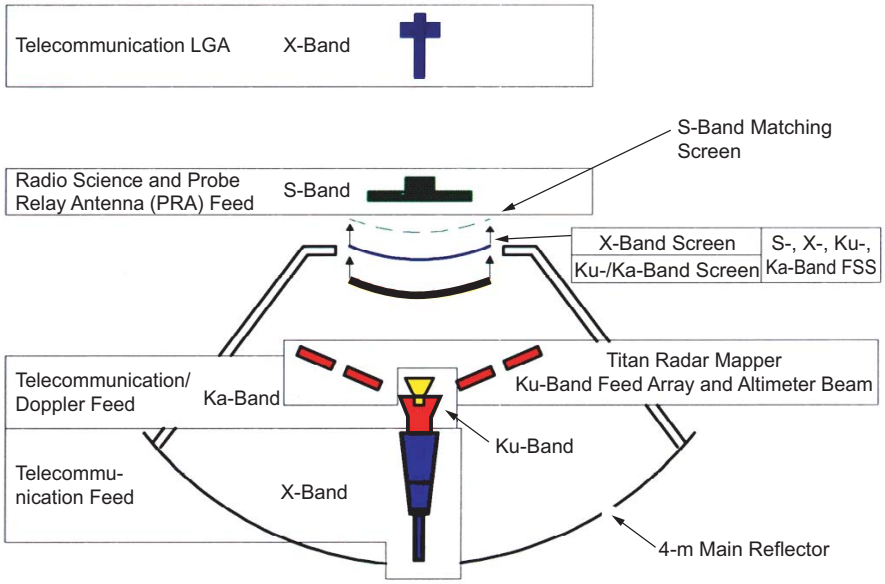

Fig. 5-33. Cassini selected HGA electrical/functional block diagram.

subreflector consists of a cascade of three frequency-selective surfaces separated by air. The first subreflector reflects Ku- and Ka-bands and is transparent at X-band. The second subreflector reflects X-band; the third subreflector is used as a matching screen to improve the overall transparency at S-band. A triple-band (X, Ku, and Ka) feed horn and 20 subarrays of slots grouped into four feed arrays of five elements each, operating at Ku-band, are arranged in the Cassegrain focal plane. For maximum coverage, the LGA1 antenna is on the top of the FSS deck.

Band allocation is dictated by the following considerations:

- X-band was Cassegrain located for maximum efficiency and minimal transmission line losses.
- Ka-band was Cassegrain located in order to avoid grating lobes from the FSS subreflector appearing in the visible space. This problem would be unavoidable if Ka-band operations were at the prime focus, considering the multiband operations. In addition, the high transmission line losses associated with a 3-m waveguide would not be tolerable at these frequencies.
- Ku-band was Cassegrain located after an extensive trade-off between a prime focus and a Cassegrain design. It was concluded that the scanning aberrations introduced by a prime focus configuration were not compatible with the sidelobe and beam-efficiency requirements for the

SAR beams (the most scanned element beam is about nine beamwidths displaced off-axis).

- S-band was located at the prime focus because the subreflector is less than four wavelengths at these frequencies and its feed aperture, of the same dimension, would be in conflict with all the other subsystems.

The selected optics geometry is shown in Fig. 5-34. It consists of a parabolic main reflector, a hyperbolic subreflector operating at Ku- and Ka-bands, and a shaped subreflector designed for X-band. Accordingly, two distinct foci are available at the X- and Ku/Ka-bands. The optics parameters are a good compromise between mechanical and technological requirements like the limited-feed axial extension and aperture dimension in the focal plane and a reasonable subreflector curvature for FSS manufacturing feasibility, as will be discussed later on.

Reflector profiles and the subreflector dimensions are constrained because the requirement for multifrequency operations. Thus, maximum performance at all the bands is not possible (see Table 5-12).

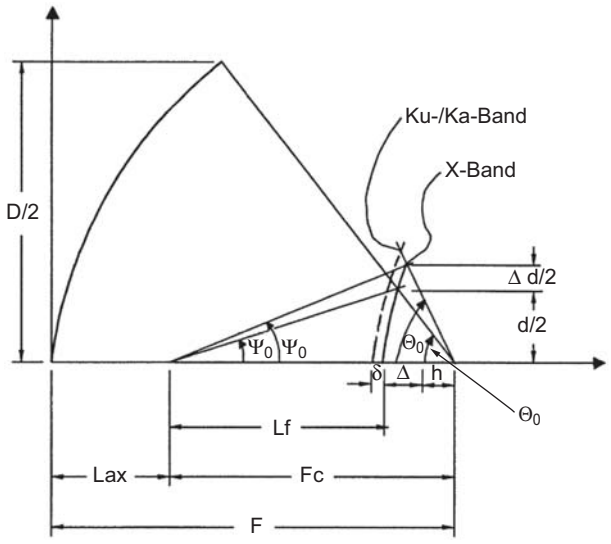

X-Band		Ku-/Ka-Band
F	= 1315 mm	1315 mm
D	= 4000 mm	4000 mm
d	= 463.5 mm	500 mm
Δ d/2	= 53.4 mm	35.6 mm
d+ Δ d	= 571.2 mm	571.2 mm
Ψ'_0	= 16.15 deg	17.44 deg
Ψ'_0	= 18.9 deg	19.3 deg
Θ_0	= 74.5 deg	74.5 deg

Fig. 5-34. Selected Cassini HGA optics geometry.

Table 5-12. Cassini Optimum reflectors profiles vs. frequency band requirements.

Frequency Band	X	Ku	Ka	S
Best optical system	Dual shaped	Dual shaped	Dual shaped or equiv. 2.5-m reflector	Parabolic main
Viable alternative(s)	Hybrid (sub shaped, main parabola)	Canonical (hyperbola/ parabola)	• Smaller (or shaped) subreflector • Defocusing 4-m canonical optics	Main with any shaping
Main characteristics	• Deep (amplitude and phase) shaping • Recovery of feed taper on aperture • Frequency (feed) dependent	• Light (phase) shaping for homogeneous patterns in different beam directions. • Oversized sub-reflector	• Light shaping • Phase error for beam broadening and/or main reflector under-illumination at ka-band	• Front-fed • Back screen FSS profiled for optimum transparency • Oversized sub-reflector
Comment/ purpose	• Highest efficiency • Uniform aperture distribution	• Good η and scan performances • Low sidelobes	• 1.6:1 beam broadening	• Highest efficiency • Avoids sub-reflector scattering at edges

In particular, X-band would ideally use dual-shaped optics [35,36] for a nearly uniform aperture field distribution. Additionally, the feed/subreflector geometry would be dimensioned to satisfy the minimum blockage condition [37], for maximum antenna efficiency.

Ku-band optics is driven by the large scan of the fan beams (up to nine beamwidths of the element beam diffraction bounded by the aperture). The idealized optics would be a multifocal dual-shaped reflector system able to minimize beam aberrations due to scan within ±9 beamwidths along the range plane. As a good compromise, a canonical hyperbola and parabola dual reflector performs much better than the dual-shaped system required at X-band. At Ku-band, the subreflector has to be adequately sized in order to provide an efficient aperture illumination even for the most displaced feed element in the Cassegrain focal plane. To this end, the subreflector edges must lie well above the optical geometrical boundaries.

The Ka-band optics require a smaller subreflector than X- or Ku-band in order to under illuminate the main reflector, to yield a useful reflector diameter on the order of 2.5 m if a focused primary illuminator is used, since a beamwidth 1.6 times that physically achievable from the 4-m aperture is

requested. Alternatively, a dual-shaped system or shaped subreflector is required at Ka-band for beam broadening. In any case, the main reflector shape is not compatible with the X-band reflector shape while the subreflector shaping degrades Ku-band performance. The bottom-line alternative consists of a defocused approach realized by a proper axial displacement of the Ka-band feed phase center with respect to the canonical (hyperbola/parabola) optics. Although two distinct foci are available at the X- and Ku/Ka-bands, an independent optimization of the triple-band feed axial position within the optics, for the requested Ka-band beam broadening and the simultaneous optimization of the Ku-band altimeter beam, is not possible because the independent subreflectors relative displacements and shapes must be consistent with a stacked layout. Additionally, the phase center of the feed at Ku-band is between the X- and Ka-band phase center, and the fan-beam feed array should not to be obscured by the triple-band feed aperture. The net result is a small degradation of the Ku-band altimeter beam peak gain.

Finally, a prime-focus S-band feed would ideally require a parabolic main reflector, even if the RF performance were only second-order sensitive to the main reflector deviations, for any shaping of the main reflector or subreflector(s). For correct prime focus operation, the subreflector(s) should be dimensioned with boundary limits well above the optical geometrical boundary in order to minimize diffraction from the edges. Advantages of subreflector over sizing have also been illustrated for Cassegrain operations [38].

Considering all those arguments, the subreflectors have been properly sized above the geometrical boundaries (see Fig. 5-34) since only Ka-band would not benefit from this solution.

A careful assessment of the degrees of freedom of the optics was carried out considering additional options provided by the capability of FSS reflection bands. In particular, X-band in conjunction with a Ku-band reflection was investigated as a potential viable alternative to the present solution. This led to analyzing the performance capabilities at X- and Ku-band of dual shaped systems versus hybrid (only subshaped) and canonical hyperbola/parabola dual reflectors [39–41]. Efficiency enhancement for the on-axis pencil beam at X-band ranged within 0.6 dB (in comparison with a canonical system), but this spreading was sensibly reduced when the constraints on the maximum feed aperture size were imposed, owing to the SAR feed array [42]. For the selected design at X-band, the hybrid optics provides a peak gain improvement of 0.25 dB at the critical downlink frequency.

5.3.3 Antenna Modeling and Subsystems Design

A photo of the HGA/LGA1 flight model (FM) is shown in Fig. 5-35. The antenna is a carbon fiber composite structure with a thin sandwich reflector and back reinforcement ribs and rings (Fig. 5-35). The reflector shell is made by a

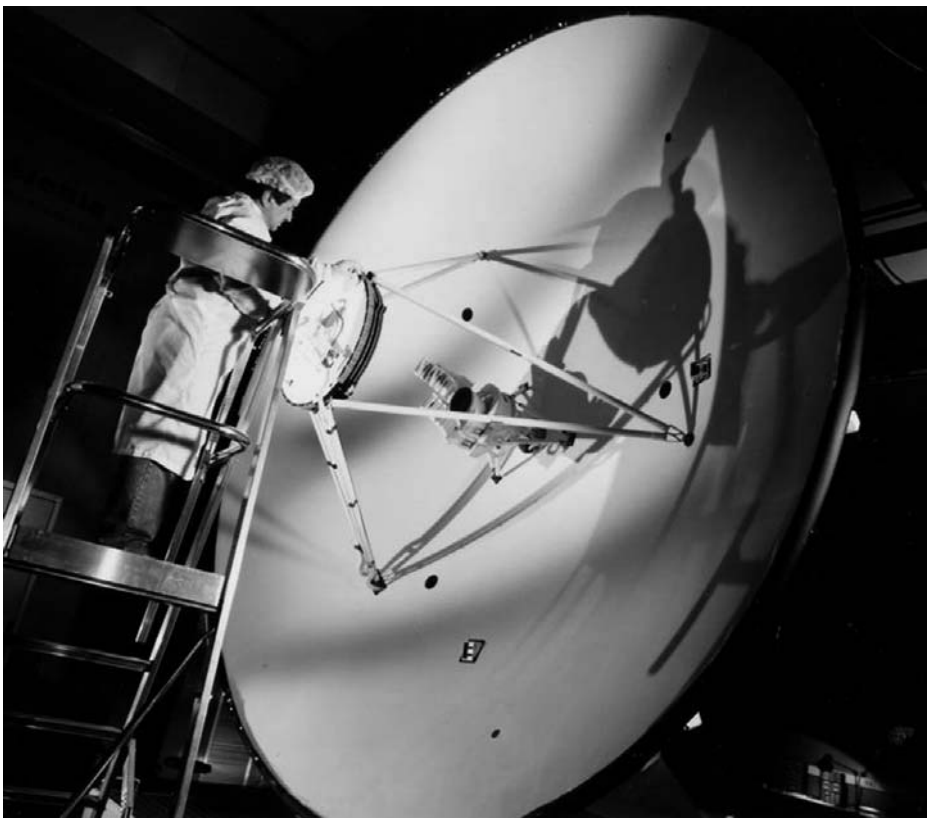

Fig. 5-35. Cassini HGA/LGA1 flight model.

lightweight sandwich, whereas the stiffening structure is a thicker sandwich. The tripod consists of six carbon-fiber-reinforced plastic (CFRP) struts having titanium end fittings connected to a Kevlar plate where the FSS subassembly, the S-band feed, and the LGA1 are mounted. The antenna mass including all RF subsystems is 103 kg, while the temperature range designed to was +160 deg C through –215 deg C.

As already anticipated, the antenna contains many complex RF subsystems, such as the FSS, a triple-band feed, and a slot-type array of 20 elements displaced in the Cassegrain focal plane.

Antenna design and performance prediction were complicated by several blocking structures inside the main reflector, including the six supporting struts of the FSS deck, the center blockage of the subreflector itself, and the asymmetrical blockage of the Cassegrain located feed assembly.

The computed main reflector geometrical optics (GO) shadow for a focused feed is illustrated in Fig. 5-36(a). It compares well to the experimental optical masking shown in Fig. 5-36(b).

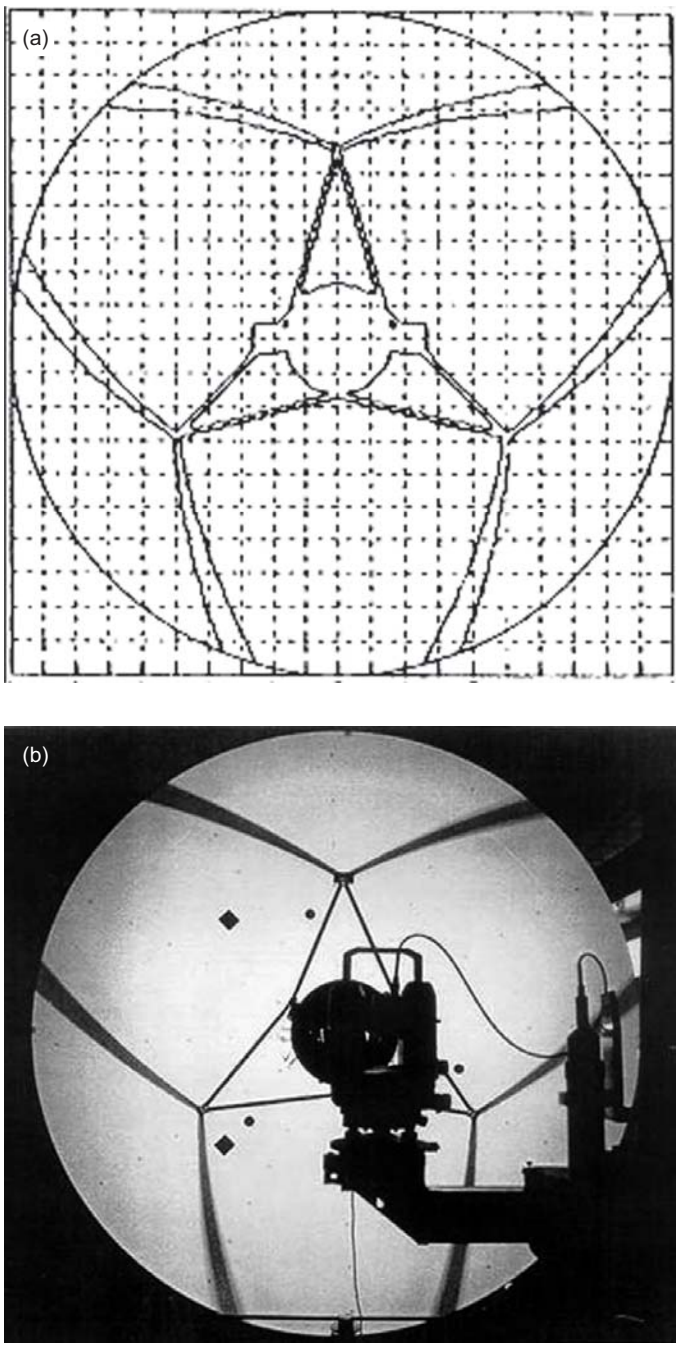

Fig. 5-36. GO shadowing of the Cassini main reflector aperture with (a) computed GO shadowing and (b) experimental optical masking.

The blockage mechanisms may be grouped into two main categories. The first—spherical-wave blockage (SWB)—is the blockage of the primary ray fields emanating from the prime-focus feed as well as from the virtual feeds. The second—plane-wave blockage (PWB)—is the blockage of the secondary ray fields reflected from the main reflector. At the time of design, the effects associated with PWB were already included in most of available reflector antenna software, such as GRASP [43], but no applications were available that dealt with SWB. SWB arises typically from the Cassegrain feeds and from the struts, which fall well inside the main reflector.

To compensate for this significant impact, customized electromagnetic (EM) software using the null-field approach [44], and a high-frequency description of the scattered field from the struts was developed [45] and validated [46]. The induced currents predicted in the physical optics (PO) approximation, were determined by the magnetic field **H** that effectively impinges on the main reflector surface. The field **H** is represented as the sum of the unperturbed field $\mathbf{H}^{\mathbf{i}}$ from the feeder plus the scattered field $\mathbf{H}^{\mathbf{s}}$ from the strut, so that, at any point, ***P***, on the main reflector, the PO currents can be described as

$$\boldsymbol{J}^{po}(\boldsymbol{P}) = \boldsymbol{J}^{poi}(\boldsymbol{P}) + \boldsymbol{J}^{pos}(\boldsymbol{P}) \tag{5.3-1}$$

where $\boldsymbol{J}^{pos}(\boldsymbol{P})$ represents the current perturbation due to the struts, and $\boldsymbol{J}^{poi}(\boldsymbol{P})$ are the currents that would ideally be induced by the feeder in the absence of the struts. In the null-field approach, the estimation of $\boldsymbol{J}^{pos}(\boldsymbol{P})$ has been simply evaluated imposing $\boldsymbol{J}^{pos}(\boldsymbol{P}) = -\boldsymbol{J}^{poi}(\boldsymbol{P})$ in the optically shadowed region, and zero elsewhere. The more accurate high-frequency (HF) formulation is detailed in [46].

The gain loss introduced by all the blockage impacts ranged between 0.4 and 0.8 dB at worst, moving from S- to Ka-band. The antenna model is also complicated by the FSS cascade, particularly at X-band, considering that a double passage through the first (Ku/Ka) screen is experienced, as schematically represented in Fig. 5-37.

At S-band, the subreflector is only a few wavelengths, and its dimensions are comparable to those of the feed aperture. As detailed below, the FSS cascade and the antenna analyses, including analysis of the dichroic subreflector were carried out using customized in-house software [47,48]. The modeling was based on accurate in-house data on the properties of RF materials (e.g., Kapton, Kevlar, adhesive). Accurate modal analysis for the evaluation of the scattering parameters of the dichroic structure was used. For the reflection bands, the radiation performance analysis of the curved surface was based on PO integration of the equivalent currents computed from the scattering

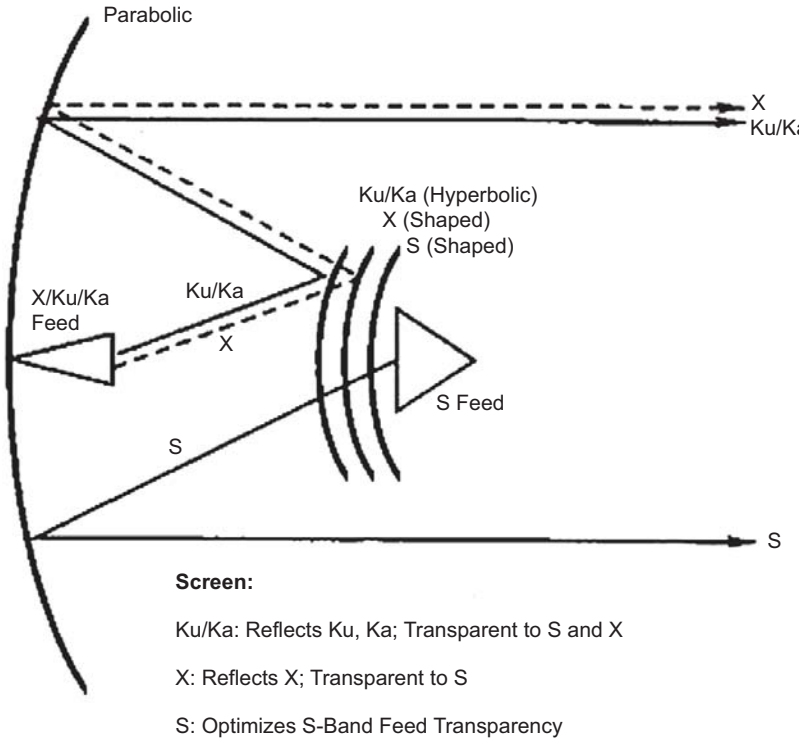

Fig. 5-37. Schematic of double passage through Cassini FSS cascade at X-band.

parameters of the dichroic cascade, making use of the scattering coefficients evaluated at the Ku-/Ka-band front screen.

The development of all the RF subsystems, including that of the complete antenna itself, was experimentally supported by customized breadboards, as detailed below.

5.3.3.1 The Four-Band Subreflector. The subreflector, designed to be reflective at X-, Ku-, and Ka-bands and transparent at S-band, is composed of three mechanically independent surfaces (screens) mounted one behind the other at precise intervals (see Fig. 5-38) so that the required reflection and transmission bands are met [49]. Each FSS screen is separated and supported by a Kevlar honeycomb structure that provides rigidity. The Ku-/Ka-band screen, mounted topmost, is composed of a double periodic array of two concentric conducting ring elements etched onto a Kapton substrate. One element is designed to be closely resonant at Ku-band, and the other at Ka-band. The exposed surface is painted with a thermal protective layer that also acts as a ground. Single-ring resonating elements are employed on the

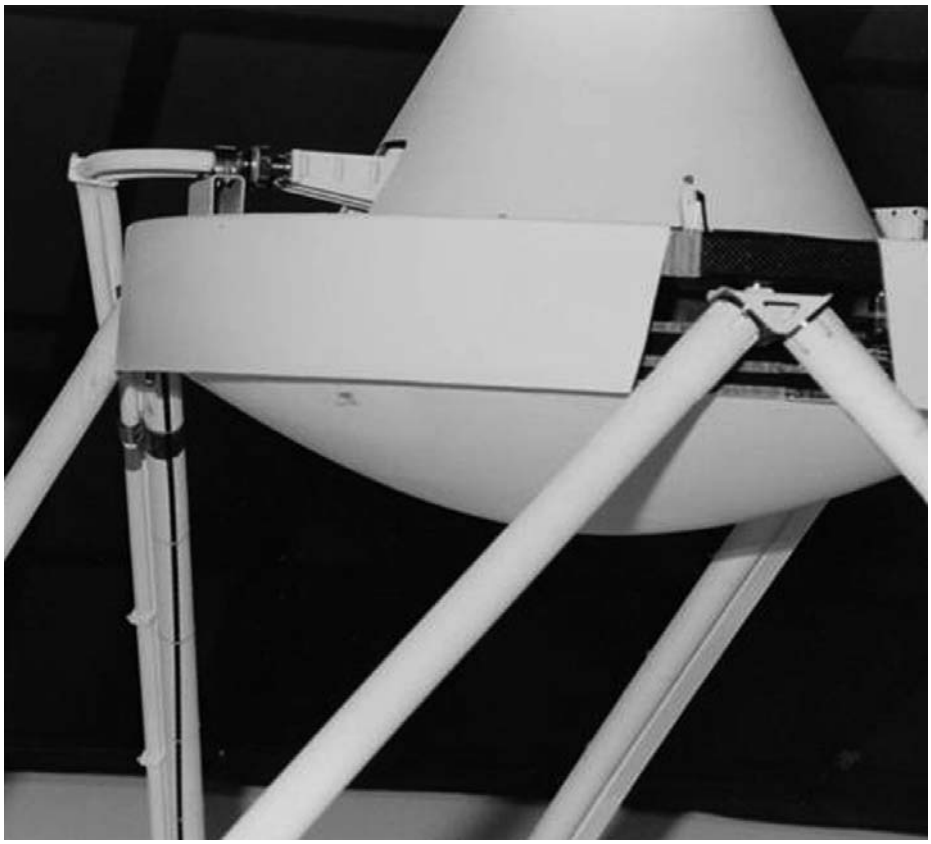

Fig. 5-38. Cassini FSS subreflector deck on HGA FM.

X-and S-band surfaces. This integration scheme was preferred to an alternative solution based on a Ka-band reflective front surface backed with an X-/Ku-band subreflector because it exhibited the lowest ohmic losses associated with the possibility of independently shaping the X-band subreflector in order to maximize the antenna gain at X-band.

From the structural point of view, the sandwich configuration forming each FSS had to be symmetrical, and each screen had to have an overall thickness greater than 4.5 mm [50]. Since the subreflector has a high curvature, a conformal transformation of the resonant elements was required. This implied the use of a regular square lattice since it had to be possible to cut the Kapton film containing these elements along parallel strips to allow forging them onto each mold, as illustrated in Fig. 5-39, where the Ku-/Ka-band screen on the assembly mold is shown.

Figure 5-40 shows the FSS computed transverse electric/transverse magnetic (TE/TM) reflection amplitude vs. frequency at 0-deg and 30-deg

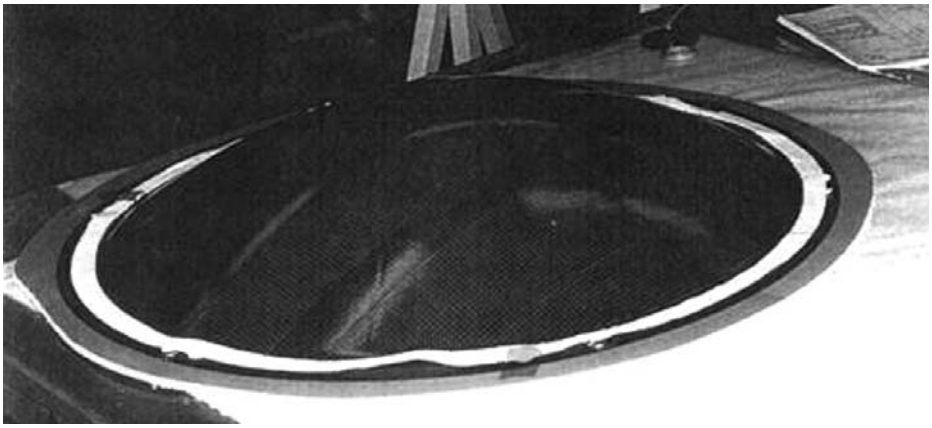

Fig. 5-39. Cassini Ku-/Ka-band FSS engineering breadboard on mold.

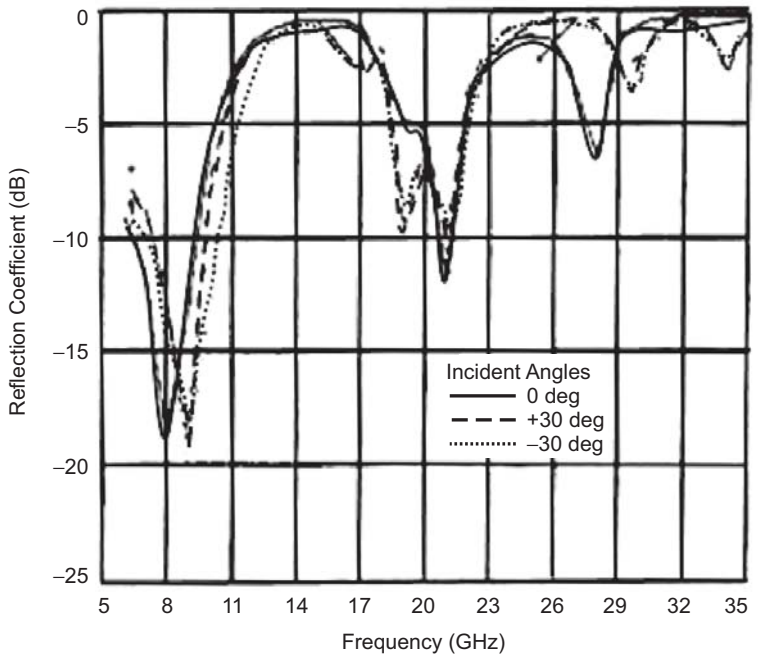

Fig. 5-40. Cassini Ku-/Ka-band FSS TE/TM reflection performance vs. frequency at 0-deg and 30-deg incidence angles.

incidence angles, referred to the Ku-/Ka-band front screen. A good transparency at X-band downlink frequency was obtained.

Although the whole subreflector is composed of the three independent reflectors, their design is not independent. At X-band, the response is a result of the constructive interference between the signal reflected by the back X-band

screen, after having been transmitted through the front Ku-/Ka-band screen, combined with the residual reflection caused by the Ku-/Ka-band screen. The ideal X-FSS would be profiled to optimize its distance from the Ku-/Ka-band FSS so as to achieve this interference as close as possible to the nominal shape dictated by the idealized shaped metallic subreflector relevant to the nominal optics. The method, which led to the definition of the optimum X-band screen shape, involved first calculating the TE/TM response of each individual screen and then cascading them to obtain the performance versus separation response of the two screens for a given incident angle. The analysis at X-band makes use of the scattering coefficients equated at the Ku-/Ka-band screen surface. The unified scattering matrix (USM) obtained using the cascading process mentioned took into account the actual separation between the Ku-/Ka- and X-band screens for each incident angle analyzed. Figure 5-41 shows the calculated S_{12} amplitude of TE/TM modes vs. X-/Ku-band, Ka-band screen separation at 0-, 30-, and 45-deg incidence angle at the downlink frequency of 8.425 GHz. From the figure it is evident that an optimum separation between the two screens, close to 4 mm at 0 deg is the best choice, but at 45 deg their separation must be doubled.

At S-band, the transmission was not optimal because the Ku-/Ka- and X-band screens were not completely transparent. For this reason, an S-band screen was used to impedance-match the response of the whole structure. This

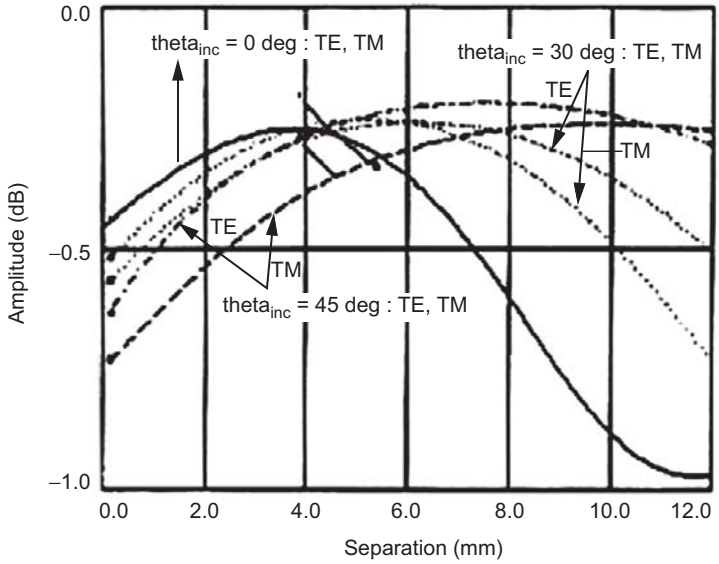

Fig. 5-41. Computed combined transmission vs. separation between Cassini X-band screen and Ku-/Ka-band screen at 0-, 30-, and 45-deg incidence angles (F = 8.425 GHz).

was achieved in the same way as for the X-band transmission although this time, of course, all three screens were cascaded to obtain the S-band screen shape that best optimized the transmission at S-band for radio science. The design curves at 2.3 GHz are illustrated in Fig. 5-42, where the S_{11} amplitude of TE/TM modes at 0-, 15-, and 45-deg incidence angles relevant to the three frequency selective subreflector cascade, is displayed. Figure 5-43 shows the final optimum subreflector profiles where, for practical reasons, the idealized spacing had to be compromised. Figure 5-44 shows the computed vs. measured amplitude and phase at the feed subreflector level.

FSS performance at ambient temperature was verified by (1) flat waveguide sample tests (S-parameter tests), (2) subassembly feed-subreflector tests (radiation performance and pattern integration), and (3) complete antenna tests (pattern and gain with regard to a metallic (for complete reflection) or no (for complete transmission) subreflector. The results, including losses due to the white paint, are summarized in Table 5-13.

In this table, the amplitude and phase-loss data, caused by the FSS subsystem, refers to the complete antenna. The losses were derived by using the experimental pattern of the subreflector subassembly in the antenna analysis at

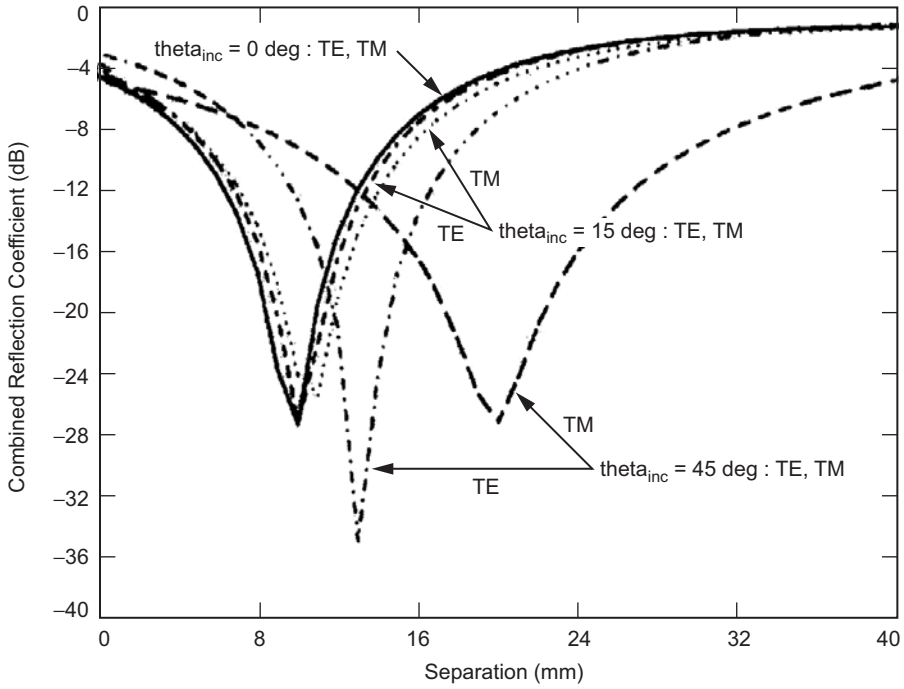

Fig. 5-42. Computed combined reflection vs. separation between Cassini S-band screen and combined X+Ku-/Ka-band screens at 0-deg, 15-deg, and 45-deg incidence angles (F = 2.298 GHz).

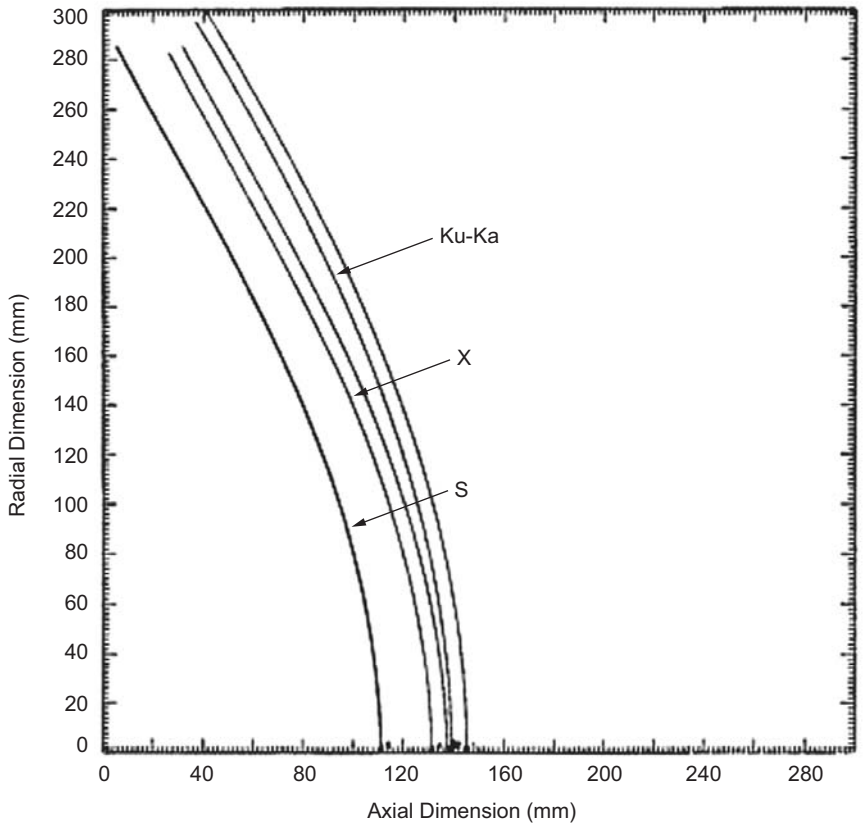

Fig. 5-43. Cassini subreflector profile (front and back layers for X-band and Ku-/Ka-band).

the secondary level. The ohmic losses were evaluated by pattern integration. The discrepancy between the results at subsystem level with regard to the tests at antenna level were consistent with the measurement accuracy.

FSS verification at cryogenic temperature (<–180 deg C) was conducted using innovative-waveguide [51] and free-space radiation [42] test methods that allowed the setup calibration and the relative measurement with respect to ideal samples in the thermal-vacuum environment. Figure 5-45(a) shows a schematic of the radiation setup.

Tests were performed using an ellipsoidal subreflector to produce a locally plane wave front to minimize the reflections from the environment. The radiating feed was placed at one of the foci. A specially designed rotating turret allowed a metallic plate and the FSS sample to be positioned at the other focus. Switching from the metallic to the FSS sample could be done at the measurement temperature since the entire assembly was placed within the thermal vacuum chamber. Considering the relative phase length between the

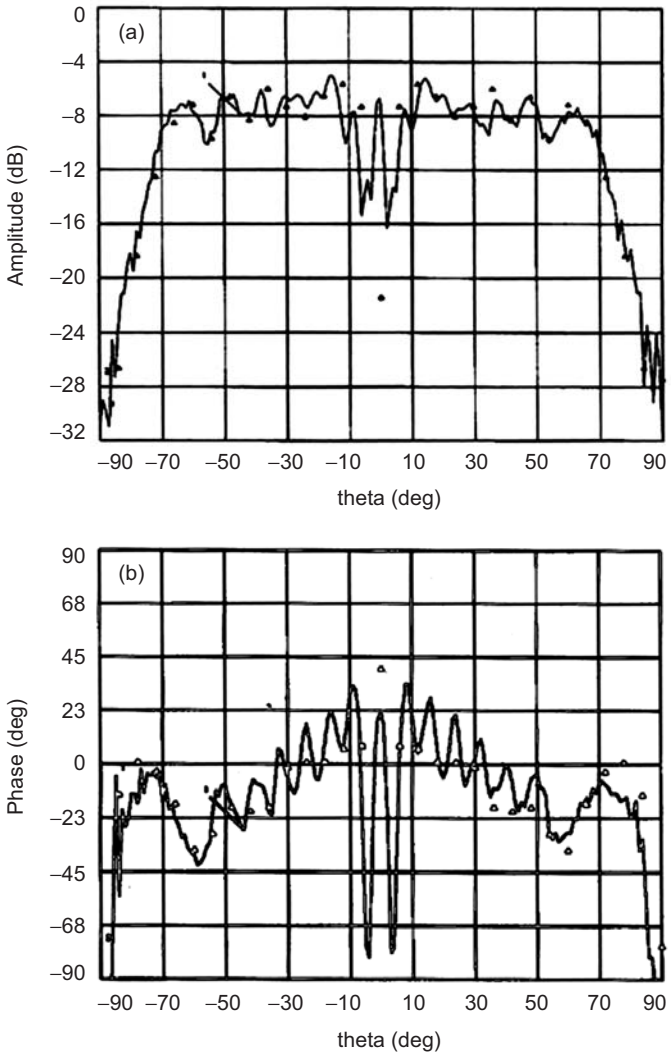

Fig. 5-44. Cassini computed (lines) vs. measured (dots) patterns at X-band of FSS subreflector cascade for (a) amplitude and (b) phase.

sample and the feed, time gating could be efficiently used to improve the measurement accuracy.

The experimental radiation setup is shown in Fig. 5-45(b). Results show a reduction in the ohmic loss of the substrate material and a decrease in the resistivity of the metallic resonant elements. The loss reduction can be explained by both a reduction in the loss tangent of the sandwich material (Kevlar and glue) and to an increased conductivity of the metals used as resonating elements.

Table 5-13. Measured Cassini FSS cascade performance relative to ideal subreflector(s).

Frequency (GHz)	At Subsystem Level		On Antenna Level	Discrepancy (dB)
	Ohmic + T/R* Loss (dB)	A & φ Loss (dB)	Total Loss (dB)	
2.040	0.26	0.14	0.5	+0.10
2.298	0.16	0.0	0.2	+0.04
7.175	0.51	0.08	0.8	+0.21
8.425	0.23	0.16	0.6	+0.11
13.7765	0.65	-	0.6	–0.05
32.028	0.55	-	0.6	+0.05
34.316	0.89	-	0.8	–0.1

*T/R transmission/reflection

This causes a marked improvement in the overall performance of the FSS at operative temperature (–200 deg C). Figure 5-46 shows the results of the radiated test on flat-panel samples (X + Ku/Ka FSS) at ambient and –180 deg C. The reduction in the loss of the FSS (–0.4 dB), with respect to the metallic reference at –180 deg C, is clearly visible.

This loss reduction is particularly evident at X-band, where the double passage through the K-band screen is experienced. At the highest frequencies (Ku- and Ka-bands) that involved only the first screen, the loss reduction is less (0.2 dB to 0.1 dB, respectively). The FSS structure was also seen to be reasonably stable in response to variation in the material and element tolerances.

5.3.3.2 The Triple-Band Feed. The triple-band feed is a dual-depth corrugated horn operating in dual circular polarization at X- and Ka-band and in linear polarization at Ku-band. The feed provides a Gaussian-like primary pattern for the generation of on-axis pencil beams at X-, Ku-, and Ka-bands [52]. The feed aperture is limited by the feed arrays of the Ku-band fan beams (see next section). The internal layout of the feed is shown in Fig. 5-47(a).

Tapered and suitably designed dual-depth corrugated sections of circular waveguides compose the main transmission line. X- and Ku-band signals are introduced at appropriate cross-sections of this line by a set of four transverse slot-coupled rectangular branch waveguides. The four branches are symmetrically arranged on the circumference of the line, thus permitting any state of polarization to be achieved through a suitable external network. Ka-band is end-launched into the line while the other end gradually flares into a dual-depth corrugated horn.

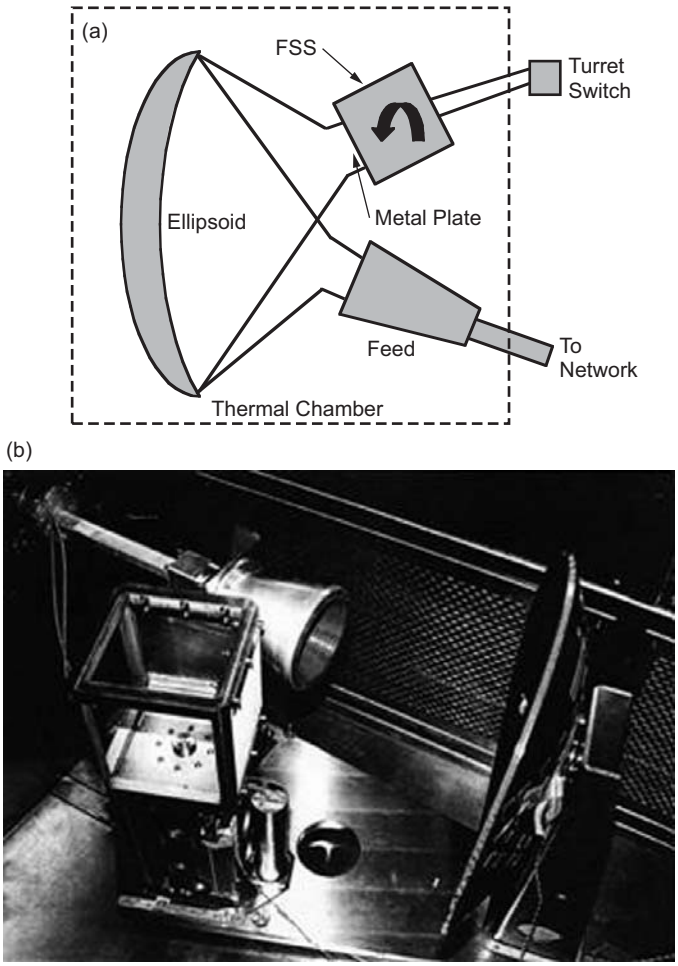

Fig. 5-45. Cassini FSS samples radiation set-up: (a) schematic and (b) photograph.

To achieve optimum simultaneous performance in three widely separated bands important design considerations are:

1) Suitable dual-depth corrugations to meet balanced hybrid boundary conditions simultaneously for Ka-, Ku-, and X-bands.
2) Radial line chokes in the X- and Ku-band transducers to isolate Ka-band as well as to minimize overmoding in the main transmission line at Ka-band.
3) Tapered sections to provide appropriate phasing of the signals at the X- and Ku-band transducers, as required for optimum coupling.
4) Independent tuning parameters in the form of step discontinuities in the rectangular branch waveguides of the X- and Ku-band transducers.

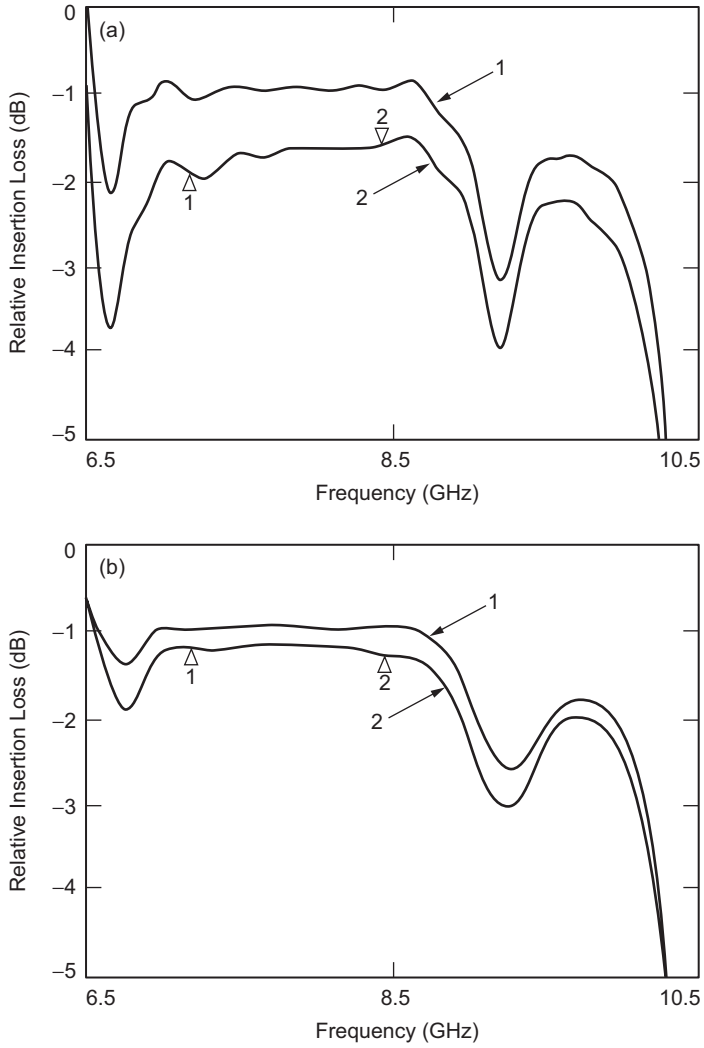

Fig. 5-46. Cassini FSS radiated test showing differential insertion loss at X-band: (a) ambient temperature and (b) at −180 deg C. Trace 1: metallic sample; Trace 2: FSS sample.

Analysis of the entire feed was done by following proper segmentation and cascading procedures. Efficient and accurate moment-method codes were used to compute the generalized scattering matrices of the segmented discontinuity modules, which were then connected in tandem by the cascading procedure to obtain the final scattering response of the integrated feed system. Radiation patterns were computed from the modal field amplitudes at the feed aperture after accounting for the fringe currents on external feed geometry whenever appropriate [52].

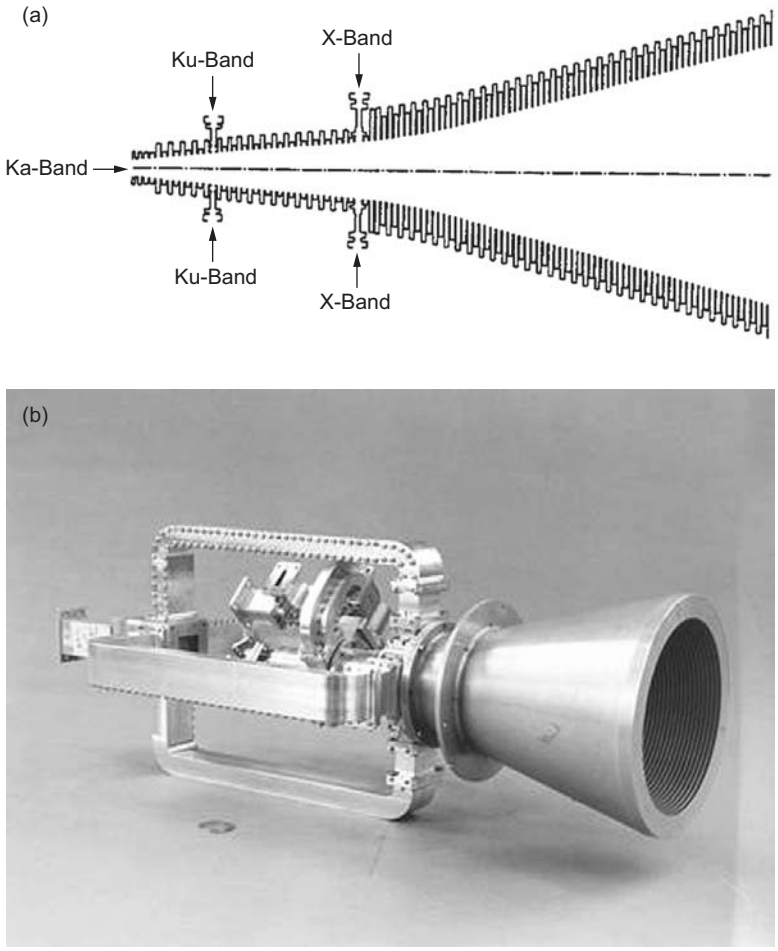

Fig. 5-47. Cassini X-/Ku-/Ka-band self-diplexed feed system (a) schematic view and (b) engineering breadboard model.

The complete feed breadboard model is shown in Fig. 5-47(b). The external microwave network at X-band consists of a septum polarizer in cascade with a radial four-port orthomode transducer (OMT). The four output arms of the OMT are connected to the four branches of the X-band feed diplexer. The Ku-band network required a 0–180-deg feeding hybrid, which was achieved by configuring a 3-dB (H-type) branch guide coupler in cascade with a 90-deg stub-type phase shifter. Ka-band dual circular polarization was achieved at the end-launched feed interface by adding an appropriate polarizer. The hardware selected for the external microwave networks guaranteed the minimum envelope in combination with the lowest insertion loss at the three bands. The feed electrical characteristics were evaluated using test setups calibrated with a

Hewlett Packard HP8510 automatic vector network analyzer for the return loss and RF isolation characteristics, and a well-equipped near- and far-field anechoic chamber for the radiation pattern measurements.

The feed exhibited high diplexing capability (>40 dB). An excellent agreement between experimental and computed RF performance was found, as illustrated in Fig. 5-48, where the primary patterns are shown.

5.3.3.3 Ku-Band Fan-Beam Subsystem. The four fan beams are generated by 20 shunt-slot subarrays grouped into 4 feed arrays each containing 5 subarrays. Each subarray was axially moved toward the subreflector in order to optimize gain and minimize scan aberrations at the element-beam level. The staircase arrangement of the slot subarrays can be seen in Figs. 5-49(a) and (b), which show the entire feed subassembly, including the triple band feed of the flight model (FM) unit and the standalone slot array on the support prior to its integration.

The 20 identical subarrays consist of five waveguides of two slots each [53]. Each waveguide is series slot fed at the center of the waveguide. In order to maximize the overlap among the adjacent element beams, a uniform distribution was synthesized along the H-plane while a Chebycheff 30-dB level sidelobe was specified along the E-plane for a minimum primary spillover and optimum far-out sidelobe level.

The subarray synthesis was carried out by using an accurate modal analysis code [54]. A detailed experimental/theoretical iteration was necessary in order to converge toward the desired sidelobe level. Corrections to the feed slot geometry were achieved with the aid of a self-impedance chart of the feeding network slot. The radiation pattern performance of the subarray was evaluated taking into account the edge effects through a geometrical theory of diffraction (GTD) model of the planar array.

Subarray performance in the feed array environment could be altered by mutual coupling and scattering among adjacent elements. Considering the aperture dimension and the relative staircase arrangement, this latter factor was recognized to be very important. In particular, a first-order impact arises from the adjacent front displaced subarray since it is in the direct radiation field of view of the back subarray. Therefore, a GTD model of this geometry was simulated. Since the subarrays had different axial displacements, this analysis was repeated for each subarray.

In Fig. 5-50, a comparison of one typical experimental pattern is overlaid on the computed one. These primary patterns were used in the fan-beam synthesis. Regarding the beam-forming network behind each feed array, a compact layout was realized by corporate feeding of the five subarrays using an integrated 10-port divider of branch-guide type to minimize mass and losses. The pattern synthesis was based on an accurate software modeling analysis; and therefore, no experimental tuning was required [55].

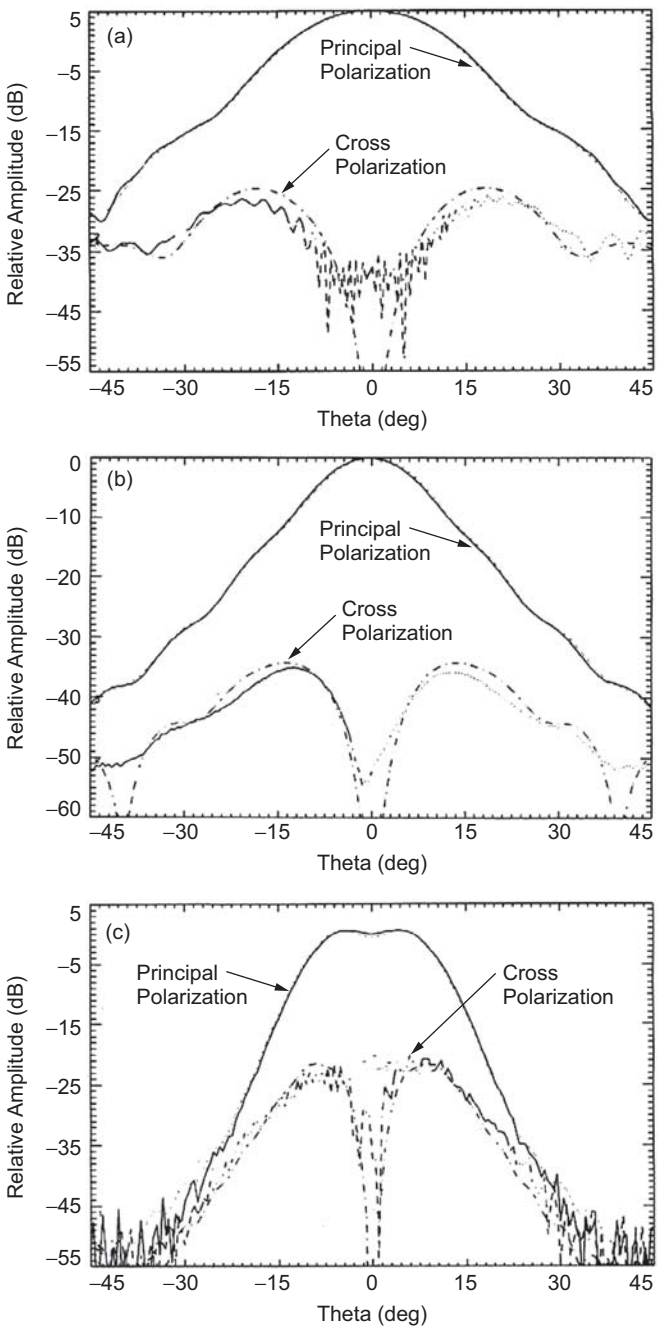

Fig. 5-48. Cassini computed (dotted line) vs. measured (continuous line) radiation patterns: (a) 8.425 GHz, (b) 13.8 GHz, and (c) 32.0 GHz.

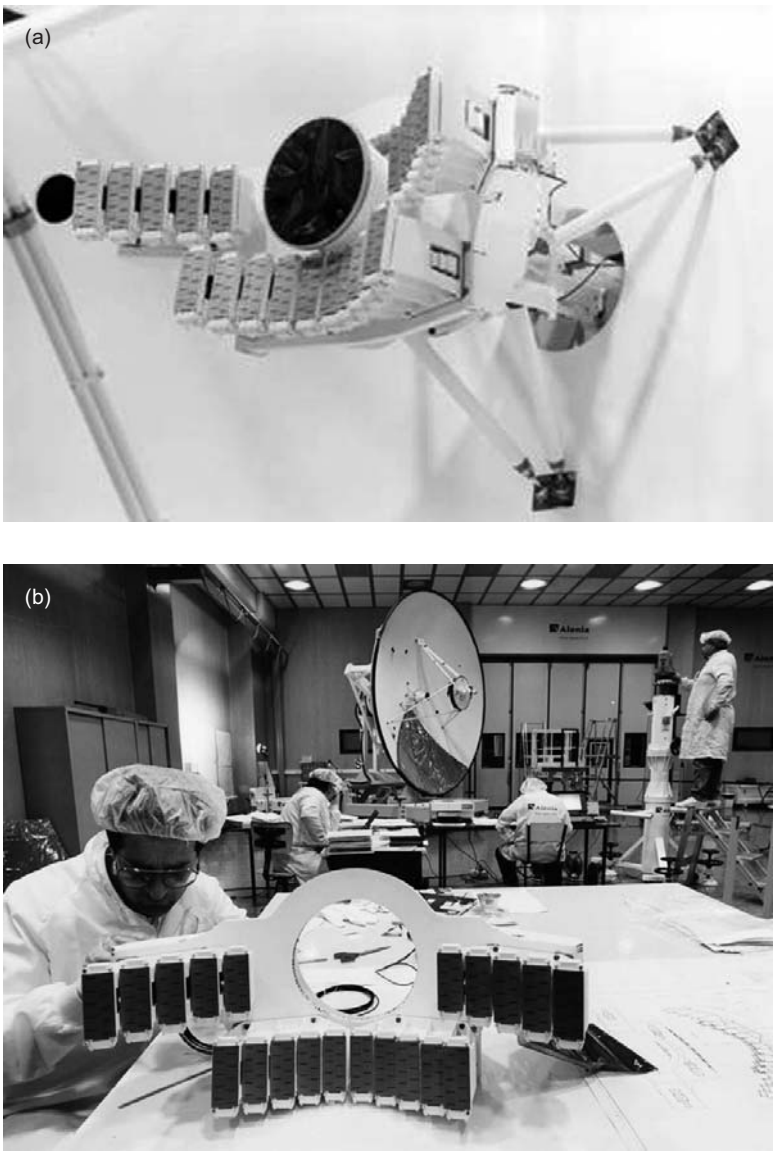

Fig. 5-49. Cassini feed system: (a) complete X-/Ku-/Ka-band feed system in the Cassegrain focal plane and (b) details of the Ku-band slot feed arrays.

5.3.3.4 S-Band Feed. The S-band feed was designed to provide a secant-squared radiation pattern in order to enhance the antenna efficiency for the short focal-length design [56]. The feed is a coaxial horn with a cylindrical waveguide and two external parasitic rings (Fig. 5-51(a)). The feed network and

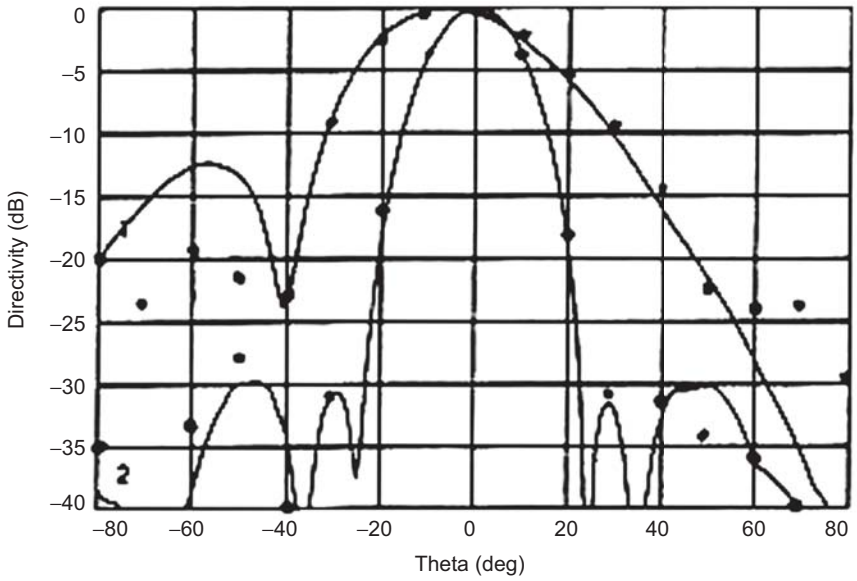

Fig. 5-50. Cassini Ku-band sub-array pattern in the feed-array environment (center element of B1/B5). E-, H-planes: ── experimental ● theoretical.

probes were made using bar-line technology (see Fig. 5-51(b)). Radiation pattern performance at the radio science frequency is shown in Fig. 5-52.

5.3.3.5 Low-Gain Antenna 1. LGA1 consists of a cylindrical waveguide with several external corrugations shaped and profiled to minimize back radiation. In Fig. 5-53, several options are illustrated. The selected configuration is shown in Fig. 5-54. The LGA1 pattern measure on the FM HGA–LGA1 antenna assembly, installed on the top of the FSS deck, for maximum coverage extension, is shown in Fig. 5-55.

5.3.4 Antenna Performance at S-Band

The S-band feed is in a prime focus configuration and has a relatively wide bandwidth. Computer modeling at feed-subreflector level showed that in order to maximize the gain throughout the bandwidth, the back FSS screen needed a thickness that varied according to incidence angle; however, variability in thickness has not been implemented in this configuration. Additionally, the parasitic coaxial feed was band-limited because, in the selected design, priority was assigned to the radio science frequency (2.3 GHz). The optimum design at 2.3 GHz was confirmed by differential on-axis gain measurements (with and without FSS), which exhibited an overall loss of about 0.2 dB at 2.3 GHz and 0.5 dB at 2.040 GHz.

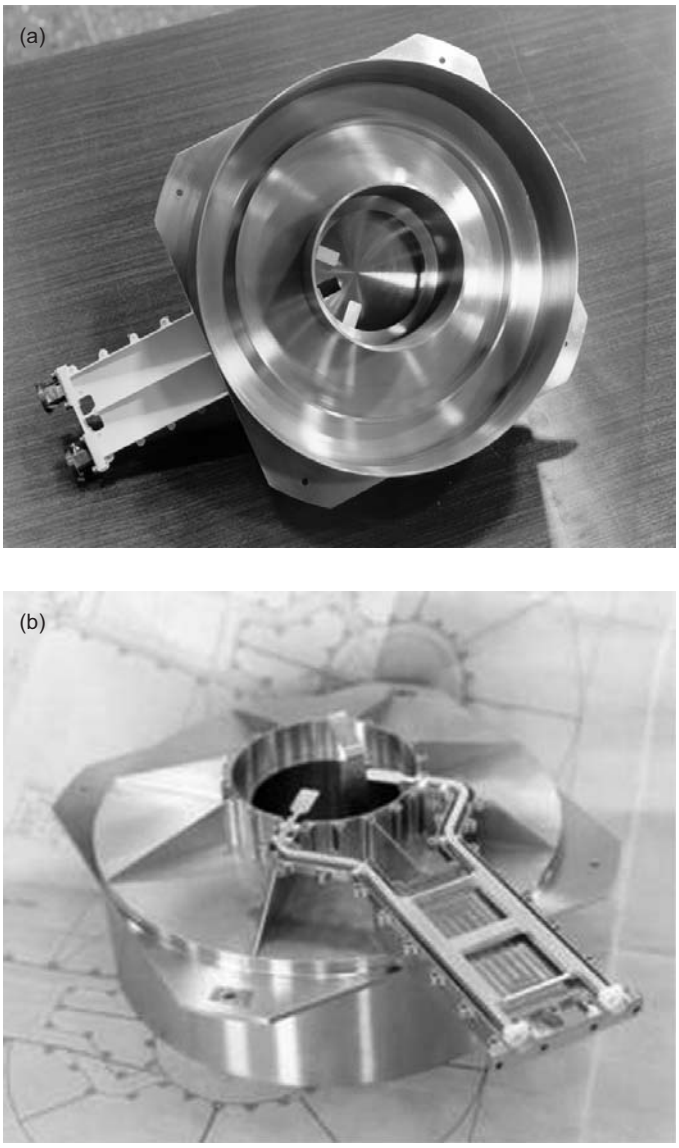

Fig. 5-51. Cassini S-band feed aperture and feeding network (a) front view and (b) rear view.

Measurements of the FM unit showed a peak gain at radio science frequency of 36.3 dBi ±0.3 dB, which corresponds to an overall antenna efficiency of 46.2 percent. At the lowest frequency, the measured peak gain was 35.0 dBi ±0.3 dB (which corresponds to an antenna efficiency of 43.1 percent).

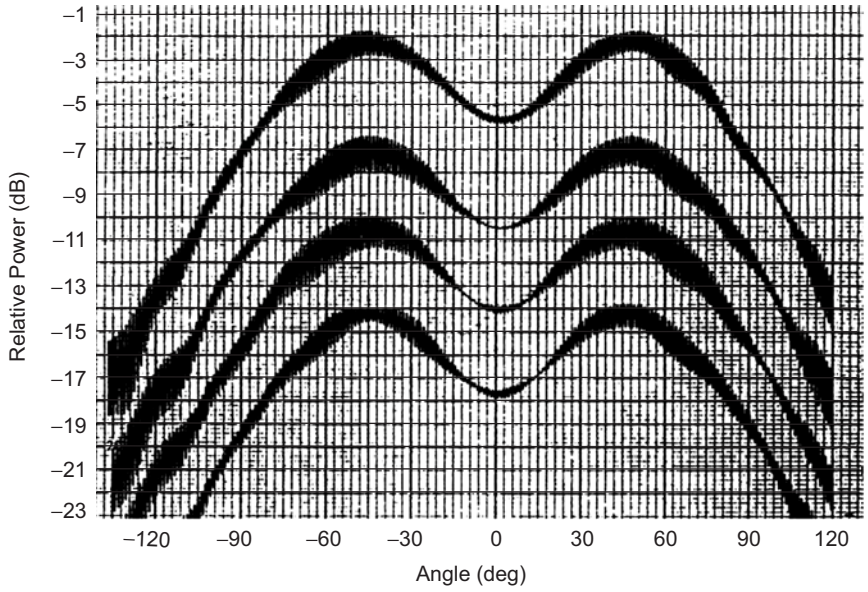

Fig. 5-52. Cassini S-band feed radiation pattern at 2298 MHz (spinning linear, four Ludwig cuts at 90 deg).

The measured antenna performance on the FM unit at 2.298 GHz (Fig. 5-56(a)) compares well with the computed pattern (Fig. 5-56(b)). Although the 2.04–2.1 GHz spectrum was not so favorable with respect to the science mission (at 2.3 GHz), excellent RF performance in terms of gain and polarization discrimination (>20 dB) have been measured on orbit at this frequency also.

5.3.5 Antenna Performance at X-Band

The requirement for multiple-frequency operation heavily constrained X-band performance, not allowing gain maximization. X-band efficiency was limited by the parabolic main reflector profile in combination with the limited feed aperture of the triple-band feed. Furthermore, a double passage through the Ku-/Ka-front screen occurred on the FSS. It was believed that if the antenna were designed to support only X-band and S-band, as for Voyager, a dual-shaped system in combination with a larger feed aperture would be able to provide a gain improvement on the order of 0.6 dB.

Additionally, a single screen FSS could be implemented in this case, producing a net improvement on the order of 0.4 dB compared with the then-current X-band design, which exhibited an overall gain loss of 0.65 dB at downlink, taking into account the double passage and the (lossy) white paint on the Ku-/Ka-band screen.

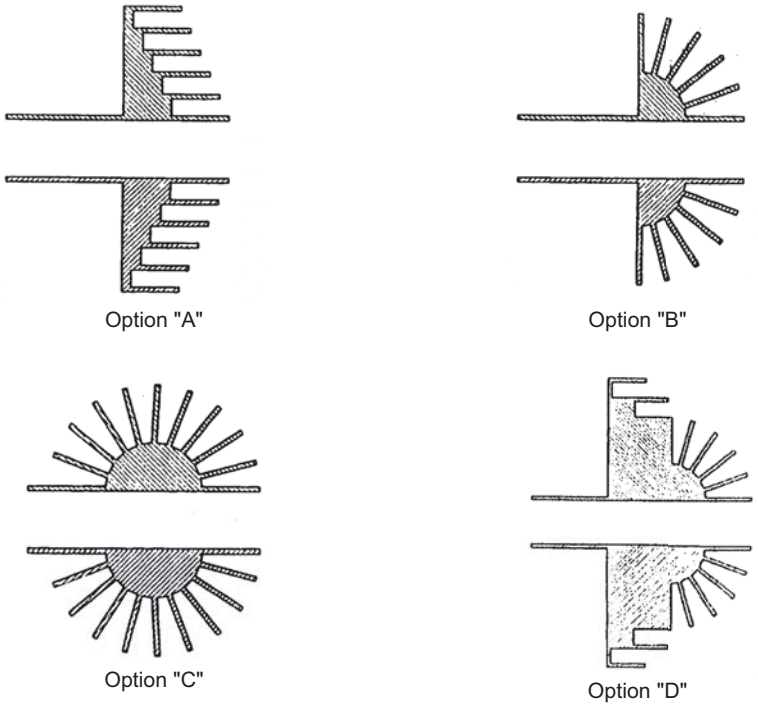

Fig. 5-53. Cassini LGA1 viable layouts.

Measurements of the FM unit showed a peak gain at a downlink frequency of 47.2 dBi ±0.3 dB (which corresponds to an overall antenna efficiency of 42.1 percent). At the uplink frequency, the measured peak gain was 45.3 dBi ±0.3 dB (which corresponds to an antenna efficiency of 37.6 percent).

A very good correlation of the computed antenna patterns with the measured patterns was obtained, as can be seen in Figs. 5-57(a) and (b), which give the experimental performance on ground and the theoretical computations. The EM analysis included an accurate primary field expansion of the triple band feed in the subreflector region, the FSS scattering through the Ku-/Ka-screen, and the blockage effects due to the struts, the feeds in the Cassegrain focal plane, and the FSS deck. A polarization discrimination better than 33 dB was also measured on orbit at the Goldstone tracking station.

5.3.6 Antenna Performance at Ku-Band

The on-axis beam efficiency of the pencil beam (B3) was limited by the integrated triple-band feed design (defocusing and non-optimum taper at subreflector edge caused a peak gain loss of 0.4 dB). Measurements of the FM unit showed a peak gain at center frequency of 50.75 dBi ±0.3 dB (which corresponds to an overall antenna efficiency of 35.6 percent).

Fig. 5-54. Cassini LGA1 engineering breadboard model.

The measured on-orbit antenna performance of the FM unit (Fig. 5-58(a)) compares well with respect to the pattern measured on ground (Fig. 5-58(b)) and the computed (Fig. 5-58(c)), demonstrating the soundness of the thermo-mechanical design.

The design of the SAR beams was based on beam contouring using a focal-fed multifeed system. The secondary pattern synthesis was carried out modeling the spherical wave component of the blockage with a null-field approach, which was then applied to each subarray. Accordingly, the projected shadowing on the antenna aperture was different for each subarray.

In order to obtain an adequate definition of the shadow boundaries, the main reflector aperture was divided into 17,762 elementary patches. The plane-wave component of the struts blockage was considered too.

Software successfully modeled the FSS subreflector as well, at analysis level. In Figs. 5-59 and 5-60, there is remarkable agreement between the measured on-orbit pattern, the measured on-ground pattern, and the computed far-field pattern at the secondary level of the two fan beams. The on-orbit patterns, processed by JPL, were measured using the radiometer mode and scanning the Sun from beyond Jupiter.

The FSS differential insertion loss (with respect to a perfectly reflective surface) is close to 0.5 dB. A peak sidelobe less than 13 dB with respect to MGL was measured on each fan beam, while the integrated sidelobe ratio figures were 8.7 dB (B2/B4), 9.3 dB (B2/B4), and 6.6 dB (B3) respectively.

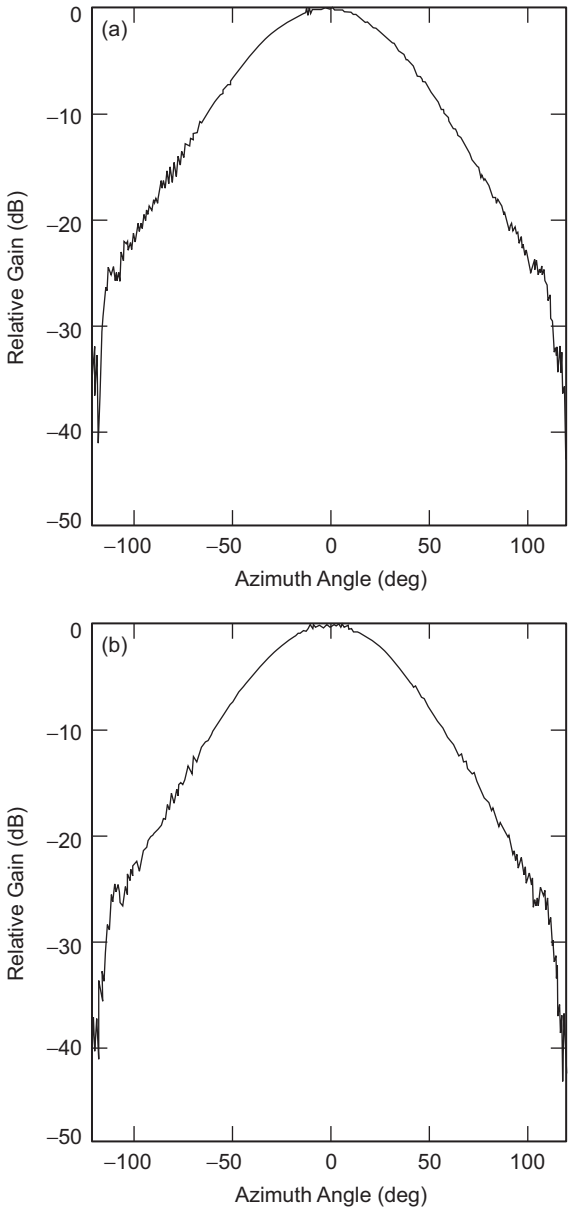

Fig. 5-55. Cassini HGA-LGA1 FM assembly. LGA1 radiation performance at (a) uplink and (b) downlink frequency.

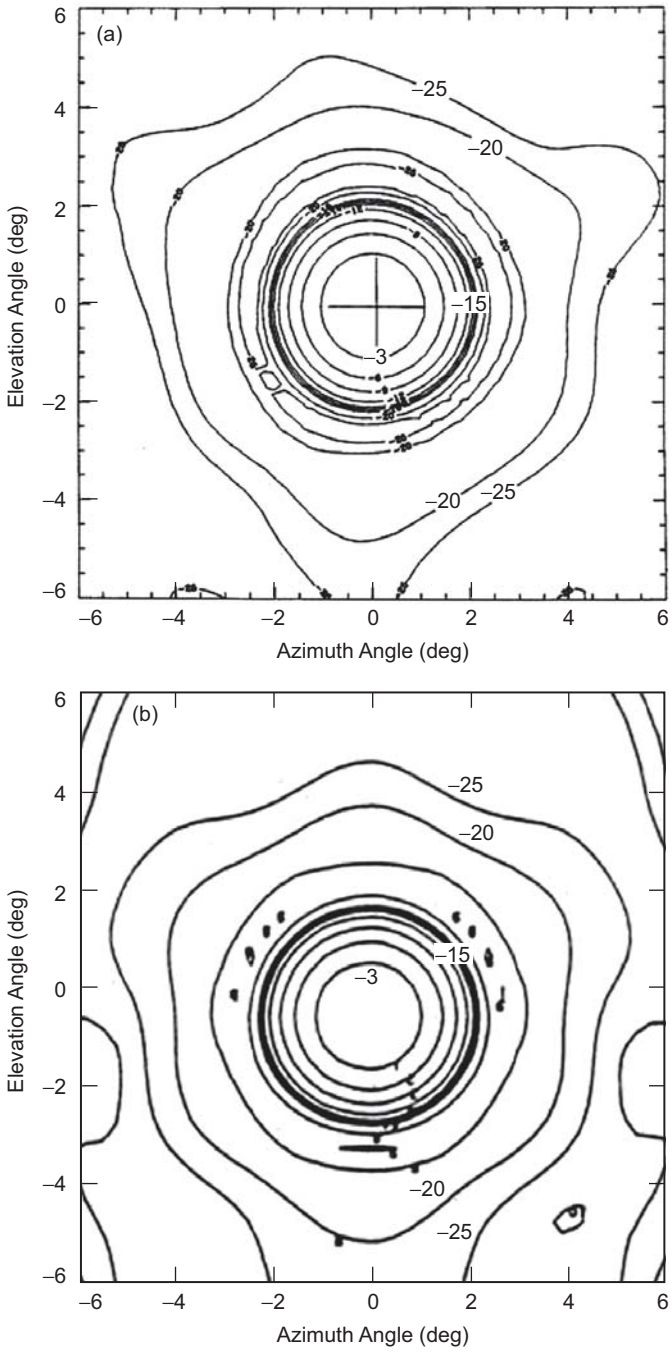

Fig. 5-56. Cassini HGA-LGA1 FM assembly of S-band radiation performance (F = 2.298 GHz): (a) measured and (b) computed.

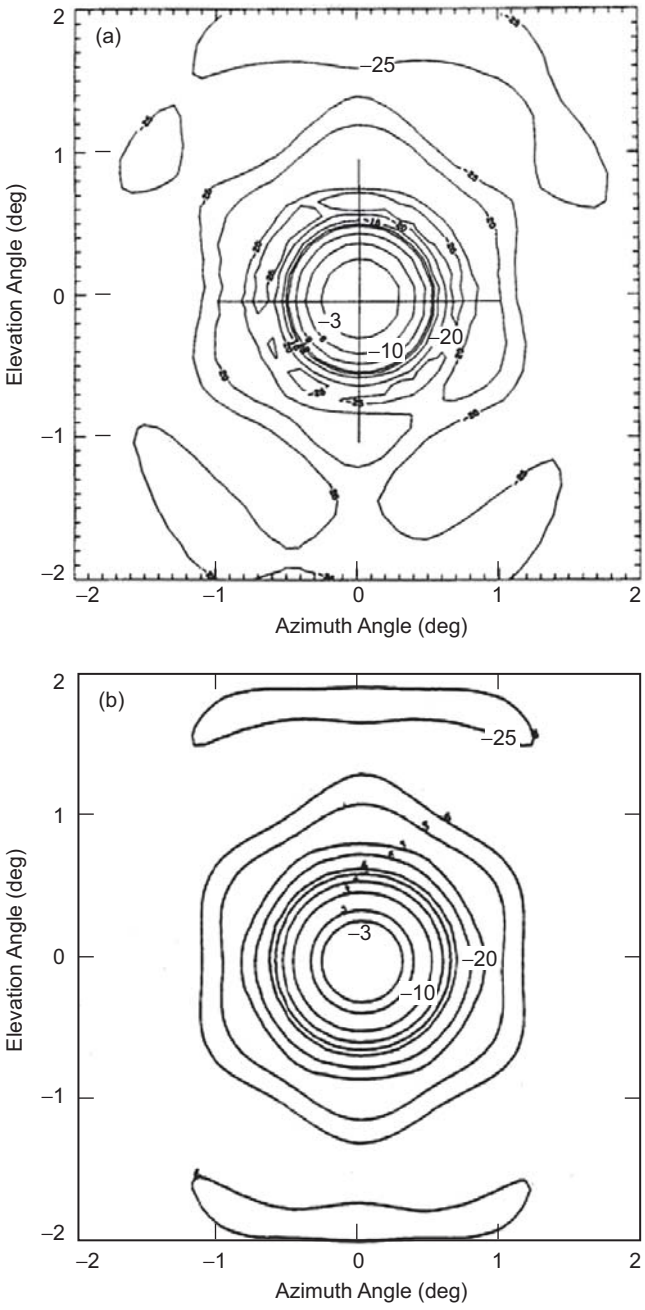

Fig. 5-57. Cassini HGA-LGA1 FM assembly X-band radiation performance (F = 8.425 GHz): (a) measured and (b) computed.

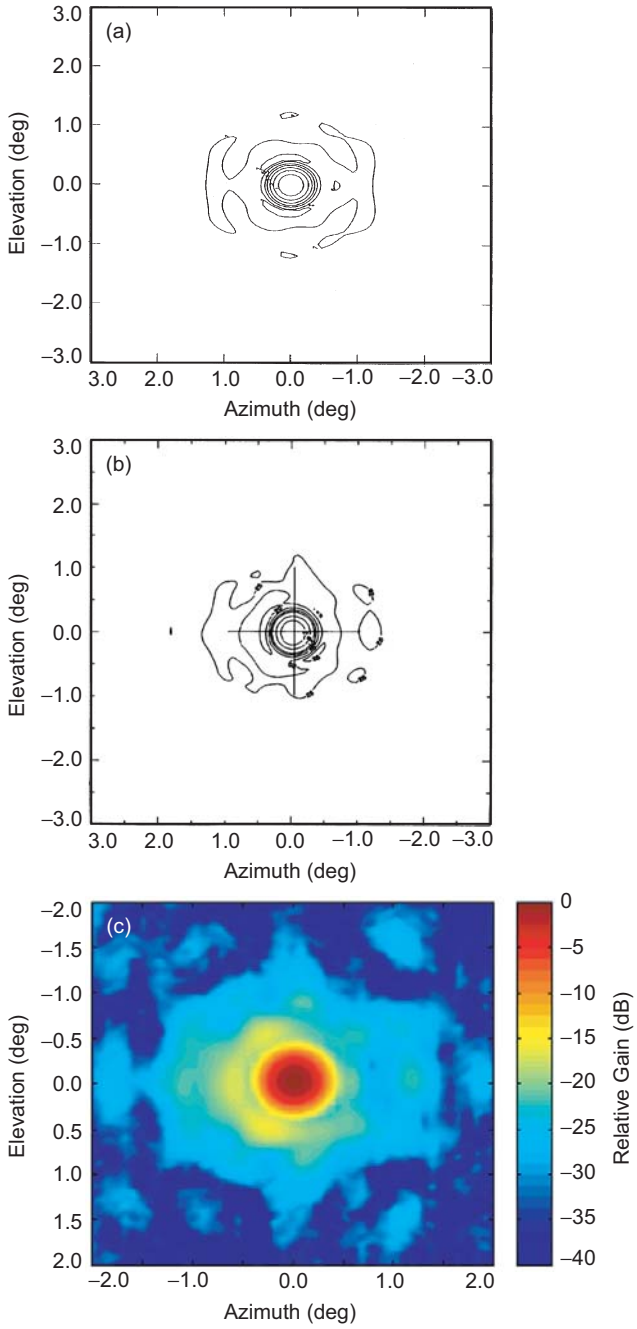

Fig. 5-58. Cassini HGA-LGA1 FM assembly B3 beam Ku-band (B3) radiation performance: (a) computed, (b) measured on ground, and (c) measured on orbit.

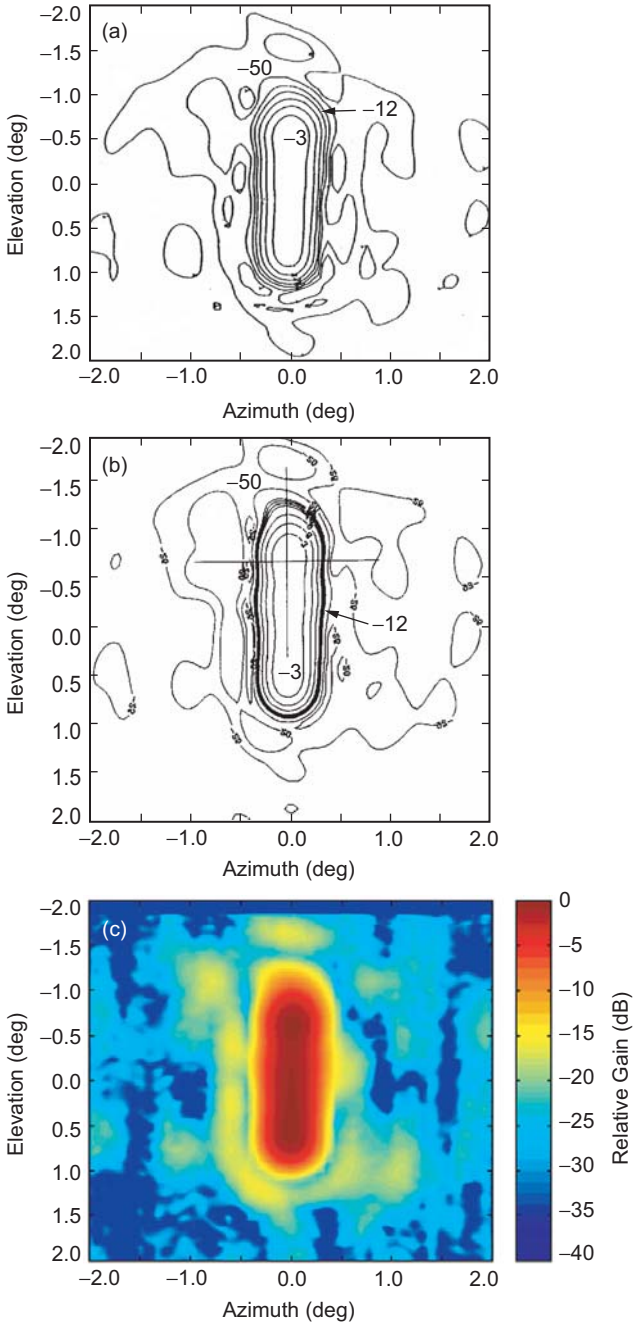

Fig. 5-59. Cassini HGA-LGA1 FM assembly B5 beam Ku-band (B3) radiation performance: (a) computed, (b) measured on ground, and (c) measured on orbit.

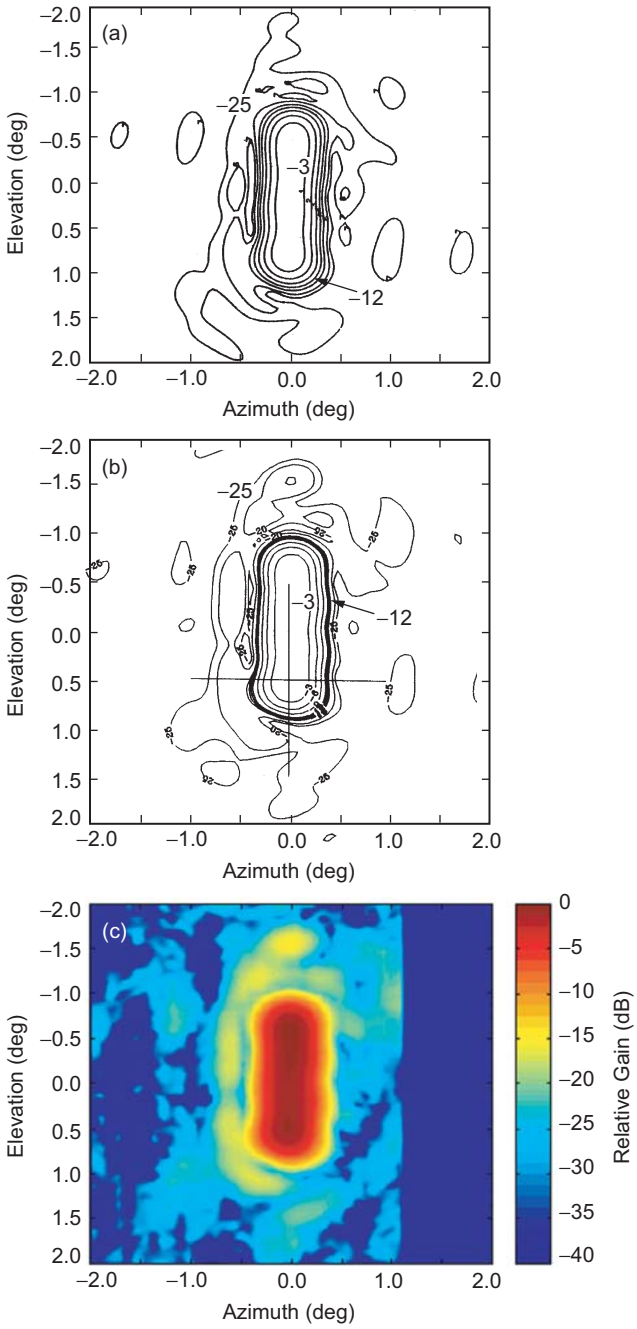

Fig. 5-60. Cassini HGA-LGA1 FM assembly B4 beam Ku-band (B3) radiation performance: (a) computed, (b) measured on ground, and (c) measured on orbit.

5.3.7 Antenna Performance at Ka-Band

Ka-band design was constrained by the parabolic main reflector profile and the hyperbolic subreflector. In the initial design, the beam broadening was achieved by defocusing the feed with respect to the optics phase center. The feed axial position was also limited by the relative interference with the Ku-band feed arrays in the focal plane and the integrated triple-band feed design. A further review of the Ka-band beamwidth requirement occurred on the FM unit, thanks to the improved spacecraft attitude control capability achieved during development. This led to reconsidering a narrower beamwidth of 0.19 deg ±0.02 deg, instead of the nominal 0.23 deg ±0.02 deg. This ultimate beam narrowing, which had a negligible impact on the other bands, was implemented through a slight axial translation of the FSS subreflector.

The final RF performance was successfully modeled (including all the blockage effects, the FSS subreflector, and an accurate reconstruction of the primary field of the triple-band feed in the near field) by means of a spherical-wave harmonics expansion. Figure 5-61 shows a typical agreement between the measured pattern at secondary level and the computed result. To achieve such a correlation, the real main reflector surface was included in the model, based on about two thousand experimental data points measured with an accurate three-dimension (3D) machine.

Figure 5-62 shows the measured downlink pattern of the FM antenna unit after the final subreflector adjustment. The measured peak gain was 56.7 dBi ±0.5 dB; this low antenna efficiency (26 percent) was caused by the desired beam broadening.

5.3.8 Conclusions

The design and performance of the Cassini multifrequency antenna has been presented. Performance estimates were validated by accurate software, able to adequately model such a complex electromagnetic environment.

In particular, modeling was successfully performed for a four-frequency-band FSS subreflector; a complex triple-band feed, and the severe scattering mechanisms due to slot arrays and struts inside the reflector (including additional blocking structures like the FSS deck).

Performance was verified using a full-scale electrical model. The agreement between the computed and the experimental results was satisfactory, confirming the validity of the assumptions. The results on the flight model (FM) unit and the correlation with the on-orbit data, demonstrated full compliance with the requirements and the validity of the electrical and thermo-mechanical design.

To date (October 2005), the Cassini spacecraft is operating superbly. It entered Saturn orbit on July 1, 2004, beginning a four-year tour of the ringed

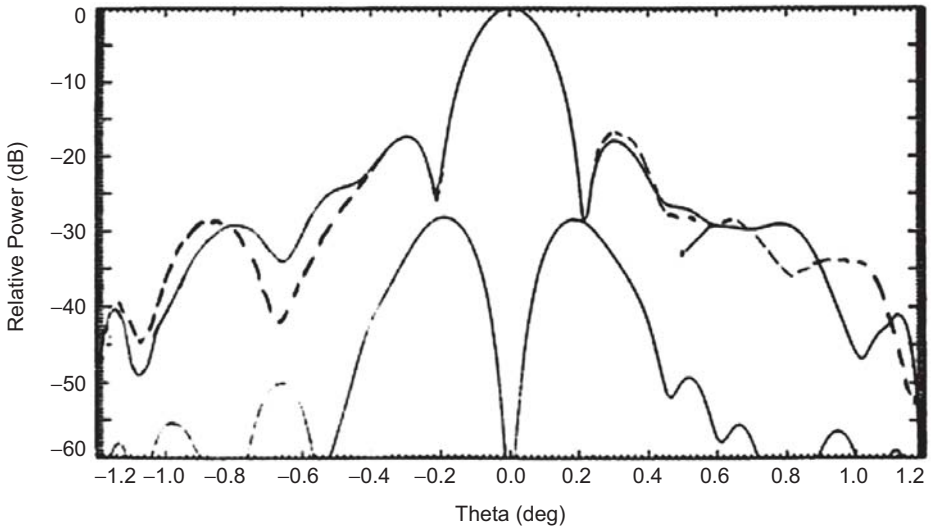

Fig. 5-61. Cassini HGA-LGA1 EBB assembly. Overlay of measured (continuous line) vs. computed (dotted line) Ka-band radiation performance at downlink (32 GHz).

planet, its mysterious moons, stunning rings, and complex magnetic environment. During the tour, Cassini will complete 74 orbits of Saturn, 44 close flybys of the mysterious moon Titan, and numerous flybys of Saturn's other icy moons. Six months after arriving at Saturn, the satellite released its piggybacked Huygens probe for descent through the thick atmosphere of Titan. The probe transmitted data from the surface of Titan.

During the transfer orbit cruise, the antenna subsystem was used several times. In particular, during the two Venus flybys, which occurred in April 1998 and June 1999, the antenna was used as thermal shield for the spacecraft. It reached a temperature of +180 deg C without any failure (in fact, all the RF subsystems operated perfectly).

By combining the multiple-frequency HGA capability with other sophisticated equipment, Cassini began its achievements even before it arrived at Saturn. One important achievement occurred in December 2000, during Cassini's passage close to Jupiter. The scientific community took advantage of Cassini's proximity to the planet by pointing its radiometer towards Jupiter, to measure cosmic synchrotron radiation, which is caused by the high-speed electrons accelerated by the intense magnetic field of the planet. The results were featured in *Nature* [57].

Additionally, Jupiter, our Solar System's most massive planet, was captured in the most detailed global color view ever seen, courtesy of NASA's high-resolution camera. Cassini acquired the views during its closest approach to the gas giant while en route to its final destination.

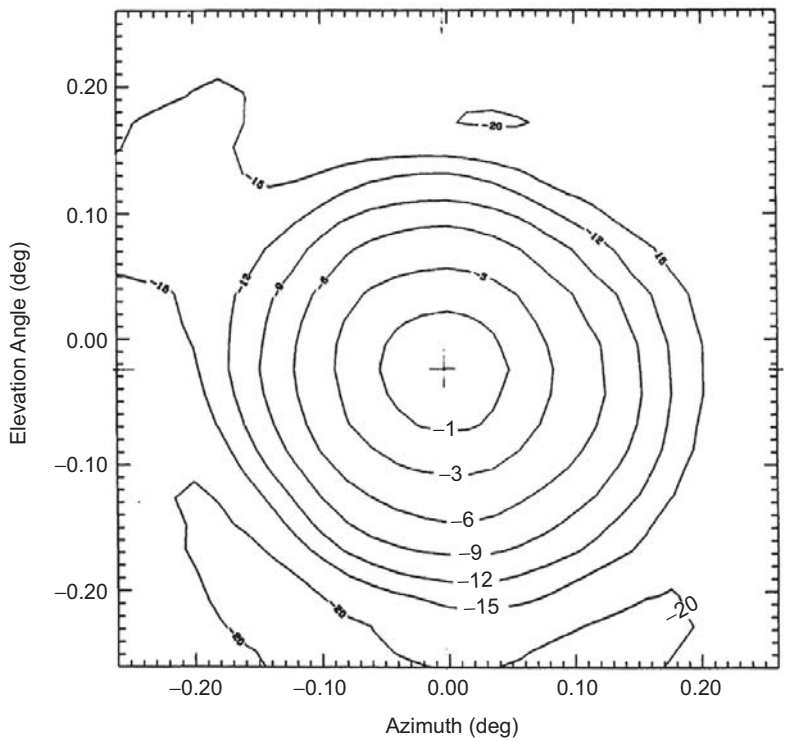

Fig. 5-62. Cassini HGA-LGA1 FM assembly measured Ka-band downlink radiation performance (after ultimate beam narrowing).

Further, a recent experiment by Italian scientists using data from Cassini, confirmed Einstein's theory of general relativity with a precision 50 times greater than that of previous measurements [58]. Past tests of general relativity had confirmed Einstein's prediction to an accuracy of one part per thousand. This accuracy was achieved in 1979 using the Viking landers on Mars. The Cassini experiment confirmed it to an accuracy of 20 parts per million.

The experiment could not have been conducted to this level of accuracy in the past because of noise on the radio link introduced by the solar corona. With the Cassini experiment, this hindrance was overcome by equipping the spacecraft communications system with multiple links at different frequencies. This new capability on the spacecraft and on the 34-m (112-ft.) diameter antenna at Goldstone allowed scientists to remove the effects of the interplanetary and solar plasma from the radio data. In addition, the noise from Earth's atmosphere was strongly reduced by a water vapor radiometer-based calibration system installed at the Goldstone complex.

References

[1] *Magellan Mission to Venus*, web site at Jet Propulsion Laboratory, Pasadena, California, accessed July 18, 2005. http://www2.jpl.nasa.gov/magellan

[2] "Synthetic Aperture Radar," *Wikipedia* web site, accessed July 18, 2005. http://en.wikipedia.org/wiki/Synthetic_aperture_radar

[3] *Venus Radar Mapper HGA-LGA Incremental Review*, Martin Marietta, Denver, Colorado, October 29, 1985.

[4] *Venus Radar Mapper Spacecraft Medium Gain Antenna PDR*, VRM-RA-004-014, Martin Marietta, Denver, Colorado, June 1985.

[5] *Venus Radar Mapper Altimeter Antenna Design Description*, DRD No. SE 014, Hughes Aircraft Company, Los Angeles, California, February 1984.

[6] J. Taylor, K.-M. Cheung, and D. Seo, *Galileo Telecommunications*, Article 5, The Deep Space Communications and Navigation Systems Center of Excellence (DESCANSO) Design and Performance Summary Series, Jet Propulsion Laboratory, Pasadena, California, July 2002 (also available at web site, accessed July 18, 2005). http://descanso.jpl.nasa.gov/DPSummary/Descanso5--Galileo_new.pdf

[7] A. G. Brejcha and C. A. Smith, "Telemetry Antennas for Deep Space Probes," *Proceedings, ITC/USA, The International Telemetry Conference* (Los Angeles, California, October 18–20, 1977), 77-06-6, p. 9, 1977.

[8] R. E. Freeland, *Industry Capability for Large Space Antenna Structures*, 710-12 (JPL internal document), Jet Propulsion Laboratory, Pasadena, California, May 25, 1978.

[9] J. C. Kievit, *Deployable High Gain Antenna Reflector Survey*, JPL D-32835 (JPL internal document), Jet Propulsion Laboratory, Pasadena, California, February 8, 1978.

[10] C. A. Smith, *Galileo SXA Deployable HGA Technology Industry Visit Summary Report*, JPL D-32836 (JPL internal document), Jet Propulsion Laboratory, Pasadena, California, April 5, 1978.

[11] W. A. Imbriale, "Phased Arrays for Satellites and the TDRSS Antennas," *Satellite Communication Antenna Technology, Proceedings of the Summer School University of Technology* (Eindhoven, The Netherlands, August 23–27, 1982), R. Mittra, W. A. Imbriale, and E. J. Maanders, editors, Elsevier Science Publishers, North-Holland, Amsterdam, the Netherlands, pp. 431–486, 1983.

[12] G. C. Levanas and M. R. Johnson, *High Gain Antenna Deploy Failure Extended Investigation: Final Report for the Galileo Mission*, JPL D-15345 (internal document), Jet Propulsion Laboratory, Pasadena, California, December 31, 1997

[13] M. R. Johnson, "The Galileo High Gain Antenna Deployment Anomaly," *The 28th Aerospace Mechanisms Symposium* (Lewis Research Center, Cleveland, Ohio), NASA-CP-3260, National Aeronautics and Space Administration, Washington District of Columbia, pp. 359–377, May 1, 1994.

[14] R. Gounley and E. Nilsen, "The Galileo High-Gain Antenna Anomaly: An Overview of the Recovery Efforts," *Third International Symposium on Space Mission Operations and Ground Data Systems* (Greenbelt, Maryland, November 14–18, 1994), Technical Report 94-0227, Jet Propulsion Laboratory, Pasadena, California, 1994.

[15] J. L. Statman, L. J. Deutsch, P. E. Beyer, D. E. Hardi, and R. L. Ticker, "Galileo Telecom Link and its Application to Future Missions," *47th International Astronautical Congress* (Beijing, China, October 7–11, 1996), IAF Paper 96-Q50, International Astronautical Federation, Paris, France.

[16] "Galileo Mission to Jupiter," *NASA Facts*, web page, Jet Propulsion Laboratory, Pasadena, California, accessed September 9, 2005.
http://www.jpl.nasa.gov/news/fact_sheets/galileo0309.pdf

[17] *Galileo Orbiter Functional Requirements Book*, JPL Document 625-205, *Functional Requirement for Galileo Orbiter Flight Equipment S/X-Band Antenna Subsystem*, GLL-4-2017, Rev E (one document in the set of internal documents), Jet Propulsion Laboratory, Pasadena, California, June 9, 1989.

[18] *Design Requirement, Project Galileo Flight Equipment S/X-band Antenna Subsystem*, GLL-2017-1 Rev E (JPL internal document), Jet Propulsion Laboratory, Pasadena, California, July 21, 1981.

[19] M. Gatti, *Galileo HGA Tip Sunshade RF Measurements*, JPL D-32837 (JPL internal document), Jet Propulsion Laboratory, Pasadena, California, December 29, 1987.

[20] Y. Rahmat-Samii, *Gain Loss Estimate for the Galileo High-Gain Antenna with Disconnected Surface Contouring Cords*, JPL D-32838 (JPL internal document), Jet Propulsion Laboratory, Pasadena, California, July 18, 1984

[21] Y. Rahmat-Samii, *Preliminary Estimate for the Effects of 4-cord Removal on the Performance of the Galileo High-Gain Antenna at X-band*, JPL D-32839 (JPL internal document), Jet Propulsion Laboratory, Pasadena, California, August 15, 1984.

[22] Y. Rahmat-Samii and M. Gatti, "Far-Field Patterns of Spaceborne Antennas from Plane-Polar Near-Field Measurements," *IEEE Transactions on Antennas and Propagation*, vol. AP-33, no. 6, pp. 638–648, June 1985.

[23] M. Gatti and Y. Rahmat-Samii, "FFT Applications to Plane-Polar Near-Field Antenna Measurements," *IEEE Transactions on Antennas and Propagation*, vol. AP-36, no. 6, pp. 781–791, June 1988.

[24] D. M. Kerns, *Plane-Wave Scattering-matrix Theory of Antennas and Antenna-Antenna Interactions*, Monograph 162, U.S. Department of Commerce/National Bureau of Standards, June 1981.

[25] Y. Rahmat-Samii, V. Galindo-Israel, and R. Mittra, "A Plane-Polar Approach for Far-Field Construction from Near-Field Measurements," *IEEE Transactions on Antennas and Propagation*, vol. AP-28, pp. 216–230, March 1980.

[26] M. Gatti, *Post-Environmental Test Results of the Galileo SXA S/N 002*, JPL D-32840 (JPL internal document), Jet Propulsion Laboratory, Pasadena, California, August 14, 1985.

[27] M. Gatti, *Galileo LGA Far Field Testing–S/N 002*, JPL D-32841 (JPL internal document), Jet Propulsion Laboratory, Pasadena, California, August 30, 1985.

[28] M. S. Gatti and D. J. Nybakken, "A Circularly Polarized Crossed Drooping Dipole Antenna," *Proceedings of the Joint Antennas and Propagation and Microwave Theory and Techniques International Symposium, and URSI Radio Science Meeting,* IEEE, pp. 254–257, May 7–11, 1990.

[29] H. Jasik, *Antenna Engineering Handbook*, First Ed., McGraw-Hill, New York, New York, pp. 31-23 to 31-25, 1961.

[30] M. Gatti, *LGA2 Engineering Model Test Data*, JPL D-32842 (JPL internal document), Jet Propulsion Laboratory, Pasadena, California, November 2, 1987.

[31] M. Gatti, *LGA2 Engineering Model Test Data–Uplink Frequency 2115 MHz*, JPL D-32843 (JPL internal document), Jet Propulsion Laboratory, Pasadena, California, January 27, 1988.

[32] "Galileo End of Mission Status," web page, Jet propulsion Laboratory, Pasadena, California, September 17, 2003, site accessed August 30, 2005. http://www2.jpl.nasa.gov.galileo/news/release/press030921.html

[33] E. H. Maize, "The Cassini-Huygens Mission to Saturn and Titan," *Space Technology and Applications International Forum—STAIF 2005*, vol. AIP Conference Proceedings 746, American Institute of Physics, Melville, New York, pp. 223–231, 2005.

[34] R. Mizzoni, "The Cassini High Gain Antenna (HGA): A Survey on Electrical Requirements, Design and Performance," *IEE Seminar on Spacecraft Antennas*, Institution of Electrical Engineers, London, England, pp. 6/1–6/10, May 9, 1994.

[35] V. Galindo, "Design of Dual Reflector Antenna with Arbitrary Phase and Amplitude Distribution," *IEEE Transactions on Antennas and Propagation*, vol. AP-12, p. 403, 1964.

[36] W. F. Williams, "High Efficiency Antenna Reflector," *Microwave Journal*, vol. 8, no. 7 p. 79, 1965.

[37] P. J. Wood, "Reflector Profiles for Pencil Beam Cassegrain Antenna," *Marconi Review*, vol. 34, no. 182, p. 121, 1972.

[38] Y. Rahmat-Samii, "Subreflector Extension for Improved Efficiencies in Cassegrain Antenna GTD/PO Analysis," *IEEE Transactions on Antennas and Propagation*, vol. AP-34, p. 1266, 1986.

[39] P. J. Wood, *Reflector Antenna Analysis and Design*, 1980, Peter Peregrims LTD, London, England.

[40] P. J. B. Clarricoats and G. T. Poulton, "High-Efficiency Microwave Reflector Antennas–A Review," *Proceeding of the IEEE*, vol. 65, no. 10, pp. 1470–1504, October 1977.

[41] D.-W. Duan, Y. Rahmat-Samii, "A Generalized Diffraction Synthesis Technique for High Performance Reflector Antennas," *IEEE Transactions on Antennas and Propagation*, vol. 43, pp. 27–40, January 1995.

[42] HGA R.F. Team (approved by R. Mizzoni), HGA-LGA1 *Electrical Design Report, Cassini Program*, Alenia Spazio, Rome, Italy, May 7, 1995.

[43] W. V. T. Rush, O. Sorensen, and J. W. M. Baars, "Radiation Cones from Feed-Support Struts of Symmetrical Paraboloidal Antenna," *IEEE Transactions on Antennas and Propagation*, vol. AP-30, no. 4, pp. 786–790, 1982.

[44] Y. C. Chang, H. V. Morrison, and R. C. Rudduck "A Hybrid Approach for the Strut Analysis of Reflector Antennas," *1986 IEEE AP-S Symposium*, Philadelphia, Pennsylvania, pp. 523–526, 1986.

[45] S. Maci, R. Mizzoni, E. Pelaca, R. Tiberio, and A. Toccafondi, "An Investigation on Blockage Effects in the Multiband Reflector Antenna for Cassini Spacecraft," *3rd ESA European Workshop* (Pisa, Italy), October 26–28, 1993.

[46] A. Toccafondi, B. Romani, R. Mizzoni, S. Maci, and R. Tiberio, "Spherical Wave Blockage in Reflector Antennas," *IEEE Transactions on Antennas and Propagation*, vol. 45, no. 5, pp. 851–857, May 1997.

[47] D. Bresciani and S. Contu, "Scattering Analysis of Dichroic Sub-Reflectors," *Electromagnetics*, vol. 5, no. 4, pp. 375–407, 1985.

[48] D. Bresciani, "A Unified Approach to the Characterization of Frequency and Polarization Selective Surfaces," *Proceedings of the IEEE-AP Symposium*, Ann Arbor, Michigan, pp. 1960–1963, 1993.

[49] G. Mascolo, S. Contu, R. Mizzoni, and S. Borchi, "A Double Dichroic Sub-Reflector Reflective at X, Ku, Ka Bands and Transparent at S-Band," *8 Journèes Internationales de Nice sur les Antennes Jina 94*, November 8–10 Nice, France, 1994.

[50] C. Bruno, S. Contu, D. Marzi, and G. Mascolo, "Design, Manufacturing and Testing of a Ku/Ka Dichroic Sub-Reflector for Space Communications," *Antennas and Propagation, Proceedings of the 8th International Conference on Antenna and Propagation* (Edinburgh, United Kingdom), Oxford University Press, Oxford, United Kingdom, pp. 178–181, March 1993.

[51] G. Mascolo and R. Flamini, "Dielectric Constant Measurements of Dielectric Substrates at Cryogenic Temperatures," *Antennas and Propagation Society International Symposium 1995 Digest* (June 1995, Newport Beach, California), vol. 4, pp. 1848–1851, 1995.

[52] K. Mahadevan, S. Ghosh, R. Mizzoni, and G. Martirano "Precision Analysis and Design of a Triple Band Feed for the High Gain Antenna of Cassini Deep Space Mission to Saturn," to appear in *JINA 94*, November 8–10, 2005, Nice, France.

[53] G. Martirano, R. Mizzoni, M. Lori, and A. Spizzichino, "The Ku-Band sub-System of the Cassini High Gain Antenna (HGA)," presented at *Progress in Electromagnetic Research (PIERS 94)*, Noordwijk, Netherlands, July 11–15, 1994.

[54] N. C. Albertsen, *Electromagnetic Modelling for Multi-Beam Slotted Waveguide Array Antennas, Final Report*, Ticra Report S-498-02, Ticra Engineering Consultants, Copenhagen, Denmark, 1992.

[55] F. Alessandri, G. Bartolucci, and R. Sorrentino, "Admittance-Matrix Formulation of Waveguide Discontinuity Problems, Application to the

Design of Branch-Guide Couplers," *IEEE Transactions on Microwave Theory and Techniques*, vol. MTT-36, pp. 394–403, February 1988.

[56] G. F. Koch, "Coaxial Feeds for High Aperture Efficiency and Low Spillover of Paraboloidal Reflector Antennas," *IEEE Transactions on Antennas and Propagation*, AP-21 no. 2, pp. 164–169, March 1973.

[57] T. W. Hill, "Magnetic Moments at Jupiter," *Nature*, vol. 415, no. 6875, pp. 965–966, February 28, 2002.

[58] B. Bertotti, L. Less, and P. Tortora, "A Test of General Relativity Using Radio Links with the Cassini Spacecraft," *Nature*, vol. 25, no. 6956, pp. 374–376, September 25, 2003.

Chapter 6
Spaceborne SAR Antennas for Earth Science

Yunjin Kim and Rolando L. Jordan

6.1 Introduction

Before the development of the first synthetic aperture radar (SAR) antenna flown in space, Jet Propulsion Laboratory (JPL) was involved in an aircraft radar program to image the Earth surface for various science applications. This radar was flown on a Convair CV-990 aircraft with the antenna attached to one of the baggage doors of the airplane. The antenna was a planar array with eight radiating elements operating at 1215 MHz and had dual-polarization capability. This system was important because it provided SAR data to prove that SAR could image ocean waves giving both the direction of wave propagation and its wavelength. These observations led to the incorporation of SAR on the Seasat spacecraft that was the first radar used to make science observations from space [1]. The development of the Seasat antenna was significant because of the unique challenges that its development required. The antenna area required was significantly larger that other similar antennas built for aircraft systems. In addition, the antenna was required to operate in a vacuum over a wide temperature range without its surface deforming significantly from out of plane, and the mass of the antenna was limited to less than 100 kg. A picture of the Seasat-A system is shown in Fig. 6-1.

Ball Aerospace developed both engineering and flight models of the Seasat antenna. The engineering model was used to verify the performance of the antenna, and the flight model was flown on the Seasat platform. Following the success of the Seasat SAR system, the first of the Shuttle Imaging Radar (SIR)

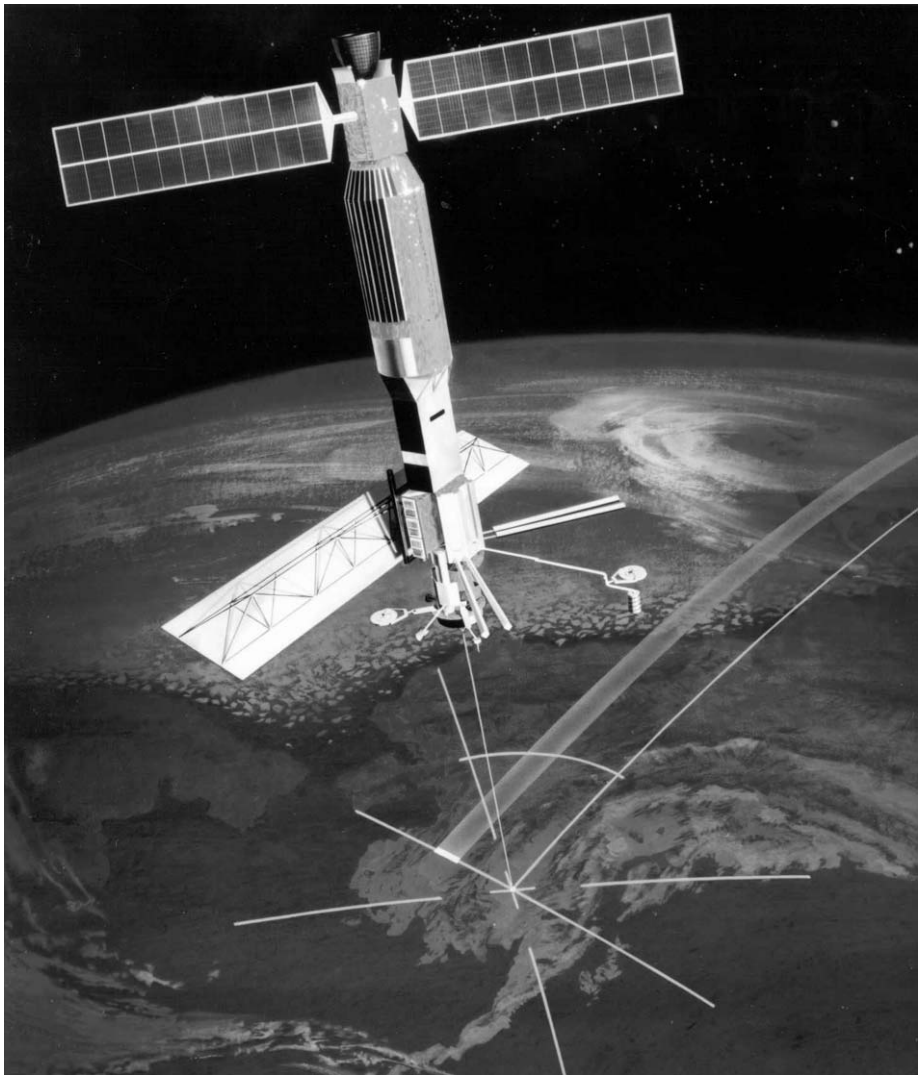

Fig. 6-1. Seasat synthetic aperture radar. The Seasat antenna is the large deployed structure near the bottom of the spacecraft.

systems, SIR-A, was flown in the Shuttle in 1981. This radar used the leftover hardware from Seasat. In particular, the antenna system used seven Seasat engineering model panels. This antenna was again flown on the Shuttle as part of the SIR-B radar instrument [2].

The SIR-C was launched on the Space Shuttle Endeavour for two 10-day missions in the spring and fall of 1994 [3]. During these two missions, radar data from more than 300 sites around the Earth were collected to investigate the

use of fully polarimetric, multi-frequency SAR to understand global environmental changes. The SIR-C antenna represents major advances in radar technology to obtain fully polarimetric SAR data from space [4]. In order to measure the weak cross-polarization signal, the SIR-C antenna must be efficient. Using transmit/receive (T/R) modules close to radiating microstrip patches, the antenna loss is reduced, and an extremely high-power transmitter is avoided. By adding a phase shifter to each T/R module, the SIR-C antenna beam can be electronically steered. Using this capability, various advanced SAR technologies (phase beam broadening, the scan mode synthetic aperture radar (ScanSAR), and spotlight operation) were tested in space. The SIR-C antenna is the world's first civilian phase-array SAR antenna in space. The SIR-C antenna was manufactured by Ball Aerospace with close technical collaboration from JPL.

The Shuttle Radar Topography Mission (SRTM), a joint project between the United States National Imagery and Mapping Agency (NIMA) and the National Aeronautics and Space Administration (NASA), used modified hardware from the C-band radar of the SIR-C system, with a 62-m long mast and a second antenna to form a single pass interferometer [5,6] (see Fig. 6-2).

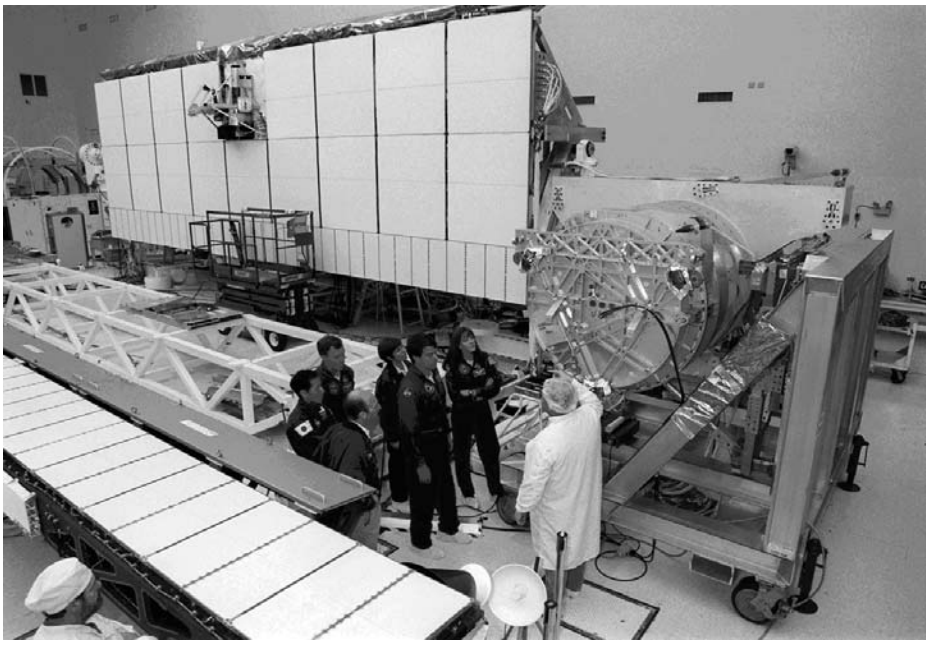

Fig. 6-2. SIR-C and SRTM phase array antennas. The SIR-C L-band (composed of larger upper panels) and C-band (smaller lower panels) phase-array antennas are shown in upper left. The SIR-C C-band antenna was used for SRTM with the outboard C-band antenna (lower left) to form a SAR interferometer.

The second antenna, known as the outboard antenna, is a receive-only phase array antenna. SRTM was the first spaceborne implementation of a single pass interferometer. It was launched in February 2000 on the Space Shuttle Endeavour. The SRTM mission acquired digital topographic data of the globe between 60 deg north and south latitudes during one 11-day Shuttle mission. The SRTM implemented the ScanSAR operation for a large swath required for the global coverage during eleven days. The major challenge of the SRTM antennas was the phase stability to form a SAR interferometer. The SRTM mission was successfully implemented, and JPL finished the processing of the global digital elevation model (DEM) data in January 2003.

Any future SAR antenna must reduce its weight and stowed volume to lower the mission cost and to enable a larger antenna required at higher orbits such as medium Earth orbit (MEO) and geosynchronous Earth orbit (GEO). Both mechanically deployable and inflatable technologies can provide a light-weight antenna structure. High efficiency, light-weight, miniaturized transmit/receive (T/R) modules are being developed for future SAR missions. These new technologies will revolutionize the future science observations. As an example, NASA formed the Solid Earth Sciences Working Group (SESWG) to formulate a scientific observational program for NASA in the next decade [7]. The SESWG final report calls for its highest priority to be "InSAR (Interferometric SAR) everywhere, all the time" to make vector surface deformation measurements of millimeter-scale accuracy over wide areas using repeat-pass SAR interferometry. New antenna technologies are required to enable continuous observations of the Earth surface for understanding global environmental changes and mitigating natural hazards.

6.2 Characteristics of Spaceborne Earth Science SAR Antennas

We start this section with the basic principles of SAR to provide SAR antenna design requirements. A conventional SAR is a two-dimensional imaging instrument that uses the time delay and the Doppler information to achieve the desired range and azimuth resolutions [8–11]. That is, the time delay between the echoes that are back-scattered from different surface elements is used to separate them in the range (cross-track) direction, and the Doppler information is used to separate surface pixels in the azimuth (along-track) direction.

First, we discuss the antenna size requirement. The antenna width (W) is determined by the illuminated swath size. The swath size can be specified by the minimum ($\theta_L^{\min}$) and the maximum ($\theta_L^{\max}$) look angles. The look angle is defined as the angle between the spacecraft nadir direction and the radar beam at the spacecraft. The minimum look angle is usually determined by science

applications and the ground topography to avoid the layover problem. In order to illuminate the desired swath, the cross-track beam width (θ_{BW}^{C}) satisfies

$$\theta_{BW}^{C} = \kappa_c \frac{\lambda}{W} = \theta_L^{\max} - \theta_L^{\min} \tag{6.2-1}$$

where κ_c is the broadening factor determined by the antenna tapering. The look angle should be calculated including the Earth curvature effect. Assuming that Earth is a sphere with the radius R, the actual curved swath can be calculated using Eqs. (6.2-2), (6.2-3), and (6.2-4). The angles shown in Fig. 6-3 are related by

$$\frac{\sin(\theta_L)}{\sin(\theta_I)} = \frac{R}{R+H} \tag{6.2-2}$$

where θ_I is the incidence angle and H is the platform altitude. The angle denoted by θ_E (see Fig. 6-3) is defined as

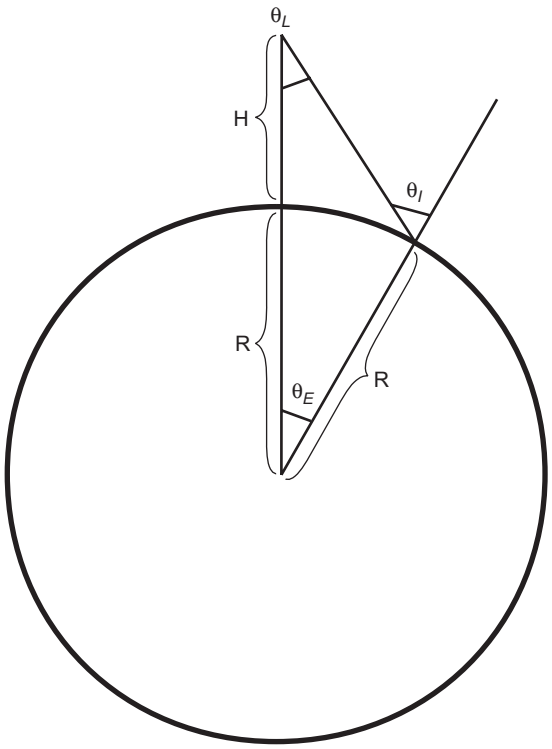

Fig. 6-3. Definition of θ_L (look angle), θ_I (incidence angle), and θ_E. The platform altitude and the Earth radius are denoted by H and R, respectively.

$$\theta_I = \theta_L + \theta_E \tag{6.2-3}$$

Then, the curved swath (S) is given by

$$S = R(\theta_E^{\max} - \theta_E^{\min}) \tag{6.2-4}$$

where the angles $\theta_E^{\min}$ and $\theta_E^{\max}$ are associated with the corresponding look angles $\theta_L^{\min}$ and $\theta_L^{\max}$. As an example, we will determine the antenna width when the platform altitude is 700 km, the desired swath is 100 km, and the minimum incidence angle is specified to be 20 deg. The Earth radius is 6378 km. For the minimum incidence angle, the minimum look angle is calculated using Eq. (6.2-2) to be 17.95 deg. Therefore, $\theta_E^{\min} = 20 - 17.95$ = 2.05 deg using Eq. (6.2-3). Then, $\theta_E^{\max}$ is calculated to be 2.95 deg by solving Eq. (6.2-4) for S = 100 km. Using Eqs. (6.2-2) and (6.2-3), the maximum look angle is 24.84 deg, and the antenna beamwidth becomes 6.89 deg. For L-band SAR with the center wavelength of 0.24 m, the antenna length must be 2 m (assuming κ_c = 1) to illuminate a 100-km swath at the altitude of 700 km.

We would like to emphasize that the antenna width can be larger than the one defined in Eq. (6.2-1) since the swath does not have to be defined by the 3-dB antenna beamwidth as long as a SAR instrument provides the adequate signal-to-noise ratio (SNR) over the entire swath. When a much larger swath is required, a ScanSAR operation can be implemented. The ScanSAR operation achieves a larger swath by moving an antenna beam electronically in a pre-determined sequence in the cross-track direction. However, this increase in the swath size causes degradation of the azimuth resolution by reducing the observation time.

The SAR azimuth resolution depends on the observation time of an imaged pixel. As a SAR instrument "sees" a pixel longer, the azimuth resolution increases. That is, the SAR synthesizes a longer antenna by observing a pixel longer to increase the resolution. The azimuth resolution (Δ_a) is given by

$$\Delta_a = L/2 \tag{6.2-5}$$

where L is the length of a SAR antenna. Equation (6.2-5) indicates that the antenna length must be smaller for better azimuth resolution. Notice also that Eq. (6.2-5) is independent of the SAR wavelength and the platform altitude. For example, if the antenna length is 14 m, the best azimuth resolution that can be accomplished is 7 m, unless a spotlight operation is implemented.

A SAR instrument is designed to transmit pulses periodically and collect the returned signals. This periodic sampling frequency is known as pulse repetition frequency (PRF). Since a SAR must sample the Doppler information

correctly without aliasing, the PRF must satisfy the Nyquist sampling requirement. This condition is given by

$$PRF \geq \frac{2V}{L} \tag{6.2-6}$$

where V is the spacecraft velocity. Due to this periodic sampling, SAR suffers two artifacts known as range and azimuth ambiguities. For a spaceborne SAR instrument, the PRF is high (>1000 Hz) since a spacecraft moves fast (7.5 km/s at low Earth orbit (LEO). Since the altitude is high and the illuminated ground area is large, many transmit pulses are in the air simultaneously. Therefore, there is a chance that several successive pulses, after being reflected from different pixels on the ground, can arrive at a SAR antenna at the same time. This artifact unique to SAR is known as the range ambiguity. In order to make sure that the range ambiguity signals are not from the half-power beamwidth (HPBW), the PRF must satisfy the condition given by

$$PRF < \frac{cW}{2\rho_m \lambda \tan(\theta_I)} \tag{6.2-7}$$

where ρ_m is the slant range between a SAR antenna and the middle point of the swath and c is the speed of light. Here, we also assume that $\kappa_c = 1$. When the condition of Eq. (6.2-7) is satisfied, the range ambiguity signal is much smaller than the desired return signal. Using Eqs. (6.2-6) and (6.2-7), a condition known as the minimum SAR antenna size can be derived as

$$LW > \frac{4V\rho_m \lambda \tan(\theta_I)}{c} \tag{6.2-8}$$

However, this condition shown in Eq. (6.2-8) is only required if the entire illuminated area (defined by the 3-dB beamwidth) is used for the SAR imaging swath. If a radar designer wants to use only part of the swath for SAR imaging, the condition shown in Eq. (6.2-8) does not have to be satisfied. Interested readers should read detailed descriptions of these SAR artifacts in [8–11].

Another condition that a SAR antenna must satisfy is that the received signal must be strong enough to provide the sufficient SNR. This condition provides the requirement on the antenna size, the antenna efficiency, the peak transmit power, and the pulse length. The condition can be derived from the radar equation given by

$$P_r = \frac{P_t G_t}{4\pi\rho^2} A_I \sigma_0 \frac{\lambda^2 G_r}{(4\pi\rho)^2} \tag{6.2-9}$$

where P_r is the radar receive power, P_t is the radar transmit power, G_t is the transmit antenna gain, ρ is the slant range, A_I is the illuminated ground area, σ_0 is the backscattering cross section, and G_r is the receive antenna gain. We explicitly show different transmit and receive antenna gains because two different antennas may be used for SAR polarimetry and SAR interferometry to be discussed later in this chapter. The illuminated ground area (A_I), under the pulse-limited condition, can be written as

$$A_I = \rho \frac{\lambda}{L} \frac{c\tau_p}{2\sin(\theta_I)} \tag{6.2-10}$$

where τ_p is the pulse length. Equation (6.2-10) is true for the pulse-limited condition where the illuminated ground (in the range direction) at any instance is limited by the pulse length instead of the antenna illuminated area. Then, the radar equation becomes

$$P_r = \frac{P_t G_t}{4\pi\rho^2} \rho \frac{\lambda}{L} \frac{c\tau_p}{2\sin(\theta_I)} \sigma_0 \frac{\lambda^2 G_r}{(4\pi\rho)^2} \tag{6.2-11}$$

The gain of a SAR antenna is related to the antenna directivity (D) as

$$G = \eta D \tag{6.2-12}$$

where η is the antenna radiation efficiency. The directivity is given by

$$D = \frac{4\pi}{\theta_r \theta_a} \approx \frac{4\pi LW}{\lambda^2} \approx \frac{4\pi A}{\lambda^2} \tag{6.2-13}$$

where θ_r and θ_a are 3-dB beamwidths in the range and azimuth directions, respectively, and A is the antenna area. From Eq. (6.2-11), in order to receive radar echoes with the sufficient SNR, the antenna area must be large, and the efficiency must be high. In addition, the peak transmit power and the pulse length are critical SAR design parameters. When a SAR instrument is designed, all four parameters (antenna area, antenna efficiency, peak transmit power, and pulse length) must be considered simultaneously to provide the sufficient SNR within available technologies. The product of the peak transmit power and the transmit gain is known as equivalent isotropically radiated power (EIRP). If the transmit power is required to be extremely high, available transmitter technologies must be considered carefully, and it is important to design the thermal management system to remove the heat properly from the radar system. Another factor to be considered for a phased-array antenna is the antenna

receiver noise figure since an excellent low-noise receiver can increase the SNR.

The antenna sidelobe is related to SAR image artifacts known as the range ambiguity and the azimuth ambiguity. As an example, the two-way antenna pattern (Φ) of a uniformly excited (no tapering) phase array is given by

$$\Phi(\theta_{RA}) = \left[\frac{\sin\left(\frac{kW}{2} \sin\theta_{RA} \right)}{\frac{kW}{2} \sin\theta_{RA}} \right]^4 \tag{6.2-14}$$

where θ_{RA} is the range angle in the cross-track direction. The range ambiguity signals can be calculated from the condition given by

$$\Delta\rho(n) = \frac{n}{2} \frac{c}{PRF} \tag{6.2-15}$$

where $\Delta\rho(n)$ is the range difference between the desired signal and the ambiguity signal, and n is a non-zero integer. For a given slant range ρ, the range ambiguity signals have the slant range defined by

$$\rho_{RA}(n) = \rho + \Delta\rho(n) \tag{6.2-16}$$

where $\rho_{RA}(n)$ is the range ambiguous slant range. For each $\rho_{RA}(n)$, the corresponding look angle can be calculated using

$$\cos(\theta_L(n)) = \frac{H^2 + \rho_{RA}^2(n) + 2RH}{2\rho_{RA}(n)(R+H)} \tag{6.2-17}$$

If the antenna is mechanically titled and the boresight is given by θ_B, the antenna angles ($\theta_A(n)$) corresponding to the ambiguities are given by

$$\theta_A(n) = \theta_L(n) - \theta_B \tag{6.2-18}$$

As an example, we consider a spaceborne platform at 800 km with an L-band (center wavelength = 0.24 m) antenna. If the antenna width is 2.5 m, and the PRF is 1350 Hz, the range ambiguities corresponding to the antenna boresight are shown in Fig. 6-4.

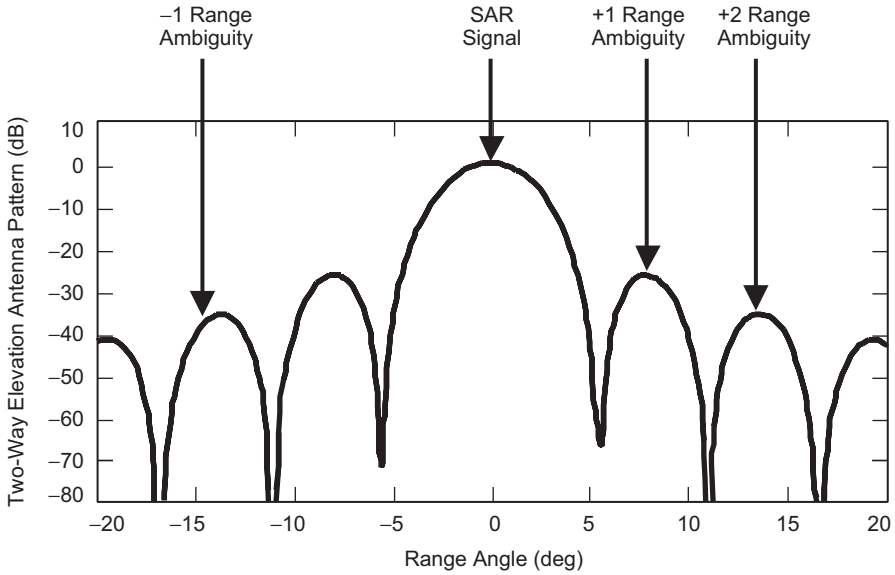

Fig. 6-4. Two-way antenna pattern with three range ambiguities. As PRF becomes lower, the range ambiguity signals move away from the antenna boresight; therefore, the overall range ambiguity is reduced. Notice that the ambiguity signals are separated by unequal angles in the range direction.

The range ambiguity ratio (*RAR*) can be calculated using

$$RAR = \frac{\sum_{n \neq 0} \frac{G_t(\theta_A(n)) G_r(\theta_A(n))}{\rho_{RA}^3(n) \sin(\theta_I(n))}}{\frac{G_t(\theta_A(0)) G_r(\theta_A(0))}{\rho^3 \sin(\theta_I)}} \tag{6.2-19}$$

Equation (6.2-19) assumes that the backscattering cross section is independent of incidence angle. From Eq. (6.2-19), it is clear that the antenna pattern must be controlled to limit the range ambiguity contamination.

The azimuth ambiguity contamination is caused by aliased signals due to a periodic sampling of Doppler information. The Doppler frequency (f_D) is given by

$$f_D = \frac{2V \sin(\theta_{AZ})}{\lambda} \tag{6.2-20}$$

where θ_{AZ} is the azimuth angle in the along track direction. The azimuth ambiguity signals can be expressed as

$$f_D \pm n \ PRF = \frac{2V \sin(\theta_{AZ}(n))}{\lambda} \tag{6.2-21}$$

where n is a non-zero integer. Since the antenna pattern is very narrow in the azimuth direction, we assume that the backscattering cross section, the slant range, and the incidence angle are constant. Under this assumption, the azimuth ambiguity ratio (*AAR*) is given by

$$AAR = \frac{\sum_{n \neq 0} \int_{PB} G_t(\theta_{AZ}(n)) G_r(\theta_{AZ}(n)) d\theta_{AZ}(n)}{\int_{PB} G_t(\theta_{AZ}(0)) G_r(\theta_{AZ}(0)) d\theta_{AZ}(0)} \tag{6.2-22}$$

where PB is the Doppler processing bandwidth.

As an example, the azimuth ambiguities of a low-Earth orbiting (orbiting velocity = 7.5 km/s) L-band SAR are shown in Fig. 6-5. The processing bandwidth identified by vertical lines is selected for the 10-m azimuth resolution. The antenna length and the PRF are 12 m and 1350 Hz, respectively. The desired Doppler signal is the area under the two-way antenna pattern over the processing bandwidth. The aliased azimuth ambiguity signals are shifted by the integer multiple of PRF.

The impulse response of a pixel in the range direction depends on the frequency transfer function of a SAR system. Therefore, the antenna frequency

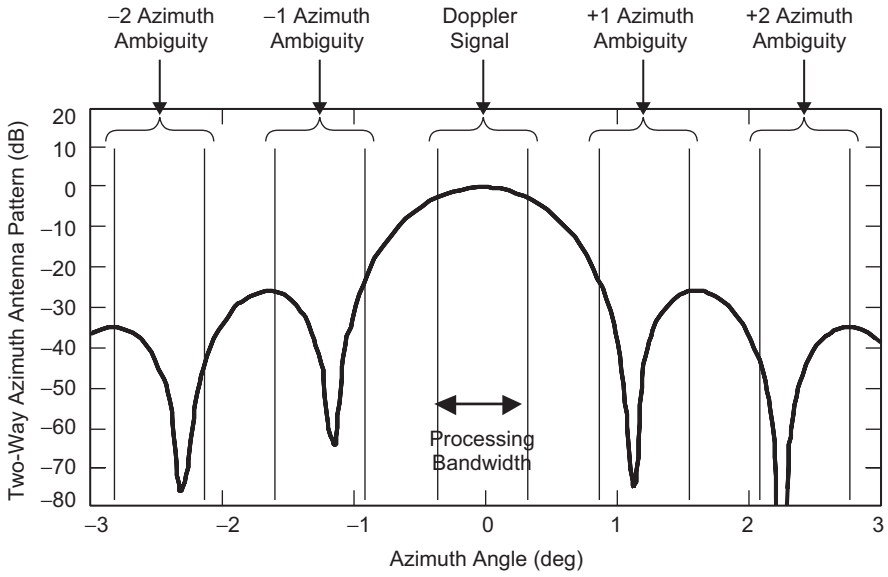

Fig. 6-5. Two-way antenna pattern with four azimuth ambiguities. As PRF increases, the azimuth ambiguities move away from the Doppler signal; therefore, the total azimuth ambiguity decreases.

response must satisfy the requirement on the integrated sidelobe level. The main product of a traditional SAR instrument is the calibrated backscattering cross section (σ_0). Since SAR measures the received power, one must derive σ_0 using the radar equation shown in Eq. (6.2-9). One of the critical components of this calibration is the antenna pattern. Therefore, the precise measurement of an antenna pattern is required before the satellite is launched. For polarimetric SAR, the cross talk between different polarization channels must be estimated and removed. A polarimetric antenna with sufficient polarization isolation will reduce the calibration burden to remove the cross talk contamination caused mainly by an antenna.

To complete the discussion on a SAR system, we provide a brief description of a SAR hardware system. A simplified radar block diagram is shown in Fig. 6-6 to illustrate the SAR hardware configuration. Received SAR signals must be coherent over the synthetic aperture length. To ensure the coherence, all radar elements are synchronized by timing signals derived from a stable local oscillator. A PRF timing signal triggers the generation of a low-frequency waveform signal. A usual waveform is a linear frequency modulation (FM) signal that is also known as a chirp signal. The bandwidth of the waveform determines the range resolution. A linear FM signal can be generated

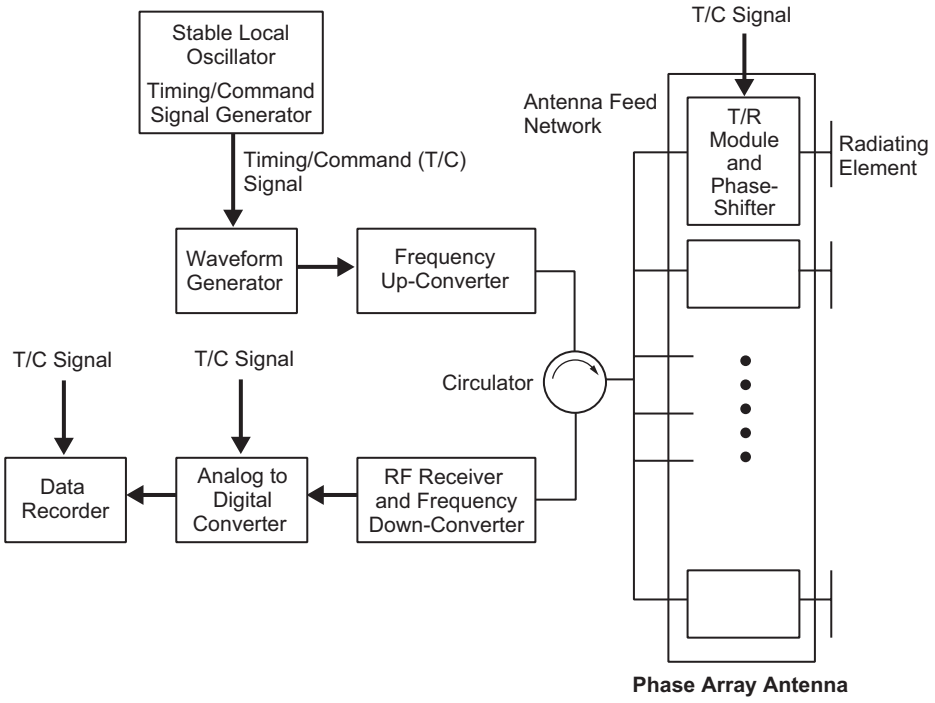

Fig. 6-6. SAR hardware block diagram including radar electronics and a phase array antenna.

using a numerically controlled oscillator (NCO). The center frequency of the waveform must be moved to the desired RF frequency using a frequency up-converter. The frequency conversion is typically performed using a mixer and a filter. An amplifier may be needed to increase the signal strength before the RF radar signal is delivered to an antenna through an antenna feed network. If the antenna contains no amplifiers, a high power transmitter such as a traveling wave tube amplifier (TWTA) is required to amplify the signal before it is delivered to the antenna. The feed network is composed of power dividers and RF cables or waveguides. For a phased-array antenna, a low-power RF signal is delivered to the antenna, and the signal is amplified and phase-shifted by transmit/receive (T/R) modules and phase shifters. This phase-shift operation is performed to send the radar signal to the desired direction. After the radar signal is reflected from the ground, the return signal is properly amplified by T/R modules. Then, the return signals are combined by the antenna feed network, and the combined signal is amplified by a low-noise amplifier (LNA). This signal is down-converted before it is digitized by an analog-to-digital converter (ADC). The digitized signal is stored at a data recorder to be processed later.

For a phased-array antenna, a T/R module is the most important element. A T/R module is composed of the control circuit, a high-power amplifier (for transmit), an LNA (for receive), and a duplexer. A duplexer can be a circulator or a T/R switch. An important factor in the T/R module design is the power efficiency (from direct current (DC) to RF conversion) and the thermal management. The receiver amplifier performance is characterized by the noise figure. A duplexer must provide the high isolation between transmit and receive paths and the insertion loss must be low. The uniformity of T/R modules is essential for producing a high gain antenna (HGA) pattern. Therefore, the root mean square (rms) amplitude and phase errors of T/R modules must be minimized. Especially, a linear phase error over the entire antenna length can cause a beam-pointing error. Since many T/R modules are required for a phased-array antenna, the cost and the weight of a T/R module is a significant design factor. The packaging and assembly of a T/R module must be simplified to produce an affordable T/R module. A typical phase shifter uses several RF switches to produce variable phase changes. For example, a four-bit phase shifter has the phase changes of 22.5, 45, 90, and 180 deg. Low insertion loss is the most important factor in selecting a phase shifter.

6.3 Seasat, SIR-A, and SIR-B Spaceborne Antennas

The Seasat SAR was the first imaging radar designed to acquire data from space to be used for scientific purposes. The Seasat satellite was a near-polar orbital platform at an 800-km altitude. The SAR instrument was designed to acquire radar backscatter data over a 100-km swath at a resolution of 25 m. The

imagery was a pictorial representation of the radar backscatter of the surface of the Earth in a map-like representation. The development of the Seasat SAR antenna was significant because it provided enabling technologies for a series of follow-on SAR systems that were flown on the Space Shuttle. Lessons learned during the Seasat SAR development phase and the analysis of the science data acquired had a large impact on the development of the later spaceborne SAR systems.

The Seasat SAR system, as shown in Fig. 6-7, includes a planar array antenna excited by 1-kW peak power transmitter. Upon reception of the return echo by the antenna, the signal was amplified by a receiver and up-converted to the downlink S-band frequency. The up-converted receiver output was then combined with timing and frequencies derived from the local oscillator for the synchronous demodulation on the ground. The data was recorded in digital format on the ground for later processing. The system was designed to acquire the 100-km swath for 10 minutes duration. This was the nominal duration for which Seasat was in view of any ground station while in orbit. The resulting data from a single pass covers an area of 4000 km by 100 km on the ground.

The Seasat SAR antenna was a 10.74-m (along-track direction) by 2.16-m (cross-track direction) planar array antenna. The antenna was composed of eight microstrip antenna panels, each 1.34 m in length and 2.16 m in width. As shown in Fig. 6-8, these panels were mounted on a composite truss structure that was deployed once in orbit. The deployed antenna was configured to fly with the long dimension along the spacecraft velocity vector, and the antenna

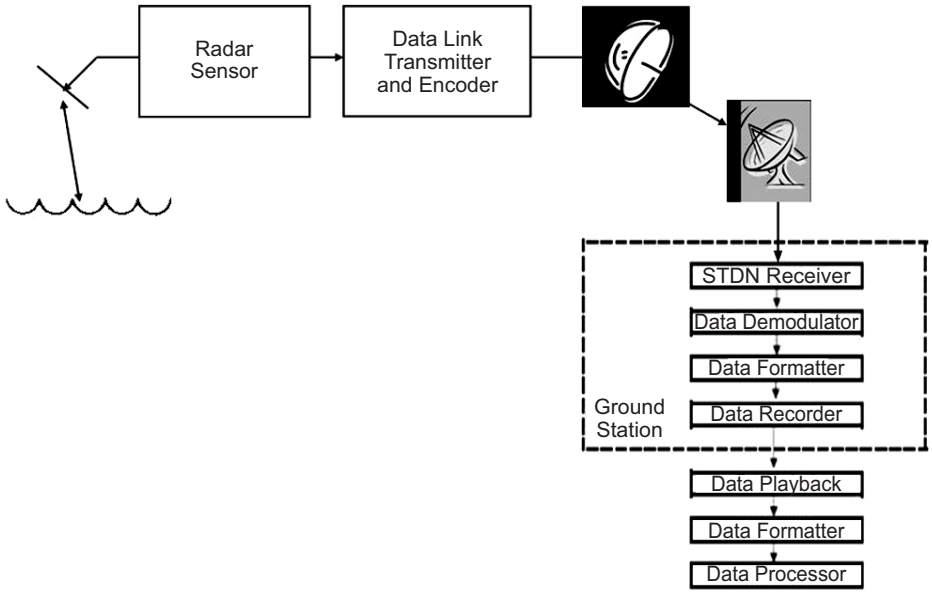

Fig. 6-7. Overall Seasat SAR operation.

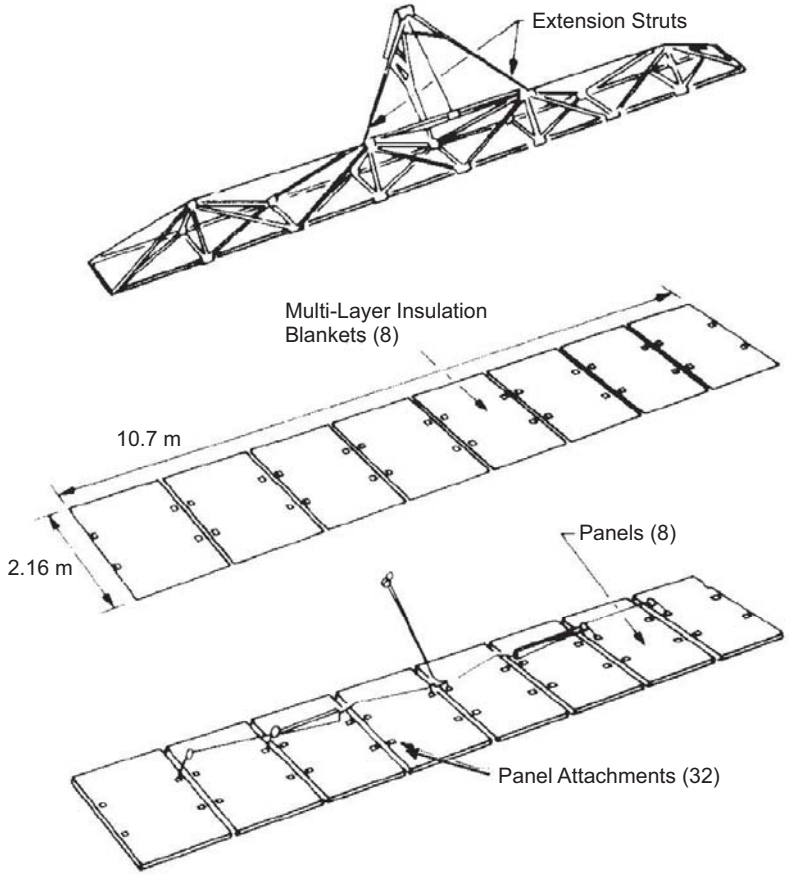

Fig. 6-8. Seasat deployment structure and eight microstrip panels. The eight panels were mounted on the composite truss structure to be deployed in space.

boresight was at a fixed angle of 20.5 deg from the nadir direction in elevation and 90 deg from the nominal spacecraft velocity vector. As discussed in Section 6.2, the antenna dimensions were set to keep the range or azimuth ambiguities to acceptably low levels. At a nominal 20.5-deg look angle from nadir, the 3-dB beam width required to illuminate the 100-km swath from an 800-km altitude is 6.2 deg. Therefore, the antenna width is 2.16 m. The swath starts from a distance of 240 km from the local nadir on the ground and ends at the far range of 340 km from this nadir point.

To form a coherent antenna beam, eight microstrip panels were fed from a coaxial corporate feed network. The construction of the microstrip panel is depicted in Fig. 6-9, and the overall antenna performance parameters are shown in Table 6-1. A significant factor in the development of this antenna was the

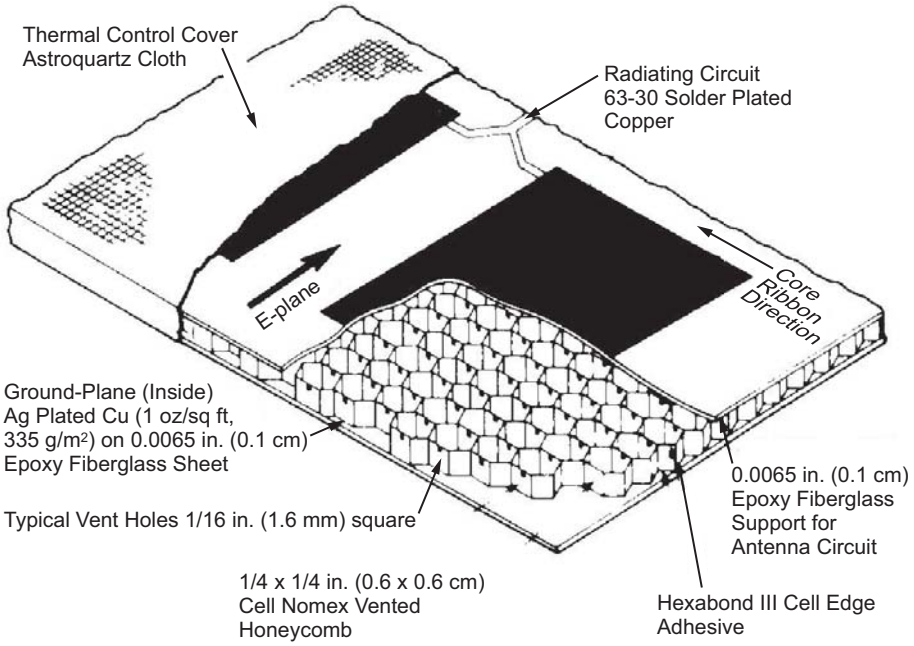

Fig. 6-9. Seasat L-band antenna panel construction using a honeycomb structure.

Table 6-1. Seasat antenna parameters.

Parameter	Value
Radiation gain	37.2 dB
Antenna efficiency	60 percent
Effective gain	35 dB at sensor electronics
Peak power	1100 W (1500 W design)
Beam width in elevation	6.2 deg
Beam width in azimuth	1.7 deg
Polarization	Horizontal polarization
Polarization isolation	20 dB
Center frequency	1.275 GHz
Bandwidth	19 MHz
Peak sidelobe	<–12.5 dB
Phase error in transfer function	±20 deg peak for quadratic error 2 deg rms for random error (higher than quadratic)
Beam pointing	90 deg in azimuth (orthogonal to the flight path) 20.5-deg mechanical tilt in look angle

need to obtain a high overall efficiency between the transmitter and the antenna radiators. The use of conventional coaxial cables for the corporate feed network was ruled out due to high loss, and a corporate feed network using vacuum as the dielectric was developed. This corporate feed network used a solid center conductor in a rectangular structure suspended by solid supports. The total losses introduced by this corporate feed network were less than 1 dB to the individual panels. The Seasat SAR system was designed to use optical processing as the principal method of generating data products on the ground. Optical processors can easily compensate for quadratic phase errors across the frequency spectrum of the transfer function; therefore, a 20-deg maximum quadratic phase error was allowed to be introduced by the antenna. This antenna phase error was removed during the processing step. Since random errors cannot be removed by optical processors, the phase error beyond the quadratic error was limited to 2-deg rms across the frequency spectrum. The Seasat antenna satisfied this phase error requirement.

A photograph of the front surface of the Seasat antenna supported by the strongback is shown in Fig. 6-10(a). A photograph of the back of the Seasat-A antenna supported by the zero-G fixture is shown in Fig. 6-10(b). Figure 6-10(b) shows the truss structure as well as the corporate feed network.

Following the success of the Seasat SAR system, the first of the Shuttle Imaging Radar (SIR) systems, SIR-A, was flown in the Shuttle in 1981. This radar used the residual hardware from Seasat. In particular, the antenna system used seven engineering model (EM) Seasat panels. The antenna was mounted on a fixed structure in the payload bay of the Shuttle and operated at a fixed angle of 50 deg from nadir. The SIR-A hardware was composed of the flight sensor (Seasat flew the engineering model sensor) from Seasat and the spare flight recorder from the Apollo 17 lunar sounder experiment. In 1984, this same antenna was flown on the Shuttle again as the SIR-B antenna.

6.4 SIR-C and SRTM Antennas

The SIR-C/X-SAR mission is a cooperative experiment between NASA, the German Space Agency (DARA), and the Italian Space Agency (ASI). The SIR-C (Shuttle Imaging Radar-C) was launched on the Space Shuttle Endeavor twice in 1994. The SIR-C data have been used to develop algorithms for understanding the global environment and its changes. SIR-C collected radar images over 300 sites around the Earth. These sites were selected to study the focused science in geology, ecology, hydrology, and oceanography. SIR-C generated fully polarimetric radar images at two frequencies (L-band and C-band) while X-band SAR data were acquired by X-SAR provided by DARA and ASI. The SIR-C data were radiometrically calibrated to produce the accurate normalized backscattering cross section of various ground objects for many science applications [12,13].

(a)

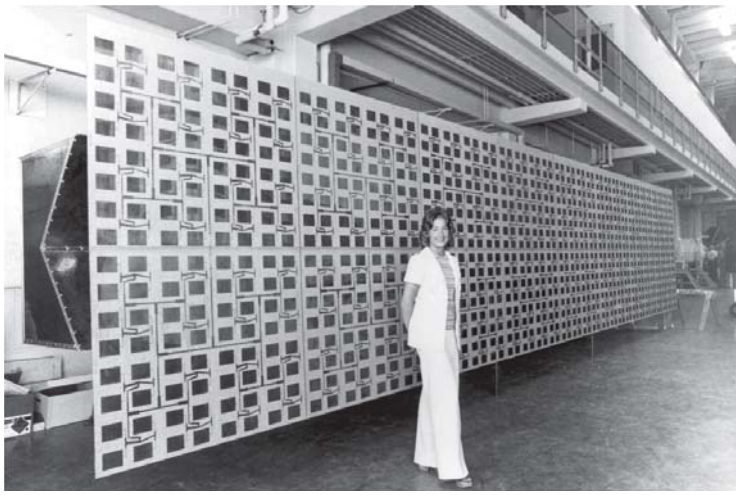

(b)

Fig. 6-10. Pictures of Seasat antenna: (a) Front antenna surface (notice that the radiation patches are fed by microstrip feed lines) and (b) back antenna surface (notice that the panels are mounted on a composite truss structure to be deployed in space). All eight microstrip panels are fed from a coaxial corporate feed network.

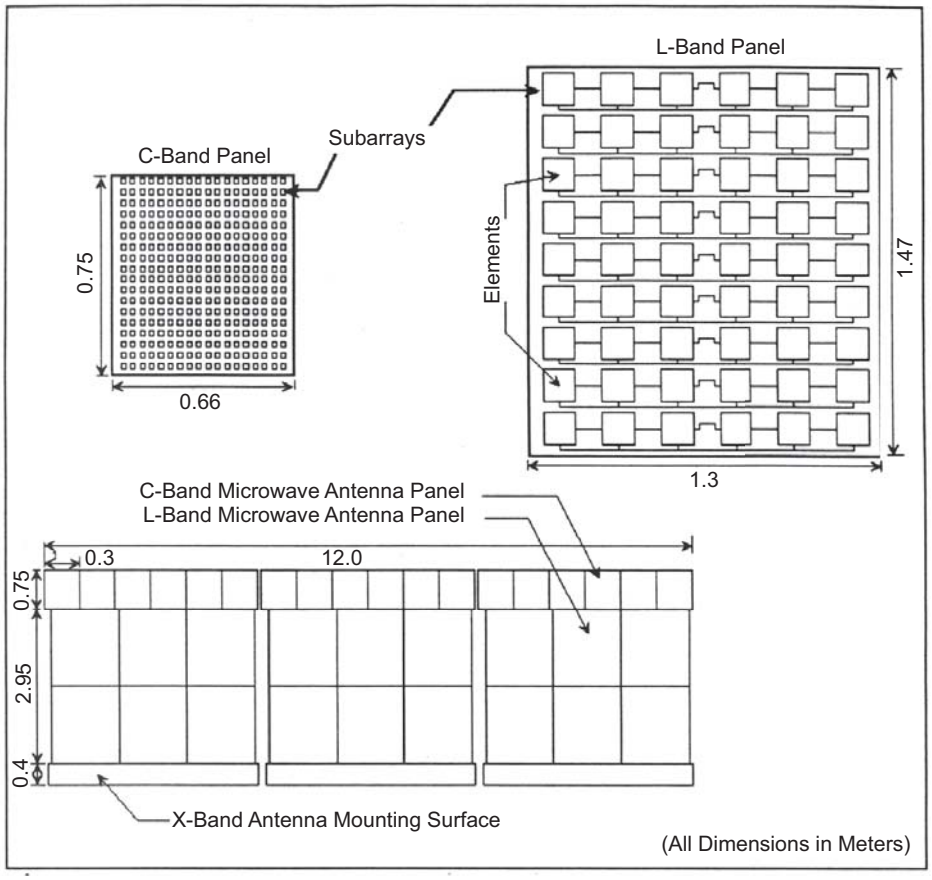

Fig. 6-11. SIR-C antenna configuration. Notice that the L-band phased array in the elevation direction is composed of two panels. Each radiation element is fed by H- and V-polarization feed lines on the front panel surface.

The SIR-C antenna is a dual linear polarized phased array. The antenna was designed and manufactured by Ball Aerospace in close collaboration with JPL. The phased array technology was selected to detect low cross-polarization returns. A phase array is highly efficient since T/R modules are placed close to radiation elements to avoid the feed loss. The SIR-C antenna is composed of 18 L-band panels and 18 C-band panels, as shown in Fig. 6-11. The C-band array size is 12 m by 0.75 m, and the L-band array size is 12 m by 2.95 m. Notice that the array size in the along-track direction is the same for both L- and C-band arrays to use the same PRF. Each L-band panel has nine radiating sticks, and each stick has six radiating elements. Each element is dual linear polarized (horizontal and vertical polarizations). Notice that there are two L-band panels in the cross-track direction. Each C-band panel has 18 sticks, and each stick has 18 radiating elements. Like L-band, a C-band radiating element

is dual polarized. The initial design of the SIR-C system was to occupy one quarter of the shuttle payload bay in its stowed configuration, and the antenna was to be deployed in space. However, during the development phase, it was decided that the antenna would be launched with the deployed configuration.

Using the phase shifters, the antenna beam can be electronically steered in both cross-track and along-track directions. Since there is one phase shifter for each stick, the azimuth steering angle is limited. The required steering angles are within ±23 degrees in the cross-track direction and within ±2 degrees in the along-track direction. One L-band panel has 7 T/R modules for each polarization as shown in Fig. 6-12 while one C-band panel has 14 T/R modules. Even though all T/R modules are identical, the arrangement of the antenna electronics, as shown in Fig. 6-12, provides the necessary antenna tapering in the cross-track direction to control the sidelobe level. Two L-band panels (tapering shown in Fig. 6-12 and its mirror image) form the complete elevation tapering, while a single C-band panel has the complete elevation tapering. The

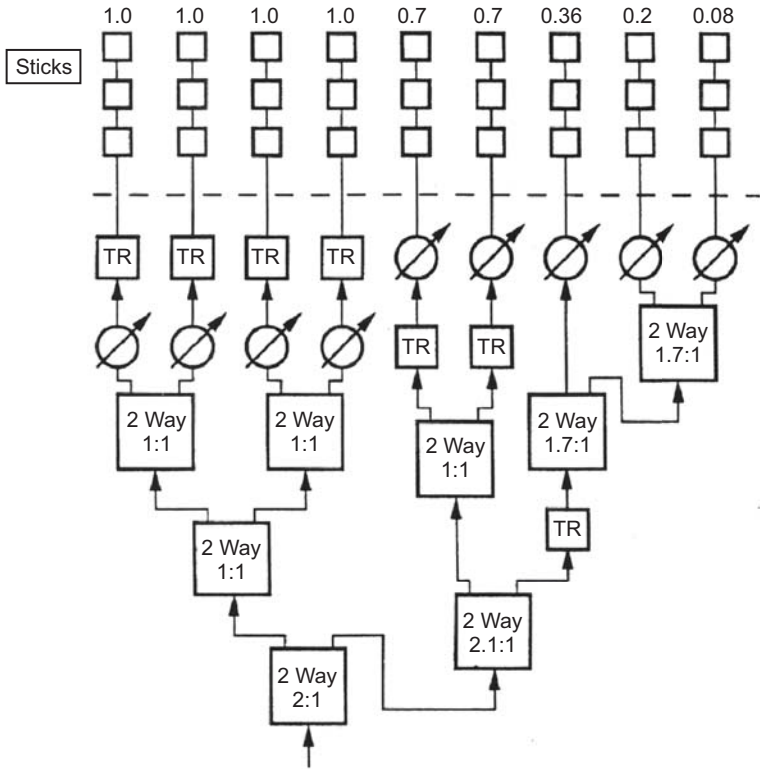

Fig. 6-12. SIR-C elevation tapering obtained by the arrangement of T/R modules, power dividers, and phase shifters. The tapering is given in power, and the amplitude tapering is the square root of the power tapering coefficients.

SIR-C phase shifter is a four-bit p-type–insulator–n-type (PIN) diode phase shifter. The elevation beam width can be changed using the phase tapering (ϕ_T) given by

$$\phi_T(n) = A_{BW} \sin\left[(n-1)\pi/17\right] \tag{6.4-1}$$

where A_{BW} takes on 0, 60, 90, 120, 150, 180, 210, or 270 deg, and n is the stick number between 1 and 18. The phase tapering is given in the half cycle of the sine function, and the larger value of A_{BW} provides a broader elevation beamwidth.

In order to calibrate the backscattering measurement accurately, we must be able to predict the SIR-C antenna patterns during the mission based on the pre-launch antenna data. The antenna patterns can be verified during the mission using ground calibration equipments and natural targets, such as rain forests. However, we could not check all the SIR-C antenna patterns due to a large number of possible antenna patterns (two polarizations, elevation steering angles, and various phase taperings). In order to predict the antenna pattern, we tested each panel separately, and the final antenna array performance was computed based on the panel data. The entire array power pattern ($P(\theta,\phi)$) can be calculated by using the stick pattern ($S(\theta,\phi)$) and the array factor given by

$$P(\theta,\phi) = F(\theta,\phi)^2 \tag{6.4-2}$$

and

$$F(\theta,\phi) = S(\theta,\phi)\sum_{n=1}^{N}\sum_{m=1}^{M} C(n.m)\exp\left[-j\frac{2\pi}{\lambda}\left(\cos(\theta)\sin(\phi)d_a(n) + \sin(\theta)d_e(m)\right)\right] \tag{6.4-3}$$

where θ is the elevation angle (cross-track direction), ϕ is the azimuth angle (along-track direction), $d_a(n)$ is the stick locations in the azimuth direction, $d_e(m)$ is the stick locations in the elevation direction, N is the number of sticks in the azimuth direction, and M is the number of sticks in the elevation direction. The elevation stick separation distance is 0.673 λ at L-band and 0.696 λ at C-band. The stick separation distance in the azimuth direction is 5.58 λ at L-band and 11.84 λ at C-band, which limits the azimuth steering angle.

In order to estimate the array antenna pattern, we first measured the stick patterns using the far-field measurement facility at Ball Aerospace. Both elevation and azimuth pattern measurements were made for four cases: two frequencies (L-and C-band) and two polarizations (horizontal and vertical). The L-band, H-polarization stick patterns are shown in Fig. 6-13.

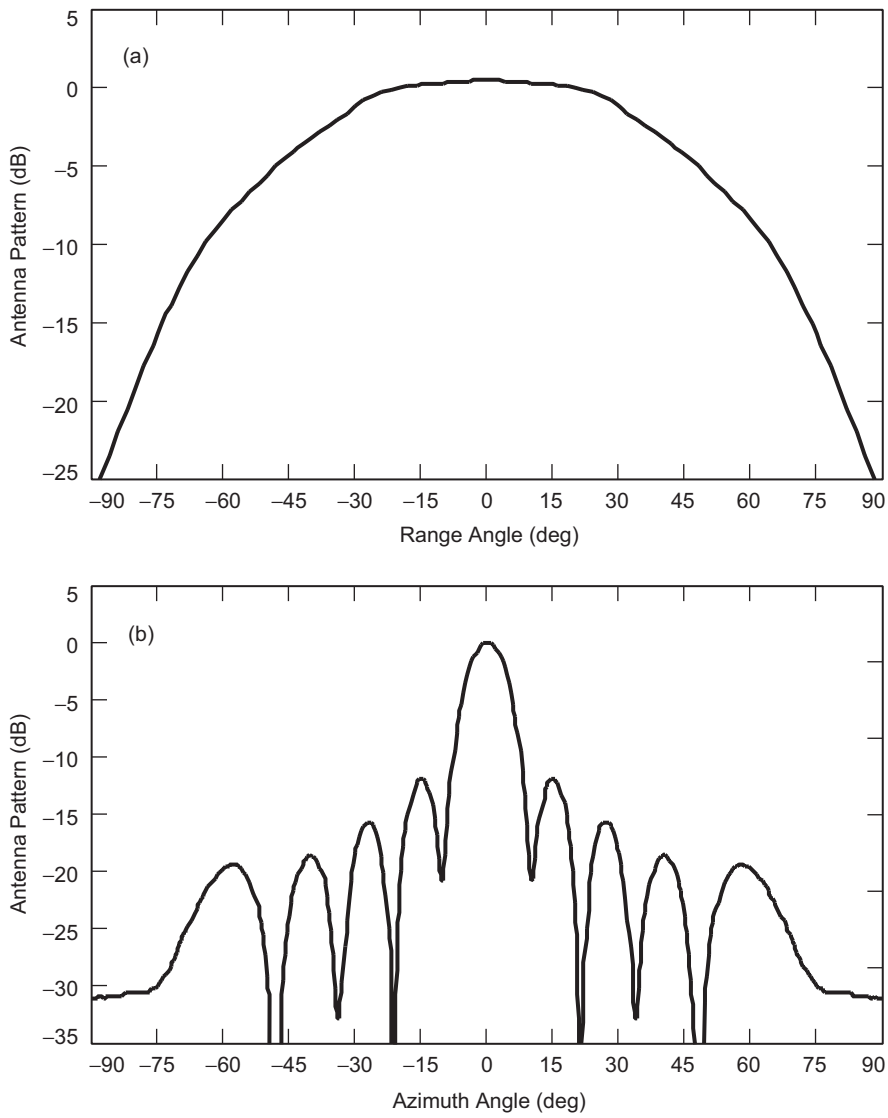

Fig. 6-13. SIR-C L-band, H-polarization measured stick patterns: (a) elevation and (b) azimuth.

As shown in Fig. 6-13, the elevation pattern is the antenna pattern of a single radiation element, and the azimuth pattern is a six element array pattern. The only unexpected stick pattern was the C-band, vertical polarization, elevation pattern (see Fig. 6-14). Two blind zones near ±25 deg are shown in Fig. 6-14. We conjecture that these blind zones are caused by the surface wave excited by a periodic structure formed within a panel. Notice that the C-band

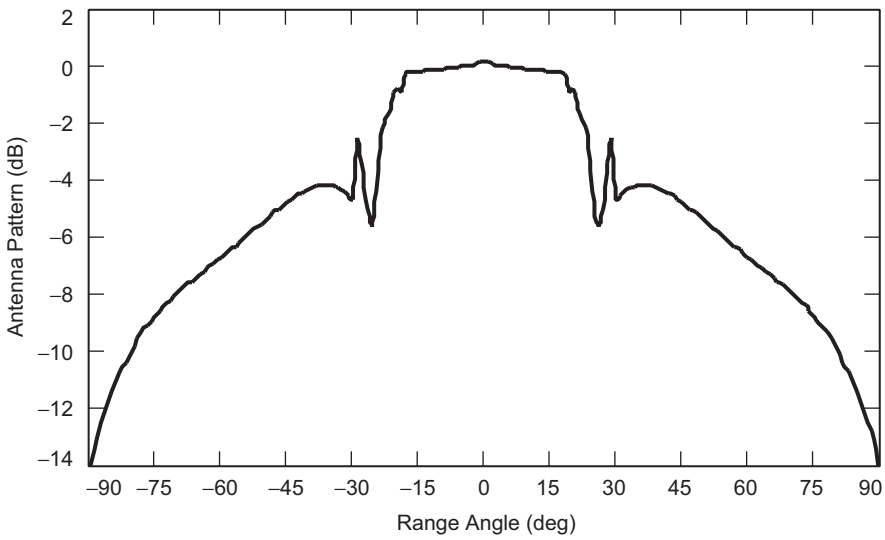

Fig. 6-14. SIR-C C-band, vertical polarization, elevation stick pattern. Notice that there are blind zones near ±25 deg.

panel has a high dielectric substrate and the radiating sticks are periodically placed on the panel.

To estimate the entire phase array antenna pattern, we need to measure the complex amplitude ($C(n,m)$) of each stick as shown in Eq. (6.4-3). The complex amplitude includes the amplitude tapering, the path length difference, the phase shifter effect, and other random errors. In order to measure the complex amplitude of each stick, Ball Aerospace developed a "near-field" probe that is almost in contact with each stick of a panel. The manual probe is shown in Fig. 6-15. This manual probe has two coupling elements that can be moved to different sticks; however, an automatic probe was developed later to measure the electromagnetic field of all the sticks in a panel without moving the coupling elements. This probe was originally developed to verify the T/R module functionality by measuring the electromagnetic field of each stick. However, with the probe-calibration technique developed by JPL and Ball, the SIR-C antenna patterns were estimated using the "near-field" probe data and Eq. (6.4-3). We calibrated the probe by comparing far-field pattern measurements with the "near-field" probe data. Using Eq. (6.4-3), one can invert the complex amplitude of each stick from the far-field measurements (amplitude and phase). Then, the ratio of these two stick fields was used to calibrate the probe element associated with each stick location.

The path length difference at the panel level is caused by the feed network and the total path length within a panel. Therefore, all antenna panels were compensated for the path length difference by inserting a phase trimmer to each panel. A separate trimmer was used for the H- and V-polarization port of each

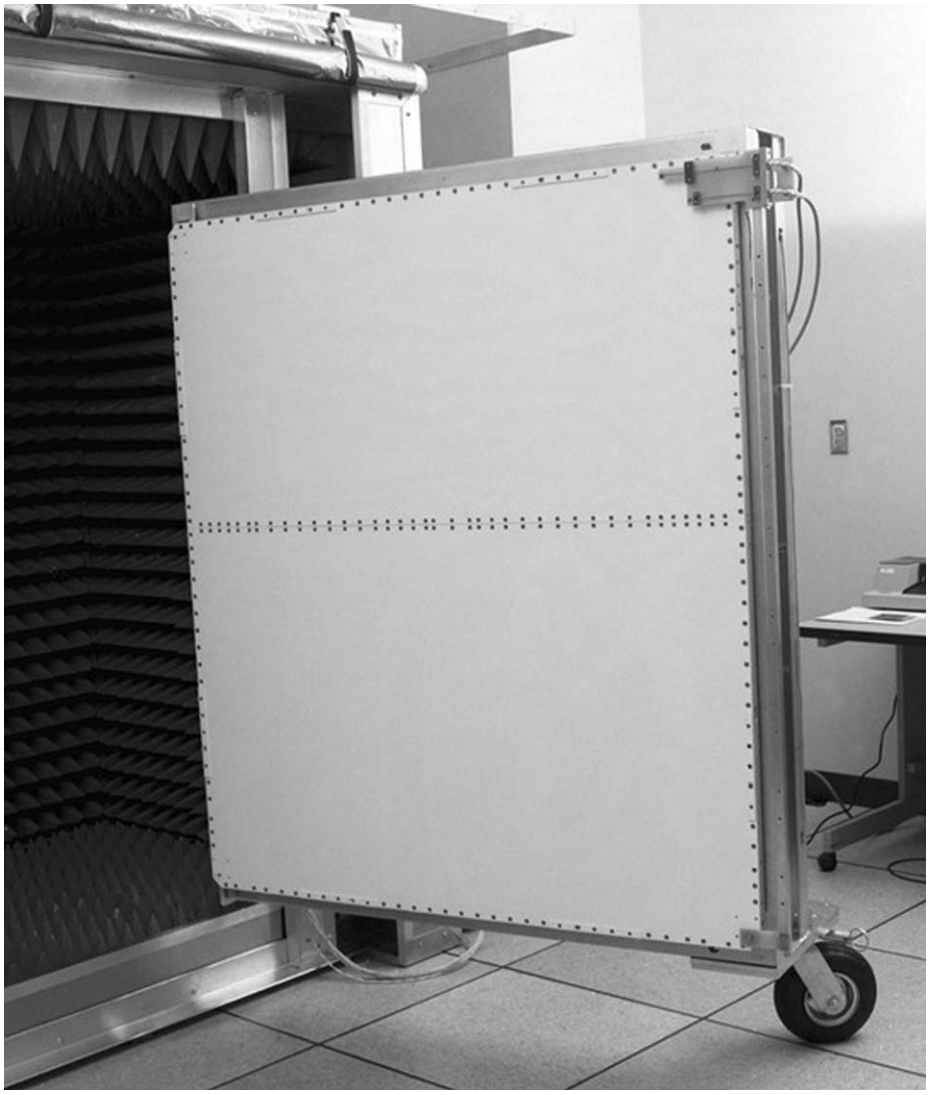

Fig. 6-15. L-band manual "near-field" probe attached to an L-band panel. The "near-field" probe is shown in the right side of the panel. At the top of the panel, two probe-coupling elements for each polarization measure the electromagnetic field of each stick.

panel. The small panel physical location variation was also compensated using the same trimmer. After all the trimmers were installed to the panels, the SIR-C array antenna pattern was estimated using the calibrated probe data as shown in Fig. 6-16. During the mission, these patterns were compared with the ground measurements and the derived patterns using rain forests. The patterns using the

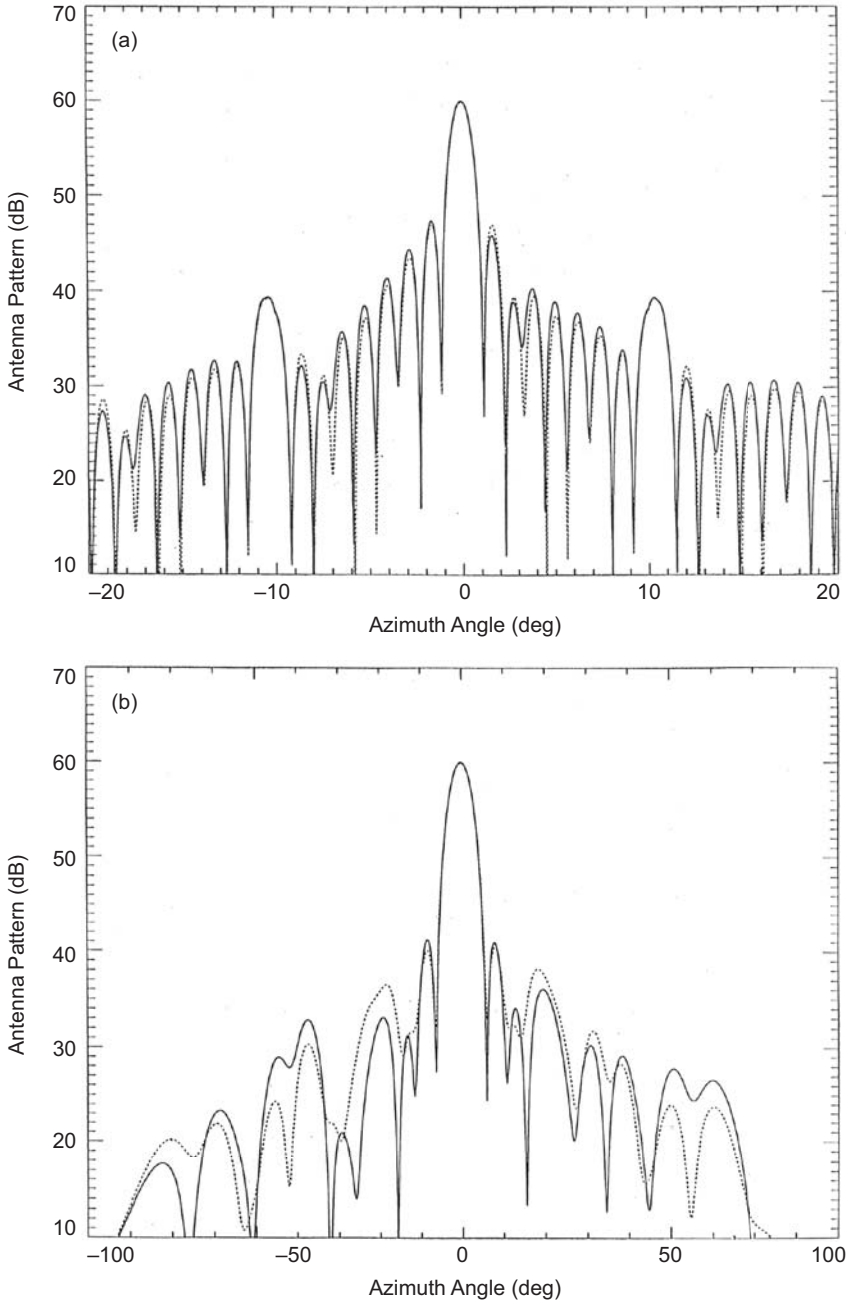

Fig. 6-16. SIR-C L-band, receive antenna patterns for H-polarization: (a) azimuth pattern and (b) elevation pattern. Notice that two patterns are shown in each plot. These two patterns were generated using two probe data sets measured at different times.

probe data compared well with the derived patterns for the low-phase tapering cases. However, for the large-phase tapering cases where the 3-dB beamwidth was significantly broadened, the estimated antenna pattern was not very accurate. During the mission, the health of all T/R modules and phase shifters was also checked using the RF built in test equipment (BITE). The BITE was incorporated into the design of each panel by including a built-in coupler to sample the power going to each of the radiation elements as well as having the ability to inject a known signal into each of the receive modules.

The SIR-C antenna performance was summarized in Tables 6-2 and 6-3. The SIR-C antenna parameters were either directly measured or derived using the analysis. These parameters were evaluated at the room temperature, and their temperature dependences were estimated using limited thermal measurements. For example, the receiver electronic gain was increased as the operating temperature decreases. The receive gain shown in Table 6-2 includes the electronic gain of T/R modules, the total insertion loss, and the antenna directivity. The receive noise temperature of a T/R module is also an important factor in determining SNR. In order to verify that the SIR-C SNR satisfies the requirement, we need to measure antenna related parameters such as EIRP, receive gain, and gain over noise temperature (G/T). The peak sidelobe level is

Table 6-2. Summary of the SIR-C L-band antenna performance.

Parameter	Specification	Performance	Uncertainty (1σ)
EIRP	>102 decibels referenced to mW (dBm)	H: 105.72 dBm V: 104.86 dBm	0.5 dBm
Receive gain	>52.8 dB	H: 57.16 dB V: 57.02 dB	0.5 dB
Polarization isolation	<–25 dB	<–25.24 dB	3 dB
Elevation beam steering accuracy	<±0.5 deg	<±0.5 deg	0.12 deg
Azimuth beam steering accuracy	<±0.1 deg	<±0.03 deg	0.014 deg
Elevation peak sidelobe	<–16 dB	<–18 dB	1 dB
Azimuth peak sidelobe	<–12 dB	<–10.36 dB	0.5 dB
G/T	>10.50 (in dB)	10.25 dB (H-polarization) 10.09 dB (V-polarization)	0.6 dB
Impulse response ISLR	<–18 dB	H: –26.43 dB V: –17.86 dB	0.1 dB

H = horizontal; V = vertical

Table 6-3. Summary of the SIR-C C-band antenna performance.

Parameter	Specification	Performance	Uncertainty (1σ)
EIRP	>105.9 dBm	H: 105.81 dBm V: 105.52 dBm	0.5 dBm
Receive gain	>64.2 dB	H: 66.8 dB V: 67.79 dB	0.5 dB
Polarization isolation	<–25 dB	–33.13 dB	0.7 dB
Elevation beam steering accuracy	<±0.5 deg	<±0.5 deg	0.25 deg
Azimuth beam steering accuracy	<±0.1 deg	<±0.02 deg	0.0004 deg
Elevation peak sidelobe	<–16 dB	<–12.93 dB	0.8 dB
Azimuth peak sidelobe	<–12 dB	<–11.32 dB	0.4 dB
G/T	>16.50 (in dB)	15.34 dB (H-polarization) 15.40 dB (V-polarization)	0.95 dB
Impulse response ISLR	<–18 dB	H: –25.98 dB V: –27.30 dB	0.1 dB

H = horizontal; V = vertical

related to the range and azimuth ambiguities. Even though the azimuth peak sidelobe level did not satisfy the specification, the SIR-C radar parameters were chosen to keep the azimuth ambiguity less than –20 dB. The time-domain impulse response was characterized by the integrated side-lobe ratio (ISLR) using the antenna frequency transfer function. However, the overall ISLR can be controlled by the range window function during the ground data processing. The transmit spurious signal was measured to be less than –35 decibels referenced to a carrier (dBc) to ensure that the SIR-C antenna did not interfere with other instruments. For a phased array, the voltage standing wave ratio (VSWR) of a panel is not very important since a low-level signal is fed into the panel. The antenna test process was designed to verify the overall radar performance within the budget limitation; therefore, the uncertainty of some parameters was allowed to be large if they were not considered critical to the overall radar performance.

The Shuttle Radar Topography Mission (SRTM) was a joint project between NASA and the National Imagery and Mapping Agency (NIMA). It was the first spaceborne implementation of a single-pass interferometer [14]. A single-pass interferometer measures two interferometric SAR datasets simultaneously using two antennas that form an interferometric baseline. The

SRTM was launched on the Space Shuttle Endeavour in February 2000. The SRTM used the modified SIR-C hardware with a 62-m long mast and a second antenna (known as "outboard antenna") to form a single-pass interferometer, as shown in Fig. 6-17. The antenna (known as the "inboard antenna") inside the Shuttle payload bay transmitted a radar signal, and both antennas (inboard and outboard antennas) received the return signal to form an interferogram. During one 11-day Shuttle mission, the SRTM acquired interferometric data between 60 deg north and south latitudes. In order to complete the global coverage within 60 deg north and south latitudes within 11 days, the SRTM implemented a ScanSAR operation to obtain a 225-km swath. JPL finished the global digital elevation model (DEM) production in January 2003, and an example of the SRTM global topographic data is shown in Fig. 6-18.

As shown in Fig. 6-17, the topographic height (z) can be measured using

$$z = H - \rho \cos\theta_L \tag{6.4-4}$$

where H and ρ are the platform altitude and the slant range, respectively. The look angle θ_L is derived from the interferometric phase measurement (ϕ) as

$$\theta_L = \alpha - \sin^{-1}\left[\frac{\lambda\phi}{2\pi B}\right] \tag{6.4-5}$$

where B and α are the baseline length and the tilt angle, respectively. For SRTM, the baseline length, the tilt angle, and the wavelength are 62 m, 60 deg, and 5.6 cm, respectively. It is important to maintain the baseline length between two antennas. That is, the phase centers of both antennas should not vary within the data-take duration since each data-take starts and ends with an ocean data-take that provides the baseline calibration. The failed T/R modules can effectively change the electrical baseline length. However, the final results showed that the phase centers of both antennas did not change within a data-take. The phase noise error of the interferometric system must be less than approximately 15–35 deg (depending upon the location within swath) to meet the vertical accuracy of the SRTM DEM. The stability of the antenna phase and the phase center location are critical factors in achieving the SRTM DEM accuracy. However, this stability is required only between ground control points that can provide the interferometric calibration.

The inboard C-band antenna was the SIR-C antenna, and the outboard antenna was designed and manufactured by Ball Aerospace specifically for SRTM. This outboard antenna is composed of 12 panels, and it is dual polarized. Each panel is 0.75 m × 0.66 m. The length of the outboard antenna is 8 m, and it is a receive-only antenna. The important consideration in this interferometric antenna system was to overlap two azimuth beams (inboard and outboard azimuth antenna beams) since the azimuth antenna pattern is

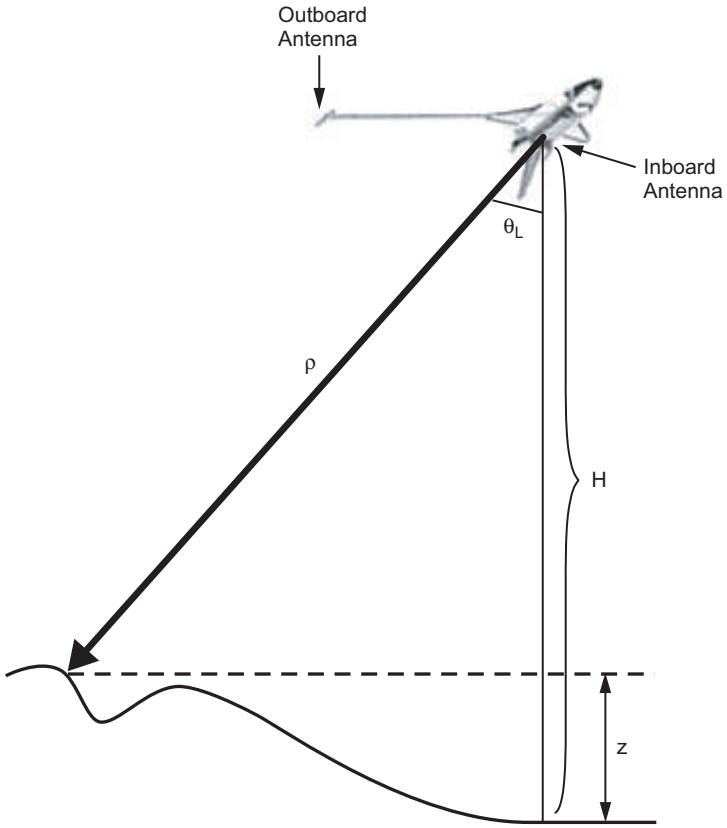

Fig. 6-17. Single-pass interferometric SAR operation. The interferometric phase determines the look angle (θ_L) and the slant range (ρ) is measured by SAR. In addition, the altitude (H) of the platform is estimated by a Global Positioning System (GPS) located near the SAR antenna.

extremely narrow. To insure that both azimuth beams overlap, the outboard antenna length is shorter than the inboard antenna length. The reason that we implemented a shorter outboard antenna instead of a shorter inboard antenna is to maintain the high SNR since the inboard antenna transmits radar signals for both antennas. The electronic scanning capability is ±20 deg in elevation and ±0.2 deg in azimuth to implement a ScanSAR operation and to ensure the azimuthal beam overlap. The outboard antenna has a capability of auto-tracking the inboard antenna azimuth beam. The antenna, in addition to electronic scanning, has the capability of increasing its beamwidth in the elevation direction using the phase tapering. Both orthogonal polarizations (horizontal and vertical) operate simultaneously with independent electronic beam steering angles to enable the four-beam ScanSAR operation as shown in Fig. 6-19.

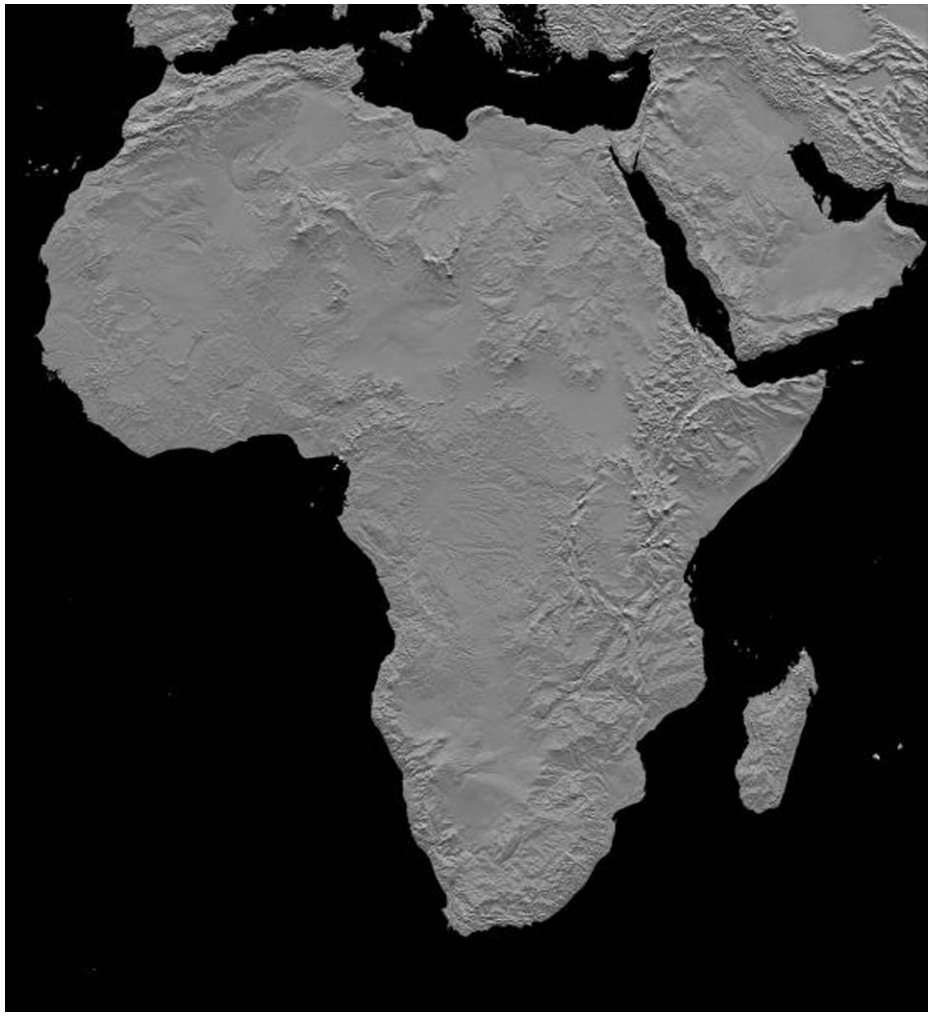

Fig. 6-18. Shaded relief image of Africa's topography measured by SRTM. The post spacing of this DEM is 30 m, and the vertical accuracy is about 7 m.

The radiating element of an outboard panel is identical to that of an inboard panel. For the antenna electronics, each stick has two monolithic microwave integrated circuits (MMIC) receive LNA/phase shifters for horizontal and vertical polarizations. The MMIC LNA/phase shifters are packaged in four modules (quad-receive module) to combine four sticks coherently. These quad-receive modules are combined by a five-way combiner to form the penta-receive module. There are two penta-receive modules (horizontal and vertical polarizations) within a panel. A lightweight panel structure was used to minimize the weight of the outboard antenna that was attached to the end of the

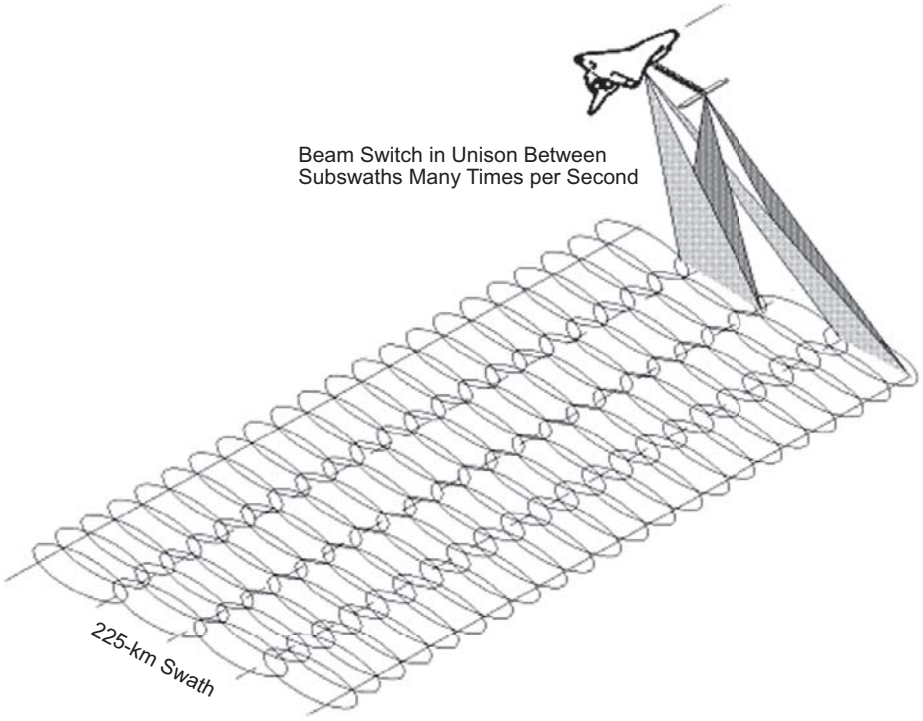

Fig. 6-19. SRTM ScanSAR operation sequence. The near and the far swaths are imaged by the horizontal polarization radar, and the two center swaths are imaged by the vertical polarization radar.

62-m mast. Since the outboard antenna is a receive-only antenna, each panel has two inputs, one for DC power and one for phase shifter commands. In addition, each panel has three outputs, one DC BITE output and two RF outputs (horizontal and vertical polarizations).

The outboard panels were combined by an equal 12-way corporate feed distribution network made up of coaxial cables and microstrip power dividers. Two independent and identical feed networks were used for horizontal and vertical polarizations. The phase balance was maintained between all paths so that the outboard array formed a coherent beam with the required sidelobe level. Unlike SIR-C, phase trimmers were not used to equalize the panel path length. Instead, the phase shifter settings of the outboard antenna were modified assuming that the path length difference does not exceed the wavelength. In order to enable the auto-tracking of two azimuth beams (inboard and outboard antenna beams), two RF signals were coupled from the main corporate feed. The outboard azimuth beam tracked the inboard beam by maximizing the received power of the outboard antenna. The polarization isolation between

horizontal and vertical polarization channels was greater than 25 dB. The steering range in the elevation (cross-track) direction from the mechanical boresight was ±20 deg with an accuracy of ±0.25 deg. In addition, the outboard antenna was capable of steering the azimuth beam electronically by ±0.5 deg in incremental steps less than 0.01 deg.

6.5 Future Antenna Technologies and Concluding Remarks

Future SAR antenna technologies depend strongly upon the antenna size. An important factor in determining the required antenna size is the spacecraft altitude. In order to shorten the revisit time, two different approaches can be implemented: low Earth orbit (LEO) constellation or SAR observations from higher altitudes. The higher altitudes include the medium Earth orbit (MEO) and the geosynchronous orbit. Here, the geosynchronous orbit does not include the geostationary orbit. Geosynchronous orbits have an orbital period equal to one Earth day. The geostationary orbit is a special case since the inclination is zero; therefore, when a satellite in a geostationary orbit is viewed from the rotating Earth, it remains fixed in the same position. Since SAR requires the relative motion between a spacecraft and Earth terrains, geosynchronous orbits will be used for SAR, not the geostationary orbit. For science and applications involved in the solid Earth and natural hazards area, NASA formed the Solid Earth Sciences Working Group (SESWG) composed of senior academic and government scientists to formulate a scientific observational program for NASA. The SESWG final report [15] calls for its highest priority being "InSAR (Interferometric SAR) everywhere, all the time" to make vector surface deformation measurements of mm-scale accuracy over wide areas using the repeat-pass interferometric SAR technology. For the near-term (5–10 years from now) requirement, an InSAR measurement system must provide the capability of daily access to anywhere on the globe. In order to satisfy the long-term (10–25 years from now) requirement, the capability must be increased to hourly global access.

To provide the frequent revisits as required by the SESWG report, a constellation of LEO satellites or higher orbit InSAR satellites are required. An optimum configuration may be a combination of both LEO and higher orbit satellites. For the LEO constellation case, a lightweight antenna with a smaller stowed volume must be developed to lower the overall InSAR life-cycle cost by reducing the capacity requirement on the spacecraft and a launch vehicle. For higher orbit InSAR satellites, a large SAR antenna is required to provide enough SNR.

One new technology that can provide lightweight antennas is an inflatable structure technology. When the inflatable structure technology is combined with the membrane electronics technology, the mass of a SAR antenna can be

reduced dramatically [16]. As an example, a roll-up membrane antenna with an inflatable structure can be stowed within a small volume. When the inflatable structure is fully inflated, the roll-up antenna is deployed to be a fully functional SAR antenna. This antenna can include the active antenna electronics such as membrane T/R modules.

A large SAR antenna technology is composed of structure, electromagnetic radiator, and radar electronics technologies. The large structure technology also includes a metrology system to measure the antenna surface deformation and the compensation method to compensate the effect of a deformed antenna surface. If a large antenna structure is rigid enough, no metrology and compensation technologies are required. The usual SAR antenna deformation that can be tolerated is 1/20 of the radar wavelength.

6.5.1 Antenna Structure Technology

Since a spaceborne SAR antenna is large, it is important to select the optimum antenna structure technology to reduce the antenna mass and the deployment risk. Due to the large size of a SAR antenna, it is necessary to deploy an antenna in space. For a typical LEO SAR antenna size (10–15 m length and 1–3 m in width), a Seasat-type deployment structure can be used for rigid panels. If a membrane panel technology is developed, an inflatable structure can be used to reduce the antenna weight and the stowed volume. However, the in-space rigidization of an inflatable structure must be demonstrated to ensure the successful deployment. Maintaining the flatness is also an important factor in evaluating the membrane panel technology.

When the antenna size becomes much larger than a typical LEO SAR antenna, the antenna structure technology becomes very complex. If the structure is not rigid enough to maintain the required antenna flatness, the antenna structure must be smart enough to correct the deformation. This is particularly true for the transmit antenna pattern since the transmit pattern must be corrected in real time. There are two methods for correcting the structure deformation in real time: mechanical correction and electrical compensation. The mechanical correction is usually accomplished by actuators, and the electrical compensation is performed using phase shifters or true time-delay elements. The choice of a phase shifter or a true time-delay element depends on the fractional bandwidth required by the SAR operation. In order to use the surface deformation correction, we need to measure the deformation in real time. Therefore, a metrology system must be developed to measure the antenna deformation accurately.

Both inflatable and mechanically deployable structure technologies are viable for very large SAR antennas. An inflatable structure is simple; however, the space inflatable technology is not mature, and the ground testing is much more complex than a mechanically deployable structure. The technology for a

mechanically deployable structure like the SRTM mast has progressed significantly enough to become reliable.

6.5.2 Electromagnetic Radiator Technology

A circular reflector antenna is not an optimum antenna for SAR since SAR requires the elongated antenna shape. If a circular reflector antenna is used, the reflector has to be partially illuminated. Therefore, the surface area is not properly used. In addition, a reflector antenna does not provide the beam agility. In order to steer the antenna beam, the reflector must be mechanically tilted, or the beam steering angle is limited, even with complex feeds. A cylindrical reflector with a phased array feed is a better candidate for SAR. This design is a compromise between a reflector antenna and a phased array. The phased array feed usually uses the microstrip radiator technology to steer an antenna beam. A reflectarray uses a reflecting surface composed of microstrip radiating elements instead of using a solid reflector. Phase shifters can be included in the radiating element of a reflectarray.

A phased array provides many important characteristics required by SAR, especially if beam agility is required. In order to reduce the antenna weight, membrane microstrip radiators can be used. To feed the membrane microstrip radiators, a multi-layer feed structure can be implemented. A radiator design comparable to lightweight structures needs to be developed to advance the phased array technology.

6.5.3 Antenna Electronics Technology

The antenna electronics include T/R modules, phase shifters, and RF/power/command distribution network. A high-efficiency T/R module needs to be developed to lower the DC power consumption. The Class E type high power amplifier (HPA) is a promising technology, especially at lower frequencies. A low-loss phase shifter is also a critical component if beam agility is needed. The micro electromechanical system (MEMS) RF switch can provide a low insertion loss for a phase shifter. The T/R module and phase-sifter packaging is also important to reduce the weight and complexity of the antenna electronics. The distribution network for RF signal, DC power, and commands must be simplified to be comparable with lightweight structures and the associated deployment mechanism. An optical-fiber distribution network is a promising future technology. The concept of a fully functional panel (including radar electronics) is being considered for an extremely large phased array antenna.

We described the spaceborne SAR antennas for Earth science applications. The planer array technology was used for earlier missions such as Seasat, SIR-A, and SIR-B. Following the success of these SAR missions, a major advancement was accomplished by the SIR-C antenna. The SIR-C antenna was

the first spaceborne, fully polarimetric, phased array antenna. By adding another antenna, the SIR-C hardware was modified to be the world's first single-pass interferometric SAR. The spaceborne SAR antenna is the most critical component to reduce the mass, stowed volume, and cost of a spaceborne SAR. Various new technologies are being developed to enable future spaceborne SAR antennas.

References

[1] R. L. Jordan, "The Seasat-A Synthetic Aperture Radar System," *IEEE Journal of Oceanic Engineering*, vol. OE-5, no. 2, pp. 154–164, April 1980.

[2] C. Elachi, T. Bicknell, R. L. Jordan, C. Wu, "Spaceborne Synthetic-Aperture Imaging Radars: Applications, Techniques and Technology," *Proceedings of IEEE*, vol. 70, no. 10, pp. 1174–1209, October 1982.

[3] E. R. Stofan, D. L. Evans, C. Schmullius, B. Holt, J. J. Plaut, J. van Zyl, S. D. Wall, and J. Way, "Overview of Results of Spaceborne Imaging Radar-C, X-Band Synthetic Aperture Radar (SIR-C/X-SAR)," *IEEE Transactions Geoscience and Remote Sensing*, vol. 33, no. 4, pp. 817–828, July 1995.

[4] R. L. Jordan, B. L. Huneycutt, and M. Werner, "The SIR-C/X-SAR Synthetic Aperture Radar System," *IEEE Transactions on Geoscience Remote Sensing,* vol. 33, no. 4, pp. 829–839, July 1995.

[5] T. G. Farr and M. Kobrick, "The Shuttle Radar Topography Mission: A Global DEM," *EUSAR 2000*, VDE-Verlag, Frankfurt am Main, Germany, pp. 41–42, 2000.

[6] *Shuttle Radar Topography Mission*, web site at Jet Propulsion Laboratory, Pasadena, California, accessed July 26, 2005. http://www2.jpl.nasa.gov/srtm/

[7] *Living on a Restless Planet*, web site at Jet Propulsion Laboratory, Pasadena, California, accessed July 26, 2005. http://solidearth.jpl.nasa.gov/seswg.html

[8] J. C. Curlander and R. N. McDonough, *Synthetic Aperture Radar Systems & Signal Processing,* Wiley & Sons, New York, New York, 1991.

[9] C. Elachi, *Spaceborne Radar Remote Sensing: Applications and Techniques*, IEEE Press, Piscataway, New Jersey, 1988.

[10] F. M. Henderson and A. J. Lewis, *Principles & Applications of Imaging Radar*, Wiley & Sons, New York, New York, 1998.

[11] J. J. van Zyl and Y. Kim, "Synthetic Aperture Radar," *Encyclopedia of Physical Science and Technology*, Third Edition, Vol. 16, Academic Press or Elsevier Inc., Burlington, Massachusetts, pp. 451–465, 2002.

[12] J. J. van Zyl, "Calibration of Polarimetric Radar Images Using Only Image Parameters and Trihedral Corner Reflector Responses," *IEEE Transactions on Geoscience and Remote Sensing,* vol. 28, no. 3, pp. 337–348, May 1990.

[13] A. Freeman, M. Alves, B. Chapman, J. Cruz, Y. Kim, S. Shaffer, J. Sun, E. Turner, and K. Sarabandi, "SIR-C Data Quality and Calibration Results," *IEEE Transactions of Geoscence and Remote Sensing,* vol. 33, no. 4, pp. 848–857, July 1995.

[14] H. Zebker and R. Goldstein, "Topographic Mapping from Interferometric SAR Observations," *Journal of Geophysical Research, vol.* 91, pp. 4993–4999, 1986.

[15] *Living on a Restless Planet: Solid Earth Sciences Working Group Report*, JPL 400-1040, Jet Propulsion Laboratory, Pasadena, California, November 2002, also at web site accessed August 30, 2005. http://solidearth.jpl.nasa.gov/PDF/SESWG_final_combined.pdf

[16] J. Huang, M. Lou, A. Feria, and Y. Kim, "An Inflatable L-band Microstrip SAR Array," *IEEE Antennas and Propagation Society International Symposium* (Atlanta, Georgia), pp. 2100–2103, June 1998.

Chapter 7
Instrument Packages

Richard E. Cofield, William A. Imbriale, and Richard E. Hodges

This chapter describes antennas used on various instrument packages for science spacecraft. The instruments have been primarily used for the Earth Observing System (EOS), a series of spacecraft to observe Earth from the unique vantage point of space. This chapter includes radiometers (7.1–7.3), scatterometers (7.4), radars (7.5), and altimeters (7.6).

7.1 Radiometers

Richard E. Cofield

Radiometry is the measurement of electromagnetic radiation using highly sensitive receivers. The blackbody radiation spectrum given by Planck's radiation law provides a reference against which the radiation spectra of real bodies at the same physical temperature are compared. The spectral, polarization, and angular variations of a scene of interest are dictated by the geometrical configuration and physical properties (dielectric and thermal) of surfaces and interior regions of (1) the materials under study, and (2) the medium (atmosphere or space) through which we make observations. Radiometer parameters (such as frequency, viewing angle, and polarization) can be chosen to relate the radiometer's output signal strength to properties of the observed scenes.

This section describes passive microwave radiometry from spaceborne instruments developed at Jet Propulsion Laboratory (JPL): passive in contrast to active (radio detection and ranging [radar] or laser induced differential absorption radar [lidar]) systems such as altimeters and the scatterometers discussed below, and microwave as a consequence of Planck's law at the

temperature ranges of natural emitters. Hence, it is convenient to express radiometric signals (radiant power per unit bandwidth) as radiances having units of temperature (kelvin, or K). These radiances vary from 0 to 500 K for Earth and atmosphere, planets and other Solar System objects aside from the Sun itself. Microwave radiometric techniques were first developed from radio astronomy programs measuring electromagnetic energy of extraterrestrial origin. Thus, the requirements levied on spaceborne microwave radiometers are similar to those found in radio astronomy: spatial requirements include resolution (beamwidth), pointing accuracy and knowledge, polarization purity, and some measure of how well the antenna rejects energy from angles other than those desired (directivity, or beam efficiency). For super-heterodyne radiometers, spectral requirements usually appear as bandwidth about the center local oscillator frequency.

7.1.1 Microwave (Atmospheric) Sounder Unit

The Television Infrared Observation Satellite (TIROS)-N microwave sounder unit (MSU) is a direct descendant of the Scanning Microwave Spectrometer (SCAMS) flown in Earth orbit aboard the NIMBUS-6 meteorological satellite in 1975 [1]; SCAMS itself descends from the microwave radiometer flown in 1962 aboard Mariner 2 for remote sensing of the atmosphere of Venus. MSU observes thermal emission on the lower-side wing of the 60-gigahertz (GHz) oxygen line complex (at 50, 54, 55, and 58 GHz) for retrieving atmospheric temperature profiles. In the vertical temperature sounding technique, the radiometer sees thermal emission from frequency-dependent depths in the atmosphere, as determined by radiative transfer with Doppler and collisional broadening of wings of the oxygen line. For the MSU frequencies, the height of atmosphere parcels contributing to radiation varies from 0 (the surface) up to about 20 km. Twelve instrument units were delivered for temperature profiling aboard National Oceanic and Atmospheric Administration (NOAA) operational satellites.

7.1.1.1 Antenna Requirements. In order to meet a mission requirement of 1 K or better long term absolute instrument accuracy, the MSU footprint along the satellite ground track was to subtend 7.5-deg half-power beamwidth (HPBW) at the antenna, with a main beam efficiency >95 percent. (For Earth remote-sensing radiometers, beam efficiency is typically defined as the fraction of radiated power within 2.5 × the HPBW; the factor relates HPBW to the width between first nulls of the Airy pattern.) Horizontal resolution is provided by scanning the antenna field of view (FOV) at 11 positions across the ground track. With a scan of ±47.5 deg, the ground footprint size from a satellite height of 830 km varies from a 109-km circle at nadir to a 177 × 323-km ellipse at the scan extrema.

Additional scan positions permit radiometric calibration by directing the radiometer view to cold space (3 K) and to an ambient temperature black-body target (290 K). The scan period, including calibration, is 25.6 s.

7.1.1.2 Antenna Design. The antennas consist of two scanning reflectors fed at a 45-deg incidence angle in the near field of two fixed corrugated feed horns, Fig. 7-1. The scan axis, feed boresight, and spacecraft velocity vector all coincide. The reflectors have projected aperture diameters of 6 cm, and they are figured as hyperbolas slightly perturbed from parabolas, in order to reduce the frequency dependence of HPBW, from 15 percent (diffraction limited) to a measured range of 6 percent residual from non-ideal horn patterns and alignment. At the throat of each feed horn, an orthomode transducer separates the signal by polarization, resulting in the final four channels, which are then Dicke-switched before detection [2].

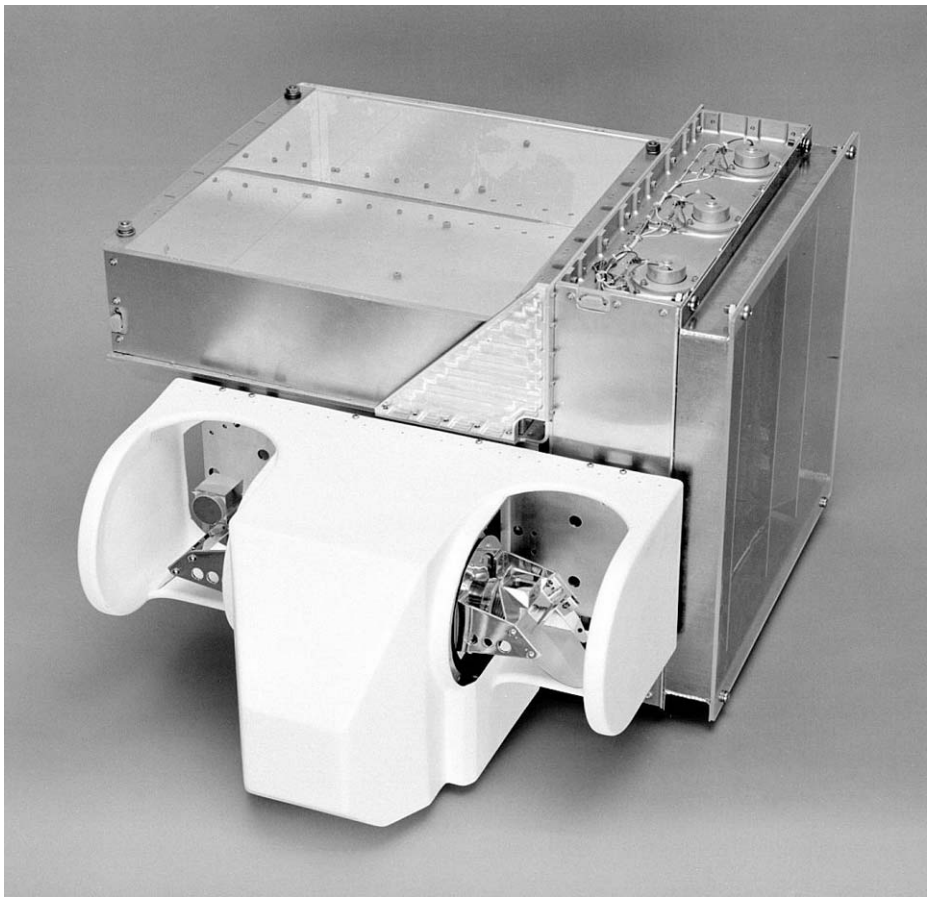

Fig. 7-1. TIROS microwave sounder unit (MSU).

7.1.1.3 Performance Estimates. The antenna patterns of the MSU instruments were measured in the far field at the JPL antenna test range. Complete patterns were measured at azimuth angle spacings of 22.5 deg for the first four units, then in principal planes and at selected scan positions for the remaining eight. The measurement's dynamic range was better than –51 dB, and amplitude measurement accuracy was 3 percent. These imply 10 percent accuracy in the knowledge of sidelobes –41 dB down from the main beam peak, corresponding to the required 95-percent beam efficiency. Angular resolution was 0.3 deg, and the polarization angle between MSU and mechanical alignment features was determined to <1 deg. Since the flight data reductions do not depend on polarization purity (atmospheric radiances for temperature sounding are uncorrelated and unpolarized), the co- and cross-polarized patterns were summed in quadrature to calculate beam efficiency (i.e., the only degradation caused here by cross-polarization is broadening of the antenna pattern). This is true of most atmospheric remote sensing of gaseous constituents (as opposed to ice clouds), with a few exceptions such as Zeeman splitting of oxygen emission in the mesosphere [3].

Antenna performance of a typical MSU is shown in Table 7-1. The beam efficiency met requirements, as did the beamwidth averaged over principal planes.

Space qualification of the MSU included extensive environmental tests, including a thermal vacuum test in which the radiometer was operated in vacuum over a temperature range exceeding that which would be seen in space. For this test, black-body targets like those used for on-board calibration were fabricated of iron-loaded epoxy and oriented for Brewster-angle incidence to achieve nearly unity emissivity. These targets were placed in front of the antennas, and their temperatures controlled in 25-K steps from 100 to 350 K to simulate cold space and the Earth [4]. This testing verified the linearity of the calibration of antenna temperatures to <1 percent, with a post fit residual of 0.5 K. Similar targets have been used for ground testing and on-board calibration in most of the spaceborne microwave radiometers subsequently flown by JPL.

Table 7-1. Antenna performance of MSU unit 4, from [2].

Frequency (GHz)	50.30	53.74	54.96	57.95
RF bandwidth (MHz)		220		
Beamwidth (deg)	7.8 × 7.1	7.3 × 7.0	7.6 × 7.3	7.3 × 7.0
Beam efficiency (percent)	95.3	95.5	95.2	97.4
Mass (kg)		29		
Power (W)		30		

7.1.1.4 Mission Status and Conclusions. The first of the TIROS-N/NOAA satellites was launched on October 13, 1978, and the MSU instruments continued to be deployed through the NOAA-J(14) satellite on December 1994, from which the MSU continues to operate to the present. Comparisons with ground truth for the first two satellites showed the MSU agreed to 0.5 K with the high resolution infrared sounder (on the same spacecraft), and to 3 K with a U.S. National Meteorological Center grid of radiosonde data. The latter improved to 1.5 K over a restricted height range corresponding to 300–700 hectopascals (hPa) pressure. This nearly meets the mission requirement of 1 K.

In a subsequent follow-on to the operational satellite series (NOAA K/L/M), the MSU has been replaced by the advanced microwave sounder unit (AMSU) for which the measurement channels extend from 50 to 183 GHz to include water vapor line spectroscopy. AMSU is supplied by an external vendor to NOAA and the Goddard Space Flight Center (GSFC), with scientific oversight by JPL.

7.1.2 Scanning Multichannel Microwave Radiometer on Seasat and Nimbus 7

The scanning multichannel microwave radiometer (SMMR) is a five-frequency imaging microwave radiometer launched on the Seasat-A and Nimbus-7 satellites. It measures dual-polarized radiation at 6.63, 10.69, 18, 21, and 37 GHz from Earth's atmosphere and surface. Geophysical quantities retrieved from these 10 channels include sea surface temperature and wind speed, sea-ice age and coverage, and atmospheric water in the forms of vapor, cloud, and rain. Sea surface temperature was the primary objective in the Seasat mission. The antenna system was designed for a 42-deg conical scan, covering a 50-deg swath angle in a sinusoidal motion of the reflector having a 4-s period. The choice of nadir angle gives an incidence angle favorable to temperature sensing [5,6]. The antenna feeds six Dicke-switched heterodyne radiometers: one for each polarization of 37 GHz, and one for each of the lower frequencies, with polarization switched on alternate scans.

7.1.2.1 Antenna Requirements. Table 7-2 summarizes the requirements for the SMMR antenna. Since collocation of footprints was critical to the science of both NIMBUS-7 and Seasat measurements, the design selected for SMMR was an offset-fed parabolic reflector coupled to a single feed horn having a novel design and arrangement of ports to accommodate the 10 radiometer channels.

In order to meet beamwidth and beam efficiency requirements, the clear aperture diameter was 79 cm. Strut brackets were attached to the periphery of the physical reflector diameter of 83 cm.

Table 7-2. SMMR antenna requirements.

Parameter	Values				
Frequency (GHz)	6.633	10.69	18	21	37
Tolerance (MHz), (1σ)	5	8	14	16	28
Antenna 3-dB beamwidth (deg)	4.2	2.6	1.6	1.4	0.8
Tolerance (deg), (1σ)	0.2	0.15	0.1	0.1	0.1
Polarization isolation (dB)	>25				
Pointing accuracy (deg), (1σ)	0.1				
Solid-angle beam efficiency	>87 percent				

The parent paraboloid diameter (D_p) of 173 cm and focal length (f) of 52 cm give f/D_p = 0:3, the minimum ratio for which reflector-induced cross-polarization would be <–25 dB as required. Reflector construction was of graphite/epoxy, with vacuum-deposited aluminum for both radio frequency (RF) performance and thermo-optical properties. The system of tubular struts, arranged to form a hexapod truss supporting the reflector at three points, was accepted despite the added blockage, after modal vibration testing of a breadboard model revealed that unacceptable deflections would occur during launch. Shims under the struts were used to boresight the beams and adjust focus. To achieve the conical scan, bearings and a drive mechanism were placed between the shim plates and the horn.

The reflector's as-manufactured contour was specified to be within 0.07 mm root mean square (rms) from the best fit paraboloid. Worst-case allowable thermal distortion was <0.25 mm to avoid pattern degradation. The antenna was to have a 100-Hz minimum resonant frequency. To minimize contamination by stray radiance, the design allowed <0.1 percent of antenna spillover energy and <7 percent of feed spillover energy to illuminate the spacecraft.

The multi-frequency feed horn (Fig. 7-2(a)) was the most innovative item in the SMMR design. A ring-loaded corrugated horn extends bandwidth beyond the octave characteristic of simple corrugations, to 3:1. Moreover, it was noted that capacitive surface impedance would recur at odd multiples of the fundamental range. Thus, if designed for 6–18 GHz, the surface should also be capacitive between 18 = 3 × 6 and 54 = 3 × 18 GHz. Orthogonal pairs of slots (one for radiometer input and another, cavity backed, for pattern symmetry) were placed at appropriate points in the side of the feed cone, along with the orthomode transducers to input the conventional highest modes through the vertex. This horn could then launch frequencies of any reasonably wide spacing with good polarization isolation.

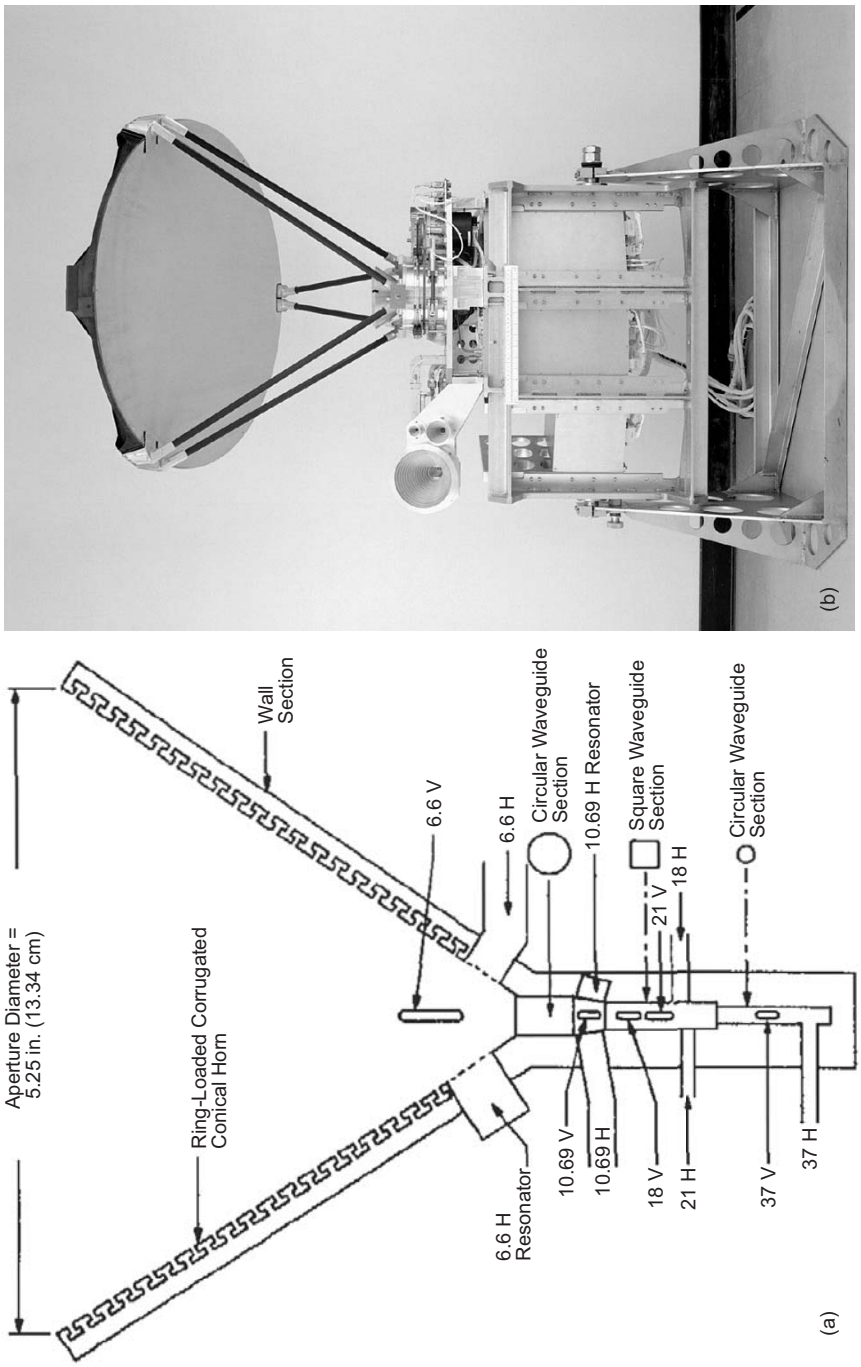

Fig. 7-2. Scanning multichannel microwave radiometer (SMMR) on Seasat-A and Nimbus-7: (a) multi-frequency feed horn (MFFH) and (b) assembled instrument.

The reflector was simulated during feed development tests using a lens sized to have the same edge taper (–22 dB) as the reflector. Coincidence of phase centers was verified by the lens collimating all frequencies simultaneously. The resulting design yielded highly efficient dual polarized primary patterns with nearly constant beamwidths at each of five frequencies needed in a 6:1 band. Near sidelobes ranged from –22 to –25 dB below the main beam [7].

Figure 7-2(b) is a photograph of the SMMR instrument. Antenna patterns of the fully assembled SMMR were measured on a 1200-foot (366-m) far-field range, over the entire 4π solid angle. Patterns at the three lowest frequencies (6.6, 10.69, and 18 GHz) showed that variation with scan angle, due to polarization rotation and to varying effects of the backup structure, was both weak and antisymmetric about a vertical plane through the antenna. Therefore, characterization for all frequencies was done at 0 deg and +25 deg only. Patterns were measured in amplitude only, since the radiances observed are incoherent; but one quantity, the relative phase between co- and cross-polarized patterns (β_p, where $p = h$ or v), was found to be needed by the data processing algorithms only after patterns were measured, and had to be estimated from subsets of in-flight data as a pseudo-geophysical quantity.

Figure 7-3 shows contours of amplitude patterns of the SMMR instrument at a particular scan position, frequency, and polarization. The pair of cross-polarization lobes about 20 dB down from the co-polarized main lobe are characteristic of offset-fed parabolic reflector antennas. The plots also show asymmetry in the sidelobes below –15 dB, which is attributed to the support struts. Numerical integration of the measured patterns provides the beam efficiencies and polarization isolations in Table 7-3. Beam efficiencies include both co- and cross-polarized power.

One science objective for the SMMR, to retrieve sea surface temperature with better than 1.5 deg C accuracy, imposed a stringent requirement for antenna pattern correction (APC), which inverts the set of antenna temperatures T_A to produce scene radiance, or (in the Rayleigh-Jeans limit) brightness temperatures T_B. These corrections can be quite large, due to (1) the disappointing beam efficiencies measured, and (2) a polarization coupling due partly to the 20-dB cross polarization but mostly to the feed horn remaining fixed while the reflector scans. The APC algorithm developed for SMMR and described in [8] corrected for these and other affects, such as spacecraft-attitude errors, Faraday rotation through the ionosphere, and retrieval of the relative phase β_p as a geophysical parameter.

In designing the SMMR, the reflector support struts had been expected to block 0.6 percent of the clear aperture area, all in the outer portion where RF illumination would be low. However, as Table 7-3 shows scattering from the

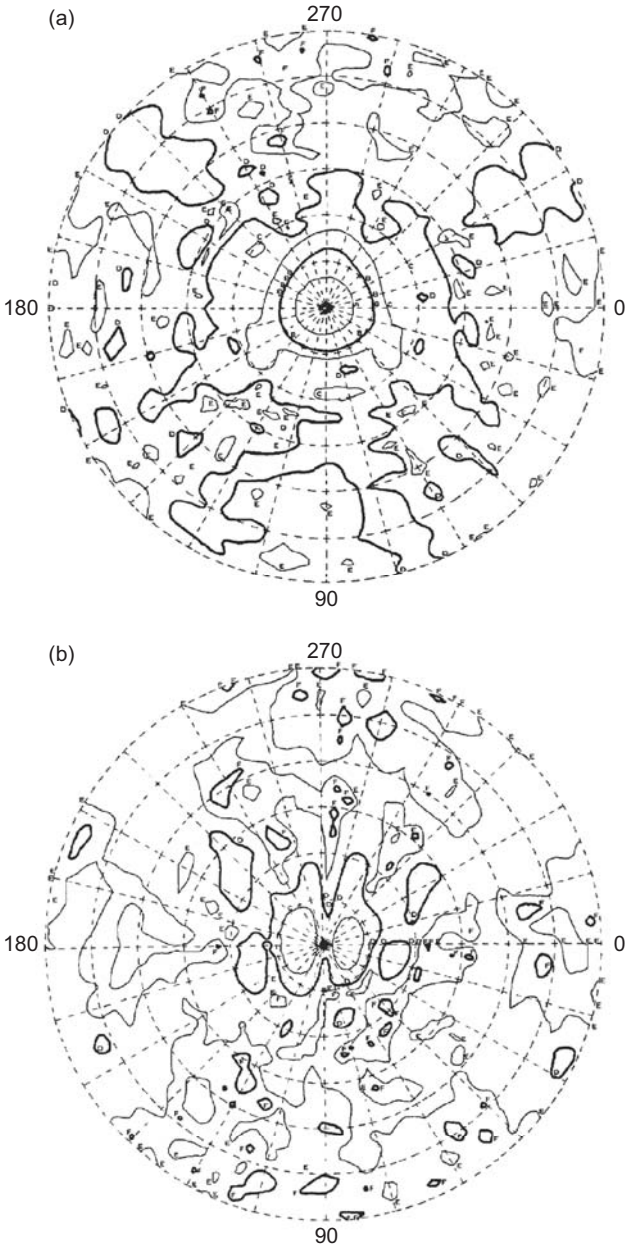

Fig. 7-3. Seasat SMMR antenna pattern contour plots at 6.6 GHz horizontal polarization, 0-deg scan position (the outer limit of the plots is at $|\theta|$ = 30 deg; contour lines are at decreasing intervals of 10 dB as follows: A = –5 dB, B = –15 dB, C = –25 dB, D = –35 dB, E = –45 dB, F = –55 dB): (a) co-polarized and (b) cross-polarized.

Table 7-3. Summary of Seasat SMMR antenna measurements.

Frequency (GHz)	Polarization	Half-Power Beamwidth (deg)	Beam Efficiency (percent)	Cross-Polarization Isolation (dB)	Dissipative Feed Loss (dB)
6.6	V	4.56	79.7	–21.5	0.55
	H	4.51	83.4	–19.9	0.55
10.69	V	2.93	83.8	–16.6	0.35
	H	2.91	86.2	–16.1	0.37
18	V	1.80	85.2	–21.2	0.50
	H	1.81	88.7	–20.1	0.52
21	V	1.50	84.2	–19.5	1.03
	H	1.49	85.8	–18.4	1.03
37	V	0.93	88.2	–17.9	0.7
	H	0.93	90.0	–17.4	0.7

H = horizontal; V = vertical

struts was a major factor in reducing the beam efficiency from the expected range (88–92 percent) to as low as 79 percent, for the 6.6-GHz V polarization. This in turn demanded high performance from the APC algorithm. In the final analysis, enough issues remained in the APC algorithm to reduce confidence in the accuracy of retrieved geophysical products. Hence, for subsequent antennas, there were significant efforts to reduce illumination of the struts or eliminate them altogether.

7.1.3 TOPEX/Poseidon Water Vapor Radiometer

The successful geophysical retrievals of the SMMR and (particularly) the radar altimeter on the Seasat mission led to proposals to use similar instruments on the Ocean Topography Explorer (TOPEX)/Poseidon mission, a joint U.S. and French effort to map ocean surface topography with precision approaching 1 cm.

Errors in the surface height measured by the altimeter result from orbit, attitude, and geoid uncertainties, from errors inherent in the radar measurement, and from inaccuracies in the time of flight of the radar signal, due to propagation effects. The TOPEX/Poseidon microwave radiometer (TMR) provides a correction to path delay due to tropospheric water vapor ranging from 5 to 50 cm, depending on temperature and humidity in the tropospheric portion of the path. After this correction (plus others due to dry air radiative transfer and ionospheric delay), the predicted accuracy of the radar altimeter was better than 1.2 cm. Experience with SMMR and the altimeter on Seasat showed unacceptably large errors due to the SMMR swath lying 42 deg ahead of the altimeter FOV at nadir; therefore the TMR configuration required co-

alignment of radiometer and altimeter boresights. The scanning capability of SMMR was also removed from the TMR [9]. The TMR reflector was a flight spare from the Nimbus-7 and Seasat SMMR programs.

The 6.6- and 10.69-GHz channels, used in SMMR for sea surface temperature and surface wind retrievals, were dropped from the TMR. Likewise, one polarization of each of the 18- and 37-GHz channels was discarded. Both polarizations were retained for the 21-GHz channel, deemed critical to the path delay retrieval, with one polarization redundant, to be activated only if the other failed. These changes also relaxed the requirements

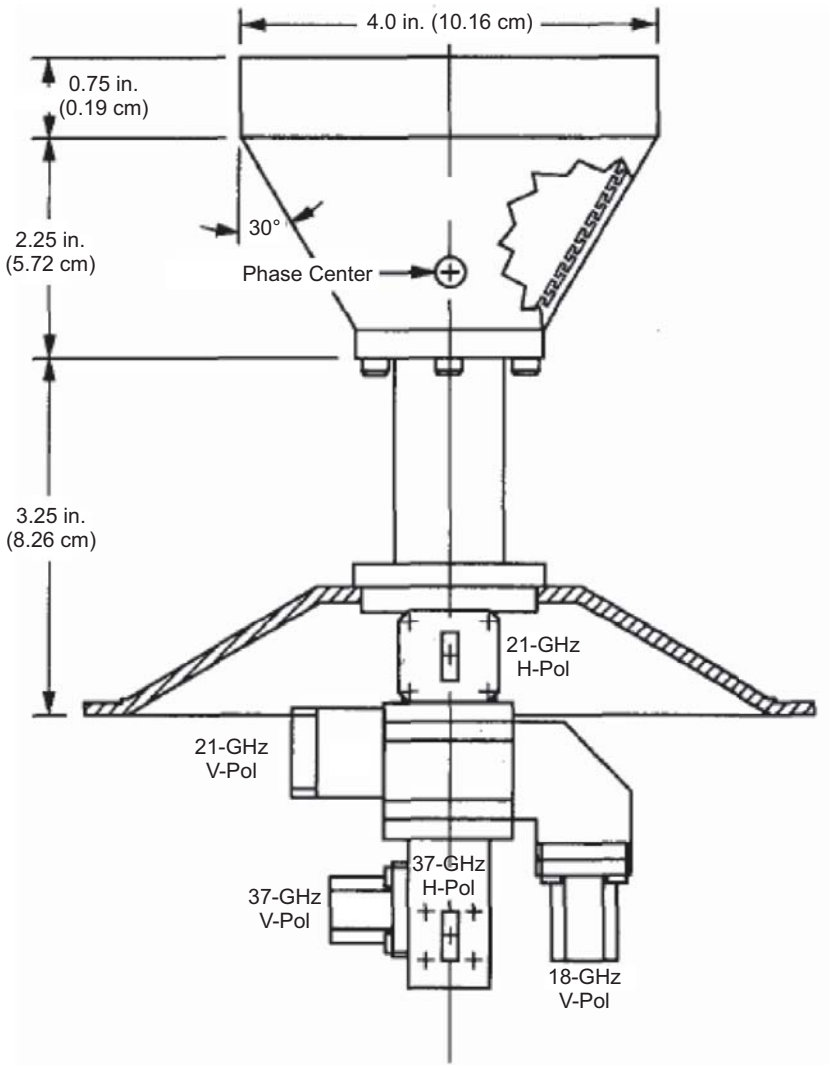

Fig. 7-4. TOPEX/Poseidon TMR multifrequency feed horn.

on the multifrequency feed horn (Fig. 7-4), for which the flare angle was reduced. Another beneficial result was to under-illuminate the reflector by 1 to 3 dB lower than SMMR, depending on frequency. This expands the HPBW by 5 percent but reduces spillover, and (with less illumination of the strut supports) it increases main beam efficiency by 2.4 percent, mitigating the need found in SMMR for extreme accuracy in the antenna pattern corrections.

Antenna patterns of all four channels of the TMR were measured on the JPL antenna range facility at a distance of 366 m, more than twice the far-field distance $2D^2/\lambda$. Patterns were measured in both polarizations over the full 4π solid angle. The effects of range asymmetry were seen in the low sidelobes between 130 and 180 deg from boresight, using the redundant pattern data obtained with the available positioner axes, and removed from the dataset used for processing of in-flight data [10]. Table 7-4 summarizes the measured performance of the TMR antenna and its lowest expected mechanical resonant frequency.

Figure 7-5 is a line drawing of the TOPEX/Poseidon spacecraft with the microwave radiometer viewed from behind its reflector. The mounting angle is for co-alignment of the radiometer and altimeter boresights. Not shown are the cold space calibration horns, which were pointed away from the Sun, to avoid radiometric contamination of the calibration noted in [6].

Radomes consisting of flat slabs of polystyrene (0.95 cm thick, with dielectric constants in the range 1.03–1.16) were also mounted in front of the multifrequency feed horn and sky horns, to reduce solar heating of these horns which results in antenna temperature fluctuations. The voltage standing wave ratio (VSWR) and insertion loss were determined radiometrically (using other ground-based water vapor radiometers) for inclusion in the antenna temperature calibration, and antenna patterns were made with radomes present. Ultraviolet

Table 7-4. TMR antenna specifications.

Parameter	Values			
Frequency (GHz)	18	H21	V21	37
Half-power beamwidth (±0.1 deg)	1.86	1.56	1.59	0.98
Solid-angle beam efficiency (percent)	91.1	89.3	87.4	90.5
Back-lobe artifact beam fraction	0.0018	0.0011	0.0017	0.0009
• Flight antenna beam fraction outside main beam	0.028	0.025	0.032	0.022
• Within Earth limb	0.005	0.003	0.003	0.004
Boresight co-alignment with altimeter (deg), (3σ)	0.4			
Minimum natural frequency (Hz)	>55			

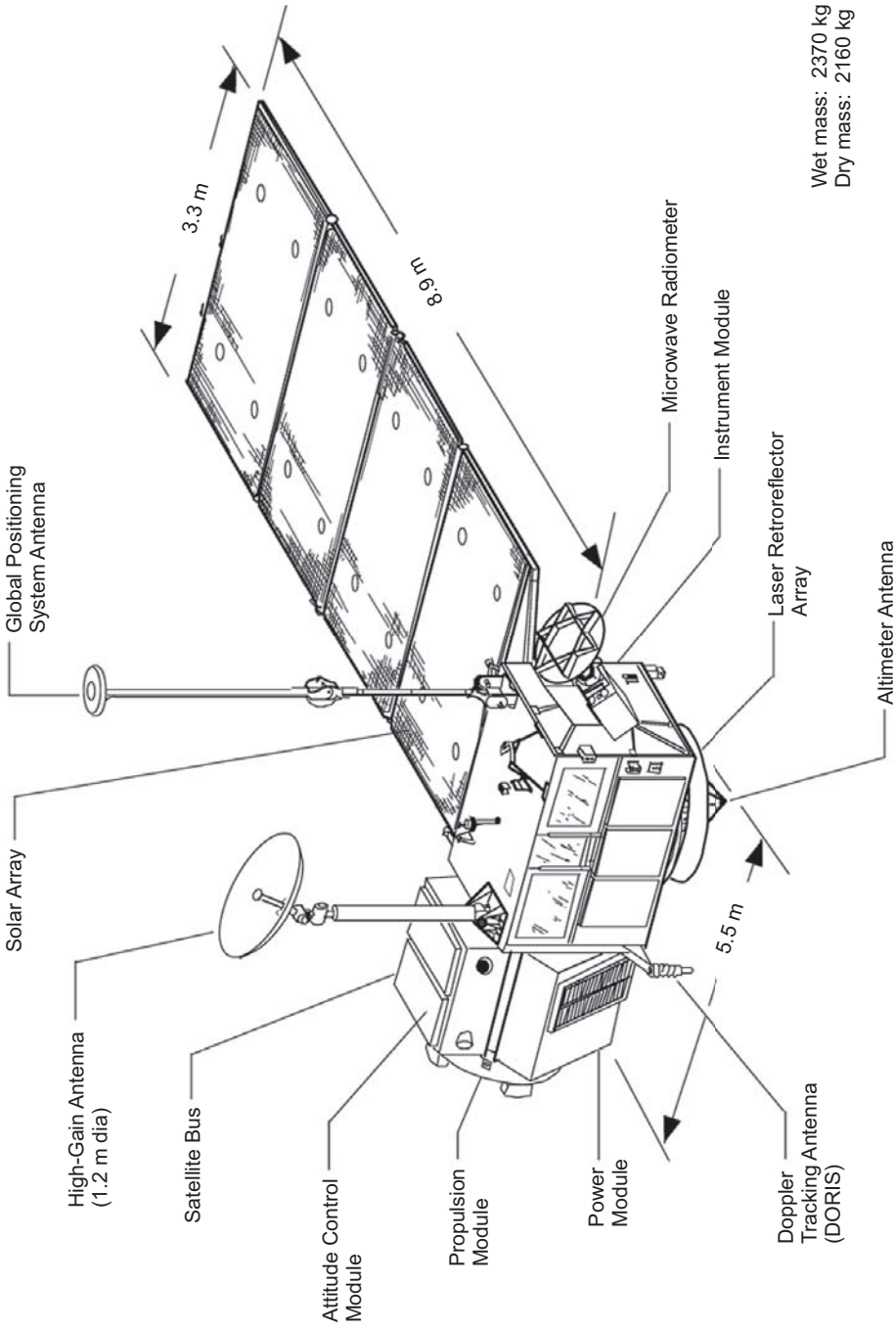

Fig. 7-5. TOPEX/Poseidon spacecraft.

exposure of the radomes, at several times the level expected in the orbital environment, resulted in some discoloration of the radome, but the darkening was self-limiting, and its ultimate effect on RF and thermo-optical performances was negligible.

Combining all known error sources from ground calibrations, the accuracy of the TMR data product was expected to be 0.57 K in antenna temperature, which when propagated through the antenna pattern-correction algorithm gives 0.77 K in brightness temperature, a significant improvement over SMMR.

TOPEX/Poseidon was launched on August 10, 1992; the TMR was activated and produced data 5 days later. Standard data sets in the final operational orbit began September 23 and have continued through the present, i.e., three times the planned prime mission lifetime of 3 years.

Engineering telemetry showed that the rate of change of antenna temperature during solar illumination of the feed and sky horns was below 0.001 deg C/s—again a significant improvement over 0.015 deg C/s experienced with SMMR and a validation of the feed redesign. The post-launch validation campaign revealed gain errors as large as 10 percent in the TMR water vapor retrieval, relative to ground truth obtained from upward-looking water vapor radiometer and radiosondes. This error was attributed partially to uncertainties in the 22-GHz water vapor absorption line strength, and partially to underestimates of the far sidelobe beam fractions of Table 7-4, which are applied in pattern correction [11]. These amendments to the ground calibration dataset were in some cases as large as a four-fold increase in the fraction of beam power missing the Earth. This reinforces the need for accurate pattern knowledge derived from both ground and in-orbit calibrations.

7.1.4 Jason Microwave Radiometer

The goal of the Jason-l mission is to further the understanding of global ocean dynamics by precise and accurate measurements of the ocean's topography, begun by the TOPEX/Poseidon mission. Jason-1 was launched in December 2001, and presently operates in tandem with TOPEX/Poseidon, which increases the data flow and allows cross checks between the two instrument platforms. As with TOPEX/Poseidon, the principal instrument carried by Jason-l is a radar altimeter, the accuracy of which is affected by the variable water content of the atmosphere, especially the troposphere. The objective of the Jason-l microwave radiometer (JMR) is passive measurement of the radiometric brightness temperature arising from water vapor and liquid water in the same FOV as the altimeter. These brightness temperatures, in turn, are converted to path-delay information required by the co-aligned altimeter for precise topography measurements. The JMR continuously measures the microwave radiation at 18.7, 23.8, and 34 GHz, and the data are used to

determine water-vapor and liquid-water content in the altimeter FOV. The JMR antenna system consists of:

1) A collecting aperture with the RF pointing axis aligned collinear with the pointing axis of the altimeter sensor.
2) A multifrequency feed assembly that illuminates the collecting aperture.
3) Multichannel microwave receivers coupled to the feed assembly.

Antenna requirements, given in Table 7-5 [12] are derived from orbital parameters for the Jason-l mission, viz.: (1) Altitude 1336 km, nominal (1000–1500 to be accommodated), (2) Inclination 66 deg.

The antenna/feed system, like that of SMMR and TMR, is an offset parabolic reflector illuminated by a single feed horn. The reflector surface consists of multiple layers of vapor-deposited aluminum and silicon dioxide. The feed horn is a multifrequency dual-polarized feed assembly that operates at both horizontal and vertical polarization, and it is designed to operate at the three center frequencies given above. Both the reflector and the feed are similar to the components flown as part of the TOPEX/Poseidon TMR.

Although TMR patterns had been measured in the far field on the JPL antenna range, JMR patterns were measured in the intermediate field (16 m «154 m= $2D^2/\lambda$) at a contractor facility. This indoor range enabled the patterns to be taken with a dynamic range of 63 dB, compared to 71 dB for TMR on the JPL range, and the beam fraction to be calculated to an accuracy of 0.25 percent vs. 0.43 percent on the JPL range. The intermediate range was operated as a spherical near-field range, in order to characterize the back lobes accurately. All performance requirements were met or exceeded on the flight model unit.

Figure 7-6 is a photograph of the JMR. Jason-1 was successfully launched on December 7, 2001, and its orbit was then adjusted to match that of TOPEX/Poseidon, with a 1-minute time separation. Both instruments then began a rigorous comparison and correlation of the two altimetry results from near-simultaneous measurements from the same altitude of the same sea surface locations. Initial results showed that the Jason altimeter and radiometer met all mission requirements. In August–September 2002 the orbit of

Table 7-5. JMR antenna requirements.

Parameter	Values			
Frequency (GHz ±25 MHz)	18.700	23.800 (H)	23.800 (V)	34.000
Pre-detection ± dB bandwidth (MHz)	200	400	400	700
Half-power beamwidth (±0.1 deg)	1.8	1.5	1.5	0.9
Solid-angle beam efficiency	>90 percent			
Boresight co-alignment with altimeter (3σ)	0.4 deg			
Minimum natural frequency	>55 Hz			

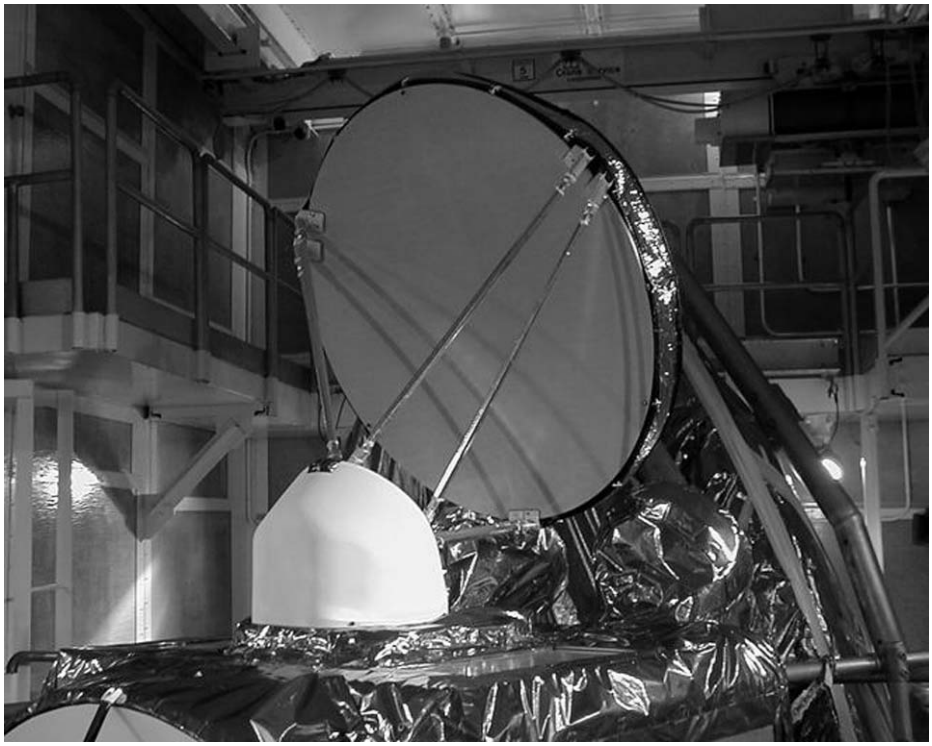

Fig. 7-6. JASON microwave radiometer (JMR) aboard JASON-1 spacecraft.

TOPEX/Poseidon was adjusted to have an orbital phase 180 deg from JASON, so that the two satellites increased global data coverage twofold.

7.1.5 Microwave Instrument for the Rosetta Orbiter

The microwave instrument for the Rosetta orbiter (MIRO) is a radiometer with millimeter and sub-millimeter receivers that will observe comet dynamics and composition; its mission also includes three planetary fly-bys and two asteroid flybys. After rendezvous with the comet at 4 AU and separation from the lander portion of the spacecraft, the orbiter will follow the comet through perihelion.

The sub-millimeter radiometer operates between 545 and 580 GHz, monitoring inner coma development by spectroscopy of several gasses at the comet, and measuring low levels of gas in the asteroid environment. A millimeter-wave radiometer operating at 190 GHz provides continuum measurements for temperature sensing and surface processes (to depths of a few centimeters at the comet nucleus or asteroid surface) [13].

7.1.5.1 Antenna Requirements. The performance requirements of the MIRO antenna and optics are made stringent by exposure to the Sun and to the cometary environment, and by the temperature extremes over which the radiometer must operate: between 100 K (comet rendezvous) and 300 K (perihelion). Further requirements for a robust mechanical design are imposed by the Ariane-5 launch vehicle, with a minimum instrument eigen-frequency of 150 Hz, and by the 15-year lifetime between launch and comet rendezvous. Table 7-6 gives the MIRO antenna requirements [14].

The antenna is completely exposed to the space environment, while the multiplexer optics and receivers are within the Rosetta spacecraft. Due to the resulting constraints on the antenna size, the requirement for low sidelobes, and a desire for main beam efficiency exceeding 90 percent, an offset Cassegrain reflector system was chosen for the design. The advantages of an unblocked optical path were shown to outweigh the penalty of an asymmetric support structure in the thermal-mechanical deformation phase of the design.

7.1.5.2 Selected Design. Both the support structure and the reflectors were made all of aluminum for lightness and to achieve a homologous deformation giving nearly constant antenna performance over temperature. For the same reason, a beamwaist was placed at the first internal mirror, close to the fixed point of the thermal deformation, keeping the phase center near the telescope focus for all environments. Supports were designed to be as symmetric as possible to minimize lateral misalignments due to thermal deformation.

Figure 7-7 is a photograph of the MIRO telescope assembly, showing primary and secondary reflectors and the hole through which the beam is focused onto the turning mirror. Figure 7-8 shows the schematic diagram of the optical system. The primary mirror is a paraboloid 300 mm in diameter, the

Table 7-6. MIRO antenna requirements.

Requirement	190 GHz	564 GHz
Loss contribution (dB)		
Spillover	0.1	0.1
Surface rms	0.1	0.3
Illumination	1.6	1.5
Total loss	1.8	1.9
Peak gain (dB)	53.7	63.0
HPBW (deg)	0.4	0.15
Tolerance limits		
Sidelobe level (dB)	–30	–30
Pointing (deg)	0.04	0.015

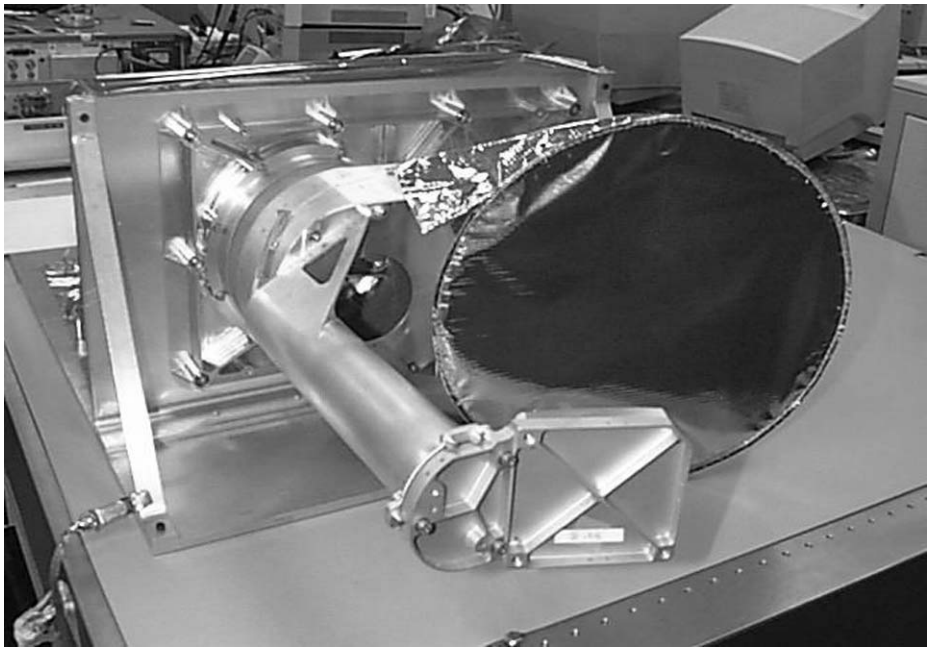

Fig. 7-7. Microwave instrument for the Rosetta Orbiter (MIRO) telescope.

secondary mirror is a hyperboloid 90 mm in diameter, and the turning mirror (at the beamwaist) is planar. This mirror is also the only moving mechanical part of the optical system; it switches radiometer views to the telescope or to either of two black-body calibration loads, which overfill the feed beams. One of these targets is kept near ambient temperature, while the other is thermally connected to cold space; their temperature difference gives two radiances, which are used for periodic radiometric calibration.

As is customary at these frequencies, the multiplexing between millimeter and sub-millimeter receivers is performed quasi-optically, using a wire-grid polarizer, to avoid ohmic losses of waveguide. Curved mirrors are used to match the large *f*/D beam, produced by the Cassegrain design, to corrugated feed horns attached to the mixer assemblies. Thermal analysis showed predicted temperature excursions of the optical bench to be small enough that alignment shifts would be negligible.

7.1.5.3 Performance Estimates. The antenna reflector surface figure was 11 μm rms, which was expected to contribute much less to sidelobe levels than larger-scale effects, such as feed pattern imperfections and distortions under vibration or thermal deformation. An extensive suite of mechanical, thermal, and RF design tools was developed to predict these changes in antenna patterns. Typically, undistorted sidelobe levels of –37.8 and –38.3 dBr respectively, for

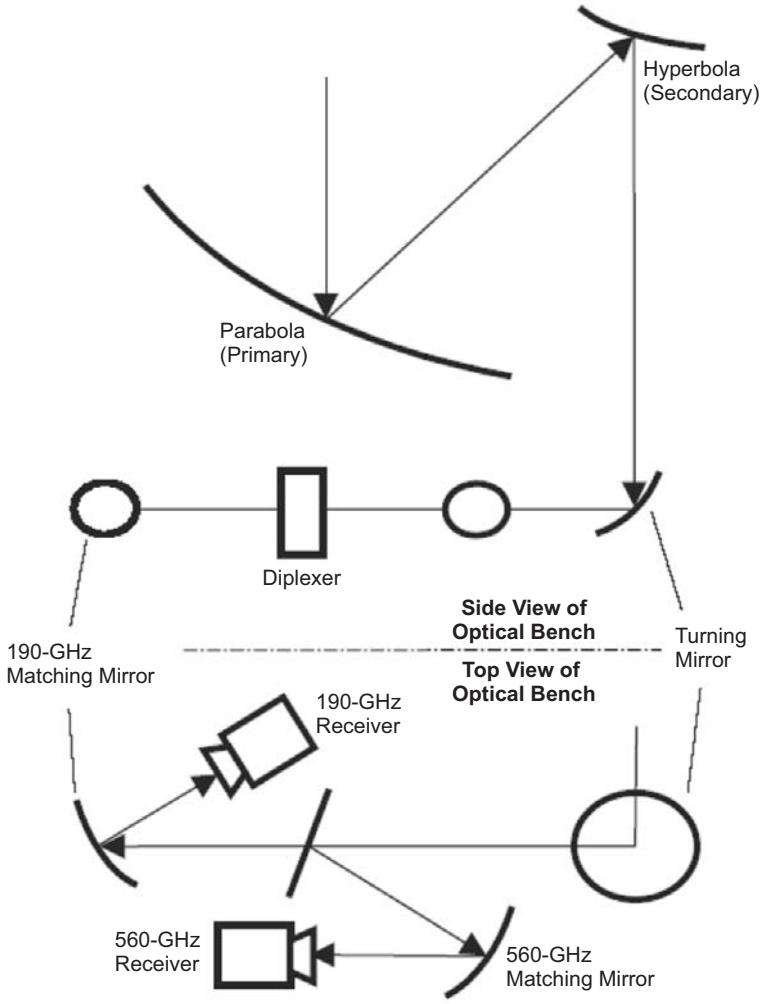

Fig. 7-8. Schematic diagram of the MIRO optical system, including side and top views of the optical bench.

the millimeter and sub-millimeter beams, would be distorted in the worst environments to just the –30 dBr level of the requirements.

Due to water vapor absorption near 550 GHz, the atmospheric path loss would be too large and too variable over even the modest $2D^2/\lambda = 360$ m required for far-field patterns. Therefore, a near-field range was obtained, and phase-locking electronics were developed at the receiver frequencies for measuring MIRO antenna patterns. Preliminary results of these patterns show HPBWs of 0.39 and 0.125, which meet the requirements of Table 7-6. Sidelobe levels range between –28 and –34 dB below the main beam, which nearly

meets the requirement. Main beam efficiency is about 92 percent, a typical value for tapered dual-offset reflector designs.

7.1.5.4 Conclusions. When the analysis of pattern measurement is completed, MIRO antenna requirements are expected to be met, although the elevation of sidelobe levels due to thermal deformation may remain an issue that cannot be resolved from pre-flight calibration.

Antenna performance under extreme environments is still verified by analysis, rather than by measurement during environmental qualification tests. However, recent advances in optomechanical metrology promise to give much better insight into the alignment of antenna components during test. This, plus the maturity of sophisticated RF scattering models over the past few decades, lets the designer expect to be able to prove much stronger statements about radiometer antenna performance in the extreme environments of deep-space missions.

The MIRO instrument was integrated with The European Space Agency's (ESA's) ROSETTA spacecraft and launched March 2, 2004, on board an Ariane-5 rocket from Europe's spaceport in Kourou, French Guiana. Rendezvous with the comet 67P/Churyumov-Gerasimenko is expected in November 2014.

7.2 Microwave Limb Sounders (MLS)

Richard E. Cofield

Microwave limb sounding is the measurement of thermal emission spectra at millimeter and sub-millimeter wavelengths by scanning the field of view (FOV) of a heterodyne radiometer instrument through a planetary atmospheric limb from above. Analysis of the measured spectra determine atmospheric profiles of temperature, pressure, wind, magnetic field, and molecular abundances, particularly of trace species with thermal emissions that can only be detected using the long path lengths involved. A strong motivation to measure such species comes from the need to understand the chemistry of ozone (O_3) destruction in Earth s stratosphere, and climate change in the upper troposphere. Thermal emission, requiring no external sources, can be observed continuously, and at these frequencies even in the presence of clouds and rain. Thus, instruments can be developed for orbiting satellites for long-term global coverage with reliable calibration [15].

For atmospheric limb sounding in optically thin spectral regions, most of the signal originates from thermal emission by that portion of the ray path which is normal to a radius vector from Earth center, i.e. tangent to a surface of constant height (or pressure). Thus, the two important heights are platform or observation height and tangent height, denoted h_0 and h_T, respectively.

Several airborne and balloon implementations of microwave limb sounders validated the technique before the first satellite implementation. They continue to provide invaluable tests as new technology evolves, plus opportunities for ground truth validation.

7.2.1 UARS MLS

The microwave limb sounder (MLS) instrument flown on the Upper Atmospheric Research Satellite (UARS) was the first spaceborne application of microwave limb sounding. MLS was one of 10 UARS instruments in a National Aeronautics and Space Administration (NASA) mission dedicated to the comprehensive and integrated study of the Earth's upper atmosphere. Table 7-7 [16] gives the measurement objectives, radiometer bands, and local oscillator (LO) frequencies of the UARS MLS. Chlorine monoxide (ClO) is the rate-limiting molecule in chlorine destruction of O_3, and MLS measurements of its abundance on a global scale indicated the rate at which chlorine destroys ozone. Simultaneous measurements of O_3 and water (H_2O) provided additional information on stratospheric ozone chemistry. Pressure measurements from molecular oxygen (O_2) provided the vertical coordinate for atmospheric profiles.

The MLS instrument is described in [17]. Figure 7-9 shows the MLS signal flow block diagram. Its antenna received radiation from the atmospheric limb and was mechanically scanned in the vertical. A switching mirror accepted radiation either from the antenna or, for calibration, from an internal target or a space view. An optical multiplexer then separated signals into the three heterodyne radiometers. Requirements for the antenna and optics design were derived directly from the functional requirements on the instrument FOV. In

Table 7-7. UARS MLS radiometer bands and mission objectives.

Radiometer	LO Frequency (GHz)	Band	Intermediate Frequency Range (MHz)	Primary (Secondary) Parameter	Measurement h_T Range (km)
1	63.283	B1	90–540	Pressure, temperature	30–60
2	203.267	B2	830–1340	ClO	15–45
		B3	1053–1563	(H_2O_2)[a]	
		B4	2610–3120	O_3	15–50[b]
3	184.778	B5	1213–1723	H_2O	15–85
		B6	145–655	O_3	21–80[b]

[a] H_2O_2 = hydrogen peroxide; was a secondary mission goal
[b] Tangent height range refined in post-launch science data analysis [16]

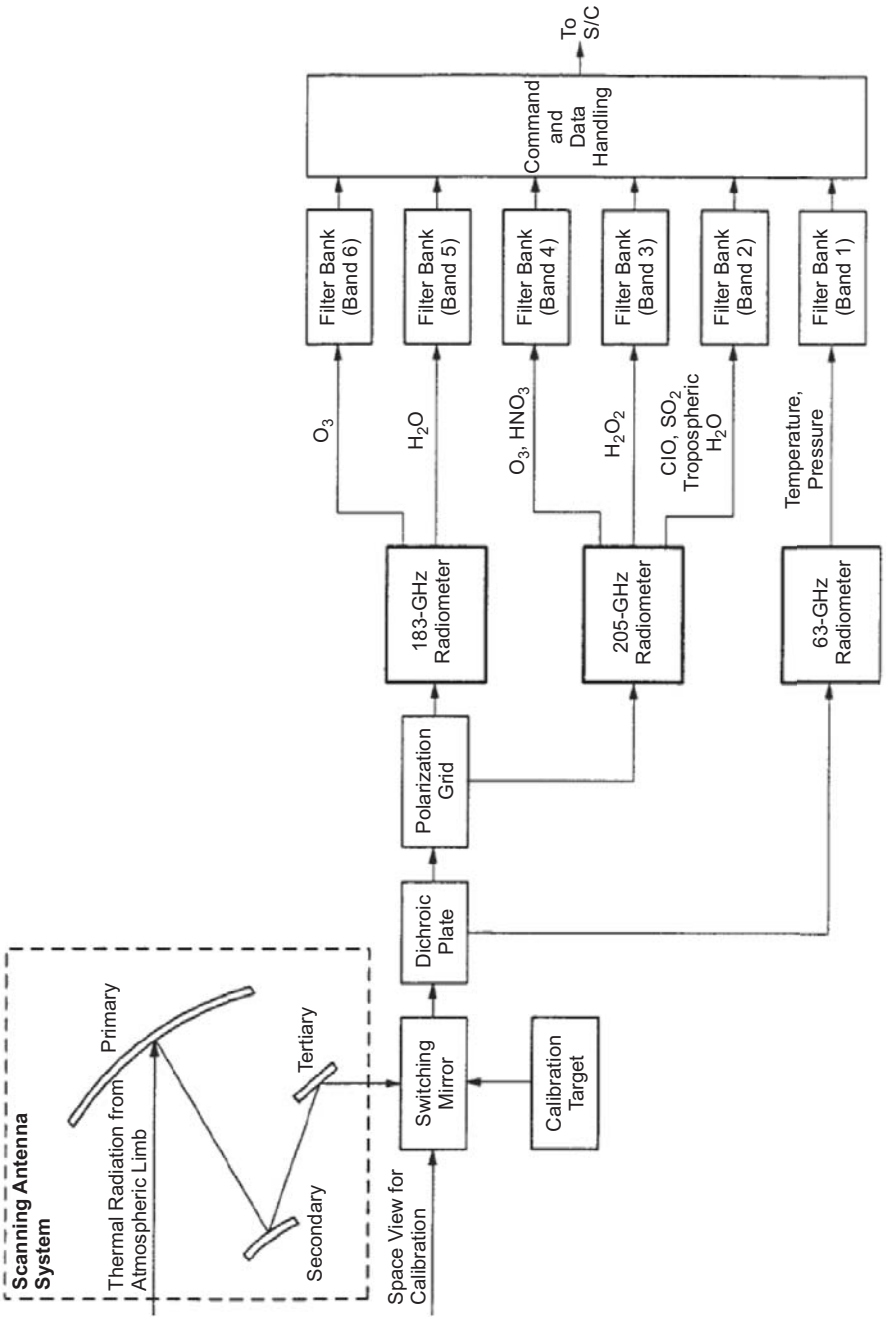

Fig. 7-9. Signal flow block diagram of the Upper Atmosphere Research Satellite (UARS) microwave limb sounder (MLS) instrument.

addition to customary requirements on HPBW, boresight direction, and beam efficiency, the algorithms for atmospheric profile retrievals levied requirements for detailed knowledge of the actual pattern shape. This was supplied by combining analysis with pattern measurements, as functions of frequency and scan angle in both polarizations and overall solid angles.

7.2.1.1 Antenna Requirements. The MLS FOV is defined as the response of the MLS as a function of direction to power received from an isotropic radiation field. This response is normalized to a maximum value of unity; hence, FOV corresponds to antenna directivity, with some qualifications for polarization in the limb-sounding application. FOV half-power beam width (HPBW) is defined as the angle between the half-power points of the FOV function. Requirements levied on the MLS HPBW are given in Table 7-8 and are converted from footprint kilometers to beam angles using the known viewing geometry. The HPBW must be known and stable to within 5 percent of its value measured during FOV calibration.

Table 7-8. UARS MLS requirements.

Radiometer Band	Vertical HPBW		Horizontal HPBW	
	km	deg	km	deg
B1 (63 GHz)	≤12	≤0.25	≤30	≤0.64
B2–4 (205 GHz)	≤3.5	≤0.075	≤10	≤0.21
B5–6 (183 GHz)	≤4.0	≤0.083	≤10	≤0.21

Boresight Pointing Accuracy	Time Scale	Vertical		Horizontal	
		km	arcsec	km	arcsec
Placement	—	3.0	225	30	2250
Knowledge	Mission	3.0	225	30	2250
Stability	65-s scan	0.3	23	3	225
Jitter	1.8-s dwell	0.3	23	3	225

Vertical Scan	
Step size	0.05 ±0.01 deg
Encoder resolution	≤0.001 deg
Dwell time between steps	1.8 ±0.1 s
Time for movement between adjacent steps	<0.3 s
h_T of scan range for atmospheric measurements	0–120 km
h_T of FOV direction for space view	>200 km
Scan axis/UARS velocity vector collinearity	±0.5 deg

FOV boresight is defined as the direction midway between half-power points in the vertical and horizontal planes. Requirements levied on the MLS FOV boresight coincidence ensured that different radiometers observe the same region of the atmosphere to within acceptable limits. The FOV boresights of all bands coincided to within 0.2 of the largest HPBW, and the coincidence was known and stable to within 4 arc seconds in the vertical plane and 20 arc seconds in the horizontal plane.

Beam efficiency is defined as that fraction of power from an isotropic source, which is collected within a specified angular range centered at the antenna boresight. For each MLS band identified in Table 7-7, the beam efficiency was required to be >0.5 within the HPBW and >0.9 within 2.5 HPBW. Beam efficiencies were required to be known and constant throughout the UARS mission to within 1 percent.

Table 7-8 also gives MLS scan requirements and tolerance requirements on FOV placement, knowledge, stability, and jitter. Finally, the lowest mechanical resonance frequency (driven for this instrument by the stiffness of the antenna support cradle) was >35 Hz.

The MLS FOV had to be determined to allow calculation, with the required accuracy, of received signal for a specified atmospheric radiation field. This determination was called FOV calibration in the MLS project, and it consisted of a mixture of antenna pattern measurements with analytical models, both in the solid-angle regions where measurement was infeasible, and of the thermal deformation of the antenna in orbit. As in the formulation for the SMMR [8], we write the antenna temperature

$$T_A = \frac{1}{4\pi} \int_{\text{all directions}} G(\Omega)\, T_B(\Omega)\, d\Omega$$

where $G(\Omega)$ describes the FOV in direction $\Omega(\theta,\phi)$ and is normalized so that $\int G(\Omega) d\Omega = 4\pi$; T_B is a brightness temperature kernel from a set of modeled atmospheric profiles, which vary only in the limb vertical direction for calculating the accuracy and resolution needed for $G(\Omega)$. The requirement is that $G(\Omega)$ be determined with sufficient accuracy and resolution to introduce less than 0.5-percent error in the calculation of T_A from the preceding equation, for FOV boresight directions encountered during the scan in orbit.

Despite this formulation of requirements, analysis of MLS data did not follow the APC method of SMMR, but rather combined FOV calibration data with spectral calibration data (filter shapes and sideband responses) in a forward model which related instrument radiances directly to geophysical parameters[15,17]. The resulting sensitivities were then used with *a priori* climatology profiles to retrieve actual profiles, with a nonlinear retrieval algorithm [16]. This approach has also been used in the successors to the UARS MLS.

7.2.1.2 Trade-off Studies. A reflector antenna system was the only candidate considered capable of producing the electrically large ($D \sim 1000\lambda$) aperture required. Reflectors were offset to avoid blockage, and a dual reflector system was used to achieve both a compact antenna and the moderately large f/D required for quasi-optical multiplexing the various bands and injecting LOs. Since the scan range (including margin and space view) was ~120 × HPBW, the beam scan deviation had to be minimized by scanning in the long f/D portion of the beam, i.e., between the secondary reflector and the multiplexer.

7.2.1.3 Selected Design. The antenna system was a dual-offset Cassegrain with a 1.6 × 0.8 m elliptical aperture. The elliptical aperture saved space in the instrument envelope but constrained the location and curvatures of subsequent mirrors that coupled antenna beams into the receiver feed horns. The primary reflector was an offset paraboloidal section of a 1-m focal length parent surface, with the aperture center offset 0.7 m from the parent axis. With the hyperboloidal secondary reflector, the antenna effective focal length was 5.9 m. A flat tertiary reflector diverted the limb radiation signal along an axis coincident with the mechanical scan axis, into a box housing the optical multiplexer and front ends of the three radiometers. The power illumination level at the primary aperture edge, when projected from the design feed pattern, was 15 dB below the level at aperture center, and it defined the limiting aperture size. The secondary and all subsequent optical elements were sized to truncate at –20 dB.

Since emission from the atmospheric limb is unpolarized (except for Zeeman splitting in the 63-GHz channels), the only degradation due to cross polarization appears as broadening of the net pattern (power sum of co- and cross-polarized patterns), i.e., degraded beam efficiency. Therefore, the angle between hyperboloid and paraboloid axes was relaxed from the Mizuguch value, which in the geometrical optics approximation cancels aperture cross-polarized fields. The actual angle permitted structural support for the secondary and tertiary reflectors with the scan bearings, in a reasonably compact envelope.

Table 7-9 gives the physical characteristics of the three antenna reflectors, and Fig. 7-10 shows the MLS instrument in flight configuration. All reflectors and structure were made of aluminum to ensure homologous deformations, so that the antenna stayed in focus over a wide range of temperatures.

The tolerance requirement for reflector surfaces was met with a net value of 28 μm (root sum square [rss] over three surfaces). Thus, upper bounds on scattering loss were 0.043 for the 183-GHz band and 0.054 for the 205-GHz band. Estimated losses were reduced further by excluding surface errors of large enough correlation length to appear in the measured antenna patterns. The signal-to-noise ratio (SNR) achieved during antenna tests imposed limits on this reduction. SNR was 55 dB for 63 GHz, 42 dB for 183 GHz, and 50 dB for

Table 7-9. UARS MLS physical antenna characteristics.

Parameter	Primary	Secondary	Tertiary
Reflector aperture (m)	1.6 × 0.8	0.45 × 0.24	0.24 × 0.20
Effective focal length (m)	5.9		N/A
Surface accuracy (μm)	23	13	8
Edge illumination (dB)	–15	–20	<–15

205 GHz patterns, resulting in estimated scattering losses of 0.001, 0.012, and 0.008, respectively [18].

Performance of the antenna under orbital heat loads was predicted by feeding temperature fields from a thermal model into a NASA structural analysis computer program (NASTRAN) structural model, which calculated deformations. In turn, these were input to an optics model. Expected changes in pointing direction and aperture phase curvature were well within allocations for all anticipated conditions. Bead-blasting in the final stages of manufacture gave the reflectors their required diffusivity. Effects of this surface treatment were a shift in focal length, corrected with shims during antenna assembly, and a small decrease in antenna reflectivity, to >0.995 per surface, measured radiometrically on witness samples using an engineering model [19].

A calibration switching mirror in the radiometer module diverted the views of radiometers from limb to cold space and ambient temperature targets, like those described above for previous instruments. Its output was separated by a quasi-optical multiplexer into the three radiometers. The multiplexer used wire grid polarizers and dichroic plates for low signal path losses, ranging from 1.0 to 1.5 dB, and included toroidal mirrors to match the elliptical astigmatic beams to the circular beams of radiometer feed horns. Horns were of a dual-mode conical design modified [20] from the Potter horn design for easy fabrication at high frequencies. LO injection for the 183- and 205-GHz frequencies was accomplished using folded ring-resonant Fabry-Perot diplexers. Gaussian beam optics were used throughout the design.

Radiometer feed patterns were measured at the subassembly level to verify proper antenna illumination, alignment sensitivity, and radiometer port spillover levels. These were repeated using the radiometer box assembly for the engineering model. Secondary patterns were characterized on far-field ranges at 3 and 1 km, at 10 scan angles, and at five frequencies within each band. Boresight directions at 63 and 205 GHz were measured to 15 arcsec relative to an optical alignment cube using a theodolite in conjunction with the RF patterns. A more stringent 2-arcsec knowledge of relative pointing between all radiometers was measured with near-simultaneous patterns using two transmitters at known separations.

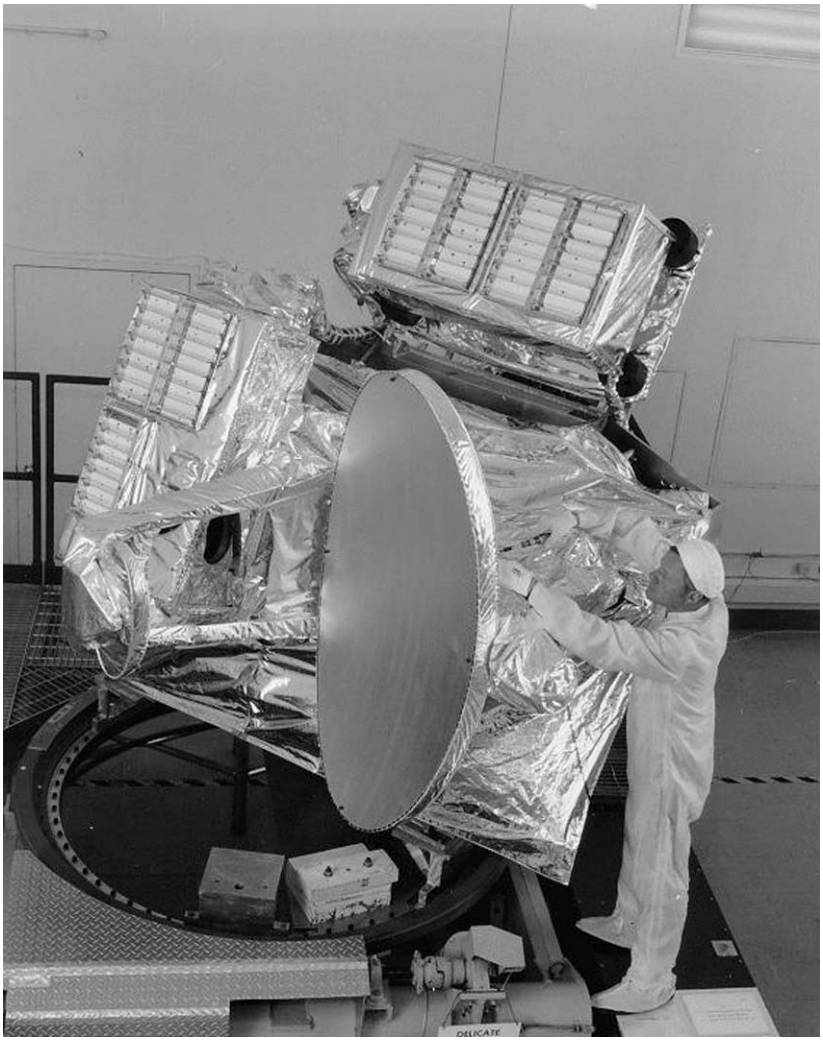

Fig. 7-10. UARS MLS in flight configuration.

Figure 7-11 shows a vertical plane cut of the UARS MLS 205 GHz antenna pattern. Table 7-10 summarizes the UARS MLS antenna performance. Beamwidths and beam efficiencies met the requirements of Table 7-8, as did boresight directions, and the FOV calibration data set sufficed to meet the most stringent mission requirement, measurement of O_3 to an accuracy of 1–3 percent [17].

UARS was launched September 12, 1991 from the space shuttle Discovery into a 600-km altitude, 57-deg inclination orbit. Useful spectra were obtained within days after activating the MLS. Ground calibration and instrument

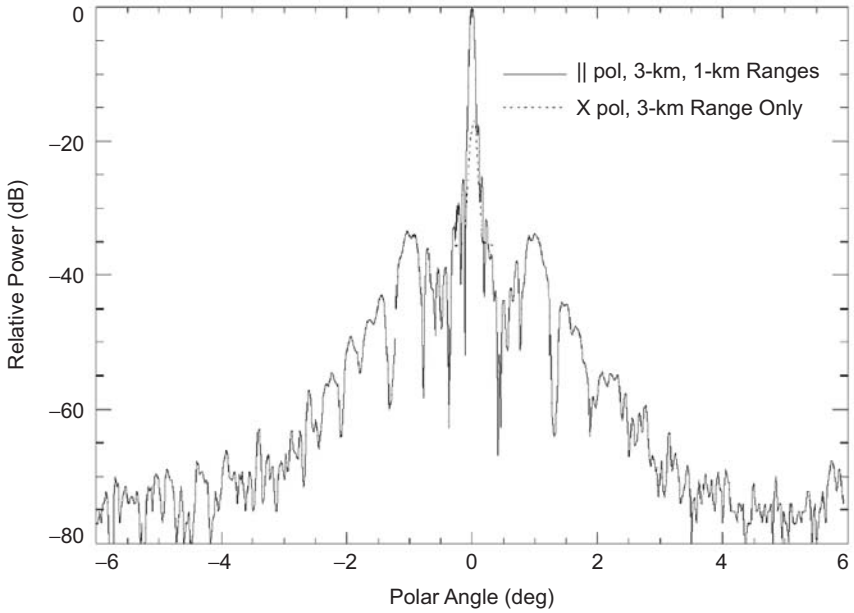

Fig. 7-11. 205-GHz limb vertical antenna pattern of UARS MLS.

Table 7-10. UARS MLS antenna performance.

Parameter	63 GHz (B1)	183 GHz (B5–6)	205 GHz (B2–4)
Vertical HPBW (deg)	0.206	0.077	0.064
1 σ uncertainty	0.002	0.001	0.001
Horisontal HPBW (deg)	0.43	0.152	0.145
1 σ uncertainty	0.008	0.002	0.003
Beam efficiency (1 σ = 0.01)	0.91	0.91	0.9
Polarization (angle from vertical of E projected from feed, at 30-km pointing) (deg)	114	1	91
Peak cross-polarization (dB)	–30	–20	–19
FOV direction knowledge elevation (deg)			
Absolute, B1 to alignment reference	0.0036	N/A	N/A
Relative to B1	N/A	0.0021	0.0016
Ohmic efficiency	0.992	0.992	0.989
Wide-angle efficiency (spillover, scattering, edge diffraction)	0.931	0.977	0.976

operations were of such high quality that several additional products were added to the UARS MLS dataset, including geopotential height, nitric acid (HNO_3), and sulfur dioxide (SO_2) during periods of significant enhancement

(such as following the eruption of Mount Pinatubo), upper tropospheric humidity, and acetonitrile (CH_3CN).

Two discrepancies between pre-launch FOV calibration and in-orbit data were found: An error in absolute pointing of 0.12 deg was attributed to uncertainty in the chain of transformations between alignment transformations from the MLS boresight to UARS reference, and it was corrected in the first few weeks of operation. The second discrepancy was a 15-percent difference in O_3 profiles retrieved from the 183-GHz and 205-GHz radiometers. This was reduced to <5 percent, in part by retrieving the relative pointing of all radiometers using the Moon as a calibration source in periods in which it drifted within range of the UARS MLS scan. The maximum resulting correction to pre-launch pointing was 0.011 deg [21]. Other investigations (using radiances from extremely high altitudes and special roll maneuvers of UARS) confirmed the low sidelobe and spillover levels in the pre-launch calibration dataset.

The UARS mission life was 18 months, set by the cryogen lifetime of the cryogenic limb array etalon spectrometer (CLAES). The MLS design lifetime was 36 months. Its 183-GHz radiometer failed after 19 months of successful operation; the cause was probably slow fracture of a solder joint between filter and a diplexer within the mixer. The MLS scan began to degrade after 3.5 years operation, due to build-up of wear products in the actuator mechanism. Following loss of the solar array drive in 1995 and aging of spacecraft battery systems, the MLS 63-GHz radiometer was switched off in 1997 to conserve power. Pressure profiles were obtained instead from linewidths in the 205-GHz radiometer. Following the most recent span of continuous operation in February 2000, MLS was put into survival mode, making no measurements but ready to be re-activated to obtain overlapping measurements with the Earth Observing System (EOS) MLS, which was launched in July 2004. However, it was never reactivated, and the UARS was scheduled for total deactivation in January of 2006.

7.3 Earth Observing System (EOS) MLS

Richard E. Cofield

A microwave limb sounder on the Aura satellite, the third in a series of satellites of NASA's Earth Observation System (EOS), continues the program of microwave limb sounding from space begun with UARS. Advances in receiver technology and reliability permit us to extend the EOS MLS observations up to 640 GHz, with fractional bandwidths increasing to almost ±10 percent to cover the many rotational molecular lines at these frequencies. The UARS MLS data quality allowed retrieval of profiles to be extended from the stratosphere down to the upper troposphere. Constituents measured by EOS MLS include pressure, temperature, geopotential height, cirrus ice, H_2O, O_3,

carbon monoxide (CO), hydrogen cyanide (HCN), nitrous oxide (N_2O), nitric acid (HNO_3), hydrochloric acid (HCl), ClO, bromine monoxide (BrO), and volcanic sulfur dioxide (SO_2). A measurement of the hydroxyl (OH) radical at 2.5 terahertz (THz) gives insight into hydrogen cycles in stratospheric chemistry.

As with the UARS MLS, the lowest target frequency comes from the vertical coordinate for profiles being pressure, obtained by EOS MLS from the 118-GHz O_2 line. Recent refinements in retrievals show this parameter can be obtained even more accurately from broadening of an isotopic O_2 line at 234 GHz.

UARS yawed 180 deg approximately every month, to keep sensors and their FOVs away from the Sun. To avoid the consequent gaps in global coverage, a polar Sun-synchronous orbit was chosen for the EOS satellites, with different orbital phases. EOS MLS scans in the orbital plane, for better coverage of the poles and with a preferred direction and period of scan. This lets orbital motion compensate for the along-track displacement of tangent points with scan angle, so that each profile is measured over one point on the Earth.

7.3.1 Antenna Requirements

Like the functional requirements of the UARS MLS, the science requirements for the EOS MLS were written explicitly to partition the instrument requirements into radiometric, spectral, and FOV requirements [22]. The latter, defined as requirements on the response to the instrument as a function of angle, were taken almost verbatim as antenna requirements. The following summary of EOS MLS antenna requirements highlights differences from the UARS MLS requirements described above.

Beamwidth requirements for EOS MLS are in Table 7-11. The EOS MLS has a single beam efficiency requirement: >0.95 within an angular range of 2.5 times the HPBW. FOV boresight is defined as the direction given by the peak

Table 7-11. EOS MLS science FOV requirements.

Radiometer Frequency	Footprint Width at 20-km Tangent Height			
	In Vertical Plane		In Horizontal Plane	
	km	deg	km	deg
118 GHz	6.5	0.123	15	0.285
190 GHz	4.5	0.085	10	0.190
240 GHz	3.5	0.066	10	0.190
640 GHz	1.5	0.028	10	0.190
2.5 THz	2.5	0.047	10	0.190

value of the Gaussian function that best fits the antenna response down to the 10-dB power points. FOV boresights of the 190-, 240-, and 640-GHz radiometers shall coincide with the 118-GHz FOV boresight to within one-fifth of the 118-GHz beamwidth. Engineering considerations make it desirable for the 2.5-THz radiometer to have separate optics, which is acceptable provided:

1) The 2.5-THz FOV boresight relative to the 118-GHz FOV boresight shall be known to within one fifth of the 118-GHz beamwidth,
2) The scan plane of the 2.5-THz boresight shall be within 10 km of that of the 118-GHz boresight at the atmospheric limb tangent point, over the tangent height range of 10 to 60 km.
3) The THz and GHz scans shall be synchronized.

The FOV scan plane shall be within 1 deg of the orbit plane. A continuous (i.e., non-stepped) scan, which emphasizes the lower stratosphere and upper troposphere and is synchronized to the orbit period, shall be used for routine atmospheric observations. The nominal scan pattern shall cover tangent heights of 2.5 to 62.5 km for the GHz radiometers and 15 to 62.5 km with 120-km space view for the THz radiometer, with more time spent at lower heights. The nominal scan, including retrace and calibration, shall have a period (24.7 s) that is 1/240 of the orbit period, and at least 75 percent of the time during this period shall be used for atmospheric measurements. The range of scan capability shall extend at least 4 deg to either side of that used for routine atmospheric observations. This provides for occasional scans outside the primary regions of interest, both for calibration purposes and for measurements over extended height ranges.

Tolerance in placement and knowledge of the tangent height of the FOV boresights, after in-orbit adjustments and accounting for Earth oblateness, is ±0.5 km at the start of each limb scan, degrading to ±1 km at the end of the limb scan.

The change in elevation of the FOV boresights with respect to nadir during each limb scan shall be known to an accuracy of 2 arcsecond (3σ), and the rate of change is known to an accuracy of 1 arcsecond per second (3σ), at time scales between 0.17 and 25 s. Jitter in the FOV boresights at time scales shorter than 0.17 s shall not exceed 2 arcsec (3σ).

The spectral and FOV responses of the instrument shall be characterized sufficiently that their separate uncertainties do not introduce uncertainties in the MLS forward model calculations of the atmospheric/Earth radiances of more than (at the 90 percent confidence level):

1) 3 K in the absolute value of the atmospheric/Earth radiances measured through each spectral channel, and
2) 1 percent (or $\Delta I_{min}/3$) in the spectrally-varying component of the atmospheric/Earth radiances measured from one channel or filter to another

throughout a given radiometer. $\Delta I_{min}/3$ is a channel-dependent allowable noise expressed in K and given in [22, Table 3.2-2].

7.3.2 Trade-off Studies

Since the EOS MLS has science requirements so similar to those for the UARS MLS, it was decided to use the same offset Cassegrain antenna system prescription for the newer instrument. The surface figure and roughness requirements were tightened to accommodate the higher frequency radiometers (240 and 640 GHz), and for EOS under-illumination was more extreme (nominal Gaussian beam truncations of –30 dB at the primary reflector and –40 dB elsewhere, versus –15 and –20 dB in the UARS MLS). This was to alleviate concerns with frequency-dependent spillovers within the optical system that could have contaminated the radiometric calibration of UARS [19]; such spillovers would be worse with the wider bandwidths of EOS MLS. In the polar orbit, solar illumination of the EOS MLS antenna, though having small seasonal variations, changes enough in each orbit to make the materials of UARS MLS infeasible (the all aluminum antenna would undergo a 25-percent change in HPBW over 1 orbit. Therefore, the primary reflector is made of graphite epoxy, with an egg-crate structure joining two skins, the front one coated with vacuum-deposited aluminum for the RF reflection and then with SiO_x for thermo-optical properties. The secondary and tertiary reflectors are diamond-turned aluminum, machined on the back to leave ribs. These reflectors are then grit-blasted to achieve the desired emissivity.

7.3.3 Selected Design

Figure 7-12 shows the signal flow diagram of EOS MLS. As with UARS, the incoming signal is split among the GHz radiometers using a multiplexer consisting of a wire grid polarizer and three dichroic plates. The feed mirrors coupling the antenna beam into corrugated horns on the GHz mixers have toric conic prescriptions, like those of UARS, to match the astigmatic beam coming from the 2:1-aspect-ratio antenna to the axisymmetric horn patterns.

A more significant departure from UARS is the antenna for 2.5-THz bands. The science requirements would have allowed use of the innermost part of the aperture for THz signal, and experience led us to expect that reflector figure errors would be dominated by components with long correlation length, so that the center portions could have a surface rms figure enough less than the entire reflector to beat back the growth of Ruze losses at a frequency four times higher than the next GHz band. However, there were enough differences in the scan pattern for OH retrieval, and the ability to perform both alignment and RF focusing through an optical surface was so attractive, that the THz instrument

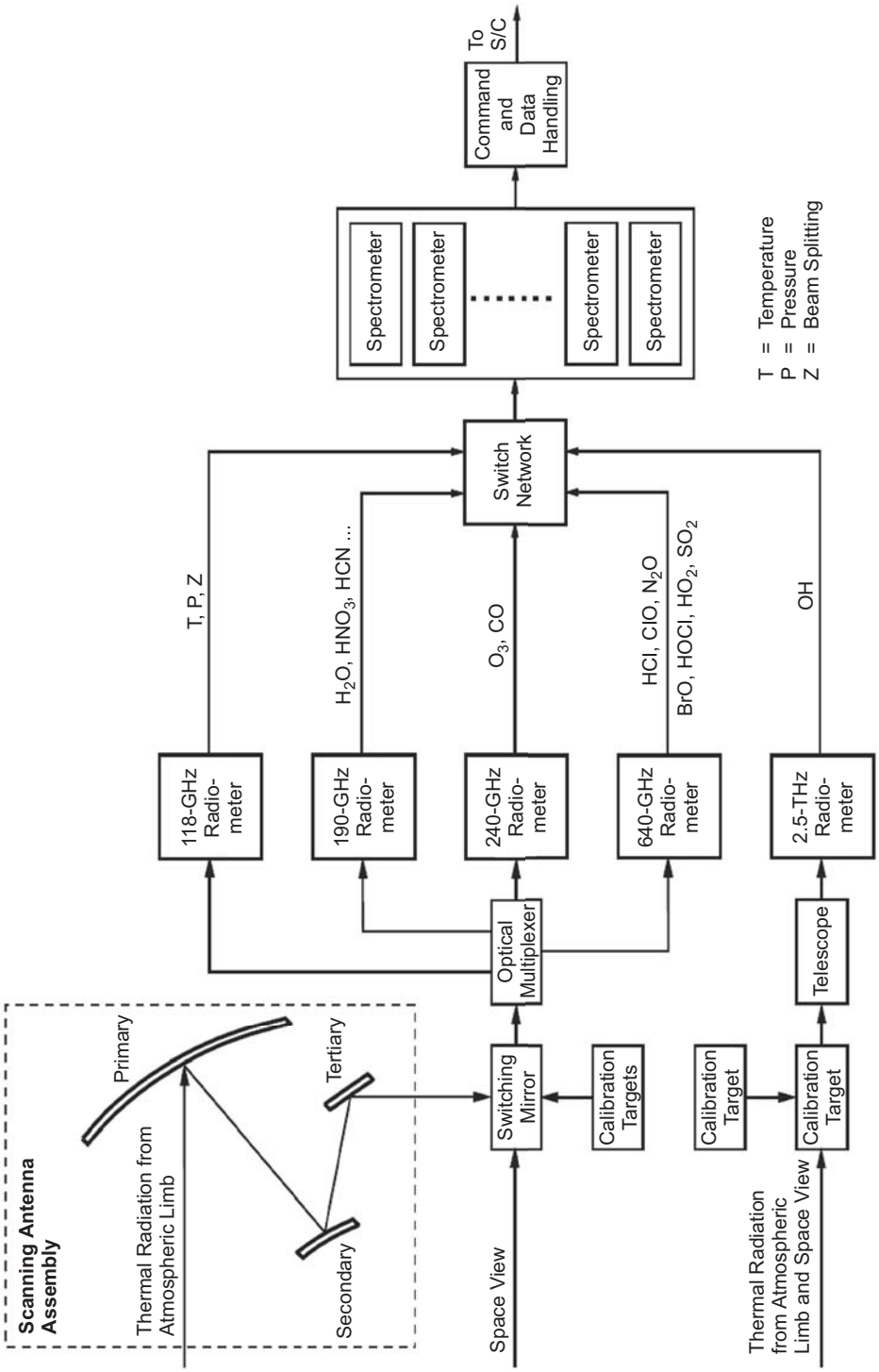

Fig. 7-12. Signal flow diagram for the Earth Observing System microwave limb sounder (EOS MLS) instrument.

was made a separate module. Another factor in separating the two modules was the environment needed for ground calibrations: Water vapor attenuates 2.5-THz signals by 1/*e* in 1 m of ambient air, so the THz calibrations, which require sources much weaker than those available at GHz frequencies, must be performed in vacuum.

Therefore, the THz optics design called for an offset Gregorian telescope with three diamond-turned mirrors, the primary having a 9-in. (22.86 cm) diameter. Beams were circular throughout the optics. The Gregorian design allowed for a pinhole (stop) between primary and secondary reflectors, which spatially filters the non-ideal feed patterns and provides a convenient reference for theodolite alignment looking into the telescope aperture. A diplexer, based on the Martin-Puplett design [23] and comprised of polarization grids and curved and roof-line mirrors, splits the signal and matches beams to two dual-mode horns. These are scaled from the UARS MLS design, and are machined into the input ports of the THz mixers. The diplexer also injects local-oscillator power from a gas laser. The THz FOV is scanned through the Earth limb, and to cold space and calibration load views using a plane scanning mirror; performing the calibration directly between telescope and limb removes the concerns with frequency-dependent spillover, which affect the GHz module optics.

Another innovation for the THz module is the use of a compact range to measure antenna patterns in the vacuum chamber. A test reflector was made with the same focal length but slightly larger than the THz primary reflector, A 900-deg C mercury arc (incoherent source) illuminated the compact range reflector through a slit to allow measurement of one-dimensional patterns with 0.01-deg sampling, using the radiometer power detection, over a range of ±1.3 deg using the scan/switching mirror. Since the radiance seen by the antenna in a limb-sounding orbit varies only in the limb vertical direction (for small horizontal angles), the slit was oriented to measure that direction of the pattern. This achieved in the test set-up what is done for the GHz module by quadrature of patterns measured in two dimensions. With this integration along the slit, the measurement technique achieved a dynamic range of –21 dB.

Water vapor attenuation precluded far-field pattern measurement for the GHz radiometer also. The attenuation is 95 dB/km in the 640-GHz bands, so atmospheric variability and even local weather make the far-field range (9 km required) infeasible. Submillimeter sources do not have sufficient power to illuminate the MLS at this distance; nor are there locations for siting transmitter and receiver in the JPL test facility without severe logistical and range reflection problems.

Using the experience of Goddard Space Flight Center (GSFC) with the Submillimeter Wave Astronomy Satellite, plus expertise gained from the microwave instrument for the Rosetta orbiter (MIRO) project described here, an 8-ft × 8-ft (2.44-m × 2.44-m) planar scanner was procured and phase-locking

electronics developed for near-field range measurement of the GHz module patterns. The planarity of the range, including scanner and electronics in the benign high bay environment, is 5 μm rms, a factor of two better than needed to meet the FOV calibration requirement. Boresight directions are determined between RF measurements using a system of theodolites that measure alignment cubes on the instrument relative to the scan plane coordinates, in which the RF pointing had been measured.

After assembly at JPL, the range was tested on the engineering model of the UARS MLS antenna, then used to baseline the pattern performance of the EOS MLS at a reduced set of scan angles and frequencies, for comparison before and after thermal vacuum tests of the GHz module.

Figure 7-13 is a photograph of the GHz engineering module of EOS MLS on the near-field range. The module is rotated 90 deg from its orientation on the Aura spacecraft to fit better with the preferred motion of the range and so that gravitational deformations affect mostly the limb horizontal plane, where requirements are less stringent.

7.3.3.1 Performance Estimates. The successful use of near-field (for GHz) and compact (for THz module) ranges was crucial in completing the FOV calibration datasets for EOS MLS. The calibration was accomplished in half the time allocated, and it gave unprecedented knowledge of the antenna performance at these frequencies. Radiometer feed patterns could be compared with the near-field patterns of the GHz module, and in one case inspection of near- and far-field patterns revealed a mechanical assembly error for one multiplexer element, which could be corrected within 2 days in the same high-bay environment. Table 7-12 compares the requirements with the measured performance for the EOS MLS beamwidths and beam efficiencies. Figure 7-14 shows principal plane co-polarized amplitude patterns at three frequencies of the 640-GHz MLS radiometer, taken in the near-field range FOV calibration of the GHz module.

Figure 7-15 shows compliance of the EOS MLS GHz boresights with the coincidence requirements, and it illustrates the pattern of footprint centers in the plane normal to boresight at the limb tangent point. The grouping of band centers corresponds to the small misalignments of polarizers and dichroic plates in the optical multiplexer. After integration on the Aura spacecraft, the THz instrument boresight co-alignment with the GHz boresights was 0.048 deg in the azimuth direction (1/4 of requirement), and was later made nearly 0 in the elevation direction by matching scan angles with spacecraft ephemeris and attitude data during flight operation.

7.3.3.2 Conclusions. Figure 7-16 is a photograph of the GHz and THz modules of EOS MLS on the Aura spacecraft prior to thermal vacuum test. A black-body target covered the THz aperture for this test.

Fig. 7-13. EOS MLS GHz module on near-field range.

EOS MLS was launched aboard the Aura spacecraft on July 15, 2004, from the Western Test Range of California's Vandenberg Air Force Base. The instrument produced useful spectra and geophysical retrievals within days after activation. In its first year of operation, the ground calibration of FOV performance was verified within pre-launch error bars, except for ohmic losses; these were overestimated for 240 GHz and underestimated for 640 GHz. The slight discrepancies have been attributed to fabrication differences between the primary reflector and the other two antenna reflectors. Calibration values were

Table 7-12. Requirements and measured performance of the EOS MLS FOV: beamwidth and beam efficiency.

GHz Band	HPBW Vertical (deg)		HPBW Horizontal (deg)		Beam Efficiency (percent)	
	Required	Measured Range	Required	Measured Range	Required	Measured Range
118 R1A	0.123	0.107–0.118	0.283	0.227–0.245	≥0.95	0.978–0.987
R1B	0.123	0.111–0.119	0.283	0.220–0.236	≥0.95	0.980–0.982
190 R2	0.085	0.074–0.084	0.189	0.147–0.168	≥0.95	0.959–0.980
240 R3	0.066	0.058–0.064	0.189	0.116–0.126	≥0.95	0.962–0.973
640 R4	0.028	0.0252–0.0271	0.189	0.0528–0.0572	≥0.95	0.962–0.967
2500 R5	0.047	0.038–0.046	0.189	N/A	≥0.95	1.0 ±0.05

corrected using special scans high above Earth's atmosphere. The correction highlights a significant contributor to stray radiance that will affect future sub-millimeter limb sounders.

7.3.4 Future Radiometer Missions

Future designs for Earth observation are driven more by the demand for greater spatial coverage than by increases in frequency (many of the spectra in [15] peak below 3 THz, above which spectral windows close rapidly due to clouds, rain, and water vapor). For the next generation of microwave limb sounding, the atmospheric region targeted by instrument concepts continues to move downward from the stratosphere to the upper troposphere, where events are more localized in both space and time, calling for greater Earth coverage than the tangent tracks of previous instruments. An azimuth-scanning version of the MLS (SMLS) under study [24] proposes to use toric symmetry in a compact multiple-offset reflector antenna system, which can be useful in the viewing geometry of limb sounding and with shorter integration times made possible by current receiver and cooler technology. An inflatable antenna concept, having a 25-m aperture in an offset parabolic torus configuration, was evaluated for remote sensing of soil moisture and ocean salinity in [25]. Both concepts avoid the need to move entire apertures mechanically for Earth coverage, preferring instead to under-utilize very large apertures having some circular symmetry. This will generate instantaneous FOVs that have moderate performance but nearly identical properties across the swath.

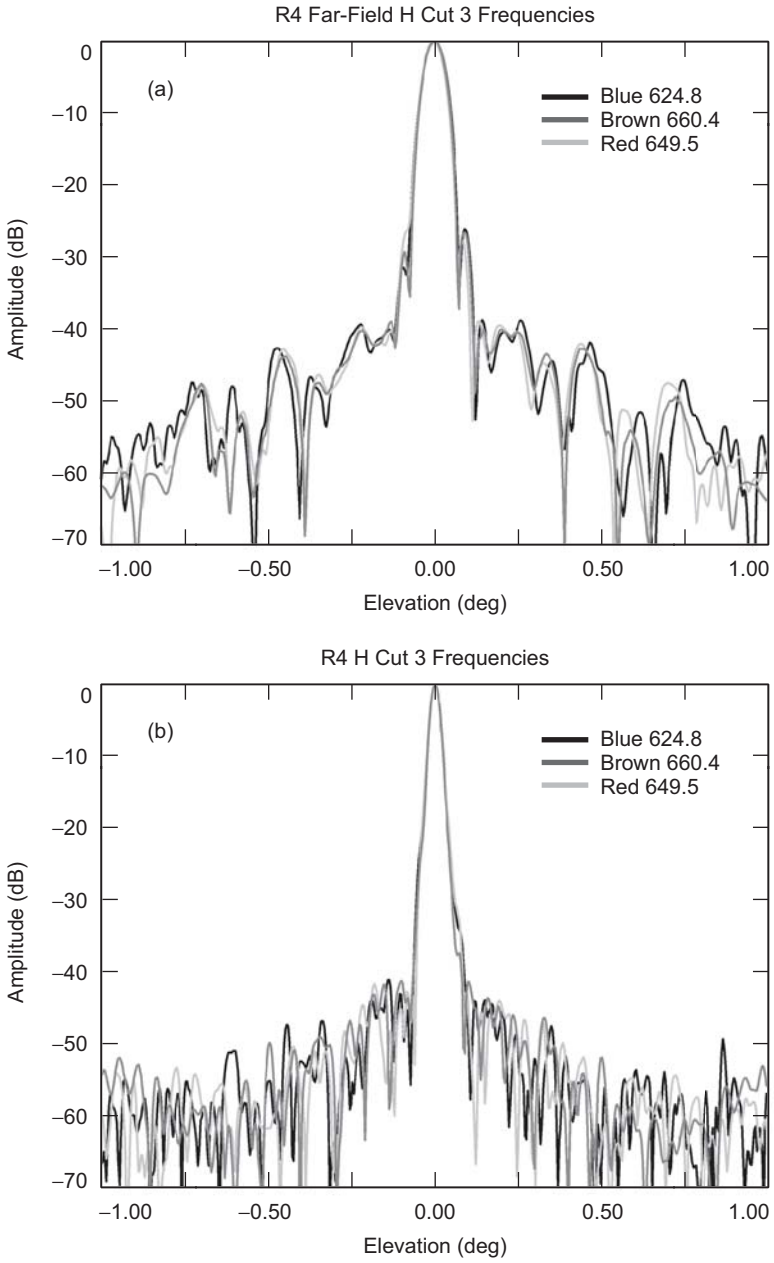

Fig. 7-14. Antenna pattern cuts in principal planes at three frequencies in the 640-GHz bands of EOS MLS: (a) V cut and (b) H cut.

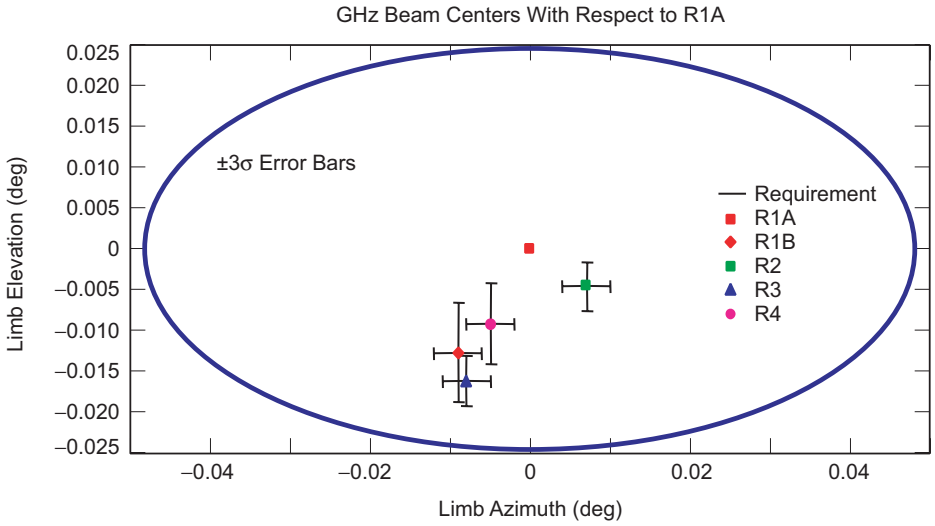

Fig. 7-15. Boresight coincidence of EOS MLS GHz radiometers.

7.4 Scatterometers

Richard E. Cofield

A scatterometer is a microwave remote sensing instrument using an amplitude-calibrated radar for measuring the scattering coefficient σ^0 (bi-static scattering cross-section per unit area). The strong dependence of σ^0 on incidence angle led to development of fan-beam Doppler antenna systems capable of simultaneous measurement over incidence angles from 5 to 60 deg. The Doppler filtering is a unique advantage of fan-beam scatterometry, using the time domain to replace multiple beam systems for horizontal resolution. An equally strong dependence of σ^0 on wind direction relative to the radar azimuth angle is the basis for measurement of vector winds by scatterometers. It was found in early experiments that the scattering coefficient at $\lambda = 2.2$ cm wavelength interacts with capillary waves induced by local winds at speeds down to 3 m/s. However, the dependence is weak, and hence the operating frequency can be chosen somewhat freely (as is not the case in radiometry) to trade radar power against antenna gain; hence, early scatterometers operated from 4 to 11 GHz; while their spaceborne descendents operate from 10 to 15 GHz.

The impetus for making scatterometers to operate from Earth orbit began with the confirmation, by a scatterometer flown aboard Skylab in 1973–1974, that the scattering coefficient varies monotonically with wind speed over the ocean—a prime candidate for global remote sensing. The measurement depends on both surface roughness and Bragg scattering from ocean surface areas

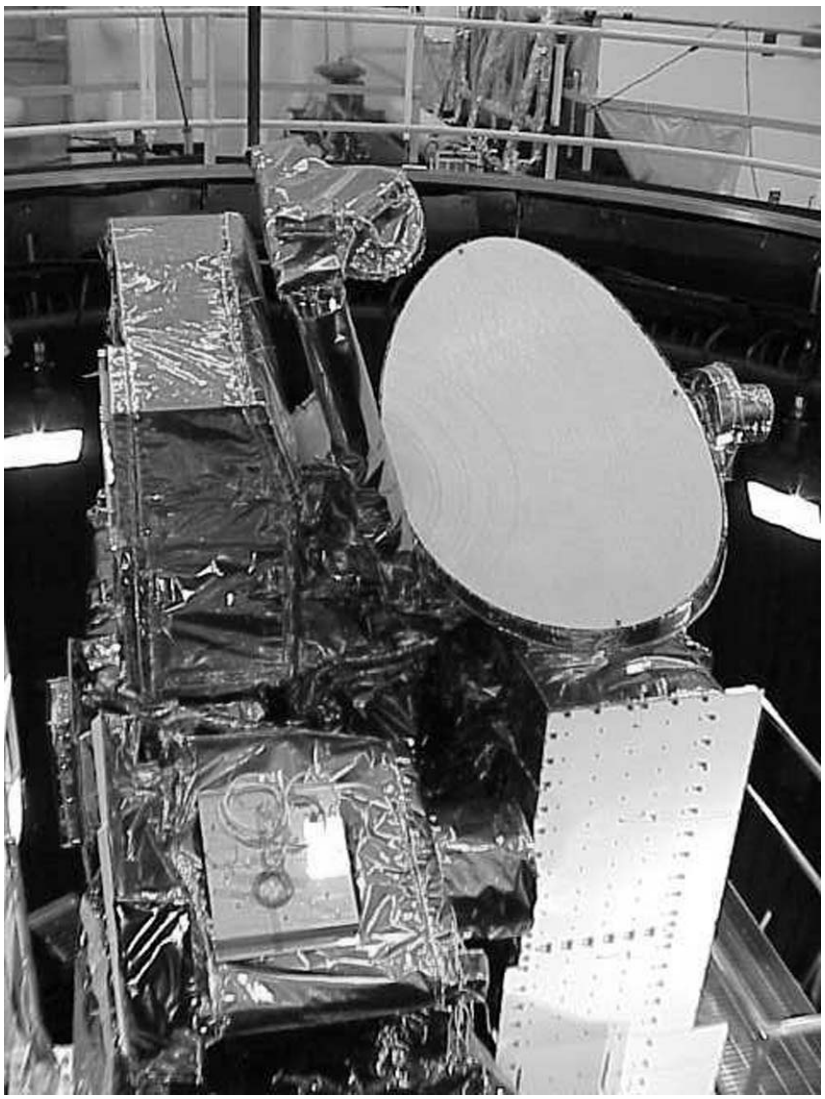

Fig. 7-16. EOS MLS GHz and THz modules on Aura spacecraft for thermal vacuum test.

spatially correlated over scales comparable to the radar wavelength, given some statistical variation of incidence angle [26].

7.4.1 Fan-Beam Instruments: Seasat-A Scatterometer

The Seasat-A scatterometer system (SASS), a Doppler scatterometer with four orthogonal fan beams, was developed for the Seasat oceanographic

satellite [27]. Wind retrieval was based on an empirical model for σ^0 as a linear function of the logarithm of wind speed, developed using results from both Skylab and other (aircraft) instruments. Mission requirements for SASS were to measure wind speed within ±2 m/s and wind directions within ±20 deg.

7.4.1.1 Requirements. Gain errors, both peak (G_0) and per-Doppler cell (G/G_0), and narrow dimension HPBW (φ_A), all contribute to fixed-bias errors. The gain knowledge errors contribute 90 percent, and HPBW 5 percent, of the sources of error contributing to ±0.84 dB rms uncertainty of σ^0. Antenna pointing errors and spacecraft attitude errors translate to errors in G/G_0. Attitude errors were not systematic, but 0.1-deg knowledge of antenna squint angle was determined in flight and found to be affected by orbital thermal variations up to 15 deg C over the length of the antenna, and 11 deg C over one orbit.

Figure 7-17 shows the viewing geometry of the Seasat-A Satellite Scatterometer (SASS). The footprints of the four antennas cover a swath extending 950 km on either side of the subsatellite track. This is divided into two swaths on either side, in which winds were to be retrieved at various speeds depending on incidence angle, and a third swath centered on the nadir track (small incidence angle θ_i). Earlier aircraft measurements had indicated that σ^0 was independent of surface roughness near $\theta_i = 10$ deg. When a constraint on SASS design provided a channel at 8 deg instead of the desired 10 deg, it was hoped that the center swath would indicate instrument stability; later refinements moved the σ^0-invariant point to 13 deg, and the center swath data was not a useful indicator of stability, except in low wind speeds of 2–10 m/s [27]. In designing subsequent fan-beam scatterometers to measure winds, the center swath, having small θ_i, was removed from mission requirements; the resulting gap later led the fan-beam design into disfavor, as described below.

Ground truth for validating performance of the SASS instrument and algorithms was obtained from 11 orbits over the Amazon jungle, for which Skylab data had shown σ^0 to be isotropic and polarization insensitive. After partitioning the data set into early-morning and afternoon passes, the scatterometry was shown to perform near theoretical limits over periods up to 150 s with long-term stability better than a few tenths of 1 dB.

The flawless performance of the SASS instrument over the short lifetime of Seasat, and success of its algorithms in meeting the mission requirements, led to JPL's next spaceborne fan-beam scatterometer.

7.4.2 Fan Beam Instruments: NASA Scatterometer (NSCAT)

The NASA scatterometer (NSCAT) project was started in 1985 with plans to build on the Seasat experience with another set of fan-beam antennas flown aboard a Navy satellite in 1988; however, several delays prompted cancellation

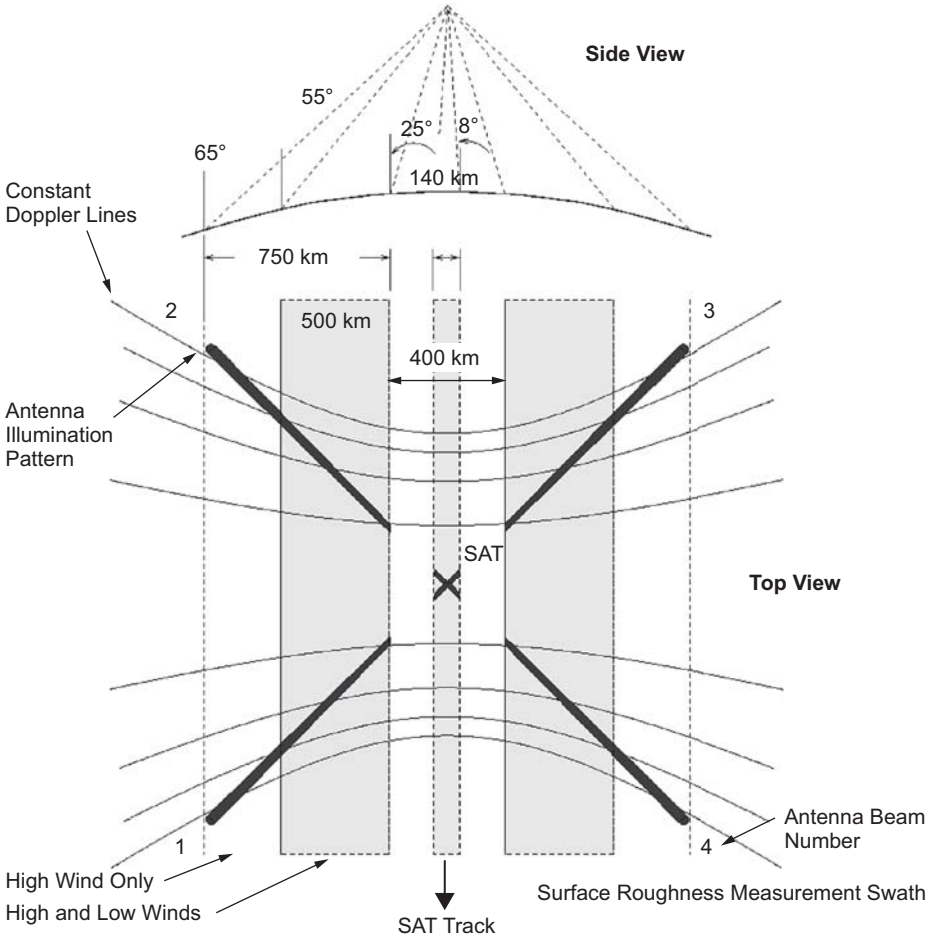

Fig. 7-17. Viewing geometry of the Seasat-A satellite scatterometer (SASS), from [27].

of that satellite program, leaving NSCAT to await a launch on the Advanced Earth Observation Satellite (ADEOS) by Japan's Space Agency NASDA.

The principal objective of NSCAT and its successors is vector winds measurement at the ocean surface, which is crucial for understanding air-surface dynamics. Altimeters and radiometers can measure wind speed but not direction except for recently developed polarimetric radiometers. Using a near-polar orbit, coverage is global, and measurements can be made in all weather conditions. Like SASS, NSCAT operates at 14 GHz. Table 7-13 gives the NSCAT mission objectives.

7.4.2.1 Trade-off Studies. Antenna systems for scatterometry have been of either the Doppler filtered-fan beam class or the scanned spot-beam class. The

Table 7-13. Major NSCAT mission objectives.

Parameter	Value
Wind speed	2 m/s rms for 3–20 m/s 10 percent for 20–30 m/s
Wind direction	20 deg rms for 3–30 m/s
Spatial resolution	25 km for σ^0 cells 50 km for wind cells
Location accuracy	25 km rms absolute 10 km rms relative
Coverage	90-percent ice-free ocean every 2 days
Mission lifetime	36 months

fan-beam design was chosen for NSCAT because of SASS heritage, particularly in the wind-retrieval algorithms.

Because scatterometry of ocean winds needs collocated radar reflections from multiple azimuths and a wide swath for global coverage, antenna design is the most severe constraint in a spaceborne scatterometer instrument. σ^0 depends weakly on wind speed and direction for near-normal incidence; this dictates large incidence angles which also incur a swath gap about the subsatellite track. The resulting instantaneous footprints are several hundred kilometers long but only few kilometers wide, and they have large variation in incidence angle near grazing incidence.

Among several enhancements of the Seasat instrument, the most significant for the antenna is addition of another antenna on each side, i.e., three antenna azimuths in each of two swaths to reduce fourfold ambiguity in wind direction in the SASS measurements.

7.4.2.2 Selected Design. Figure 7-18 is an artist's concept of the NASA scatterometer on the ADEOS spacecraft, showing antennas deployed plus footprints and swath coverage of the Earth NSCAT beam geometry: Each of two 600-km swaths on each side is swept out by three antennas: one at 45-deg azimuth from the orbit plane and H-polarization; one at 135-deg azimuth, V-polarization; and one at 65-deg azimuth, (forward one side, backward the other), H and V-polarization; For horizontal resolution, the 600-km swath is divided into 24 cells, each 25 km wide. In the 795-km orbit (101-minute period) of the ADEOS platform, the ground track velocity is 6.7 m/s, hence to make the along-track resolution also 25 km, NSCAT must cycle through all eight antennas in 3.74 s [28].

The NSCAT Antenna subsystem consists of six identical fan-beam antennas and associated deployment mechanisms. Each antenna is composed of two separate horns fed by a slotted waveguide array; only one polarization is

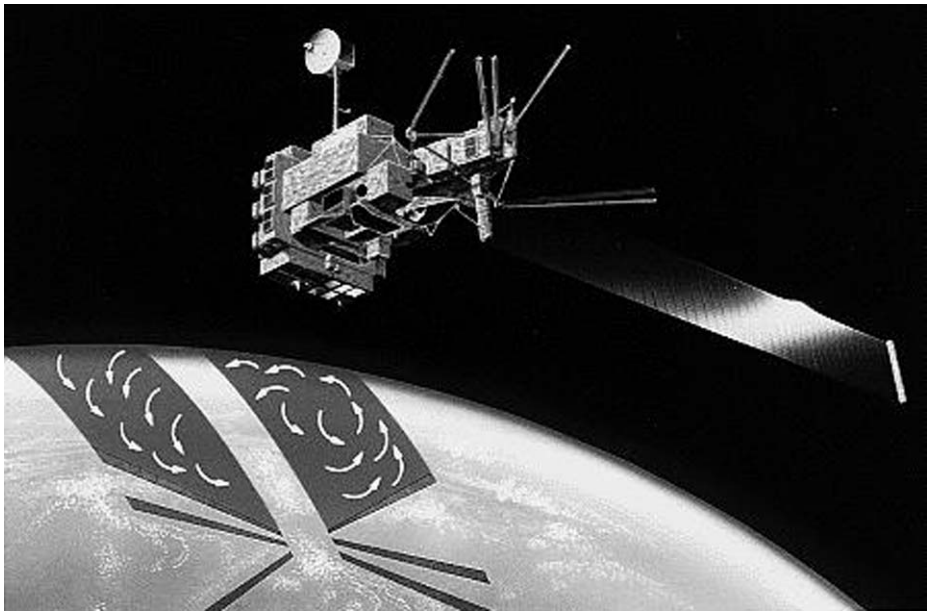

Fig. 7-18. NSCAT scatterometer on the ADEOS spacecraft.

used for all but the two 65-deg azimuth antennas. The horn walls are made of graphite-epoxy for dimensional stability in the orbital thermal environment. Thin aluminum foil provides the conducting surface inside the horn, and the 202-slot waveguide is also aluminum. Horn dimensions are 120 in. (305 cm) long, 2.5 in. (6.35 cm) wide, and 4.5 in. (11.43 cm) deep, to produce the desired fan beam. Figure 7-19 is an end view of one dual-horn flight antenna.

Nominal peak gain is 33.5 dB, tilted toward the far swath to compensate for longer slant range there. The first sidelobes have relative intensities of –15 and –20 dB in the wide and narrow beams, respectively. Antenna requirements and performance measured by the vendor are in Table 7-14, from [29]. These results were duplicated and augmented with alignment information when the antennas were calibrated on the cylindrical near-field range at JPL.

Transforming the NSCAT mission requirements into antenna specifications revealed two key performance requirements: (1) Signal-to-noise ratio (SNR) shall exceed –8 dB for 3 m/s winds, and (2) the combined rms variation due to antenna pattern knowledge, beam pointing, and other non-antenna effects shall not exceed 0.5 dB, 1 σ over 8 minutes. With the long delay between antenna fabrication and integration of NSCAT on a new platform, it was necessary to repeat antenna measurements in a more rigorous fashion before delivery, in order to demonstrate compliance with these requirements.

Antenna gain was calibrated during ground test to 0.25 dB, with in-orbit gain variations to be corrected using temperature data from sensors mounted

Fig. 7-19. Dual-polarized NSCAT flight antenna, end view.

Table 7-14. Required and measured performance of the NSCAT antennas.

		H-Polarization			V-Polarization		
			Flight Predict.[a]			Flight Predict.[a]	
Parameter	Required	Measured	Low	High	Measured	Low	High
Frequency			13.995 ±5 MHz				
HPBW (narrow beam) (deg)	0.41 ±0.02	0.41 ±0.01	0.40	0.42	0.42 ±0.01	0.40	0.42
Squint (narrow beam) (deg)	1.75 ±0.25	1.81 ±0.01	–1.78	–1.81	–1.72 ±0.01	1.69	1.72
Gain (dBi)	33.5, Goal 34	33.64 ±0.37	33.62	33.53	34.1 ±0.37	34.15	34.16
Sidelobes (dB)	–20 below peak	–20.2 ±0.7	–22.3	–19.9	–22.6 ±0.7	–22.1	–21.9

[a] Low predicted temperature of –129 deg F (–89 deg C); high predicted temperature of 182 deg F (103 deg C).

along the horn length. The ground patterns were measured on a cylindrical near-field range coaxial with the phase center line along the slotted waveguide. [30]

Alignment of the range fixture and waveguide mechanical features to alignment cubes gave knowledge of the RF and mechanical boresights with respect to the interface with the deployment hinge. Further cube-to-cube

alignments then allowed this alignment knowledge to be transformed back to the attitude control system of ADEOS.

One issue which arose late in the program of pattern calibration was whether to fly with or without covers over the horn apertures; this has been a perennial question with radiometer missions also. Expected thermal deformations made the covers highly desirable, but as the original vendor measurements of Table 7-14 show, a small price would be paid in sidelobe level at extreme temperatures. The principal effect of the covers, a pointing change, was accounted for by the alignment portion of the calibration. NSCAT was flown with covers. This is in contrast to the radiometer missions: despite much smaller horn throats at the higher frequencies, the degradation in voltage standing wave ration (VSWR) and resultant spectral baseline were deemed even worse than the risk of contamination, so the radiometer instruments have flown without horn covers.

Table 7-15 shows how uncertainties in pre-launch calibrations of antenna gain, beamwidth, and pointing contributed to bias and time-varying components of uncertainty in σ^0.

NSCAT was launched August 16, 1996 aboard the ADEOS spacecraft from Tanegashima, Japan. It operated from September 1996 until failure of the spacecraft power system on June 30, 1997. A post-launch calibration campaign, begun shortly after turn-on, confirmed the ground calibrations of antenna gain, sidelobes, and nominal antenna deployment. Antenna pointing was calibrated in orbit by three methods:

1) A calibration ground station was deployed, capable of both transmitting to and receiving from NSCAT. Antenna gain patterns in the narrow-beam

Table 7-15. Pre-launch calibration of the NSCAT antennas.

Antenna Calibration Parameter	Pre-launch Calibration Bias		Time-Varying Calibration Error	
	Parameter Error	σ^0 Error	Parameter Error	σ^0 Error
Peak gain	0.35 dB	0.7 dB (2-way)	0.10 dB	0.20 dB (2-way)
Broad-beam pattern	0.02 dB/dB	0.40 dB max (2-way)		
Beam width	0.015 deg	0.16 dB	0.005 deg	0.05 dB
Squint	0.05 deg	0.09 dB max	0.007 deg	0.01 dB
Pointing	0.05 deg each axis	0.05 dB	0.08 deg each axis	0.13 dB
Other contributors, rss	—	0.61	—	0.19
rss sums	Pre-launch bias = 1.03 dB		K-factor = 0.31 dB	

Uncertainty of post-launch bias removal: 0.2 dB beam-to-beam, 0.5 dB absolute

direction were measured during NSCAT overpasses and the beam peak used to infer spacecraft attitude.

2) Natural targets, such as the Brazilian rain forest (as described previously for SASS) and central Russia, were observed along with beam-to-beam bias over open ocean.
3) Attitude was determined independently, using raw housekeeping data.

All three methods indicated that attitude varied over one orbit by as much as a few tenths of 1 deg—an order of magnitude higher than the reported ADEOS stability. This resulted in uncertainty in σ^0 of a few tenths of a dB. Comparison of NSCAT wind vectors with *in-situ* data, from 27 moored open-ocean buoys, indicates that NSCAT met science requirements for wind speed and direction accuracy [31].

7.4.3 Pencil-Beam Scatterometers: QuikSCAT and SeaWinds

The SeaWinds on QuikSCAT mission was a "quick recovery" mission to fill the gap created by the loss of data from the NASA Scatterometer (NSCAT), when ADEOS lost power in June 1997, until a second SeaWinds could be deployed on the ADEOS-II satellite. SeaWinds instruments for QuikSCAT and ADEOS-II are functionally identical, but the platform attitude controls differ: a star tracker on QuikSCAT gives 0.05 deg attitude knowledge (3σ), whereas ADEOS-II used Sun/Earth sensors and gyros to attain 0.2 deg (3σ) [32]. Table 7-16 summarizes the science requirements of the SeaWinds missions, which are very similar to those of NSCAT.

Scatterometers developed at JPL after NSCAT were designed with conically-scanned pencil beams, to avoid several drawbacks of the fan-beam approach: With satellite motion, two conically scanned beams (which can share

Table 7-16. SeaWinds science requirements.

Measurement Parameter	Performance Requirement	Instrument Performance
Wind field resolution	50 km; 25 km goal for data products	3-dB beamwidth + pulse modulation
Wind speed accuracy	The greater of 2 m/s and 10-percent rms of wind speed	Post-launch science analysis to show requirement is met
Wind direction accuracy	Less than 20 deg rms	Post-launch science analysis to show requirement is met
Coverage; revisit period	90 percent of global sea surface every 2 days	Orbit design and swath coverage of 1800 km
Mission life	3 years; 5 years goal	Flight qualified parts and materials; key electronics redundancy

the same reflector antenna system) trace out helical footprint paths which overlap at different points along the orbit track, meeting the scatterometry requirement to measure each surface element from different azimuths. Moreover, a full conical scan will measure at a given ocean surface point twice, once from the forward and once from the backward-looking part of the scan. The nadir gap vanishes, directional accuracy is inherent in the beam and not a function of Doppler gating, and the retrieval is simplified by having measurements at a small number of incidence angles. Finally, the pencil-beam concept occupies much less space on the platform, since a compact dish replaces the multiple fan-beam antennas. Cost and risk are less for the continuously rotating conical scan mechanism than for the older concept, which involved one-time deployment and had greater susceptibility to orbital thermal gradient [33].

Table 7-17 gives the measurement geometry and antenna specifications for the SeaWinds scatterometer. Figure 7-20(a) shows the conical spot-beam illumination. The antenna designed for the SeaWinds instruments (Fig. 7-20(b)), is a parabolic reflector with an elliptical projected aperture. The antenna is built of composite lightweight material (this includes the reflector surface shells, waveguides, struts, and feed horns) and has an rms surface error of 0.2 mm. It is oriented at an angle of 43 deg from nadir, as illustrated. The

Table 7-17. Viewing geometry and antenna specifications for the SeaWinds scatterometer.

Parameter	Inner Beam	Outer Beam
Polarization	H	V
Half-cone angle from nadir	40 deg	46 deg
Surface incidence angle	47 deg	55 deg
Slant range	1100 km	1245 km
3-dB footprint dimensions (az × el)	34 × 44 km	37 × 52 km
Rotation rate	18 rpm	
Along track spacing	22 km	
Along scan spacing	15 km	
Instrument frequency	13.402 ±0.5 GHz	
Expected range of σ^0	–37 to –2 dB	
3-dB beam dimensions (az × el)	1.8 deg × 1.6 deg	1.7 deg × 1.4 deg
Antenna peak gain	38.5 dBi	39 dBi
Antenna peak side lobe	–15 dB or less	
Minimum antenna resonant frequency	>94 Hz	

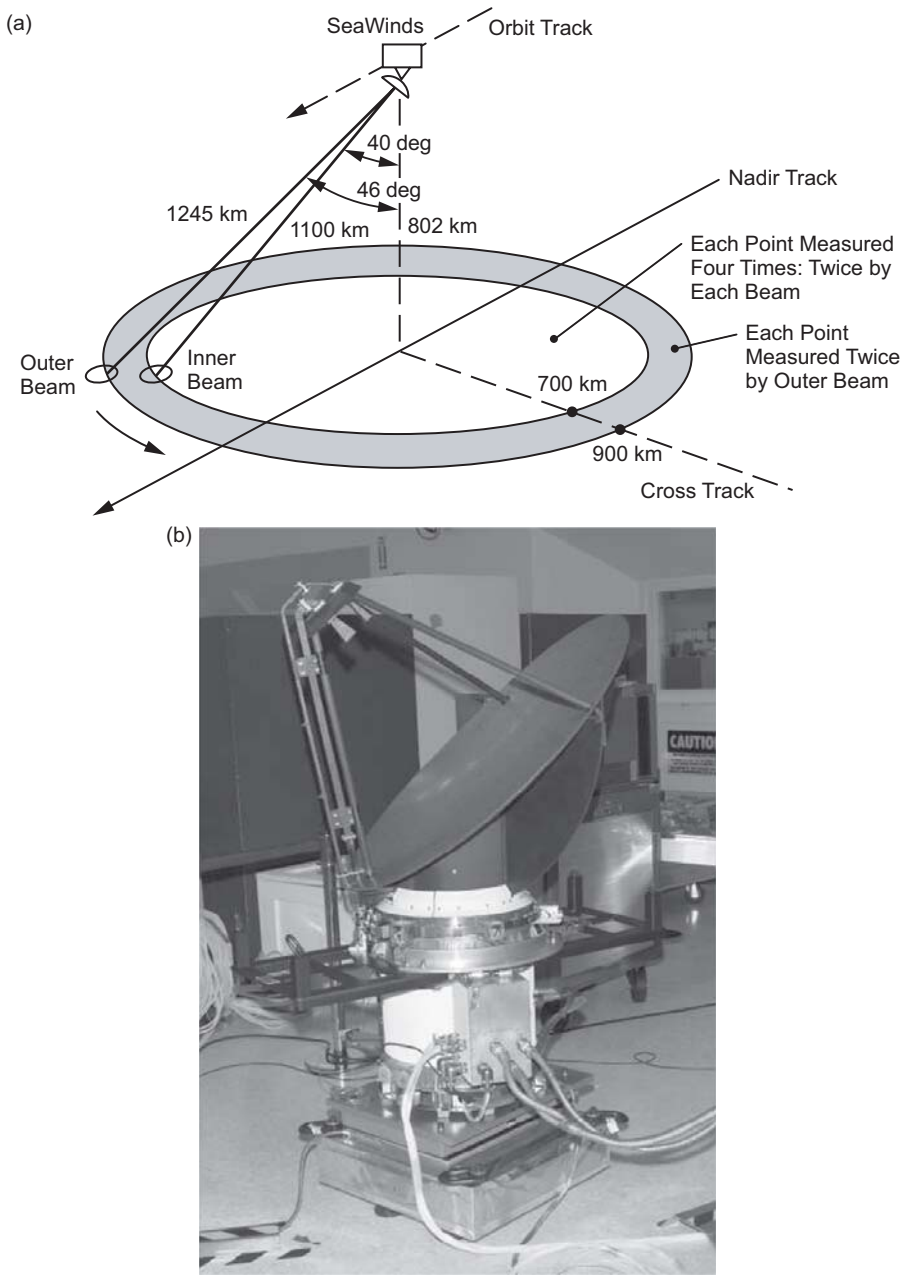

Fig. 7-20 (a) SeaWinds conical-scan spot-beam scan pattern and (b) 1.07 m x 0.96 m Ku-band SeaWinds dual-feed reflector antenna. The reflector shell, waveguides, and feeds are made of lightweight composite material (total weight is 6.40 kg).

projected elliptical aperture of the antenna is 1.07×0.96 m for the major and minor axis, respectively. Two feed horns are each displaced 0.0345 m from the boresight axis of the antenna to produce two independent pencil beams at angles of 40 deg and 46 deg from nadir. The inner beam (beam closer to nadir) has horizontal polarization; the outer has vertical [34].

SeaWinds antenna patterns were measuring using a cylindrical near-field range (CNFR) developed for NSCAT. This range was qualified for SeaWinds by measuring both a standard gain horn and the SeaWinds antenna, on both the CNFR and a 3000-ft (915-m) far-field range at JPL (9 times longer than $2D^2/\lambda$).

Figure 7-21 shows the principal plane cuts of the SeaWinds antenna beams, from both near- and far-field measurements. Coma lobes are evident in the elevation plane patterns, as expected for scanning 2 to 3 times HPBW in an $f/D \sim 1$ system. Even though inner and outer beam feeds were displaced symmetrically from the focus of the paraboloid, the outer beam's first sidelobe is higher by 5 dB. Nevertheless, at –15 dB down from main beam peak it still meets the requirement. Table 7-18 summarizes requirements and measured performance of the SeaWinds antenna for both inner and outer beams, before and after vibration tests.

QuikSCAT was launched on June 19, 1999, from Vandenberg Air Force Base, California, into a nearly polar orbit with a maximum altitude of about 800 kilometers, and it has continued operation to the present. The second SeaWinds instrument was launched December 14, 2002, aboard ADEOS-II, renamed Midori-2, and it operated until a solar storm in October 2003 caused permanent loss of the satellite.

7.4.4 Future Scatterometer Missions

Loss of the Midori-2 spacecraft left JPL with only the QuikSCAT scatterometer operational and has created a loss of coverage in measurement of vector winds. Currently planned JPL missions are addressing this gap with concepts involving large deployed apertures in pencil-beam configuration, possibly teamed with next-generation radiometers (for atmospheric and oceanic science) as was done in the 1978 Seasat mission.

7.5 CloudSat

William A. Imbriale

CloudSat (scheduled for launch in the fall of 2005) is a multisatellite, multisensor experiment designed to measure those properties of clouds that are critical for understanding their effects on both weather and climate. The mission's primary science goal is to furnish data needed to evaluate and improve the way clouds are parameterized in global models, thereby contributing to better predictions of clouds and thus to the poorly understood cloud-climate feedback problem.

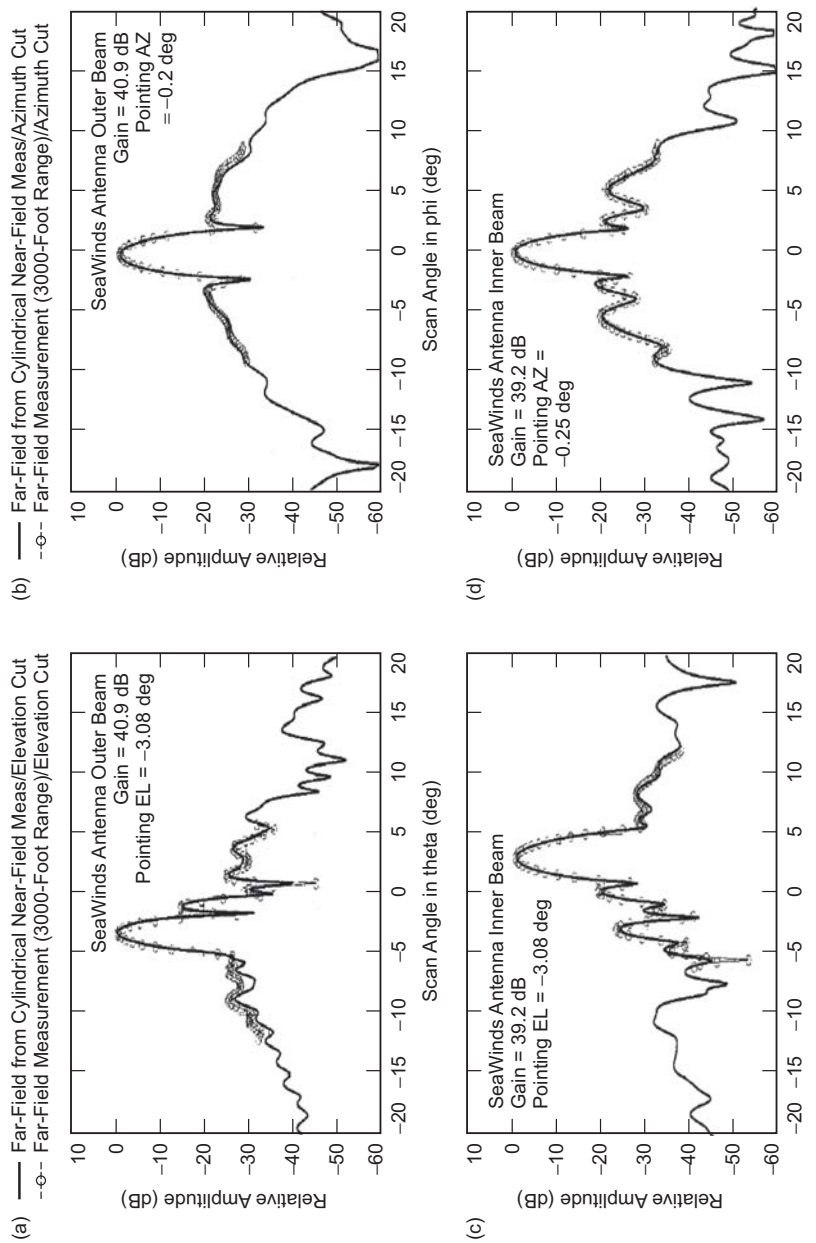

Fig. 7-21. Antenna pattern cuts of inner and outer beams of the SeaWinds antenna, from [30]. Co-polarized principal plane cuts from both near- and far-field measurements are shown: (a) outer beam, elevation; (b) outer beam, azimuth; (c) inner beam, elevation; and (d) inner beam, azimuth.

Table 7-18. SeaWinds antenna performance through vibration tests.

	Gain	X-pol*	Beamwidth		Pointing	
	dBi	dB	Az (deg)	El (deg)	El (deg)	Az (deg)
V-Polarization						
Requirement	>39.5	<–20	1.4 ±0.1	1.7 ±0.1	46 ±0.1	—
Post-vibration	40.91	–25.63	1.35	1.69	46.08	–0.05
Pre-vibration	40.86	–25.56	1.34	1.7	46.08	+0.05
Difference	0.05	0.07	0.01	0.01	0.00	0.1
H-Polarization						
Requirement	>39.2	<–20	1.6 ±0.1	1.8 ±0.1	40 ±0.1	—
Post-vibration	39.27	–26.97	1.66	1.76	40.01	0.00
Pre-vibration	39.22	–26.54	1.66	1.76	40.02	+0.10
Difference	0.05	0.42	0.0	0.0	0.01	0.1

* relative to co-polarized beam peak

The key observations are the vertical profiles of cloud liquid water and ice water contents and related cloud physical and radiative properties. The spacecraft payload consists of a 94-GHz cloud profiling radar (CPR). CloudSat will fly in tight formation with the Cloud-Aerosol Lidar and Infrared Pathfinder Satellite Observation (CALIPSO) [35] satellite (formerly known as PICASSO-CENA/ESSP3) carrying a backscattering lidar, and these two satellites will follow behind the Aqua satellite [36] in a somewhat looser formation. The combination of data from the CloudSat radar with coincident measurements from CALIPSO and Aqua provides a rich source of information that can be used to assess the role of clouds in both weather and climate.

7.5.1 Cloud Profiling Radar (CPR)

The CloudSat cloud profiling radar (CPR) [37] provides calibrated radar reflectivity (i.e., radar backscatter power) as a function of distance from the spacecraft. The design has a strong heritage derived from existing ground-based [38] and airborne cloud radars [39].

The choice of radar frequency, 94 GHz, is a trade-off between sensitivity, antenna gain, atmospheric transmission, and radar transmitter efficiency. Sensitivity and antenna gain increase with frequency while atmospheric transmission and transmitter efficiency decrease with frequency. Since a space-based platform sets strong constraints on antenna size, a frequency of 94 GHz provides an optimum compromise between the competing factors. An international frequency allocation at 94 GHz has recently been set aside for spaceborne radar use. The choice of frequency means that a small percentage of

the time when very thick clouds or heavy precipitation is present, CPR will not be able to penetrate to the cloud base. The mission objective dictates this choice.

The CPR consists of six primary subsystems. The digital subsystem performs the timing and control of the radar, and acquires and processes the reflectivity data. The upconverter generates and up-converts the lower frequency pulse to 94 GHz. The high-power amplifier consists of an extended interaction klystron (EIK), which amplifies the 3.33-μs long transmitted pulse to 1.5 kW peak, and a high-voltage supply that provides 16 kV. The power distribution unit supplies power to all the low-voltage electronics.

The antenna subsystem, which is shown in Figs. 7-22 and 7-23, consists of a quasi-optical transmission line (QOTL) and a collimating antenna. The QOTL couples the transmitted (or received) signal to (from) the collimating antenna and provides the required duplexing function to separate the transmitted and received 94-GHz radar pulses. The QOTL has three mirrors, a ferrite Faraday rotator, and a wire-grid polarizer. The collimating antenna focuses the radiation and reception of the 94-GHz pulses with the required gain and radiation pattern. It has three mirrors: a large shaped primary (M1) that implements an ~1.85-m wide noncircular radiating aperture, a shaped secondary (M2), and a third mirror (M3) that is used to properly relay the energy to the QOTL.

7.5.2 Antenna Requirements

The CloudSat instrument is driven by several mission and science requirements. Particularly relevant to the antenna system is the 1.5-dB absolute reflectivity measurement accuracy goal, the less than 2-km diameter instantaneous Earth surface radar footprint, the low sidelobe envelope (50 dB below gain peak for angles larger than 7 deg from boresight), and the –26 dBZ minimum detectable cloud reflectivity at the end of the 2-year mission (dBZ is a weather radar unit that corresponds to decibels relative to a reflectivity factor Z of 1 mm^6/m^3 [40]). These requirements drive the 94-GHz frequency choice, the collimating antenna topology and aperture size, and the required antenna system efficiency. The details of the antenna subsystem design and the performance measurements were derived from [41] and the various design review packages.

7.5.3 Quasi-Optical Transmission Line

The QOTL performs two functions in the CPR: signal relaying and duplexing. More specifically, when the CPR transmits, the QOTL delivers the RF energy pulse from the EIK to the collimating antenna. When the CPR receives, the QOTL delivers the reflected signal from the collimating antenna to the receiver. Since the radiated transmitted and received signals have identical frequency and linear polarization, the required duplexing is accomplished

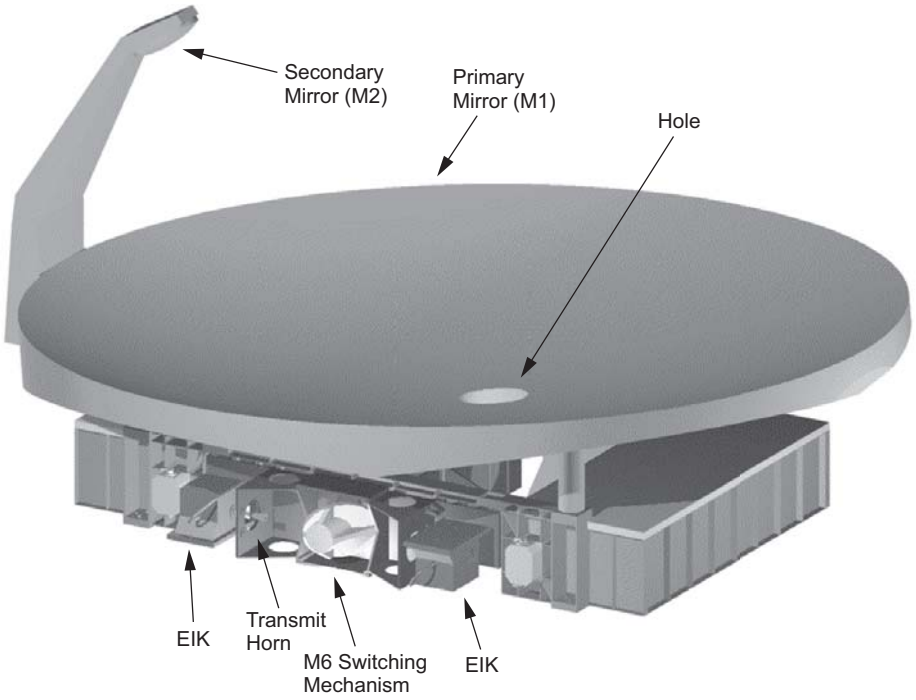

Fig. 7-22. CloudSat antenna system (EIK = extended interaction klystron).

through the use of a non-reciprocal component (a Faraday rotator) and a polarization grid located in the path common to both the transmitted and received signals [42]. The Faraday rotator creates a spatially orthogonal polarization relationship between the transmit and received signals, which are then separated by the polarization grid. Distinct feed horns are used to transmit and receive. To increase reliability, the CPR has two independent EIKs and associated feed horns, which are selected by the mirror M6 (see Fig. 7-22) and its switching assembly. Note that all horns are identical, as well as mirrors M5 and M6.

The schematic drawing of Fig. 7-24 details the operation of the QOTL. The transmitted 94-GHz pulse emanates from the active EIK through its corresponding feed horn. The pulse then reflects at the switching mirror, passes through the polarizing grid, and then passes through the Faraday rotator, which spatially rotates the linear polarization by 45 deg. From the Faraday rotator the beam heads to the collimating antenna. The returned radar pulse is received by the collimating antenna and routed to the Faraday rotator, where the field is rotated an additional 45 deg in the same direction as the transmitted pulse. The pulse leaving the Faraday rotator is then spatially filtered by the polarization grid, which reflects towards the receive horn only the component orthogonally

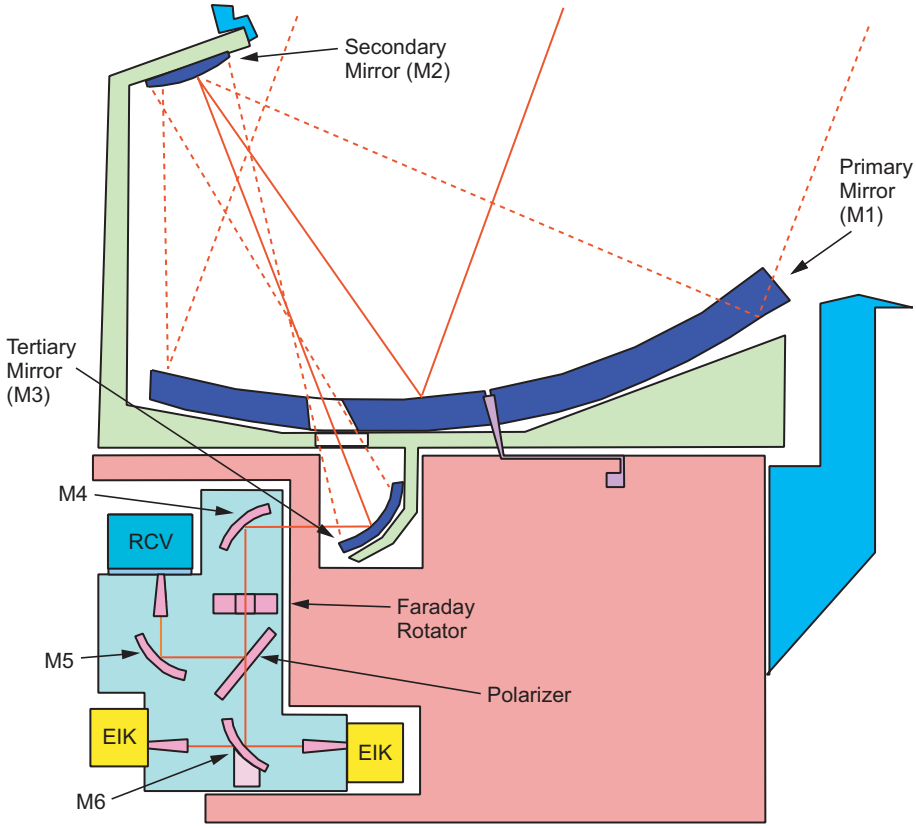

Fig. 7-23. CloudSat antenna system block diagram.

polarized to the transmitted signal at the polarization grid. Because of the net 90-deg rotation, the pulse that reaches the receive horn is co-polarized with the transmitted pulse at the collimating antenna aperture. The actual implementation of the QOTL (as shown in Fig. 7-22) uses extra mirrors M4 and M5 to route the signals in the proper direction.

The pulse-relaying and duplexing tasks of the QOTL can in principle be accomplished by waveguides and circulators. However, the relatively large physical size of the EIKs determined their location on the CloudSat spacecraft bus and would have imposed relatively long waveguide runs. Since a typical WR-10 waveguide has about 3.3 dB/m of loss at 94 GHz, the utilization of the QOTL (with its free-space propagation advantage) yields substantially less loss to the antenna system.

7.5.3.1 Requirements. The requirements for the QOTL are summarized below:

- Transmit loss: 0.5 dB

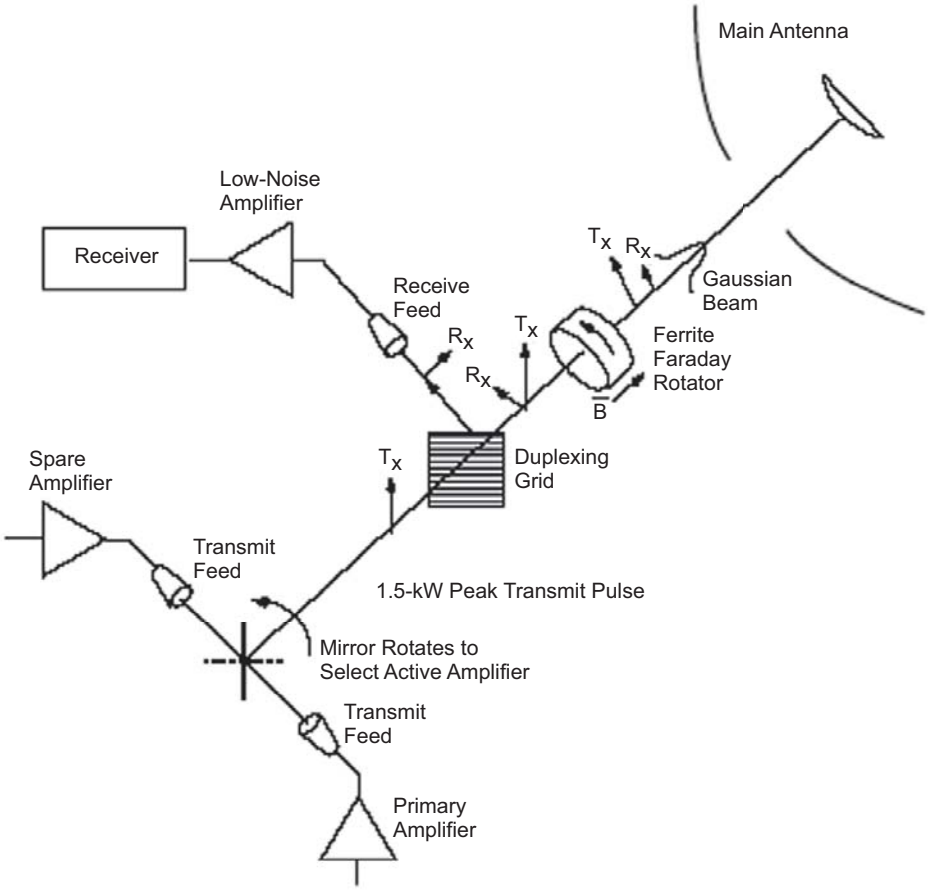

Fig. 7-24. CloudSat quasi-optical transmission line schematic drawing.

- Receive loss: 0.5 dB
- Isolation: 35 dB
- Power handling capacity: 2.0 kW, peak
- Operating temperature: –20 to +65 deg C
- Vibration: 9.8 grms, first mode: 70 Hz
- Magnetic: residue dipole < 0.1 A/m^2, 25 G demagnetized

To facilitate the QOTL and collimating-antenna development efforts, a circular corrugated test horn was designed to provide test excitation to both mirror M4 of the QOTL and mirror M3 of the collimating antenna. Use of this horn allowed the QOTL and collimating antenna to be developed and tested almost independently of each other, and combined only in the last stages of the program (an important convenience since the two systems were developed separately). This was possible because in the ideal case where the radiation

pattern of M4 (with the QOTL transmitting) and the radiation pattern of M3 (with the collimating antenna receiving a plane wave) are conjugate matched, the coupling of the QOTL and the collimating antenna will have no loss due to pattern mismatch [43]. The design goal was then to have the QOTL and the collimating antenna match the pattern of the test horn, which was designed for a nearly invariant radiation pattern from the far zone up to 100 mm from the horn aperture. The calculated radiation pattern of the test horn is depicted in Fig. 7-25.

7.5.3.2 Polarizer Design. The polarizer separates the received signal from the transmitted signal, and it is made from a periodic array of parallel conductors that reflects signals polarized parallel to the conductors, and transmits signals polarized perpendicular to the conductor axis.

A free-standing wire grid polarizer was used to minimize losses. Commercial polarizers were available with conductor spacing of 8 per mm, giving 24 conductors per wavelength (at 94 GHz, $\lambda = 3.18$ mm). This is sufficient density for low transmission and reflection losses.

A square aperture with all wires the same length is used to match the mechanical resonant frequency from wire to wire. The polarizer was fabricated with gold-plated tungsten wires. The gold plating gives lower transmission loss than bare-tungsten designs.

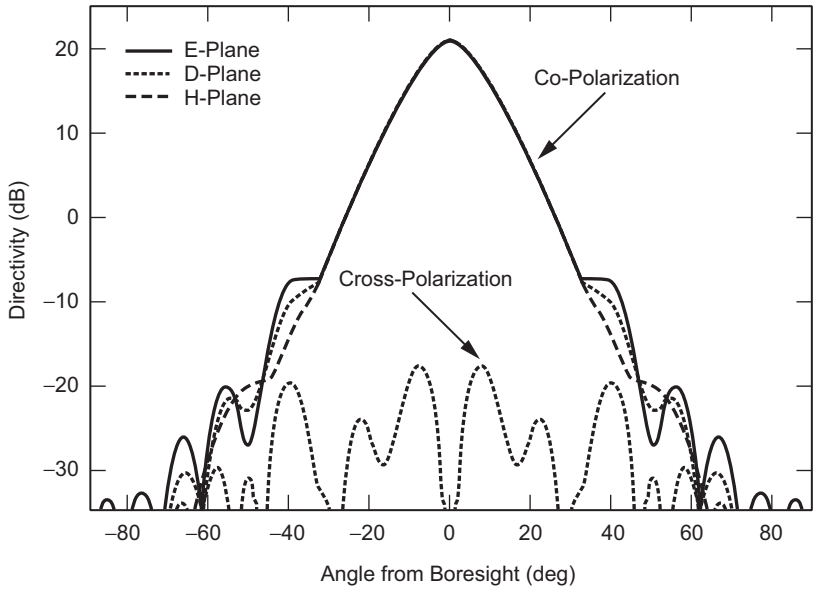

Fig. 7-25. CloudSat test horn radiation pattern, calculated on a 130-mm radius sphere centered on the phase center.

7.5.3.3 Faraday Rotator Design. The Faraday rotator (schematic shown in Fig. 7-26) consists of a ferrite disc, two quartz quarter-wave plates, and a bias permanent magnet; with axial-beam propagation. The Faraday rotation angle of a ferrite disc is given by:

$$\theta = \frac{\pi\sqrt{\varepsilon}}{c}\gamma 4\pi M_S T$$

where: γ = gyromagnetic ratio (28 GHz/T)
$4\pi M_S$ = ferrite saturation magnetization
T = Thickness

The bias field exceeds the saturation magnetization of the ferrite to provide adequate bias over the volume and minimize perturbations from external fields. The rotator is made from a 1-kilogauss (kG) permanent magnet, a rotator disc of 8.7-mm thick Transtec G-4259 ferrite, and quartz quarter-wave plates 0.406 mm thick.

7.5.3.4 Performance. The estimated losses of the QOTL are shown in Table 7-19. The radiation pattern of M4 calculated on a 130-mm radius sphere centered at the phase center is shown in Fig. 7-27.

7.5.4 Collimating Antenna

In the initial proposal for the CloudSat mission, an axially symmetric Cassegrain collimating antenna was suggested. Due to blockage by the subreflector and its supporting structure, the axially symmetric Cassegrain has inherently higher sidelobe levels and larger pattern prediction uncertainty than a clear-aperture geometry. Since in a spaceborne atmospheric radar a large

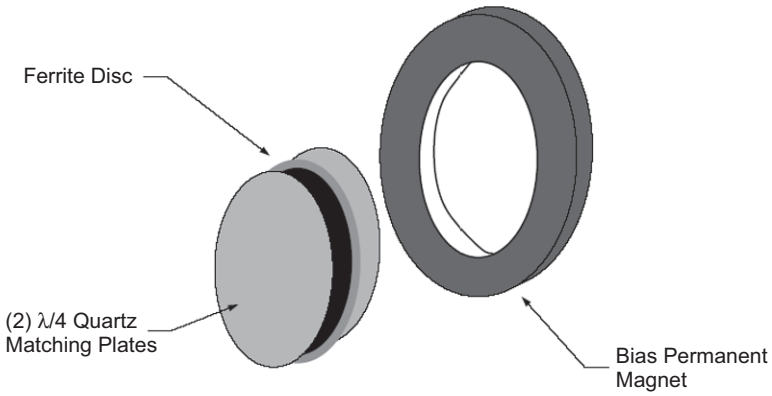

Fig. 7-26. Schematic of the CloudSat rotator design.

Table 7-19. QOTL losses.

Component	Loss, dB	Notes
Rotator ferrite	0.27	For $4\pi M_S = 800$ gauss, $\varepsilon_r = 14.8$, $\mu_r = 38$, $\tan\phi = 0.00015$, 8.7-mm thick
Quartz plates	0.03	For $\varepsilon_r = 3.79$, $\tan\phi = 0.001$, 0.41-mm thick
Mismatch	0.001	$r = 0.0087$
Angle error	0.03	5-deg error
Polarizer	0.2	From MLS, bare tungsten wire
Total	**0.53**	**Slightly over requirement**

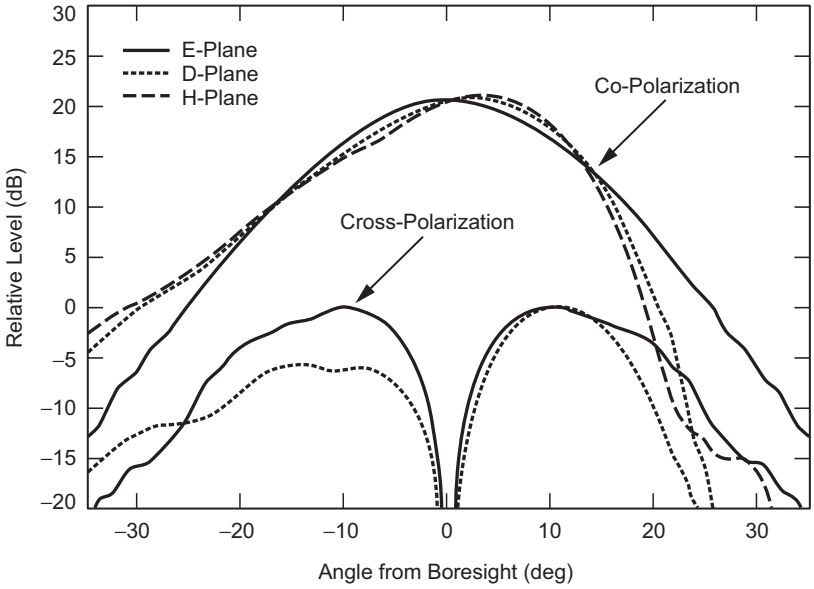

Fig. 7-27. Radiation pattern of M4, calculated on a 130-mm radius sphere centered on the phase center (EIK 1 path).

amount of Earth surface clutter comes through the antenna sidelobes, the axially symmetric Cassegrain geometry may yield intolerable sidelobe levels. To overcome this potential problem, the CloudSat designers planned on implementing a frequency diversity scheme in its digital subsystem, where a slight frequency shift would be impressed in the sequence of transmitted pulses. This would allow the cloud reflection to be separated from the surface clutter, alleviating the antenna sidelobe requirement. However, after the radar program was initiated, the use of an offset collimating antenna was proposed. The clear aperture of the offset geometry yields low sidelobes that can be accurately modeled. Due to this, the additional electronics needed to support the frequency diversity were removed.

The collimating antenna is severely constrained by the available spacecraft envelope (the translucent surface shown in Fig. 7-28), and several clear-aperture options were considered. Since there was no severe cross-polarization requirement, the highly compact open Cassegrain geometry was chosen [44]. This offset configuration, which is depicted in Figs. 7-22 and 7-28, offers excellent packaging characteristics and, although requiring a hole in mirror M1, is free of all the other blockage-related scattering problems present in an axially symmetric configuration. The M1 hole increases the radiated sidelobe levels, but the hole can be made quite small, and its scattering characteristics can be predicted with high degree of confidence. In fact, this high degree of confidence allowed the collimating antenna to be manufactured without the usual engineering and breadboard models, producing significant savings in both cost and implementation time.

The collimating antenna is depicted in the scale drawing of Fig. 7-29. The mirror M3 surface is ellipsoidal and, in the transmit mode of operation, transforms the QOTL (or test horn) pattern from about 21 dBi directivity to about 34 dBi directivity at the surface of M2. The mirror M2 is shaped to provide an almost uniform amplitude illumination of the collimating antenna aperture. M1 is also shaped to correct the phase error introduced by the shaped M2. To maximize the gain, the rim of M1 is also shaped to optimize the

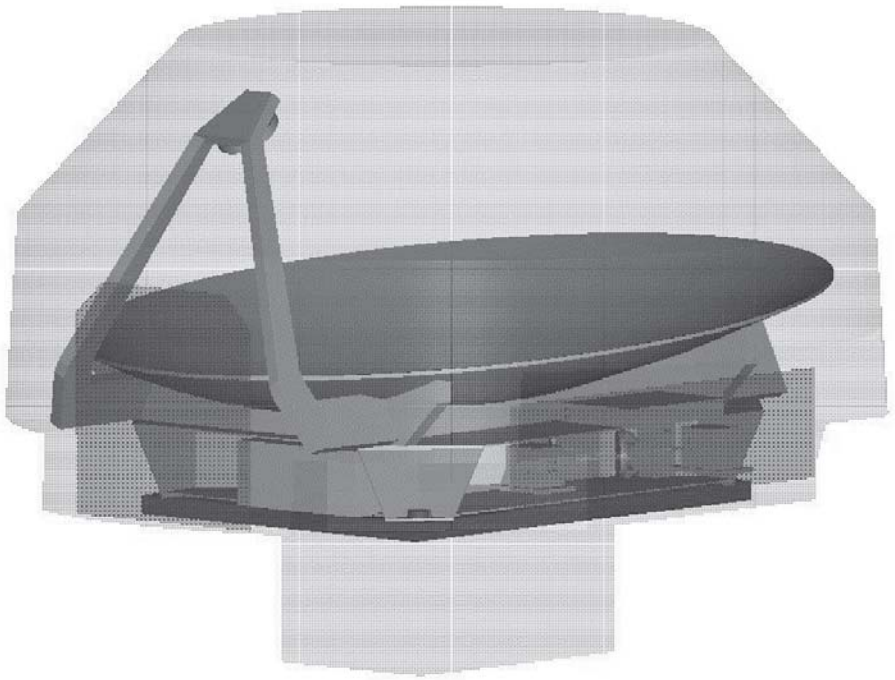

Fig. 7-28. CloudSat instrument in spacecraft envelope.

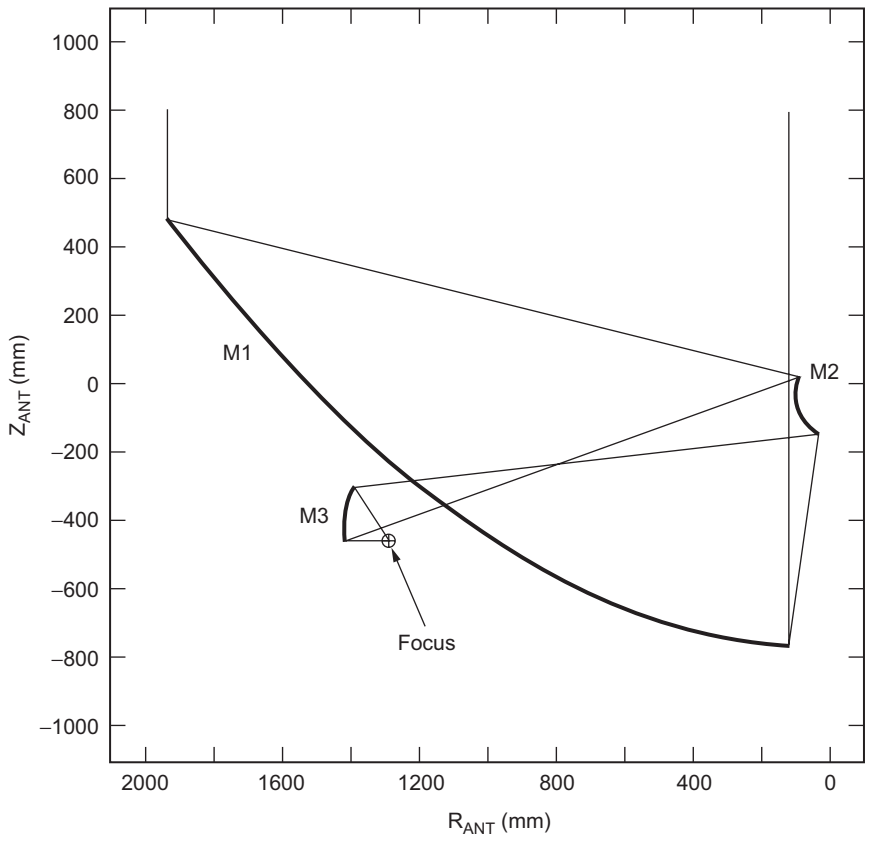

Fig. 7-29. Scale drawing of the CloudSat collimating antenna (shaped reflector system geometry in Y = 0 plane).

utilization of the available spacecraft fairing envelope (the projected M1 aperture is not circular). The end result is a projected collimating antenna aperture area of 2,798,018 mm^2, which yields a predicted 64.70 dBi directivity (85-percent efficiency since the maximum theoretical directivity of this aperture is 65.39 dBi) when excited by the test horn. This number does not include mechanical imperfections.

Due to the large asymmetry and non-circular projected rim, none of the shaping methods available in the literature (for example Section 1.2.4) can be applied to the collimating antenna; consequently, a new shaping method was developed for this antenna.

Since the surface area of M1 is much larger than the area of M2, M2 controls the amplitude of the aperture field, and M1 controls the phase of the aperture field. The shaping method developed uses numerical optimization with scattering tools to generate the shape of M2 and M1 that maximizes the

collimating antenna directivity. Since a numerical optimization is employed, arbitrary M1 and M2 rims can be used.

The numerical procedure is as follows. The radiation pattern of the test horn illuminating M3 at 94.05 GHz was determined and used as a "shaping feed'' (with an imposed spherical wavefront). The M2 surface was defined by 20 adjustable points and an interpolator based on thin-plate deformation theory [45].

These adjustable points were the optimization variables (symmetry was used to half the optimization variables). One M2 point was held fixed to establish the M2 location (nine optimization variables). The path length from the shaping feed to the aperture was held fixed and determined using geometrical optics on M2. This established the M1 shape and its position. Physical optics was used to determine the antenna directivity (on both M1 and M2). The directivity is the parameter to be maximized during the optimization process. To reduce computation time the shaping was performed at 24.05 GHz (and required ~14 hours on a 450-MHz personal computer (PC)).

As mentioned previously, the radiation of M3 reaches M2 through a hole on the surface of M1. The hole is approximately elliptical in shape and has an aperture-projected major axis of about 110 mm. This assures small scattering by the hole and allows the collimating antenna to meet the sidelobe envelope requirement with more than 10 dB margin at 7 deg from boresight. The edge tapers on M3 and M2 are 25 dB and 23 dB, respectively (space loss not included). On the hole, the M3 radiation has a 30-dB edge taper. These high edge taper values yield a total spillover loss of only 0.16 dB for the entire collimating antenna (i.e., M3 + hole + M2 + M1).

The near-boresight and far-from-boresight radiation patterns of the collimating antenna, when excited by the test horn, are depicted in Figs. 7-30 and 7-31, respectively. The electric field is polarized in the paper plane of Fig. 7-29. The near-boresight pattern was computed by sequentially using the physical optics (PO) technique starting from the test horn pattern and proceeding to M1 (the radiation of M3 through the M1 hole was modeled using the equivalence principle). Fig. 7-30 depicts the scattering of M1 and its hole, which are the only significant scattering effects in the angular range shown.

The far-from-boresight pattern of Fig. 7-31 is a composite result of two patterns that were computed using a combination of geometrical theory of diffraction (GTD) and PO scattering techniques [46]. This is needed because, for angles far from boresight, the required integration grid over M1 is very dense; and hence, the computation time to determine the radiation pattern becomes prohibitively large. The first pattern of the composite was the radiation of M1 and its hole. It was obtained by first computing the radiation over M2, emanating from the M1 hole, as described for the near-boresight pattern. This pattern was then used to excite M2, and its scattering over M1

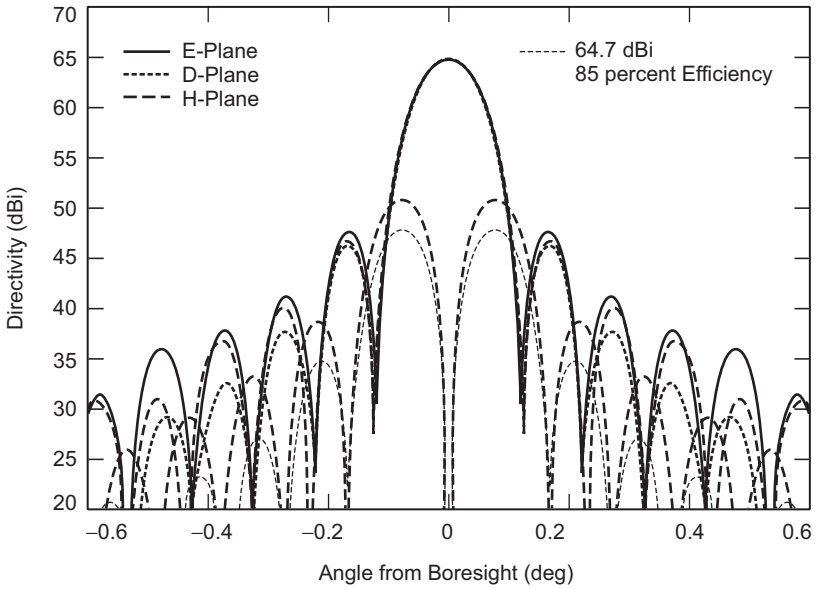

Fig. 7-30. CloudSat collimating antenna calculated near-boresight far-zone radiation pattern (excited by the test horn).

determined using GTD. The radiation from M1 and its hole was then determined using PO and plotted in Fig. 7-31. The second pattern of the composite is the M2 scattering and its spillover. It was determined as described for the near-boresight pattern and also plotted in Fig. 7-31. This composite pattern then shows, as an envelope, the dominant pattern of the two parts of the composite. Clearly seen in Fig. 7-31 is the effect of the M1 hole (oscillations that peak at about every 2 deg, and can be seen between approximately –30 and +30 deg), the M2 spillover (in the neighborhood of –70 deg), and the M1 top-rim spillover (beyond about +65 deg). Although the shaped rim increases the sidelobes, the –50 dB sidelobe envelope requirement (relative to peak gain) for angles greater than 7 deg is met with ~12 dB of margin (worst case). Since the edge of the Earth is at about 65 deg from nadir, the M1 and M2 spillovers do not significantly contribute to clutter.

The mirror M1 and its associated support structure was manufactured using composite materials to reduce weight while yielding an rms surface accuracy better than 50 μm.

The surface of M1 was coated with a vacuum-deposited aluminum film to provide a highly reflective surface at W-band. The mirror M2 was machined in aluminum to an accuracy better than 25 μm. Both the M1 and M2 surfaces were subsequently made Lambertian to reduce coherent scattering at infrared wavelengths, and hence minimize thermal loading. All other mirror surfaces

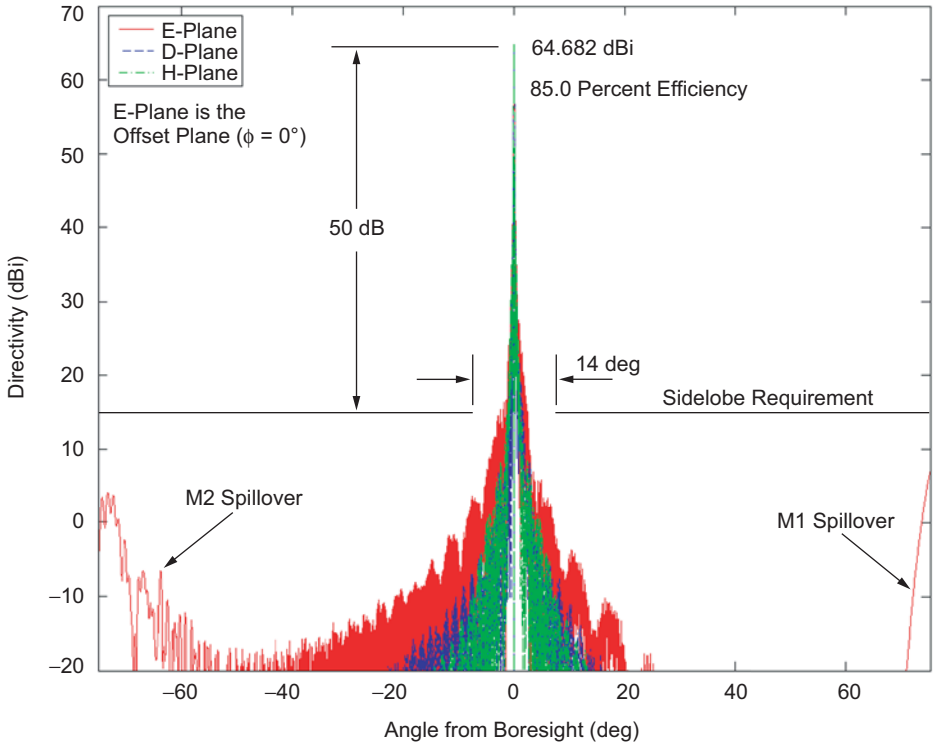

Fig. 7-31. CloudSat collimating antenna far-from-boresight radiation pattern (excited by the test horn).

(i.e., M3–M6) were machined of aluminum to an accuracy significantly better than that of M1 and M2.

Table 7-20 summarizes the expected performance of the CPR antenna system, and provides a breakdown of its various loss components. As mentioned previously, the QOTL paths for the EIK 2 and the receiver have the worst performance with an overall gain of 63.1 dBi. The EIK 1 path has a better performance with a gain of 63.2 dBi. These numbers correspond to overall efficiencies for the CPR antenna system of 59.0 percent and 60.5 percent, respectively.

7.5.5 Measured Performance

The gain, sidelobes, and pointing were measured on both the near-field range and a quasi-far-field range at JPL. Measurements were also made before and after the vibration test. The results were:

1) Gain met specification, with close to promised uncertainty.

Table 7-20. Gain loss budget for the CPR antenna system.

Loss/Gain Path Elements	EIK 1 (dB)	EIK 2 (dB)	RCVR (dB)
Collimating antenna directivity	64.70	64.70	64.70
Primary – mirror M1			
Reflectivity	–0.04	–0.04	–0.04
Surface error	–0.10	–0.10	–0.10
Secondary – mirror M2			
Reflectivity	–0.012	–0.012	–0.012
Surface error	–0.05	–0.05	–0.05
Tertiary – mirror M3			
Reflectivity	–0.02	–0.02	–0.02
Surface error	–0.012	–0.012	–0.012
QOTL to collimating antenna coupling	–0.25	–0.45	–0.45
QOTL mirror M4			
Spillover	–0.05	–0.03	–0.03
Reflectivity	–0.02	–0.02	–0.02
Surface error	–0.012	–0.012	–0.012
Faraday rotator			
Ferrite dielectric loss	–0.26	–0.26	–0.26
Matching plates	–0.03	–0.03	–0.03
Reflectivity	0.00	0.00	0.00
Angular error	–0.03	–0.03	–0.03
Duplexing polarizer	–0.20	–0.20	–0.20
QOTL mirror M5			
Spillover			–0.11
Reflectivity			–0.02
Surface error			–0.012
QOTL mirror M6			
Spillover	–0.11	–0.11	
Reflectivity	–0.02	–0.02	
Surface error	–0.012	–0.012	
Feed horn waveguide flange pair	–0.10	–0.10	–0.10
Feed horn and waveguide losses	–0.12	–0.12	–0.12
Total overall gain (dBi)	**63.2**	**63.1**	**63.1**

2) Pre-post vibration gain differences well within uncertainty, and pattern shapes tracked well.
3) Patterns had some sidelobe discrepancies.
4) On elevation and azimuth cuts, sidelobe levels were exceeded.
5) Outermost sidelobe specification met (>7 deg).

6) Pre-post vibration change in pointing within uncertainty. Pointing uncertainty somewhat larger than anticipated.
7) Beam co-pointing within specification (±0.01 deg)

7.6 Wide Swath Ocean Altimeter

Richard E. Hodges

The Ocean Surface Topography Mission (OSTM) [47] is a cooperative effort between NASA, the National Oceanic and Atmospheric Administration (NOAA), the European organization for the Exploitation of Meteorological Satellites (EUMETSAT), and the Centre National d'Etudes Spatiales (CNES), the space agency of France. OSTM is a follow-on to Jason [48] and will provide continuity of ocean topography measurements beyond Jason and TOPEX/Poseidon [49]. OSTM will measure sea surface height to an accuracy of <4 cm every 10 days. Sea surface topography, as measured by satellite altimeters, has numerous applications important to global environmental monitoring, including predicting hurricane intensification, improving tide models, mapping deep-ocean bathymetry, monitoring, and forecasting El Niño Southern Oscillation, measuring the rate of global sea-level rise, and charting surface currents.

OSTM will carry six scientific instruments. NASA will provide the advanced microwave radiometer (AMR), the global positioning system payload (GPSP), the laser retroreflector array (LRA), and the experimental wide swath ocean altimeter (WSOA). CNES will provide the nadir altimeter and the Doppler orbitography and radio positioning integrated by satellite (DORIS) instruments. The nadir altimeter will provide vertical measurements of sea-surface height. The AMR will provide atmospheric correction for the nadir altimeter. The GPS payload, the LRA, and the DORIS will provide precision orbit determination, and the WSOA will demonstrate new high-resolution measurement of ocean surface topography. The following describes the development of the WSOA.

WSOA is a cross-track interferometer with a 6.4-m baseline. WSOA will produce a full three-dimensional map of ocean height, which will provide key information on oceanic energy transport and eddy currents.

An enabling technology for this instrument is the pair of antennas used to form the Ku-band interferometer operating at 13.285 GHz. WSOA requires two 2.2- by 0.35-m projected apertures that are stowed by folding and that provide dual-beam, dual-polarization, ~20-dB sidelobes, and 50-percent aperture efficiency in a low mass package. A unique offset-fed reflectarray antenna design was developed to meet these needs and also minimize overall system mass and moment of inertia. Each antenna has two feeds located off the focal point to produce two beams scanned ±3.3 deg from nadir.

Each antenna is comprised of a reflectarray and two slotted waveguide feeds. A reflectarray is a relatively new type of antenna that uses non-Snell's law reflection optics to enable a flat surface to function as a focused reflector comparable to a traditional parabolic reflector [50–52]. The reflectarray is realized using a uniform array grid of variable-sized microstrip patch elements. These elements are designed to reflect an incident field with the phase shift needed to collimate a beam. An important discovery in this work is that a flat offset-fed reflectarray provides dramatically better scan performance than a comparable reflector antenna. Indeed, for this application a parabolic reflector antenna is not viable because the scan loss from positioning the feeds off-focus to obtain ±3.3 deg beam positions is ~3 dB.

An experimental breadboard of the reflectarray was built and successfully demonstrated that the performance requirements can be achieved using this new technology. The reflectarray antennas are made up of five separate flat panels, which can be folded for compact stowage and ease of deployment. The panels consist of an aluminum honeycomb core and a thin dielectric substrate upon which the square patch elements are etched. The slotted waveguide feeds utilize Taylor amplitude weighting to achieve low spillover. Since the reflectarray surface is in the near field of the feeds, a cylindrical phase taper is used on the feed aperture to focus the feed pattern at the 2.8-m reflectarray focal distance.

7.6.1 Antenna Requirements

WSOA is a cross-track interferometer that requires a pair of dual-polarized antennas separated by a 6.4-m baseline as illustrated in Fig. 7-32. The key antenna electrical requirements are summarized in Table 7-21. A projected aperture size of approximately 2 m × 0.35 m is needed to achieve the gain and beamwidth requirements.

To obtain a 39.2-dB gain with this aperture, the antenna must realize an overall efficiency of approximately 50 percent. To accommodate the length and baseline separation of these apertures, the antennas must fold up for launch stowage and be compatible with a mast deployment mechanism. Spacecraft mass allocation, moment of inertia, and center of gravity lead to requirements for very low mass (<14 kg).

Several options (including a reflector, a microstrip patch array, and a waveguide array) were considered for the WSOA. A reflectarray design was selected because it is the only option that meets all of the requirements. For example, a reflector antenna cannot fold flat for stowage and does not meet requirements for two beams in the offset configuration. A microstrip patch array and waveguide array could not meet the mass requirements. The key drawback of the reflectarray design option is lack of flight heritage—to date, a reflectarray has not been flown on a space flight mission.

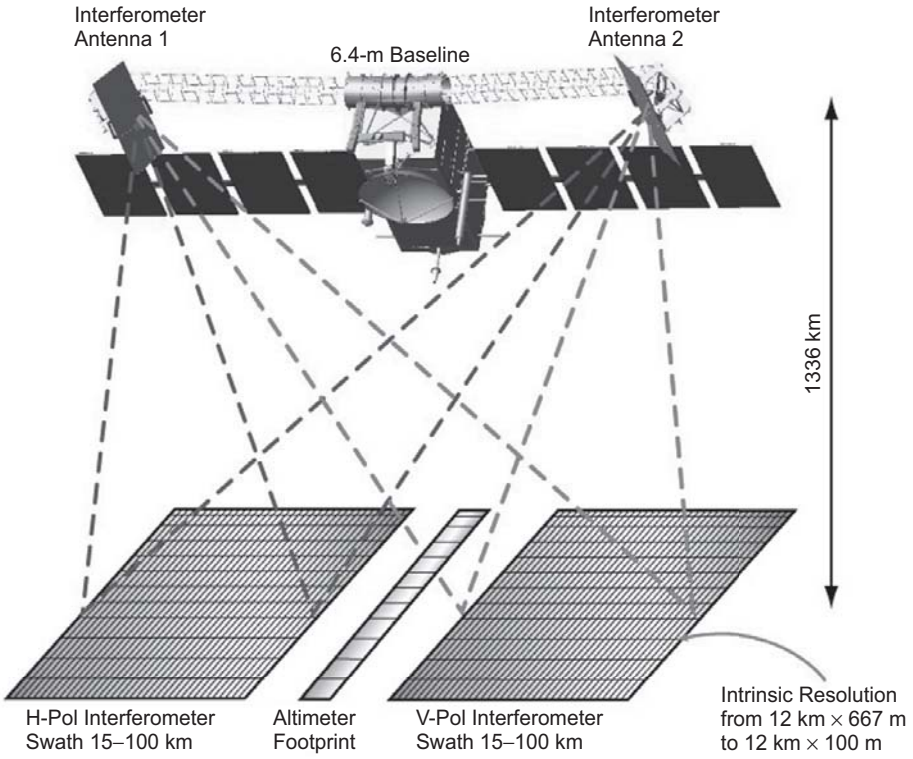

Fig. 7-32. WSOA system concept.

Table 7-21. WSOA antenna requirements.

Parameter	Value
Center frequency	13.285 GHz
Bandwidth	20 MHz
Gain per antenna	≥39.2 dBi
Elevation 3-dB beamwidth	≥3.8 deg
Azimuth 3-dB beamwidth	<0.65 deg
Beam pointing (V-polarization/H-polarization)	±3.3 deg
Sidelobe ratio (elevation)	–13 dB
Sidelobe ratio (azimuth)	–20 dB
Cross polarization	–20 dB
Return loss	>20 dB
Peak power handling	130 W
Panel mass (10 panels)	11.26 kg
Feed mass (4 feeds)	2.5 kg

Two concepts were developed to meet the system requirements. The initial concept was a symmetric-fed antenna design [53]. Although this design was proven in breadboard testing, the placement of electronics and cabling could not meet system requirements. To overcome this problem, a novel offset-fed reflectarray design was developed. Although this design significantly increased the technical risk, the design software developed for the symmetric design enabled rapid development of the offset-fed design.

Figure 7-33 illustrates the offset-fed reflectarray antenna design developed for the WSOA interferometer [54,55]. The offset-fed design improves spacecraft antenna accommodation by arranging the reflectarray optics to locate the focal point near the spacecraft bus. The focal length is 2.8 m, and the two feeds are offset from the focal point in order to realize a ±3.3-deg elevation beam scan (Fig. 7-34). This feed placement allows all transmitter and receiver electronics to be co-located on the spacecraft bus, which eliminates the need for separated electronics boxes and associated cables to distribute RF, power, and control signals along the mast. If the reflectarray panels are sufficiently low mass, this results in reduced mass and moment of inertia. In addition, the flexibility to reposition the panels enables a designer to adjust instrument center of gravity.

7.6.2 Panel Design

Each reflectarray is comprised of five panels and a two feeds, one feed for vertical polarization and one for horizontal polarization. A mechanical deployment mechanism is used to fold the flat panels into a stowage

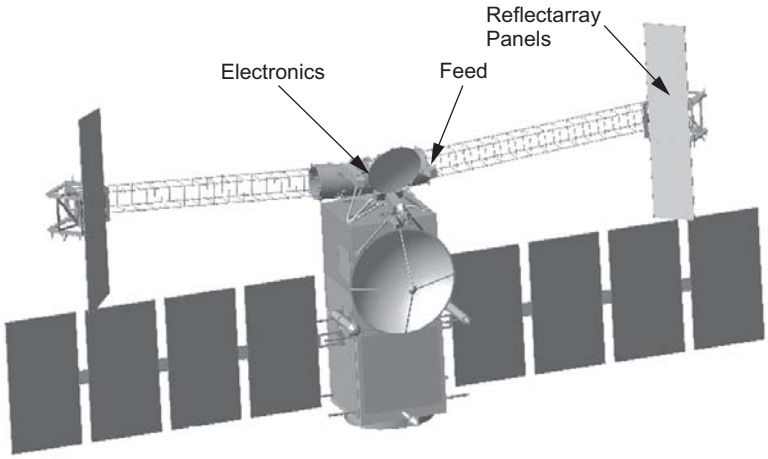

Fig. 7-33. Illustration of WSOA offset-fed reflectarray antennas spacecraft accommodation.

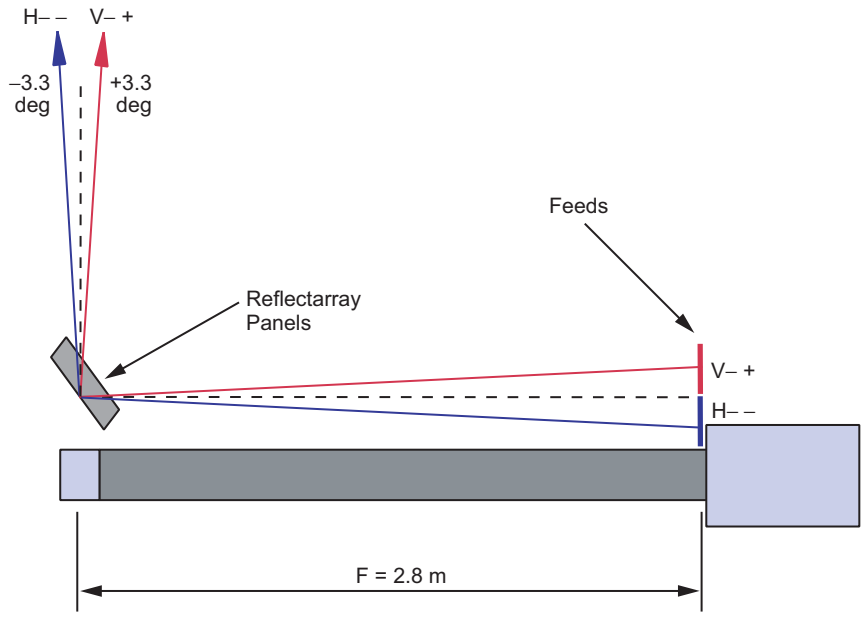

Fig. 7-34. WSOA offset-fed feed scanning arrangement.

configuration for launch. The panels use variable-sized square patch reflectarray elements printed on dielectric substrates. Unlike in the symmetric configuration [53], a piecewise parabolic configuration will not work for the offset-fed reflectarray because excessive scan loss precludes the ±3.3-deg elevation beam scan. Fortunately, it was found that a flat reflectarray geometry yields acceptable scan loss, and therefore, enables one to obtain the required ±3.3-deg elevation beam scan.

Pozar's variable patch design procedure was used for the reflectarray electrical design [52]. The procedure uses infinite array (Floquet mode) reflection coefficients to determine the phase of the field scattered by each patch. This approximation introduced risk because reflectarray element sizes vary over the array face, thus creating a non-periodic array environment. Since patch elements can only generate ~360-deg phase shift, "phase wraps" occur when the required phase shift exceeds this value.

7.6.3 Feed Design

A waveguide slot array was selected as the feed design for an appropriate combination of high efficiency, relatively low mass, higher power-handling capability, and an ability to control the pattern shape by adjusting the amplitude and phase coefficients at each radiating slot. It also provided a simple geometry that could be easily modeled with basic array theory in the calculation of the secondary reflectarray pattern.

The interferometric baseline and availability of space on the flight vehicle set the geometry shown in Fig. 7-35. Basic system requirements specified the scan angle and beamwidth for both the azimuth and elevation directions. The design task was to provide an illumination on the reflectarray to satisfy these requirements.

A Taylor distribution was used to determine the slot amplitudes in both the azimuth and elevation directions, while a cylindrical phase taper was used to focus the beam at the center of the reflectarray to minimize spillover. An iterative approach was then used to vary the feed position and amplitude weighting on the slots to achieve the required scan angles and beamwidths. Simple array theory was used for each iteration to calculate the resulting field at each patch element for use in calculation of the secondary reflectarray pattern.

Once the correct patterns were established, then the waveguide feed network that fed the slots could be designed by combining various waveguide components (such as T-splitters and couplers) to transfer power between different waveguide layers in the feed. Four unique feed designs are needed for WSOA—two V-pol and two H-pol. One feed of each polarization is described below. The other two feeds use the same basic design, but the number of rows is varied to adjust the beamwidth needed to obtain the desired reflectarray illumination.

7.6.3.1 Vertical-Polarization Feed. The geometry selected for the radiating slot layer of the vertical-polarization (V-pol) feed is an offset longitudinal-shunt

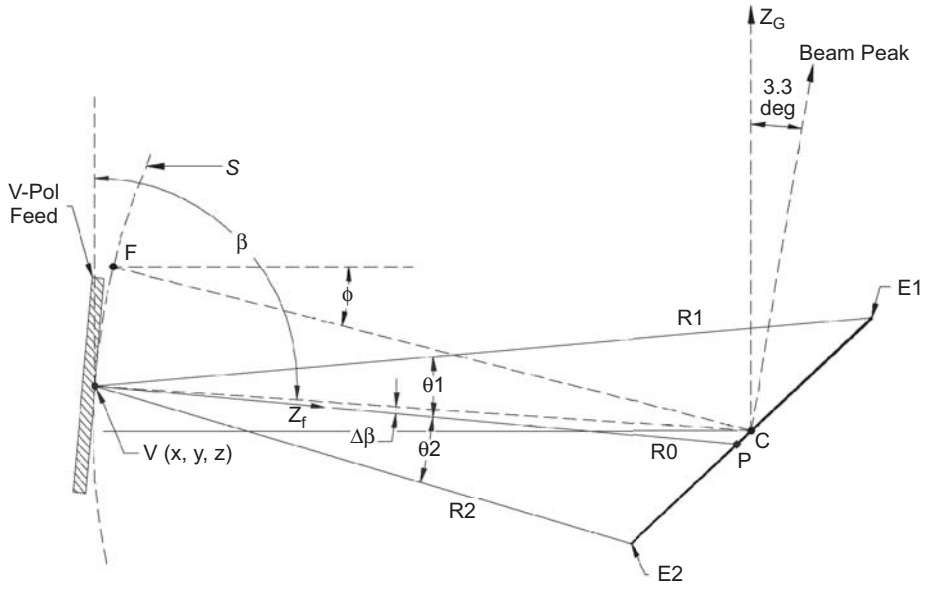

Fig. 7-35. WSOA basic geometry and design parameters (not to scale).

slot array. There are a total of eighteen three-by-one subarrays. A full-wave moment method procedure was used to design the required slot offsets, and the calculated patterns showed excellent agreement with those from array theory. An 18-way power divider with the appropriate power splits and phase delays provides the correct input excitation to each subarray.

The final breadboard configuration consists of four machined aluminum layers, with couplers transferring the power between the layers. Silver paint is used to provide electrical contact between the layers for breadboard testing. The flight hardware will use dip-brazed aluminum fabrication to minimize mass and ensure consistent electrical contact between all parts.

The performance of the assembled feed was excellent. The input return loss was 24 dB, which met the specification of 20 dB. The measured patterns, shown in Fig. 7-36, also agreed very well with those calculated by the moment method. Note that the elevation patterns are de-focussed in the far-field but are properly focused in the near feed at a radius of 2.8 m due to the cylindrical phase aperture illumination. The measured gain of 24.1 dB was also in good agreement with the calculated gain of 24.2 dB. The silver-painted breadboard feed achieved an efficiency of 87 percent.

7.6.3.2 Horizontal Polarization Feed. A design procedure similar to V-pol was followed for the horizontal-polarization (H-pol) feed. The feed geometry selected for the H-pol feed is a 4 × 16 element array comprised of eight 4 × 2 subarrays. Each 4 × 2 subarray consists of four 1 × 2 longitudinal-shunt slot subarrays. The eight 4 × 2 subarrays are fed from another layer consisting of eight rows of series-shunt angled coupling slots–four slots per row. An eight-way power divider on a third layer provides the correct amplitude and phase taper to each of the eight angled coupling slot rows.

The final H-pol configuration consists of four machined aluminum layers, with couplers transferring the power between the layers. The resulting patterns are shown in Fig. 7-37. The measured gain of 24.8 dB agreed very well with the calculated gain of 24.9 dB. The return loss was 17 dB at the design frequency but was 23 dB about 0.1 GHz higher, which can be tuned in a future iteration.

7.6.4 Breadboard Test Results

A breadboard model of the offset-fed antenna was designed, built, and tested to verify the accuracy of the modeling capability. Figure 7-38 shows the breadboard test antenna mounted in the NASA/JPL cylindrical near-field test facility. The panels and feeds are supported by a rigid aluminum frame structure to maintain the proper geometrical orientation of the panels relative to the feeds. The frame is covered with absorber material to eliminate spurious scattering lobes in the antenna pattern.

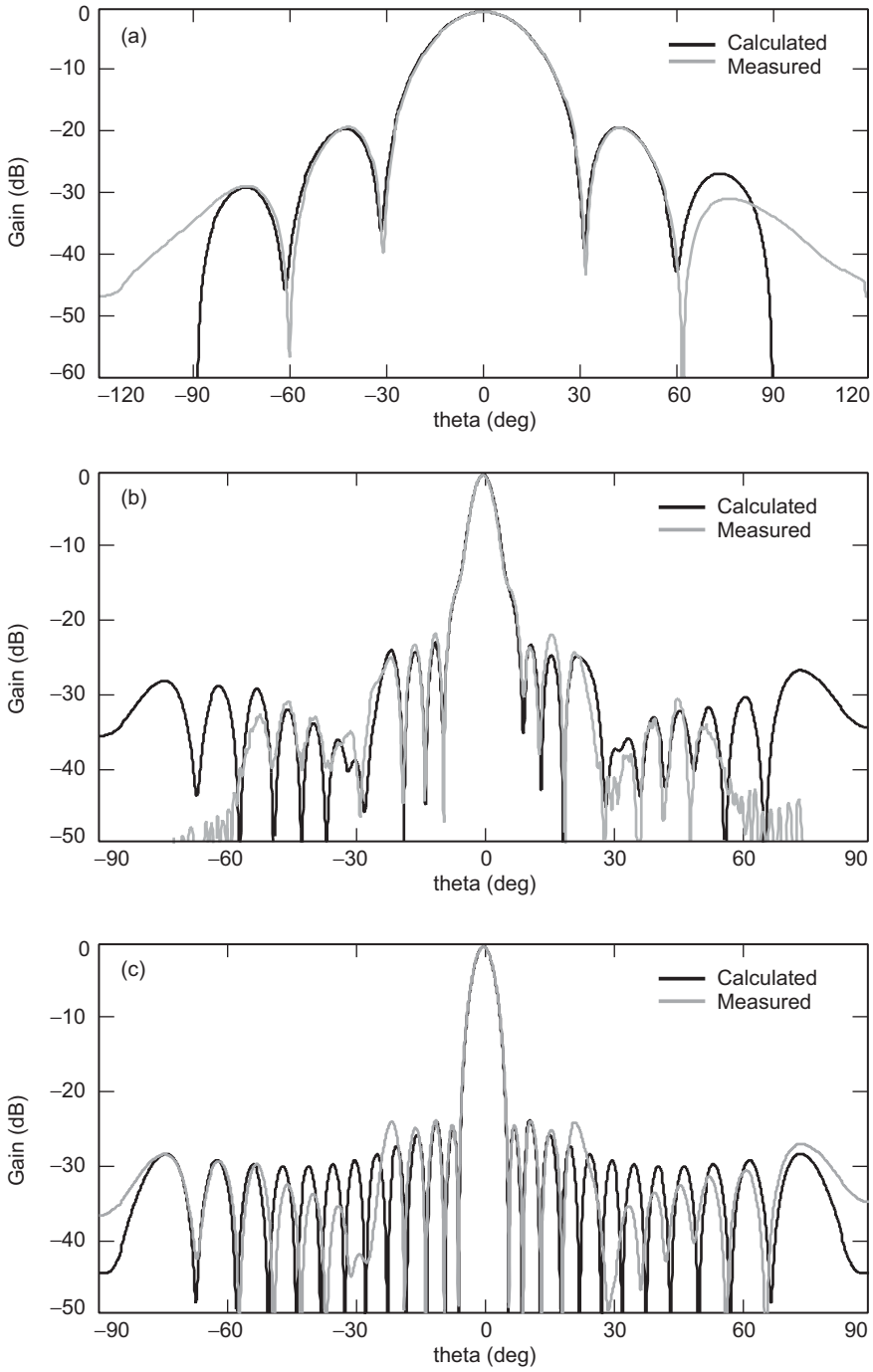

Fig. 7-36. WSOA measured vs. calculated feed patterns with V-polarization: (a) azimuth, (b) far-field elevation, and (c) near-field elevation.

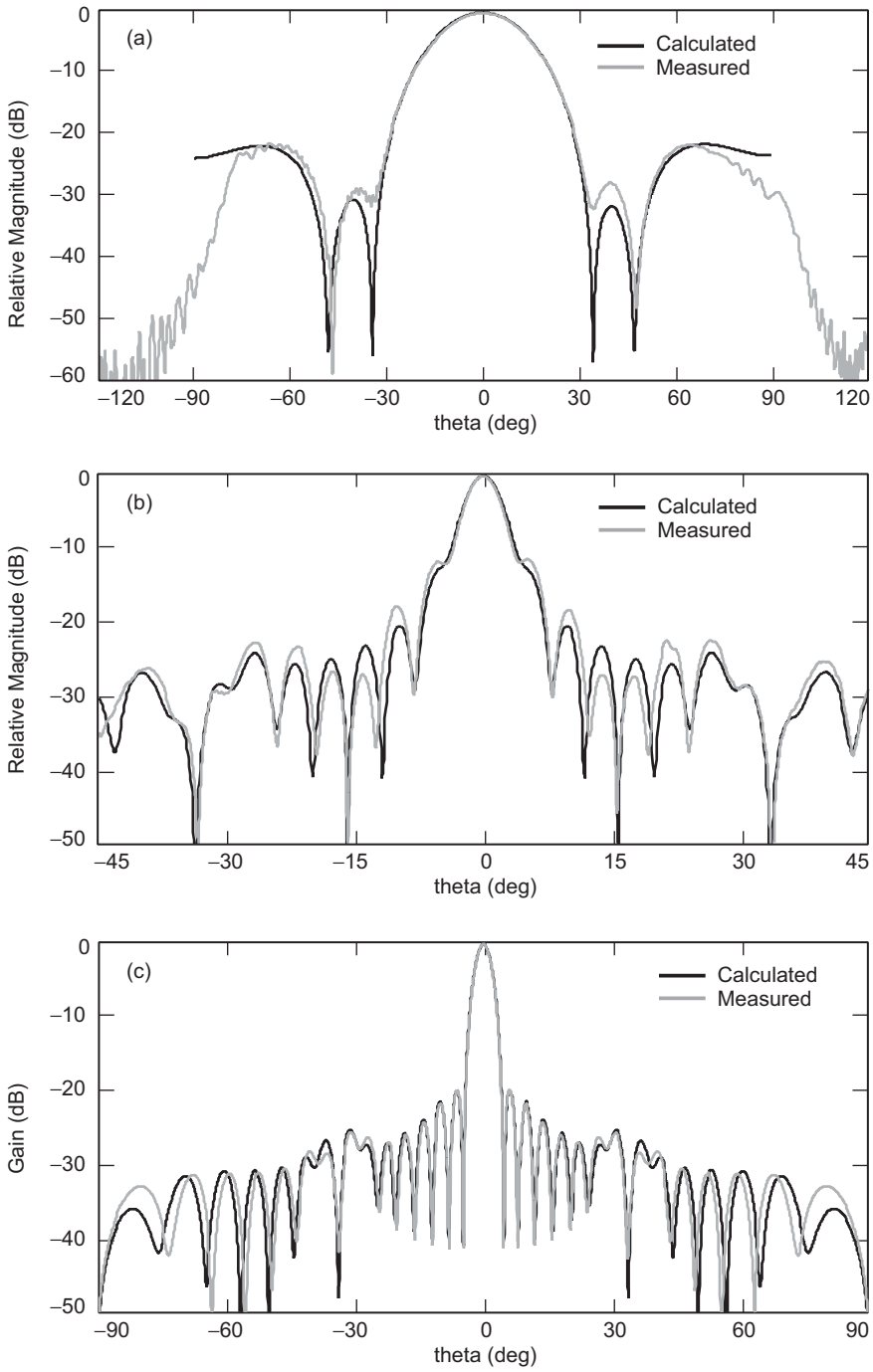

Fig. 7-37. WSOA measured vs. calculated feed patterns with H-polarization: (a) azimuth, (b) far-field elevation, and (c) near-field elevation.

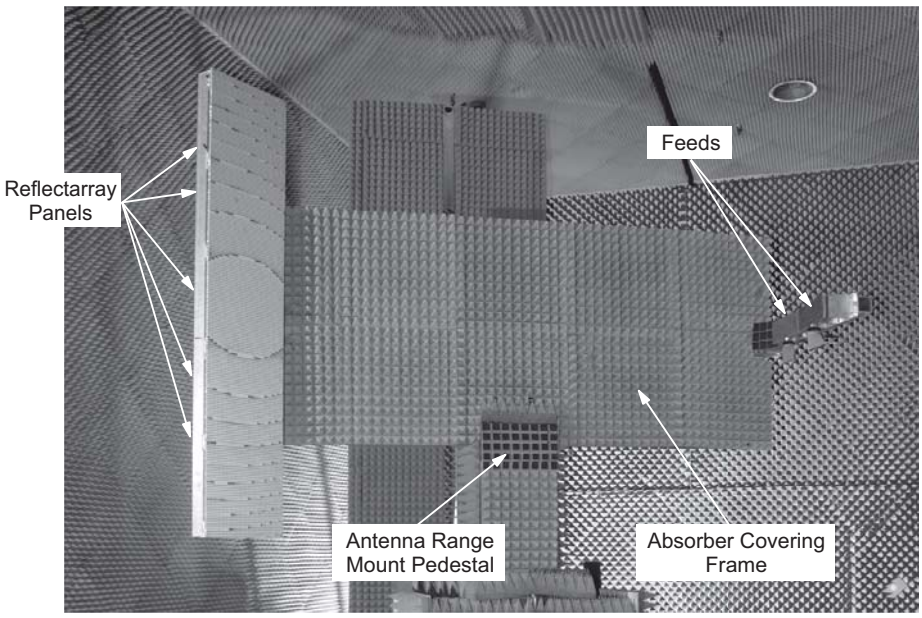

Fig. 7-38. WSOA offset-fed reflectarray breadboard mounted in NASA JPL cylindrical near-field test facility.

Figures 7-39 and 7-40 compare measured and calculated antenna patterns using the V-pol feed of the breadboard antenna. The patterns for H-pol are similar. The data show excellent agreement with predicted patterns. It should be noted that predicted patterns are calculated entirely from theoretical models, and do not account for errors in surface flatness or feed misalignment which were measured by a laser metrology system. The results tabulated in Tables 7-22 and 7-23 demonstrate good agreement between predicted and measured performance, and more importantly show that the specifications in Table 7-21 can be achieved. Note that the projected aperture is 2.2×0.35 m, so that the measured aperture efficiency is 48 percent for V-pol and 51 percent for H-pol. Efficiency is expected to improve slightly with flight-model feeds that are brazed instead of silver painted.

7.6.5 Conclusions

A reflectarray antenna offers a unique combination of advantages that can be a mission-enabling antenna design concept. The key characteristics of a properly designed reflectarray include relatively simple to obtain dual polarization, improved scan capability, low mass, good launch stowage, good efficiency (~50 percent), and relatively low cost.

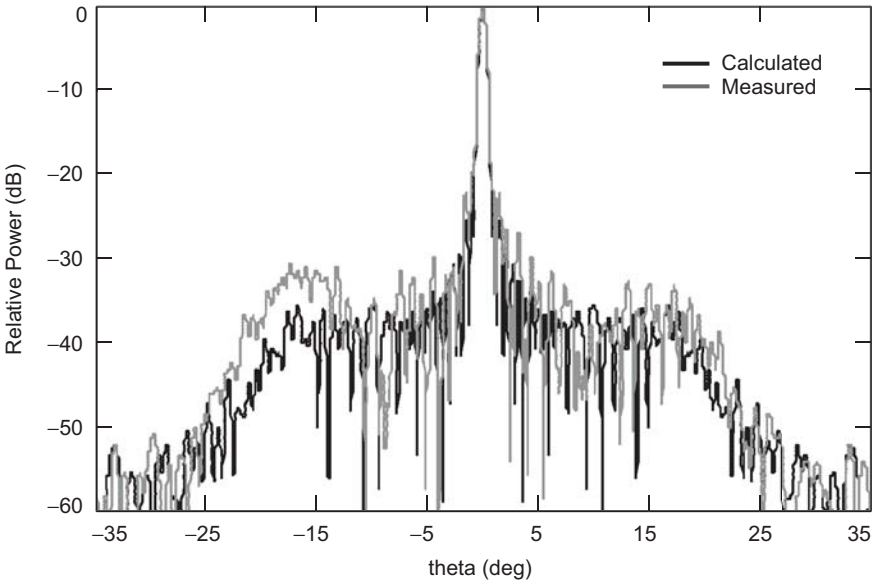

Fig. 7-39. Comparison of WSOA measured vs. calculated breadboard offset-fed reflectarray antenna patterns (V-pol azimuth).

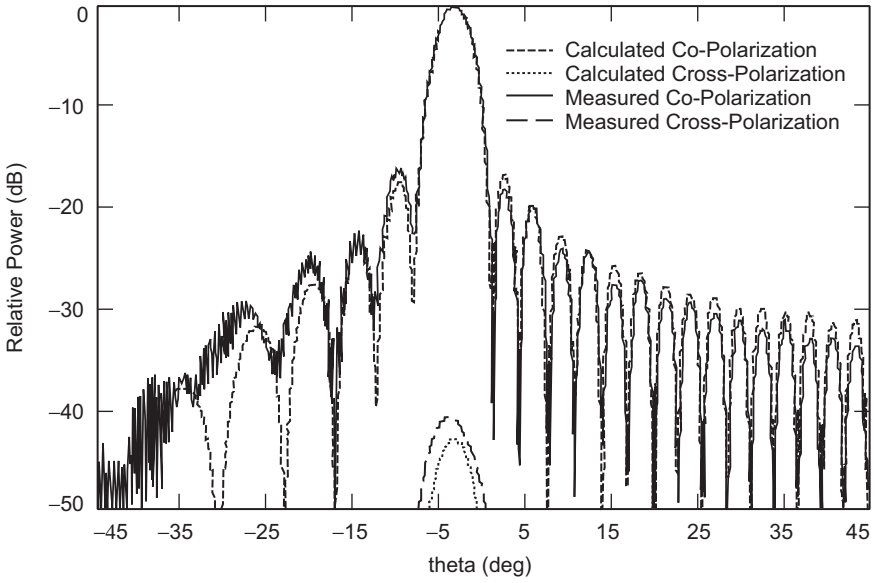

Fig. 7-40. Comparison of WSOA measured vs. calculated breadboard offset-fed reflectarray antenna patterns (V-pol elevation).

Table 7-22. V-pol reflectarray performance summary.

	Predicted	Measured
Gain	39.81 dB	39.31 dB
El beamwidth	3.85 deg	3.88 deg
Az beamwidth	0.625 deg	0.626 deg
El sidelobes (max)	–18.0 dB	–16.9 dB
Az sidelobe (max)	–21.90 dB	–19.5 dB

Table 7-23. H-pol reflectarray performance summary.

	Predicted	Measured
Gain	40.15 dB	39.53 dB
El beamwidth	3.84 deg	3.93 deg
Az beamwidth	0.616 deg	0.630 deg
El sidelobes (max)	–21.7 dB	–21.3 dB
Az sidelobe (max)	–21.5 dB	–18.7 dB

Compared to a reflector antenna, the reflectarray has smaller frequency bandwidth [56,57] and lower aperture efficiency. However, reflectarray fabrication is lower cost because it uses standard planar printed circuit fabrication techniques and does not require precision molds and custom lay up processes needed to produce lightweight composite reflectors.

7.7 Summary

Richard E. Cofield

In conclusion, JPL's development of radiometer and scatterometer antennas for instrument packages has combined an extensive heritage of theory and experience from JPL's telecommunications antenna programs, with the rigorous and ambitious regimens for qualifying spaceborne observational instruments. The following points distinguish these instruments' antennas from their ground-based predecessors.

Antenna performance requirements for scatterometers and radiometers generally differ slightly from those for telecommunications antennas. Radiometers typically view extended sources, especially in Earth remote-sensing applications. Therefore, requirements are often set for beam efficiency, rather than gain. Moreover, the atmospheric sounders can tolerate substantial cross-polarized power, as long as it is accurately known. In contrast, scatterometers typically have stringent gain and polarization isolation requirements but less demanding requirements on sidelobe level.

An important part of the development of spaceborne instrument antennas is pattern (or FOV) calibration. With the environment and observation scene often very different in space than during ground calibration, the analysis of flight data often requires the antenna performance knowledge as a mixture of measured patterns plus estimates of far-angle scattered power envelope. In many cases this demands an in-flight calibration campaign, using ground calibration sources (active or passive), known properties of homogeneous scenes for ground truth, or celestial objects (Sun, Moon, etc.) for in-orbit verification of the antenna pattern shape or its pointing.

Signals for radiometry in current instruments lie increasingly in submillimeter bands between windows for optical and telecommunications applications. With the need to fly as few receivers as possible, this drives us to broader bandwidths rather than for antennas in the other applications.

The expense of launch and the difficulty of instrument retrieval continue to make it critical to verify performance requirements through environmental tests, and to understand interactions between instrument and spacecraft. For antennas, this makes the following crucial:

1) FOV calibration must be properly sequenced with environmental qualification (such as vibration and thermal vacuum tests). The engineer must demonstrate with ever-increasing clarity how the antenna meets requirements before, during, and after these tests.
2) Alignment of the antenna boresight to spacecraft reference combines optomechanical methods with RF patterns. For extreme orbital environments these results must be interpreted using thermal and mechanical models of the spacecraft in flight, augmented where possible with temperature or dynamic-telemetry data. Alignment instruments packaged for hostile environments promise to help in this interpretation.
3) Analysis of flight data depends on both placement and knowledge of the alignment of co-aligned multiple sensors. Until now, this has been successful on a single platform, but future missions call for formation flying, which will increase the difficulty of co-alignment.

We expect that the synergy between spaceborne instrument antennas and their ground-based and telecommunications counterparts will continue to benefit both programs as JPL continues developing space missions.

References

[1] D. Staelin, P. W. Rosenkranz, F. T. Barath, E. J. Johnson, J. W. Waters, “Microwave Spectroscopy Imagery of the Earth,” *Science*, vol. 197, no. 4307, pp. 991–993, 1977.

[2] P. Swanson, W. Harris, and E. Johnston, "The Tiros-N Microwave Sounder Unit," *1980 MTT-S International Microwave Symposium Digest,* vol. 80, no. 1, pp. 123–125, 1980.

[3] M. J. Schwartz, W. V. Snyder, and W. G. Read, *EOS MLS Mesosphere-Specific Forward Model Algorithm Theoretical Basis Document*, JPL D-28534 (internal document), version 1, Jet Propulsion Laboratory, Pasadena, California, also available on line, June 4, 2004, accessed September 15, 2005. http://mls.jpl.nasa.gov

[4] P. Goldsmith and R. Kot, "Microwave Radiometer Blackbody Calibration Standard for Use at Millimeter Wavelengths," *Review of Scientific Instruments*, American Institute of Physics, vol. 50, no. 9, pp. 1120–1122, September 1979.

[5] P. Gloersen and F. Barath, "A Scanning Multichannel Microwave Radiometer for Nimbus-G and Seasat-A," *IEEE Journal of Oceanic Engineering*, vol. 2, no. 2, pp. 172–178, 1977.

[6] E. Njoku, J. Stacey, and F. Barath, "The Seasat Scanning Multichannel Microwave Radiometer (SMMR): Instrument Description and Performance," *IEEE Journal of Oceanic Engineering*, vol. 5, no. 2, pp. 100–115, 1980.

[7] K. Green, *Final Report on Design Study of NIMBUS-G SMMR Antenna Subsystem*, Technical Report, Microwave Research Corporation, North Andover, Massachusetts, 1975.

[8] E. Njoku, E. Christensen, and R. Cofield, "The Seasat Scanning Multichannel Microwave Radiometer (SMMR): Antenna Pattern Corrections Development and Implementation," *IEEE Journal of Oceanic Engineering*, vol. 5, no. 2, pp. 125–137, 1980.

[9] C. Ruf, S. Keihm, and M. Janssen, "TOPEX/Poseidon Microwave Radiometer (TMR). I. Instrument Description and Antenna Temperature Calibration," *IEEE Transactions on Geoscience and Remote Sensing*, vol. 33, no. 1, pp. 125–137, 1995.

[10] M. Janssen, C. Ruf, and S. Keihm, "TOPEX/Poseidon Microwave Radiometer (TMR). II. Antenna Pattern Correction and Brightness Temperature Algorithm," *IEEE Transactions on Geoscience and Remote Sensing*, vol. 33, no. 1, pp. 138–146, 1995.

[11] C. Ruf, S. Keihm, and B. Subramanya, "TOPEX Microwave Radiometer in-Flight Performance Evaluation," *International Geosciences and Remote Sensing Symposium*, (IGARSS) 1993, pp. 1759–1761, 1993.

[12] F. Soltis and S. Kaki, *Jason-1 Project Microwave Radiometer Functional Requirements*, JPL D-14917 (internal report), Jet Propulsion Laboratory, Pasadena, California, October 1997.

[13] C. L. Kahn, "Challenges in Developing the Microwave Instrument for the Rosetta Orbiter," *IEEE Aerospace Conference Proceedings*, vol. 2, pp. 2-575–2-582, 2002.

[14] V. Jamnejad, "A Dual Band Telescope for Microwave Instrument on Rosetta Orbiter (MIRO)," *IEEE Aerospace Conference Proceedings*, vol. 3, pp. 3-265–3-269, 1999.

[15] J. W. Waters, "Microwave Limb Sounding," *Atmospheric Remote Sensing by Microwave Radiometry*, M. A. Janssen, editor, chapter 8, John Wiley, New York, New York, 1993.

[16] N. Livesey, W. G. Read, L. Froidevaux, J. W. Waters, M. L. Santee, H. C. Pumphrey, D. L. Wu, Z. Shippony, R. F. Jarnot, "The UARS Microwave Limb Sounder Version 5 Data Set: Theory, Characterization, Validation," *Journal of Geophysical Research*, vol. 108, no. D13, article no. 4378, pp. ACH 2-1–ACH 2-21, 2003.

[17] R. F. Jarnot, R. E. Cofield, J. W. Waters, D. A. Flower, and G. E. Peckham, "Calibration of the Microwave Limb Sounder on the Upper Atmosphere Research Satellite," *Journal of Geophysical Research*, vol. 101, no. D6, pp. 9957–9982, April 1996.

[18] F. T. Barath, M. C. Chavez, R. E. Cofield, D. A. Flower, M. A. Frerking, M. B. Gram, W. M. Harris, J. R. Holden, R. F. Jarnot, W. G. Kloezeman, G. J. Klose, G. K. Lau, M. S. Loo, B. J. Maddison, R. J. Mattauch, R. P. McKinney, G. E. Peckham, H.M. Pickett, G. Siebes, F. S. Soltis, R. A. Suttie, J. A. Tarsala, J. W. Waters, and W. J. Wilson, "The Upper Atmosphere Research Satellite Microwave Limb Sounder Instrument," *Journal of Geophysical Research*, vol. 98, no. D6, pp. 10751–10762, June 20, 1993.

[19] R. F. Jarnot and R. E. Cofield, *Microwave Limb Sounder (MLS) Instrument Calibration Report*, JPL. D-9393, version 1.0 (internal document), Jet Propulsion Laboratory, Pasadena, California, August 28, 1991.

[20] H. M. Pickett, J. C. Hardy, and J. Farhoomand, "Characterization of a Dual-Mode Horn for Submillimeter Wavelengths," *IEEE Transactions on Microwave Theory and Techniques*, vol. 32, pp. 936–937, August 1984.

[21] R. E. Cofield, "Field of View Calibration of the Microwave Limb Sounder on the Upper Atmosphere Research Satellite," *International Geoscience and Remote Sensing Symposium (IGARS)*, August 1994.

[22] J. W. Waters and R. F. Jarnot, *Science Requirements on the EOS Microwave Limb Sounder*, JPL D-14421, Rev. 2.0 (internal document), Jet Propulsion Laboratory, Pasadena, California, September 15, 1999.

[23] D. H. Martin and E. Puplett, "Polarized Interferometric Spectrometry for the Millimetre and Submillimetre Spectrum," *Infrared Physics*, vol. 10, p. 105, 1969.

[24] R. E. Cofield, T. A. Cwik, and N. A. Raouf, "Toric Offset Three-Reflector Antenna for an Advanced Microwave Limb Sounder," *Proceedings of SPIE*, vol. 4849, *Highly Innovative Space Telescope Concepts*, pp. 235–244, August 2002.

[25] E. Njoku, Y. Rahmat-Samii, J. Sercel, W. Wilson, and M. Moghaddam, "Evaluation of an Inflatable Antenna Concept for Microwave Sensing, " *IEEE Transactions on Geoscience and Remote Sensing*, vol. 37, no. 1, pp. 63–78, 1999.

[26] F. T. Ulaby, R. K. Moore, and A. K. Fung, *Microwave Remote Sensing, Active and Passive*, Addison-Wesley, Reading, Massachusetts, 1981.

[27] J. Johnson, J. Williams, L. E. Bracalente, F. Beck, and W. Grantham, "Seasat-A Satellite Scatterometer Instrument Evaluation," *IEEE Journal of Oceanic Engineering*, vol. 5, no. 2, pp. 138–144, 1980.

[28] F. Naderi, M. Freilich, and D. Long, "Spaceborne Radar Measurement of Wind Velocity over the Ocean: An Overview of the NSCAT Scatterometer System," *Proceedings of the IEEE*, vol. 79, no. 6, pp. 850–866, 1991.

[29] W. Crosswell, R. Roddewig, C. Pewsey, R. Moye, and W. Jones, "A Waveguide Fed Composite Horn Antenna," *Antennas and Propagation Society International Symposium 1988, International Symposium Digest: Antennas and Propagation*, vol. 1, pp. 338–341, 1988.

[30] Z. Hussein and Y. Rahmat-Samii, "Application of Cylindrical Near-Field Measurement Technique to the Calibration of Spaceborne Radar Antennas: NASA Scatterometer and SeaWinds," *IEEE Transactions on Geoscience and Remote Sensing*, vol. 37, no. 1, pp. 360–373, 1999.

[31] W.-Y. Tsai, J. Graf, C. Winn, J. Huddleston, S. Dunbar, M. Freilich, F. Wentz, D. Long, and W. Jones, "Postlaunch Sensor Verification and Calibration of the NASA Scatterometer," *IEEE Transactions on Geoscience and Remote Sensing*, vol. 37, no. 3, pp. 1517–1542, May 1999.

[32] C. Wu, Y. Liu, K. Kellogg, K. Pak, and R. Glenister, "Design and Calibration of the SeaWinds Scatterometer," *IEEE Transactions on Aerospace and Electronic Systems*, vol. 39, no. 1, pp. 94–109, 2003.

[33] M. Spencer, C. Wu, and D. Long, "Tradeoffs in the Design of a Spaceborne Scanning Pencil Beam," *IEEE Transactions on Geoscience and Remote Sensing*, vol. 35, no. 1, pp. 115–126, 1997.

[34] Z. Hussein, Y. Rahmat-Samii, and K. Kellogg, "Design and Near-Field Measurement Performance Evaluation of the SeaWinds Dual-Beam Reflector Antenna," *Antennas and Propagation Society International Symposium Digest*, vol. 2, pp. 852–855, 1997.

[35] CALIPSO Home page, Langley Research Center, Hampton, Virginia, site accessed August 4, 2005. http://www-calipso.larc.nasa.gov

[36] M. R. Schoeberl, "The AURA Mission and the A-Train," *The World Space Congress* (Houston, Texas), October 10–19, 2002.

[37] E. Im, S. L. Durden, C. Wu, and T. R. Livermore, "The 94 GHz Cloud Profiling Radar For the CloudSat Mission," *2001 IEEE Aerospace Conference Proceedings* (Big Sky, Montana, March 10–17, 2001), pp. 1803–1809, 2001.

[38] J. B. Mead, A. L. Pazmany, S. M. Sekelsky, and R. E. McIntosh, "Millimeter-Wavelength Radars for Remotely Sensing Clouds and Precipitation," *Proceedings of the IEEE*, vol. 82, no. 12, pp. 1891–1906, 1994.

[39] G. A. Sadowy, R. E. McIntosh, S. J. Dinardo, S. L. Durden, W. N. Edelstein, F. K. Li, A. B. Tanner, W. J. Wilson, T. L. Schneider, and G. L. Stephens, "The NASA DC-8 Airborne Cloud Radar: Design and Preliminary Results," *Proceedings of the International Geoscience and Remote Sensing Symposium (IGARSS),* Singapore, August 3–8, 1997, pp 1466–1469, 1997.

[40] R. Meneghini and T. Kozu, *Spaceborne Weather Radar*, Chapter 2, Artech House, Inc., Boston, Massachusetts, 1990.

[41] S. Spitz, A. Prata, Jr., J. Harrell, R. Perez, and W. Veruttipong, "A 94 GHz Profiling Radar Antenna System," *2001 IEEE Aerospace Conference Proceedings* (March 10–17), pp. 2-685–2-694, 2001.

[42] G. M. Smith, C. P. Unsworth, M. R. Webb, and J. S. G. Lesurf, "Design, Analysis and Application of High Performance Permanently Magnetized, Quasi-Optical, Faraday Rotators," *1994 IEEE MTT Symposium Digest*, pp. 293–296, 1994.

[43] M. K. Hu, "Near-Zone Power Transmission Formulas," *1958 IRE National Convention Record* (New York, New York, March 24–27, 1958), Part 8, pp. 128–138, 1958.

[44] W. V. T. Rusch, T. S. Chu, A. R. Dion, P. A. Jensen, and A. W. Rudge, "Quasi-Optical Antenna Design and Applications," *The Handbook of Antenna Design*, edited by A. W. Rudge, K. Milne, A. D. Olver, and P. Knight, Peter Peregrinus Ltd., London, England, Chapter 3, 1982.

[45] A. R. Keith and A. Prata, Jr., "Interpolation of Reflector Surfaces Using Deformed Plate Theory,'' *Proceedings of the International IEEE AP-S Symposium* (Newport Beach, California, June 18–23, 1995), pp. 885–888, 1995.

[46] W. V. T. Rusch and P. D. Potter, *Analysis of Reflector Antennas*, Academic Press, New York, New York, 1970.

[47] *Ocean Surface Topography from Space: Missions–OSTM*, Jet Propulsion Laboratory, Pasadena, California, web site accessed August 4, 2005. http://topex-www.jpl.nasa.gov/mission/ostm.html

[48] *Ocean Surface Topography from Space: Missions–Jason-1*, Jet Propulsion Laboratory, Pasadena, California, web site accessed August 4, 2005. http://topex-www.jpl.nasa.gov/mission/jason-1.html

[49] *Ocean Surface Topography from Space: Missions–TOPEX/Poseidon*, Jet Propulsion Laboratory, Pasadena, California, web site accessed August 4, 2005. http://topex-www.jpl.nasa.gov/mission/topex.html

[50] R. E. Munsen, H. Haddad, and J. Hanlen, "Microstrip Reflectarray for Satellite Communications and RCS Enhancement or Reduction," U.S. Patent 4684952, August 1987.

[51] J. Huang, "Microstrip Reflectarray," *IEEE International Symposium on Antennas and Propagation*, Ontario, Canada, June 1991, pp. 612–615, 1991.

[52] D. M. Pozar, S. D. Targonski, and H. D. Syrigos, "Design of Millimeter Wave Microstrip Reflectarrays," *IEEE Transactions on Antennas and Propagation*, vol. AP-45, no. 2, pp. 287–296, February 1997.

[53] R. E. Hodges and M. S. Zawadzki, "Design of a Large Dual Polarized Ku Band Reflectarray for Space Borne Radar Altimeter," *Antennas and Propagation Society Symposium* (Monterey, California, June 20–25), vol. 4, pp. 4356–4359, 2004.

[54] R. E. Hodges and M. S. Zawadzki, "Scanning Properties of Large Reflectarray Antennas," *URSI Symposium Digest* (Monterey, California), June 20–25, 2004.

[55] R. E. Hodges and M. S. Zawadzki, "A Reflectarray Antenna for use in Interferometric Ocean Height Measurement," *2005 IEEE Aerospace Conference* (Big Sky, Montana), March 2005.

[56] J. Huang, "Bandwidth Study of Microstrip Reflectarray and a Novel Phased Reflectarray Concept," *1995 IEEE International Antennas and Propagation Symposium Digest* (Newport Beach, California, June 1995), pp. 582–585, 1995.

[57] D. M. Pozar, "Bandwidth of Reflectarrays," *Electronic Letters*, vol. 39, no. 21, pp. 1490–1491, October 16, 2003.

Chapter 8
Mechanical Development of Antenna Systems

Gregory L. Davis and Rebekah L. Tanimoto

Previous chapters in this book have described primarily the radio frequency (RF) development of antennas used on Jet Propulsion Laboratory (JPL) spacecraft since the first Explorer flight in 1958 to the present. In this chapter, that description broadens to include issues related to the mechanical development of these and other spaceborne antenna systems. In particular, this chapter surveys historically significant antenna systems, delineates the current mechanical state-of-practice, describes antenna mechanical technology development, and finally tries to anticipate the directions of future mechanical developments for antenna systems.

8.1 Historically Significant Antenna Systems

Several structural concepts for spaceborne antennas began to surface in the late 1950s and early 1960s as the development of rocket propulsion and guidance systems allowed for the insertion of spacecraft into Earth orbit. This new capability made it realistic to start considering antenna technologies that could potentially provide a new level of satellite-based global communication [1]. Throughout the following years, the need for new antenna capabilities was always on the horizon, whether it was the desire for a structure that was larger, cheaper, lighter, more durable, or more precise. In response to these technical challenges, a variety of companies and institutions—both large and small—developed an array of innovative spaceborne antenna designs. The evolution of some of these historically significant antenna systems is outlined below [2,3].

8.1.1 Echo Balloons

The Echo balloon is significant as a National Aeronautics and Space Administration (NASA) forerunner to more modern rigidizable/inflatable (RI) antenna structures. After many years of development and seven major failures, Echo was able to reflect radio transmissions between various locations on Earth, beginning in August 1960 [4]. Echo I, shown in Fig. 8-1, was a 100-ft (31-m) diameter inflated sphere, weighed 136 lb (62 kg), and was made from 0.5-mil (0.013-mm) Mylar. It was covered with a layer of vapor-deposited aluminum (Al) to provide RF reflectivity. Echo was inflated by the sublimation of 20 lb (9.1 kg) of anthraquinone and 10 lb (4.5 kg) of benzoic acid, which provided enough internal pressure to keep its spherical shape during its high-velocity orbit [5].

Significantly, new methods for packaging and deployment were also developed during the Echo program. Preflight packaging and deployment challenges for Echo I included fitting the balloon into a 28-in. (71-cm) diameter canister for launch and designing a safe and effective way to release the balloon when in orbit. A storage method was devised that required the balloon to be folded into a long narrow strip and packed into a seamed spherical canister, where a V-shaped explosive charge was placed to separate the hemispheres on command [4].

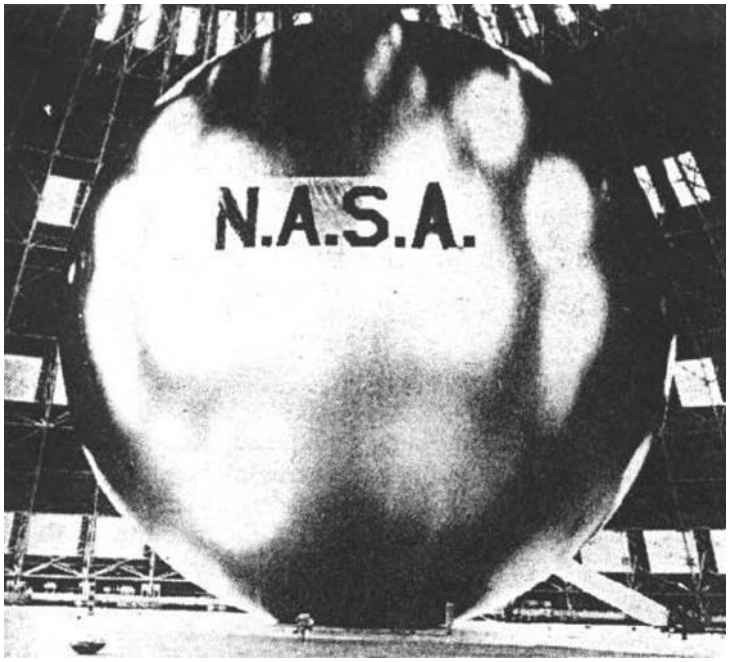

Fig. 8-1. An inflated Echo balloon.

One of the problems faced with Echo I was that it lost its spherical shape after days of service. In an effort to address this problem, NASA developed Echo II, a 135-ft (41-cm) diameter balloon that theoretically would be able to remain rigid after plastic deformation beyond its elastic limit, even after losing some inflation gas. Echo II was launched in 1964, served as a communications satellite (comsat) for a full year, and (as with Echo I) also served as a valuable instrument for geodetic studies. Even though the Echo balloons were at the forefront of communications satellite technology when they were first launched, by the time they fell to Earth in the late 1960s, they had already been replaced by active-repeater satellites [6].

8.1.2 Orbital Construction Demonstration Article

In the 1970s, Grumman conducted a study on the concept of a 100-m diameter parabolic antenna, shown in Fig. 8-2, under the Orbital Construction Demonstration Study (OCDS). This project was significant in that it addressed the challenge of designing a very large antenna—on the order of 100 m—using a small number of shuttle flights. Since such a structure would require a nearly perfect packing efficiency, Grumman decided that the best solution was to

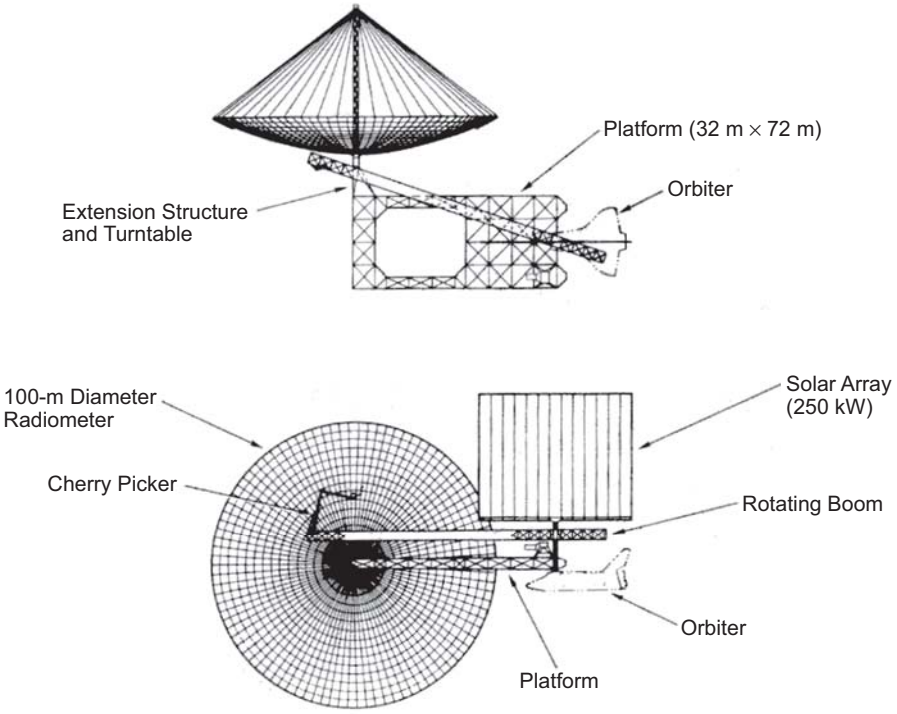

Fig. 8-2. The Grumman orbital construction demonstration study antenna concept.

design an antenna structure that could be assembled in space. With in-space assembly, only the materials, which could be packaged more efficiently than a completely assembled structure, would need to be transported into orbit. Once in orbit, simple robotics could be utilized to attach the pieces together [7].

The space-assembled elements would include 94 ribs and 16 circumferential members, which were each attached to a core module with the help of a turntable and indexed with specific positions. This extended core would make up the support structure over which an RF-reflective mesh would spread, tensioned by ties connecting its outer edge to the top of a deployable Astromast (developed by Astro Aerospace, Carpenteria, California). The contour of the parabolic antenna would be actively controlled by a laser surface-sensing system, and a free-flying satellite would be used to evaluate its structure and performance from a distance of 200 km [8].

8.1.3 Electrostatically Figured Membrane Reflector

With the desire to significantly reduce the mass and increase the precision of very large diameter spaced-based reflecting antennas, the Massachusetts Institute of Technology (MIT) initiated the Electrostatically Figured Membrane Reflector (EFMR) Program in January 1978 [9]. The EFMR design is depicted in Fig. 8-3. The program strove to develop a deployable antenna with either a very thin mesh or a 2- to 10-μm-thick-film reflector, thereby minimizing its mass per unit reflecting area and in turn, significantly reducing the overall antenna mass [8]. A novel feature of this design was the introduction of an auxiliary command surface behind the main reflecting surface to enhance its shape tolerance.

For the reflecting surface to attain a precise shape, it had to be actively controlled and remain stable when disturbed by external noise sources. This control would be done through the stiffer, similarly shaped command surface several meters to the rear and almost parallel to the reflector surface. This command surface would be made up of approximately 10^4 to 10^6 insulated conducting segments that could be controlled individually by an electron beam. The entire reflector configuration would be supported by a deployable “maypole”-type support structure [8].

8.1.4 Lockheed Wrap-Rib Antenna

In the 1960s, Lockheed began to develop the wrap-rib antenna concept as an innovative demonstration of a kinematically simple structure with a very high packing efficiency [10]. This antenna, shown in Fig. 8-4, consists of a series of ribs which, prior to deployment, are wrapped around a rotating spool. The ribs are stored, along with the mesh, in a central hub, which also serves as a support point and holds the deployment and refurl mechanisms. Driven by their own stored strain energy, the ribs are released to form a parabolic support

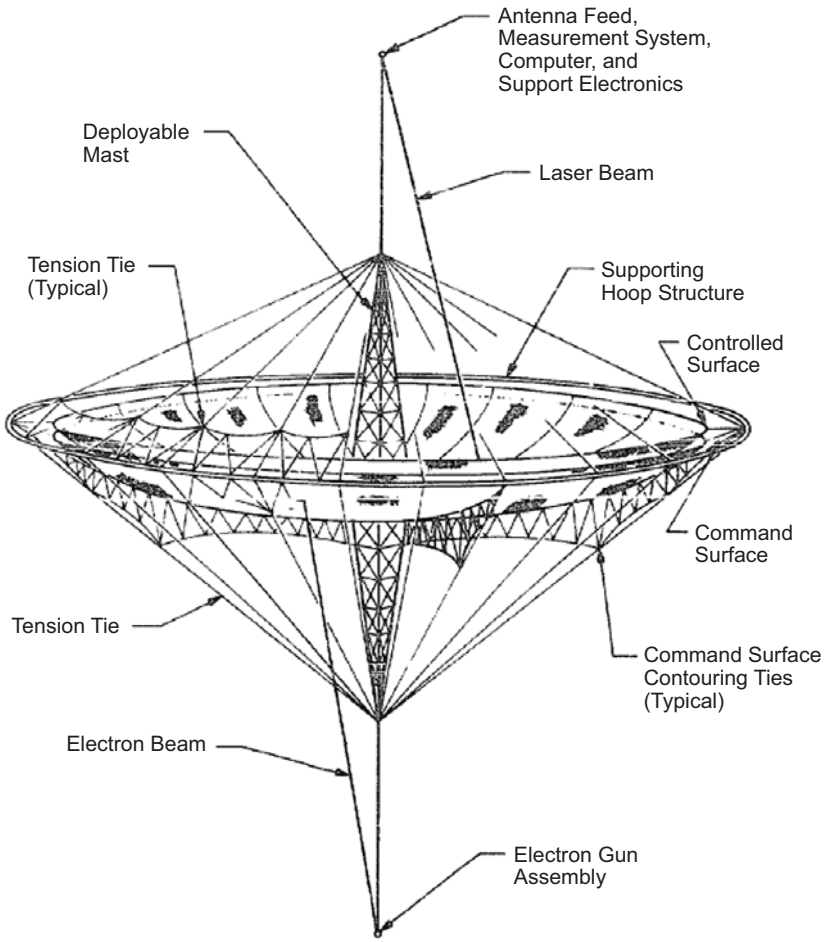

Fig. 8-3. The MIT controlled thin-film antenna concept.

structure for the lightweight reflective mesh surface. The number of ribs used depends on the required root mean square (RMS) surface accuracy, which will also determine the gain of the antenna. The feed system, located at the prime focus of the paraboloid, can be supported by one or two deployable booms of various types, and it is thermally controlled or is fabricated from materials with very low coefficients of thermal expansion.

A surface contour evaluation and adjustment system was also developed to evaluate antennas of sizes 20 m or greater while deployed in space. This system is necessary because the shape fidelity of such large structures cannot be assessed on the ground due to the effects of gravity on the ribs and mesh. This system accounts for thermal distortions and, with information from a laser ranging system, can correct the shape of the paraboloidal surface by rotating or translating the ribs [8].

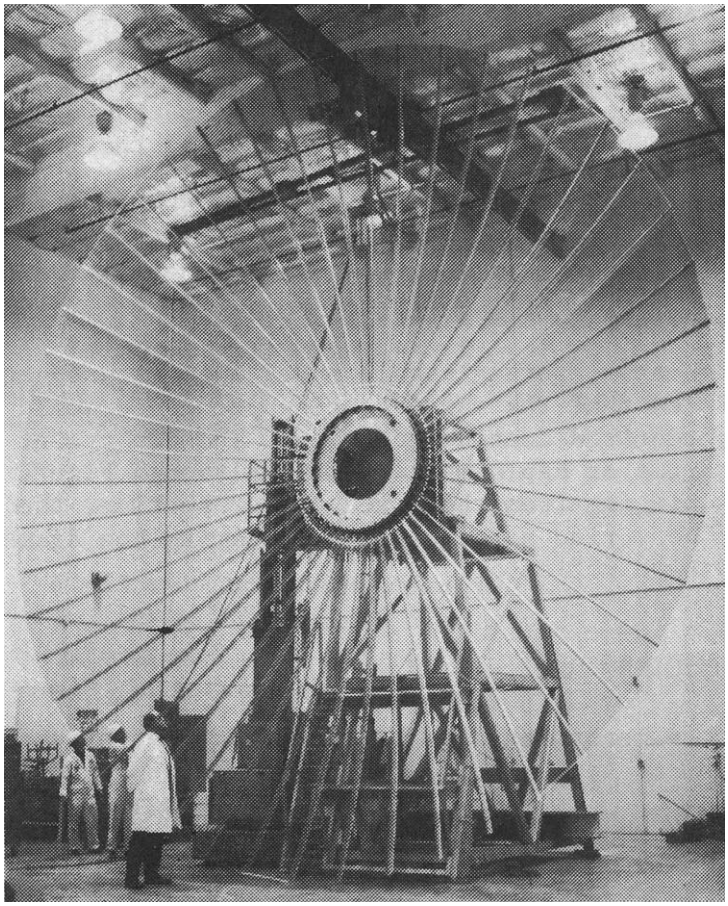

Fig. 8-4. The hub, rib, and mesh structure for LMSC ATS-6 flight antenna reflector.

In the early 1980s, NASA demonstrated this technology in its Large Space System Technology (LSST) with a 55-m wrap-rib antenna. Subsequently, in the early to mid 1990s, Lockheed made a final attempt with its 6- to 7-m mobile satellite (MSAT), which lasted until a group parted to form their own company. Today the concept is not patented or copyrighted, and it is open for anyone to use [10].

8.1.5 AstroMesh Reflector

Beginning in the 1990s, Astro Aerospace Corporation made a significant contribution to the development of deployable mesh reflector technology by experimenting with new structural and materials concepts through their work on the AstroMesh deployable reflector, shown in Fig. 8-5. This design was a result of more than 6 years of hardware development that, in the end, proved to

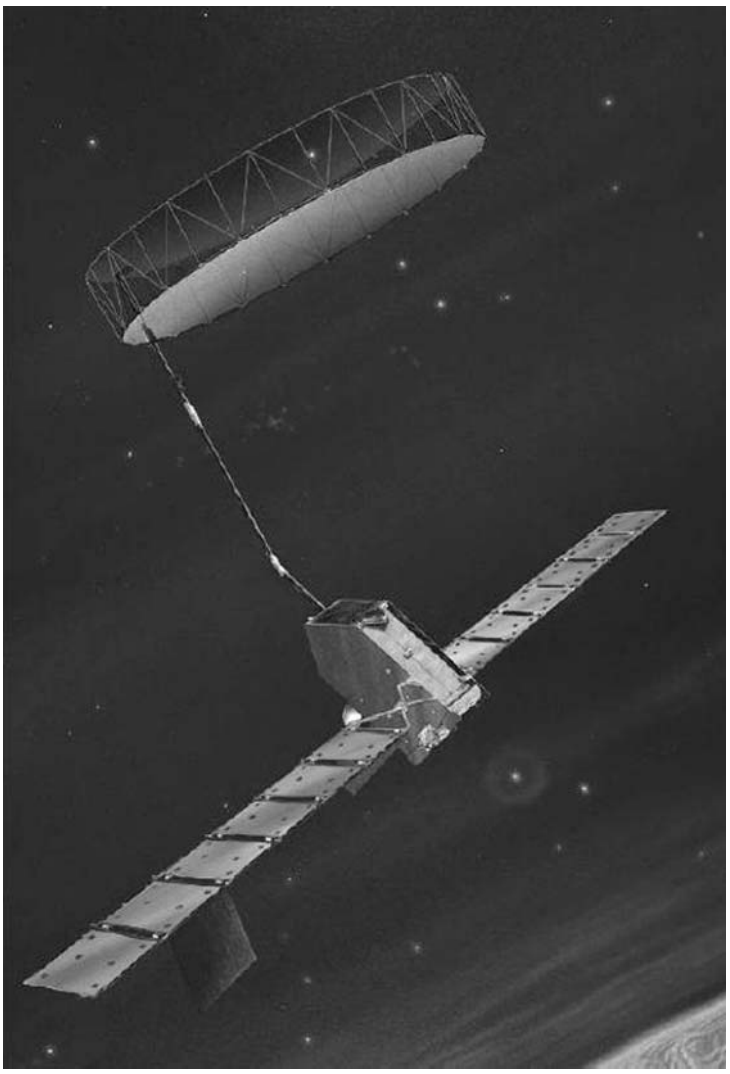

Fig. 8-5. The AstroMesh in deployed configuration on Euro-African Satellite Telecommunications (EAST) System.

be revolutionary with its low mass and stowed volume, high stiffness, thermal stability, and low cost. Flight models of 6- and 12-m offset circular aperture were developed and could be scaled to apertures up to 150 m without changes to their fundamental design. The two models were qualified by a number of electrical and environmental tests, and the 6-m reflector was shown to provide an RMS surface accuracy of less than 0.6 mm.

The main reflector structure consists of two doubly curved composite 'nets' placed back-to-back across a deployable graphite-epoxy ring truss. A highly

RF-reflective mesh, made of gold-plated molybdenum is stretched onto the convex side of the front net structure, creating a number of flat triangular facets to approximate a desired parabolic shape. Tension ties are attached between the nets to apply approximately normal forces to produce a rigid drum-like structure with outstanding structural efficiency and a high stiffness-to-weight ratio.

The AstroMesh is stowed in a very compact, over-stowed manner, allowing for gentle expansion upon release. The truss members are packaged adjacent to each other in a narrow cylinder, and the end members are preloaded against stiffening hoops that also serve as debris shields [11].

The AstroMesh reflector is still in use today. Most recently, a 12-m version was successfully deployed aboard Space Systems/Loral's Mobile Broadcasting Satellite (MBSAT) for a digital broadcasting service [12].

8.1.6 Inflatable Antenna Experiment

In recognition of the growing need for very large, low-cost spaceborne antenna structures, NASA began development on a new class of self-deployable structures beginning in 1989. Taking inflatable antenna concepts that had been in development by L'Garde, Inc. of Tustin, California, NASA sponsored the Inflatable Antenna Experiment (IAE) as part of its In-Space Technology Experiments Program (IN-STEP).

The basic antenna configuration, shown in its on-orbit deployed configuration in Fig. 8-6, consisted of a 14-m inflatable antenna membrane reflector and canopy (lenticular structure); an inflatable toroidal perimeter support; three inflatable struts; and a canister that provided antenna stowage,

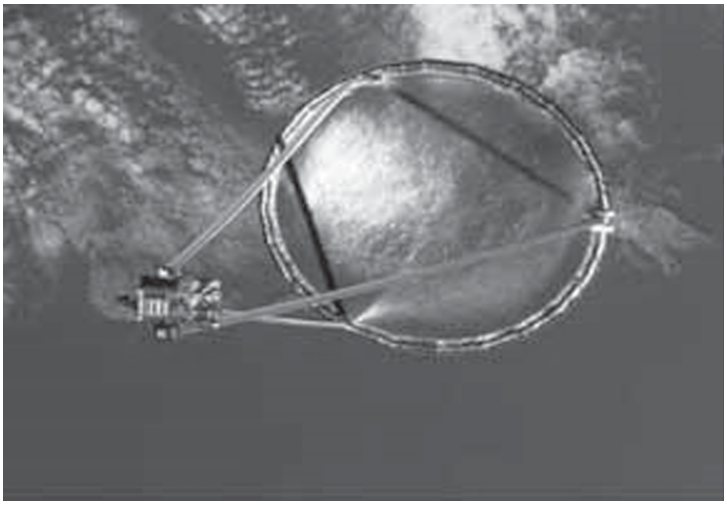

Fig. 8-6. Deployed orbital configuration of IAE.

measurement instrumentation, and an interface with the Spartan spacecraft. The antenna was designed to inflate sequentially with nitrogen gas and residual air in approximately 5 minutes. The antenna was observed from the orbiter using high-resolution photography and video recording.

IAE flew aboard Space Shuttle Endeavour as part of the Space Transportation System (STS)-77 mission, launched in May 1996. JPL, which managed this project for NASA with help from L'Garde, successfully deployed the 14-m diameter offset parabolic reflector in a zero-gravity environment. This very significant in-space demonstration verified that a very large inflatable antenna structure could be built on the order of $1M, be very efficiently packaged, be successfully deployed, and have its reflector surface precision measured with a resolution of 0.1 to 0.2 mm in a true thermal environment.

Despite some minor flaws in the inflation process, IAE proved to be not only an overall success with respect to its main objectives; but also drew a significant amount of attention to a new kind of technology that although had been recognized mechanically, needed a successful in-space demonstration to draw serious interest [13].

8.1.7 Large Radar Antenna Program

With the success of NASA's Inflatable Antenna Experiment, the Department of Defense (DoD) saw potential in that demonstrated technology and initiated the Large Radar Antenna (LRA) Program. Its goal was to evaluate the current mechanical packing and deployment methods for very large reflector-antenna systems. LRA achieved this through the study of an RI perimeter support truss integrated with a mesh/net parabolic reflector, as shown in Fig. 8-7. This program was significant for its ground-breaking work in RI materials characterization for space applications and its exploration of the performance envelope for hybrid RI/mechanical systems [14].

L'Garde, Inc., which had previously assisted with the IAE, developed the LRA baseline truss configuration, with the goal of optimizing it with a low mass and a high packing efficiency. First, a method developed by Astro Aerospace Corp. for their AstroMesh Reflector, involving two "back-to-back" mesh/net structures tied in multiple locations, was integrated into the LRA baseline configuration. Second, a characterization of various truss types was carried out, resulting in the selection of a standard truss configuration as the perimeter structure. The University of Colorado also contributed to the design with their innovative tension drum, which served to structurally decouple the mesh/net from the RI perimeter truss to achieve a higher reflector precision and reduce the required RI stiffness.

In addition to the development of the truss configuration, studies were also performed to characterize and validate different methods of material rigidization for the truss structural elements. Two of the most promising

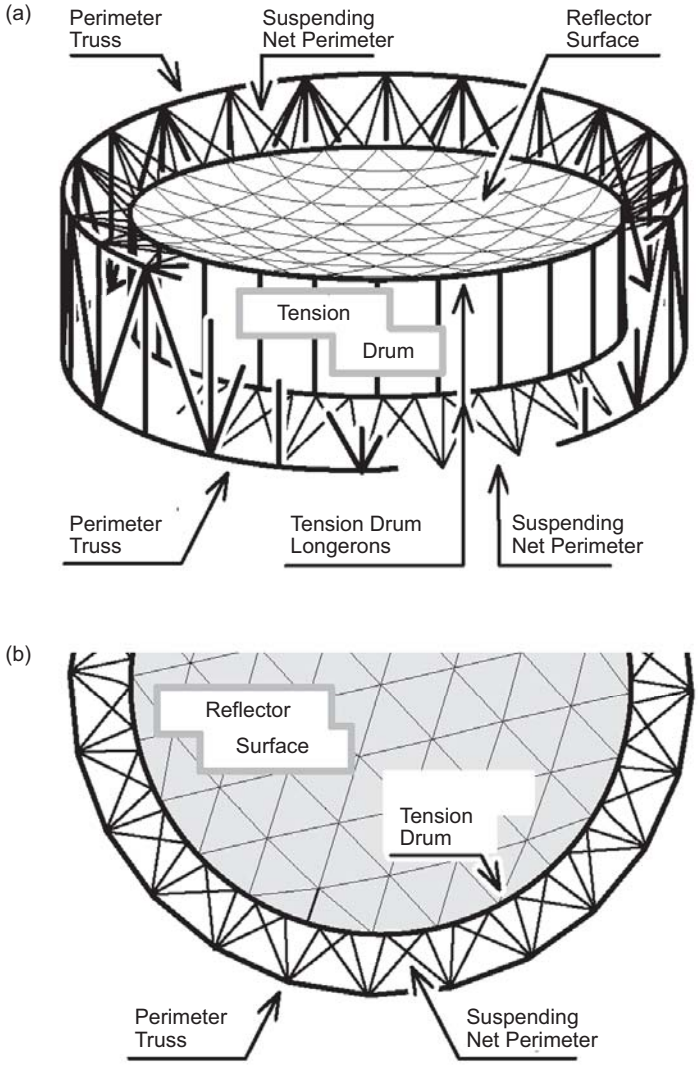

Fig. 8-7. LRA configuration: (a) isometric view and (b) top view.

concepts involved the use of sub-T_g rigidizable/thermoplastics, and ultraviolet (UV)-cured and heat-cured plastics. Further investigation of these materials resulted in the confirmation of their ability to withstand orbital radiation and to provide high modulus truss members on-orbit [14].

As a follow-on to LRA, in 2001 the Defense Advanced Research Projects Agency (DARPA) initiated the Innovative Space-based Radar Antenna Technology Program (ISAT) to further study the potential for RI technology. As of this writing, the ISAT program is in progress and represents an excellent

case study for describing antenna technology development work, to be discussed in Section 8.3.

8.2 Current State-of-Practice

8.2.1 Mechanical Configurations

During the course of the just-outlined evolution of spaceborne antenna systems, a variety of innovative designs matured to yield the current state-of-practice. A convenient way to describe the mechanical configuration trade space for these designs is to plot antenna operating frequency as a function of antenna diameter [15], as shown in Fig. 8-8.

Of course, this classification scheme is only one of many that can be used; other important design variables include mass, deployed stiffness, thermal and

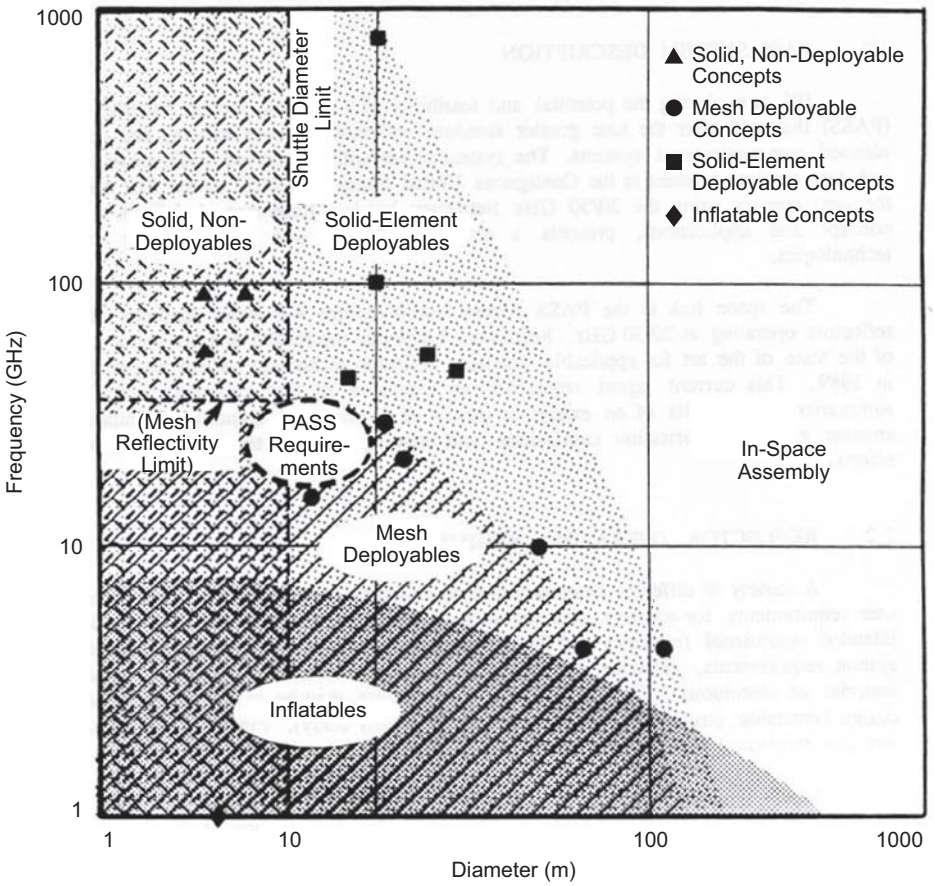

Fig. 8-8. The mechanical configuration trade space for spaceborne antennas (PASS = Personal Access Satellite System).

coefficient of thermal expansion (CTE) characteristics, joint tolerance and dimensional repeatability, and deployed surface-alignment/precision. As Fig. 8-8 shows, the mechanical configuration regimes can be arranged into solid non-deployable, mesh deployable, solid-element deployable, and RI categories. Generally speaking, the type of reflecting surface will be determined by the operating frequency of interest; whether the antenna is deployable or not will be determined by its aperture size. Notice that the options in the configuration trade space become fewer—regardless of the frequency—as the aperture size increases. A brief description follows of the salient characteristics of each spaceborne antenna type, with some noteworthy examples [15].

8.2.1.1 Solid Non-Deployable Antennas. Solid non-deployable antennas are among the earliest of spaceborne antenna designs. In this design, a lightweight backing structure is mated to a high-precision reflecting surface. The backing structure is typically a composite constructed of graphite epoxy face sheets bonded to a nomex or aluminum honeycomb core. For applications requiring less surface precision, a variation of this design incorporates a stiffening rib structure bonded to a single face sheet. The reflecting surface is typically laid up by hand on a very precise tool or mandrel. Local roughness errors are a function of the tool's machined surface precision; global surface errors are more influenced by thermal effects during the curing cycle. RMS surface errors in the reflecting surface are very manufacturing-process dependent, and can vary up to several orders of magnitude between the ranges of 5 μm and 500 μm. Characteristics of some noteworthy solid non-deployable antennas are summarized in Table 8-1. The Advanced Communications Technology Satellite (ACTS) reflector is shown in Fig. 8-9.

8.2.1.2 Mesh Deployable Antennas. Mesh deployable antennas are an excellent design solution for spaceborne antennas that require larger aperture sizes operating at frequencies below approximately 30 GHz. Because of launch vehicle shroud size limitations, deployable antennas are essential for apertures exceeding approximately 4.6 m. A metallic reflecting mesh has the mechanical virtue of being lightweight, easily folded, and reflective to RF at frequencies below approximately 30 GHz. At frequencies above 30 GHz, RF losses become excessive because of manufacturing limitations in creating a sufficiently fine mesh grid. Typical mesh grid materials are gold-plated molybdenum or beryllium copper wire. A variety of techniques can be used to shape the mesh, including deployable trusses, ribs, or hoops. Sometimes a secondary membrane type surface connected to the main reflecting surface with auxiliary ties or cables is used to assist in mesh-shape control. Characteristics of some noteworthy mesh deployable antennas are summarized in Table 8-2. The TDRSS and ATS structural thermal models are shown in Fig. 8-10 and Fig. 8-11, respectively.

Table 8-1. Noteworthy solid non-deployable antennas.

Vendor	Name	Notable Features	Size	Surface Precision
Composite Optics	ACTS reflector	Composite panel with rib stiffeners	2.2–3.3 m	60–70 μm
Boeing	Precision antenna reflector	Rib-stiffened shell	2.0–2.5 m	50–75 μm
Space Systems/Loral	Voyager antenna	Longest operating antenna in deep space	3.7 m	250 μm
Dornier	First reflector panels	Graphite epoxy aluminum honeycomb construction	2.3 × 3.1 m offset paraboloid	8.9 μm

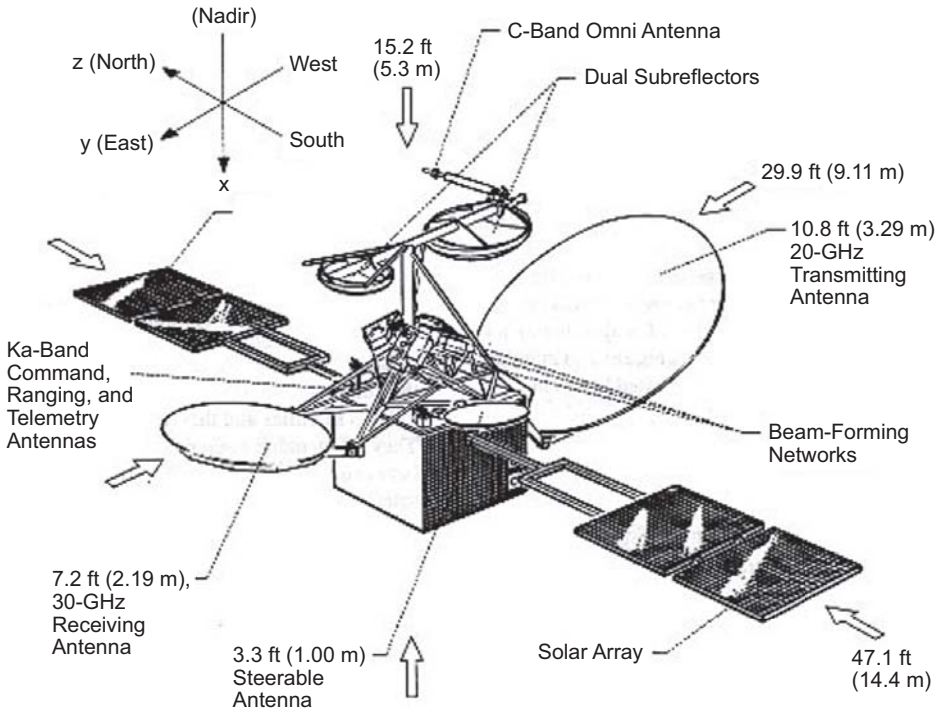

Fig. 8-9. ACTS spacecraft schematic.

8.2.1.3 Solid Element Deployable Antennas. Solid-element deployable antennas are an excellent design solution for spaceborne antennas that require larger aperture sizes operating at frequencies above approximately 30 GHz. The deployable aspect of this design allows for apertures exceeding 4.6 m, and the solid-element aspect—with its greater surface precision—allows for RF

Table 8-2. Noteworthy mesh-deployable antennas.

Vendor	Name	Notable Features	Size	Surface Precision/ Frequency
Harris	Tracking Data Relay Satellite System (TDRSS) (Fig. 8-10)	Surface precision independent of ribs	6 m	15 GHz
Lockheed	Applications Technology Satellite (ATS) (Fig. 8-11)	Al ribs and Cu-coated Dacron mesh	9 m	1.52 mm RMS
TRW (now Northrop-Grumman Space Technology (NGST))	Fleet Satellite Communications (FLTSATCOM) (Navy)	Stainless steel ribs and mesh	4.9 m	0.3 GHz
Mitsubishi	Tension truss antenna	Radial deployable ribs	10 m	22 GHz

operations at frequencies well above 30 GHz, the performance limit for meshes. The solid elements themselves are usually lightweight composite structures, typically graphite-epoxy-aluminum-honeycomb-core. The element shape can vary, ranging from simple folding edges (as in the ETS-VI antenna) to more complex, nested polygonal shapes (as in the TRW Sunflower); see Figs. 8-12 and 8-13. Characteristics of some noteworthy solid-element deployable antennas are summarized in Table 8-3.

8.2.1.4 Inflatable Antennas. RI structures present a potentially very attractive design solution for spaceborne antennas that require large apertures operating in the low- to mid-frequency regime. The Echo balloon (shown in Fig. 8-1)—one of the earliest satellites of the space age—was an inflatable antenna structure, and interest in this class structures has increased since the successful in-space demonstration of the IAE (shown in Fig. 8-6) in 1996. RI structures are important because of their potential to enable a new class of lightweight large aperture structures requiring very high packaging efficiency with variable stowed geometry. The RI structural paradigm hinges on employing materials that are flexible and easily packaged for launch, and capable of being inflation-deployed and rigidized in space. Currently, the most promising materials are two classes of composites: sub-T_g rigidizable thermoplastics and elastomerics, and UV and heat-cured thermoset plastics. Recent materials technology work has validated their use as high modulus truss elements suitable for the space environment [14]. Characteristics of several noteworthy inflatable antennas are summarized in Table 8-4.

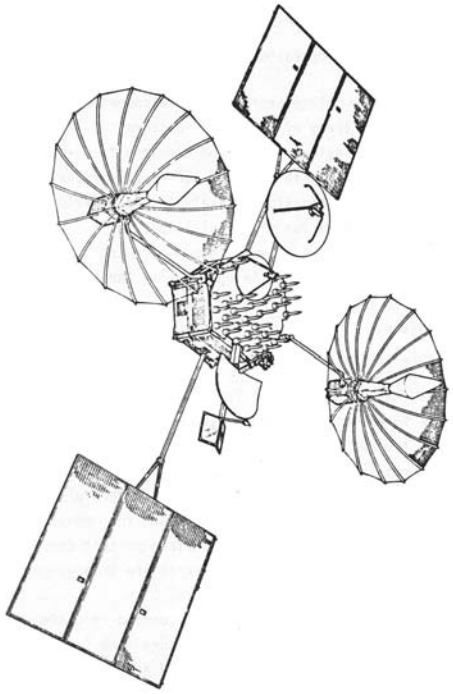

Fig. 8-10. TDRSS.

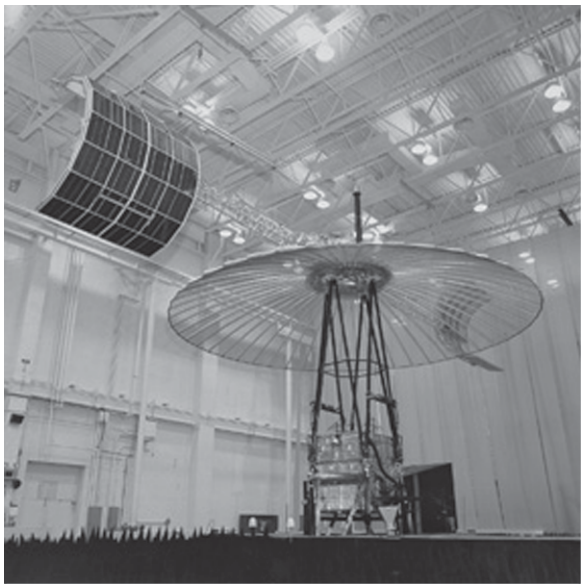

Fig. 8-11. ATS structural thermal model.

Fig. 8-12. ETS-VI with edge-folded antenna.

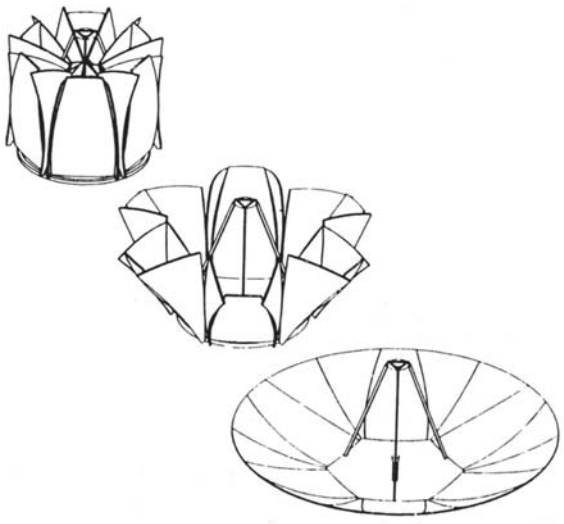

Fig. 8-13. TRW sunflower antenna diagram.

Table 8-3. Noteworthy solid-element deployable antennas.

Vendor	Name	Notable Features	Size	Surface Precision/ Frequency
TRW (now NGST)	Advanced sunflower deployable reflector	Graphite-epoxy precision deployable antenna	10 m	50–75 μm
Dornier	Daisy deployable	Graphite-epoxy precision deployable telescope	8 m	8 μm
Toshiba	Solid deployable reflectors	Graphite-epoxy Al honeycomb core petals with backup truss structure	5 m	20–30 GHz
Nippon Telegraph and Telephone Corporation (NTT)	ETS-VI 20-GHz reflector	Graphite-epoxy Al honeycomb core petals	3.5 m	0.17 mm

Table 8-4. Noteworthy rigidizable/inflatable antennas.

Vendor	Name	Notable Features	Size	Surface Precision/ Frequency
Sheldahl, Grumman	Echo balloon	First inflatable, passive communications satellite	30.5–41.1 m diameter	960–2390 MHz frequency (passive)
L'Garde	Inflatable Antenna Experiment	First in-space demonstration of a large inflation-deployed structure	14 m diameter	0.1–0.2 mm

8.2.2 Other Mechanical Design Considerations

8.2.2.1 Thermal Control. Thermal design for spaceborne antennas consists of maintaining the antenna subsystem within its allowable flight temperatures (AFT) and minimizing thermally induced shape distortions. For the majority of antennas, the traditional thermal control techniques of using paints, multi-layer insulation (MLI), and low-coefficient-of-thermal-expansion (CTE) materials are sufficient. When using MLI, aluminized kapton must not be situated in the antenna beam path, as it is not transparent to RF.

Solid non-deployable and solid-element deployable antennas can usually be controlled thermally with a combination of paint and MLI. White paint, having negligible effect on RF transmission or reflection, is typically applied to the front reflecting surface to minimize dish heating and temperature gradients;

MLI is typically applied to the back surface to maximize radiative insulation. Newer generation composite antenna structures may have minimal temperature control features because they are made from low-CTE materials.

Mesh deployable antennas can be controlled thermally with paint and selected use of MLI. The gold-plated molybdenum or beryllium copper wire in the mesh itself is usually left untreated, since applying a thermal coating to that fine grid is difficult. Either paint or MLI can be applied to the supporting structural ribs (often composite), although paint is preferred because of its less intrusive effects on antenna packaging and deployment. Regardless of antenna type, a structural-thermal analysis is nearly always required to ensure that the antenna operates within its AFT and that thermally induced shape distortions are within tolerances for RF performance [16].

Thermal distortion can be a significant problem for large spaceborne antenna systems, particularly those configured with RF transmitting/receiving panels attached to a backing structure. Although interface forces between the panels and the backing structure can be minimized using kinematic joints, the CTE mismatch between the two can still lead to shape distortions in the system, adversely affecting RF performance. This problem remains an ongoing challenge.

8.2.2.2 Deployment. Controlling deployment dynamics is key to mitigating the risk associated with any deployable space antenna structure. Two approaches to this problem have evolved historically: *sequential* and *synchronous* and deployment [17].

Sequential deployment refers to releasing discrete elements of a deploying structure in series from a stowage canister or deployment cage to manage system deployment dynamics. The ancillary stowage or cage structure provides (1) a mechanical infrastructure for staging deployment on a localized scale and (2) a robust mechanical interface to minimize deployment-induced reactions to both the deploying structure and its host spacecraft.

Synchronous deployment refers to simultaneously releasing all deploying structural elements by controlling their relative positions and velocities. Typically, cable driven or distributed motor systems are used to drive the deployment. This deployment technique is appealing in that it seeks to minimize (1) the potential for kinematic lockup of contiguous structural elements and (2) the mass penalty associated with a stowage canister or deployment cage.

Recently, with the advent of unique and very large deployable antenna structures, hybrid techniques utilizing both deployment approaches have evolved.

8.2.2.3 Testing. Environmental testing of stowed antenna systems, typically done at the spacecraft system level, is usually very straightforward. If the

system is deployable, subsequent to stowed system testing, deployment testing and deployed performance verification ideally should be demonstrated in a space environment. However, it becomes increasingly unrealistic to implement this "fly as you test, test as you fly" rule with the advent of larger and larger structures. Practical difficulties in implementing the classical testing approach for very large structures include finding very large environmental test facilities, properly simulating a zero-g environment with mechanical ground support equipment, and reversing irreversible deployment effects (particularly for RI structures). When traditional deployment testing is impracticable, a combination of substructure characterization, demonstration testing, and predictive analysis must be used (see Section 8.4).

8.3 Antenna Technology Development

Despite the varied nature of the once state-of-the-art spaceborne antennas described in 8.1, the technology development process used for each of these systems contains several unifying elements. These common elements can be categorized as assessing the mission technology drivers, determining the critical technologies and requirements, assessing the state-of-the-art, and specifying the technology development approach [18]. As a case study for illustrating this process, the technology development for the DARPA-sponsored ISAT program, in progress as of this writing, is described below [14].

8.3.1 Mission Technology Drivers

In the integrated radar technology roadmap shown in Fig. 8-14, all of the radar product lines indicate an emphasis on increasing aperture size for future missions. Although this technology roadmap is oriented towards Earth-science applications, the same conclusions can be drawn for military applications. This desire for larger and larger aperture sizes created a mission "pull" for using new and innovative structural technologies. Consequently, in 2001 DARPA created the ISAT Program to assess the risk of using RI materials as the structural support for a very large, active planar radar array. The ISAT baseline configuration, a concept envisioning a linear radar aperture hundreds of meters long by several meters wide, is shown in Fig. 8-15.

8.3.2 Critical Technologies and Requirements

The configuration shown in Fig. 8-15 argues for a truss backing as an efficient structural solution for the linear radar array. The critical guidelines for the ISAT structural configuration are as follows:

- A free-free fundamental frequency of 0.05 Hz
- Strut buckling strength to 0.001 g
- Strut slenderness ratio (L/d) $\leq$100

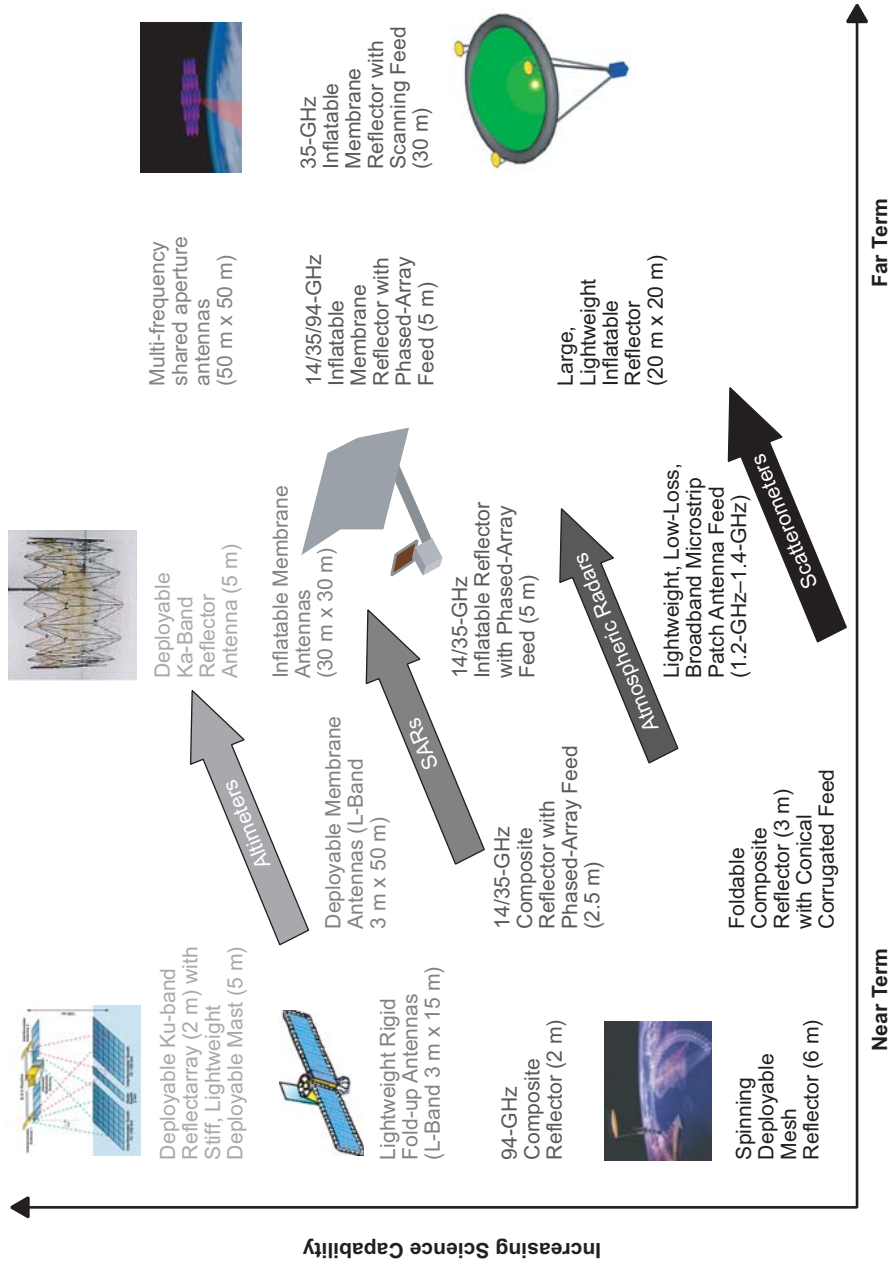

Fig. 8-14. Integrated radar technology roadmap for earth science.

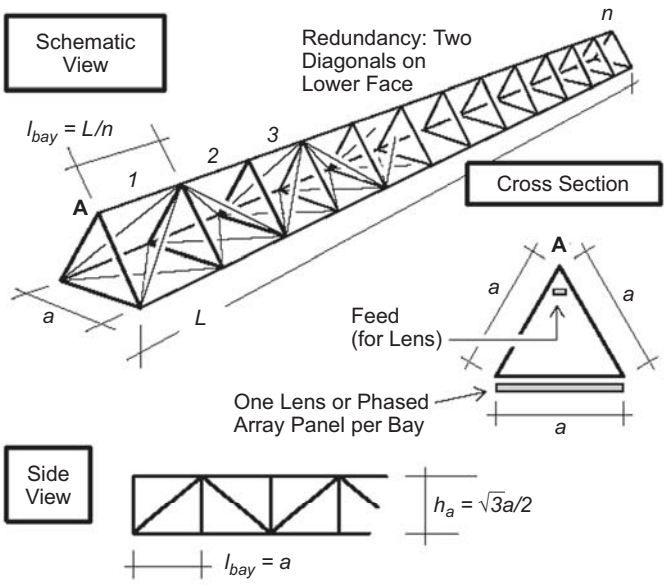

Fig. 8-15. ISAT baseline configuration.

- Optimal stowage volume
- Controlled deployment
- Thermal stability
- Dimensional stability

Given this set of guidelines, RI structural technologies—with their high packing efficiencies and potential for variable stowed geometries—were identified as a potentially attractive solution. After a careful assessment of the state-of-the-art, activities in the technology elements of truss structure concept definition, RI materials evaluation, and structural performance simulation were initiated to mitigate the risks associated in the overall RI technology area.

8.3.3 Assessing the State-of-the-Art

Generalizing beyond ISAT for a moment, Freeland [19] has proposed an assessment of current antenna technology capability for large deployable antennas, adapted and summarized in Table 8-5.

As can be seen from this very generalized assessment, the number proven and existing concepts that can be modified or applied, and the number of new concepts that can be developed becomes fewer and fewer as antenna size becomes larger and larger. These limitations are explored in more detail in Section 8.4. Returning to ISAT, because the current state-of-the-art offered extremely limited design solutions for its very large aperture size, RI materials

Table 8-5. Current technology assessment for large deployable antennas.

Antenna Size	Concept Design Maturity			Comments
	Increasing	→	Decreasing	
Small (<10 m)	Modification of a number of proven concepts	Adoption of a number of existing concepts Modification of a number of existing concepts	Adoption of a number of new concepts Development of simple new concepts	
Medium (10–25 m)	Direct application of a limited number of proven concepts Modification of a limited number of proven concepts	Direct application of a limited number of existing concepts Modification of a limited number of existing concepts with limited scaling	Development of very simple new concepts	Radial rib, planar array, small number of articulations
Large (>25 m)	Direct application of a very limited number of proven concepts Minor modification of a very limited number of proven concepts	Direct application of a very limited number of existing concepts Minor modification of a very limited number existing concepts	Very limited	Very limited options because of cost and development time constraints

were selected in large part for their potential to provide breakthrough structural-design solutions.

8.3.4 Technology Development Approach

Discipline experts were selected to manage and develop each of the three critical technology elements. More specifically, truss structure concept definition addressed the optimal truss design consistent with critical ISAT structural guidelines listed in Section 8.3.2. RI materials evaluation addressed specific concepts for the on-orbit rigidization of flexible materials, and structural performance simulation addressed on-orbit analytical prediction of structural performance. Each technology element was further comprised of sub-elements according to the taxonomy given in Table 8-6. After a prescribed development period, both the technical maturity and the remaining development risk of each critical ISAT element and sub-element technology was assessed. Technical maturity was evaluated using the widely used NASA technical readiness level (TRL) scale, summarized in Table 8-7. Remaining development risk, both technical and programmatic, was evaluated qualitatively. These evaluations are summarized in Table 8-8.

Table 8-6. Critical ISAT element and sub-element technologies.

Element	Sub-Elements
Truss structure concept definition	—
RI materials evaluation	Micro-mechanical analysis
	Column design, manufacturing, and database
	Materials technology assessment
	Truss tube experiment characterization
Structural performance simulation	Structural performance design tool
	Aperture distortion error shape analysis

Table 8-7. NASA technical readiness levels.

TRL Level	Description
1	Basic principles observed and reported
2	Technology concept and/or application formulated
3	Analytical and experimental critical function and/or characteristic proof-of-concept
4	Component and/or breadboard validation in laboratory environment
5	Component and/or breadboard validation in relevant environment
6	System/subsystem model or prototype demonstration in a relevant environment (ground or space)
7	System prototype demonstration in a space environment
8	Actual system completed and "flight qualified" through test and demonstration (ground or space)
9	Actual system "flight proven" through successful mission operations

As can be seen from Table 8-8, most of ISAT's critical element and sub-element technologies were judged sufficiently mature at the TRL 3−5 level to validate the design approach underlying the baseline configuration. The remaining development risk spanned all ranges, with the highest risk items concentrated in the area of characterizing the on-orbit rigidization process of the RI structural elements. As of this writing, the ISAT program is preparing to down-select to one or more structural preliminary design(s) from several competing concepts. The activities to date have demonstrated the viability of RI technologies for meeting the mission mechanical requirements; however, additional risk-reduction activities are required to mature the critical technologies to a flight readiness state. Ultimately, because of scale limitations and the great difficulty of accurately reproducing a zero-g space environment on the ground, a demonstration flight to validate the design will be needed [14].

Table 8-8. Critical ISAT technology maturity and risk assessment matrix.

Truss Structure Concept Definition	TRL/ Risk	RI Materials Evaluation	TRL/ Risk	Structural Performance Predict	TRL/ Risk
ISAT functional configuration	4 L	Space radiation durability	3–4 L	Structural system stiffness	4 L
Optimized structural system	4–5 L	Mechanical constitutive properties database	3 L	Structural system dynamic characteristics	2–3 L
Mechanical packaging techniques	2–3 M	RI structures folding capability	3–4 L/H	Structural system thermal stability	3 L
Deployment control	2–3 L/M	RI structures stiffness/strength	4–5 L	Aperture mounting precision / alignment	2 M/H
Panel alignment	3 L	Outgassing	4–5 L	Structural element deployment simulation	1 M/H
Mechanical/thermal stability	2 L	Long-term dimensional stability	0.5 L		
		Manufacturability	3 M/H		

Risk Rating: L = low, M = medium, H = high

From this example, one can inductively adapt the just-described process of assessing mission technology drivers, determining critical technologies and requirements, assessing the state-of-the-art, and specifying a technology-development approach to other spaceborne antenna systems. This technology development process helps to provide insights into directions for future mechanical developments.

8.4 Future Antenna Systems Developments

An overriding common theme underlies the future technical thrust for spaceborne antenna systems operating in any wavelength regime for nearly all end end-users: the need for larger and larger apertures. The overarching advantage afforded by large apertures can be seen, for example, by examining the radar equation for synthetic aperture radar (SAR), which can be formulated as

$$P_{av}^{T} A_E^2 \geq 4\pi \frac{kT_0 F_N L(S/N)_{\min}}{\rho \delta_r \delta_{az} \sin\psi} \cdot 2v\lambda\delta_{az} \cdot R^3$$

where the product $kT_0F_NL(S/N)_{\min}$ represents the minimum detectable signal energy, R is the range to the target, v is the velocity of the SAR platform

(relative to the target), ρ denotes the surface reflection coefficient, $\delta_r \delta_{az}$ is the area of the resolution cell, and ψ is the grazing angle. $P_{av}^T A_E^2$ is known as the power aperture product, where P_{av}^T is the average transmitted power. The underlying physics is straightforward: to rapidly scan large solid angles and detect small targets at long ranges, one needs a large power aperture, which, in a power-limited system, implies a large physical aperture. This fundamental physical condition has significant implications for future mechanical development. Consider for example, an integrated radar technology roadmap for earth science, with its various product lines, shown in Fig. 8-15.

8.4.1 Radar Altimeters

Radar altimeters can be used to measure ocean topography at Ku-band and river discharge at Ka-band. For these applications, very lightweight deployable Ku-band and Ka-band antennas are required. For the wide-swath interferometer altimeter, a very stiff interferometric mast is also required.

8.4.2 Synthetic Aperture Radars

L-band interferometric SAR can be used to measure surface deformation and topography, L-band and Ku-band polarimetric SAR can be used to measure snow properties, and P-band SAR can be used to measure deep-soil moisture and carbon cycle. For these applications, large scanning phased-array antennas are required. Current technology enables relatively large antennas using rigid-panel construction with integrated electronics and complex feed networks deployed with conventional truss structures. To enable increased science capability, these antennas may be replaced with very lightweight, flexible-membrane apertures deployed with ultra-lightweight structures. These missions also require compact, very high efficiency front-end component technologies to enable very high transmit powers. These technologies must be compatible with membrane antennas for both electronic beam scanning and advanced beam control/calibration techniques. These very large antennas can eventually be incorporated into geosynchronous SAR missions for timely global monitoring of surface changes, snow cover, soil moisture, and carbon cycle.

8.4.3 Atmospheric Radar

Atmospheric radar can be used to measure cloud and precipitation properties at multiple frequencies (14, 35, 94 GHz) as well as to monitor hurricanes and severe storms with continuous global coverage. For these applications, large, lightweight, reflector antennas with multi-frequency scanning feeds are required. Current state-of-the-art antennas use moderately large composite, non-deployable antennas with fixed nadir pointing. Beam pointing is accomplished with a phased-array feed. To enable increased science

capability, these reflector antennas may be replaced with very lightweight flexible membrane apertures deployed with ultra-lightweight structures. These missions also require compact, very high-efficiency front-end component technologies (particularly the transmit/receive module) to enable dual-frequency beam-scanning capability. These very large antennas can eventually be incorporated into geosynchronous atmospheric radar missions for timely global monitoring of hurricanes and severe storms.

8.4.4 Scatterometers

Scatterometers can be used to measure ocean surface winds at Ku-band and soil moisture and sea surface salinity at L-band. To measure low-resolution ocean-vector winds, no new technologies are required. To achieve very large coverage (swath), the antennas must be rotated. Currently, the high-resolution requirements can be met by using large (6 m) spinning mesh antennas for soil moisture measurement or by using rigid reflectors (3 m) operated in a "push-broom" geometry for ocean-salinity measurement. These antennas must be very low loss and broadband (for example, 1.2–1.4 GHz for soil moisture and ocean salinity measurement) to enable simultaneous radar and radiometric measurements. To enable increased science capability, these reflector antennas may be again replaced with very lightweight flexible membrane apertures deployed with ultra-lightweight structures.

8.5 Concluding Remarks

Observe that across these diverse mission sets, there is a "pull" for large, lightweight deployable apertures. This trend becomes even stronger when one accounts for payload size limitations in current launch vehicles. The same developments can be observed for missions in the defense sector. This mission "pull" supplies a "push" for mechanical technologies that enable high packing ratios; large, lightweight structural support; reliable deployments; and precise surface control. To move toward this goal, many spaceborne antenna technology roadmaps show a transition from small, mechanically deployed structures in the near term to large gossamer-inflation deployed structures in the longer term. In this author's opinion, the mechanical technology trade space is more complex than that, with many performance tradeoffs among solid non-deployable, mesh deployable, solid-element deployable, and inflatable designs. For the near-term future, there are promising developments for large antenna structures in several areas.

The state-of-the-art for large mechanical structural systems continues to progress, providing an important alternative to RI structural systems. State-of-the-art deployable SAR antennas have been flown having diameters of approximately 10 m. Notable examples are the 15-m Radarsat-1 antenna (1996), the 15-m Radarsat-2 antenna planned for 2005 [19], and the 10.7-m

Seasat-A antenna, launched in 1978 [2]. The Seasat-A L-band antenna, despite its 25-year old design, is remarkable for the high packing efficiency that was obtained from its eight-panel, z-fold design. Novel near-term conceptual designs for linear apertures include the 50-m dual-use L-band synthetic aperture radar/moving target indicator (SAR/MTI) antenna under development by JPL and the Air Force Research Laboratory (AFRL) [20]. State-of-the-art, deployable reflector antennas have been flown also having diameters of approximately 10 m. Notable examples are the 12.2-m AstroMesh reflector deployed from the Thuraya-2 geosynchronous Earth orbiting (GEO) communications satellite in 2003, and the dual 12-m Harris reflectors deployed from the Asia Cellular Satellite (ACeS) communication satellite in 2000. These antennas obtain high packing efficiencies; for example, the AstroMesh reflector measures only 1.1 m in diameter when stowed for launch. Representative ongoing near-term research efforts in deployable reflectors include Harris' advanced hoop truss reflector, measuring 25 m or more in diameter when deployed. These developments argue for continued progress on the mechanical front.

The state-of-the-art for large RI structural systems also continues to progress, particularly with the advent of shaped-memory polymers (SMP). SMPs are relatively new materials that achieve both a high deployed-to-packed volume ratio and a high structural-stiffness-to-mass ratio. Shape memory materials typically consist of graphite fibers imbedded in an SMP resin. Uniquely, these materials retain memory of their manufactured shape. When the SMP is above its glass transition temperature or T_g, its modulus becomes extremely low, allowing the structure to be packed into a small volume using conventional flattening, folding, and/or rolling techniques. This packed shape may then be "frozen" into place by cooling the SMP to below its T_g. If the structure is manufactured in its desired on-orbit configuration, it will return to its deployed shape once heated above its T_g. For large structures, the restoring force of the SMP resin, or "memory" may not be enough to ensure a complete return to the as manufactured shape. Consequently, a mechanical aid (such as an inflation gas) is used to assist in deployment. For reflecting apertures, SMP materials manufactured in thin-shell form also show promise, providing a viable alternative to membrane materials. Advantages of SMP materials include mechanical simplicity and their ability to be repeatedly heated and cooled, thereby enabling ground-based deployment testing.

Integrated modeling techniques and predictive performance analysis tools will continue increasing in importance for the development of large antenna systems. Because of increasingly strict requirements for high-precision dimensional performance, multi-disciplinary modeling techniques integrating nonlinear thermal transients, static, dynamic, structural, and RF elements will become critical to verifying the overall design of these systems. Because their

increasingly large size makes ground-based deployment testing impractical, predictive analysis tools incorporating the properties of very accurately characterized materials, joint micromechanics, and nonlinear structures will become critical to verifying the deployment performance of large antenna systems.

In this author's opinion, as spaceborne antenna systems continue to grow in size, the trend toward the intermediate term future of integrating advanced metrology with active/adaptive structural control will strengthen. This development is driven by the fact that precision antenna systems incorporating lightweight structural technology may still have residual surface errors on the order of $\lambda/10$ or greater at radar wavelengths. With the aid of an advanced metrology system, such as those used for current interferometers, an active/adaptive structural control system can reduce these errors to approximately $\lambda/20$. In the limit, for optical wavelengths, active/adaptive structural control can provide the critical intermediate step permitting the quasi-static and dynamic control necessary to enable capture for precision wavefront sensing.

Finally, for the longer term future, there may be a renewed emphasis on in-space assembly of modular structures for the construction of large spaceborne antenna systems. Significant advances in the state-of-the-art for both autonomous control and robotic systems make this option more viable than it was in the mid 70s, when Grumman first proposed the OCDS (see Section 8.1). With in-space assembly, only the material inventory (which can be packaged much more efficiently than a completely assembled structure) need be transported into orbit. Once in orbit, autonomous robotic operation of varying complexity can be utilized for space-assembly operations. For this to be a truly viable option, payload delivery costs will need to continue to decline significantly.

References

[1] J. A. Shortal, *A New Dimension, Wallops Island Flight Test Range: The First Fifteen Years*, NASA Reference Publication 1028, National Aeronautics and Space Administration, Washington, District of Columbia, 1978.

[2] M. R. Hachkowski and L. D. Peterson, *A Comparative History of the Precision of Deployable Spacecraft Structures*, CU-CAS-95-92, Center for Aerospace Structures, College of Engineering, University of Colorado. December 1995, also at University of Colorado web site accessed August 6, 2005.
http://sdcl.colorado.edu/Publications/1995/CAS_Reports/CU-CAS-95-22.pdf

[3] G. Tibert, *Deployable Tensegrity Structures for Space Applications*, Doctoral Thesis, TRITA-MEK Technical Report 2002:04, Department of Mechanics, Royal Institute of Technology, Stockholm, Sweden, 2002, also at Royal Institute web site accessed August 6, 2005. http://www2.mech.kth.se/~gunnart/TibertDocThesis.pdf

[4] J. R. Hansen, "The Big Balloon: How Project Echo taught NASA the value of a glitch," *Air & Space*, vol. 9, no. 1, pp. 70–77, April/May 1994.

[5] L. Jaffe, "Project Echo results," *Astronautics*, vol. 6, no. 5, pp. 32–33, 80, May 1961.

[6] A. Wilson, "A History of Balloon Satellites," *Journal of the British Interplanetary Society*, vol. 34, pp. 10–22, January, 1981.

[7] R. E. Freeland, *Orbital Construction Demonstration Study, Final Report*, NAS 9-14916, prepared by Grumman Aerospace Corp for Johnson Space Center, Houston, Texas, June 1977.

[8] R. E. Freeland, *Industry Capability for Large Space Antenna Structures*, 710-12 (internal document), Jet Propulsion Laboratory, Pasadena, California, 1978.

[9] *Status Report Concerning Research on Electrostatically-Figured Membrane Reflectors and Large Space Structure Control Systems*, Research Laboratory of Electronics, Massachusetts Institute of Technology, Cambridge, Massachusetts, 1982.

[10] R. E. Freeland, *Final Report for Study of Wrap Rib Antenna Design*, LMSC D714613, Contract No. 955345, prepared by Lockheed Missiles and Space Company for Jet Propulsion Laboratory, Pasadena, California, December 12, 1979.

[11] M. W. Thomson, "The AstroMesh Deployable Reflector," *Proceedings of the Fifth International Satellite Conference* (June 6–18, 1997, Pasadena, California), JPL Publication 97-11, Jet Propulsion Laboratory, Pasadena, California, pp. 393–398, 1997.

[12] Northrop Grumman, "2004. Northrop Grumman's AstroMesh Reflector Successfully Deployed on MBSAT Satellite," Northrop Grumman web site, site accessed August 6, 2005. http://www.irconnect.com/noc/press/pages/news_releases.mhtml?d=54953

[13] R. E. Freeland, G. D. Bilyeu, G. R. Veal, M. D. Steiner, and D. E. Carson, "Large Inflatable Deployable Antenna Flight Experiment Results," *Proceedings of the 48th International Astronautical Congress* (October 6–10, Turin, Italy), IAF Paper 97-1.3.01, International Astronautical Federation, Paris, France, 1997.

[14] R. E. Freeland, R. G. Helms, P. B. Willis, M. M. Mikulas, W. Stuckey, G. Steckel, and J. Watson, "Inflatable Space Structures Technology Development For Large Radar Antennas, IAC Paper 04-IAF-I.1.10, *55th IAF Congress* (October 4–8, 2004, Vancouver, Canada), International Astronautical Federation, Paris, France, 2004.

[15] C. M. Satter, and R. E. Freeland, *PASS Spacecraft Antenna Technology Study*, JPL D-8490 (internal document), Jet Propulsion Laboratory, Pasadena, California, August 1, 1991.

[16] D. G. Gilmore, *Spacecraft Thermal Control Handbook: Fundamental Technologies*, 2nd edition, Aerospace Press, Los Angeles, California, 2002.

[17] R. E. Freeland, *Deployable Space Structures: Deployment Control of the DARPA Radar Antenna*, White Paper, JPL D-33751 (internal document), Jet Propulsion Laboratory, Pasadena California, October 9, 2005.

[18] B. K. Wada and R.E. Freeland, "Technology Requirements for Large Flexible Space Structures," IAF Paper 83-404, *34th IAF Congress* (October 10–15, 1983, Budapest, Hungary), International Astronautical Federation, Paris, France, 1983.

[19] L. Brule and H. Baeggli, "RADARSAT-2 Mission Update," *Geoscience and Remote Sensing Symposium*, 2001 (IGARSS '01) (July 9–13, 2001), IEEE, Piscataway, New Jersey, Vol. 6, pp. 2581–2583, 2001.

[20] P. A. Rosen and M. E. Davis, *AFRL/JPL Space-based Radar Development, 2002–2003 Final Technical Report*, AFRL-SN-RS-TR-2003-307, Air Force Research Laboratory Sensors Directorate, Rome Research Site, Rome New York, January 2004.

Chapter 9
Miscellaneous Other Antennas

William A. Imbriale and Daniel J. Hoppe

This chapter describes a few unique antennas that do not readily fit into any of the other categories. Included are the Solar Probe antenna and the Deep Impact antenna.

9.1 Solar Probe Antenna

William A. Imbriale

Although the Solar Probe Mission is in a state of limbo at this time and there are no plans to fly this antenna, it represents such a unique design that it is worthy of being included.

9.1.1 Solar Probe Mission Description

The destination of the Solar Probe is the atmosphere of the Sun. It will approach the Sun within 2 million kilometers of the surface (a perihelion radius of 4 solar radii) while traversing its atmosphere or corona to make fundamental observations of the most important and the least-understood environment in the Solar System [1,2].

The most significant technology challenge is the thermal shield that will protect the spacecraft from the flux of 3000 suns (400 W/cm^2) at perihelion while allowing the spacecraft subsystems to operate at near room temperature. The Solar Probe spacecraft configuration is shown in Fig. 9-1, with the large thermal shield dominating the configuration. The shield is a section of a parabola of revolution (paraboloid) that has a dual function as a shield and as a high-gain antenna (HGA) [3]. The spacecraft trajectory is chosen so that near

the Sun the nadir of the spacecraft always faces the Sun and the HGA always points toward Earth.

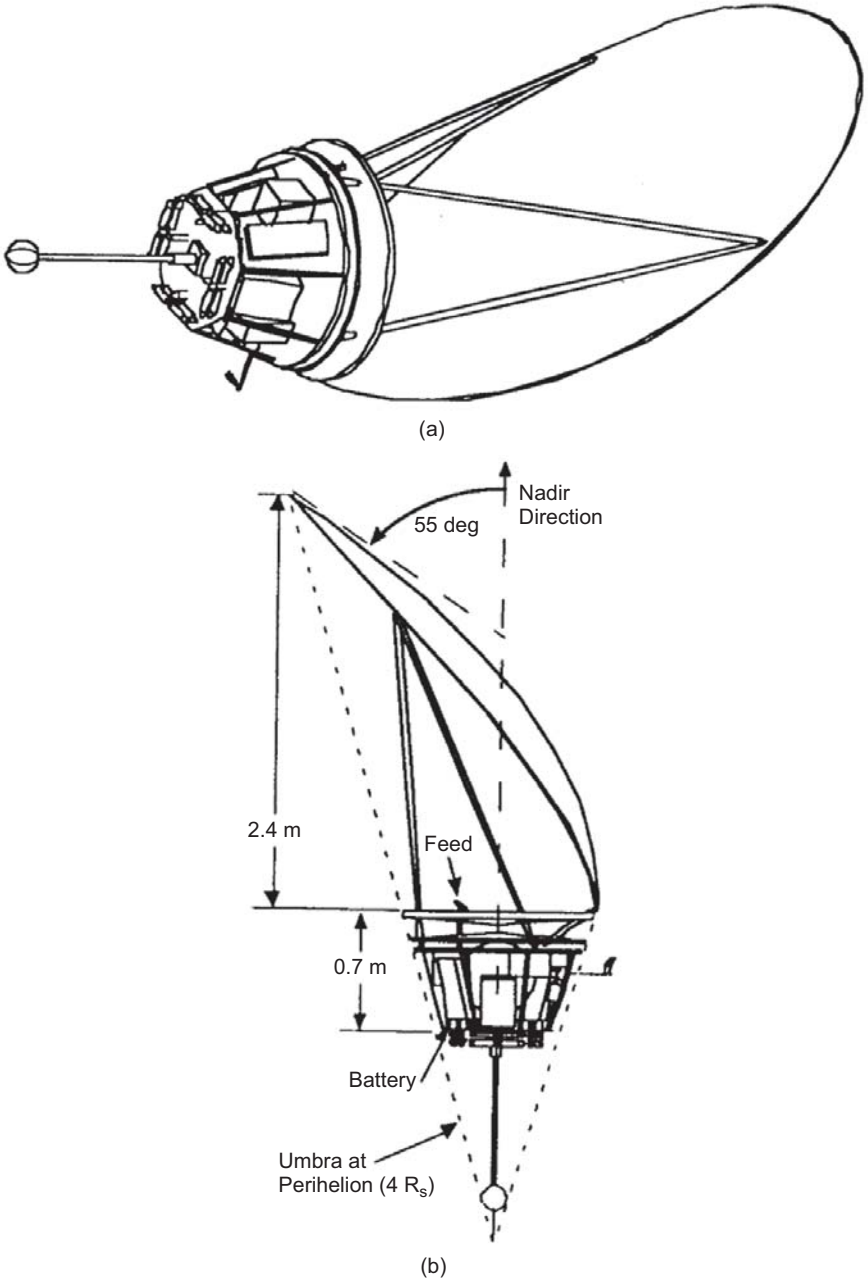

Fig. 9-1. Solar Probe spacecraft configuration: (a) isometric view and (b) side view.

9.1.2 Antenna Requirements

Measurements of the plasma environment including the birth and acceleration of the solar wind are the principle scientific objectives of this mission. To accomplish these measurements, the spacecraft must not produce excessive outgassing or sublimation that could ionize and contaminate the natural plasma environments that are to be measured. The scientific community has suggested the magnitude of contamination that is acceptable and has given a total mass loss specification of less than 2.5 mg/s at perihelion.

Traveling to a perihelion radius of four solar radii (4Rs) requires a very high-energy launch capability. In order to maximize the launch capability and minimize launch costs, the spacecraft must be small and lightweight as possible while satisfying the scientific payload accommodation requirements. Thus, the shield must be made of lightweight materials such as composites. In addition, for a spacecraft traveling to 4Rs and maintaining its electronics at room temperature (approximately 300 K), a shield is required to shade the electronics while the shield itself will be operating at extremely high temperatures (greater than 2000 K). The combination of these requirements led to the selection of carbon-carbon as the ideal shield material because of its low density, high strength, and excellent high-temperature characteristics.

The antenna geometry is detailed in Fig. 9-2. It is an offset reflector with a focal length of 0.8 m situated on top of the spacecraft. The feed is also shielded from the Sun, but because the feed is outside the spacecraft thermal blankets, it still gets to a fairly high temperature (1400 K) at perihelion.

9.1.3 The Solar Probe Heat Shield/Parabolic Antenna

The heat shield must be designed to minimize its mass loss while operating at more than 2000 K at perihelion. An architectural characteristic of the spacecraft and mission suggested that if the heat shield could have the shape of a paraboloidal shell, it could also function as an off-axis HGA for X-band communications at perihelion. The main shell of the shield consists of a high-density carbon-carbon material with a thickness of about 1 mm that forms a parabolic structure having an “elliptical” planform with about 2 m by 3 m axes. Following an extensive program to screen various carbon-carbon shield materials, a candidate material was chosen that promised to have optical properties that would minimize the operating temperatures at the high solar fluxes, thereby minimizing the mass loss at these high temperatures. The testing program confirmed the desired characteristics of this carbon shield material and a specific material was selected for the shield. The material is fabricated with a densification process using chemical vapor infiltration (CVI). A final chemical vapor deposition (CVD) process produces a pyrolytic graphite coating to minimize the absorptivity/emissivity ratio at high temperatures. No additional coatings are necessary to satisfy the design requirements. The CVD process

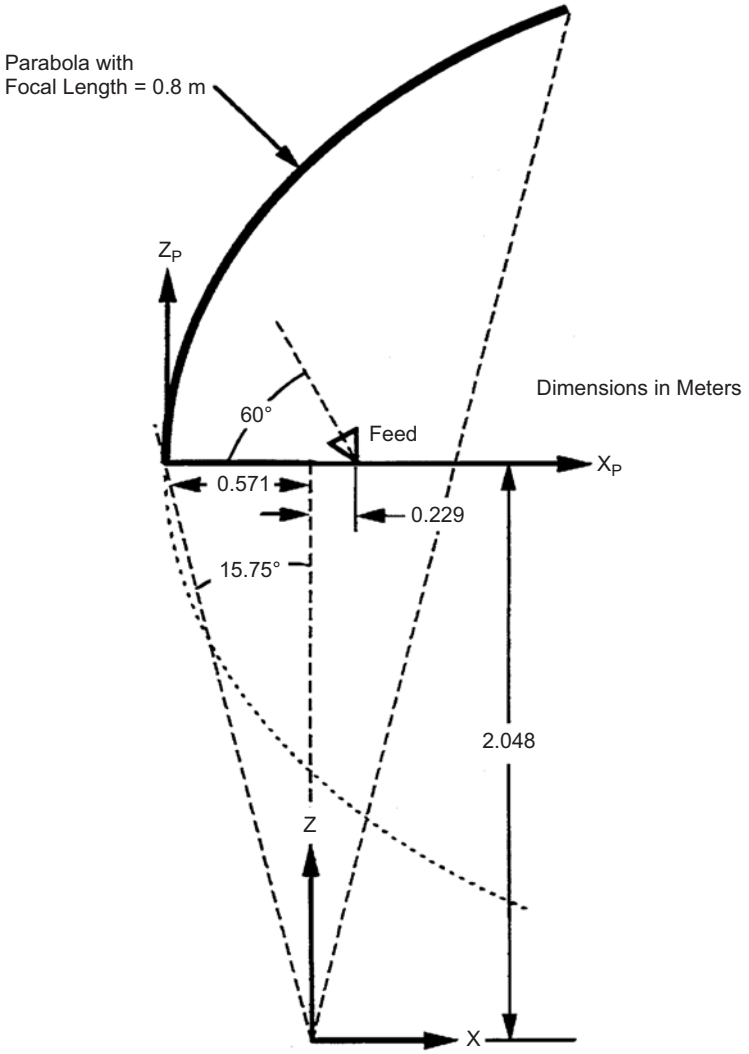

Fig. 9-2. Solar Probe antenna geometry.

also promises to minimize the mass loss (sublimation) at these operating temperatures. The radio frequency (RF) reflectivity of the material at the X-band frequency (~8 GHz) is sufficient to allow the shield to operate as an antenna at temperatures greater than 2000 K. A more complete description of the history of the shield development, the materials fabrication process, the materials selection process, and the shield-design concept can be found in [4].

9.1.4 Frequency and Feed Specifications

Since X-band was chosen as the primary communications band, including both transmit and receive functions, the frequency range of the feed is 7.145 to 8.5 GHz. To properly illuminate the reflector, a feed gain of about 10 dB is required. The feed is to have left-hand circular polarization (LHCP) with an axial ratio of less than 2 dB and a return loss of less than –15 dB. The feed must operate at a peak temperature of 1400 K. A number of low-gain feed designs were considered including a horn, a crossed dipole in a cup, and a helical antenna. A horn was ruled out because it would require a polarizer to generate the circular polarization, and the combination of the horn and polarizer would be considerably larger than the other two designs and extend too far above the spacecraft platform. To cover both the transmit and receive bands with the crossed dipole requires a hybrid to combine the two arms of the crossed dipole 90 deg out of phase to achieve circular polarization, whereas the helix is inherently circular polarized. In addition, the helix is inherently wider in bandwidth and thus less sensitive to length changes due to thermal variations. The helix could also be constructed using very high temperature capable metal. For these reasons the helix was chosen as the feed element.

9.1.5 Feed Design

A schematic of the feed is shown in Fig. 9-3. It consists of a helical antenna, a coax, a coax-to-waveguide transition joint, and a short piece of high-temperature-capable waveguide with a short bend. Thermal shields on the top of the spacecraft bus separate the helix from the waveguide. The coax size was chosen to minimize the penetration hole in the thermal shields. A thermal block (choke air gap) separates the feed assembly from the room temperature waveguide in the spacecraft bus. A two-phase contract was given to Composite Optics, Inc. Phase 1 investigated key technologies to determine which materials and component designs would satisfy the feed antenna requirements [5], and phase 2 culminated with the fabrication and delivery of a working prototype [6].

9.1.5.1 Plating. The plating development effort investigated and determined a plating process for nickel on ceramic matrix composite (CMC) materials. Neither copper nor aluminum could withstand the high temperature (1400 K). Adhesion of the nickel was verified at –173 deg C, +525 deg C, and +1125 deg C.

9.1.5.2 Waveguide and Feed Element Design. The basic design consists of a coax-fed helical feed element coupled to a plated ceramic waveguide. The conductor for the helical feed element would be inserted into the coax with low dielectric, high temperature spacers to attach/align the center conductor in

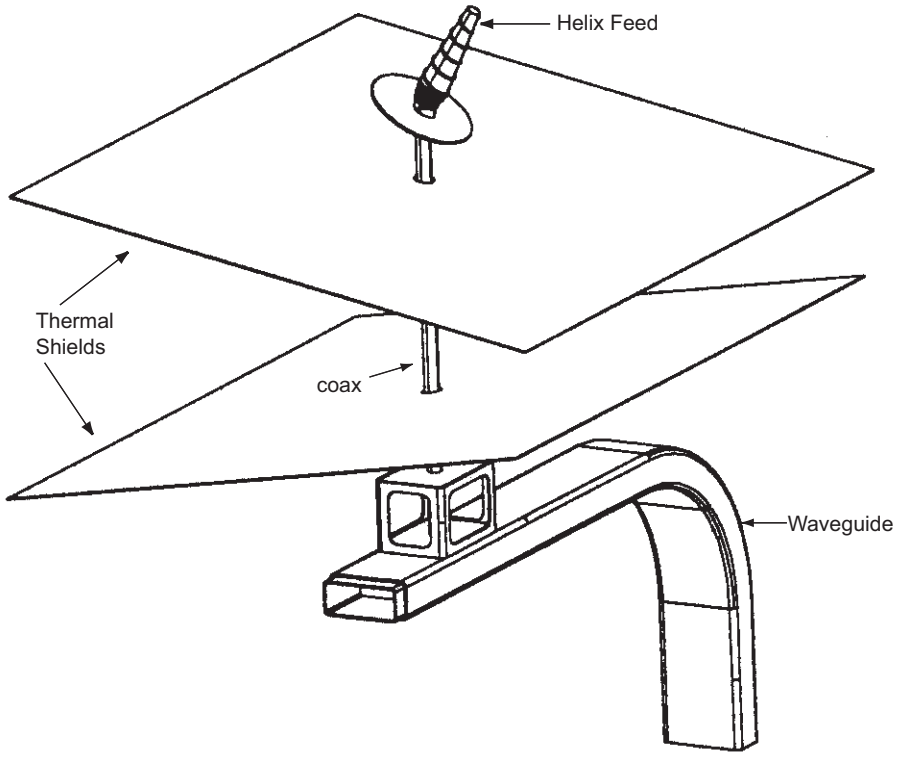

Fig. 9-3. Solar Probe waveguide and antenna design.

place. Additional low-dielectric material would be used in the waveguide to latch the center conductor probe.

9.1.5.3 Choke Joint Design. Typically, the waveguide/coaxial cable/helix assembly would be a unitized construction having no openings from the RF path to the outside except at the antenna. A coaxial choke joint was added at the helix interface because of the need to periodically extract the helix/center conductor assembly from the waveguide/outer conductor assembly without using screw fasteners or temperature-sensitive bonding agents.

The key feature is the choke joint section that alleviates the need for a continuous conductive bond between the waveguide and the coaxial outer conductor. The choke joint also makes possible blind mating of the two components for easy assembly and removal of the coaxial center conductor/antenna assembly. See [6] for more details on the choke design.

9.1.5.4 Helical Antenna. Generally, helical antennas are constructed from a single uniform diameter wire, such as copper, and wound in a consistent shape. However, due to the design and temperature requirements of the Solar Probe

antenna feed assembly, a conventional helical antenna could not satisfy these requirements. Based on work completed in Phase I of the program, a non-uniform diameter helical antenna design with variable pitch and a construction of the antenna from tungsten material, would satisfy these requirements.

9.1.5.5 RF Analysis. RF analysis was performed prior to fabricating the Solar Probe prototype. The purpose of this analysis was to establish a viable initial solar probe design without having to fabricate numerous expensive prototypes. The Solar Probe antenna feed assembly comprises of the following key components:

1) waveguide to coaxial transition,
2) tapered air dielectric coaxial cable,
3) coaxial choke joint.

For reasons of computational efficiency, the problem was split into two parts. The first being a waveguide-to-coaxial cable transition coupled with a 14-in. (35.6-cm) length of tapered air-dielectric coaxial cable terminated in 100 Ω, and the other being a 100-Ω coaxial choke joint.

Finite element models of these two components were constructed so that field propagation and scattering parameters (S-parameters) could be calculated in the transmit and receive frequency bands. The basic models were dimensioned for lab ambient temperature. S-parameters were calculated for lab ambient temperature and with the probe depth dimension adjusted for the maximum specified temperature so that temperature-induced changes in insertion loss and match could be evaluated. Worst-case matching conditions were assumed in order to predict the performance of the fully integrated assembly. Based upon the results of the analysis, the final assembly was fabricated and tested.

Return loss and insertion loss measurements were performed on the completed Solar Probe feed assembly prototype. The return loss shown in Fig. 9-4 was measured at the input to the WR-112 waveguide. To measure the insertion loss, the helix port was shorted while the return loss was measured at the input to the waveguide. Dividing the measured return loss (in decibels) by 2 and plotting as shown in Fig. 9-5, approximated the net loss. Rapid variations were due to mismatches in the integrated feed and helix that were not modeled. Return loss was nominally –12 dB across the band, and insertion loss was approximately –1.0 dB.

9.1.5.6 Measured Radiation Patterns. The measured transmit and receive radiation patterns of the feed assembly are shown in Fig. 9-6. Utilizing these measured radiation patterns in a physical optics calculation and estimating a total additional loss of 2 dB from insertion loss, reflector reflectivity, etc., the

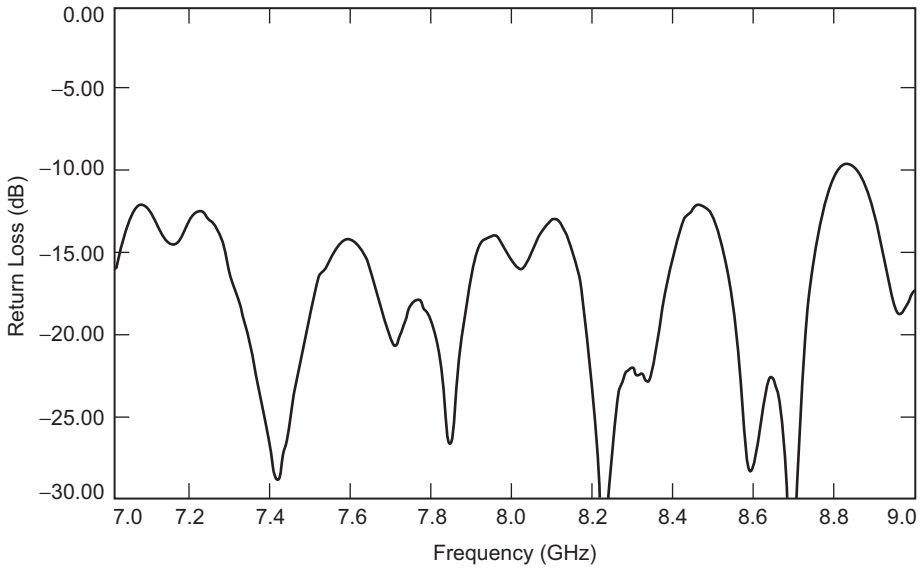

Fig. 9-4. Measured Solar Probe feed assembly return loss.

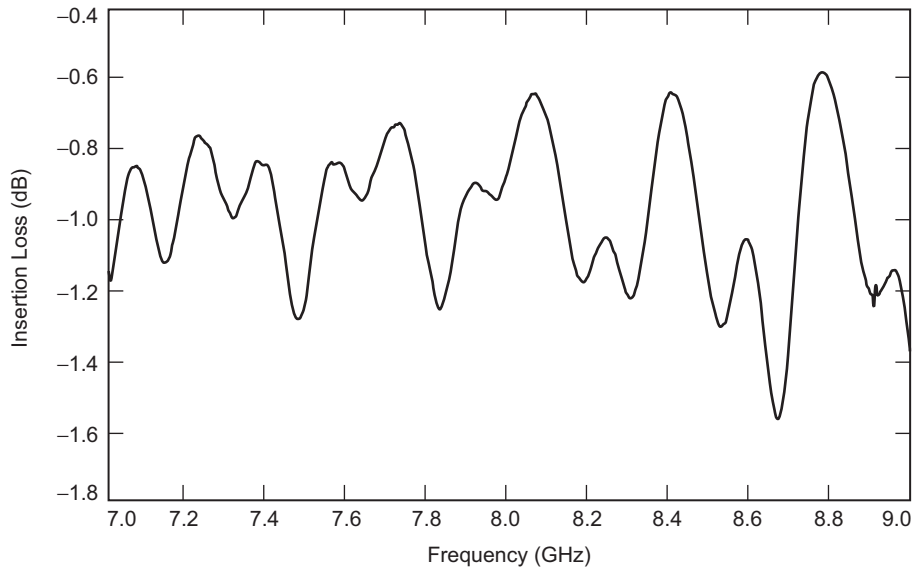

Fig. 9-5. Measured Solar Probe feed assembly insertion loss.

estimated gains are 41.3 dB at the transmit frequency (8.425 GHz) and 39.6 dB at the receive frequency (7.145) [7]. A picture of the completed prototype feed assembly is shown in Fig. 9-7.

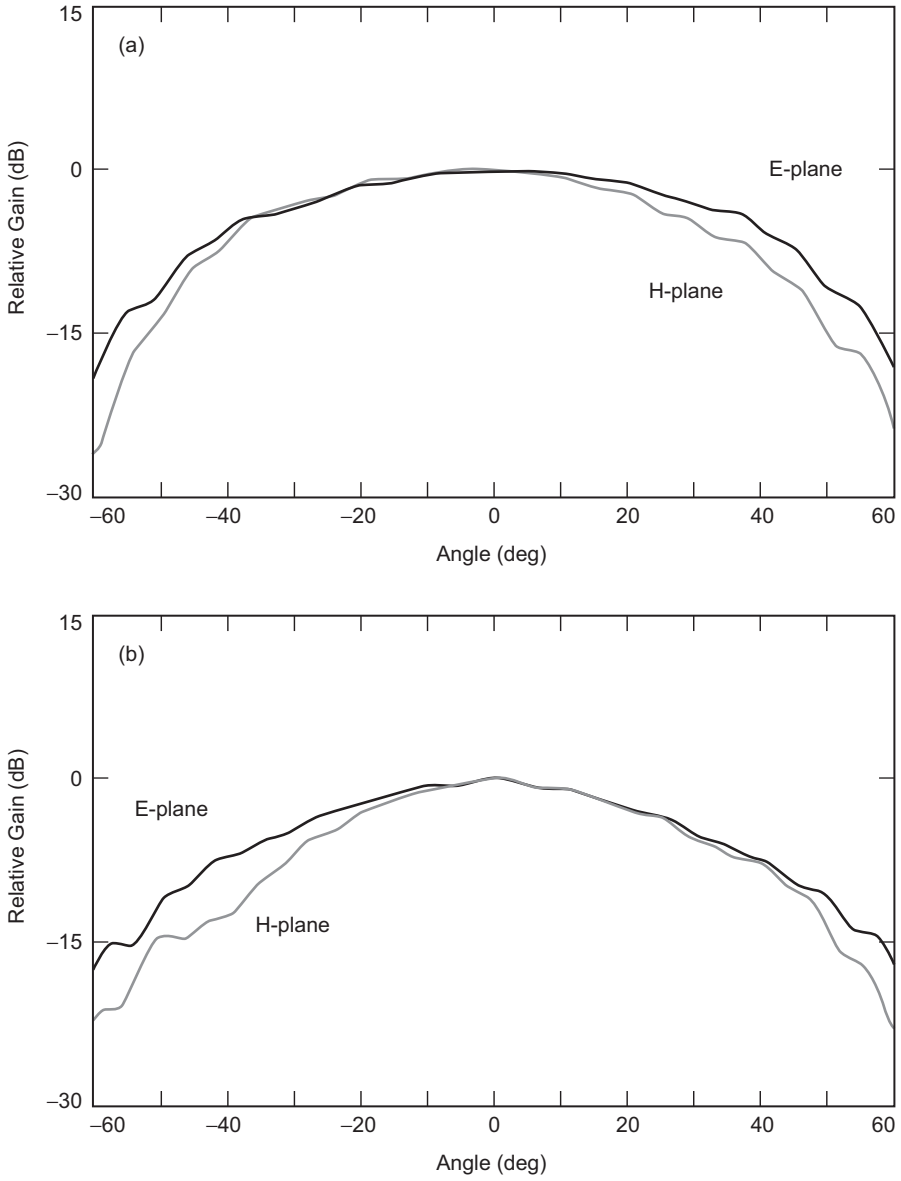

Fig. 9-6. Solar probe feed element radiation patterns: (a) receive frequency 7.145 GHz and (b) transmit frequency 8.425 GHz.

Fig. 9-7. Solar Probe antenna feed assembly prototype.

9.2 Deep Impact S-Band Patch Array Antenna

Daniel J. Hoppe

9.2.1 Deep Impact Mission Description

The Deep Impact mission's science goal was to increase our understanding of comets, particularly the composition of their interior, [8]. The science goals were accomplished using a two-part spacecraft, a 370-kg impactor and a flyby spacecraft, Fig. 9-8. The impactor was released by the flyby spacecraft and struck the target comet, Temple-1, creating a large crater, ejecting ice and other debris from the interior of the comet. The flyby spacecraft recorded the impact using conventional photography and spectrometers, characterizing the comet's

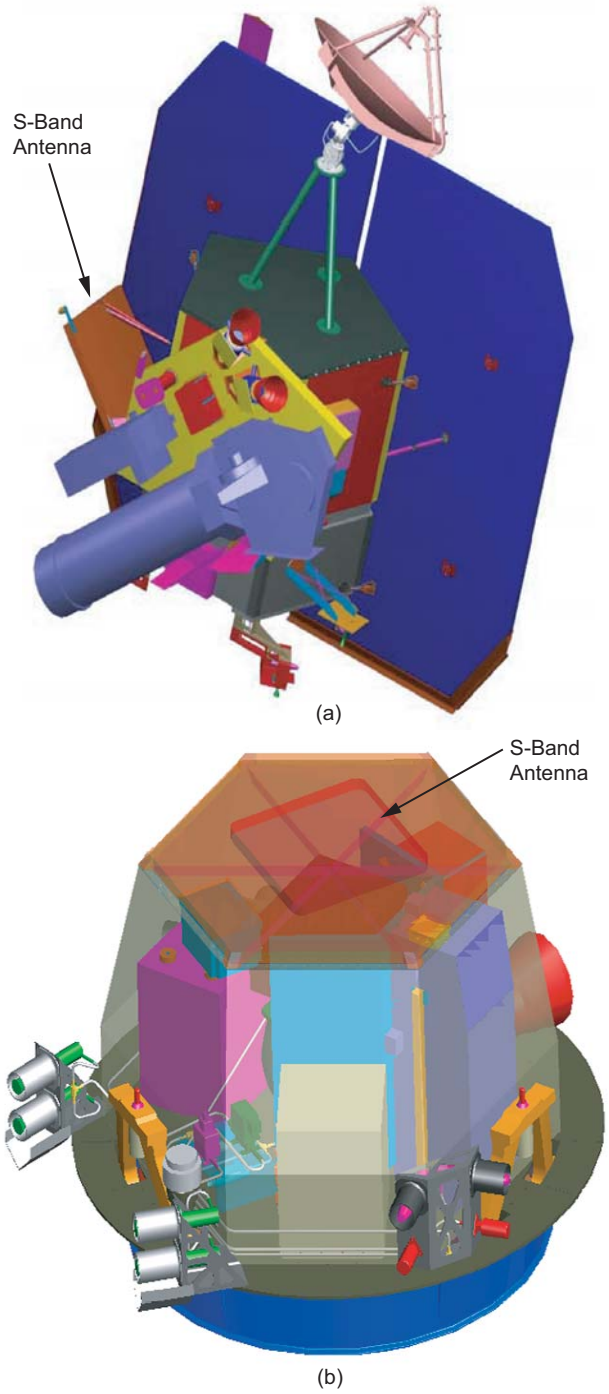

Fig. 9-8. Deep Impact: (a) flyby spacecraft and (b) impactor.

material. The flyby spacecraft made these observations from a distance of approximately 500 km. In addition, cameras on the impactor relayed images of the comet's nucleus to the flyby spacecraft until just seconds before impact. The S-band patch array described in this chapter is part of the impactor-flyby link used to transmit these images. Identical antennas were placed on both the impactor and flyby spacecraft, as shown in Fig. 9-8. Details of the link requirements are provided in the next section.

Deep Impact was launched December 2004. Impact with the comet Temple-1 occurred in July 2005. The Sun illumination angle and Earth position were designed to be optimum at the date of impact. The overall mission lifetime was approximately 7 months. After the encounter, the trajectory of the flyby spacecraft was adjusted to fly past Earth in December 2007. Proposals by NASA for future use of the spacecraft will be solicited in the near future.

9.2.2 Antenna Requirements

The performance requirements for the antenna are described in Table 9-1. Two narrow bands of operation are specified, 2.105 GHz for 64 kilobits per second (kbps) impactor-to-flyby communication, and 2.28 GHz for a 16-kbps command interface from the flyby spacecraft to the impactor. In general, all performance trade-offs in the design were made to favor the impactor-to-flyby band which was used to transmit the images to the flyby spacecraft. The command link was used three times during the encounter to provide timing updates. Since the impactor was to be spinning during its journey to the comet circular polarization was chosen for both bands. Maximum ellipticity of 3 dB was specified in both bands in order to limit the coupling loss between the two spacecraft as they rotated relative to each other. In order to support the expected data rates, a gain of 19 decibels referenced to isotropic radiator (dBi) was specified for the 2.105-GHz band and 16- to 19-dBi gain was specified for the 2.28-GHz band. A voltage standing-wave ratio (VSWR) of less than 2 was specified for both bands, once again to minimize signal loss in the link. The 2-to-1 aspect ratio of the antenna was chosen to satisfy the beamwidth requirements in the table below. Maximum transmit power in the 2.28-GHz band was 2 W continuous wave (CW).

Table 9-1. Antenna requirements.

Parameter/Band	2.105 GHz	2.280 GHz
Gain	19 dBi	16–19 dBi
Ellipticity	<3 dB	<3 dB
VSWR	<2 to 1	<2 to 1
Power	Receive only	2 W CW
Data Rate	64 kbps	16 kbps

In order to minimize cost, a single antenna design was used for both ends of the link. The environmental conditions experienced by the impactor and flyby antennas were considerably different however; and therefore, the design for both spacecraft had to operate under environmental extremes. For example, the impactor antenna was illuminated by the Sun during the encounter and was fairly warm, while the flyby antenna was shielded and thermally isolated from the spacecraft and operated at temperatures as low as –160 deg Celsius. Vibration and acoustic levels consistent with the Delta II launch vehicle were also specified.

9.2.3 Antenna Design

Although the 19-dBi gain and polarization requirements could be met by a variety of antennas, a microstrip patch array antenna was chosen, [9]. The patch array has a low profile that was compatible with the mounting requirements imposed by both spacecraft. The disadvantages of the patch array include high loss and low bandwidth. Since the bandwidth of a single microstrip patch is not sufficient to cover the two frequencies of interest for this application, a dual stacked rectangular patch arrangement was chosen, [10]. In this configuration the upper patch is designed to resonate in the high frequency band while the lower patch resonates in the lower band and also serves as the ground plane for the upper patch. A number of approaches for feeding the patches were also considered, including slot coupling [11] and four-probe coupling. The final design uses a single pair of probes to excite the lower patch with the upper patch excited through parasitic coupling with the lower one. This feeding approach offers simplicity but sacrifices some polarization purity relative to a four-probe feed. Microstrip and strip-line were both considered for realization of the microwave circuits needed to feed the array. Microstrip was chosen in the final design since it offered a superior mechanical design, simplifying fabrication. The final array contains 18 patches in a 3-by-6 configuration. Element spacing is approximately 4.2 in. (10.668 cm) in the broad dimension of the array and 4.5 in. (11.430 cm) in the narrow dimension, providing for efficient use of the overall antenna area and minimizing coupling for this fixed-beam array. The following sections provide more detail about the various components making up the array.

9.2.3.1 Mechanical Configuration/Stack-up. A cross section through the stack of materials making up the array antenna is depicted in Fig. 9-9. All metal structures were fabricated using 0.002-in. (0.0051-cm) thick sheets of Kapton (DuPont High Performance Materials, Circleville, Ohio) material coated with 0.5 oz. (14.17 g) copper. Working from the bottom of the structure up, the microstrip circuit is formed by a ground plane in the form of a copper-coated Kapton sheet, a layer of Astro Quartz (Bryte Technologies, Inc., Morgan Hill,

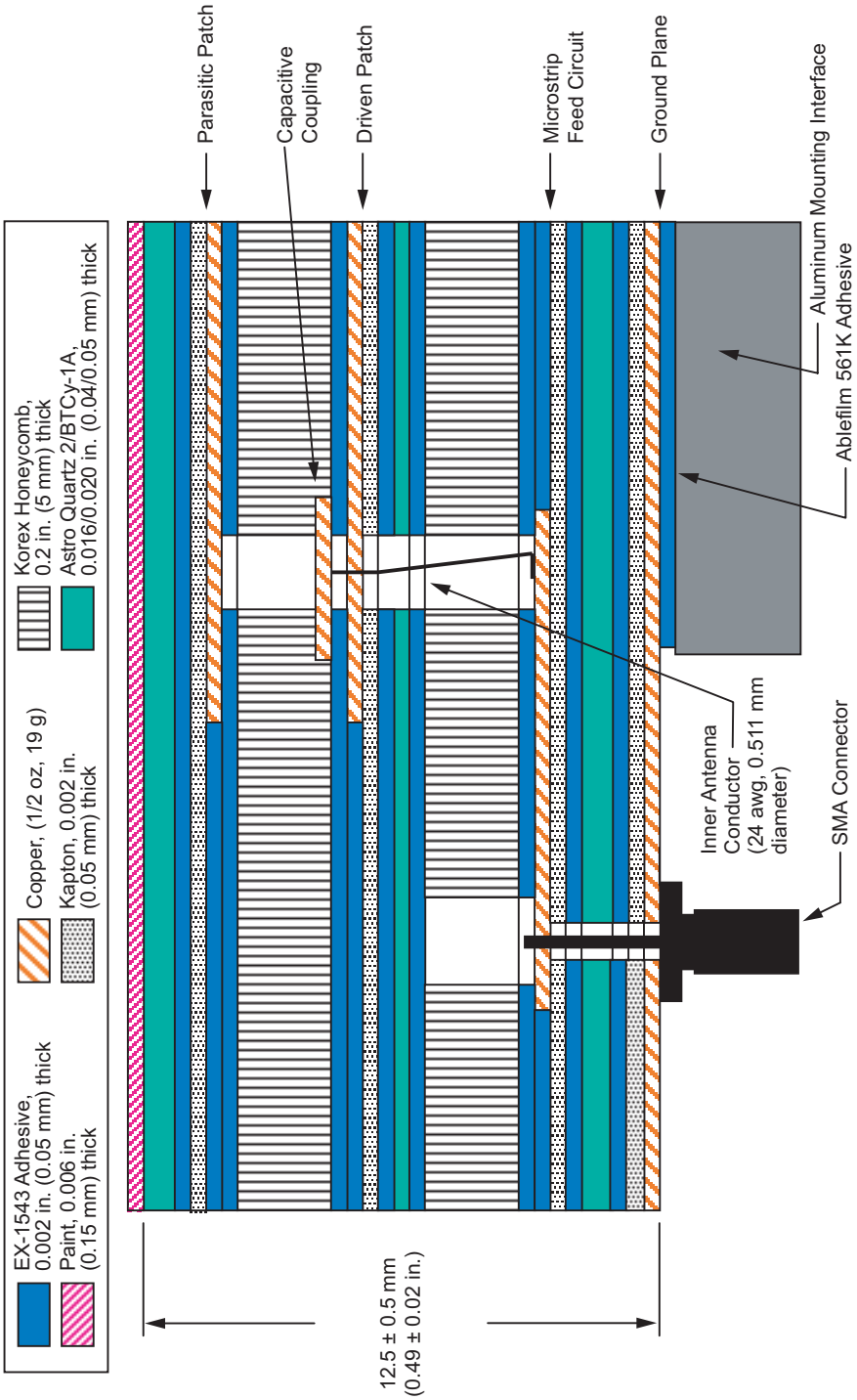

Fig. 9-9. Deep Impact antennas mechanical configuration.

California), the circuit layer containing the printed structures, and another layer of copper-coated Kapton. The driven patch layer is separated from the microstrip layer by a 0.2-in. (0.508-cm) thick layer of Korex honeycomb material. A layer of Astro Quartz provides stiffness for the honeycomb. The second, parasitic patch layer is supported similarly and covered with a final layer of Astro Quartz that serves as a radome. Although a thin layer of conductive paint was considered during the design, and is shown in the figure, it was not ultimately included in the flight antennas. All layers are bonded with EX1543 adhesive from Bryte Technologies, Inc. The complete antenna is bonded to the aluminum mounting interface using adhesive. The array was fed using a single sub-miniature version A (SMA) connector. A model of the entire stack-up, including glue layers, was used in the electromagnetic simulation using Ansoft's Ensemble, [12]. Figure 9-10 depicts the construction sequence and layer configuration for the overall antenna.

9.2.3.2 Patch and Microstrip Circuit Details. Figure 9-11 depicts the computer model of a single 3-dB hybrid/stacked-patch element. The structure is fed through port 1, and two equal amplitude in-quadrature signals are generated at the output ports of the hybrid. These signals are then used to excite the two orthogonal modes of the stacked patches. The hybrid's output is connected to the driven patch by a unique and simple coupling mechanism. A thin wire is soldered to the top of the microstrip line, passed through the patch, and terminated using a capacitive disc. This capacitive coupling compensates for the inductance of the coupling wire. The upper patch is excited parasitically through the lower one. No direct RF connection is made. The fourth port of the hybrid is terminated with a 50-Ω chip resistor. Instead of shorting the second lead of the chip resistor to ground using a via, an open-circuited stub was used to provide an effective short. This arrangement gave acceptable performance and simplified construction of the array. In this configuration, reflections from the patch are terminated in the load and do not appear at the input connector. Alternatively, shorting the fourth port of the hybrid would re-radiate the reflected power in the cross-polarized sense. Figure 9-12 shows a photo of the overall microwave circuit layer and details of the hybrid. As depicted in the figure all line lengths were carefully matched throughout the array. Eight three-way and a single two-way splitter were required to feed the 18-element array. Both splitters are reactive, and contain no load material. All bends in the circuit are optimized miter bends.

9.2.3.3 Predicted Performance. Figure 9-13 shows the computed return loss for the single patch element depicted in Fig. 9-11. Excellent return loss is achieved in the 2.105-GHz band with an acceptable return loss of approximately 12.5 dB at 2.28 GHz. As was stated previously, the 2.105-GHz

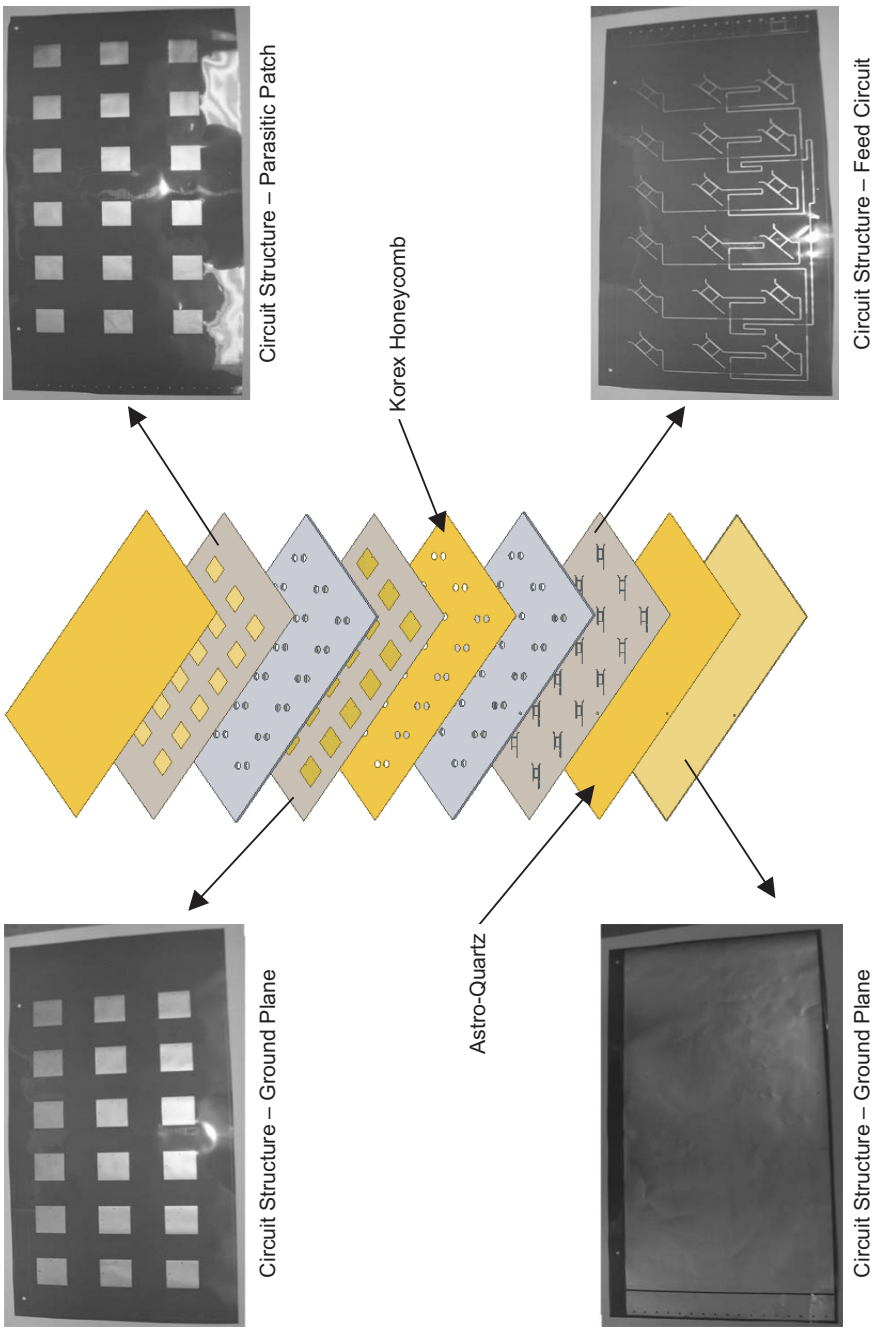

Fig. 9-10. Deep Impact antennas fabrication sequence.

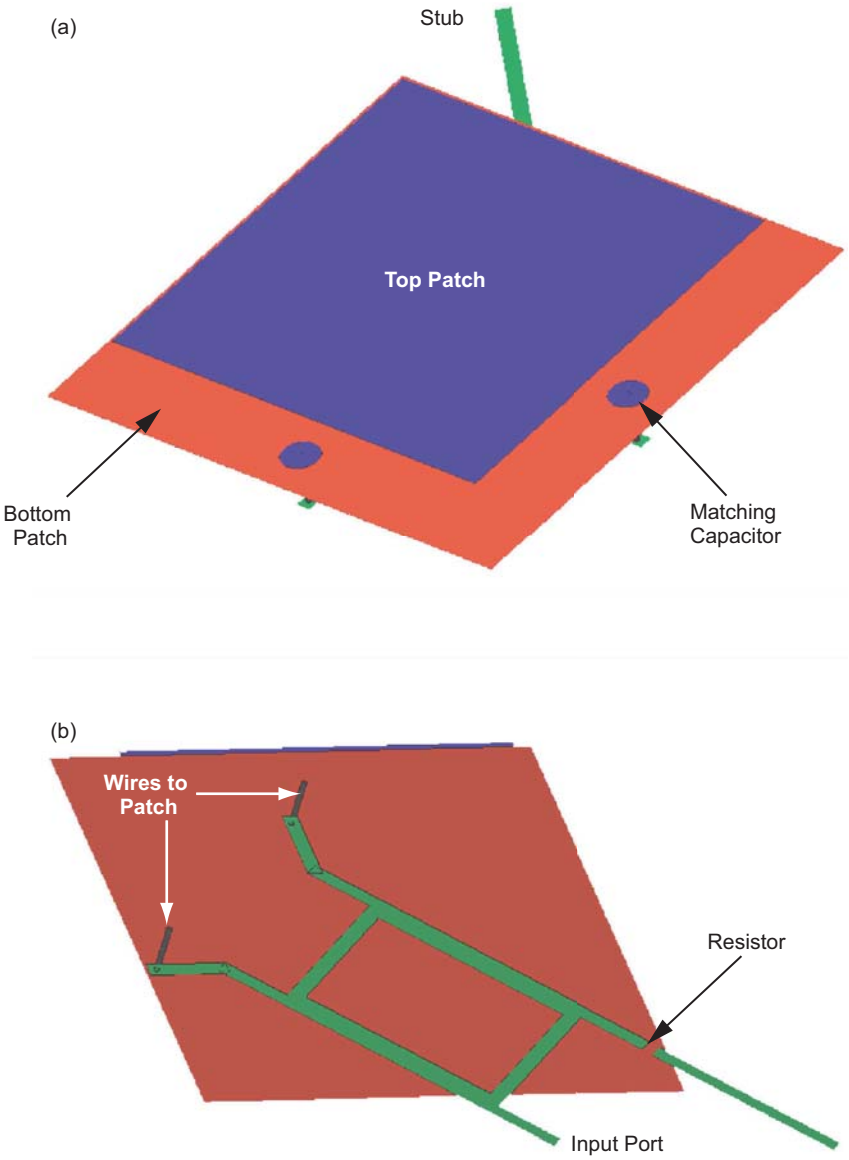

Fig. 9-11. Details of Deep Impact antenna patch configuration: (a) top view and (b) bottom view.

band was favored in the design, as evidenced in Fig. 9-13. The computed axial ratio is shown in Fig. 9-14. In this case the hybrid dimensions and probe locations were designed to produce an excellent axial ratio near 0.5 dB at 2.105 GHz. The axial ratio at 2.28 GHz is limited to approximately 2.8 dB due

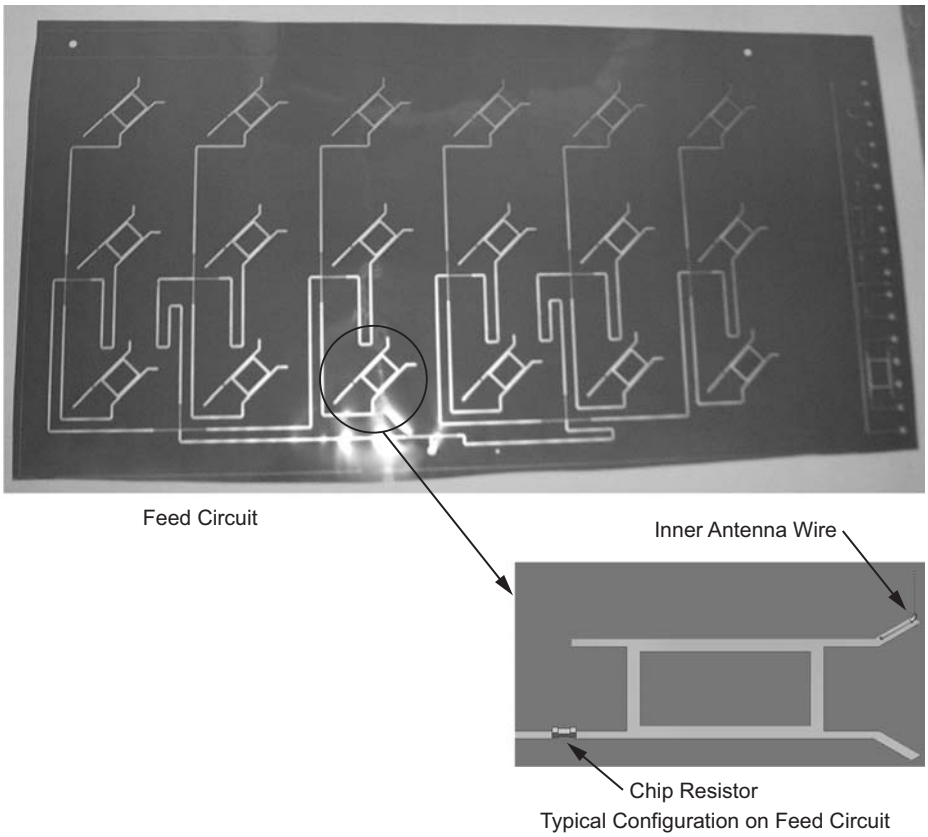

Fig. 9-12. Details of Deep Impact microstrip hybrid.

to the bandwidth of the hybrid and unwanted coupling between the two probes. A four-probe feed or rotation of adjacent patches relative to each other [13], would have reduced this axial ratio significantly. In the interest of simplicity and schedule the slight loss in link efficiency caused by this axial ratio was accepted in the 2.28-GHz band. As indicated in Table 9-1 a tradeoff between axial ratio and antenna gain is possible in this low-data-rate band. Further discussion of this the effect of axial ratio on link efficiency is given in the following section. An estimate of the expected gain of the array was made by creating a model of the patch elements and models for the various circuit elements and transmission lines. The overall gain is driven by circuit loss, and it can vary significantly depending on the loss parameters assumed for the various materials in the structure. In particular, no independent measurements of the loss tangent for Astro Quartz and EX5143 adhesive were available. Manufacturer's loss tangent values for Astro Quartz and for the adhesive were assumed and an overall gain in the 18.5–19.5 dB range was computed, based upon various other assumptions in the model.

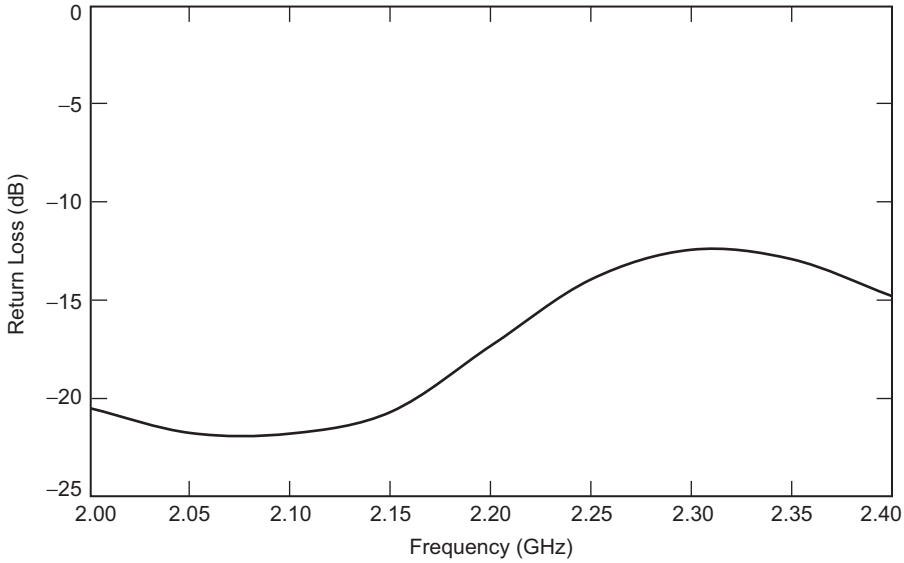

Fig. 9-13. Computed return loss of an individual Deep Impact patch-hybrid element.

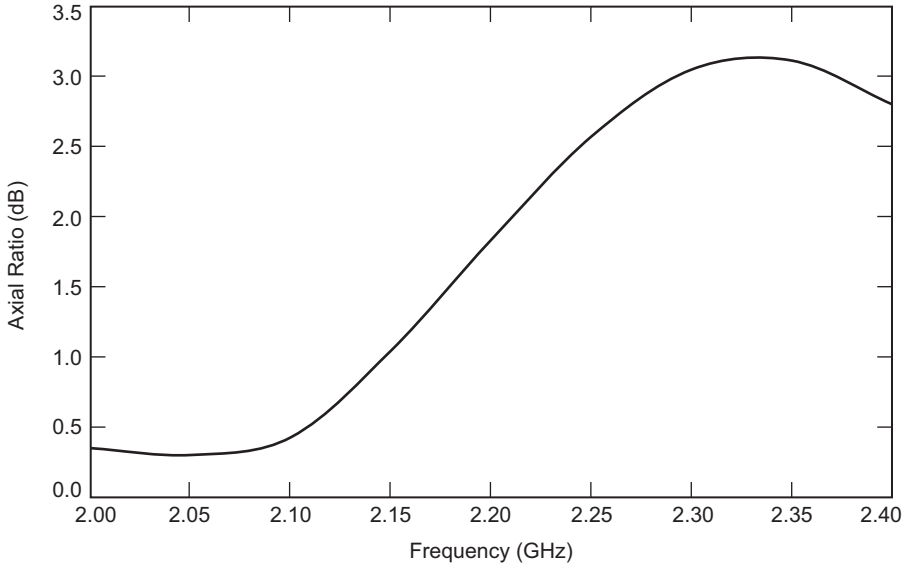

Fig. 9-14. Computed axial ratio for an individual Deep Impact patch-hybrid element.

9.2.4 Measured Performance

After the initial design phase two breadboard antennas were fabricated, one full array and another half-array with a number of additional test points. The measured gain for the full array was 18.5 dBi at 2.105 GHz and 18.6 dBi at 2.280 GHz. The measured axial ratios were 1.65 dB and 4.0 dB, respectively. Although the axial ratio in the high-frequency band was slightly outside the specification, the relatively high gain in that band relative to the minimum required value of 16 dBi mitigates this effect on the overall link performance, and the overall antenna was deemed acceptable. Next, an engineering model of the antenna was fabricated for environmental testing. The performance of this model exceeded that of the breadboard, with gains of 18.7 and 19.3 dBi in the two bands, and axial ratios of 0.2 and 2.78 dB in the two bands. After significant testing of the engineering model (EM) unit, two flight units were fabricated. In all respects except gain the performance of the flight units was identical to the EM unit. Excess loss was detected in both flight units, reducing their gain by approximately 2.5 dB in both bands. The origin of this excess loss was investigated through additional RF testing, X-ray photography of the units, and materials testing. Unfortunately, the results of this testing were inconclusive as to the cause of the excess loss. The flight antennas were then put through environmental testing and delivered to the project. As a compromise, the engineering model was flown along with one of the flight units, with the other flight unit acting as a spare. The excellent performance of the EM unit and other margin available in the link allowed the data rates required by the project despite the unexpected gain loss.

9.2.4.1 S-Parameter Testing. The scattering parameters (S-parameters) of individual components were measured on the breadboard antenna, and the overall match presented at the input port to the overall array was measured on every array produced. Figures 9-15 and 9-16 show the phase and amplitude performance of an individual 3-dB hybrid. The phase difference between ports is maintained within a few degrees of quadrature across the entire band while the amplitude balance is optimum near 2.105 GHz. The quality of this response from the first fabricated unit indicate not only the quality of the modeling software, but also the accuracy of the fabrication and material parameters used in the design process. Excellent results were also achieved for the three-way splitter. A balance of better than 0.1 dB was measured at 2.105 GHz, deteriorating slightly to 0.2 dB at 2.280 GHz. Figure 9-17 shows the measured return loss at the SMA connector for the complete EM antenna. The return loss is optimum near 2.105 GHz, and is better than –15 dB at 2.280 GHz, easily meeting the requirements. The measured return loss for all of the fabricated arrays was quite similar to that shown in the figure.

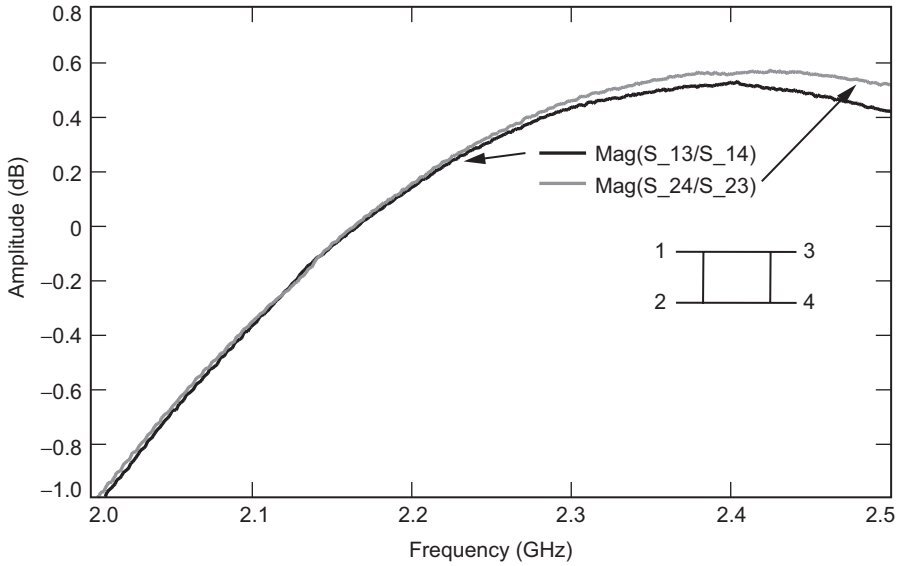

Fig. 9-15. Measured amplitude balance of Deep Impact hybrid.

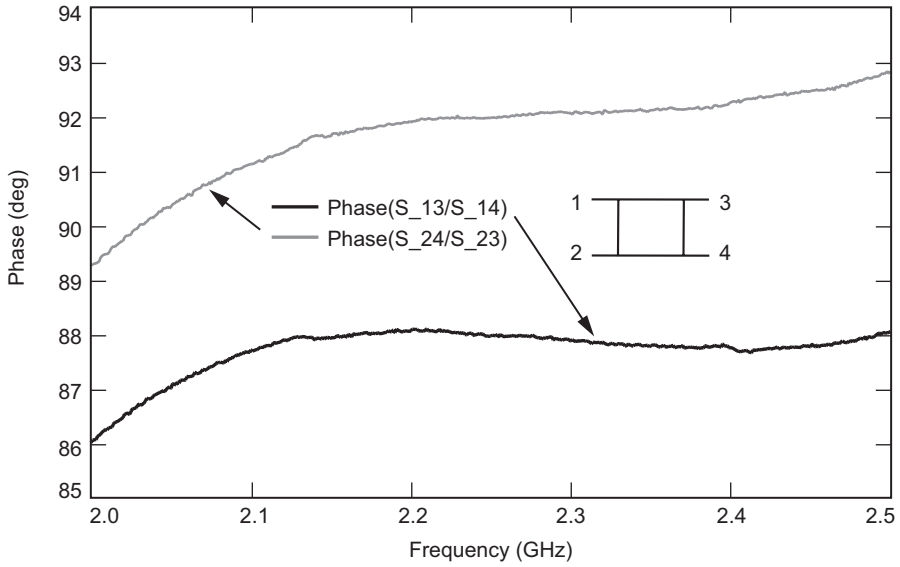

Fig. 9-16. Measured phase balance of Deep Impact hybrid.

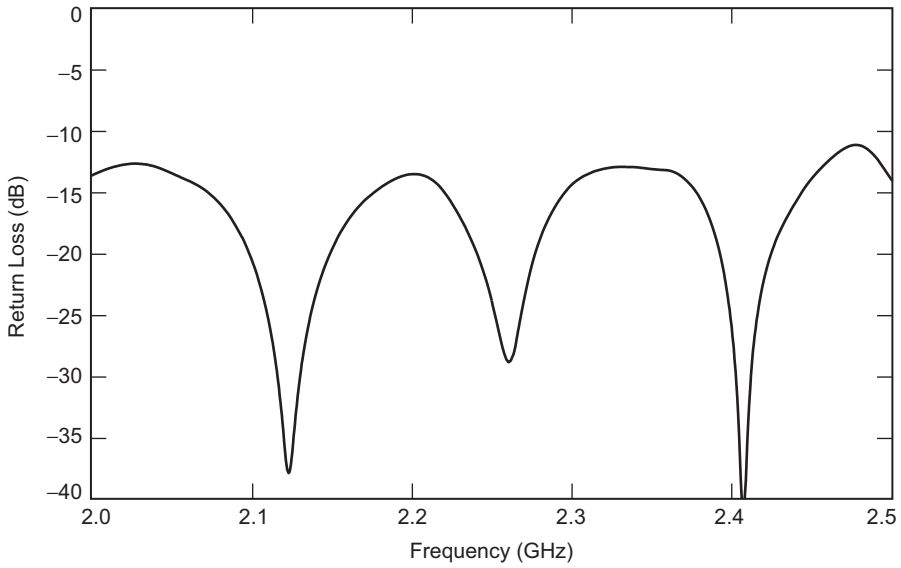

Fig. 9-17. Measured return loss of complete Deep Impact engineering model antenna.

9.2.4.2 Radiation Pattern Testing. Radiation patterns and axial ratio were measured on all antennas fabricated and both prior to and after the complete environmental testing sequence for the EM and flight units. Measurements were carried out at JPL's outdoor antenna test range. Figures 9-18 and 9-19 depict the horizontal component's radiation pattern in the two principal planes of the array at 2.105 GHz. The measured 3-dB beamwidths were approximately 12 and 24 deg. The level of the first sidelobe was approximately –13 dB, as expected, indicating a nearly uniform aperture illumination. Figure 9-20 shows the narrow beam cut once again, this time using a spinning linearly polarized receiver. The lack of ripple in the main beam of the pattern is indicative of the excellent axial ratio of the antenna in this band. Radiation patterns in the 2.280-GHz band were quite similar to those of Figs. 9-18 to 9-20, with the exception of the somewhat degraded axial ratio. All fabricated arrays had virtually identical radiation patterns.

9.2.4.3 End-to-End Link Testing. A final RF test was conducted to verify the gain of the antennas and the effects of axial ratio on the performance of the link. The test setup consisted of one antenna on a rotating positioner and the other antenna fixed. An automatic network analyzer was used to measure the antenna-to-antenna transmission versus frequency and rotation angle, simulating the amplitude variation expected when one of the two spacecraft in the link is spinning. The results of the test are depicted in Fig. 9-21. A peak-to-

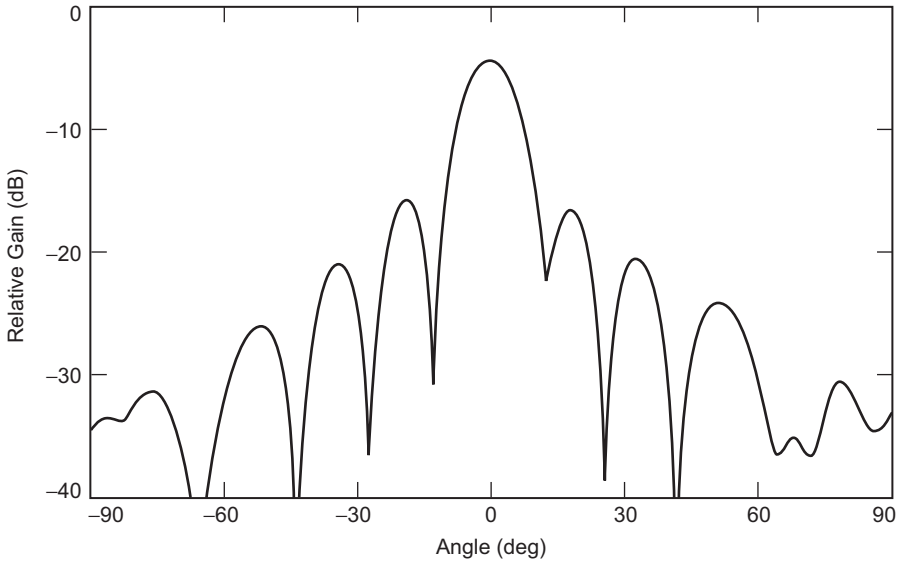

Fig. 9-18. Measured linearly polarized (LP) radiation patterns of Deep Impact engineering and flight models at 2.105 GHz.

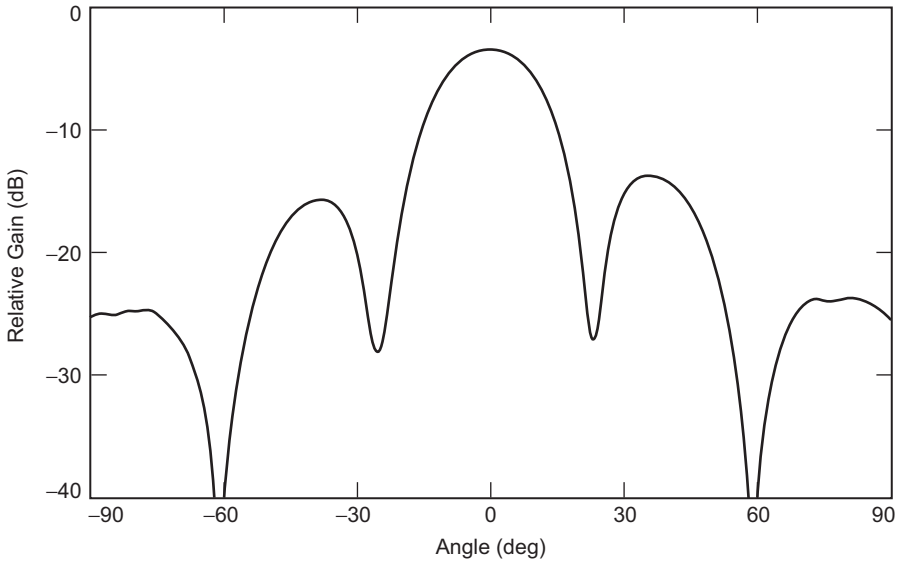

Fig. 9-19. Measured linearly polarized (LP) radiation patterns of Deep Impact engineering and flight models at 2.105 GHz.

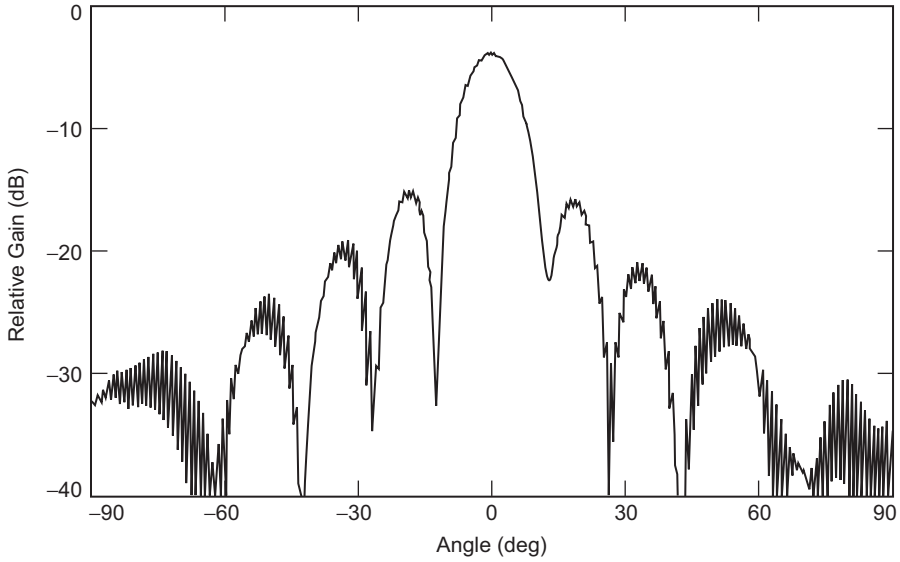

Fig. 9-20. Measured circularly polarized (CP) radiation patterns at 2.105 GHz.

peak ripple of 0.2 dB was measured at 2.105 GHz, and approximately 1 dB was measured at 2.280 GHz. These results are consistent with the measured axial ratio in each band. In addition, this calibrated transmission measurement provided independent confirmation of the gain values measured on the antenna range.

9.2.5 Environmental Testing

Environmental testing was performed on the EM and each of the two flight units. In addition some early tests were performed on one of the breadboard units to verify operation at –160 deg C, an area of significant concern. Environmental testing included thermal-vacuum testing, vibration testing in all three axes, and acoustic testing. A full set of antenna radiation patterns was measured before and after the full set of environmental tests. Return loss was measured before and after each of the three axis tests in vibration, and before and after the acoustic test. RF performance was monitored continuously during the thermal vacuum tests.

9.2.5.1 Vibration Testing. The EM and flight models of the antenna array were subjected to both a sine wave survey and random vibration over a frequency range of 20–2000 Hz. Vibration tests were conducted over a one-minute interval along each of the three axes. In all cases the measured return loss of the antenna after vibration was essentially indistinguishable from that before vibration, indicating a successful test.

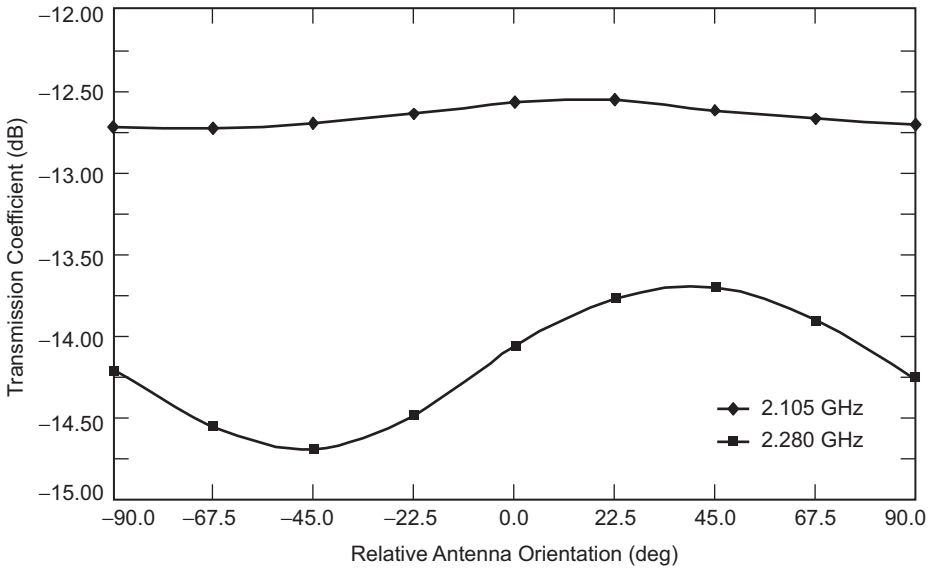

Fig. 9-21. Measured antenna coupling versus relative rotation between Deep Impact antennas.

9.2.5.2 Acoustic Testing. The engineering model of the antenna was also subjected to acoustic testing. The tests were carried out in JPL's 10,000-ft^3 (283-m^3) reverberation chamber. Acoustic energy with a specified spectral density, covering the range between 30 and 10,000 Hz, was delivered to the antenna while it was suspended inside the chamber. Once again, return loss measurements verified that no damage was sustained by the array during the acoustic test. The flight units were not subjected to acoustic testing.

9.2.5.3 Thermal Vacuum Testing. The most severe environmental constraint placed on the antenna was the wide temperature range expected. While the impactor antenna's temperature could reach as much as 70 deg C when illuminated by the Sun, the flyby spacecraft antenna's temperature could plunge to –160 deg C when shaded from the Sun. The thermal vacuum test was intended to verify the antenna's survival and performance over several cycles covering this extreme temperature range. Figure 9-22 shows the EM antenna inside the thermal vacuum chamber. During the thermal vacuum test, the antenna's temperature was measured at several locations using thermocouples. In addition, a dipole antenna was placed inside the chamber, and the RF transmission between the array and dipole (as well as the return loss of the array) were measured continuously throughout the test. The temperature profile throughout the test is shown in Fig. 9-23. More than 300 data points are included in the plot. These data were taken at 5-minute intervals, representing

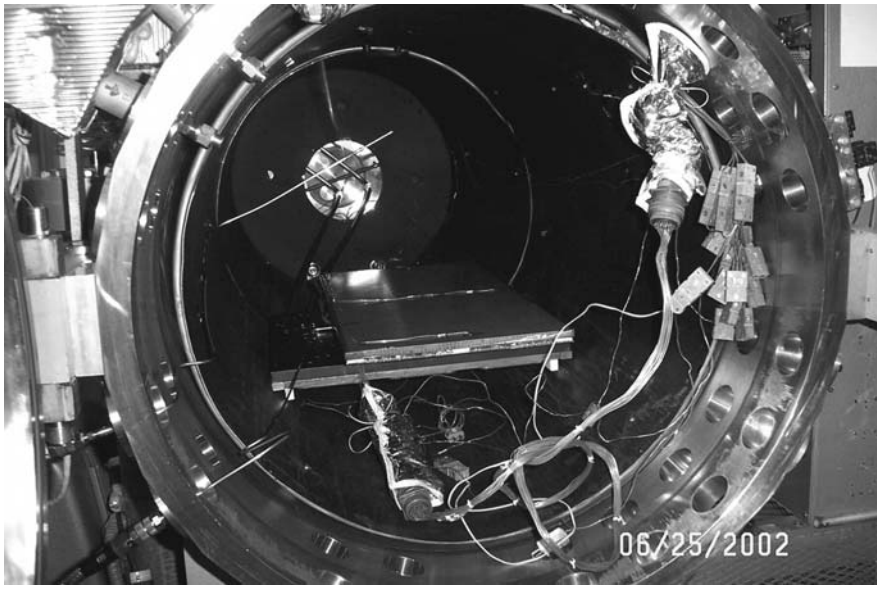

Fig. 9-22. Deep Impact thermal vacuum test configuration.

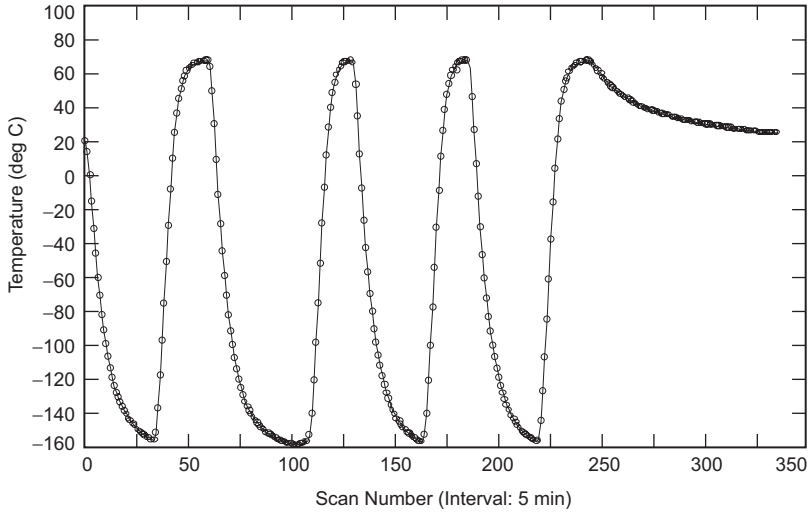

Fig. 9-23. Deep Impact thermal vacuum test temperatures.

over 27 hours of data. The temperature extremes depicted on the plot are +70 deg C and –160 deg C, as indicated above. Figure 9-24 shows the measured return loss and transmission throughout the test. The top two plots

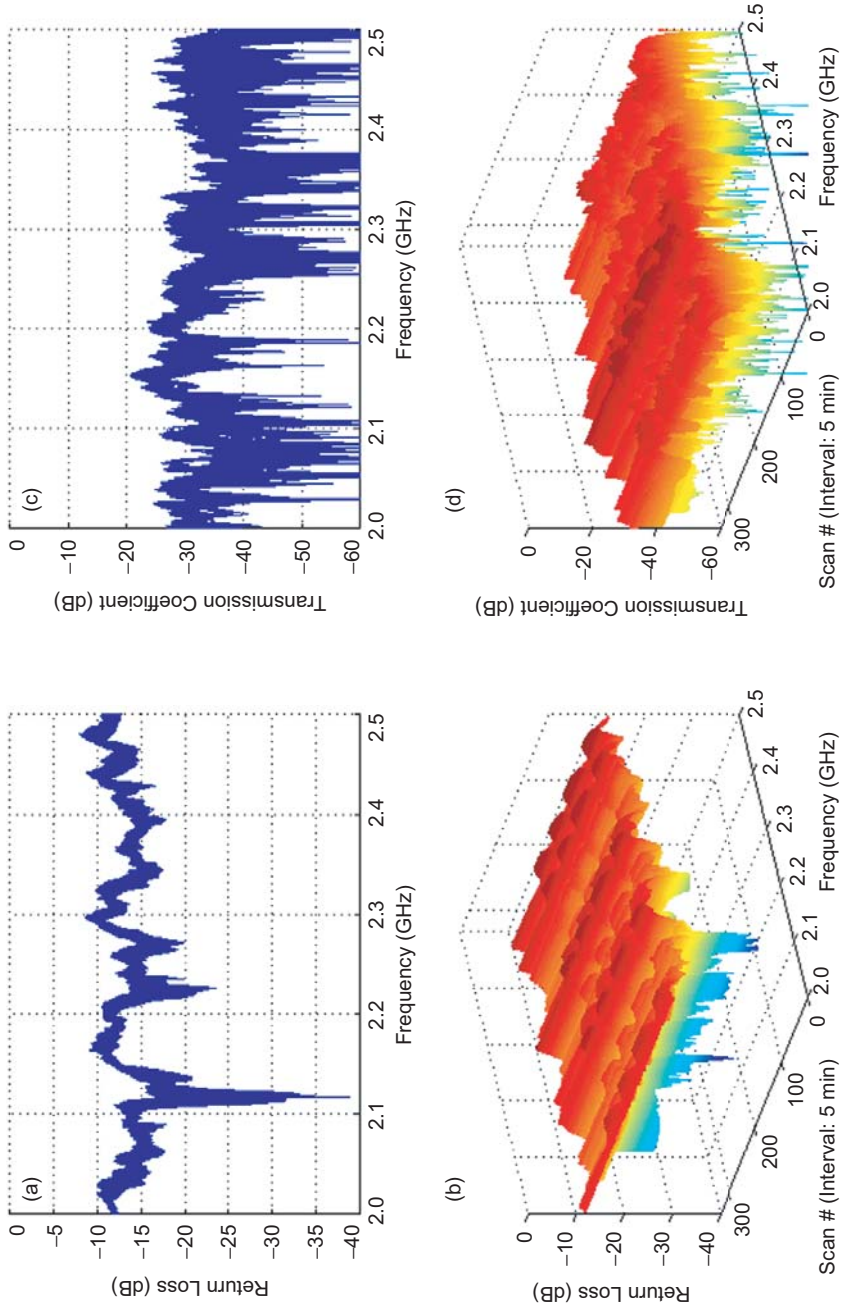

Fig. 9-24. Deep Impact measured antenna performance during thermal vacuum testing: (a) thermal-vacuum return loss, (b) thermal-vacuum return loss over time, (c) thermal-vacuum return loss transmission coefficient, and (d) thermal-vacuum transmission over time.

overlay a large number of frequency sweeps taken at 5-minute intervals; while the bottom plots are a three-dimensional representation of measured frequency response versus time throughout the test. The oscillatory behavior versus time depicted in the lower plots mimics the temperature profile of the test. As expected, slight shifts in the frequency response are seen in both the measured parameters. No discontinuities, which would be indicative of an intermittent connection or failure, were observed. As expected, the transmission between antennas increased at cryogenic temperatures due to the decreased copper loss at these temperatures. Comparison of the return loss measured before and after the thermal vacuum test further verified the success of the test.

9.2.6 Current Status

The Deep Impact spacecraft was successfully launched from the Kennedy Space Center in Florida on January 12, 2005. The impactor spacecraft successfully collided with comet Tempel-1 on July 4, 2005. The Deep Impact flyby spacecraft suffered only light damage in its proximity to Tempel-1, and the spacecraft control team is attempting to maneuver it to an additional flyby of comet 85P/Boethin.

References

[1] J. E. Randolph, J. A. Ayon, K. Leschly, R. N. Miyake, B. T. Tsurutani, "Innovations on the Solar Probe Mission," *Proceedings of the SPIE*, vol. 3442, Missions to the Sun II (San Diego, California, July 22, 1998), C. M. Korendyke, editor, pp. 13–21, November 1998.

[2] J. Randolph, J. Ayon, G. Harvey, W. Imbriale, R. Miyake, R. Mueller, B. Nesmith, P. Turner, R. Dirling, S. Rawal, and W. Vaughn, "The Solar Probe Mission and System Design History," *American Institute of Physics Proceedings*, vol. 387, p. 123, 1997.

[3] J. Randolph, J. Ayon, R. Dirling, W. Imbriale, R. Miyake, D. Le Queau, G. Olalde, E. Pierson, S. Rawal, B. Rivoire, J. Robert, C. Royere, R. Taylor, P. Valentine, and W. Vaughn, "The Solar Probe Shield/Antenna Materials Characterization," *CARBON*, vol. 37, pp. 1731–1739, 1999.

[4] J. Randolph, W. Imbriale, R. Miyake, E. Pierson, and R. Dirling, "The Solar Probe Heat Shield Development," presented at the Tri-Service *Sponsored Symposium on Advancements in Heatshield Technology* (Redstone Arsenal, Alabama), May 10, 2000.

[5] E. Embuido, *Phase I Solar Probe Feed Assembly Final Report*, contractor report from Composite Optics, Inc., JPL D-32848 (internal document), Jet Propulsion Laboratory, Pasadena, California, October 1999.

[6] E. Embuido, *Phase II Solar Probe Feed Assembly Final Report*, contractor report from Composite Optics, Inc., JPL D-32849 (internal document), Jet Propulsion Laboratory, Pasadena, California, January 2001.

[7] W. Imbriale, J. Randolph, and E. Embuido, "The Solar Probe Antenna," *IEEE International Symposium on Antennas and Propagation* (Monterey, California), pp. 3007–3010, June 2004.

[8] Deep Impact web site, Jet Propulsion Laboratory, Pasadena, California, web site accessed August 15, 2005. http://deepimpact.jpl.nasa.gov/

[9] R. E. Munson, "Conformal Microstrip Antennas and Microstrip Phased Arrays," *IEEE Transactions on Antennas and Propagation*, vol. AP-22, no. 1, pp. 74–78, January 1974.

[10] S. A. Long and M. D. Walton, "A Dual-Frequency Stacked Circular-Disc Antenna," *IEEE Transactions on Antennas and Propagation*, vol. AP-27, no. 2, pp. 270–273, March 1979.

[11] S. D. Targonski and D. M. Pozar, "Design of Wideband Circularly Polarized Aperture-Coupled Microstrip Antennas," *IEEE Transactions on Antennas and Propagation*, vol. AP-41, No. 2, pp. 214–220, February 1993.

[12] Ansoft, Pittsburg, Pennsylvania, web site accessed August 9, 2005. http://www.ansoft.com/

[13] J. Granholn, and K. Woelders, "Dual Polarization Stacked Microstrip Patch Antenna Array with Very Low Cross-Polarization," *IEEE Transactions on Antennas and Propagation*, vol. AP-49, no. 10, pp. 1393–1402, October 2001.

Chapter 10
Spacecraft Antenna Research and Development Activities Aimed at Future Missions

John Huang

Space missions of the Jet Propulsion Laboratory (JPL) of the National Aeronautics and Space Administration (NASA) can be categorized into two major areas: deep-space exploration and Earth remote sensing. As scientists have learned from the previous missions, higher capabilities and more stringent system requirements are being placed on future missions, such as longer distance communications, higher data rate, and finer radar imaging resolution. Almost all these stringent requirements call for higher-gain and larger-aperture spacecraft antennas. At the same time, however, lower mass and smaller stowage volume for the spacecraft antenna are demanded in order to reduce payload weight and reduce required shroud space, and thus minimize overall launch cost. To meet these goals, several space-deployable antenna concepts [1] have been investigated over the past several decades. To name a few, there were the Harris Corporation's hoop-column umbrella type, Lockheed's wrapped-rib version, TRW's sunflower antenna, and the more recent Astro mesh. All these deployable antennas are of the parabolic reflector type with metalized mesh reflecting surfaces. Because they have been parabolic with a relatively small focal length, they lack wide-angle beam scanning ability—only a few beamwidths can be scanned. The mesh surface also limits the upper frequency of operation to Ku-band or lower. In addition, some of these concepts suffer from higher risk because of too many mechanical components. One good example of mechanical component failure is the Galileo spacecraft,

which used the Harris radial rib mesh reflector that failed to deploy in space. To remedy these drawbacks, several new antenna concepts are being investigated at JPL for possible future-mission applications. These antenna concepts, separately discussed below, are the inflatable array antenna, foldable thin-membrane array, and reflectarray. The mechanical characteristics of inflatable antennas are discussed in Chapter 8. In addition, the wide swath ocean altimeter (WSOA) a reflectarray developed for, but not used on, the Ocean Surface Topography Mission (OSTM) is discussed in Section 7.6.

10.1 Inflatable Array Antenna

A deployable antenna using inflatable parabolic reflector concept was introduced [2] in the mid 1980s for achieving large aperture with low mass and small stowage volume. This concept was later demonstrated in a space shuttle (Endeavour STS-77 mission) experiment in 1996 [3] called the In-space Antenna Experiment (IAE), which used a 14-m diameter thin-membrane reflector (see also Section 8.1.6). The antenna, as shown in Fig. 10-1, had an annular inflatable tube to support a thin-membrane parabolic surface and three inflatable tubular struts to support a possible feed. This large-aperture antenna was successfully deployed in space, but, by a large margin, failed to meet the required surface tolerance. Thus, the full implementation of this concept is still hampered by the inability to achieve and maintain the required surface accuracy. In particular, it is believed that it would be difficult to maintain the

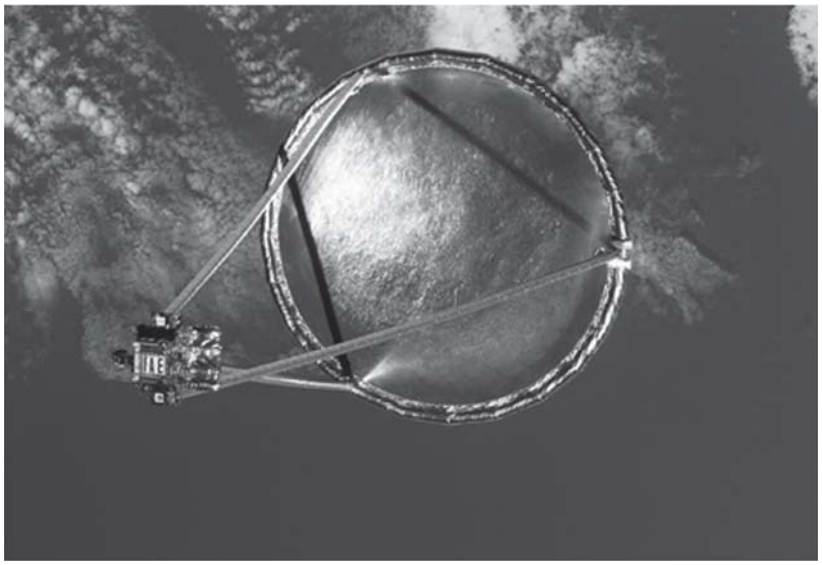

Fig. 10-1. Actual space-flight photo of the 14-m inflatable parabolic reflector (a Space Shuttle experiment in 1996).

desired surface accuracy of a large thin-membrane parabolic surface over the duration of a long space flight. To mitigate the difficulty associated with curved surfaces, a new class of deployable planar array technology is being developed [4,5]. It is believed that it would be significantly more reliable to maintain the required surface tolerance of a flat "natural" surface, such as a planar array, than a specifically curved "non-natural" surface, such as a parabolic reflector. In addition, a planar array offers the possibility of wide-angle beam scanning, which cannot be easily achieved by a parabolic reflector.

At JPL, two types of inflatable planar array antennas have recently been developed [6]. One is the inflatable synthetic aperture radar (SAR) multilayer microstrip array for Earth remote sensing at the L-band frequency. The other is the inflatable microstrip reflectarray for deep-space telecom application at the Ka-band frequency. Most of the radio frequency (RF) capabilities and a portion of the space-environment mechanical capabilities have already been demonstrated for these two antenna types under JPL efforts. The RF designs and the aperture membrane surfaces of these antennas were developed at JPL, while the inflatable structure developments and antenna integrations were mostly accomplished by ILC Dover, Inc. and L'Garde Corp. under JPL contracts. All these antennas were constructed and developed in a similar fashion with each basically constructed from an inflatable tubular frame that supports and tensions a multilayer thin-membrane RF radiating surface. They are deployed by a "rolling" mechanism, rather than by the "folding" mechanism. Multi-folding of the thin membrane radiating surface has not been used here to avoid the forming of large creases on the printed patch elements and transmission lines. Any large crease may significantly degrade the impedance matching of the microstrip circuit and hence the overall RF performance. As is shown later, these antenna developments have demonstrated that inflatable thin-membrane arrays are feasible across the microwave and millimeter-wave spectra. Further developments of these antennas are deemed necessary, in particular, in the area of qualifying the inflatable structures for space environment usage. The detailed description and performance of these two types of inflatable array antennas are separately presented in the following subsections.

10.1.1 Inflatable L-Band SAR Arrays

10.1.1.1 Antenna Description. The inflatable L-band SAR array, having an aperture size of 3.3 m × 1.0 m, is a technology demonstration model with 1/3 the size of the future full size (10 m × 3 m) array. Two such inflatable arrays were recently developed: one by ILC Dover, Inc. and the other by L'Garde Corp. For both antennas, the concepts and electrical designs were accomplished at JPL, while the inflatable structures were developed by the two companies. The ILC Dover unit is shown in Fig. 10-2, and the L'Garde unit is shown in

Fig. 10-3. Both units are very similar, and each basically is a rectangular frame of inflatable tubes that supports and tensions a three-layer thin-membrane radiating surface with microstrip patches and transmission lines. The inflatable tube of the ILC Dover unit has a diameter of 13 cm and is made of 0.25-mm thick urethane coated Kevlar material. The L'Garde's inflatable tube has a diameter of 9 cm and is made of 0.08-mm-thick rigidizable stretched aluminum material. The inflatable tubes need to be rigidized once they are deployed in space so that they could avoid the need of constant air pressure and the concern of air leakage due to space debris damage. This technology of tube rigidization is further discussed in Section 10.1.3.2. The three membrane layers are separated 1.27 cm between the top radiator layer and the middle ground-plane layer and 0.635 cm between the middle layer and the bottom transmission-line layer. The bottom transmission lines excite the top radiating patches, not by rigid feed-through pins, but by a set of aperture coupling slots [7] so that no

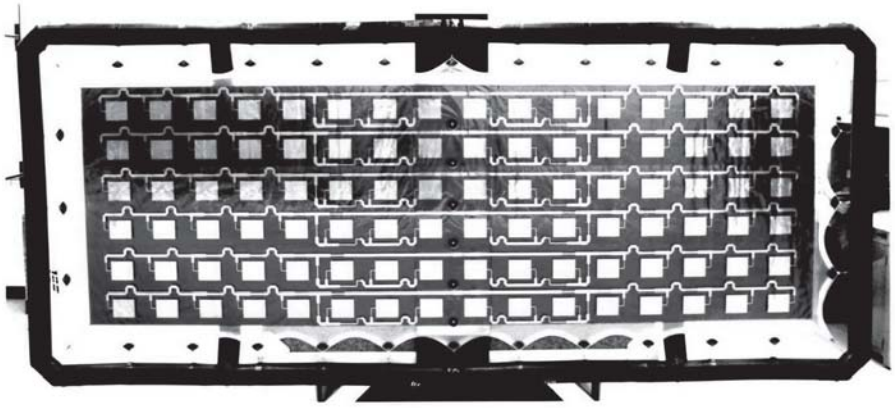

Fig. 10-2. Inflatable L-band SAR array (3.3 m × 1 m) developed by JPL and ILC Dover Inc.

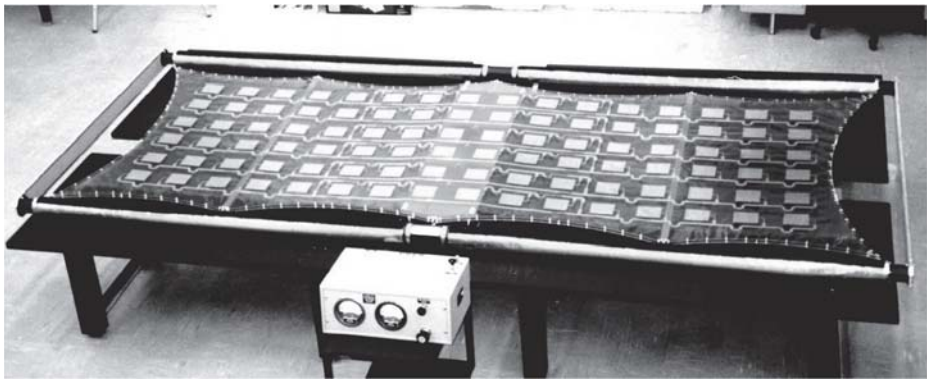

Fig. 10-3. Inflatable L-band SAR array (3.3 m × 1 m) developed by JPL and L'Garde Corp.

soldering is required here. The connection between the edges of these membranes and the inflated tubular frame is made by a series of catenary attachment points and tensioning cords. The required spacings between the three membranes are maintained by the tensioning of the catenary cords, the honeycomb spacing panels and bars, and small spacer blocks at each of the catenary points. The membrane material used is a thin film of 5-μm thick copper cladding on a 0.13-mm thick Kapton dielectric material. It should be noted that all metal claddings (radiating elements, transmission lines, and ground plane) should have a minimum thickness of at least twice the skin depth at the operating frequency. Otherwise, radiation will leak through the thin metal and reduce the antenna efficiency.

10.1.1.2 Antenna Test Results. The L'Garde unit achieved a total antenna mass of 11 kg with an average mass density of 3.3 kg/m^2. The ILC Dover unit has a slightly higher mass. The surface flatness of the L'Garde unit was measured to be ±0.28 mm, which is better than the requirement of ±0.8 mm. The ILC Dover's surface flatness was measured to be ±0.7 mm. Both antenna units achieved bandwidths slightly wider than the required 80 MHz, and achieved port isolation between the two orthogonal polarizations of greater than 40 dB within the required bandwidth. The radiation patterns of the ILC Dover unit measured in two principal planes at 1.25 gigahertz (GHz) are given in Fig. 10-4. Sidelobe levels of –14 dB in the azimuth plane and –12 dB in the elevation plane are reasonable for this uniformly distributed array. The cross-polarization level of less than –20 dB within the main beam region is also considered acceptable for this radar application. Patterns measured at frequencies from 1.21 to 1.29 GHz are very similar to those shown in Fig. 10-4 without significant degradation. The measured peak gain of ILC Dover's unit is 25.2 dB at 1.25 GHz, which corresponds to an aperture efficiency of 52 percent. L'Garde's unit has a peak gain of 26.7 dB and an aperture efficiency of 74 percent. The better efficiency of L'Garde's unit is the result of better surface tolerance and more precise membrane spacing. Nevertheless, both units are considered quite good as they are the first demonstration models ever developed. Both these inflatable array antennas had masses less than half of those with rigid structures, while achieving similar radiation efficiencies. Although another type of deployable antenna with mesh structure achieved similar, or even in some cases smaller masses, these mesh antennas can only be used as reflectors but not as arrays.

10.1.2 Ka-Band 3-m Reflectarray

10.1.2.1 Antenna Description. The details of the reflectarray antenna technology are discussed further in Section 10.4. The reflectarray is used here because of its unique feature of having a flat reflecting aperture. A photograph

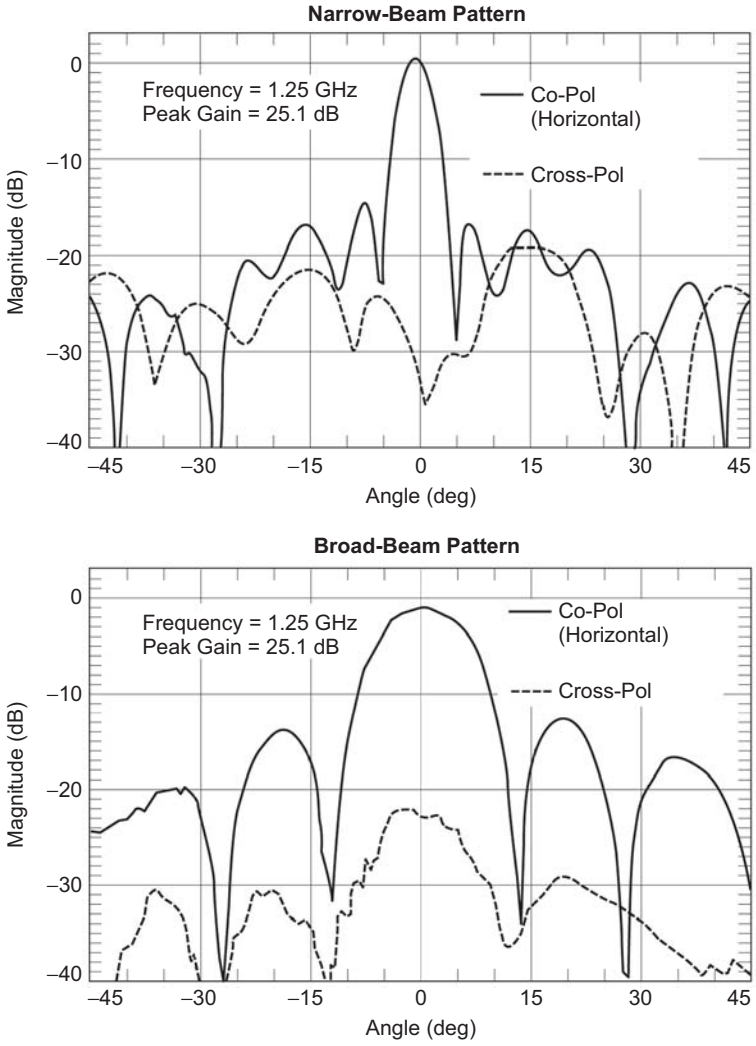

Fig. 10-4. Measured two principal-plane patterns of the ILC Dover inflatable array for (a) narrow-beam pattern, (b) broad-beam pattern.

of the inflatable Ka-band reflectarray antenna with a 3-m diameter aperture is shown in Fig. 10-5. This antenna was co-developed by JPL and ILC Dover, Inc. It consists of a horseshoe shaped inflatable tube that supports and tensions a 3-m aperture membrane. The tube, 25 cm in diameter, is made of urethane-coated Kevlar and is inflated to 3.0 pound-per-square-inch (psi) (21 kPa) pressure, which translates to about 90 psi (620 kPa) of tension force to the aperture membrane. The inflatable tube is connected to the aperture membrane at 16 catenary points with spring-loaded tension cords. Each connecting point has displacement adjustment capability in the x, y, z directions so that the

Fig. 10-5. Inflatable Ka-band 3-m reflectarray antenna. The white-colored structure in front of the aperture is a membrane-flatness measurement device.

circumference of the circular aperture membrane can be made into a single plane orthogonal to the feedhorn axis. The single-layer aperture membrane is a 5-mil (0.13-mm) thick Uplex dielectric material (a brand of polyimide) with both sides clad with 5-μm thick copper. The copper on one side is etched to form approximately 200,000 microstrip patch elements, while the copper on the other side is un-etched and serves as the ground plane for the patch elements. Portion of the microstrip elements are shown in Fig. 10-6. The elements use a variable rotation technique [8] to provide the needed electrical phases. The inflatable tripod tubes, asymmetrically located on the top portion of the horseshoe structure, are used to support a Ka-band corrugated feedhorn. The horseshoe-shaped main tube structure and the asymmetrically connected tripod tubes are uniquely designed in geometry to avoid membrane damage and flatness deviation when the deflated antenna structure is rolled up.

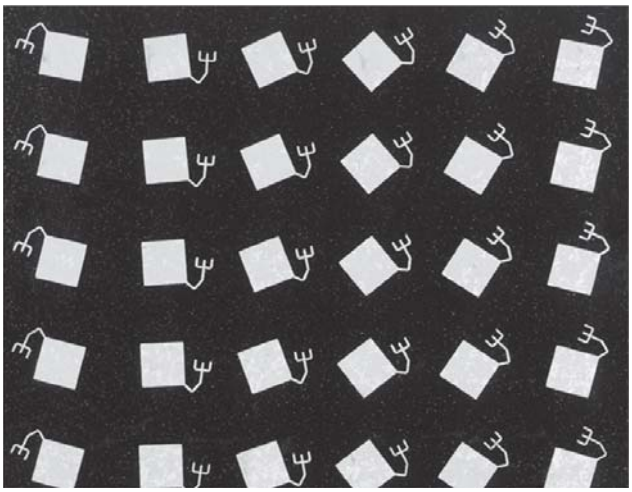

Fig. 10-6. Close-up view of the Ka-band reflectarray patch elements. A rotational technique is used to achieve the desired element electrical phase.

10.1.2.2 Antenna Test Results. The antenna's RF tests were performed at the in-door compact range of Composite Optics, Inc. (COI), where antennas as large as 10 m can be tested. Figure 10-7 shows a typical elevation pattern of the antenna with measurements of a 0.22-deg beamwidth. The sidelobe level is –30 dB or lower below the main beam peak, and the cross-polarization level is –40 dB or lower. All patch elements are circularly polarized and are identical in dimensions. Their angular rotations are different and are designed to provide correct phase delays to achieve a co-phasal aperture distribution. The antenna gain was measured versus frequency. The results show that the antenna is tuned to the desired frequency of 32.0 GHz with a –3-dB bandwidth of 550 MHz. A peak gain of 54.4 decibels referenced to a circularly polarized, theoretical isotropic radiator (dBic) was measured. This measured antenna gain indicates an aperture efficiency of 30 percent, which is lower than the expected 40 percent. This relatively lower efficiency was the result of large element resistive loss due to the poor loss-tangent material of Kapton used, non-optimal substrate thickness, large feed-struts blockage, and non-optimal feed illumination. The phase delay line that is attached to each patch element has a certain amount of impedance mismatch to the patch, and thus, sends a certain amount of RF power into undesirable cross-polarization energy, and this results in poor radiation efficiency. It is quite certain that future development can improve the efficiency to the expected 40 percent or higher. The measured surface flatness data of the antenna aperture shows a root mean square (RMS) value of 0.2 mm, while the required surface RMS value is 0.5 mm. This good surface flatness is also reflected by the well-formed far-field pattern with

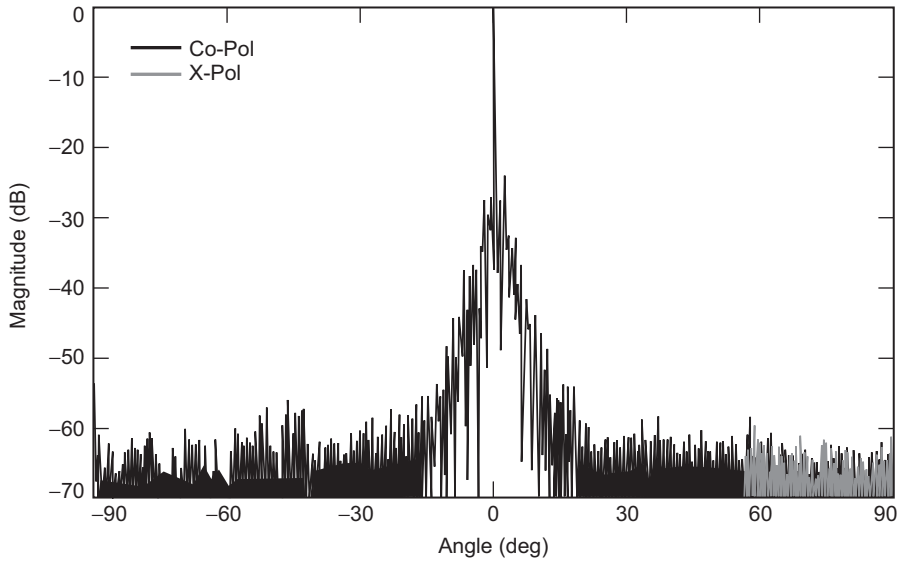

Fig. 10-7. Measured radiation pattern of the 3-m Ka-band inflatable reflectarray.

expected main beamwidth and low sidelobe level. A solid antenna can certainly achieve surface flatness better than 0.2 mm rms, but with significantly increased mass. Although the aperture efficiency of the inflatable reflectarray was not as expected, the achievement of excellent membrane flatness indicates that inflatable array antenna at Ka-band is now feasible.

10.1.2.3 Improved Ka-Band 3-m Reflectarray. The above Ka-band 3-m inflatable reflectarray was built primarily for laboratory demonstration of its RF performance only. Since then, a second model was developed to demonstrate its mechanical integrity. There are two major differences in the models. One is that the second model has its inflatable reflectarray surface deployed without the deployment of a tripod-supported feed. The offset feed is fixed on the spacecraft bus as illustrated in Fig. 10-8, where the inflatable surface, shown in Fig. 10-9, can be rolled up and down as a movie screen. The second major difference is that the inflatable tubes are made of rigidizable aluminum reinforced internally by using carpenter extendable-ruler tapes as shown in Fig. 10-10. This type of tube is named spring-tape reinforced (STR) boom. Once the booms are inflated in space, the aluminum membrane soon rigidizes (see Section 10.1.3.2), and the inflation gas is no longer needed. In addition, in the event that the tubes are penetrated by small space debris, they will remain rigid to provide proper support for the reflectarray membranes. The carpenter tapes are used as reinforcement to provide additional axial load capacity as well as some orthogonal load capacity to each tube.

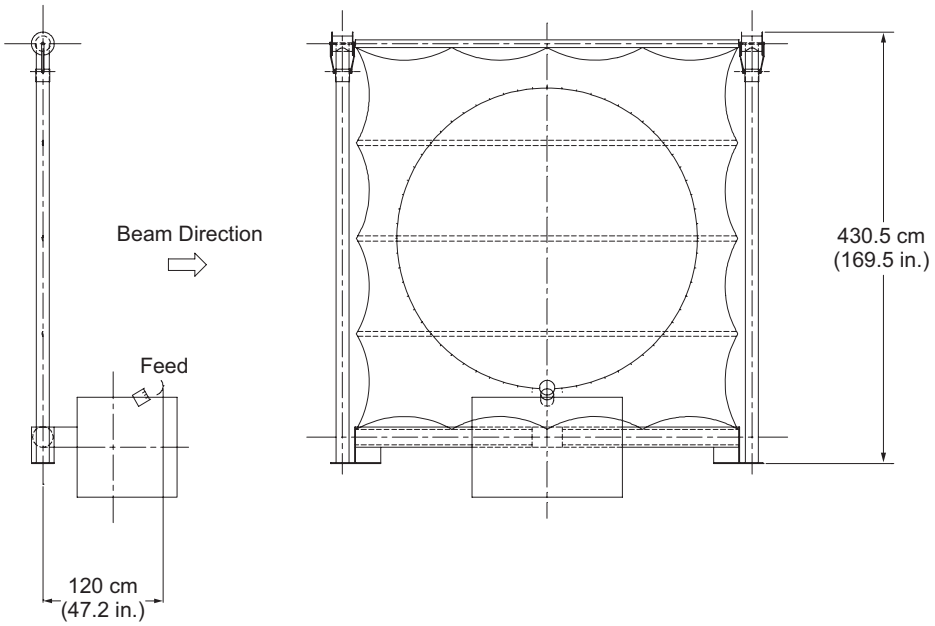

Fig. 10-8. Configuration of offset-fed inflatable reflectarray on spacecraft (rectangular box). Inflatable tubes allow the aperture to roll up.

10.1.2.4 Thermal Analysis of the Inflatable Reflectarray. The most critical structural components of the 3-m inflatable reflectarray antenna, illustrated in Fig. 10-8, are the two STR aluminum laminate inflatable/self-rigidizable booms [9]. Due to other mechanical reasons, these two booms cannot be thermally protected with thermal blankets and will undergo thermal distortions in space. This section presents results of a study of structural integrity of these booms under space thermal environments, as well as the effects of thermal distortion of the booms on surface deviation of the RF membrane [10].

The in-space structural integrity of these booms is first investigated. After in-space deployment of the antenna, the two STR booms are continuously loaded by axial forces that react to the tension in the RF membrane. The two booms will also bow due to the circumferentially uneven thermal expansions. This leads to significant reductions in the buckling capabilities of the booms. The Earth orbit's thermal load condition was used to calculate the temperature distributions and gradients of a single boom as shown in Fig. 10-11. The bending of the boom introduced by temperature gradients was then determined. The buckling capability of the bended boom was subsequently calculated to be 916 N. The baseline STR boom is capable of taking the required load, which is 156 N. Since the Earth application has the most severe thermal environment among all near-term mission applications, it was concluded that the STR booms

Fig. 10-9. 3-m Ka-band reflectarray membrane with 200,000 elements supported by two rigidizable inflatable tubes (shown on the right and left sides of the photo).

with current design and configuration are structurally strong enough for both near-Earth and deep-space applications in terms of buckling capability.

The thermally introduced deviation of the RF membrane is also investigated in this study. The case in which the antenna membrane aperture directly faces the Sun is identified as the worst situation because at that moment the inflatable antenna structure has the least moment of inertia to resist the thermal loads. The RF membrane deviations of the antenna, equipped with baseline STR booms, was analyzed. Figure 10-12 provides a rough illustration of how the bending occurs. The membrane tilt angle is calculated to be 0.758 deg, which is three times larger than the antenna beam-width (0.22 deg). This large tilt angle would lead to unacceptable degradation of RF performance and must be reduced. There are several ways to remedy this undesirable situation, including: (1) replacing steel spring tapes of the boom with composite spring tapes, since composite material is less sensitive to temperature change, (2) mechanically adapting the feed position to the membrane, and (3) electronically adapting the feed by using an array of feeds with a phase-compensation technique. However, replacing steel spring tapes of the boom with composite spring tapes is the most feasible and simplest way. To validate this, two antennas (one with the baseline STR booms and the other with booms that have their steel spring tapes replaced by composite tapes) were analyzed

Fig. 10-10. Rigidizable inflatable aluminum tubes reinforced by carpenter tapes. Right tube shows the end cap.

for thermal environments of the Earth, Mars, and Jupiter orbits. It was concluded from the results of these analyses that the current booms with steel tapes are not acceptable for Earth missions, but are acceptable for Mars and Jupiter missions. Conversely, the boom design with composite spring tapes is acceptable for all Earth, Mars, and Jupiter missions.

10.1.2.5 Recent Development of a 10-m Structure. It is envisioned that future inflatable antennas will not be limited to the size of 3 m as presented above. Sizes in the order of 5, 10, 20 m, etc., are likely to occur, depending on the distance that the spacecraft will travel and the needed data capacity. Analysis has shown that, each time the inflatable antenna size is increased approximately by twice, new challenges will be encountered. A new program was initiated in late 2004 to develop a larger inflatable reflectarray with a diameter in the order of 10 m. Several mechanical challenges are being studied. The most important one is the development of the 10-m long inflatable boom. This 10-m boom and its recent development are discussed in the following paragraph.

As the antenna aperture size increases, the strength of the inflatable booms also need to be increased in order to provide proper support and tensioning forces to the reflectarray surface. Analysis indicates that not only the boom diameter needs to be increased, the strength of the axial “carpenter” tapes also need to be enhanced by increasing either the tape size or its quantity. Furthermore, it was determined that in addition to these axial carpenter tapes, circumferential tapes are needed to enhance the boom’s strength in the non-

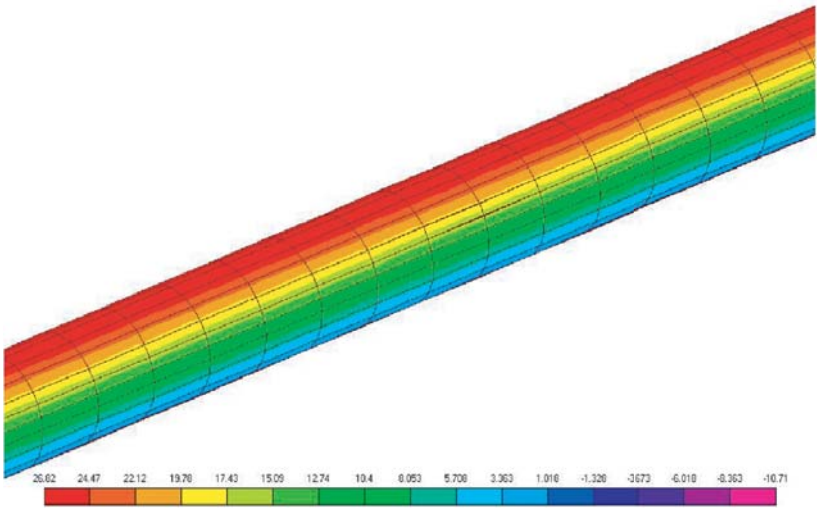

Fig. 10-11. Close-up view of temperature distribution of the 3.5-m inflatable boom. The dark color on top of the boom indicates the Sun's illumination with a temperature of 26.82 deg C, while the bottom of the boom's shadow region has a temperature of –10.71 deg C.

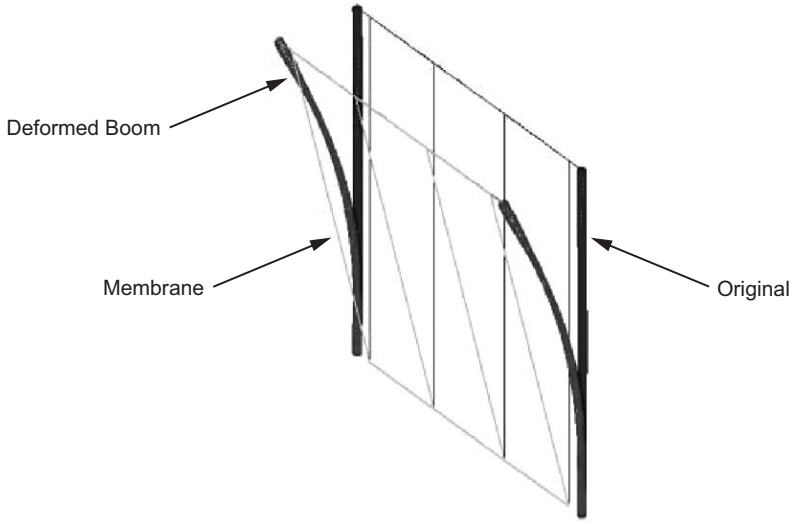

Fig. 10-12. Bending of the reflectarray membrane aperture due to thermally deformed inflatable booms.

axial direction so that buckling of the boom would not occur. This new boom structure, with both axial and circumferential tapes, is illustrated by a drawing and an actual photo in Fig. 10-13. Consequently, a 10-m long boom has been

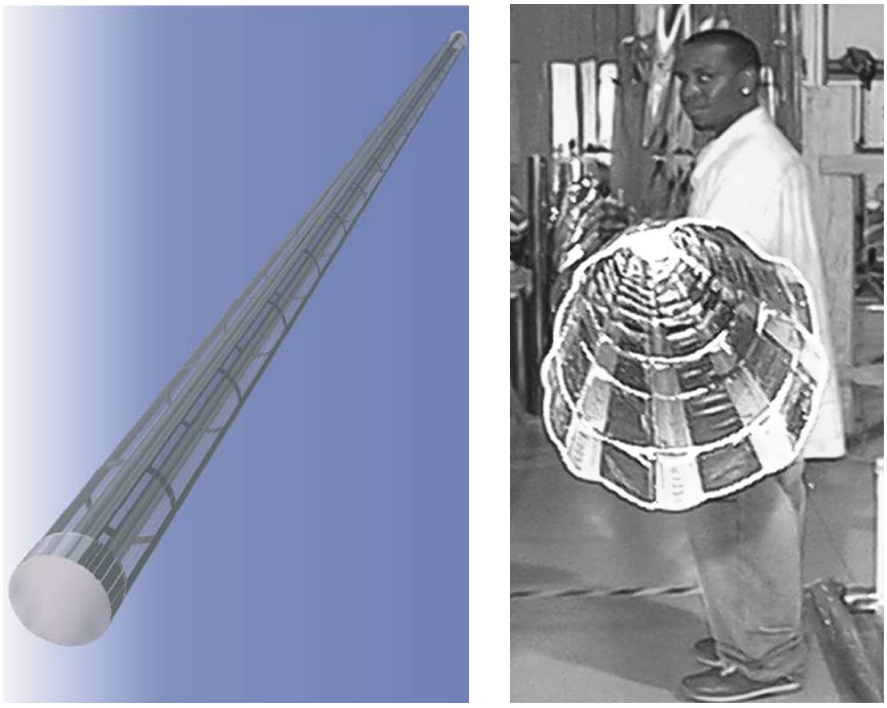

Fig. 10-13. Inflatable boom with axial and circumferential tapes.

constructed with rigidizable aluminum foil and both axial and circumferential tapes as shown in Fig. 10-14. This boom, having a diameter of 25 cm, will be tested under vibration to determine its mechanical resonant modes and strength. To carry out the vibration test under zero gravitational-force (0-g) effect, a special boom-support structure as shown in Fig. 10-14 was constructed. The 10-m long boom is hung along its length inside the support structure by many flexible bungee cords. A vibrating "gun" is used to hit one end of the boom horizontally. In this way, the boom will vibrate and show resonant modes in the horizontal direction with minimum g-force effect.

10.1.3 Technical Challenges for Inflatable Array Antennas

The above subsections presented two different types of inflatable arrays with each being a multilayer planar aperture surface that is supported and tensioned, through a catenary system, by several inflated tubular elements. In order to successfully develop these types of inflatable array antennas at any frequency throughout the microwave and millimeter-wave spectrums, several technical challenges must be addressed and resolved in the future. These challenges are separately discussed in the following subsections.

Fig. 10-14. 10-m inflatable boom and its support structure for vibration test.

10.1.3.1 Membrane Flatness and Separation. In order for a planar array to maintain certain required aperture efficiency and sidelobe/cross-polarization levels, the aperture membrane must maintain certain flatness accuracy. This required flatness, depending on the requirements, should generally be between

1/20th and 1/40th of a free-space wavelength. For a multilayer membrane aperture, specific membrane separation distances must also be maintained, especially for a microstrip array. If microstrip patches are separated with slightly different distances from their ground plane, they will resonate at different RF frequencies, which implies a very inefficient array aperture at the required operating frequency. Generally, the required membrane separation tolerance should be smaller than 1/20th of the absolute separation distance.

The above stringent flatness requirement is currently being addressed primarily by the tension force of the inflatable tube. The tighter the flatness requirement, the larger the tension force required, which implies that a larger inflation tube and stronger tube material are needed. All these will result in larger antenna mass, which is undesirable. The required membrane separation tolerance is currently met by, in addition to the tension force, using sparsely located small spacers. Tighter membrane separation tolerance implies that larger tension force and more spacers are needed, which also implies larger antenna mass. In the future, innovative techniques are needed for maintaining the required membrane flatness and layer separation without significantly increasing the antenna mass.

10.1.3.2 Inflatable Tube In-Space Rigidization Techniques. For any long-term space application, the inflatable tube needs to be rigidized once it is inflated in space. This is to avoid deflation and loss of tension force due to leaks in the inflatable structure or structures caused by impacting micrometeoriods and space debris. If the inflatable tubes are rigidized upon the completion of deployment, the need to carry a large amount of make-up gas to compensate for the leaks can thus be eliminated.

There are several rigidization techniques. One early technique was enabled by the development of several polymers that can be cured by space environments [11], such as vacuum, ultraviolet (UV) light, and cold temperature. A second technique is the use of stretched aluminum [12]. When thin aluminum foil is stretched by inflation pressure just above the aluminum's yield point, it rigidizes. Unfortunately, when the thin-wall aluminum tube becomes very long, it cannot carry large non-axial or bending loads. Aluminum with reinforced laminate material needs to be investigated. The third method is called hydro-gel rigidization [13], which uses woven graphite fabric impregnated with a water-soluble resin (hydro-gel). When evaporation of the water content occurs in space vacuum environment, the dehydrated gel fabric rigidizes to give structural stiffness. This rigidization technique, as well as the stretched aluminum, is a reversible process, which will allow several ground deployment tests prior to space flight. The fourth technique uses heat-cured thermoplastic material. Heating wires or electric resistive wires are imbedded into a soft plastic material, which rigidizes when heated to a certain

temperature. This curing process is also reversible; however, it may require a large amount of electric power depending on the size of the inflatable structure.

All the above techniques have certain advantages, as well as disadvantages. They require continued investigation and improvement. For each particular mission, their performance parameters, such as mass density, curing time, and bending stiffness, need to be subjected to a tradeoff study for selecting an optimal technique. Regardless of the rigidization technique, one major challenge is for the deployed structure to maintain its original intended structure shape and surface accuracy after rigidization.

10.1.3.3 Controlled Deployment Mechanism. In a space mission, there is a high probability that an uncontrolled inflation of a large inflatable structure might lead to self-entanglement, as well as damage to other spacecraft hardware. Thus, an inflatable antenna must be deployed in a well-controlled manner in both time and space domains. There are several controlled development mechanisms. One uses the compartmental valve control technique where the long inflatable tube is divided into a series of sectional compartments with a pressure-regulated valve installed at the beginning of each compartment. As the inflation gas enters, the tube gets sequentially deployed in a controlled manner. A second mechanism uses long coil springs, which are embedded along the inner walls of the inflatable tube. A controlled deployment of the tube is achieved by balancing the inflation pressure and the restoring force of the spring. The third technique is to use a long Velcro strip glued to the outside and along the long dimension of the tube wall. As the tube becomes inflated, the Velcro strip provides a certain amount of resistance force and thus achieves the controlled deployment. This technique, which already has space flight heritage, offers a significant advantage over the coil spring method because the Velcro strip, unlike the coil spring, will not impose any restoring force on the deployed tube when the inflation deployment is completed. The fourth technique of controlled deployment, proposed by L'Garde Corp., involves the use of a mandrel. During the deployment process, the inflation tube is forced to go over a guiding mandrel, which introduces a frictional force to balance the inflation pressure and to achieve the controlled deployment.

Research efforts should continue in the above controlled-deployment mechanisms, and improved or innovative concepts should be developed to minimize the mechanism's mass and risk impacts to the overall antenna system.

10.1.3.4 Packaging Efficiency. The inflation-deployment techniques currently used for array-type antennas are limited to the roll-up mechanism. No folding of the membrane is currently allowed in order to avoid the formation of large creases and cracks in the very thin copper traces on the membrane surface. Therefore, when the antenna is rolled up, its packaged minimum-achievable dimension is the short dimension of a rectangular aperture or the diameter of a

circular aperture. For examples, for a 10-m by 3-m aperture antenna, the packaged best-achievable dimension would be 3 m long. For a 10-m by 10-m aperture, the best-packaged dimension would be 10 m long, which can hardly fit into any current launch rocket. Therefore, it is imperative that innovative deployment techniques must be developed for future very large inflatable-array antennas.

10.1.3.5 Membrane Mountable Transmit/Receive (T/R) Modules. One of the major advantages of the inflatable-array antenna over that of the inflatable-reflector antenna is that the array antenna has the capability of achieving wide-angle beam scanning. To achieve beam scanning in both principle planes of a large array, many transmit/receive (T/R) amplifier modules with phase shifters need to be installed throughout the array aperture. Although current state-of-the-art technologies provide various miniaturized T/R modules, the packaged configurations of these modules, with significant mass and volume, preclude mounting onto the thin membrane surface. Very thin and low mass T/R modules should be developed in the future to preserve the beam-scanning capability of the array antenna. A very recent development of placing discrete amplifier and phase shifter components on thin membrane is to be presented in Section 10.3.

10.1.3.6 Modeling and Simulation of Static and Dynamic Space Environmental Effects. Inflatable antennas are a fairly new mechanical structure, and their structural form may vary significantly from one antenna to another. Accurate mathematical modeling and simulation techniques must be developed to predict the in-space static and dynamic effects for a variety of inflatable antenna types. Orbital and deep-space thermal effects, as discussed earlier, may distort the shape of the inflatable tubes or fatigue the aperture membranes. Spacecraft maneuvering will induce a natural vibration of the inflatable structure, which may also distort or damage the antenna. The effects of these static and dynamic forces on the inflatable structure need to be well understood through accurate calculation and/or simulation.

10.1.3.7 RF Design Challenges. Bandwidth performance is always an issue when an array antenna is involved. For example, with inflatable synthetic aperture radar (SAR) arrays, the technique of using series/parallel feed lines with good bandwidth for very large aperture antennas is still a challenging task. In the area of inflatable reflectarray, due to the use of phase delay lines, instead of time delay lines, bandwidth of more than 5 percent is very difficult to achieve. Dual-band or even triple-band reflectarray technology should be developed in the future to counter the bandwidth issue.

10.2 Foldable Frame-Supported Thin-Membrane Array

For Earth remote-sensing applications, a SAR typically employs an antenna with a fairly long along-track aperture in order to achieve the required resolution, swath width, and data rate. 10-m-long antennas, such as those for Seasat [14] and the SIR-A, -B, and -C [15] series, have been flown previously, and 50-m-long to 100-m-long apertures are being planned for the future. To maintain an acceptable electrical flatness across these long apertures, very massive antenna support and deployment structures have been and will be needed. For example, the fixed-beam L-band Seasat antenna, which used a microstrip array with a honeycomb substrate and 10-m × 3-m aperture, had a mass of 250 kg (including deployment mechanism). The electronic-beam-scanning L/C/X-band shuttle-based SIR-C antenna with similar aperture size is much heavier and had a mass of 1800 kg. These massive antenna systems generally require a launch vehicle with large stowage volume and heavy-payload-lift capability. On the other hand, in order to achieve high launch-volume efficiency and to reduce payload weight, low-mass inflatable array antennas are currently being developed as presented in the previous sections. However, it is unlikely that a beam-scanning inflatable phased array will be achieved in the near future prior to the availability of membrane-mountable electronics, T/R modules, and phase shifters. The concept presented in this section would achieve a deployable antenna with extreme light weight and, at the same time, have the capability of electronic beam scanning. This concept uses foldable low-mass rigid frames to support a set of multi-layer thin-membrane radiating apertures. The phase shifters and T/R modules can be rigidly mounted onto the frames. The frames are deployed by using the novel "carpenter tape" hinge, which is a simple, low cost, low mass, and reliable deployment and latching mechanism. With this foldable thin-membrane array concept [16], it is believed that Earth remote-sensing SAR antennas, in the near future, can achieve electronic beam scanning with low mass and large deployable apertures.

10.2.1 Antenna Description

The complete array antenna, with an aperture of 10 m × 2.85 m, would consist of 14 foldable panels that are made deployable by using the carpenter-tape hinges. Prior to deployment, these panels could be folded up to form a relatively small stowed volume of 2.85 m × 0.7 m × 0.9 m. In this development effort, instead of the full-size array, only a half array with 7 panels was fabricated and tested. This half array, shown in a photograph in Fig. 10-15, has a total radiating aperture of 5 m × 2.85 m. Each panel of this half array, sketched in Fig. 10-16, is a rectangular rigid frame that supports a two-layer, thin-membrane, L-band subarray aperture. The rigid frame is made of very low-

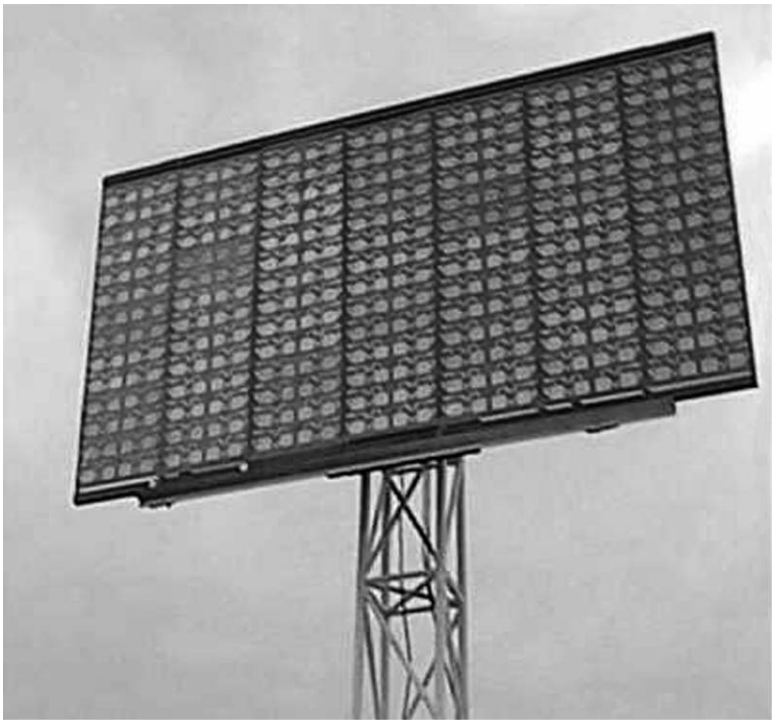

Fig. 10-15. Photograph of the half-size thin-membrane array with seven foldable panels, shown on a test fixture at an outdoor far-field range.

mass graphite composite material with honeycomb core and graphite epoxy face sheets. Each framed aperture has an aperture size of 2.85 m × 0.71 m and 14 rows of microstrip patch radiators with each row consisting of two 1 × 2 series-fed dual-polarized subarrays. The spacing between any two adjacent rows is 0.8 free-space-wavelength at the center operating frequency of 1.25 GHz. The spacing between adjacent patches in the horizontal direction is 0.74 free-space-wavelength. Each 1 × 2 subarray, as sketched in Fig. 10-16, can be connected to T/R modules that may be rigidly mounted onto the frame. The chief advantage of this "frame" concept is that each frame is able to rigidly support an appropriate number of T/R modules and phase shifters for achieving the desired beam scan. With this particular design, the complete array is able to scan its beam to ±20 deg in the vertical direction and a few degrees in the horizontal direction. In this development, however, T/R modules and phase shifters were not used, and all the 1 × 2 subarrays were connected together behind the ground plane via coax cables and discrete power dividers. For the two-layer thin-membrane structure, as shown in the photograph in Fig. 10-17, the top layer has all the radiating patches and microstrip transmission lines, while the bottom layer serves as the ground plane. Both layers are made of

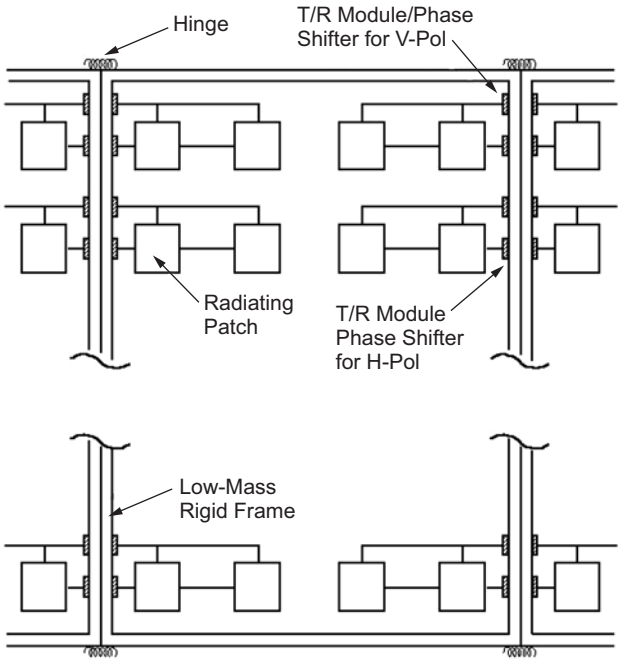

Fig. 10-16. Sketch of each framed panel with major components.

5-μm-thick copper deposited on 0.05-mm-thick Kapton membrane. The two layers are separated 1.3 cm apart for the purpose of achieving the required 80-MHz RF bandwidth.

To deploy the foldable panels, the novel but simple "carpenter tape" hinges were used. Figure 10-18 shows the carpenter tape hinge in its deployed and folded positions. Each hinge is comprised of two tape stacks with their concave side facing inward. Each of the stacks may have one to four layers of tapes. The tape hinge has two distinct performance regimes: When folded, it exhibits nonlinear behavior, with the ability to store significant amounts of energy in the tape deformation, which is released upon deployment. When latched after deployment, it acts as a rather stiff composite beam (linear behavior) to support the panels.

10.2.2 Antenna Performance Results

The half-size (5 m × 2.85 m) breadboard array antenna, shown in Fig. 10-15, was measured for its radiation characteristics at an outdoor far-field range. The typical measured patterns at 1.25 GHz for the vertically polarized array in both the E- and H-plane cuts are shown in Figs. 10-19 and 10-20, respectively. The peak sidelobe is about –12 dB, which is close to that expected

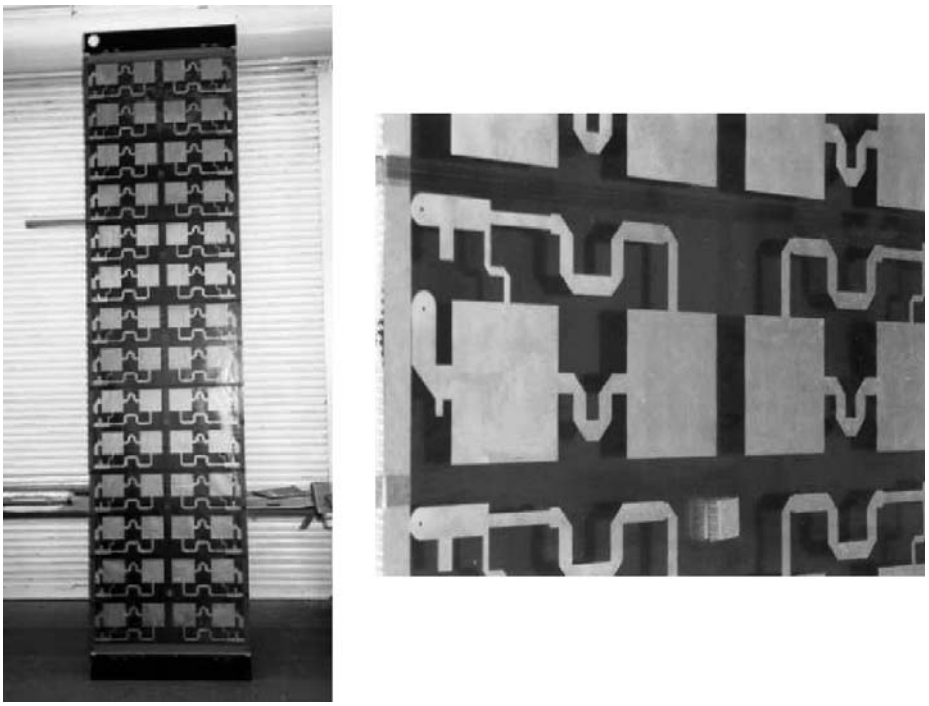

Fig. 10-17. Photographs of a single framed panel and a close-up view of the two-layer membrane patch elements.

for a uniformly distributed array. The cross-polarization lobes are mostly below –20 dB in the H-plane pattern, but they show –15 dB level in the E-plane. For SAR application, reduction of this –15 dB cross-polarization radiation to –20 dB level is needed in future development of this array. The measured 3-dB beamwidths in the E-plane and H-plane directions are 4.47 deg and 2.44 deg, respectively, which are very close to those expected for a uniformly distributed aperture of 2.85 m × 5 m. The input return losses measured at the inputs of the 1×2 subarray are below the required –10 dB level over a bandwidth of ±40 MHz centered at 1.25 GHz. The measured array efficiency (not including the losses of the coax cables and discrete power dividers) is 85 percent, which is considered quite good.

10.3 Thin-Membrane Array Antenna for Beam Scanning Application

An electronic beam scanning phased-array antenna with very large apertures (10 m to 100 m dimensions) will provide a wide range of radar capabilities for NASA's future Earth science missions, as well as deep-space planetary missions. For these very large arrays, the antenna mass, volume, and

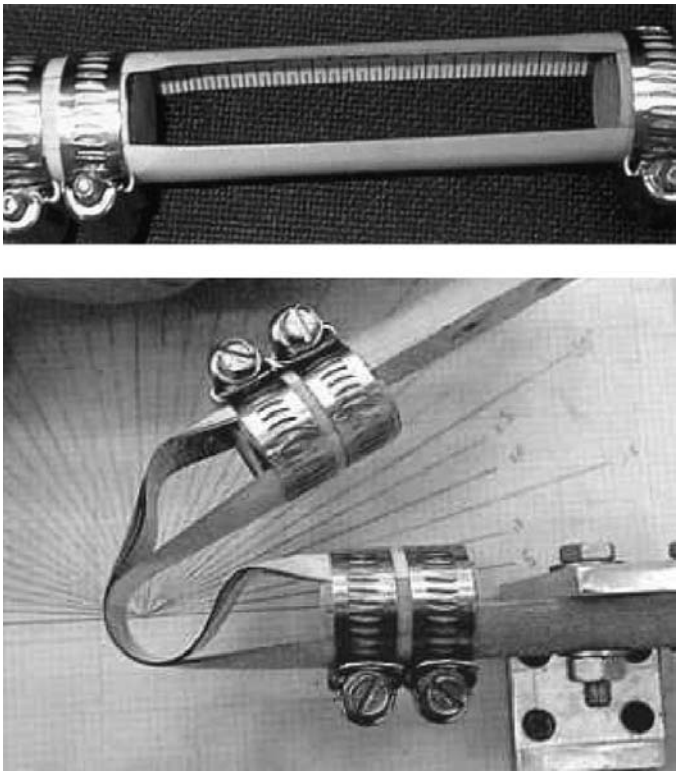

Fig. 10-18. The "carpenter tape" hinge.

cost will be prohibitive if the technology relies on previous rigid-panel phased arrays, such as the SIR-C antenna [17]. Previously developed membrane-based deployable passive array antennas [6] provided a means to reduce mass, launch-vehicle stowage volume, and overall cost compared to rigid antenna systems. However, to realize beam-scanning capability with thin-membrane-mounted active components, one of the challenges, as mentioned previously, is to develop T/R modules having the ability to integrate with thin-membrane patch arrays. The thin-membrane arrays must also be configured for easy integration with the T/R modules. As an initial effort, JPL has recently successfully developed a small L-band T/R-module-mounted thin-membrane array with 4×2 patch elements [18,19].

To avoid the use of many rigid coax feeding pins and associated solderings on thin membranes, aperture-coupling [7] is the ideal method for a large set of microstrip lines to feed a large array of microstrip patch elements. This aperture-coupling technique is employed here for the 4×2 array. Previously developed inflatable L-band array antennas [6] used three layers of thin

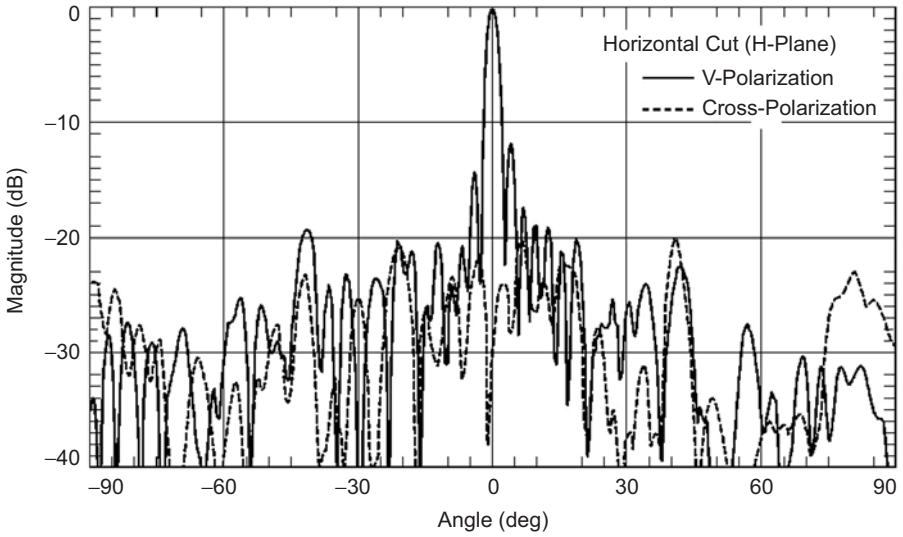

Fig. 10-19. Measured vertical-polarization pattern in the horizontal cut of Fig. 10-13.

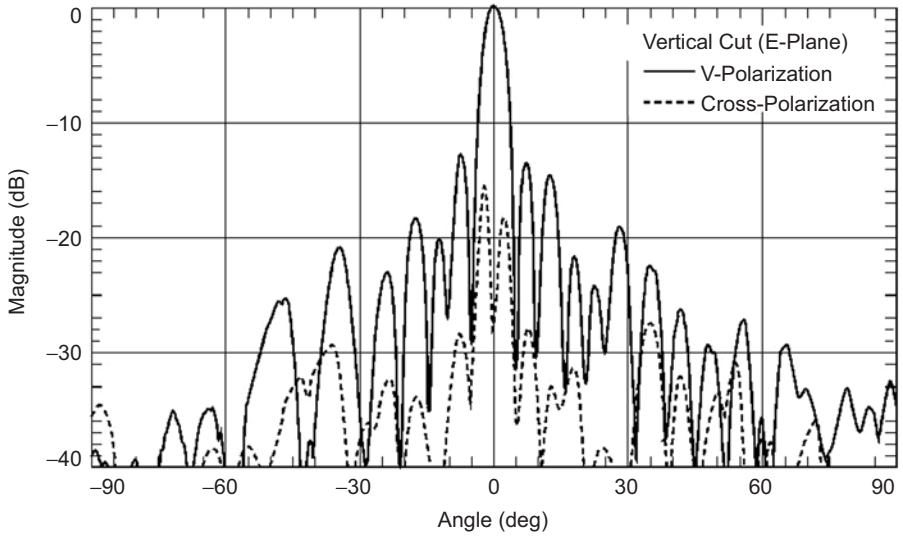

Fig. 10-20. Measured vertical-polarization pattern in the vertical cut of Fig. 10-13.

membranes as sketched in Fig. 10-21. These three layers, at the low microwave frequency of L-band, are separated with relatively large empty spaces of 0.64 cm and 1.27 cm. These large spaces make it difficult to integrate with small-size T/R modules, since small T/R modules with many electronic circuits

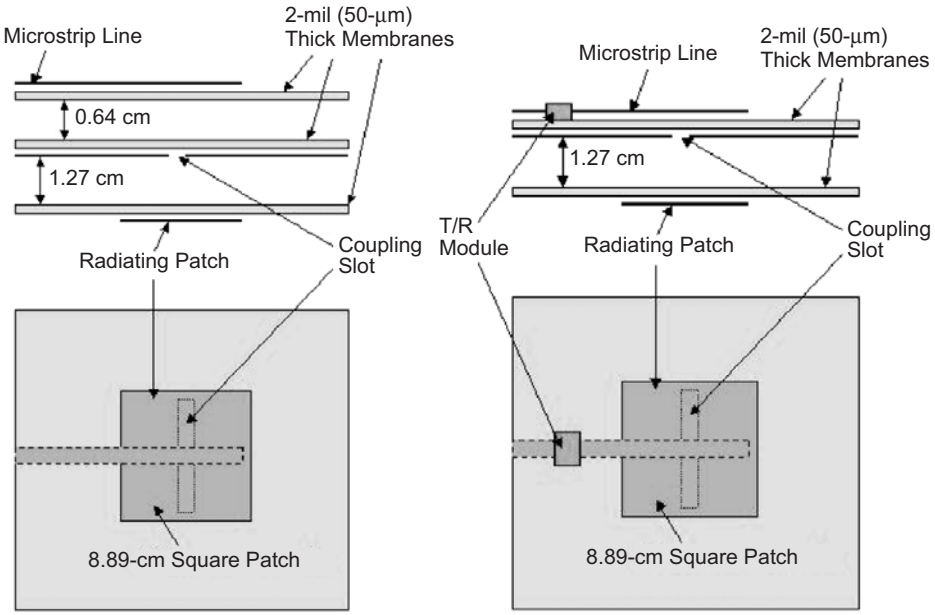

Fig. 10-21. Sketches of thin-membrane patch antennas. Left sketch is the previous three-layer approach; right sketch is the current two-layer approach.

function better with small separation distances from the ground plane. This development effort presents a new approach where only two thin-membrane layers are needed for the array elements. With this approach, as shown in Fig. 10-21, the top layer has both the microstrip lines and the slotted ground plane, while the bottom layer has only the patch elements. On the top layer, the microstrip lines are separated from the slotted ground plane via a very thin membrane substrate (0.05 mm). The microstrip line couples the energy to the patch through the slot in the ground plane. This approach allows easier integration with the membrane-based T/R modules where a single-layer co-planar waveguide (CPW) or microstrip transmission-line system is used [18]. This two-layer approach also allows the large-aperture antenna to be more easily rolled up with a smaller stowage volume than the previous three-layer system.

10.3.1 Antenna Description

Figure 10-22 shows the photograph of a single aperture-coupled membrane patch element with the left picture showing the bottom layer and the right picture showing the top patch layer. It can be observed that the coupling slot is very thin. It has dimensions of 79.5 mm by 0.48 mm with a length-to-width ratio of 160. The 4×2 array uses this same element design with linear polarization and an E-field parallel to the long dimension of the array. Two

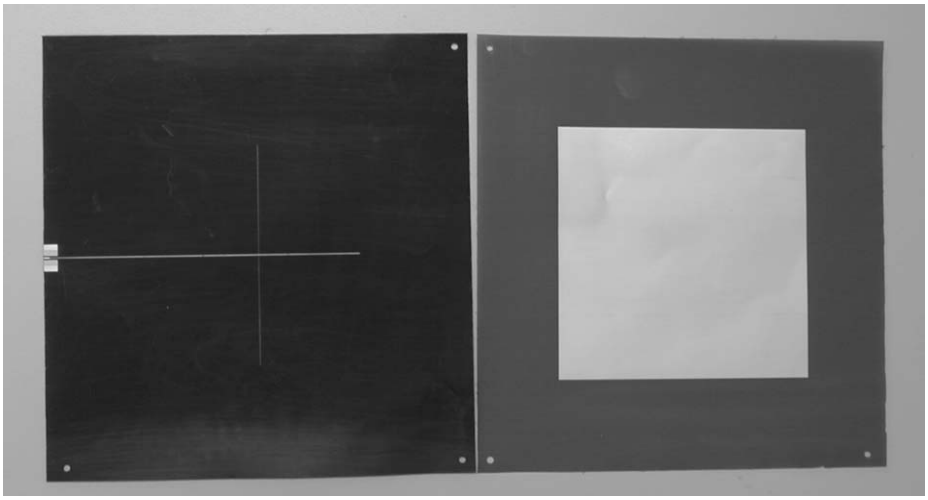

Fig. 10-22. Photograph of the single patch element showing two separated membrane layers.

4 × 2 arrays were fabricated and tested with one being a passive array and the other an active array. The active array is identical to the passive array except it has T/R modules integrated between the aperture-coupling slots and the power divider. Figure 10-23 gives both front and rear views of the 4 × 2 array, where the element spacing is 15.24 cm (0.64 λ_0) in both the vertical and horizontal planes. This spacing is selected to accommodate the T/R-module-required real estate while allowing the beam to scan to a relatively wide angle of 30 deg. Each patch is a square with a dimension of 8.89 cm and has a resonant frequency centered at 1.26 GHz. The array of elements is fed by a corporate microstrip power divider system with uniform amplitude distribution. The two membrane layers are each a 0.05-mm-thick polyimide material (Pyralux) having a relative dielectric constant of 3.4. On each membrane, the deposited copper is 5 μm thick. Both membranes are supported and tensioned by a framed catenary system to maintain the required membrane flatness (<5 mm rms) and membrane spacing (1.27 cm). The T/R module components, such as the amplifiers and phase shifters, are all commercially available devices. They are integrated onto JPL-designed membrane circuits. A close-up view of the T/R module circuitry is shown in Fig. 10-24 where it indicates that all components are small enough for the membrane to be rolled up.

10.3.2 Antenna Performance Results

The measured input return loss of the 4 × 2 passive array is given in Fig. 10-25 where it shows that the –10-dB return-loss bandwidth is about 100 MHz (8 percent) with a deep resonance occurring at 1.26 GHz. Due to the

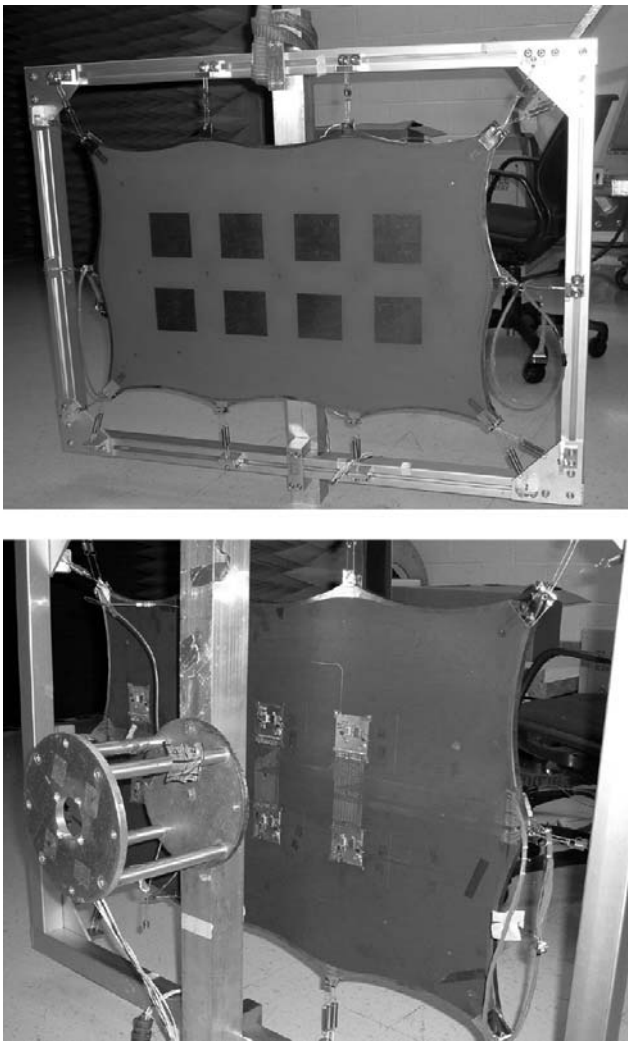

Fig. 10-23. Front (top) and rear (bottom) views of the 4 × 2 membrane array.

relative high loss material of the polyimide membrane substrate, the corporate power divider incurred a 2.5-dB insertion loss. The passive array achieved a measured gain of 12.1 dB (include the power divider loss). Both calculated and measured two-principal-plane radiation patterns at 1.26 GHz for 0-deg cut and 90-deg cut are shown in Fig. 10-26. The calculation was done by the moment-method-based Ensemble software. For the active array, the 4-bit phase shifters were adjusted for the main beam to scan to 15, 30, and 45 deg in the E-plane of the array. Both calculated and measured patterns for these three scanned beam

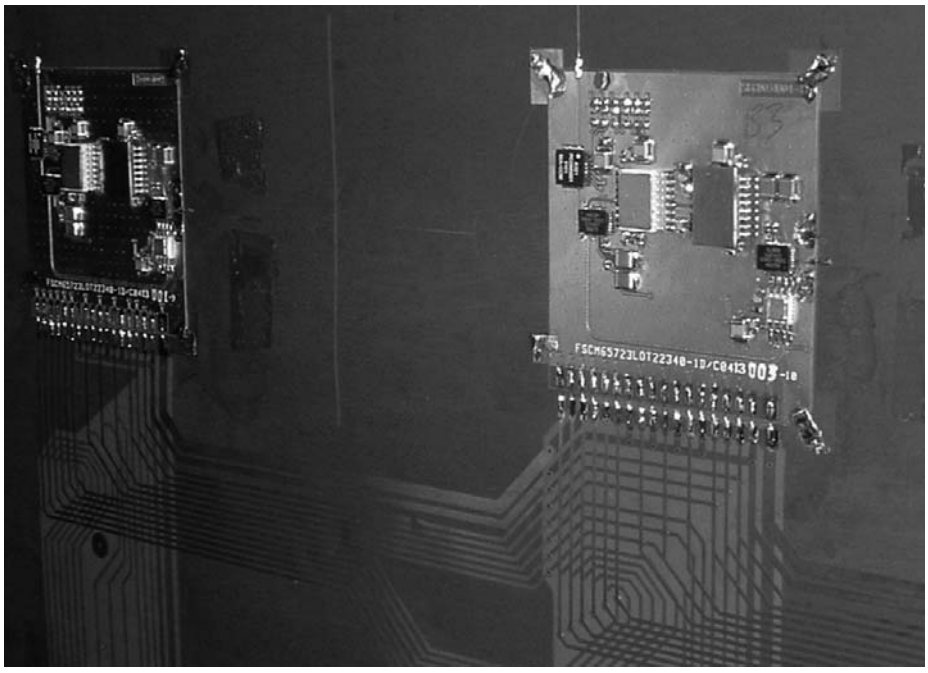

Fig. 10-24. Close-up view of the membrane array showing T/R module components.

positions are shown in Figs. 10-27, 10-28, and 10-29, respectively. The calculations agree well with the measured values. The 45-deg scanned beam has a significant drop in gain of about 3.0 dB. This is because, in order to achieve wide bandwidth with a relatively thick air substrate, the element pattern [19] formed a relatively narrow beam of ±42 deg, which suppresses the array's 45-deg-scanned beam. In addition, due to the element spacing of 0.64 λ_0, the grating lobe starts to form, which further reduces the main beam gain. Nevertheless, the 4×2 active array has successfully demonstrated that the membrane-based beam-scanning array is very feasible.

10.4 Printed Reflectarray Antenna

Since the printed reflectarray is a fairly new antenna concept, this section gives a more detailed discussion and an overview of the development history and key design methodologies for this antenna. The reflectarray antenna consists of a flat or slightly curved reflecting surface and an illuminating feed as shown in Fig. 10-30. On the reflecting surface, there are many isolated elements (e.g., open-ended waveguides, printed patches, dipoles, or rings) without any power division transmission lines. The feed antenna illuminates these isolated elements, which are designed to scatter the incident field with

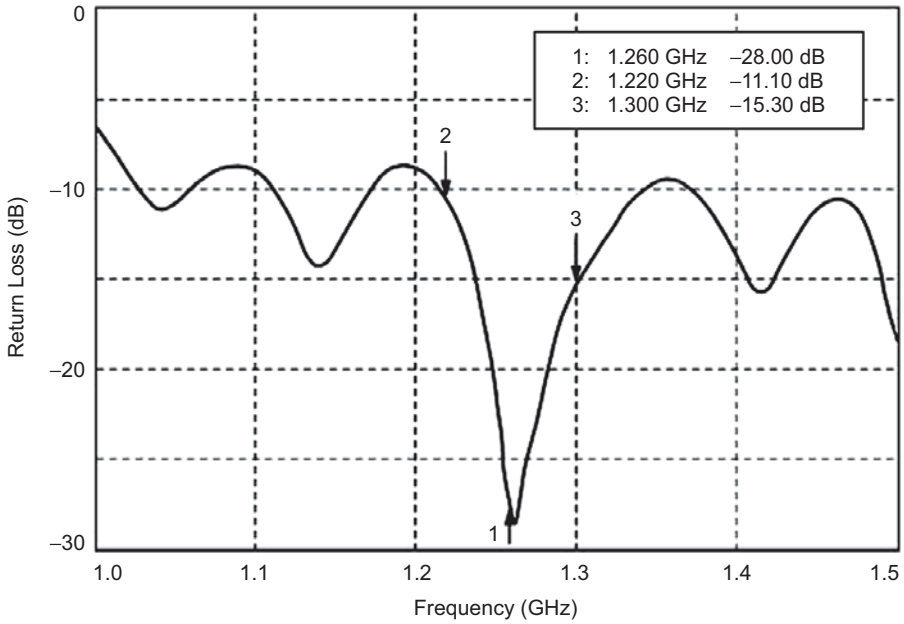

Fig. 10-25. Measured input return loss of the 4 × 2 membrane passive array.

electrical phases that are required to form a planar phase front in the far-field distance. This operation is similar in concept to the use of a parabolic reflector that naturally reflects and forms a planar phase front when a feed is placed at its focal point. Thus, the term "flat reflector" is sometimes used to describe the reflectarray, which utilizes both technologies of reflector and array. As shown in Fig. 10-31, there are several methods for reflectarray elements to achieve a planar phase front. For example, one is to use identical microstrip patches with different-length phase-delay lines attached so that they can compensate for the phase delays over the different paths from the illuminating feed. The other is to use variable-size patches, dipoles, or rings so that elements can have different scattering impedances and, thus, different phases to compensate for the different feed-path delays. The third method, for circular polarization only, the reflectarray has all identical circularly polarized elements but with different angular rotations to compensate for the feed path length differences.

10.4.1 Advantages/Disadvantages of Printed Reflectarrays

To achieve a low-reflecting surface profile and a low antenna mass, reflectarrays using printed microstrip elements have been developed. These reflectarrays combine some of the best features of the traditional parabolic reflector antenna and the microstrip-array technology. As with the parabolic reflector, the reflectarray can achieve very good efficiency (>50 percent) for

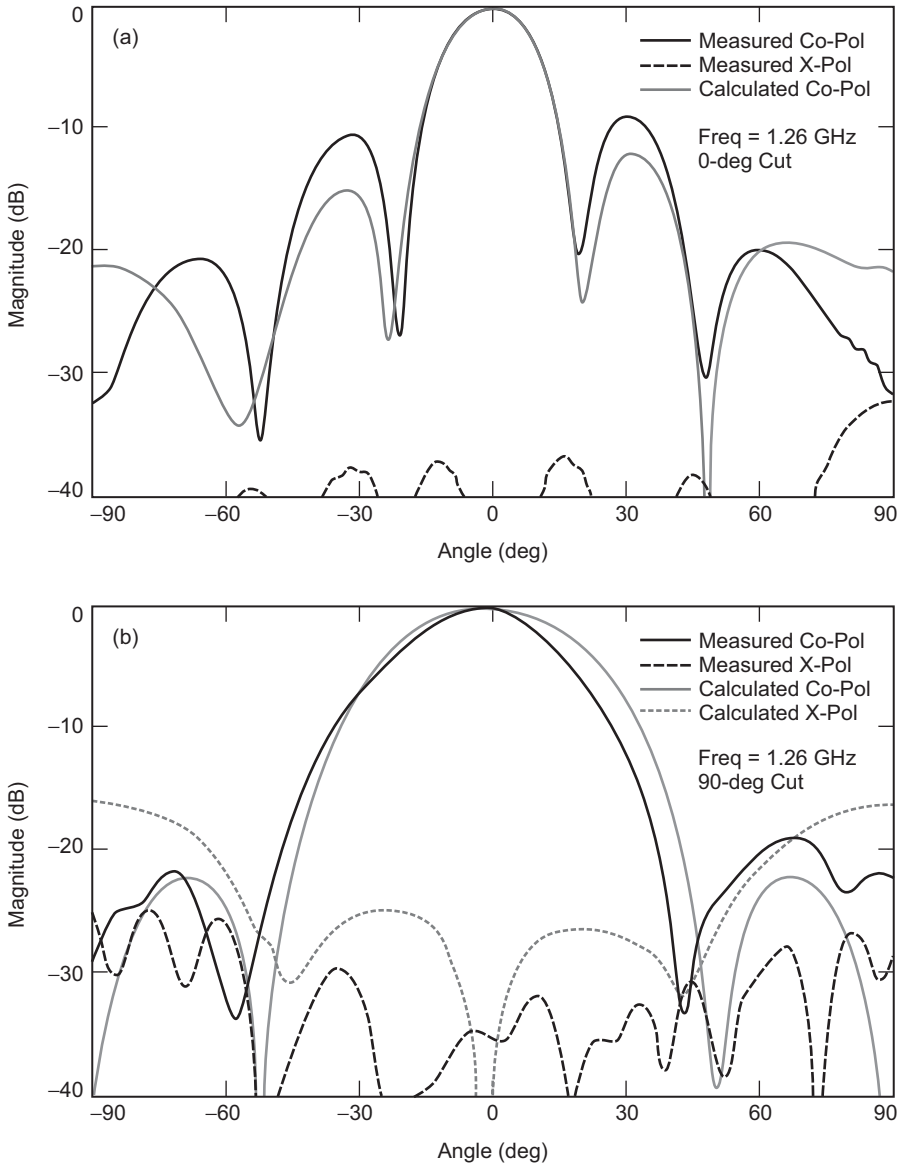

Fig. 10-26. Two-principal-plane patterns of the 4 × 2 membrane passive array radiation patterns for (a) 0-deg cut and (b) 90-deg cut.

very large aperture since no power divider is needed and thus very little resistive insertion loss is encountered here. On the other hand, very similar to an array antenna, the reflectarray can have its main beam designed to tilt at a large angle (>50 deg) from its broadside direction. Low-loss electronic phase

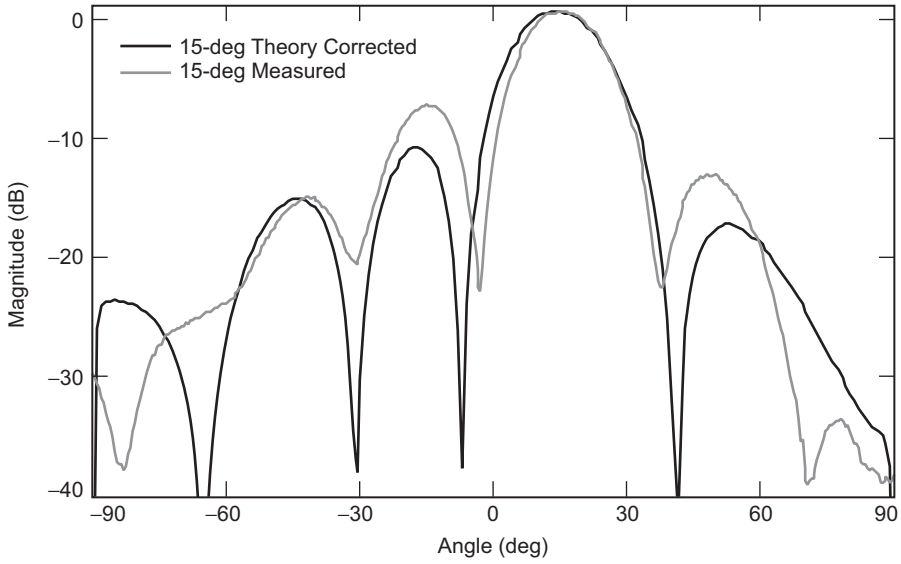

Fig. 10-27. 15-deg scanned pattern of the 4 × 2 active array.

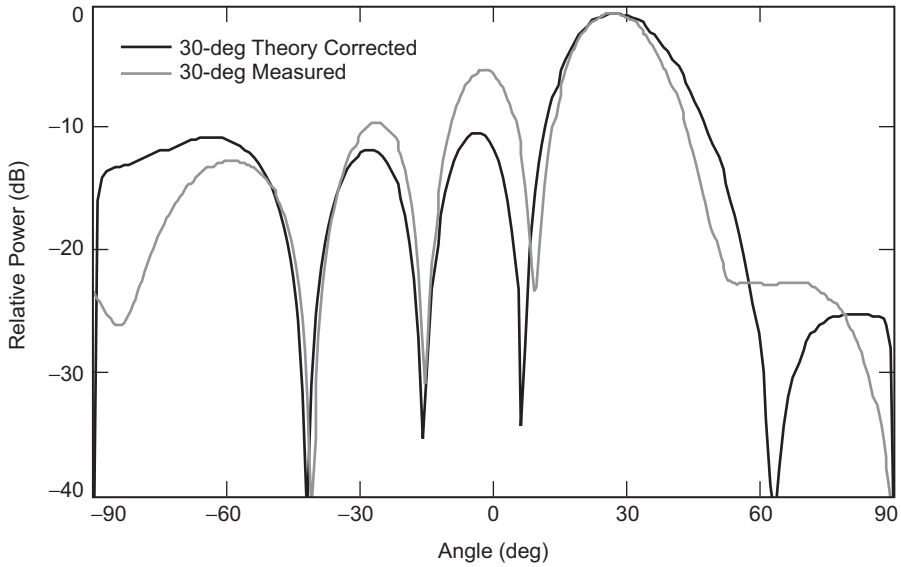

Fig. 10-28. 30-deg scanned pattern of the 4 × 2 active array.

shifters can be implanted into the elements for wide-angle electronic beam scanning. With this beam scanning capability of the reflectarray, the complicated high-loss beamforming network and high-cost transmit/receive

(T/R) amplifier modules of a conventional phased array are no longer needed. One significant advantage of the printed reflectarray is that, when a large aperture (e.g., 10-m size) spacecraft antenna requires a deployment mechanism, the flat structure of the reflectarray allows a much simpler and more reliable

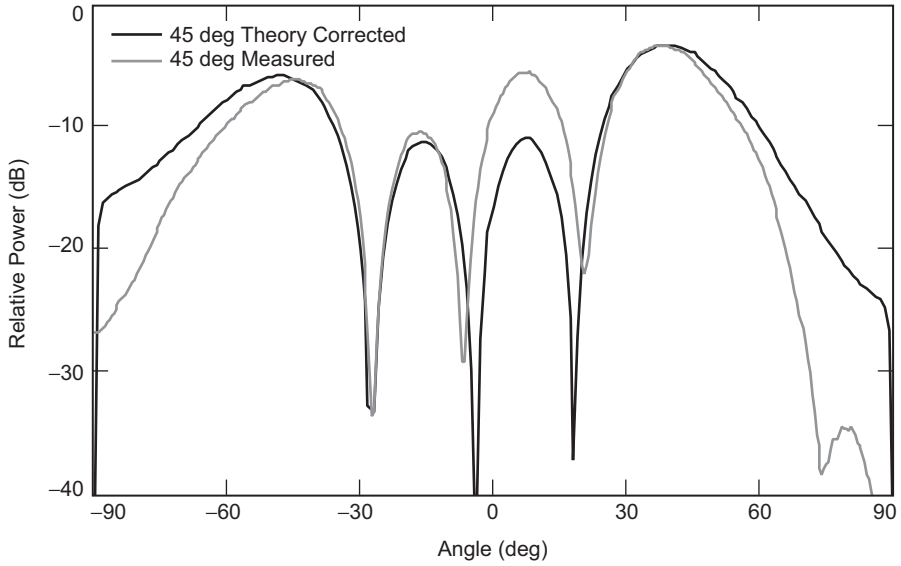

Fig. 10-29. 45-deg scanned pattern of the 4 × 2 active array.

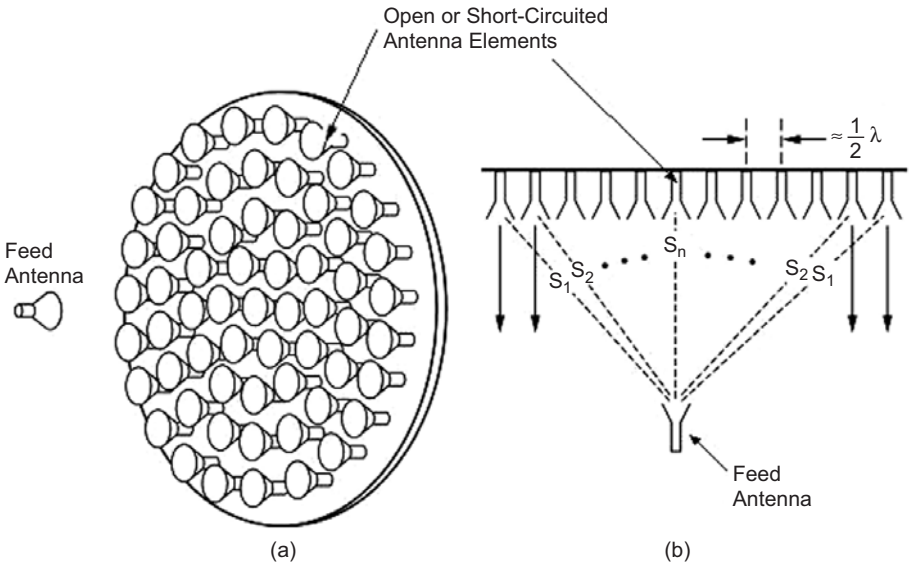

Fig. 10-30. Configuration of a reflectarray antenna in (a) three-dimensional view and (b) two-dimensional view.

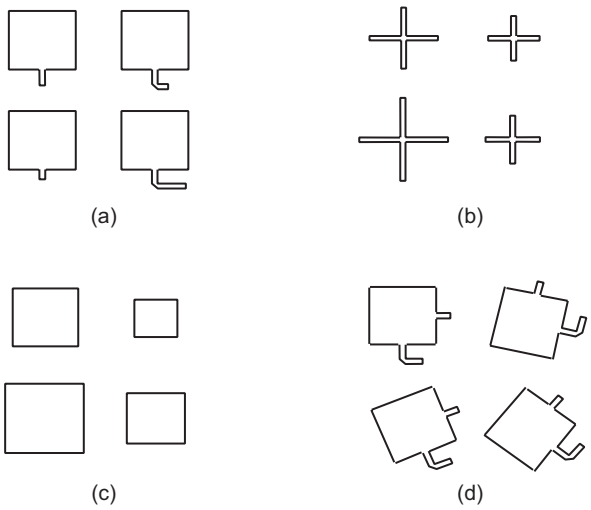

Fig. 10-31. Various reflectarray elements: (a) identical patches with variable-length phase delay lines; (b) variable-size dipoles; (c) variable-size patches; (d) variable angular rotations.

folding or inflation mechanism than the curved surface of a parabolic reflector. The flat reflecting surface of the reflectarray also lends itself to flush mounting onto an existing flat structure without adding significant mass and volume to the overall system structure. The reflectarray, being in the form of a printed microstrip antenna, can be fabricated with a simple and low-cost etching process, especially when produced in large quantities. Another major feature of the reflectarray is that, with hundreds or thousands of elements in a reflectarray having phase adjustment capability, the array can achieve very accurate contour beam shape with a phase synthesis technique. With all the above capabilities, there is one distinct disadvantage associated with the reflectarray antenna. This is its inherent narrow bandwidth, which generally cannot exceed much beyond ten percent. This narrow bandwidth behavior is discussed further in 10.4.4 Although the reflectarray has narrow bandwidth, due to its multitude of capabilities, the development, research, and application of the printed reflectarray antenna would be boundless in the future.

10.4.2 Review of Development History

The reflectarray antenna concept, shown in Fig. 10-30, was first demonstrated during the early 1960s [20]. Open-ended waveguide elements with variable-length waveguides were used to demonstrate the capability of achieving co-phasal re-radiated far-field beams. Since, during this early time, most wireless operations were done at relatively low microwave frequencies,

the large-waveguide reflectarrays resulted in very bulky and heavy antennas. In addition, the efficiencies of these reflectarrays were not studied and optimized. More than ten years later (in the mid 1970s), the very clever concept of the "spiraphase" reflectarray was developed [21], in which switching diodes were used in an eight-arm spiral or dipole element of a circularly polarized reflectarray to electronically scan its main beam to large angles from the broadside direction. This is possible because, by angularly rotating a circularly polarized radiating element, its propagating electrical phase will also change by an amount proportional to the amount of rotation. However, due to the thick spiral cavity and large electronic components, the spiraphase reflectarray was still relatively bulky and heavy. Its aperture efficiency was still relatively poor. Thus, no continued development effort was followed. It should be noted here that, in order to have good efficiency for the reflectarray, the intricate relations between the element phasing, element beamwidth, element spacing, and focal length/diameter (f/D) ratio must be well designed; otherwise, a large backscattered component field or a mismatched surface impedance would result.

Due to the introduction of the printable microstrip antennas, the technologies of reflectarray and microstrip radiators were combined, and a typical configuration is illustrated in Fig. 10-32. Various printed microstrip reflectarray antennas were developed in the late 1980s and early 1990s for the purpose of achieving reduced antenna size and mass. These printed reflectarrays came in various forms, as shown in Fig. 10-31, but all have flat low-profile and low-mass reflecting surfaces. The reflectarrays that used identical patch elements with different-length phase delay lines [22–27] have

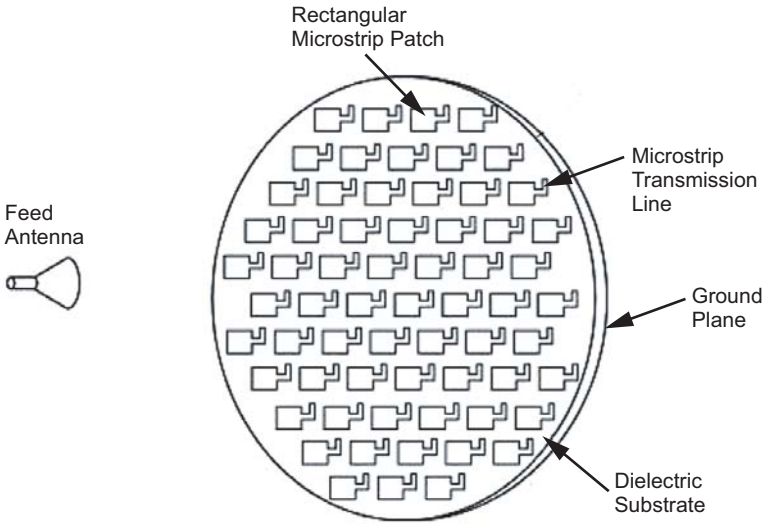

Fig. 10-32. Configuration of printable microstrip reflectarray antenna.

their elements similar to those shown in Fig. 10-31(a). The phase delay lines, having lengths on the order of a half-wavelength long or less, are used to compensate for the phase differences of different path lengths from the illuminating feed. The second approach, shown in Fig. 10-31(b), used elements that are made of printed dipoles with variable dipole lengths [28]. Different dipole lengths yield different scattering impedances, which then provide the different phases needed to compensate for the different path-length delays. Similarly, microstrip patches with variable patch sizes [29], shown in Fig. 10-31(c), were also developed. Circularly polarized microstrip patches with identical size but variable angular rotations [8,30], shown in Fig. 10-31(d), were designed to form a co-phasal far-field reflectarray beam. In addition to those shown in Fig. 10-31, several other reflectarray or equivalent developments during the 1990s are worth mentioning here. Printed variable-length dipole elements were used to form a frequency-scanned grating-reflector antenna with an offset feed [31]. Printed annular rings of variable diameters arranged in Fresnel zone configuration were also used to focus the beam [32]. In the 1996 Phased Array Conference, a 94-GHz monolithic reflectarray [33], using a 1-bit p-type, intrinsic, n-type (PIN) diode phase shifters, was reported to achieve wide-angle (±45 deg) electronic beam scanning. In the same conference, a 35-GHz reflectarray, using waveguide/dielectric elements with 3-bit ferrite phase shifters [34], was also reported to achieve ±25-deg beam scanning. One proposed technique [30], although not yet developed, is worth mentioning here. By using the angular rotation technique with circularly polarized elements, miniature or micro-machined motors could be placed under each element to achieve wide-angle beam scanning without the need of T/R modules and phase shifters. For application in the spacecraft area, a deployable and low-mass 1-meter diameter inflatable reflectarray antenna [35] at the X-band frequency was developed. Another unique spacecraft application of the reflectarray was conceived [36] and developed [37] by using its many elements, with a numerical phase synthesis technique, to form a uniquely shaped contour beam. From all the above developments, it can be seen that, at the beginning of the Twenty-First Century, the reflectarray antenna technology is becoming mature enough and has a variety of possible applications throughout the microwave and millimeter-wave spectra.

By early 2000, the development of reflectarray had mushroomed and several performance improvement techniques are worth mentioning here. One used multi-layer stacked patches to improve the reflectarray bandwidth from a few percent to more than ten percent [38]. As an extension to the 1-m X-band inflatable reflectarray mentioned above, a 3-m Ka-band inflatable reflectarray consisting of 200,000 elements was also developed [39], which is currently known as the electrically largest reflectarray. An amplifying reflectarray was developed [40] for each element of the reflectarray to amplify the transmitted signal and, thus, achieving very high overall radiated power. In order to achieve

good antenna efficiency, the most critical segment of the reflectarray design is its elements. The element performance was optimized by using the genetic algorithm technique [41]. The reflectarray using a subreflector and array feed configuration to achieve fine beam scanning was also studied [42]. To combat the shortcoming of narrow bandwidth, dual-band multi-layer reflectarrays using annular rings [43] and crossed dipoles [44] are also being developed. Another development that is worth mentioning here is a folded reflectarray configuration [45], where two reflecting surfaces are used to reduce the overall antenna profile due to the feed height of a conventional reflectarray.

10.4.3 Analysis and Design Procedures

The design and analysis of a reflectarray can be separated into four essential steps, which are separately discussed below:

10.4.3.1 Element Characterization. The most important and critical segment of the reflectarray design is its element characterization. If the element design is not optimized, it will not scatter the signal from the feed effectively to form an efficient far-field beam. Its beamwidth must correlate correctly with the reflectarray's f/D ratio to accommodate all incident angles from the feed. Its phase change versus element change (patch size, delay line length, etc.) must be calibrated correctly. One of the most popular techniques to calibrate the phase is to use the infinite-array approach [29,46] to include local mutual coupling effects due to surrounding elements. It is not yet feasible for computers to provide a complete rigorous solution including all the mutual coupling effects of all elements since the reflectarray generally consists of too many elements. The infinite array approach can be done by using the method of moment technique [29,46] or equivalently done by a finite-difference time-domain (FDTD) analysis on a unit cell of a single element [47]. A mathematical waveguide simulator, which simulates the infinite array approach, can also be adapted by using the commercial software—HFSS (a finite element technique) to achieve the element-phase information. All these techniques are used to derive the phase-versus-element-change curve, which is generally an S-shaped curve with nonlinear relationship, as illustrated in Fig. 10-33. The antenna designer should minimize the slope at the center of the curve so that the phase change will not be overly sensitive to the element change. If the curve is too steep, the element change or fabrication tolerance may become an issue, in particular at high microwave frequencies.

10.4.3.2 Required Phase Delay. The path lengths from the feed to all elements are all different, which lead to different phase delays. To compensate for these phase delays, the elements must have corresponding phase advancements designed in according to a unique S-curve similar to that shown in Fig. 10-33.

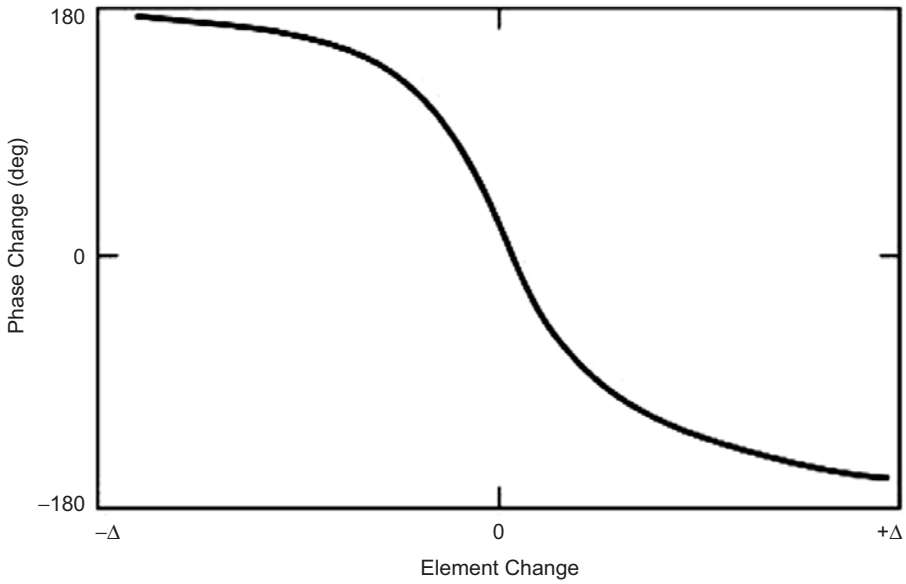

Fig. 10-33. A typical S-curve of a reflectarray element phase-change versus element-change.

The following gives an example of how the compensating phase is calculated for each element of a reflectarray with a broadside-directed beam. The differential path length for each element is given as:

$$\Delta L_{m,n} = L_{m,n} - L_{0,0} \tag{10.4-1}$$

where:

$L_{m,n}$ = distance between the feed and the *mn*-th element, which can be obtained by using simple geometry;

$L_{0,0}$ = distance between the feed and a reference point on the reflectarray surface (e.g., the center point).

$\Delta L_{m,n}$ = differential feed path length for the *mn*-th element.

To achieve a collimated radiation, the phase advancement $\Delta\Phi_{mn}$ needed for the *mn*-th element is given by

$$\Delta\Phi_{mn} \text{ in degrees } = \left[\frac{\Delta L_{m,n}}{\lambda_0} - \text{integer of}\left(\frac{\Delta L_{m,n}}{\lambda_0}\right)\right] \times 360 \tag{10.4-2}$$

The above indicates that the compensating phase can be repeated every 360 deg, and the portion that is an integer multiple of a wavelength or 360 deg can be deleted.

10.4.3.3 Pattern Calculation. With the compensating phases of all elements known, the far-field radiation patterns can be calculated by the conventional array theory [48], where the radiations of all elements are summed together as follows. Consider a planar array consisting of $M \times N$ elements that are non-uniformly illuminated by a low-gain feed at position vector $\vec{r}_f$. Let the desired beam direction be specified by unit vector $\hat{u}_0$. Then, the far field of the reflectarray in the direction will be of the form:

$$E(\hat{u}) = \sum_{m=1}^{M} \sum_{n=1}^{N} F\left(\vec{r}_{mn} \bullet \vec{r}_f\right) \cdot A\left(\vec{r}_{mn} \bullet \hat{u}_0\right) \cdot A\left(\hat{u} \bullet \hat{u}_0\right) \cdot \exp\left[jk\left(\left|\vec{r}_{mn} - \vec{r}_f\right| + \vec{r}_{mn} \bullet \hat{u}\right) + j\alpha_{mn} \right] \tag{10.4-3}$$

where F is the feed pattern function, A is the reflectarray element pattern function, $\vec{r}_{mn}$ is the position vector of the mn-th element, and α_{mn} is the required compensating phase of the mn-th element calculated by Eq. (10.4-2). $\cos^q \theta$ factor is used for both F and A functions with no azimuth (φ) dependence.

10.4.3.4 Reflectarray Geometry Design. To determine the geometry of a reflectarray is basically to determine its f/D ratio, which is governed by its desired aperture efficiency. The aperture efficiency (η_a) can be defined as the product of the illumination (η_I) and spillover (η_s) efficiencies: $\eta_a = \eta_I \times \eta_s$. By integrating the pattern function of Eq. (10.4-3), the illumination efficiency for a center-fed reflectarray can be obtained in a close form [48] as given by

$$\eta_I = \frac{\left[\dfrac{1+\cos^{q+1}\theta_e}{q+1} + \dfrac{1-\cos^{q}\theta_e}{q} \right]^2}{2\tan^2\theta_e \dfrac{1-\cos^{2q+1}\theta_e}{2q+1}}, \tag{10.4-4}$$

and the spillover efficiency is given by

$$\eta_s = 1 - \cos^{2q+1}\theta_e \tag{10.4-5}$$

where q is the exponent of the feed pattern function represented by $\cos^q \theta$ and θ_e is half of the subtend angle from the feed to the reflectarray aperture. The

reflectarray element is approximated by the cosine function. Equations (10.4-4) and (10.4-5) are calculated by assuming a circular aperture only for the demonstration of the design procedures. Similar closed-form equations can be easily obtained for square, rectangular, or elliptical apertures by performing proper integrations. To give an example about how Eqs. (10.4-4) and (10.4-5) can be utilized to optimize a reflectarray design, Fig. 10-34 shows the calculated curve of spillover and illumination efficiencies versus the feed pattern factor q (feed beamwidth) for a half-meter 32-GHz reflectarray with a fixed f/D ratio of 1.0 ($\theta_e = 26.6$ deg). It demonstrates that the maximum aperture efficiency is achieved at $q = 10.5$ or when the feed has a –3-dB beamwidth of 29 deg. Another curve, shown in Fig. 10-35, gives aperture efficiency as a function of f/D ratio for the same half-meter 32-GHz reflectarray when the feed beamwidth is fixed at 33.4 deg with $q = 8$. In this case, the maximum aperture efficiency is achieved when the f/D ratio is 0.87. It can be seen that curves derived from Eqs. (10.4-4) and (10.4-5) are essential in obtaining an optimum efficiency design. The above discussion has been limited to center-fed reflectarray. Offset reflectarrays can also be optimally designed by using equations similar to Eqs. (10.4-4) and (10.4-5).

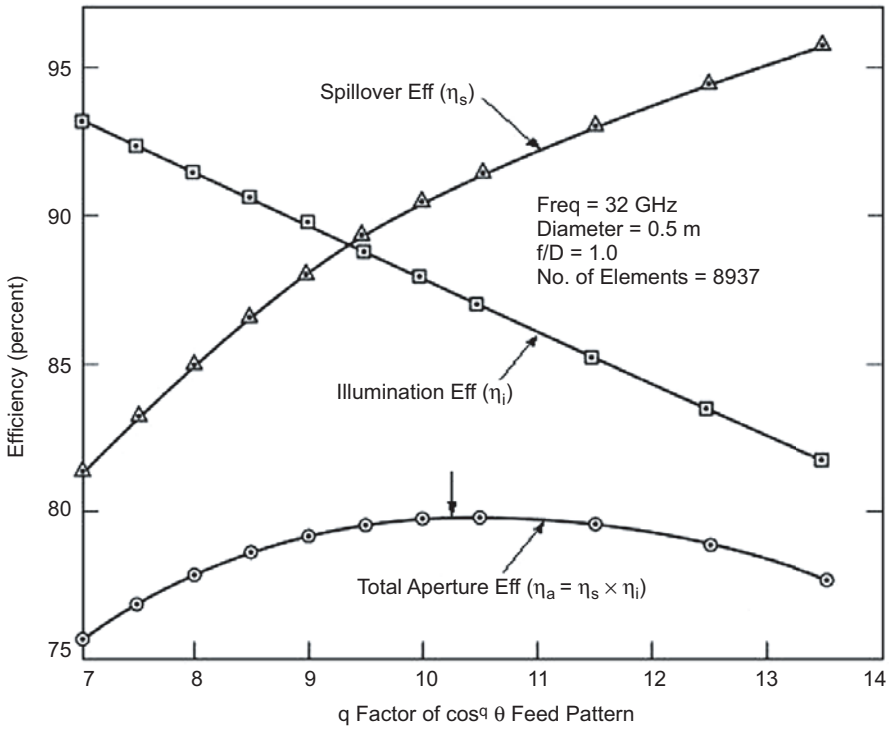

Fig. 10-34. Spillover and illumination efficiencies versus feed pattern shape.

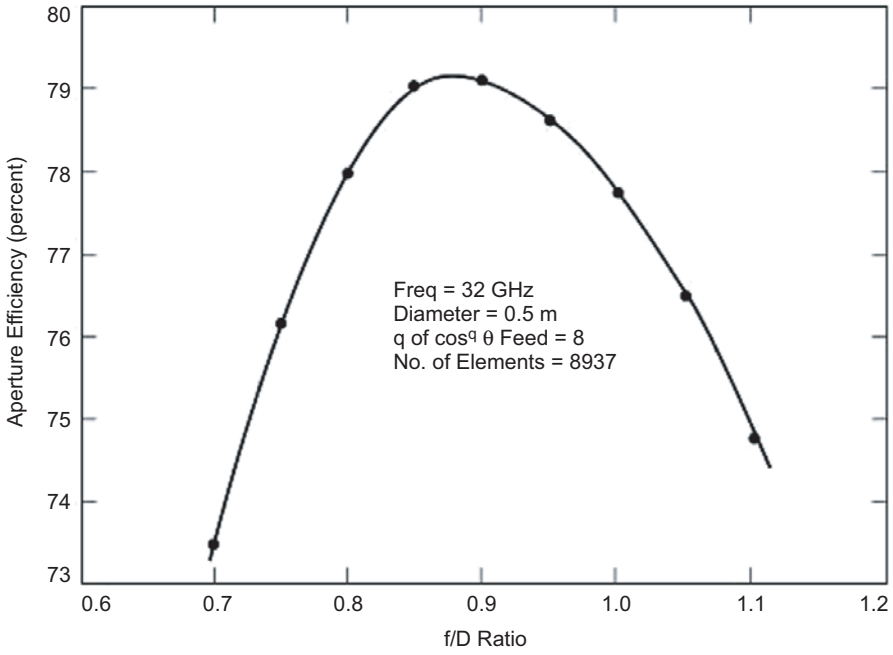

Fig. 10-35. Aperture efficiency versus f/D ratio.

10.4.4 Bandwidth Issues

The bandwidth performance of a reflectarray [30] is no match for that of a parabolic reflector, where theoretically infinite bandwidth exists. For a printed microstrip reflectarray, its bandwidth is primarily limited by two factors. One is the narrow bandwidth of the microstrip patch elements on the reflectarray surface, and the other is the differential spatial phase delay. The microstrip patch element generally has a bandwidth of about 3 to 5 percent. To achieve wider bandwidth for a conventional microstrip array, techniques such as using thick substrate for the patch, stacking multiple patches, and using sequentially rotated subarray elements have been employed. Bandwidths greater than 15 percent have been reported. The second reflectarray-limiting factor, the differential spatial phase delay, can be best explained by referring to Fig. 10-36 where the differential spatial phase delay, ΔS, is the phase difference between the two paths S_1 and S_2 from the feed to the reflectarray elements. This ΔS can be many multiples of the wavelength (λ) at the center operating frequency. It can be expressed as $\Delta S = (n + d)\lambda$ where n is an integer and d is a fractional number of a free-space wavelength λ. At each element location, d is compensated by an appropriate phase delay achieved by the reflectarray element design (achieved by variable patch size, variable phase delay line length, etc.). As frequency changes, the factor $(n + d)\lambda$ becomes $(n + d)(\lambda + \Delta\lambda)$. Since the design and the compensating phase for each element is fixed

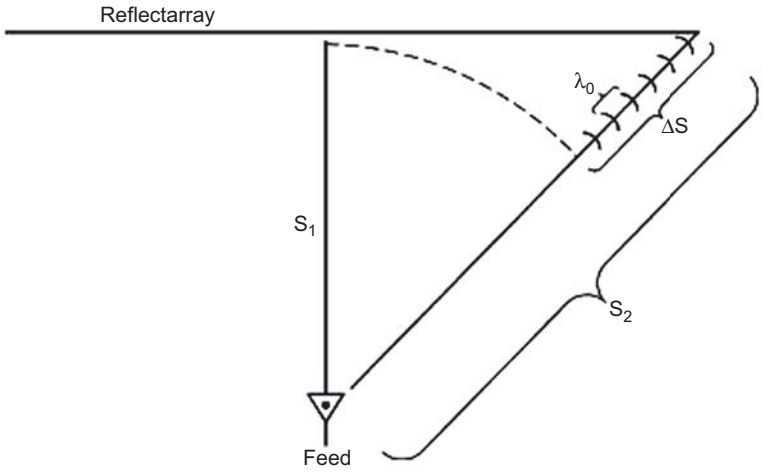

Fig. 10-36. Differential spatial phase delay limits the bandwidth of a reflectarray.

for the center frequency, a frequency excursion error will occur in the re-radiated phase front. The amount of phase change in each path when compared to a reference path, say S_1, is $(n + d)\Delta\lambda$, which can be a significant portion of a wavelength or 360 deg.

To reduce the amount of frequency excursion error mentioned above, the integer number n must be reduced. There are several methods to reduce n. One is to design the reflectarray with a larger f/D ratio and hence to minimize the difference between paths S_1 and S_2. The second way is simply to avoid the use of a reflectarray with a large electrical diameter. The effect of f/D ratio on bandwidth performance was given previously in Fig. 10-35. The third method to reduce frequency excursion error is to use time-delay lines or partial-time-delay lines instead of the phase delays. In other words, when using the phase delay line technique (not the variable patch size technique), instead of using $d\Delta\lambda$ for the delay line length, $(n + d)\Delta\lambda$ could be used for the delay line. Certainly, additional line-insertion loss and needed real estate for the lines are issues to be encountered. Another method to increase the bandwidth is to use, instead of a complete flat reflectarray surface, a concavely curved reflectarray with piecewise flat surfaces. This curved reflectarray has advantages over a curved parabolic reflector; such as its beam is able to be scanned to large angles with a phase shifter inserted into each element, and, for a space-deployable antenna, the piecewise flat surfaces in some cases are easier to fold into a smaller stowed volume. In order to mitigate the bandwidth problem, a recent technique of using multi-layer stacked-patch element [38] not only has increased the element bandwidth but also has reduced the effect of differential spatial phase delay. As a net result, the bandwidth has increased from a few percent to more than ten percent. Multi-band techniques can also be applied to

the reflectarray. Recently, two dual-band techniques have been developed for the X- and Ka-band frequencies. One used double-layer with two different-size rings and variable angular rotations [43], and the other also used double-layer with X-band crossed dipoles over Ka-band patches [44]. To summarize, although the narrow bandwidth characteristic is the primary shortcoming of a reflectarray, several techniques can be employed to improve the bandwidth performance.

10.5 Applications and Recent Developments

In addition to those possible reflectarray applications mentioned in the introduction and review sections, there are several other important applications and recent developments. One is a Ka-band circularly polarized inflatable reflectarray [39] with a 3-m-diameter aperture developed by the JPL for NASA's future spacecraft communication antenna application. As shown in Fig. 10-5, the antenna uses a torus-shaped inflatable tube to support and tension a 3-m thin-membrane reflectarray surface. This circularly polarized reflectarray, having approximately 200 thousand elements using variable angular rotation technique [8,39], is considered electrically the largest reflectarray ever build. Because the reflectarray has a "natural" flat surface, it is much easier for the inflatable structure to maintain its required surface tolerance (0.2 mm rms in this case) than a "non-natural" parabolic surface; in particular, for long-duration space flight. This inflatable antenna was later improved to equip with rigidizable inflatable tubes [39,49] in order to survive the hazardous space environment, such as bombardment by space debris and strenuous thermal effects. This reflectarray achieved an aperture efficiency of 30 percent with room for improvement and excellent far-field pattern shape with average sidelobe and cross-polarization levels below–40 dB, as shown in Fig. 10-7.

A second important development of the reflectarray is the achievement of a shaped contour beam by using a phase-synthesis technique. This reflectarray, shown in Fig. 10-37, was developed by the University of Massachusetts [37] for a commercial application to provide Earth contour-beam coverage. A typical calculated contour beam transmitted by this antenna, using a phase synthesis technique, is given in Fig. 10-38. Since a reflectarray generally has many thousands of elements, it thus has many degrees of freedom in design to provide an accurate and uniquely required contour beam.

A third important development is a dual-frequency reflectarray, where the two frequencies are widely separated, such as the X-band and Ka-band. The prototype antenna developed, shown in Fig. 10-39, is circularly polarized and uses variable-angularly-rotated annular rings [43]. It was developed by the Texas A&M University for JPL/NASA's future space communication application. This antenna, with a diameter of 0.5 m, uses a multi-layer technique in which the X-band annular rings are placed above the Ka-band

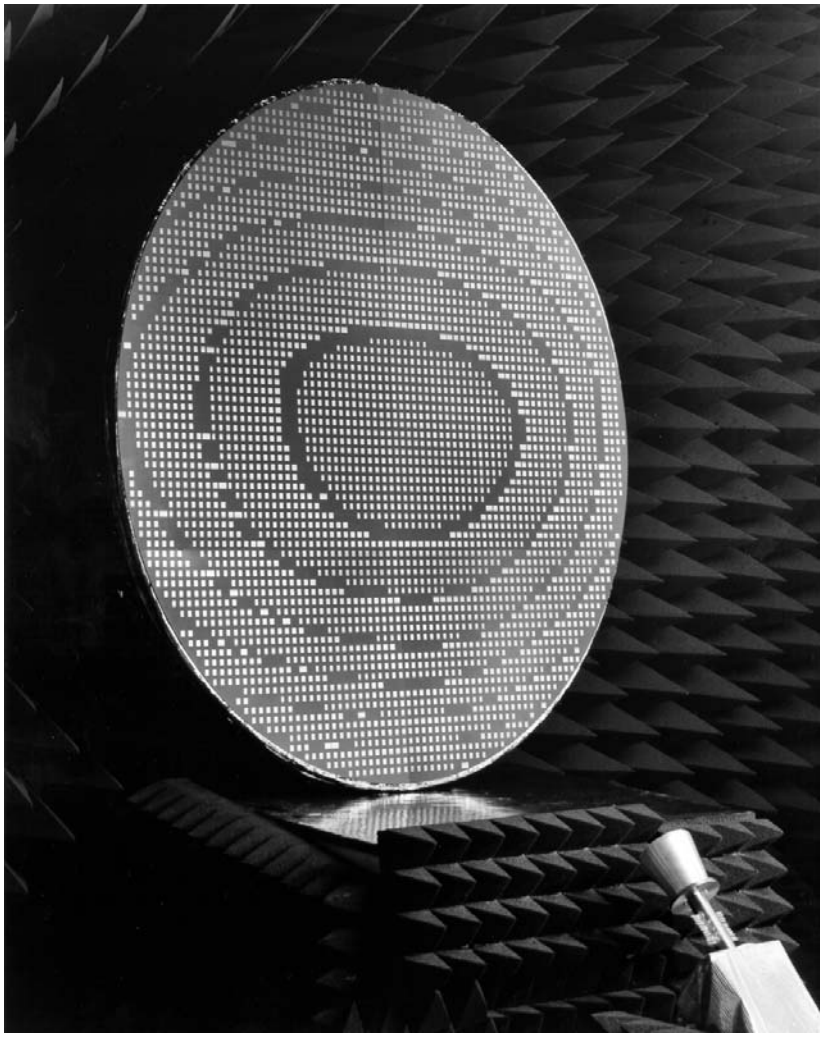

Fig. 10-37. Ku-band reflectarray with shaped contour beam capability [37]. (Courtesy of Professor Dave Pozar, Univ. of Massachusetts)

rings and serve as a frequency-selective surface to let the Ka-band signal pass through. The measured results indicate that the presence of the Ka-band elements has very little impact on the X-band performance. The measured radiation patterns of the Ka-band reflectarray without and with the X-band layer are shown in Figs. 10-40 and 10-41, respectively. There is no significant difference between the two patterns. However, the measured Ka-band gain of the dual-frequency dual-layer antenna is about 1.0 dB lower than the Ka-band alone antenna. The Ka-band alone reflectarray has a measured aperture

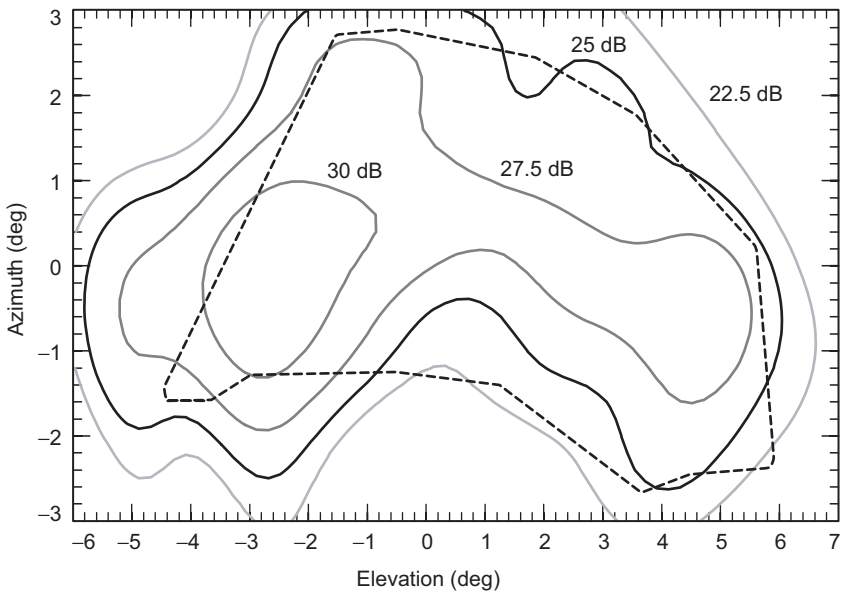

Fig. 10-38. A measured contour beam plot of the reflectarray shown in Fig. 10-26.

efficiency of 50 percent, while the dual-frequency dual-layer antenna has a Ka-band efficiency of about 40 percent. In other words, the X-band annular rings did impact the Ka-band performance somewhat. Future development work is needed to minimize this impact.

One final recent development is a reflectarray having a rectangular aperture intended for the NASA/JPL Wide Swath Ocean Altimeter (WSOA) radar application. This reflectarray uses variable-size patches as elements. The required rectangular aperture, as shown in Fig. 10-42, consists of five flat sub-apertures that are connected together to form a curved reflectarray [50]. The curving of the long dimension of the rectangular surface is to minimize the incident angles from the feed for the end elements, and thus, to optimize the radiation efficiency for all elements. The radiation efficiency here indicates the measured amount of energy of each element that is reradiated in the desired main beam direction. The advantage of using a reflectarray with flat subapertures is that it allows mechanically folding of the flat panels into a compact structure for spacecraft launch-vehicle stowage. Preliminary test data indicate that this reflectarray is functioning properly and some minor improvements are currently being carried out.

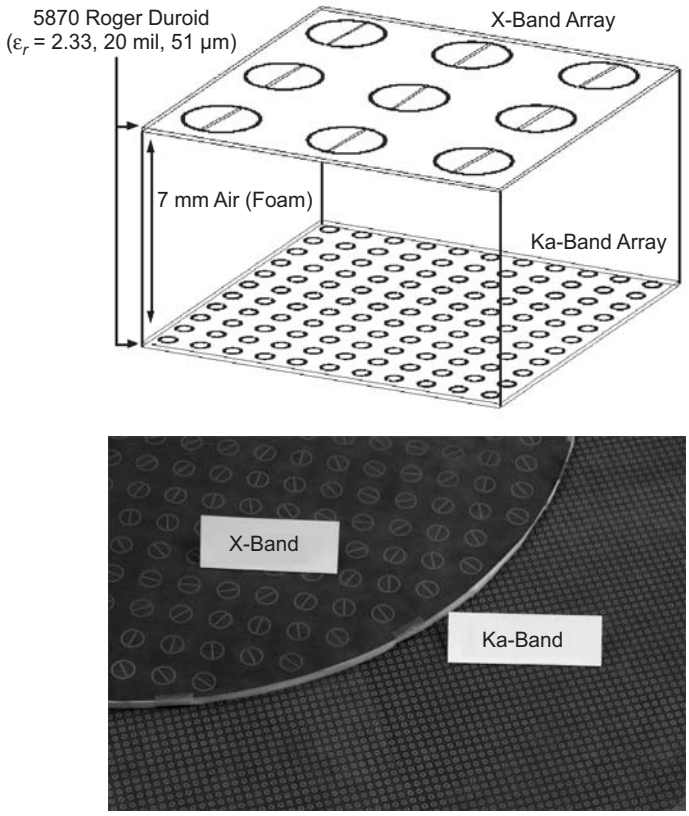

Fig. 10-39. The sketch and photo of the X/Ka dual-band two-layer reflectarray antenna using annular ring elements.

10.6 Summary

The reflectarray antenna has come a long way. However, its development and application had not been widely adapted until about the mid 1990s when the printable microstrip reflectarray was introduced. Except for its narrow bandwidth characteristic, the reflectarray has many advantages over a parabolic reflector antenna type. The main beam of a reflectarray can be designed to tilt to a large angle from its broadside direction. Phase shifters can be implanted into the elements for wide-angle electronic beam scanning. For large-aperture spacecraft antenna applications, the reflectarray's flat surface allows the antenna to be made into an inflatable structure, and it is easier to maintaining its surface tolerance than a curved parabolic surface. Its flat surface also can be made of multiple flat panels for ease in folding into a more compact structure

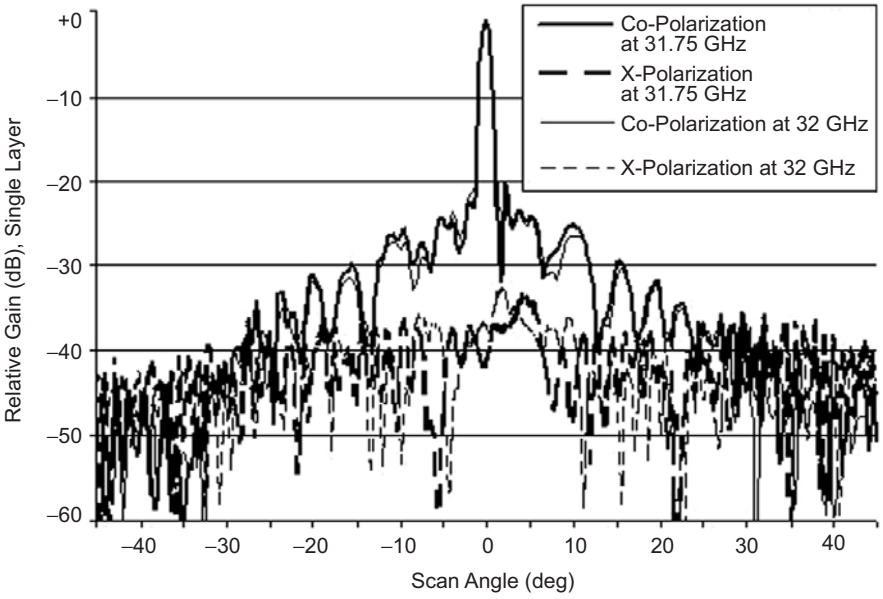

Fig. 10-40. Measured radiation pattern of the single-layer Ka-band reflectarray without the top X-band layer.

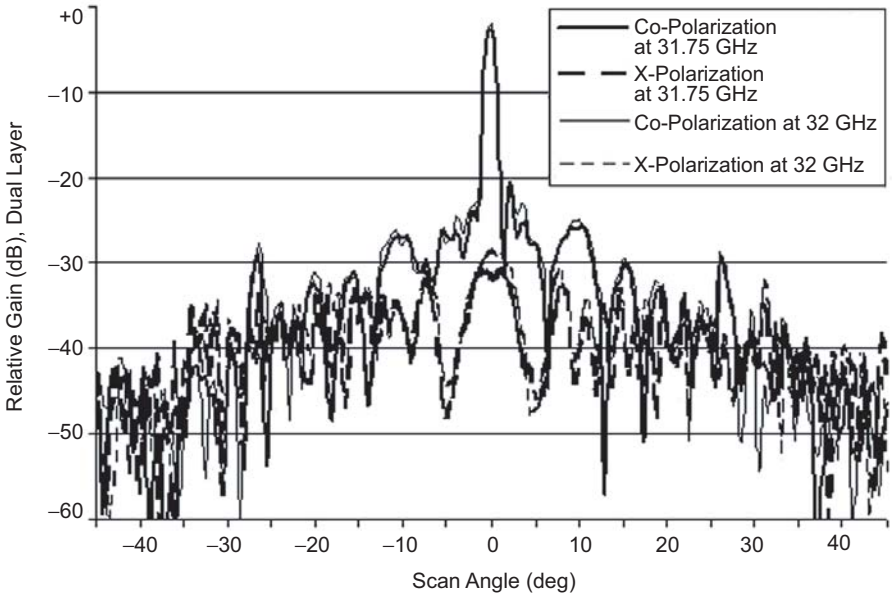

Fig. 10-41. Measured Ka-band radiation pattern of the two-layer X-/Ka-dual-band reflectarray.

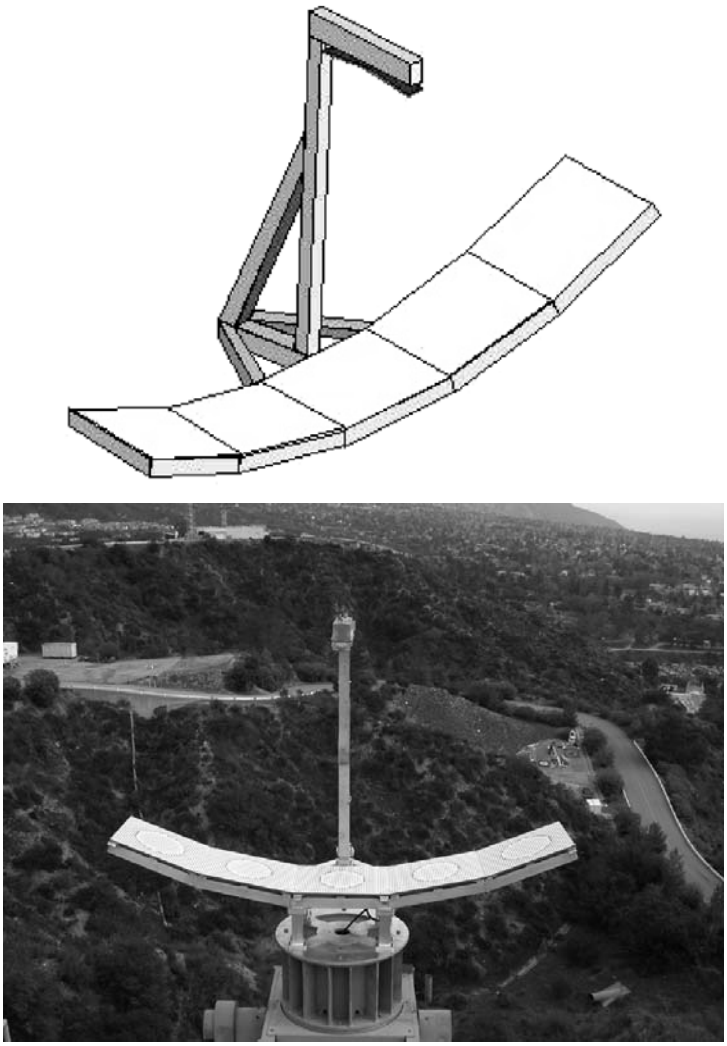

Fig. 10-42. Drawing and photo of the piece-wise flat reflectarray for space application.

for launch vehicle stowage. Very accurate beam shape can be achieved with phase synthesis for Earth-contour beam-coverage applications. Due to these many capabilities, the door has just opened for the development, research, and application of printed reflectarray antennas. Two major areas that need continuing improvement of the reflectarray performance are its bandwidth and its radiation efficiency.

References

[1] R. A. Russell, T. G. Campbell and R. E. Freeland, "A Technology Development Program for Large Space Antennas," *International Astronautical Congress*, 31st (Tokyo, Japan), IAF Paper 80-A-33, International Astronautical Federation, Paris, France, September 1980.

[2] G. Veal and M. Thomas, *Highly Accurate Inflatable Reflectors, Final Report*, AFRPL Report TR84-021, Air Force Rocket Propulsion Laboratory (renamed Air Force Astronautics Laboratory in 1987), Edwards Air Force Base, California, May 1984.

[3] R. E. Freeland, G. D. Bilyeu, and G. R. Veal, "Large Inflatable Deployable Antenna Flight Experiment Results," IAF paper 97-1.3.01, *48th Congress of the International Astronautical Federation* (Turin, Italy), International Astronautical Federation, Paris, France, October 1997.

[4] J. Huang, M. Lou, and E. Caro, "Super-Low-Mass Spaceborne SAR Array Concepts," 1997 *IEEE Antennas and Propagation Society International Symposium Digest*, 1997, vol. 2, pp. 1288–1291, July 13–18, 1997.

[5] J. Huang, "Emerging Array Antenna Technologies at JPL," *Antenna Technology and Applied Electromagnetics (ANTEM) Symposium* (Ottawa, Canada), August 1998.

[6] J. Huang, "The Development of Inflatable Array Antennas," *IEEE Antennas and Propagation Magazine*, vol. 43, pp. 44–50, August 2001.

[7] D. M. Pozar, "Microstrip Antenna Aperture-Coupled to a Microstripline," *Electronics Letters*, vol. 21, pp. 49–50, January 1985.

[8] J. Huang and R. J. Pogorzelski, "A Ka-Band Microstrip Reflectarray with Elements Having Variable Rotation Angles," *IEEE Transactions on Antennas and Propagation*, vol. 46, pp. 650–656, May 1998.

[9] H. Fang, M. Lou, J. Huang, L. Hsia, and G. Kerdanyan, "An Inflatable/Self-Rigidizable Structure for the Reflectarray Antenna," *10th European Electromagnetics Structure Conference* (Munich, Germany), EADS Deutschland GMbH, Munich, Germany, pp. 166–174, October 2001.

[10] H. Fang, M. Lou, J. Huang, U. Quijano, and L. Hsia, "Thermal Distortion Analysis of a Three-meter Inflatable Reflectarray Antenna," *44th AIAA/ASME/ASCE/AHS Structure and 4th AIAA Gossamer Spacecraft Forum* (Norfolk, Virginia), Paper 2003-1650, American Institute of Aeronautics and Astronautics, Reston, Virginia, April 2003.

[11] S. Schwartz, "Space Rigidization Techniques for Expandable Structures," *Modern Plastics*, vol. 46, p. 11, November 1969.

[12] W. F. Hinson and L. S. Keafer, Large Inflated Antenna Systems, NASA Report N84-17234, National Aeronautics and Space Administration, Washington, District of Columbia, 1984.

[13] L. B. Keller, S. Schwartz, A. Olivitch, and S. Allinikov, "Space Rigidizable Resin Fiberglass Sandwich Materials," *Journal of Spacecraft and Rockets*, vol. 3, pp. 513–518, April 1966.

[14] R. L. Jordan, "The Seasat-A Synthetic Aperture Radar System," *IEEE Journal of Ocean Engineering*, vol. OE-5, pp. 154–164, April 1980.

[15] E. R. Caro, "SIR-C, the Next Generation Spaceborne SAR," *The 2nd Spaceborne Imaging Radar Symposium*, Jet Propulsion Laboratory, Pasadena, California, pp. 203–217, 1987.

[16] J. Huang, M. Lou, B. C. Lopez, and E. Gama, "Foldable Frame-Supported Thin-Membrane Array," *Proceedings of 2000 International Symposium on Antennas and Propagation (ISAP 2000)* (Fukuoka, Japan), Communications Society of the Institute of Electronics, Information, and Communication Engineers (IEICE), Japan, pp. 213–216, August 2000.

[17] R. L. Jordan, B. L. Huneycutt, and M. Werner, "The SIR-C/X-SAR Synthetic Aperture Radar System," *IEEE Transactions on Geoscience and Remote Sensing*, vol. 33, pp. 829–839, July 1995.

[18] A. Moussessian, G. Sadowy, L. Del Castillo, J. Huang, S. Madsen, W. Edelstein, and A. Shapiro, "Transmit/Receive Membranes for Large Aperture Scanning Phased Arrays," *Earth Science Technology Conference (ESTC)* (College Park, Maryland), National Aeronautics and Space Administration Headquarters, Washington, District of Columbia, June 2003.

[19] J. Huang and A. Moussessian, "Thin-Membrane Aperture-Coupled L-Band Patch Antenna," *IEEE 2004 Antennas and Propagation Society Symposium Digest* (June 20–25, 2004, Monterey, California), vol. 3, IEEE, pp. 2388–2391, 2004.

[20] D. G. Berry, R. G. Malech, and W. A. Kennedy, "The Reflectarray Antenna," *IEEE Transactions on Antennas and Propagation*, vol. AP-11, pp. 645–651, November 1963.

[21] H. R. Phelan, "Spiraphase Reflectarray for Multitarget Radar," *Microwave Journal*, vol. 20, pp. 67–73, July 1977.

[22] R. E. Munson and H. Haddad, "Microstrip Reflectarray for Satellite Communication and RCS Enhancement and Reduction," United States patent 4,684,952, Washington, District of Columbia, August 1987.

[23] J. Huang, "Microstrip Reflectarray," *1991 IEEE Antennas and Propagation Symposium*, (London, Ontario, Canada), IEEE, pp. 612–615, June 1991.

[24] T. A. Metzler, *Design and Analysis of a Microstrip Reflectarray*, Ph. D. Dissertation, University of Massachusetts, Amherst, September 1992.

[25] Y. Zhang, K. L. Wu, C. Wu, and J. Litva, "Microstrip Reflectarray: Full-Wave Analysis and Design Scheme," *IEEE AP-S/URSI Symposium* (Ann Arbor, Michigan), pp. 1386–1389, June 1993.

[26] R. D. Javor, X. D. Wu, and K. Chang, "Beam Steering of a Microstrip Flat Reflectarray Antenna," *1994 IEEE International Antennas and Propagation Symposium* (AP-S/URSI, Seattle, Washington), pp. 956–959, June 1994.

[27] D. C. Chang and M. C. Huang, "Multiple Polarization Microstrip Reflectarray Antenna with High Efficiency and Low Cross-Polarization," *IEEE Transactions on Antennas and Propagation*, vol. 43, pp. 829–834, August 1995.

[28] A. Kelkar, "FLAPS: Conformal Phased Reflecting Surfaces," *Proceedings of the 1991 IEEE National Radar Conference* (Los Angeles, California), pp. 58–62, March 1991.

[29] D. M. Pozar and T. A. Metzler, "Analysis of a Reflectarray Antenna Using Microstrip Patches of Variable Size," *Electronics Letters*, pp. 657–658, April 1993.

[30] J. Huang, "Bandwidth Study of Microstrip Reflectarray and a Novel Phased Reflectarray Concept," *IEEE AP-S/URSI Symposium* (Newport Beach, California), pp. 582–585, June 1995.

[31] F. S. Johansson, "A New Planar Grating-Reflector Antenna," *IEEE Transactions on Antennas and Propagation*, vol. 38, pp. 1491–1495, September 1990.

[32] Y. T. Gao and S. K. Barton, "Phase Correcting Zonal Reflector Incorporating Rings," *IEEE Transactions on Antennas and Propagation*, vol. 43, pp. 350–355, April 1995.

[33] J. M. Colin, "Phased Array Radars in France: Present and Future," *IEEE Symposium on Phased Array Systems and Technology* (Boston, Massachusetts), pp. 458–462, October 1996.

[34] A. A. Tolkachev, V. V. Denisenko, A. V. Shishlov, and A. G. Shubov, "High-Gain Antenna System for Millimeter-Wave Radars with Combined Electrical and Mechanical Beam Steering," *IEEE Symposium on Phased Array Systems and Technology* (Boston, Massachusetts), pp. 266–271, October 1996.

[35] J. Huang and A. Feria, "A 1-m X-Band Inflatable Reflectarray Antenna," *Microwave and Optical Technology Letters*, vol. 20, pp.97–99, January 1999.

[36] J. Huang, "Capabilities of Printed Reflectarray Antennas," *IEEE Symposium on Phased Array Systems and Technology* (Boston, Massachusetts), pp. 131–134, October, 1996.

[37] D. M. Pozar, S. D. Targonski, and R. Pokuls, "A Shaped-Beam Microstrip Patch Reflectarray," *IEEE Transactions on Antennas and Propagation*, vol. 47, pp. 1167–1173, July 1999.

[38] J. A. Encinar, "Design of Two-Layer Printed Reflectarray Using Patches of Variable Size," IEEE Transactions on Antennas and Propagation, vol. 49, pp. 1403–1410, October 2001.

[39] J. Huang, V. A. Feria, and H. Fang, "Improvement of the Three-Meter Ka-Band Inflatable Reflectarray Antenna," *IEEE AP-S/URSI Symposium* (Boston, Massachusetts), pp. 122–125, July 2001.

[40] M. Bialkowski, A. W. Robinson, and H. J. Song, "Design, Development, and Testing of X-Band Amplifying Reflectarrays," *IEEE Transactions on Antennas and Propagation*, vol. 50, pp. 1065–1076, August 2002.

[41] R. E. Zich, M. Mussetta, M. Tovaglieri, P. Pirinoli, and M. Orefice, "Genetic Optimization of Microstrip Reflectarrays," *IEEE AP-S/URSI Symposium* (San Antonio, Texas), pp. III-128–III-131, June 2002.

[42] B. Khayatian and Y. Rahmat-Samii, "Characterizing Reflectarray Antenna Radiation Performance," *IEEE AP-S/URSI Symposium* (Columbus, Ohio), vol. 3, pp. 298–301, June 2003.

[43] C. Han, B. Strassner, K. Chang, and J. Huang, "A Dual-Frequency 7/32 GHz Reflectarray Antenna," *Progress in Electromagnetics Research Symposium (PIERS)* (Honolulu, Hawaii), p. 526, October 2003.

[44] M. Zawadzki and J. Huang, "A Dual-Band Reflectarray for X- and Ka-Bands," *Progress in Electromagnetics Research Symposium (PIERS)* (Honolulu, Hawaii), p. 525, October 2003.

[45] W. Menzel, D. Pilz, and M. Al-Tikriti, "Millimeter-Wave Folded Reflector Antennas with High Gain, Low-Loss, and Low Profile," *IEEE Antennas and Propagation Magazine*, vol. 44, no. 3, pp. 24–29, June 2002.

[46] D. Pozar, S. D. Targonski, and H. D. Syrigos, "Design of Millimeter Wave Microstrip Reflectarrays," *IEEE Transactions on Antennas and Propagation*, vol. 45, pp. 287–296, February 1997.

[47] E. Girard, R. Moulinet, R. Gillard, and H. Legay, "An FDTD Optimization of a Circularly Polarized Reflectarray Unit Cell," *IEEE AP-S/URSI Symposium* (San Antonio, Texas), pp. III-136–III-139, June 2002.

[48] J. Huang, "Analysis of a Microstrip Reflectarray Antenna for Microspacecraft Applications," *The Telecommunications and Data Acquisition Progress Report 42-120, October–December 1994*, Jet Propulsion Laboratory, Pasadena, California, pp. 153–173, February 15, 1995. http://ipnpr.jpl.nasa.gov/progress_report/

[49] H. Fang, M. Lou, J. Huang, L. M. Hsia, and G. Kerdanyan, "An Inflatable/Self-Rigidizable Structure for the Reflectarray Antenna," *10th European Electromagnetic Structure Conference* (Munich, Germany), October, 2001.

[50] R. Hodges and M. Zawadzki, "Design of a Large Dual Polarized Ku-Band Reflectarray for Spaceborne Radar Altimeter," *IEEE AP-S Symposium* (Monterey, California), pp. 4356–4359, June 2005.

Acronyms and Abbreviations

2-D	two-dimensional
3-D	three-dimensional
A	amp
AAR	azimuth ambiguity ratio
ABMA	Army Ballistic Missile Agency
ACeS	Asia Cellular Satellite
ACTS	Advanced Communications Technology Satellite
ADC	analog-to-digital converter
ADEOS	Advanced Earth Observation Satellite
AFRL	Air Force Research Laboratory
AFT	allowable flight temperatures
ALTA	(Magellan) altimeter antenna
AMR	(Ocean Surface Topography Mission) advanced microwave radiometer
AMSU	advanced microwave sounder unit (flown in Earth orbit on NOAA K/L/M weather satellites)
APC	antenna pattern correction
ARPA	Advanced Research Projects Agency

ASI	Italian Space Agency
AU	astronomical unit
AUT	antenna under test
BITE	built in test equipment
CAD	computer-aided-design
CALIPSO	Cloud-Aerosol Lidar and Infrared Pathfinder Satellite Observation (satellite)
CCSDS	Consultative Committee for Space Data Systems
CFRP	carbon-fiber-reinforced plastic
CH_3CN	acetonitrile
CLAES	(UARS) cryogenic limb array etalon spectrometer
ClO	hypochlorite
CMC	ceramic matrix composite
CNES	Centre National d'Etudes Spatiales (French space agency)
CNFR	cylindrical near-field range
CO	carbon monoxide
CO_2	carbon dioxide
COI	Composite Optics, Inc.
comsat	communications satellite
CPR	(CloudSat) cloud profiling radar
CPW	co-planar waveguide
CRM	(Galileo) central release mechanism
cross-pol	cross-polarization
CTE	coefficient of thermal expansion
CVCM	collected volatile condensable materials
CVD	chemical vapor deposition
CVI	chemical vapor infiltration

CW	continuous wave
DARA	German Space Agency
DARPA	Defense Advanced Research Projects Agency
dB	decibel
dBc	decibels referenced to carrier
dBi	decibels referenced to an isotropic radiator
dBic	decibels referenced to a circularly polarized, theoretical isotropic radiator
DC	direct current
DEA	(Mars Pathfinder) descent antenna
DEM	digital elevation model
DoD	Department of Defense
DORIS	(Ocean Surface Topography Mission) Doppler orbitography and radiopositioning integrated by satellite
DSN	(Jet Propulsion Laboratory) Deep Space Network
DTE	direct-to-Earth (link)
EDL	entry, descent, and landing
EFMR	electrostatically figured membrane reflector
EIK	extended interaction klystron
EIRP	effective isotropic radiated power or equivalent isotropically radiated power
EM	engineering model
EMF	electromotive force
EOS	Earth Observing System
ESA	European Space Agency
ESD	electrostatic discharge
EUMETSAT	European organization for the Exploitation of Meteorological Satellites

F / D	focal length to diameter (ratio) (f/D is also acceptable)
FDTD	finite-difference time domain
FE	finite element
FLTSATCOM	(Navy) Fleet Satellite Communications
FM	flight model
FM	frequency modulation
FOV	field of view
FSS	frequency selective surface
GALCIT	Guggenheim Aeronautical Laboratory, California Institute of Technology (organization that became the Jet Propulsion Laboratory)
GB	gigabyte
GEO	geosynchronous Earth orbit
GHz	gigahertz
GO	geometrical optics
GPSP	(Ocean Surface Topography Mission) global positioning system payload
GSFC	Goddard Space Flight Center
G/T	gain over noise temperature
GTD	geometrical theory of diffraction
H_2O	water
HCl	hydrochloric acid
HCN	hydrogen cyanide
HF	high frequency
HFCD	hybrid-fed crossed dipole
HGA	high-gain antenna
HNO_3	nitric acid

HPA	high power amplifier
HPBW	half-power beamwidth
IAE	Inflatable Antenna Experiment
IGARS	International Geoscience and Remote Sensing Symposium
IMP	imager for Mars Pathfinder
InSAR	Interferometric SAR
ISAP	International Symposium on Antennas and Propagation
IN-STEP	In-Space Technology Experiments Program
ISAT	Innovative Space-based Radar Antenna Technology Program
ISLR	integrated side-lobe ratio
ITU	International Telecommunication Union
IUS	Inertial Upper Stage
JMR	Jason-l microwave radiometer
JPL	Jet Propulsion Laboratory
kG	kilogauss
kW	kilowatt
LEO	low-Earth orbit
LGA	low-gain antenna
LHCP	left-hand circular polarization
lidar	laser induced differential absorption radar
LMRE	(Mars Pathfinder) lander microwave receive antenna
LNA	low-noise amplifier
LO	local oscillator
LRA	(Department of Defense) Large Radar Antenna (Program)

LRA	(Ocean Surface Topography Mission) laser retroreflector array
LSST	Large Space System Technology
Mbps	megabits per second
MBSAT	(Space Systems/Loral) Mobile Broadcasting Satellite
MEMS	Micro-electro-mechanical systems
MEO	medium-Earth orbit
MER	Mars Exploration Rover(s) (Spirit and Opportunity)
MGA	medium-gain antenna
MGL	minimum gain along the range plane line
MGS	Mars Global Surveyor
MHz	megahertz
MIRO	microwave instrument for the Rosetta orbiter
MIT	Massachusetts Institute of Technology
MLI	multi-layer insulation
MLS	microwave limb sounder
MMIC	monolithic microwave integrated circuit
MO	Mars Observer
MPL	Mars Polar Lander
MRO	Mars Reconnaissance Obiter
MSAT	mobile satellite
MSU	microwave sounder unit (flown in Earth orbit on the TIROS-N meteorological satellite)
N_2O	nitrous oxide
NASA	National Aeronautics and Space Administration
NASDA	Japan's Space Agency
NASTRAN	NASA structural analysis computer program

NCO	numerically controlled oscillator
NGST	Next Generation Space Telescope
NIMA	National Imagery and Mapping Agency
NIST	National Institute of Standards and Technology
NOAA	National Oceanic and Atmospheric Administration
NSCAT	NASA Scatterometer (project)
NTT	Nippon Telegraph and Telephone Corporation
O_2	molecular oxygen
O_3	ozone
OCDS	Orbital Construction Demonstration Study
OH	hydroxyl radical
OMT	orthomode transducer
ONR	Office of Naval Research
OSTM	Ocean Surface Topography Mission
Pa	pascal
PASS	Personal Access Satellite System
PC	personal computer
PDT	Pacific Daylight Time
PIN	p-type, intrinsic, n-type diode
PLGA	(Mars Exploration Rover) petal low-gain antenna
PO	physical optics
PRF	pulse repetition frequency
psi	pounds per square inch
PTFE	polytetrafluoroethylene
PWB	plane-wave blockage
PWS	plasma wave search-coils

QOTL	quasi-optical transmission line
radar	radio detection and ranging
RAM	random-access memory
RAR	range ambiguity ratio
RCS	radar cross section
RF	radio frequency
RFS	(Voyager, Galileo) radio frequency subsystem
RHCP	right-hand circular polarization
RI	rigidizable/inflatable
rms	root mean square
rss	root sum square
RTG	radioisotope thermoelectric generator
RTV	reentry test vehicle
SAR	synthetic aperture radar
SAR/MTI	synthetic aperture radar/moving target indicator
SASS	Seasat-A scatterometer system
SCAMS	scanning microwave spectrometer (flown in Earth orbit aboard the NIMBUS-6 meteorological satellite
SESWG	(NASA) Solid Earth Sciences Working Group
SGA	standard gain antenna
SIR	Shuttle Imaging Radar
SMA	sub-miniature version A
SMLS	azimuth-scanning version of the microwave limb sounder
SMMR	(Seasat and Nimbus 7) scanning multichannel microwave radiometer
SMP	shaped-memory polymers
SNR	signal-to-noise ratio

SO_2	sulfur dioxide
SRTM	Shuttle Radar Topography Mission
SSPA	solid-state power amplifier
STR	spring-tape reinforced (boom)
STS	Space Transportation System
SWB	spherical-wave blockage
SXA	(Voyager, Galileo) S-/X-band antenna subsystem
TDRSS	Tracking and Data Relay Satellite System
THz	terahertz
TIROS	Television Infrared Observation Satellite
TML	total mass loss
TMM	thermoset microwave material
TMR	(TOPEX/Poseidon) microwave radiometer
TNC	threaded Neill-Concelman (connector)
TOPEX)/ Poseidon	Ocean Topography Explorer mission (a joint U.S. and French effort to map ocean surface topography)
T/R	transmit/receive
TRL	technical readiness level
TWTA	traveling wave tube assembly **[in 3]** amplifier **[in 4]**
UARS	Upper Atmospheric Research Satellite
UHF	ultrahigh frequency
USM	unified scattering matrix
UV	ultraviolet
VEEGA	Venus, Earth, Earth gravity assist
VOIR	Venus Orbiting Imaging Radar
VRM	Venus Radar Mapper

VSWR	vertical standing wave ratio
W	watt
WEB	warm electronics box
WSOA	(Ocean Surface Topography Mission) wide swath ocean altimeter
WVR	water vapor recovered
XSDC	(Galileo) X/S downconverter subsystem